

ADDRESS OF PUBLISHER  
& EDITOR'S OFFICE:

GDAŃSK UNIVERSITY  
OF TECHNOLOGY

Faculty of Ocean Engineering  
& Ship Technology  
G. Narutowicza 11/12  
80-233 Gdańsk, POLAND

EDITORIAL STAFF:

Wiesław Tarełko  
| Editor in Chief  
Janusz Kozak  
| Deputy Editors-in-Chief  
Wojciech Litwin  
| Deputy Editors-in-Chief

Price:  
single issue: 25 PLN

Prices for abroad  
single issue:  
- in Europe EURO 15  
- overseas USD 20

WEB:  
[pg.edu.pl/pmr](http://pg.edu.pl/pmr)

e-mail : [pmr@pg.edu.pl](mailto:pmr@pg.edu.pl)

ISSN 1233-2585

## CONTENS

6	<b>Erdem Üçer</b> <i>LYAPUNOV FUNCTION BASED CRITERIA FOR SHIP ROLLING IN RANDOM BEAM SEAS</i>
15	<b>Zhuo Wang, Bo Zhang, Tao Wang</b> <i>ANALYSIS AND EXPERIMENTS OF EMBEDDED GRIPPING MECHANISM USED IN LARGE-SCALE TOOLS HOLDING UP PILE FOUNDATION IN OCEAN</i>
22	<b>Stanisław Gucma</b> <i>CONDITIONS OF SAFE SHIP OPERATION IN SEAPORTS – OPTIMIZATION OF PORT WATERWAY PARAMETERS</i>
30	<b>Czesław Dymarski</b> <i>A CONCEPT DESIGN OF DIESEL – HYDRAULIC PROPULSION SYSTEM FOR PASSENGER SHIP INTENDED FOR INLAND SHALLOW WATER NAVIGATION</i>
39	<b>Piotr Bzura</b> <i>DIAGNOSTIC MODEL OF CRANKSHAFT SEALS</i>
47	<b>Agnieszka Maczyszyn</b> <i>ENERGY LOSS COEFFICIENTS <math>K_1</math> IN A DISPLACEMENT PUMP AND HYDRAULIC MOTOR USED IN HYDROSTATIC DRIVES</i>
56	<b>Nguyen Thi Ngoc Hoa, Vu Ngoc Bich, Tran Ngoc Tu, Nguyen Manh Chien, Le Tat Hien</b> <i>NUMERICAL INVESTIGATING THE EFFECT OF WATER DEPTH ON SHIP RESISTANCE USING RANS CFD METHOD</i>
65	<b>Ang Li, Yunbo Li</b> <i>NUMERICAL AND EXPERIMENTAL STUDY ON SEAKEEPING PERFORMANCE OF A HIGH-SPEED TRIMARAN WITH T-FOIL IN HEAD WAVES</i>
78	<b>Fengli Wang</b> <i>PULSATION SIGNALS ANALYSIS OF TURBOCHARGER TURBINE BLADES BASED ON OPTIMAL EEMD AND TEO</i>
87	<b>Luyun Chen, Hong Yi</b> <i>DYNAMIC CHARACTERISTIC STUDY OF RISER WITH COMPLEX PRE-STRESS DISTRIBUTION</i>
98	<b>Olgun Konur, Murat Bayraktar, Murat Pamik, Barış Kuleyin, Mustafa Nuran</b> <i>THE ENERGY EFFICIENCY GAP IN TURKISH MARITIME TRANSPORTATION</i>
107	<b>Esmail Homayoun, Hassan Ghassemi, Hamidreza Ghafari</b> <i>POWER PERFORMANCE OF THE COMBINED MONOPILE WIND TURBINE AND FLOATING BUOY WITH HEAVE-TYPE WAVE ENERGY CONVERTER</i>

**ADDRESS OF PUBLISHER  
& EDITOR'S OFFICE:**

**GDAŃSK UNIVERSITY  
OF TECHNOLOGY**

**Faculty of Ocean Engineering  
& Ship Technology  
G. Narutowicza 11/12  
80-233 Gdańsk, POLAND**

- 115 **Bin Mei, Licheng Sun, Guoyou Shi, Xiaodong Liu**  
*SHIP MANEUVERING PREDICTION USING GREY BOX FRAMEWORK VIA  
ADAPTIVE RM-SVM WITH MINOR RUDDER*
- 128 **Eligiusz Mieloszyk, Marcin Abramski, Anita Milewska**  
*CFGFRPT PILES WITH A CIRCULAR CROSS-SECTION AND THEIR APPLICATION  
IN OFFSHORE STRUCTURES*
- 138 **Ireneusz Pielecha, Jerzy Merkisz**  
*OPTIMIZING THE SHAPE OF A COMPRESSION-IGNITION ENGINE  
COMBUSTION CHAMBER BY USING SIMULATION TESTS*
- 147 **Jan P. Michalski**  
*PARAMETRIC METHOD APPLICABLE IN CALCULATING BREAKOUT FORCE  
AND TIME FOR LIFTING AXISYMMETRIC OBJECTS FROM SEABED*
- 153 **Dimov Stojce Ilcev**  
*INTRODUCTION TO COASTAL HF MARITIME SURVEILLANCE RADARS*
- 163 **Hossein Nejatbakhsh Esfahani, Rafal Szlapczynski**  
*MODEL PREDICTIVE SUPER-TWISTING SLIDING MODE CONTROL FOR AN  
AUTONOMOUS SURFACE VEHICLE*
- 172 **Aleksandr Ursolov, Yuriy Batrak, Wieslaw Tarelko**  
*APPLICATION OF THE OPTIMIZATION METHODS TO THE SEARCH OF  
MARINE PROPULSION SHAFTING GLOBAL EQUILIBRIUM IN RUNNING  
CONDITION*
- 181 **Oleksandr Cherednichenko, Serhiy Serbin, Marek Dzida**  
*APPLICATION OF THERMO-CHEMICAL TECHNOLOGIES FOR CONVERSION  
OF ASSOCIATED GAS IN DIESEL-GAS TURBINE INSTALLATIONS FOR OIL  
AND GAS FLOATING UNITS*
- 188 **Ivana Ćipranić, Marija Jevric, Goran Sekulic, Sreten Tomovic**  
*THE PROBLEM OF BALLAST WATER  
IN MONTENEGRO PORTS AND POSSIBILITY OF ITS TREATMENT*

---

## Editorial

POLISH MARITIME RESEARCH is the scientific journal with a worldwide circulation. This journal is published quarterly (four times a year) by Gdansk University of Technology (GUT). On September, 1994, the first issue of POLISH MARITIME RESEARCH was published. The main objective of this journal is to present original research, innovative scientific ideas, and significant findings and application in the field of :

### Naval Architecture, Ocean Engineering and Underwater Technology,

The scope of the journal covers selected issues related to all phases of product lifecycle and corresponding technologies for offshore floating and fixed structures and their components.

All researchers are invited to submit their original papers for peer review and publications related to methods of the design; production and manufacturing; maintenance and operational processes of such technical items as:

- all types of vessels and their equipment,
- fixed and floating offshore units and their components,
- autonomous underwater vehicle (AUV) and remotely operated vehicle (ROV).

We welcome submissions from these fields in the following technical topics:

- ship hydrodynamics: buoyancy and stability; ship resistance and propulsion, etc.,
- structural integrity of ship and offshore unit structures: materials; welding; fatigue and fracture, etc.,
- marine equipment: ship and offshore unit power plants: overboarding equipment; etc.

---

### Scientific Board

**Chairman : Prof. JERZY GIRTLEK - Gdańsk University of Technology, Poland**

**Vice-chairman : Prof. CARLOS GUEDES SOARES, Universidade de Lisboa, Lisbon, Portugal**

**Vice-chairman : Prof. MIROSŁAW L. WYSZYŃSKI - University of Birmingham, United Kingdom**

**Prof. POUL ANDERSEN**  
Technical University of Denmark  
Kongens Lyngby  
Denmark

**Prof. STOJCE DIMOV ILCEV**  
Durban University of Technology  
Durban  
South Africa

**Prof. JERZY EDWARD MATUSIAK**  
Aalto University  
Espoo  
Finland

**Prof. JIAHN-HORNG CHEN**  
National Taiwan Ocean University  
Keelung  
Taiwan

**Prof. YORDAN GARBATOV**  
Universidade de Lisboa,  
Lisbon  
Portugal

**Prof. JERZY MERKISZ**  
Poznan University of Technology  
Poznan  
Poland

**Prof. VINCENZO CRUPI**  
University of Messina  
Messina  
Italy

**Prof. STANISŁAW GUCMA**  
Maritime University of Szczecin  
Szczecin  
Poland

**Prof. VALERI NIEKRASOV**  
Admiral Makarov National University  
of Shipbuilding  
Mikolaiv  
Ukraine

**Prof. MAREK DZIDA**  
Gdansk University of Technology  
Gdansk  
Poland

**Prof. ANTONI ISKRA**  
Poznan University of Technology  
Poznan  
Poland

**Prof. JOZEF SZALA**  
UTP University of Science and  
Technology  
Bydgoszcz  
Poland

**Prof. ODD MAGNUS FALTINSEN**  
Norwegian University of Science and  
Technology  
Trondheim  
Norway

**Prof. JAN KICINSKI**  
Institute of Fluid-Flow Machinery -  
Polish Academy of Sciences  
Gdansk  
Poland

**Prof. TADEUSZ SZELANGIEWICZ**  
Maritime University of Szczecin  
Szczecin  
Poland

**Prof. MASSIMO FIGARI**  
University of Genova  
Genova  
Italy

**Prof. ZBIGNIEW KORCZEWSKI**  
Gdansk University of Technology  
Gdansk  
Poland

**Prof. DRACOS VASSALOS**  
University of Strathclyde  
Glasgow  
United Kingdom

**Prof. HASSAN GHASSEMI**  
Amirkabir University of Technology  
Tehran  
Iran

**Prof. JOZEF LISOWSKI**  
Gdynia Maritime University  
Gdynia  
Poland



## GDAŃSK UNIVERSITY OF TECHNOLOGY FACULTY OF OCEAN ENGINEERING AND SHIP TECHNOLOGY

- 1200 students
- 100 academic Staff
- 35 technical staff
- 3 BSc Courses (7 semesters)
  - Ocean Engineering
  - Power Engineering (in cooperation with Mechanical Eng. and Electrical Eng. faculties), both in Polish and English
  - Marine Transport
- 4 MSc courses (3 or 4 semesters)
  - Ocean Engineering, both in Polish and English
  - Power Engineering (in cooperation with Mechanical Eng. and Electrical Eng. faculties)
  - Marine Transport
  - Coastal and Offshore Engineering (in cooperation with Faculty of Civil and Environmental Eng.), both in Polish and English
- New and modern facilities, including new towing tank, ship technology, equipment, systems and power plants laboratories, propulsion system simulator and access to up-to-date CAE and CFD software
- Close cooperation with ship design offices, shipyards, ports, terminals, manufacturers and industrial partners like as GE or REMONTOWA Holding, as well classifications societies including PRS, DNV.GL, ABS and RINA
- Vast possibilities for students activities, including Students Research Centre in Iława on a large lake, Student Scientific Clubs KORAB, PIKSEL and SYNERTECH, participation in international solar regatta and waterbike regatta
- Well-indexed open-access Polish Maritime Research!

### FACULTY OF OCEAN ENGINEERING AND SHIP TECHNOLOGY

Gdańsk University of Technology  
address: G. Narutowicza 11/12, 80-233 Gdańsk, Poland  
phone: +48 58 3471567  
fax: +48 58 3486372  
e-mail: [dziekoce@pg.edu.pl](mailto:dziekoce@pg.edu.pl)  
[www.pg.edu.pl/international/study-in-english](http://www.pg.edu.pl/international/study-in-english)

[www.oio.pg.edu.pl](http://www.oio.pg.edu.pl)





## **MSc IN OCEAN ENGINEERING**

Specialization: Ship Technology and Offshore Engineering  
 Specialization: Marine Engineering and Offshore Energy

➤ Degree to be obtained	▪ Master of Science
➤ Duration	▪ 2 years (4 semesters)
➤ Language	▪ English
➤ ECTS points	▪ 120 ECTS
➤ Programme description	▪ The aim is providing advanced engineering knowledge in the field of Ocean Engineering including two main specializations: Ship Technology and Offshore Engineering, Marine Engineering and Offshore Energy. Students will gain detailed knowledge within the subjects such as Marine Applied Informatics, CAE and Design Tools, Ship and Offshore Power Systems Design, Dynamics of Ship and Offshore Structures, Advanced Mechanics of Marine Structures, Ship and Offshore Structures Design, Marine and Offshore Systems and Equipments, Modelling and Simulation in Ocean Engineering, Reliability, Safety and Risk Analysis, Advanced Material Engineering and Manufacturing Technology, Marine and Intermodal Transport, Finance and Economy in Engineering Design, Maritime Environmental Protection and Optimisation in Engineering Design. Students deal with a real design process and prepare the final thesis in cooperation with the industrial partners of the Faculty.
➤ Entry requirements	▪ B.Sc. in Naval Architecture, Marine Engineering, Mechanical Engineering, Civil Engineering, Energy/Power Engineering, Electrical Engineering, Transport (or similar fields of study)
➤ Comments	<ul style="list-style-type: none"> <li>▪ The programme is supported and organised in cooperation with Det Norske Veritas – Germanischer Lloyd (DNV GL)</li> <li>▪ Details of the programme and admission process are available online: <a href="http://oio.pg.edu.pl/en">oio.pg.edu.pl/en</a></li> </ul>



## LYAPUNOV FUNCTION BASED CRITERIA FOR SHIP ROLLING IN RANDOM BEAM SEAS

Erdem Üçer

Istanbul Technical University, Faculty of Naval Architecture and Ocean Engineering, Turkey

### ABSTRACT

*The aim of this study is to present a Lyapunov function which can be used to derive an intact stability criterion for a ship in random beam seas. First, the mathematical model of the rolling motion of ships in random beam seas is introduced. The random wave excitation is described by a spectrum which is depended on the wave energy spectrum and the amplitude of the moment of roll. This spectrum is generated by a second order linear filter. Second, the methodology of creating a Lyapunov function is explained briefly. Then, there is outlined the way by which Lyapunov function can be used as the intact stability criterion for a ship. The proposed criterion is derived by considering the weather criteria for German naval vessels. Finally, the coherence of the boundary of safe basin obtained by Lyapunov function with the numerical results obtained by Euler-Maruyama Method is presented. From the results it can be deduced that the Lyapunov function can be used to define an intact stability criterion.*

**Keywords:** random beam sea, wave energy spectrum, Lyapunov function, intact stability criterion

### INTRODUCTION

Modelling the dynamic behaviour of ships and offshore structures in their real working environment such as random seas and winds have always been a popular study subject since 1960s [3].

The earliest milestones on the investigation of ship rolling in random seas are the studies of Haddara [11], Odabasi [21] and Roberts [24].

Lyapunov Direct Method or Lyapunov functions [18, 25] are used since 1970s to determine the conditions of stability against capsizing of ships. The studies of Odabasi [21], Ozkan [22] and Caldeira-Sariava [4] are the earliest examples of the usage of Lyapunov functions to investigate the rolling motions of ships. The more recent studies are the studies of Yilmaz [29] and Ucer [28].

The form parameters of fishing ships are analyzed by Yilmaz [29] to establish a practical stability criterion in preliminary design stage.

In the study of Ucer [28], the transverse stability of BSRA trawlers are analyzed by using both numerical and analytical safe basin concepts and it is also demonstrated how the concept of safe basin can be utilized for the assessment of the stability of trawlers in regular beam seas.

The dynamic behaviour of elastic ocean structures of single degree of freedom is treated by an analytical approach based on the stochastic averaging of the energy envelope according to Moshchuk et al. [20]. The system is considered to be subject to a narrow-band random process modelled as the output of shaping filter. Three different shaping filters (first, second and fourth order) possessing Pierson-Moskowitz spectrum are employed to model Gaussian random sea waves.

The large-amplitude rolling and capsize dynamics of ships in random beam seas are investigated by using a nonlinear single-degree-of-freedom model by Jiang et al. [13]. In their work a criterion of capsizing is derived by using Melnikov function and phase-space transport techniques.

The general non-linear model of parametric excited roll motions in head or following random seas is derived in the study of Dostal and Kreuzer [9]. The irregular waves are modelled in terms of a continuous time autoregressive moving average process. The resulting model of stochastic differential equations is investigated numerically by local statistical linearization.

An analytical criterion is provided by Dostal et al. [10] for ship and sea state parameters, which indicates the large roll amplitudes or capsizing and determines the mean time to these events.

The subject of this study, the rolling motion of a ship in random beam seas is recently investigated by Chai et al. [5–8].

The stochastic roll response and reliability of a ship in random beam seas is studied by using a four-dimensional (4D) path integration (PI) approach in the studies of Chai et al. [5–8] where a 4D Markov dynamic system is established by combining the single-degree-of freedom model used to represent the ship rolling behaviour in random beam seas with a second-order linear filter used to approximate the stationary roll excitation moment.

In this study, firstly the roll motion in beam seas is represented by the mathematical model derived by Chai et al. [5–8]. Secondly, the methodology of constructing a Lyapunov function of randomly exerted system is outlined. Then, it is presented how that Lyapunov function can be used as a tool for intact stability criterion similar to the weather criteria for German naval vessels [2]. Finally, the coherence of the boundary of safe basin of the ship, obtained by Lyapunov function, with the numerically determined safe basin is presented for two ships and three sea states.

## MATHEMATICAL MODEL

While establishing the mathematical model, the couplings between the roll motion and other modes of ship motion are ignored to make the equation of roll motion simpler [5–9]. This assumption is based on the idea that roll motion has a greater influence on the ship stability in beam seas rather than the other modes of ship motion. Another reason for this simplification are the difficulties encountered when the complete hydrodynamic forces are accurately determined [15]. Although the coupling between the roll and sway motions is strong, it is possible to reduce one DOF by defining a virtual roll centre as indicated in the studies of Jiang [14], Hutchison [12] and Balcer [1].

The single degree of freedom (SDOF) roll motion equation in random beam seas can be represented by the equation (1) [5–8].

$$I(\tilde{\omega}) \ddot{\phi}(t) + B_{44}(\tilde{\omega}) \dot{\phi}(t) + B_{44q}(\tilde{\omega}) \phi(t) + \Delta GZ(\phi) = M(t) \quad (1)$$

where  $\phi$  is the rolling angle with respect to calm sea surface (rad), roll angular velocity (rad/s),  $I$  denotes the virtual mass moment of inertia including the added mass moment in roll,  $B_{44}(\tilde{\omega})$  and  $B_{44q}(\tilde{\omega})$  are the linear and quadratic damping

coefficients, respectively,  $\Delta$  is the displacement of the ship,  $\omega$  is the wave circular frequency,  $GZ$  is the righting arm as a function of the roll angle which can be defined by a single cubic polynomial and  $M(t)$  is the external random wave excitation moment described by the spectrum  $S_{mm}(\omega)$ . The excitation moment spectrum is related to the wave energy spectrum by the relationship shown in Eq. (2).

$$S_{mm}(\omega) = |F_{roll}(\omega)| S_{\xi\xi}(\omega) \quad (2)$$

where  $|F_{roll}(\omega)|$  represents amplitude of the moment of the roll motion per unit wave height at frequency  $\omega$  and  $S_{\xi\xi}(\omega)$  is the wave energy spectrum [5–9].

The equation (3) is the spectrum of the relative wave excitation moment  $S_{mm}(\omega)$  generated by a second-order linear filter shown in equation (4) and (5) [5–9].

$$S_{mm}(\omega) = \frac{1}{2\pi} \frac{\gamma^2}{(\alpha - \omega^2)^2 + (\beta\omega)^2} \quad (3)$$

$$dx_3 = (x_4 - \beta x_3) dt + \gamma dW \quad (4)$$

$$dx_4 = -\alpha x_4 dt \quad (5)$$

where  $x_3$  and  $x_4$  are the state variables in filter equation with  $x_3$  representing the output term  $m(t)$ ,  $dW(t) = W(t+dt) - W(t)$  represents an infinitesimal increment of a standard Wiener process,  $\alpha$ ,  $\beta$  and  $\gamma$  are the parameters of the linear filter [5–9].

With the aid of linear filtering technique, the roll motion equation (1) is described by the following four dimensional state space equations (6–9) [5–8].

$$dx_1 = x_2 dt \quad (6)$$

$$dx_2 = (-b_{44}x_2 - b_{44q}x_2 | x_2 | - c_1x_1 + c_3x_1^3 + x_3) dt \quad (7)$$

$$dx_3 = (x_4 - \beta x_3) dt + \gamma dW \quad (8)$$

$$dx_4 = -\alpha x_4 dt \quad (9)$$

Where  $x_1$  is the roll angle  $\phi(t)$ ,  $x_2$  is the roll angular velocity  $x_2 = \dot{\phi}(t)$ ,  $x_3$  is the ratio of the external random wave excitation moment and the virtual mass moment of inertia  $x_3 = M(t)/I$ , the damping moment coefficients  $b_{44}$  and  $b_{44q}$  are equal to  $B_{44}/I$  and  $B_{44q}/I$ , respectively, the righting arm coefficients  $c_1$  and  $c_3$  are equal to  $\Delta GM/I$ , and  $-\Delta GM/(I\phi_v^2) = c_1/\phi_v^2$ , respectively.

## LYAPUNOV FUNCTION OF RANDOM PROCESS

Let the  $dx = f(x,t)dt + \sigma(x,t)dz$  be the stochastic differential (Ito) equation.

In order to derive a Lyapunov function,  $V(x)$ , the following assumptions are made [16]:

- $V(x)$  should be a non-negative and continuous function, satisfying  $V(0) = 0$ ,  $V(x) > 0$  at  $x \neq 0$
- $V(x)$  should have continuous first partial derivatives in  $Q_m \equiv \{x: V(x) < m\}$   $m < \infty$ .

When the derivative of Lyapunov function  $L V(x)$  is smaller and equal to a continuous positive function  $k(x)$ , the system is stable.

The differential generator of the random process is given by the following equation [16, 25]:

$$L = \sum_i f_i(x, t) \frac{\partial}{\partial x_i} + \frac{1}{2} \sum_{i,j} S_{i,j}(x, t) \frac{\partial^2}{\partial x_i \partial x_j} \quad (10)$$

where  $S(x) = \{S_{ij}(x)\} = \sigma'(x) \sigma(x)$

## CONSTRUCTION OF LYAPUNOV FUNCTION OF RANDOM ROLL MOTION OF A SHIP

In this section the determination of analytical safe basin for forced non-linear rolling motion by using Lyapunov function is presented. Firstly, a positive analytical function is determined [4, 21–22, 25, 28–29]. Secondly, the derivative of this analytical function is obtained. When the derivative of this analytical function is negative, the ship is assumed to be stable [28].

The positive analytical function, Lyapunov function of the equation system (6–9), is assumed as the expression given in equation (11).

$$V = (1 + k_3 x_3^2 + k_4 x_4^2) \frac{x_2^2}{2} + k_1 \frac{x_1^2}{2} \quad (11)$$

The above given function is non-negative continuous and satisfying  $V(0) = 0$  and  $V(x) > 0$  at  $x \neq 0$  and also has continuous first partial derivatives.

By using the differential generator (10), the derivative of the Lyapunov function is found as:

$$\begin{aligned} LV = & (1 + k_3 x_3^2 + k_4 x_4^2) (-b_{44} x_2^2 - b_{44q} |x_2| x_2^2 - c_1 x_1 x_2 \\ & + c_3 x_1^3 x_2 + x_3 x_2) + k_1 x_1 x_2 + k_3 x_3 x_4 x_2^2 - k_3 \beta x_2^2 x_3^2 \\ & + \frac{\gamma^2}{2} k_3 x_2^2 - \alpha x_3 x_4 k_4 x_2^2 \end{aligned} \quad (12)$$

When the coefficient  $k_3$  is assumed equal to  $\alpha k_4$ , the equation (12) is simplified and the following expression is obtained:

$$\begin{aligned} LV = & (1 + k_3 x_3^2 + k_4 x_4^2) (-b_{44} x_2^2 - b_{44q} |x_2| x_2^2 - c_1 x_1 x_2 \\ & + c_3 x_1^3 x_2 + x_3 x_2) + k_1 x_1 x_2 - k_3 x_2^2 (\beta x_3^2 - \frac{\gamma^2}{2}) \end{aligned} \quad (13)$$

Let  $1 + k_3 x_3^2 + k_4 x_4^2$  be smaller than any positive real number  $K$  smaller than infinity. On this assumption and regrouping the parentheses the equation (13) turns into the

equation (14). When the expression given by the equation (14) is smaller and equal to zero, the system is stable.

$$\begin{aligned} LV = & K (-x_2^2 (b_{44} + b_{44q} |x_2|) - x_2 (c_1 x_1 - c_3 x_1^3 - x_3)) \\ & + k_1 x_1 x_2 - k_3 x_2^2 (\beta x_3^2 - \frac{\gamma^2}{2}) \leq 0 \end{aligned} \quad (14)$$

When the both sides of the above given equation is divided by  $K$  positive constant and after regrouping the parentheses, the following expression is obtained:

$$\begin{aligned} -x_2^2 (b_{44} + b_{44q} |x_2|) - x_2 ((c_1 - k_1^*) x_1 - c_3 x_1^3 - x_3) \\ - k_3^* x_2^2 (\beta x_3^2 - \frac{\gamma^2}{2}) \leq 0 \end{aligned} \quad (15)$$

where  $k_1^* = k_1/K$  and  $k_3^* = k_3/K$

Let's assume  $x_{3m}$  is the greatest value of  $x_3$  and put into the equation (15) in the place of  $x_3$ . Then, the equation (15) turns into the equation (16).

$$\begin{aligned} -x_2^2 (b_{44} + b_{44q} |x_2|) - x_2 ((c_1 - k_1^*) x_1 - c_3 x_1^3 - x_{3m}) \\ - k_3^* x_2^2 (\beta x_{3m}^2 - \frac{\gamma^2}{2}) = 0 \end{aligned} \quad (16)$$

After regrouping parentheses and dividing both sides of the equation (16) by  $x_2$ , the equation (17) is obtained.

$$\begin{aligned} x_2 (b_{44} + b_{44q} |x_2| + k_3^* (\beta x_{3m}^2 - \frac{\gamma^2}{2})) \\ = [x_{3m} - ((c_1 - k_1^*) x_1 - c_3 x_1^3)] \end{aligned} \quad (17)$$

When the above given condition is satisfied, the ship can be assumed stable. Hence, the two unknown parameters of the equation (17),  $k_1^*$  and  $k_3^*$ , should be determined. The determination of the parameters is explained in the next section.

## LYAPUNOV FUNCTION BASED CRITERIA

The graphical representation of the right hand side of the equation (17) is shown in Fig. 1.

In the figure,  $x_{1st}(\phi_{st})$  is the static heel angle which is represented by the intersection point of the line of maximum value of the external excitation  $x_{3m}$  and the modified restoring arm curve ( $gz^* = (c_1 - k_1^*) x_1 - c_3 x_1^3$ ). According to the weather criteria for German naval vessels,  $x_{1ref}(\phi_{ref})$ , the reference angle and  $h_{res}$ , the residual arm between the restoring and the excitation moment are determined by means of the equation (18) or (19) [2].

$$\phi_{ref} = 35^\circ \text{ and } h_{res} = 0.1 \text{ m for } \phi_{st} \leq 15^\circ \quad (18)$$

$$\phi_{ref} = 2 \times \phi_{st} + 5^\circ \text{ and } h_{res} = 0.01 \times \phi_{st} - 0.05, \phi_{st} > 15^\circ \quad (19)$$

where both  $\phi_{st}$  and  $\phi_{ref}$  are expressed in degrees.

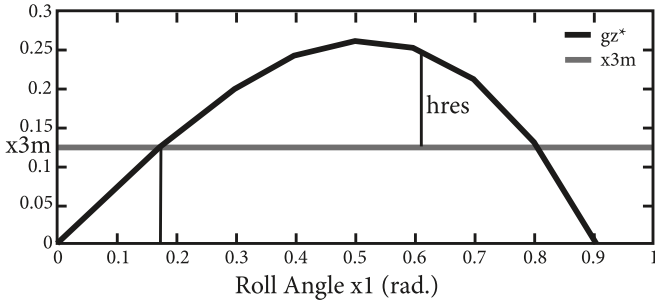


Fig. 1. Modified restoring arm curve with external excitation

The unknown parameters  $k_1^*$  and  $k_3^*$  are determined by the numerical solution of the system of the equations (20)–(25) which are derived by making the following assumptions:

- $x_{1st}$  is the intersection point of the modified  $gz$  curve and the maximum external excitation lever  $x_{3m}$  determined by the equation (20).
- The roll angular velocity  $x_2$  gets its highest value ( $x_{2m}$ ) when the roll angle is zero. Then, the equation (21) is obtained by putting  $x_{2m}$  and 0 instead of  $x_2$  and  $x_1$ , respectively, in the equation (17).
- It is assumed that the ship must have the half of the maximum roll angular velocity ( $x_{2m}$ ) at the reference angle of heel ( $x_{1ref}$ ). Then, the equation (22) is obtained by putting ( $x_{2m}/2$ ) and  $x_{1ref}$  instead of  $x_2$  and  $x_1$ , respectively, in the equation (17).
- In the equation (23), it is stated that the ship must have the residual arm  $h_{res}$  at the roll angle  $x_a$ . The value of  $h_{res}$  is determined by the following condition:  
 $x_{1st} \leq 15^\circ$  then  $h_{res} = 0.01$   
 $x_{1st} > 15^\circ$  then  $h_{res} = 0.01 x_{1st} - 0.05$ .
- The equation (24) shows that the coefficient  $k_1^*$  depends on  $x_{2m}$  and  $x_b$  and is obtained by dividing the equation (11) by  $K$  constant and assuming that the energy on the boundary is equal to  $(x_{2m}^2/2)$  and the width of safe basin is  $x_b$ .
- The width of the safe basin ( $x_b$ ) is assumed to be equal to the expression represented by the equation (25). When  $x_a$  and  $x_{1st}$  get higher values, the width of safe basin decreases.

$$(c_1 - k_1^*) x_{1st} - c_3 x_{1st}^3 - x_{3m} = 0 \quad (20)$$

$$-x_{2m} (b_{44} + b_{44q} |x_{2m}|) - x_{3m} - k_3^* x_{2m} (\beta x_{3m}^2 - \frac{\gamma^2}{2}) = 0 \quad (21)$$

$$\frac{x_{2m}}{2} (b_{44} + b_{44q} |x_{2m}|) + k_3^* (\beta x_{3m}^2 - \frac{\gamma^2}{2}) \quad (22)$$

$$- [x_{3m} - ((c_1 - k_1^*) x_{1ref} - c_3 x_{1ref}^3)] = 0$$

$$(c_1 - k_1^*) x_a - c_3 x_a^3 - x_{3m} - h_{res} = 0 \quad (23)$$

$$k_1^* = (x_{2m}/x_b)^2 \quad (24)$$

$$x_b = 0.8 x_v - x_{1st} - x_a \quad (25)$$

here  $x_v$  is the vanishing stability angle, the coefficients  $k_1^*$  and  $k_3^*$  should be positive.

The input values to the above equation system are the restoring and damping coefficients, second order linear filter parameters and the maximum external excitation value  $x_{3m}$ . The output of the equation system is  $x_{1st}$ ,  $x_{2m}$ ,  $x_a$  and  $k_3^*$ . It is also possible to easily obtain  $x_b$  by putting the values of  $x_{1st}$  and  $x_a$  into the equation (25).

Whether the ship has a safe region or not can easily be understood by looking at the values  $x_{2m}$  and  $x_b$ .

## DATA FOR ROLLING MOTION EQUATION

In this study, the data of a fishery research vessel [6] is used to test the criteria based on Lyapunov function. The main parameters of the ship model are given in Tab. 1.

Tab. 1. List of ship parameters

$I$	$5540 \times 10^7 \text{ kg m}^2$
$\Delta$	$2017 \times 10^7 \text{ N}$
$b_{44}$	$0.095 \text{ s}^{-1}$
$b_{44q}$	0.0519
$c_1$	$1.153 \text{ s}^{-2}$
$c_3$	$0.915 \text{ s}^{-2}$
$\omega_0$	1.074 rad/s
$x_v$	1.1 rad

The parameters  $\alpha$ ,  $\beta$  and  $\gamma$  in the second order linear filter equation (4) and (5) are presented in Tab. 2 [6].

Tab. 2. List of second order linear filter parameters

Sea States	$H_s$ (m)	$T_p$ (s)	$\alpha$	$\beta$	$\gamma$
Sea State 1	4.0	11.0	0.495	0.366	0.0432
Sea State 2	5.0	12.0	0.441	0.364	0.0498
Sea State 3	6.0	13.0	0.390	0.365	0.0555

## RESULTS

In this section, for three sea states [6], the safe basins of roll motion of the fishery vessel are obtained from both the numerical solutions of the equation system (6)–(9) and the equation system (20)–(25) created by means of Lyapunov Direct Method. Then, the safe basins of roll motion of the fishery vessel, obtained in different ways, are compared.

Firstly, the equation system (20)–(25) are numerically solved with different initial conditions of  $x_{2m}$ ,  $x_a$  and  $x_{3m}$ .

The output of the equation system (20)–(25) for the fishery vessel is presented for different initial conditions in Tab. 3–6 for Sea state 1 and Tab. 7–8 for Sea state 3. In each table, the highest values of  $x_{2m}$  and  $x_b$  which gives the largest safe basin are marked bold.

Tab. 3. The outputs for Sea state 1 with the initial values of  $x_{1st} = 0.1$ ,  $k_3=0.2$ ,  $x_a = 0.5$  and  $x_{3m} = \gamma / (2\alpha\sqrt{2\beta})$

Initial $x_{2m}$	$x_{1st}$ (rad)	$x_{2m}$ (rad/s)	$x_a$ (rad)	$x_b$ (rad)
0.1	0.126	0.301	0.397	0.357
0.2	0.119	0.308	0.397	0.364
0.3	0.114	0.312	0.397	0.369
0.4	0.104	0.322	0.396	0.380
0.5	0.119	0.311	0.395	0.366
<b>0.6</b>	<b>0.108</b>	<b>0.326</b>	<b>0.388</b>	<b>0.384</b>
0.7	0.106	0.323	0.394	0.380
0.8	0.122	0.311	0.392	0.366
0.9	0.121	0.312	0.393	0.366
1.0	0.114	0.318	0.394	0.373

Tab. 6. The outputs for Sea state 1 with the initial values of  $x_{1st} = 0.1$ ,  $k_3=0.2$ ,  $x_a = 0.75$  and  $x_{3m} = \gamma / (\alpha\sqrt{2\beta})$

Initial $x_{2m}$	$x_{1st}$ (rad)	$x_{2m}$ (rad/s)	$x_a$ (rad)	$x_b$ (rad)
0.1	0.182	0.210	0.433	0.265
0.2	0.191	0.207	0.431	0.259
0.3	0.191	0.204	0.432	0.257
0.4	0.168	0.219	0.436	0.276
0.5	0.176	0.210	0.439	0.265
0.6	0.173	0.211	0.440	0.266
0.7	0.178	0.212	0.435	0.267
0.8	0.199	0.198	0.433	0.248
<b>0.9</b>	<b>0.161</b>	<b>0.229</b>	<b>0.431</b>	<b>0.288</b>
1.0	0.193	0.204	0.431	0.256

Tab. 4. The outputs for Sea state 1 with the initial values of  $x_{1st} = 0.1$ ,  $k_3 = 0.2$ ,  $x_a = 0.75$  and  $x_{3m} = \gamma / (2\alpha\sqrt{2\beta})$

Initial $x_{2m}$	$x_{1st}$ (rad)	$x_{2m}$ (rad/s)	$x_a$ (rad)	$x_b$ (rad)
0.1	0.131	0.304	0.393	0.356
<b>0.2</b>	<b>0.105</b>	<b>0.323</b>	<b>0.394</b>	<b>0.381</b>
0.3	0.108	0.320	0.395	0.377
0.4	0.114	0.312	0.397	0.369
0.5	0.121	0.309	0.395	0.364
0.6	0.119	0.310	0.395	0.366
0.7	0.122	0.308	0.394	0.363
0.8	0.123	0.308	0.394	0.363
0.9	0.123	0.309	0.394	0.364
1.0	0.125	0.303	0.399	0.356

Tab. 7. The outputs for Sea state 3 with the initial values of  $x_{1st} = 0.1$ ,  $k_3 = 0.2$ ,  $x_a = 0.5$  and  $x_{3m} = \gamma / (2\alpha\sqrt{2\beta})$

Initial $x_{2m}$	$x_{1st}$ (rad)	$x_{2m}$ (rad/s)	$x_a$ (rad)	$x_b$ (rad)
0.1	0.165	0.234	0.425	0.289
0.2	0.169	0.233	0.423	0.288
0.3	0.162	0.236	0.426	0.292
0.4	0.158	0.243	0.423	0.299
0.5	0.155	0.246	0.423	0.302
<b>0.6</b>	<b>0.154</b>	<b>0.247</b>	<b>0.422</b>	<b>0.304</b>
0.7	0.167	0.238	0.421	0.292
0.8	0.174	0.235	0.419	0.287
0.9	0.173	0.235	0.419	0.288
1.0	0.173	0.235	0.419	0.288

Tab. 5. The outputs for Sea state 1 with the initial values of  $x_{1st} = 0.1$ ,  $k_3=0.2$ ,  $x_a = 0.5$  and  $x_{3m} = \gamma / (\alpha\sqrt{2\beta})$

Initial $x_{2m}$	$x_{1st}$ (rad)	$x_{2m}$ (rad/s)	$x_a$ (rad)	$x_b$ (rad)
0.1	0.178	0.203	0.443	0.259
0.2	0.182	0.203	0.441	0.257
0.3	0.185	0.206	0.434	0.261
<b>0.4</b>	<b>0.171</b>	<b>0.214</b>	<b>0.437</b>	<b>0.272</b>
0.5	0.182	0.209	0.434	0.264
0.6	0.174	0.213	0.436	0.270
0.7	0.182	0.210	0.433	0.264
0.8	0.180	0.210	0.436	0.264
0.9	0.193	0.206	0.429	0.258
1.0	0.193	0.201	0.434	0.253

Tab. 8. The outputs for Sea state 3 with the initial values of  $x_{1st} = 0.1$ ,  $k_3=0.2$ ,  $x_a = 0.75$  and  $x_{3m} = \gamma / (2\alpha\sqrt{2\beta})$

Initial $x_{2m}$	$x_{1st}$ (rad)	$x_{2m}$ (rad/s)	$x_a$ (rad)	$x_b$ (rad)
0.1	0.177	0.234	0.417	0.285
0.2	0.200	0.218	0.415	0.265
0.3	0.170	0.238	0.419	0.292
0.4	0.169	0.238	0.420	0.292
<b>0.5</b>	<b>0.152</b>	<b>0.251</b>	<b>0.420</b>	<b>0.308</b>
0.6	0.157	0.244	0.423	0.301
0.7	0.176	0.233	0.419	0.285
0.8	0.177	0.232	0.419	0.285
0.9	0.167	0.239	0.420	0.293
1.0	0.158	0.246	0.420	0.302

The highest values of  $x_{2m}$  and  $x_b$  are presented for different maximum excitation levers ( $x_{3m}$ ) in Tab. 9–14 for Sea state 1, Sea state 2 and 3, respectively. As can be seen from the tables, the percentage difference between the highest values of  $x_{2m}$  and  $x_b$  obtained by using the initial value of  $x_a = 0.5$  and  $x_a = 0.75$  is less than 2. The solution of the equation system shows the same characteristics for different initial conditions.

The size of the safe basins is highly dependent on the selection of the value of  $x_{3m}$  which is the greatest value of  $x_3$  (the ratio of the external random wave excitation moment and the virtual mass moment of inertia). Selecting small value of  $x_{3m}$  results in not representing of sea state and also that the safe basin is greater than expected whereas selecting bigger value of  $x_{3m}$  causes safe basin smaller than expected.

While comparing the safe basins obtained by the numerical solutions of the equation system (3)–(6) and equation system (19)–(25), the value of  $x_{3m}$  is assumed equal to  $\gamma / (2\alpha\sqrt{2\beta})$ . The values of  $x_{2m}$  and  $x_b$  used for obtaining the safe basins are presented in Tab. 15.

Tab. 9. The highest values of  $x_{2m}$  and  $x_b$  for Sea state 1 with the initial values of  $x_{1st} = 0.1$ ,  $k_3 = 0.2$  and  $x_a = 0.5$

$x_{3m}$	$x_{1st}$ (rad)	$x_{2m}$ (rad/s)	$x_a$ (rad)	$x_b$ (rad)
$\gamma/(3\alpha\sqrt{2\beta})$	0.062	0.383	0.377	0.441
$\gamma/(2\alpha\sqrt{2\beta})$	0.108	0.326	0.388	0.384
$\gamma/(\alpha\sqrt{2\beta})$	0.171	0.214	0.437	0.272
$3\gamma/(2\alpha\sqrt{2\beta})$	0.199	0.156	0.467	0.213

Tab. 10. The highest values of  $x_{2m}$  and  $x_b$  for Sea state 1 with the initial values of  $x_{1st} = 0.1$ ,  $k_3 = 0.2$  and  $x_a = 0.75$

$x_{3m}$	$x_{1st}$ (rad)	$x_{2m}$ (rad/s)	$x_a$ (rad)	$x_b$ (rad)
$\gamma/(3\alpha\sqrt{2\beta})$	0.064	0.375	0.382	0.434
$\gamma/(2\alpha\sqrt{2\beta})$	0.105	0.323	0.394	0.381
$\gamma/(\alpha\sqrt{2\beta})$	0.161	0.229	0.431	0.288
$3\gamma/(2\alpha\sqrt{2\beta})$	0.208	0.145	0.474	0.198

Tab. 11. The highest values of  $x_{2m}$  and  $x_b$  for Sea state 2 with the initial values of  $x_{1st} = 0.1$ ,  $k_3 = 0.2$  and  $x_a = 0.5$

$x_{3m}$	$x_{1st}$ (rad)	$x_{2m}$ (rad/s)	$x_a$ (rad)	$x_b$ (rad)
$\gamma/(3\alpha\sqrt{2\beta})$	0.083	0.355	0.383	0.414
$\gamma/(2\alpha\sqrt{2\beta})$	0.115	0.291	0.413	0.352
$\gamma/(\alpha\sqrt{2\beta})$	0.182	0.183	0.457	0.241
$3\gamma/(2\alpha\sqrt{2\beta})$	No Region for some initial conditions ( $x_{2m} = 0.8$ )			

The boundary of the analytical safe basin is determined by Eq. (26).

$$x_2 = x_{2m} \sqrt{1 - \left(\frac{x_1}{x_b}\right)^2}, \quad x_1 \in [0, x_b] \quad (26)$$

Secondly, the initial condition for rolling is selected by defining the bounded area ( $A_B$ ) as follows:

$$A_B = \{(x_1, x_2): 0 \leq x_1 \leq 1, 0 \leq x_2 \leq 1\} \quad (27)$$

where  $A_B$  is divided into the mesh of  $58 \times 58$  points which are taken as the initial values for the solutions of the four-dimensional state space equations (6–9).

The equation system of rolling motion in random beam seas are numerically integrated by using the Euler Maruyama (EM) method [17] for different initial conditions as defined in Eq. (27) in order to investigate existence of a safe basin until either the roll angle exceeds a capsizing criterion reaching the point where the ship is assumed to capsize or the simulation end time (equal to 3000s in this study) is reached, in which it is assumed that the ship will remain upright [15, 19, 23, 26–28].

Tab. 12. The highest values of  $x_{2m}$  and  $x_b$  for Sea state 2 with the initial values of  $x_{1st} = 0.1$ ,  $k_3 = 0.2$  and  $x_a = 0.75$

$x_{3m}$	$x_{1st}$ (rad)	$x_{2m}$ (rad/s)	$x_a$ (rad)	$x_b$ (rad)
$\gamma/(3\alpha\sqrt{2\beta})$	0.082	0.346	0.394	0.404
$\gamma/(2\alpha\sqrt{2\beta})$	0.112	0.299	0.410	0.358
$\gamma/(\alpha\sqrt{2\beta})$	0.190	0.176	0.458	0.232
$3\gamma/(2\alpha\sqrt{2\beta})$	No Region for some initial conditions ( $x_{2m} = 0.7$ )			

Tab. 13. The highest values of  $x_{2m}$  and  $x_b$  for Sea state 3 with the initial values of  $x_{1st} = 0.1$ ,  $k_3 = 0.2$  and  $x_a = 0.5$

$x_{3m}$	$x_{1st}$ (rad)	$x_{2m}$ (rad/s)	$x_a$ (rad)	$x_b$ (rad)
$\gamma/(3\alpha\sqrt{2\beta})$	0.100	0.327	0.393	0.387
$\gamma/(2\alpha\sqrt{2\beta})$	0.154	0.247	0.422	0.304
$\gamma/(\alpha\sqrt{2\beta})$	0.216	0.138	0.473	0.192
$3\gamma/(2\alpha\sqrt{2\beta})$	No Region for some initial conditions ( $x_{2m} = 0.8$ )			

Tab. 14. The highest values of  $x_{2m}$  and  $x_b$  for Sea state 3 with the initial values of  $x_{1st} = 0.1$ ,  $k_3 = 0.2$  and  $x_a = 0.75$

$x_{3m}$	$x_{1st}$ (rad)	$x_{2m}$ (rad/s)	$x_a$ (rad)	$x_b$ (rad)
$\gamma/(3\alpha\sqrt{2\beta})$	0.104	0.319	0.399	0.376
$\gamma/(2\alpha\sqrt{2\beta})$	0.152	0.251	0.420	0.308
$\gamma/(\alpha\sqrt{2\beta})$	0.213	0.134	0.481	0.186
$3\gamma/(2\alpha\sqrt{2\beta})$	No Region for some initial conditions ( $x_{2m} = 0.8$ )			

Safe basin is a set of initial conditions defined in the space of roll angle and roll angular phase [15, 19, 23, 26–28]. The safe initial conditions which are represented by white points do not cause the ship to capsize, whereas unsafe initial conditions leading to capsizing of the ship are represented by black points [15, 23, 26–28].

The numerically and analytically obtained safe basins of the ship are shown in Figs. 2–4. In the figures the analytically determined boundaries are represented by a black line and the black points are the unsafe initial conditions. As can be seen from these figures, the number of the initial conditions causing the ship to capsize rapidly increases by the increment of sea state and also the analytically obtained safe basin appears smaller. It can be deduced from these figures that the boundary of safe basin obtained by Lyapunov’s function is coherent with the numerical results, though more conservative.

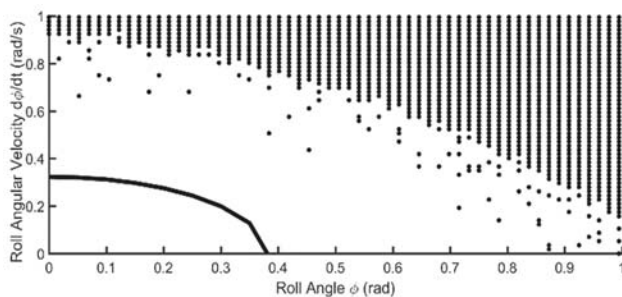


Fig. 2. Boundary of safe basin for Ship 1 and Sea state 1

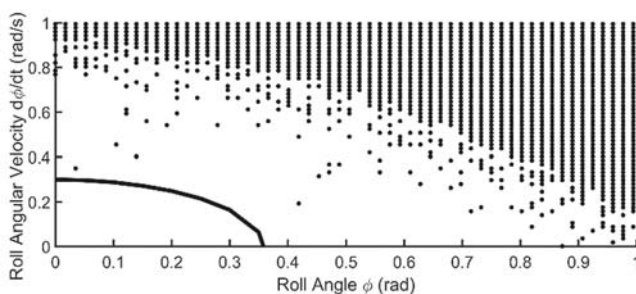


Fig. 3. Boundary of safe basin for Ship 1 and Sea state 2

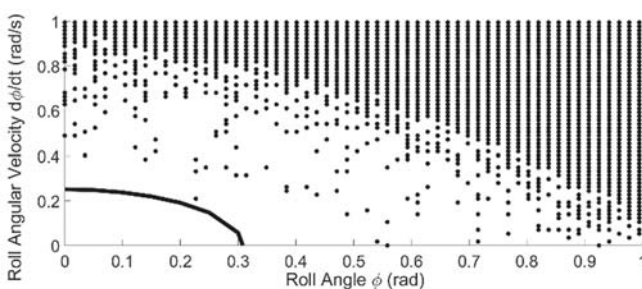


Fig. 4. Boundary of safe basin for Ship 1 and Sea state 3

## CONCLUSIONS

In this study, the Lyapunov function is derived for the 4D system describing the roll motion in beam seas. The Lyapunov function is derived under the following assumptions:

- $x_{1st}$  is the intersection point of modified restoring arm and maximum value of external excitation arm.
- The roll angular velocity reaches its highest value ( $x_{2m}$ ) when the roll angle is zero.
- The ship must have the half of the maximum roll angular velocity at the reference angle of heel determined by  $x_{1st}$ .
- The ship must have a residual arm of  $h_{res}$  at the roll angle  $x_a$ . The magnitude of  $h_{res}$  is determined by  $x_{1st}$ .

The Lyapunov function is derived by the maximum roll angular velocity ( $x_{2m}$ ) and the width of safe basin ( $x_b$ ). Values of  $x_{2m}$  and  $x_b$  are obtained from the solution of the equation system (20)–(25).

The necessary parameters of the equation system are: the restoring moment coefficients ( $c_1, c_3$ ), damping moment coefficients ( $b_{44}, b_{44q}$ ), linear filter parameters ( $\alpha, \beta, \gamma$ ), the greatest value of the ratio of the external random wave excitation moment and the virtual mass moment of inertia ( $x_{3m}$ ), as well as initial values of  $x_2, x_{1st}, k_3^*$  and  $x_a$ . The way of selection of  $x_{3m}$  and initial values of  $x_2, x_{1st}, k_3^*$  and  $x_a$  is explained in Section 5.

With the existence and size of the safe basin obtained by Lyapunov function, it is possible to define whether the ship is stable or not in an examined sea state.

From the results of this study it can be concluded that the existence and size of the safe basin obtained by Lyapunov function can be used to derive an intact stability criterion to define a rule for the intact stability of ships.

## REFERENCES

1. Balcer L.: *Location of ship rolling axis*, Polish Maritime Research, vol. 11, no. 1, pp. 3–7, 2004.
2. Biran, A. B.: *Ship Hydrostatics and stability*. Butterworth-Heinemann, Oxford, 2003.
3. Belenky, V. L. and N. B. Sevastianov *Stability and Safety of Ships: Risk of Capsizing* (2<sup>nd</sup> ed), SNAME, Jersey City, 2007.
4. Caldeira-Sariava, F.: *The boundedness of solutions of a Leinard Equation arising in the theory of ship rolling*. IMA J. Appl. Math, 36, pp. 126–139.
5. Chai W., Naess A. and Leira B. J.: *Filter models for prediction of stochastic ship roll response*, Probab. Eng. Mech., 41, pp. 104–114, 2015.
6. Chai W., Naess A., and Leira B. J.: *Stochastic dynamic analysis and reliability of a vessel rolling in random beam seas*, J. Ship Res., 59(2), pp. 113–131, 2015.
7. Chai W., Naess A. and Leira B. J.: *Stochastic nonlinear ship rolling in random beam seas by the path integration method*, Probab. Eng. Mech., 44, pp. 43–52, 2016.
8. Chai W., Naess A. and Leira B. J.: *Long-term extreme response*

- and reliability of a vessel rolling in random beam sea*, J. Offshore Mech. and Arctic Eng., 140, 11601, pp. 1–9, 2018.
9. Dostal L. and Kreuzer E.: *Probabilistic approach to large amplitude ship rolling in random seas*, Proceedings of the Institution of Mechanical Engineers. Part C, Journal of Mechanical Engineering Science, 225, pp. 2464–2476, 2011.
  10. Dostal L., Kreuzer E. and Namachchivaya: *Non-standard stochastic averaging of large-amplitude ship rolling in random seas*, Proceedings of the Royal Society A, 258, pp. 1–25, 2012.
  11. Haddara M.: *Modified approach for the application of Fokker – Plank equation to the nonlinear ship motions in random waves*. Int. Shipbuilding Prog., 21(242), pp. 283–288, 1974.
  12. Hutchison B. L.: *The transverse plane motions of ships*, SNAME Marine Tech., vol. 28, No. 2, pp. 55–72, 1991.
  13. Jiang C., Troesch A. and Shaw, S.: *Capsize criteria for ship models with Memory-Dependent Hydrodynamics and Random Excitation*, Philos. Trans. R. Soc. Lond. Ser. A, 358(1771), pp. 1761–1791, 2000.
  14. Jiang C.: *Highly nonlinear rolling motion leading to capsizing*, University of Michigan, Ann Arbor, 1995.
  15. Karakas S. C., Pesman E. and Ucer E.: *Control design of fin roll stabilization in beam seas based on Lyapunov's direct method*, Polish Maritime Research, No 2(73) Vol. 19, pp. 25–30, 2012.
  16. Kushner H. J.: *Stochastic stability and control*, Academic Press, New York, 1967.
  17. Kloden PE, Platen E: *Numerical solution of stochastic differential equations*. New York: Springer; 1995.
  18. La Salle, J.P. and Lefschetz, S.: 1961. *Stability by Lyapunov's Direct Method with Applications*. Academic Press, New York.
  19. Long, Z.Z., Lee, S.K., Kim, J.Y.: *Estimation of survival probability for a ship in beam seas using the safe basin*, Ocean Eng. Vol: 37, 418–424, 2010.
  20. Moshchuk N., Ibrahim R. A. and Khazminskii R.: *Response statistics of ocean structures to nonlinear hydrodynamics loading Part I: Gaussian ocean waves*, Journal of Sound and Vibration, 184(4), pp. 681–701, 1995.
  21. Odabasi, A.Y.: *Stochastic stability of ships in following seas*, Schiff & Hafen, 3, pp. 223–226, 1979.
  22. Ozkan, I.R.: *Total (practical) Stability of ships*, Ocean Eng., 8, pp. 551–598.
  23. Rainey, R.C.T., Thompson, J.M.T.: *The transient capsizing diagram- a new method of quantifying stability analysis*. J. Ship Res. 35 (1), pp. 58–92. 1991.
  24. Roberts J.: *A Stochastic Theory for Nonlinear Ship Rolling in Irregular Seas*, J. Ship Res., 26(4), pp. 229–245, 1982.
  25. Schurz H.: *Verification of Lyapunov functions for the analysis of stochastic Lienard equations*. J Sound Vib., 325: pp. 938–49, 2009.
  26. Soliman, M.S., Thompson, J.M.T.: *Transient and steady state analysis of capsizing phenomena*. Appl. Ocean Res. 13 (2), 82–92, 1991.
  27. Thompson, J.M.T.: *Loss of engineering integrity due to the erosion of absolute and transient basin boundaries*, Proceedings of IUTAM Symposium on the Dynamics of Marine Vehicles and Structures in Waves, pp. 313–320, 1989.
  28. Ucer E.: *Examination of the trawlers in beam seas using safe basins*, Ocean Eng., 38(17-18), pp. 1908–1915, 2011.
  29. Yilmaz H.: *Analyzing form parameters of fishing vessels point of view of practical stability criteria in preliminary design stage*, Yildiz Technical University, Istanbul, 1998.

**CONTACT WITH THE AUTHORS**

**Erdem Üçer**

*e-mail: ucerer@itu.edu.tr*

Istanbul Technical University  
Faculty of Naval Architecture and Ocean Engineering  
Ayazaga Campus, 34469 Istanbul  
**TURKEY**

# ANALYSIS AND EXPERIMENTS OF EMBEDDED GRIPPING MECHANISM USED IN LARGE-SCALE TOOLS HOLDING UP PILE FOUNDATION IN OCEAN

Zhuo Wang

Bo Zhang

Tao Wang

Harbin Engineering University, China

## ABSTRACT

*With the rapid development of the marine economy and continuous improvement of the industry, the scale of the offshore engineering is increasing. This raises interest in studying, theoretically and experimentally, gripping and bearing mechanisms for large-scale holding and lifting tools used in foundation pile installations. In this paper, the embedded gripping mechanism is studied based on the theory of elastic-plastic mechanics. The embedded and bearing performance of the tooth is simulated and the influence factors are studied. In addition, the device used in the simplified embedded experiment on the tooth of the embedded block is designed. The relationship between embedded depth, load, and tooth profile angle is identified and validated. Meanwhile, the embedded performance of linear and ring type teeth is compared experimentally in order to select the suitable type of tooth for various situations. This comparison makes the basis for designing an upending gripper for the marine pile foundation, which can realize the operation of holding the pile to prevent its falling.*

**Keywords:** pile foundation; gripping; embedded mechanism; embedded depth; upending gripper

## INTRODUCTION

With the development of economy, the demand for energy increases. The exploitation of offshore oil and wind becomes an important direction of energy development [1, 2]. Underwater installation of marine foundation piles is one of the key technologies used in installation of offshore platforms and wind turbines [3]. Since the marine foundation piles have several characteristic features, such as large diameter, length, and weight, large-scale holding and lifting tools are used for their installation [4]. In this context, it is advisable to study, theoretically and experimentally, gripping and bearing mechanisms for large-scale holding and lifting tools used for installation of foundation piles in offshore areas.

There are numerous foreign large-scale holding and lifting tools, but their specific principles and research methods are seldom available [5, 6, 7]. In China, many domestic scholars have done theoretical and experimental research in this area

[8, 9, 10]. The contact pressure and extrusion conditions of the pressing block tooth have been obtained based on the finite element analysis. In 2006, an optimal design was introduced into the structure of the pressing block tooth for underwater skirt pile gripper by some scholars from Harbin Engineering University. In 2007, Liang, F.H. et al. of Tianjin University proposed making a tooth or groove on the piston surface to increase friction. In that paper, the finite element analysis was used to choose the number of hydraulic pressure vats distributed in the pile gripper [11]. In 2008, Jiang, Y.C. et al. of Tianjin University put forward a design of the controlled friction skirt pile gripper, and used ANSYS software to obtain the relationship between stress, strain, and force for different pile diameters and wall thickness [12]. In 2009, Li, H.L. et al. of CNOOC completed the experimental examination of mechanical performance of the clamping block [13]. The ultimate load experiment was concluded with the relation between the clamping force and the maximum lifting force

for clamping blocks made of different materials. In 2011, the mechanical model of contact between pressing block teeth and a steel pile was developed by Jiang, P.R. and Fang, X.M. of Harbin Engineering University [14]. The mechanical performance of the pressing block teeth and the steel pile was examined. In 2013, Li, T.Q. of CNOOC worked out the structural design of the suspension tool. He also analyzed variations of the clamping force, which increased with the increase of the angle between the pile and the horizontal plane [15]. The clamping performance of the Pile Pending Device (PPD) was researched by the company IHC in 2015 [16]. The conclusion from their research was that when the number of uniformly distributed wedge assemblies covers more than 50% of the circumference of the base ring, the clamping effect is better [17].

Up to the present, most researches have focused on the principle and feasibility of large-scale holding and lifting tools, and on contact problems between the pressing block teeth and the steel pile. Another research issue was optimization of pressing block tooth type via the finite element analysis and experimental validation. A few researches investigated damages to the foundation piles and their bearing capacity introduced by the embedded gripping mechanism. In this paper, the damage to the foundation piles is researched in the simplified experiment on the tooth of the embedded block. Moreover, the embedded performance of linear and ring type teeth is compared. The embedding process performed with the embedded gripping mechanism is analyzed using the finite element simulation.

## SIMPLIFIED METHOD OF EXPERIMENT ON EMBEDDED BLOCK TOOTH

As Fig. 1 shows, the device used in the simplified experiment on the tooth of the embedded block was designed not only to simulate the force acting between the tooth and the pile, but also to examine the pile deformation and damage.



Fig. 1. Device used in simplified embedded experiment

In practice, the diameter of the pile is very large, compared to the size of the embedded block. Therefore, plates were used in the experiment instead of piles, as shown in Fig. 2. When measuring the embedded depth, the material of the used plates was Q235, the yield strength of which is relatively low and the embedded depth was larger than that of the pile

material. As shown in the figure, different embedded blocks with different types of teeth and tooth profile angles were examined to find the relationship between the embedded performance and the tooth type and profile angle.



Fig. 2. Plates of piles and embedded block

During the experiment, the embedded block was placed on the wedge-shaped slider which was installed respectively on both sides of the fixed wedge block, as shown in Fig. 3.



Fig. 3. Diagram of indirect measurement of embedded depth

The plate representing the pile was placed in the main framework to contact with the tooth of the embedded block. The hydraulic jack was installed on the main framework to apply load, which then was measured by the pressure sensor. The embedded depth was calculated by measuring the distance between the wedge-shaped slider and the pile plate before and after the experiment. To extend the range of generality of the results of the experiment, different embedded blocks with different tooth types and profile angles were used.

## RESULTS OF THE EXPERIMENT ON EMBEDDED BLOCK TOOTH

As shown in Tab. 1, in the simplified experiment on the tooth of the embedded block, the embedded blocks of the same linear tooth type but with different tooth profile angles were examined under different pressures. The embedded depth corresponding to each load step was recorded. The average value was obtained from the data of several experiments. Finally, the curve representing the relationship between the load and the embedded depth was drawn.

When the tooth profile angle was the same, the load increase resulted in the increase of the embedded block depth. When the load was the same, the increase of the tooth profile angle resulted in the decrease of the embedded block depth, as shown in Fig. 4.

Tab. 1. Embedded depth of different angle of tooth profile

Angle of tooth profile (°)	Load (T)	Emb- edded depth (mm)	Angle of tooth profile (°)	Load (T)	Emb- edded depth (mm)
75	1.20	0.12	85	1.20	0.10
	1.50	0.20		1.48	0.16
	1.60	0.23		1.62	0.18
	1.68	0.25		1.72	0.20
	1.78	0.28		1.84	0.22
	2.02	0.31		2.10	0.26
	2.09	0.33		2.20	0.28
	2.44	0.35		2.44	0.31
	2.60	0.38		2.67	0.33
	2.83	0.40		2.80	0.35
	3.00	0.42		2.96	0.38
3.17	0.45	3.36	0.42		
3.47	0.47	3.55	0.44		
95	1.15	0.08	105	1.18	0.06
	1.35	0.11		1.48	0.09
	1.50	0.14		1.57	0.11
	1.69	0.16		1.67	0.12
	1.80	0.18		1.81	0.13
	2.02	0.21		2.07	0.16
	2.36	0.24		2.38	0.18
	2.54	0.25		2.52	0.20
	2.69	0.27		2.65	0.22
	2.97	0.30		2.95	0.24
	3.14	0.32		3.13	0.27
	3.30	0.34		3.40	0.29
	3.55	0.37		3.53	0.30

Tab. 2. Embedded depth of different type of the tooth

Linear type of tooth	Load (T)	Emb- edded depth (mm)	Ring type of tooth	Load (T)	Emb- edded depth (mm)
	1.20	0.10		1.37	0.09
	1.48	0.16		1.50	0.11
	1.62	0.18		1.61	0.13
	1.72	0.20		1.74	0.14
	1.84	0.22		1.93	0.15
	2.10	0.26		2.05	0.17
	2.20	0.28		2.26	0.19
	2.44	0.31		2.48	0.21
	2.67	0.33		2.66	0.23
	2.80	0.35		2.77	0.24
	2.96	0.38		2.98	0.27
	3.36	0.42		3.36	0.31
	3.55	0.44		3.50	0.32

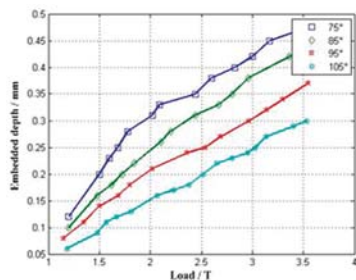


Fig. 4. Curve between the load and the embedded depth

During the experiment, no embedded block breakup was recorded, as shown in Fig. 5. The indentation of the embedded block for the tooth profile angle of 75° was deep and narrow, while for the angle of 105° it was shallow and wide. In practice, deep and narrow indentation has higher stress concentration, therefore a larger tooth profile angle should be chosen, provided that the bearing load condition is met.



Fig. 5. Indentation of embedded blocks

The embedded performance of the linear and ring type teeth was compared experimentally. The embedded blocks with the same tooth profile angles but of different tooth type were examined under the same pressure. The embedded depth corresponding to each load step was recorded.

The experimental data shown in Tab. 2 reveal that the embedded depth of the ring type tooth is significantly smaller than that of the linear type tooth. The reason is that the contact length of the ring type tooth is longer than that of the linear type tooth, consequently the damage of the plate is smaller under the same load.

When the parallelism between the tooth and the pile plate was deteriorated in the experiment, the phenomenon of uneven contact occurred. Since the contact trace of the linear type tooth was a straight line, this reduced the phenomenon of uneven contact to a certain extent, as shown in Fig. 6.



Fig. 6. Uneven indentation of embedded blocks

In practice, the plate damage caused by the ring type tooth was small, and the ring type tooth could withstand forces in all directions. In cases when the load changes in various directions, the ring type tooth should be chosen. The ring type tooth is structurally simple and convenient in processing. When the parallelism between the tooth and the pile plate is poor but the direction of load does not change, the linear type tooth should be chosen.

## ALYSIS AND DISCUSSION ON THE EMBEDDED GRIPPING MECHANISM

The analysis on the embedded mechanism between the embedded block tooth and the pile. The embedded block increased the friction and provided the bearing capacity for the pile by embedding into the pile. The embedded mechanism between the tooth of the embedded block and the pile had the following characteristics:

- 1) Compared to the size of the pile, the size of the tooth was very small and sharp.
- 2) The stress in the pile caused by the tooth was larger than the yield strength of the pile, as a consequence of which the tooth embedded into the pile.

When the pile was clamped, it formed the interactive compression between the tooth and the pile. Therefore, the pile yielded and the tooth embedded into the pile. With the increase of the embedded depth, the metal of the pile slipped on the face of the tooth and the contact area increased. Once the limit load was reached, the plastic deformation of the pile stopped and the metal stopped slipping. Meanwhile, the tooth stopped embedding into the pile and the process reached the equilibrium state.

The embedding process between the tooth and the pile is a complex contact process. It can be simplified to the plane contact problem. The formula of the embedded depth can be obtained using the slip line method.

As shown in Fig. 7 (a) and (b), the embedded block with tooth profile angle  $2\gamma$  was under the pressure  $N_n$  to embed into the pile. The embedded depth was  $t$ , and the normal stress of the contact surface was  $q$ . Considering the frictional force of the contact surface, the friction shear stress was  $k$ .

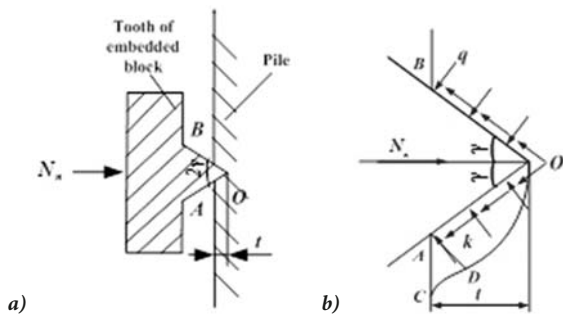


Fig. 7. Force diagram between the tooth and the pile

Due to the symmetry of the problem, the direction of the pile slip line was determined by examining half of the tooth.  $AD$  was the slip line of the area  $ADC$ , according to the direction of the maximum principal stress. Then,  $AO$  was the slip line of the area  $AOD$ , according to the direction of the maximum shear stress.

The average stress on the boundaries  $AC$  and  $AO$  can be illustrated by the boundary normal stress component  $\sigma_n$ , the yield stress of pile material  $\tau_s$ , the angle  $\theta$  between the slip line and the  $x$ -axis, and the angle  $\varphi$  between the boundary normal and the  $x$ -axis.

$$\sigma = \sigma_n + \tau_s \sin 2(\theta - \varphi) = -\tau_s \quad (1)$$

$$\sigma = \sigma_n + \tau_s \sin 2(\theta - \varphi) = -q \quad (2)$$

Along with the slip line, the equation can take the form of the Hencky equation:

$$\sigma + 2k\theta = C_\beta \quad (3)$$

By considering (1), (2) and (3), the equations can be set up as:

$$\begin{cases} -\tau_s + 2\tau_s \left( -\frac{3\pi}{4} \right) = C_{\beta 1} \\ -q + 2\tau_s \left( -\frac{\pi}{2} + \gamma \right) = C_{\beta 2} \end{cases} \quad (4)$$

If the slip line is straight,  $\sigma$ ,  $\theta$ ,  $C_\alpha$ , and  $C_\beta$  are constant along the line. Consequently,  $C_{\beta 1} = C_{\beta 2} = \text{constant}$ .

Therefore, the equation can take the form:

$$q = \tau_s \left( \frac{\pi}{2} + 2\gamma + 1 \right) \quad (5)$$

Based on the known condition, the force equilibrium equation was set up:

$$N_n = (l_{OA} + l_{OB}) (q \sin \gamma + \tau_s \cos \gamma) \quad (6)$$

where,  $l_{OA} = l_{OB} = \frac{t}{\cos \gamma}$ .

The formula of the embedded depth can be obtained after substituting (5) into (6):

$$t = \frac{N_n}{2\tau_s \left( \frac{\pi}{2} \tan \gamma + 2\gamma \tan \gamma + \tan \gamma + 1 \right)} \quad (7)$$

The curved surface shown in Fig. 8 represents the relationship between the embedded depth of the block, the applied load, and the used tooth profile angle.

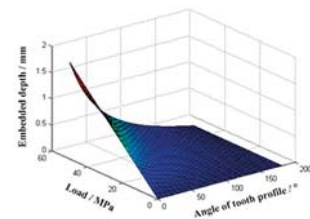


Fig. 8. Curve of the embedded depth

It reveals that the embedded block depth increases with the increase of load and the decrease of tooth profile angle. This result is consistent with the experiment, on the whole. In order to avoid pile failure and the decrease of ultimate bearing capacity of the tooth caused by improper embedded depth, the embedded blocks with appropriate tooth profile angles should be chosen, and appropriate loads should be applied.

**The simulation analysis on the embedding process of embedded block tooth.** The embedding process of the tooth

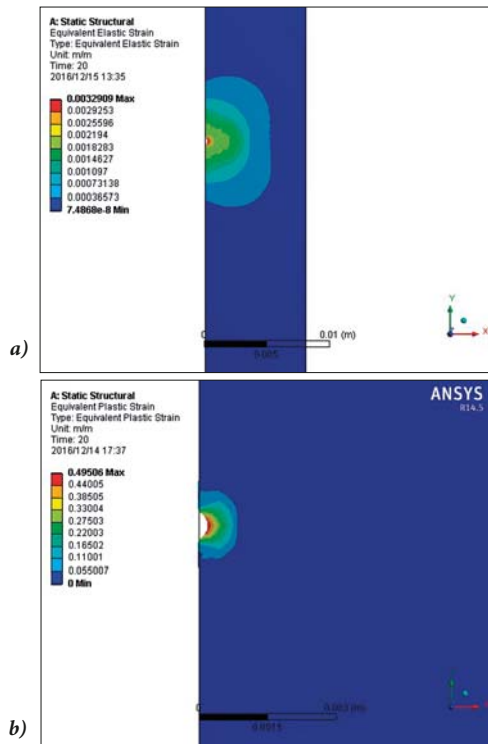


Fig. 9. Elastic and plastic strain of the pile

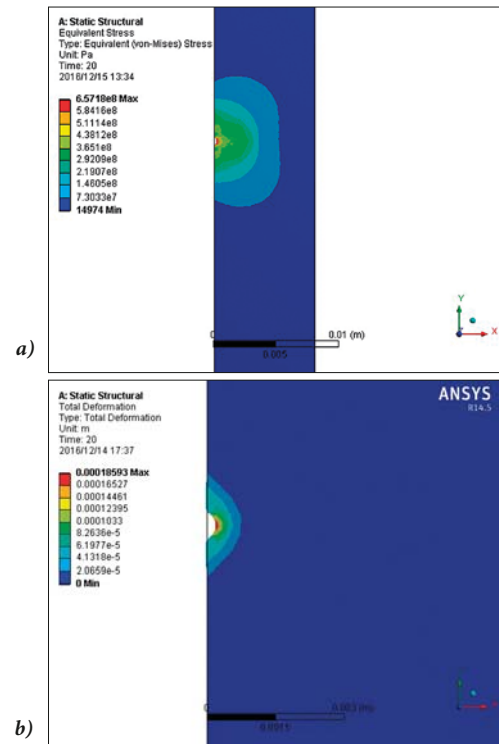


Fig. 10. Equivalent stress of the pile and embedded depth

belongs to the category of nonlinear processes, which not only require advanced and time-consuming calculations, but are also difficult to converge. Therefore, the finite element models of the tooth and the pile were described by plane elements. To improve the calculation accuracy and speed, the mesh was refined at the location where the tooth embedded into the pile, while in other places, a coarsened grid was used. The contact model between the tooth and the pile was established, in which the tooth and the pile were the contact body and the target body for each other.

The simulation analysis was carried out with the tooth of the embedded block and the pile. In the simulation, the embedded block with tooth profile angle of  $90^\circ$  was under the pressure of 30 MPa. To find the embedded depth of the tooth, the pile was analyzed separately.

The pile generated elastic deformation at the location where the tooth embedded into it under the applied load. When the elastic deformation reached the maximum, the pile entered the stage of plastic deformation. The elastic and plastic strain regions are shown in Fig. 9. The region of elastic strain is obviously larger than that of plastic strain. The maximum of elastic strain was 0.0033, and the maximum of plastic strain was 0.495, as shown in the figure.

The equivalent stress of the pile gradually increased along the direction of thickness at the location where the tooth was embedded under the applied load, as shown in Fig. 10. The equivalent stress reached a maximum of 657.18 MPa and was above the yield strength of the pile material, as a consequence of which the tooth embedded into the pile to the depth of 0.186 mm.

A small axial displacement was subjected to the top of the pile. The ultimate bearing capacity of the tooth was obtained

by applying the constraint force in the simulation. It was equal to 313.93 kN under the pressure of 30 MPa.

Similarly, different loads were applied to the embedded blocks with different tooth profile angles to simulate the embedding process. The curved surface of the embedded depth, load, and tooth profile angle obtained from the simulations is shown in Fig. 11.

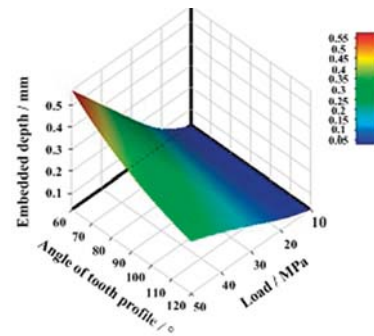


Fig. 11. Curve of the embedded depth

Changes of the theoretical value, the simulation value, and the experimental value of the embedded depth were basically the same. However, the experimental value was larger than the theoretical value and the simulation value. The theoretical value, which was studied by the slip line method, was closer to the experimental value. The embedded depth measured in the experiment included not only the deformation of the pile, but also the elastic deformation of the tooth. Besides, the embedded depth was obtained by indirect measurement in the experiment. The measurement errors made the experimental value larger than the theoretical value and the simulation value.

**Design of the pile upending gripper.** During pile installation, the pile upending gripper clamps the pile and turns it from horizontal to vertical position. This reduces difficulties and improves the efficiency of the installation process. When the gripper upends the pile, it clamps the pile to prevent pile dropping.

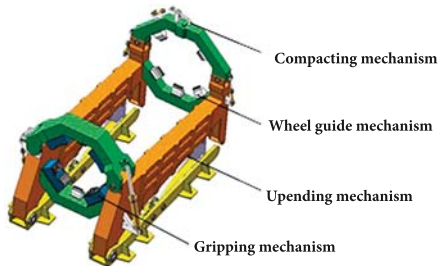


Fig. 12. Schematic of the pile upending gripper

As shown in Fig. 12, the pile upending gripper was designed by using the embedded gripping mechanism to increase friction and clamping force. The pile upending gripper includes gripping mechanism, wheel guide mechanism, compacting mechanism, and upending mechanism.

When the pile upending gripper upends the pile, the gripping mechanism clamps the pile in order to prevent pile slipping. The gripping mechanism is mainly composed of clamping jaw, frame connecting jaw, jaw opening hydraulic cylinder, clamping hydraulic cylinders, embedded blocks, boxes, and wheels. The clamping hydraulic cylinder piston rods and the mounting plate of the embedded blocks are in threaded connection. The embedded blocks are uniformly arranged in the groove of the mounting plate, as shown in Fig. 13.

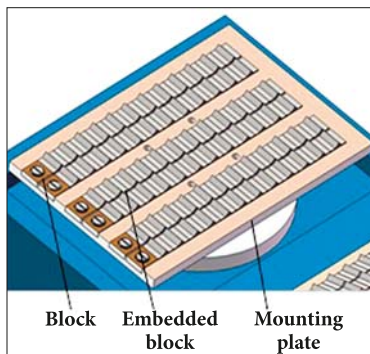


Fig. 13. Arrangement of embedded blocks

When the clamping hydraulic cylinders clamp the pile, the blocks embed into the pile. The resistance to bend and shear is produced to increase friction.

## CONCLUSIONS

The paper analyses the embedded gripping mechanism and the damage done by it to the foundation piles. Based on that, the pile upending gripper is proposed. The conclusions are as follows: the damage to the foundation piles is very small when using the embedded gripping mechanism which can

effectively increase friction. With the increase of load and the decrease of tooth profile angle, the embedded block depth increases. The embedding performance of the linear and ring type teeth is different. Therefore, they should be used in different situations.

## ACKNOWLEDGEMENT

The research was financed by the National Natural Science Foundation of China, within the framework of the project entitled “Research on ultimate bearing capacity and parametric design for the grouted clamps strengthening the partially damaged structure of jacket pipes” (NSFC Grant No. 51879063) and “Research on analysis and experiments of gripping and bearing mechanism for large-scale holding and lifting tools on ocean foundation piles” (NSFC Grant No: 51479043).

## REFERENCES

1. Sarkar, A., Gudmestad, O. T. *Installation of monopiles for offshore wind turbines – by using end-caps and a subsea holding structure*. ASME 2011 International Conference on Ocean, Offshore and Arctic Engineering, 2011: 309–315.
2. Sarkar, A., Gudmestad, O. T. *Study on a new method for installing a monopile and a fully integrated offshore wind turbine structure*. Marine Structures, 2013, 33(10): 160–187.
3. Hezarjaribi, M., Bahaari, M. R., Bagheri, V., et al. *Sensitivity analysis of jacket-type offshore platforms under extreme waves*. Journal of Constructional Steel Research, 2013, 83: 147–155.
4. Wang, W., Yang, M., *Review and discussion on key technologies in foundation design of offshore wind power*, Journal of Hydroelectric Engineering, 2012,31(06): 242–248.
5. Natskâr, A., Moan, T., Alvær, P. *Uncertainty in forecasted environmental conditions for reliability analyses of marine operations*. Ocean Engineering, 2015, 108(2): 636–647.
6. <http://www.knudehansen.com/references/offshore-offshore-wind-vessels/mono-pile-upending-trolley/.2017>.
7. <http://www.ihchs.com/wind/deck-equipment/pile-guiding-and-positioning-frame/.2017>.
8. Sun, Z. J., Meng, Q.X., Zhou, D. *Contact finite element analysis of the pressing block tooth in underwater skirt pile gripper of offshore oil platform*. Machinery, 2006, (12): 1–4.
9. Sun, Z. J., Meng, Q.X., Zhou, D. *Structure optimization of the pressing block tooth in underwater skirt pile gripper of offshore oil platform*. Machine Design and Research, 2006, (06): 102–105.

10. Sun, Z.J., Meng, Q.X., Zhou, D. *Contact nonlinear finite element analysis on the pressing block tooth in underwater skirt pile gripper*. Journal of Petrochemical Universities, 2006, (03): 72–75.
11. Liang, F.H., Yan, X.G., Zheng, W. *Mechanical analysis of jacket pile gripper and choice of the number of hydraulic pressure vats*. The Ocean Engineering, 2007, (01): 82–87.
12. Jiang, Y.C., Tian, Y.F., Yang, S.G., *The skirt pile gripper design of jacket platform*. China Offshore Platform, 2008, (05): 19–22+26.
13. Li, H.L., Yu, W.T., Wang, L.Q., et al. *Experimental research on clamping block of underwater leveling equipment*. China Offshore Oil and Gas, 2009, (01): 57–60.
14. Jiang, P.R., Fang, X.M. *Analysis and experimental study grip function of an underwater skirt the gripper*. Journal of Harbin Engineering University, 2011, (09): 1228–1232.
15. Li, T.Q. *Research of unilateral clamping lifting tool of great steel tube stake at sea*. Modern Manufacturing Engineering, 2013, (08): 79-82+59.
16. Mulderij, K. J. Pile upending device: WO, WO/2014/084738[P], 2014.
17. Stefan, A., Constantin, D., Grigore, L. S. *Aspects of kinematics and dynamics of a gripping mechanism*. Electronics, Computers and Artificial Intelligence (ECAI), 7th International Conference on, 2015: WF-1-WF-4.

## CONTACT WITH THE AUTHORS

**Zhuo Wang**  
*e-mail: 2958219945@qq.com*

Harbin Engineering University  
 Road Nantong 145, District Nangang  
 150001 Harbin  
**CHINA**

## CONDITIONS OF SAFE SHIP OPERATION IN SEAPORTS – OPTIMIZATION OF PORT WATERWAY PARAMETERS

Stanisław Gucma

Maritime University of Szczecin, Poland

### ABSTRACT

*A seaport is presented in this article as a system composed of various types of waterways. The author has defined relationships between port waterway system elements and conditions of safe operation of ships in port. Relationships were determined between the conditions of safe operation of ships and the parameters of the following port waterways: anchorage, fairways (approach and inner channels, port entrances), turning area and port basin. The identified relationships between port waterway system and conditions of safe ship operation provided a basis for formulating the objective function of waterway parameter optimization during port design. In practice, these relations were used to determine the parameters of the Outer Container Terminal being built in Świnoujście, where two optimization problems were to be solved:*

1. *The optimization of approach channel parameters,*
2. *The optimization of parameters of the port entrance, turning area and port basin.*

*The Outer Container Terminal in Świnoujście is expected to handle ocean-going ships with a length overall  $L_o = 400$  m, and its projected capacity is estimated at 1.5 million TEU per year, a figure that can be doubled in the future.*

**Keywords:** marine traffic engineering, sea port, waterways, optimization of port parameters, simulation methods of optimization.

### INTRODUCTION

The seaport is a system consisting of set of various waterways (harbour areas) such as: anchorages, fairways, turning areas and basins. The parameters of individual types of waterways are a function of the safe operation of ships manoeuvring in these waterways [Gucma S. 2015].

Conditions for the safe operation of ships are defined by basic parameters of a 'maximum ship' that can safely maneuver on a given waterway in the allowable for this manoeuvre hydrometeorological conditions. Conditions for the safe operation of ships in particular types of waterways differ and are otherwise determined.

Conditions for the safe operation of ships in port regarded as a system composed of various types of waterways are dependent on the conditions of safe operation of ships on

each specific waterway within the port, while the parameters of each waterway belonging to the port are determined by the conditions of safe operation of ships manoeuvring in that area.

The article defines and determines the above relations, i.e.:

- conditions for safe operation of ships manoeuvring in a port as a waterway system,
- conditions for safe operation of port waterways,
- relationships between port waterway parameters and the conditions for their safe operation.

These relationships enable optimisation of port parameters, i.e. the functional division of the port, formulation of the objective function of the functional parts and the optimization of individual waterways, components of the port.

The defined dependencies of waterway parameters on the conditions for safe operation of the port and port waterways

were used in the optimization of the parameters of the Outer Container Terminal under construction in Świnoujście.

## THE SEAPORT AS A SYSTEM COMPOSED OF VARIOUS WATERWAYS

The seaport in terms of marine traffic engineering is a system consisting of a set of the following types of waterways (port areas), where ships perform characteristic maneuvers (Fig.1):

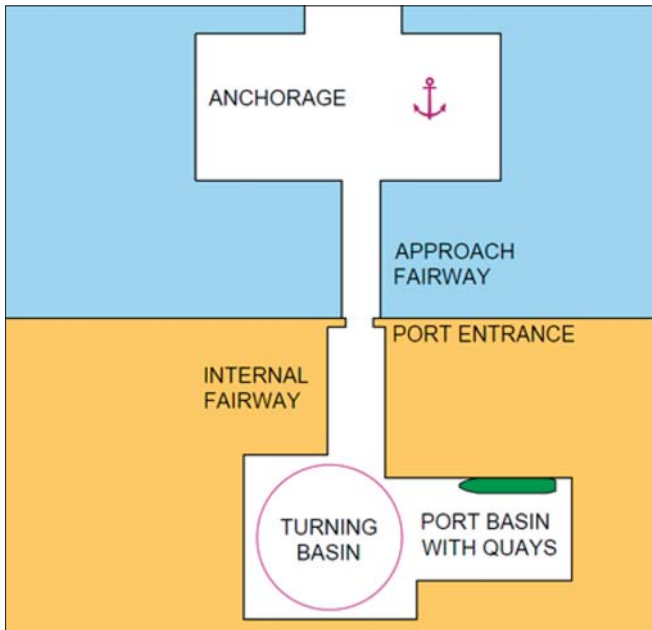


Fig. 1. System of port waterways

- anchorage (roadstead) – anchoring manoeuvre,
- approach channel – passage along the channel,
- port entrance – port entry manoeuvre
- internal fairway (port channel) – port channel passage manoeuvre,
- turning basin – turning maneuver
- port basin and berth – berth approach and berthing manoeuvres.

In the port regarded as a system of sea waterways, different port areas make up separate waterway sections that can be classed by a number of criteria [Gucma S. et al.: 2015]:

- technical parameters of the port area,
- technical parameters of navigation systems used,
- prevailing hydrometeorological conditions,
- conditions of safe operation.

Each of the sections of the waterway is composed of two basic elements [Gucma S. 2014]:

1. waterway subsystem,
2. navigational subsystem (ship position determination subsystem).

These elements affect each other and have an important impact on the system properties.

The parameters of elements (subsystems) of each port waterway section define conditions for safe operation of ships in the port system. Therefore, the vector of the conditions of safe ship operation is a function of the port waterway system parameters:

$$W_i = F \begin{bmatrix} A_i \\ N_i \end{bmatrix} \quad (1)$$

where

$W_i$  – vector of safe ship operating conditions in  $i$ -th section of the port waterway,

$A_i$  – subsystem of the area (the  $i$ -th section of the port waterway),

$N_i$  – navigational subsystem (of  $i$ -th section of the port waterway).

Conditions for the safe operation of ships in ports are subject to two restrictions [IMO 2002; Tsinker G.P. 2004; Thoresen C.A. 2014; Gućma S. 2015]:

1. The principal maximum parameters (length, breadth, draft) of vessels that can safely enter the port must be the same in all waterway sections,
2. Hydrometeorological conditions that allow ships to manoeuvre are identical for all port waterway sections except for anchorage (roadstead).

Sea going ferries are considered separately, as allowable hydro – meteorological conditions for ferries are stricter and established individually for each ferry, depending on their parameters and manoeuvrability.

Given the above limitations, conditions for safe operation of ships in port regarded as a waterway system can be written in the form of a vector [Gucma S. 2015]:

$$W^p = [L_o, B, T, H^p] \quad (2)$$

where:

$W^p$  – vector of safe ship operating conditions for the whole port as a waterway system,

$L_o$  – maximum length overall of the ship that can safely enter the port,

$B$  – maximum breadth of the ship that can safely enter the port,

$T$  – maximum draft of the ship that can safely enter the port,

$H^p$  – set of hydrometeorological conditions acceptable for port manoeuvres of a ‘maximum ship’, i.e. ship whose at least parameter:  $L_o, B, T$  has the maximum value.

wherein:

$$H^p = [s, V_w, V_c, \Delta h] \quad (3)$$

where:

$s$  – allowable visibility,

$V_w$  – allowable wind speed,

$V_c$  – allowable current speed,

$\Delta h$  – allowable drop of water level.

For anchorages, values  $V_w, V_c$  and  $\Delta h$  are adopted without restrictions concerning the conditions prevailing in the anchorage area.

## CONDITIONS OF THE SAFE OPERATION OF SHIPS IN PORT WATERWAYS

The subsystems of port waterway areas ( $A_i$ ) and the vectors of safe ship operating conditions ( $W_i$ ) are defined differently depending on the type of waterway, which involves different kind of manoeuvres performed by the ship. Port waterways are divided into four differently defined groups: These are:

1. Anchorages,
2. Fairways, approach channels, inner channels and port entrances
3. Turning basins,
4. Port basins with quays (berths).

An **anchorage** is defined by two system components (area and navigation subsystems), which are a function of the conditions of safe operation of vessel performing anchoring manoeuvre:

$$\begin{bmatrix} A^a \\ N^a \end{bmatrix} = f(W^a) \quad (4)$$

The anchorage area subsystem is described by a set of parameters:

$$A^a = \begin{bmatrix} D^a \\ h^a \end{bmatrix} \quad (5)$$

where:

$D^a$  – available navigable area of the anchorage (meeting a condition of minimum depth),

$h^a$  – minimum depth of anchorage.

The navigation subsystem of the anchorage is defined by a set of parameters:

$$N^a = \begin{bmatrix} M_{oj} \\ m_j \end{bmatrix} \quad (6)$$

where:

$M_{oj}$  – circular error of ship position determined at anchorage using the  $j$ -th navigation system,

$m_j$  – availability of  $j$ -th navigational system at any time of day for various visibility conditions.

The conditions of safe ship operation at anchorage during anchoring manoeuvres and staying at anchor are expressed by the vector of the ‘maximum ship’ safe operating conditions.

$$W^a = [L_o, B, T, H^a] \quad (7)$$

where:

$H^a$  – the set of hydrometeorological conditions acceptable for manoeuvring of a ‘maximum ship’ at anchorage.

The set of allowable hydrometeorological conditions of anchoring  $H^a$  is limited for some anchorages only by allowable maximum wind speed ( $V_w^a$ ) and allowable water level drop ( $\Delta h^a$ ); in such a case:

$$H^a = [V_w^a, \Delta h^a] \quad (8)$$

**Fairways** and port entrances, like anchorages, are defined by the area and navigation subsystems, a function of the conditions of safe operation of vessels manoeuvring therein.

$$\begin{bmatrix} A_i^f \\ N_{ij}^f \end{bmatrix} = f_1(W_i^f) \quad (9)$$

The area subsystem is described by this set of parameters:

$$A_i^f = \begin{bmatrix} t_i \\ l_i \\ D(l)_i \\ h_i \end{bmatrix} \quad (10)$$

where:

$t_i$  – type of  $i$ -th fairway section,

$l_i$  – length of  $i$ -th fairway section,

$D(l)_i$  – width of the available navigable area of  $i$ -th fairway section as a function of its length,

$h_i$  – minimum depth of  $i$ -th fairway section.

From the viewpoint of marine traffic engineering, the following types of waterways are distinguished in this group [Gucma S. et al.: 2015]:

• fairway:

– straight section,

– bend,

• entrance to the port (straight, a bend or combined bends).

The navigation subsystem of the fairway is described by a set of parameters:

$$N_{ij}^f = \begin{bmatrix} p(l)_{ij} \\ m_{ij} \\ n_{ij} \\ w_{ij} \end{bmatrix} \quad (11)$$

where:

$p(l)_{ij}$  – accuracy of  $j$ -th navigational system in  $i$ -th section of the fairway defined as a function of fairway length  $l$  (directional error perpendicular to the fairway centre line at a specific level of confidence),

$m_{ij}$  – availability of  $j$ -th navigational system in  $i$ -th section of the fairway (dependent on the day/night time, visibility and ownership of the system),

$n_{ij}$  – reliability of the  $j$ -th navigational system in  $i$ -th section of the fairway (technical reliability),

$w_{ij}$  – integrity of the  $j$ -th navigational system in  $i$ -th section of the fairway (measure of confidence in the correctness of information provided by the system).

The conditions of safe ship operation in a fairway are described by a set of conditions for the safe operation of a maximum ship in  $i$ -th section of the fairway, which is written as [Gucma S. et al.: 2015]

$$W_i^f = [t_{yp}, L_o, B, T, H_{st}, V_p, C_p, H_i^f] \quad (12)$$

where

$t_{yp}$  – type of ‘maximum ship’,

$H_{st}$  – airdraft of ‘maximum ship’ (for passage under bridges),

$V_i$  – allowable speed of ‘maximum ship’ in  $i$ -th fairway section,

- $C_i$  – tug assistance in  $i$ -th section of the fairway, if it is required (required number and bollard pull of tugs),  
 $H_i^f$  – set of hydrometeorological conditions acceptable for a ‘maximum ship’ in  $i$ -th waterway section.

$$\mathbf{H}_i^f = [d/n, s, \Delta h_i, V_{wi}, V_{pi}, h_{fi}] \quad (13)$$

where:

- $d/n$  – allowable time of day (day or no restrictions),  
 $s$  – allowable visibility,  
 $\Delta h_i$  – allowable drop of water level in the  $i$ -th section of the fairway,  
 $h_{wi}$  – allowable wave height in  $i$ -th section of the fairway.

Conditions of the safe ship operation, defining the parameters of marine waterway system components, are defined separately for one-way and two-way traffic. For two-way traffic the conditions of safe fairway operation can be written as follows:

$$\begin{bmatrix} \mathbf{A}_i^f \\ \mathbf{N}_i^f \end{bmatrix} = \mathbf{f}_2 \begin{bmatrix} t_{yp}^{in}, L_c^{in}, B^{in}, T^{in}, V^{in} C_i^{in} \mathbf{H}_i^f \\ t_{yp}^{out}, L_o^{out}, B^{out}, T^{out}, V^{out} C_i^{out} \mathbf{H}_i^f \end{bmatrix} \quad (14)$$

whereby *in* means a ship entering the port and *out* refers to a departing ship.

**Turning basins**, like anchorages and fairways, are defined by two elements, which are a function of the conditions of safe operation of vessels manoeuvring therein:

$$\begin{bmatrix} \mathbf{A}^t \\ \mathbf{N}^t \end{bmatrix} = \mathbf{f}(\mathbf{W}^t) \quad (15)$$

The subsystem of the turning basin is defined similarly to the anchorage area subsystem, that is:

$$\mathbf{A}^t = \begin{bmatrix} \mathbf{D}^t \\ h^t \end{bmatrix} \quad (16)$$

the navigational subsystem, similarly to the fairway, i.e.:

$$\mathbf{N}^t = \begin{bmatrix} M_{oj} \\ m_j \\ n_j \\ w_j \end{bmatrix} \quad (17)$$

where:

$M_{oj}$  – accuracy of  $j$ -th navigational system (circular error of position).

The conditions of the safe ship operation in a turning basin are defined by the vector of maximum ship safe operating conditions:

$$\mathbf{W}^t = [L_o, B, T, \mathbf{H}^t] \quad (18)$$

while the set of allowable conditions of a turning manoeuvre can be written as follows:

$$\mathbf{H}^t = [d/n, s, \Delta h, V_w, V_c] \quad (19)$$

**A port basin with quays** is defined by three subsystems: area, navigation, quay, which are a function of the conditions of safe operation of vessel manoeuvring therein.

$$\begin{bmatrix} \mathbf{A}^{bp} \\ \mathbf{N}^{bp} \\ \mathbf{K}^{bp} \end{bmatrix} = \mathbf{f}(\mathbf{W}^{bp}) \quad (20)$$

The subsystem of the port basin is defined by a set of parameters, like in the case of turning area:

$$\mathbf{A}^{bp} = \begin{bmatrix} \mathbf{D}^{bp} \\ h^{bp} \end{bmatrix} \quad (21)$$

The navigation subsystem is defined similarly to that of fairways, except that the accuracy of the  $j$ -th navigational system is represented by the directional error of ship position, perpendicular to the berth line and the error of speed evaluation, the normal to the berth line.

The subsystem of berth and its equipment is described by a set of parameters:

$$\mathbf{K}_i^{bp} = \begin{bmatrix} T_i \\ k_i \\ b_i \\ E_i \\ q_i \\ v_i \end{bmatrix} \quad (22)$$

where:

- $T_i$  – type of the structure of  $i$ -th berth,  
 $k_i$  – length of the line of mooring of  $i$ -th berth,  
 $b_i$  – fender spacing at  $i$ -th berth,  
 $E_i$  – allowable kinetic energy absorbed by the fender at  $i$ -th berth,  
 $q_i$  – allowable reaction force on 1 m<sup>2</sup> of the fender front panel on  $i$ -th berth (allowable unit pressure on the hull),  
 $v_i$  – allowable speed of propeller streams at the bottom of the approach area.

The conditions for the safe operation of a ‘maximum ship’ manoeuvring in a port basin and coming to a given berth are written as a vector:

$$\mathbf{W}^{bp} = [r, L_o, B, T, H_{st}, F, M, M_{st}, n_h, U_h, \mathbf{H}^{bp}] \quad (23)$$

where:

- $r$  – type of maneuvers of the maximum ship coming to a given berth,  
 $F$  – lateral windage of ‘maximum ship’,  
 $M$  – main propulsion power of ‘maximum ship’,  
 $M_{st}$  – power of bow thrusters of ‘maximum ship’,  
 $n_h$  – number of tugs assisting the berthing of ‘maximum ship’,  
 $U_h$  – total bollard pull of tugs involved in berthing,  
 $\mathbf{H}^{bp}$  – the set of hydrometeorological conditions acceptable during manoeuvring of ‘maximum ship’ to a given berth.

Hydrometeorological conditions permitted for berthing manoeuvres of the 'maximum ship' are defined similarly to the case of fairway passage:

Specifying the conditions of safe ship operation in the port waterway system we distinguish the following berthing manoeuvres, also dependent on the number of propellers and thrusters of the ship [Clark I.C. 2009]:

- twin-propeller ships with bow thrusters – berthing without assistance,
- single-propeller ships with bow thrusters – berthing without assistance,
- single-propeller ships without thrusters – berthing without assistance.
- ships berthing with tug assistance.

Depending on the type of berthing ships the vector of safe operating conditions may be written in various ways (different set of parameters).

### PORT PARAMETER OPTIMIZATION: THE CASE OF OUTER CONTAINER TERMINAL CONSTRUCTION IN ŚWINOUJŚCIE

The optimization of parameters of a typical port including anchorage, approach channel, port entrance, turning basin and port basin is performed in two parts:

- optimization of parameters of the approach channel,
- optimisation of parameters of the port basin and turning basin.

The common characteristics of both optimisation procedures are:

- conditions of safe ship operation:

$$W^p = [L_p, B, T, H^p] \quad (24)$$

- the expected traffic intensity of ingoing vessels:

$$I = [I_p, I_m, I_s] \quad (25)$$

which is usually determined for vessel size groups: large ( $I_p$ ), medium ( $I_m$ ) and small ( $I_s$ ). This division depends on the projected port capacity and calling ships.

When the port parameter optimization problems are divided into two parts, port entrance is combined with approach channel in cases where ships manoeuvre on their own, or with port and turning basins if ships are to manoeuvre assisted by tugs.

The parameters of an anchorage are usually determined and optimized separately. Anchorage parameters, such as capacity (horizontal dimensions) and minimum depth are a function of the conditions of the safe operation of maximum ships at the anchorage, projected vessel traffic intensity and associated time of ship delays [Groenveld R., Hoek C.V.A. 2000].

For the purpose of optimizing parameters of a newly designed outer container port in Świnoujście, safe operation conditions for ingoing ships were determined as follows:

type    Lo    B    T

$$W^p = [\text{container ship, 400m, 60m, 13.0m, } H^p] \quad (26)$$

while the allowable hydrometeorological conditions for the entry of maximum ships into that port can be written as follows (no res. – no restrictions):

d/n    s    Δh    Vw    Vp    hf

$$H^p = [\text{no res., 1Nm, 0.5m, 10m/s, 1knot, no res.}] \quad (27)$$

To determine the parameters of the outer container port in Świnoujście two optimisation problems were solved:

1. optimization of the port entrance parameters (with tugs), turning area and port basin including the berth,
2. optimization of the approach channel parameters.

Such a set of problems results from a differently formulated objective function and different methods used to solve them.

#### The optimization of parameters: port entrance, turning basin and port basin with berths of the Outer Container Terminal in Świnoujście.

Objective functions for this type of sea waterways system can be written this form [Gucma S., Ślęczka W. 2015; Gućma S. et al. 2015]:

$$Z = (A + N + S) \rightarrow \min \quad (28)$$

with the constraints:

- safety of ship manoeuvring (one of two),  
– condition of navigational safety:

$$\left. \begin{array}{l} \mathbf{d}_{lkz(1-\alpha)} \subset \mathbf{D} \\ \wedge \quad h_{xy} \geq T_{xy} + \Delta_{xy(1-\alpha)} \\ p(x,y) \in \mathbf{D}(t) \end{array} \right\} \quad (29)$$

- condition of the navigational risk:

$$R_i \leq R_{akc} \quad (30)$$

- safety of ship's mooring.  
– condition of the allowable wave height:

$$h_w \leq h_{w akc} \quad (31)$$

where:

- Z – cost of the construction and operation of the waterways system,
- A – cost of the construction (reconstruction) of a waterway,
- N – construction cost of ship position determination subsystem (navigation systems),

- $S$  – ship’s operating costs associated with the passage through the waterway (waiting for passage, pilotage, tug assistance, etc.),
- $D_i(t)$  – navigable area in  $i$ -th section of the waterway (condition of safe depth at instant  $t$  is satisfied),
- $d_{ikz(1-\alpha)}$  – safe maneuvering area of  $k$ -th ship performing a maneuver in  $i$ -th section of the waterway in  $z$ -th navigational conditions determined at the confidence level  $1-\alpha$ ,
- $R_i$  – navigational risk when passing  $i$ -th section of the waterway,
- $R_{akc}$  – acceptable navigational risk,
- $h_{xy}$  – area depth at point  $(x, y)$ ,
- $T_{xy}$  – ship’s draft at point  $(x, y)$ ,
- $\Delta_{xy(1-\alpha)}$  – underkeel clearance at point  $(x, y)$  determined at the confidence level  $1-\alpha$ ,
- $h_w$  – wave height at berth,
- $h_{wakc}$  – wave height acceptable for a particular vessel at berth.

The costs of construction of the port waterway system of the outer container terminal in Świnoujście depend on the size of the navigable area ( $D$ ), depth of that area ( $h_{xy}$ ) and the sheltering breakwater length ( $l_{br}$ ), therefore we can write:

$$Z = F(D, h_{xy}, l_{br}) \rightarrow \min \quad (32)$$

In the particular case of Świnoujście Outer Container Terminal the area depth was determined by the depth of Pomeranian Bay and accepted as equal to  $h_{xy} = 14.5$  m. In this connection the objective function can be written as:

$$Z = F(D, l_{br}) \rightarrow \min \quad (33)$$

with two constraints:

- safety of manoeuvring ships:

$$d_{i(1-\alpha)} \square D_i \quad (34)$$

- safety of mooring ships:

$$h_w \leq h_{wakc} \quad (35)$$

The parameter optimization of the Outer Container Terminal made use of a method specially developed for the purpose – a two-stage simulation method of optimization [Report...2017]. In this method the safe maneuvering area ( $d_{ikz(1-\alpha)}$ ) was determined on the basis of simulation test results conducted on full mission bridge simulators with 3D visualization, operated at the Marine Traffic Engineering Centre in Szczecin. Wave heights at berths were determined on the basis of wave analysis carried out using mathematical models developed at the IBW PAN (Polish Academy of Sciences).

Figure 2 presents the optimal shapes and parameters of the entrance, turning basin and berths of the Outer Container Terminal in Świnoujście.

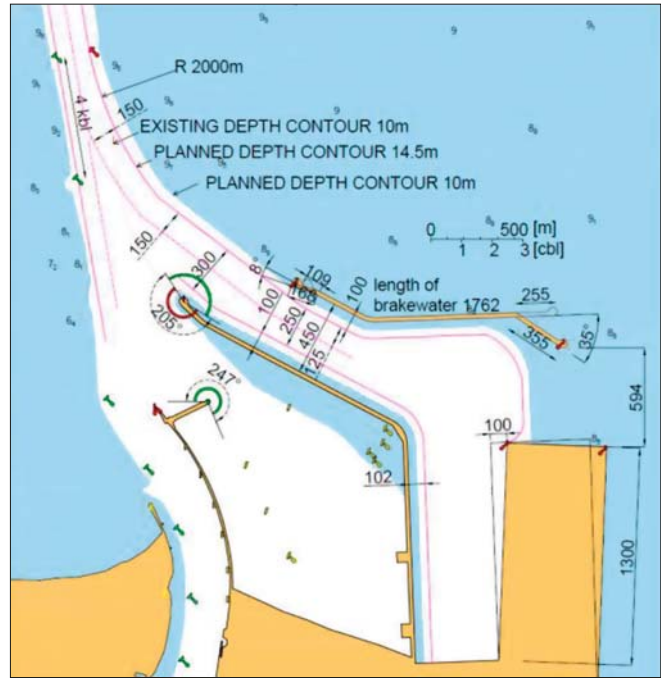


Fig. 2. Outer Container Terminal in Świnoujście dimensioned as a result of parameter optimization of the entrance, turning area and the mooring basin (navigable area  $D$  is bounded by a red line) [Report Maritime University of Szczecin (2017): Detailed specification of parameters and conditions for safe operation of the Świnoujście Outer Container Port.]

### The optimization of parameters of the approach channel leading to the Outer Container Terminal in Świnoujście.

The objective function applied in optimisation problems related to parameters of a fairway composed one-way and two-way sections is to minimise the cost of its construction and operation costs accounting for delays of ships for each size group and projected traffic intensity can be written as follows [Gucma S. et. al. 2015; Gućma L. et. al. 2016]:

$$Z_r = (A_r + N_r + K_s) \rightarrow \min \quad (36)$$

with the constraints dependent on the type of fairway traffic:

- one-way fairway,

$$\left. \begin{aligned} D_j &\geq d_{j(1-\alpha)} + 2d_r \\ h &\geq T + \Delta \end{aligned} \right\} \quad (37)$$

- two-way fairway,

$$\left. \begin{aligned} D_j &\geq d_{j(1-\alpha)}^{in} + d_{j(1-\alpha)}^{out} + d_r^{in} + d_r^{out} + d_r^s \\ h &\geq T + \Delta \end{aligned} \right\} \quad (38)$$

- $Z_r$  – annual construction costs of waterway (fairway) system and annual costs of ship delays,
- $A_r$  – annual depreciation of the fairway (construction costs divided by 30 years of depreciation period),
- $N_r$  – annual depreciation of non-autonomous navigation systems (construction costs of these systems divided by 15 years of depreciation period),

- $K_s$  – annual delay costs for ships using the designed fairway,
- $D_j$  – available width of the fairway at the bottom at  $j$ -th point of the fairway centre line (the condition of safe depth at instant  $t$  is satisfied),
- $d_{j(1-\alpha)}$  – safe fairway width the at bottom of a ‘maximum ship’ manoeuvring in preset navigational conditions at  $j$ -th point of fairway centre line, determined at the confidence level  $1-\alpha$ ,
- $d_r, d_r^{in}, d_r^{out}$  – margin of ship’s manoeuvring areas allowing for the bank effect,
- $d_r^s$  – traffic separation zone allowing for ship suction effect,
- $h$  – depth of the fairway,
- $\Delta$  – underkeel clearance.

Annual costs of the delays of ships using a specific variant of the fairway design are calculated from this relationship:

$$K_s = \sum_{l=1}^n l_l \cdot t_l \cdot k_l \quad (39)$$

where

- $l_l$  – projected number of ships in  $l$ -th group using the designed waterway within one year,
- $t_l$  – mean time of delay of  $l$ -th group ship,
- $k_l$  – unit costs of delay of  $l$ -th group ship.

Annual costs of delays of ships using the real variant of the designed waterway construction are calculated by the method of computer simulation of vessel traffic flows (for 10 year vessel traffic forecast).

The solution of the objective function resulted in an optimal division of the approach channel into the following sections (Fig. 3):

- one-way traffic, 2.1 km ÷ 11.0 km of the fairway,
- two-way traffic 11.0 km ÷ 35.6 km of the fairway (buoy N2).

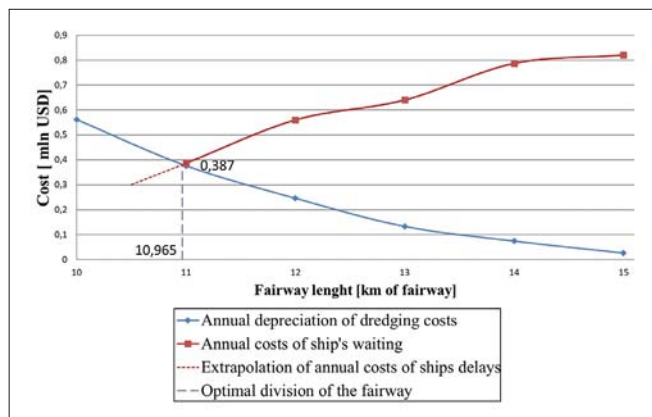


Fig. 3. The optimal length of two-way approach channel to Świnoujście (from buoy N2 to 11 km point of the channel) [Report Maritime University of Szczecin (2017): Detailed specification of parameters and conditions for safe operation of the Świnoujście Outer Container Port.]

The navigable width at the bottom in the approach channel to the Outer Container Terminal in Świnoujście determined by empirical relationships [PIANC 2014; Zalewski P. 2012] is, respectively:

- one-way section (2.1 km ÷ 11.0 km)  $D = 220$  m,
- two-way section (11,0 km ÷ 35,6 km of)  $D = 500$  m.

## SUMMARY

The article defines the port as a system composed of set of various waterways (anchorage, approach channel, entrance to the port, turning basin, and port basin with berths). The conditions have been specified for safe ship operation in port waterway system and in particular types of port waterways. In this connection, relationships between the parameters of individual types of waterway and conditions of safe operation of ships have been defined. Based on these relations, the objective function of two port optimization problems has been calculated.

- optimization of parameters of the port entrance, turning basin and port basin with berths,
- optimization of parameters of the approach channel.

The optimal division of an approach channel into one-way and two-way sections is made by the method of computer simulation of vessel traffic flows.

Optimal parameters of the port entrance, turning basin and port basin are determined using dedicated two-phase simulation optimisation methods, in which simulation experiments are carried out on a ship-handling simulator with 3D visualization.

The developed methods have been used to determine optimal parameters of the Outer Container Terminal currently under construction in Świnoujście, where the annual container handling capacity is estimated at 1.5 million TEU. The port is expected to operate ocean-going container ships with a length overall  $L_c = 400$  m and breadth  $B = 60$  m.

## REFERENCES

1. Gucma L., Bąk A., Sokołowska S., Hajduk J. (2016): *Stochastic model of ship traffic congestion in waterways applied to determine the influence of Liquefied Petroleum Gas tanker introduction on ship traffic on the Świnoujście–Szczecin waterway*. Scientific Journal of Maritime University of Szczecin No. 45 (117), 2016.
2. Gucma S. (2014): *System approach to sea waterways*. Scientific Journal of Maritime University of Szczecin No. 38(110)2014.
3. Gucma S. (2015): *Port basin as waterway system component*. Scientific Journals of the Maritime University of Szczecin, No. 41(113)2015.
4. Gucma S. et al. (2015): *Morskie Drogi Wodne. Projektowanie i eksploatacja w ujęciu inżynierii ruchu morskiego*. Fundacja Promocji Przemysłu Okrętowego i Gospodarki Morskiej, Gdańsk.

5. Gucma S., Ślącza W. (2015): *Methods for optimization of sea waterway systems and their application*. Polish Maritime Research, No. 3(87)2015 Gdańsk.
6. PIANC (2014): *Harbour Approach Channels Design Guidelines*. PIANC Report No. 121–2014 PIANC Secretariat General. Bruxelles.
7. Report Maritime University of Szczecin (2017): *Detailed specification of parameters and conditions for safe operation of the Świnoujście Outer Container Port*.
8. Thoresen C.A. (2014): *Port Designer's Handbook ICE Publishing*. London.
9. Tsinker G.P. (2004): *Port Engineering, Planning, construction, Maintenance, and Security*. John Wiley and Sons, INC.
10. Zalewski P. (2012): *Algorithms for analytical method of waterway design parameters determination*; Scientific Journals of the Maritime University of Szczecin No. 29(101)2012.
11. Groenveld R., Hoek C.V.A. (2000): *A simulation tool to assess nautical safety in port approaches*, Seminar of the Permanent Commission for Development and Cooperation of PIANC, Argentina.
12. International Maritime Organization (IMO, 2002): *Resolution Standards for Ship Maneuverability*, MSC.137(76) 4.
13. Clark I.C. (2009): *Mooring and anchoring ships*, Vol 1 (Principles and Practice) The Nautical Institute, London.

## CONTACT WITH THE AUTHORS

**Stanisław Gucma**

*e-mail: s.gucma@am.szczecin.pl*

Maritime University of Szczecin  
 Wały Chrobrego 1-2  
 70-500 Szczecin  
**POLAND**

# A CONCEPT DESIGN OF DIESEL – HYDRAULIC PROPULSION SYSTEM FOR PASSENGER SHIP INTENDED FOR INLAND SHALLOW WATER NAVIGATION

Czesław Dymarski  
Gdańsk University of Technology, Poland

## ABSTRACT

*This paper presents an analysis of environmental and technical conditions necessary for working out a possibly most favourable propulsion system for a two – segment passenger ship intended for navigation between Berlin and Kaliningrad. There are presented various types of propulsion systems for small ships as well as analyzed their possible applications and consequences. In this work there were taken into account system’s reliability, efficiency, dimensions, mass and costs of manufacturing, assembling and possible replacing the system components as well as an impact on maneuverability and natural environment. With taking into account the above mentioned criteria it was finally found that the diesel-hydraulic system fitted with two azimuthal ducted solid propellers is the most favourable. There are also presented a schematic propulsion and control diagram, three-dimensional arrangement drawing of system components as well as assembly drawing of the designed azimuthal propulsion system.*

**Keywords:** ship propulsion systems, hydraulic drive and control, azimuthal propulsion systems

## INTRODUCTION

In the contemporary world economy, water transport, especially intercontinental one plays crucial role as it makes practically unlimited transport of different goods in different forms under the lowest cost and possibly lowest unfavourable influence on natural environment, possible. The favourable features deal also, however to a lesser degree, with inland waterway transport. In the West European countries this mode of transport has a high share in total amount of transport. In Poland, because of insufficiently developed inland waterways, this mode of transport plays a marginal role, and the worse, its share in the overall goods transport turnover in the years 2000–2014–2015 decreased from 0,8 to 0,4% and 0,3%, respectively[1]. However it should be hoped that owing to EU transport policy a chance appears for restoring proper navigation features of Polish inland waterways and an appropriate position of Polish inland waterways navigation, which would mitigate the

today negative consequences of transport development, i.e. a distinct domination of car transport both in carrying goods and passengers.

An European document presently in force which indicates directions for transport development, including inland waterways transport, is the so called “White Book” [2], in which crucial challenges for the transport system up to 2050 are diagnosed. There is taken into account a. o. the necessity of unification of transport systems of West and East Europe, limitation of dependence on crude oil as well as reduction of emission of greenhouse-effect gases. Moreover, there is also postulated to shift long-range road transport of over 300 km in distance to other transport modes, e.g. water or railway transport, in the amount of 30% up to 2030.

The present Polish government plans to build in Poland a network of “water highways”. The international waterways have to be developed on the rivers: Vistula, Bug, Oder, Warta and Notec. Cost of the undertaking is estimated at abt. 70–90 billion zlotys. On 6.03.2017, Andrzej Duda, the

Polish President signed the ratification act concerning the European agreement on the matter of main inland waterways of international importance (AGN). The convention makes it possible for its partners to apply for river development funds. Hence, favourable conditions are formed to undertake works on improving technical state of waterways as well as designing and building modern, more efficient transport means, more suitable for navigation over Polish inland waterways.

It should be underlined that already in the years 2003–2006 similar research and design projects were carried out by the team of the Ocean Engineering and Ship Technology Faculty, Gdansk University of Technology, in the frames of the EU-supported EUREKA project INCOWATRANS – E!3065 (*A NEW GENERATION OF ENVIRONMENT FRIENDLY INLAND & COASTAL SHIPS FOR POLISH EAST-WEST WATERWAYS*).

The project was conducted in cooperation with Warsaw University of Technology and Wrocław University of Technology, Polish Maritime Institute, SINUS design office as well as the firm INFERT GmbH Rostock. And, after initial analyzes Gdansk University of Technology was assigned to work out a design project of two-segment passenger ship intended for inland waterways navigation on the route between Berlin and Kaliningrad.

One of the most important and simultaneously difficult tasks was to design a propulsion system most suitable for the ship in question. A decisive difficulty of the task resulted from the fact that the depth of Polish sections of the intended route did not exceed 1,2 m in some spots. To solve the problem it was necessary to work out and analyze several variants of the system in order to select finally the most appropriate. In view of the fact that since that time the state of the waterways has not been improved and the development plans still cover also inland waterways transport, this author decided to remind the systems which were earlier considered the most favourable in the respect of many important criteria, and to analyze their usefulness.

## ENVIRONMENTAL AND TECHNICAL CONDITIONS FOR THE PROPULSION SYSTEMS

While designing inland navigation ships it is necessary to be aware of technical state of an intended navigation route, particularly its depth, dimensions of locks, minimum clearance under bridges to be met along the route as well as other factors, including ecological. The enumerated factors decisively impacts construction of the ship and its propulsion and steering systems, in particular.

For the selected route, apart high environmental requirements, values of three most important characteristic parameters were as follows:

- minimum water depth – 1,2 m,
- length of the shortest lock – 60 m,
- minimum under bridge clearance over mean water level – 3,87 m.

With taking into account the above data, a general concept of the ship consisting of two mutually connected segments, namely: hotel barge and its pusher of the following technical parameters, was worked out:

- length and breadth of each segment  $L \times B = 56 \times 9$  m,
- draught  $T = 1,0$  m,
- ship displacement at the draught  $T = 1$  m  $D_{1.0} = 440$  t,
- designed speed of the ship at the draught  $T = 1$  m  $V = 14$  km/h,
- effective propulsion power demand  $P = 300$  kW.

## ANALYSIS OF THE CONSIDERED PROPULSION SYSTEMS AND SELECTION OF THE MOST FAVOURABLE VARIANT

The very small draught of the ship is an important limitation in selecting an appropriate main propulsion system. The condition practically eliminates a system with cycloidal propellers placed under ship hull, whereas it rather prefers

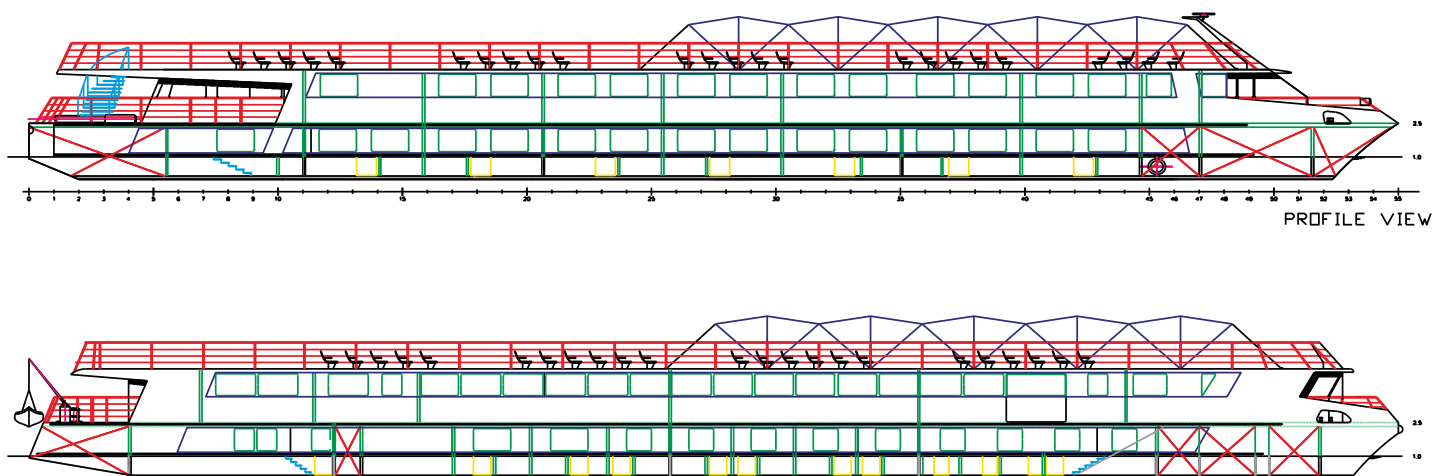


Fig. 1. Concept design of the two-segment inland navigation ship [3]

waterjet propulsion which provides high manoeuvrability properties without danger of hitting water bottom with screw propeller blades. Such propulsion system is not favourable from the point of view of ecology. The sucking out of large amount of water from under ship bottom and fast discharging it off cause that the water bed structure and surrounding biological life may be damaged. The factor is as much important that the designers decided to resign from applying the waterjet propulsion.

Therefore the systems fitted with a typical screw propeller were considered. When applying such typical system with a single screw propeller working in under-cavitation zone its diameter necessary to execute the ship's tasks should be greater than 1.4 m. In view of the small draught of the ship this diameter value is not acceptable. Hence it was concluded that to be able to fulfil the assumptions it is necessary to apply a twin-propeller system. Such solution would allow to effectively reduce diameters of screw propellers to 0.83–0.85 m under the condition of placing them within Kort nozzles, maintaining their capacity of transmitting the assumed power. Based on the preliminary documentation of the unit in question it turned out that the outer diameter of the nozzle would reach 1,045 m, which means that it would be somewhat greater than the nominal value of ship draught of 1 m, but it seems not to be a significant obstacle if only an appropriate forming the ship hull is used.

Such solution has many merits. The twin-propeller system ensures a greater manoeuvrability and reliability. Placing the propellers in nozzles substantially reduces danger of hitting the waterway bed with propeller blades, which usually results in blade damage and necessity of replacing the propeller. Such system also mitigates unfavourable impact of propeller race onto waterway bed.

A next issue which should be analyzed was selection of an optimum type of the propeller, namely, whether to use a solid screw propeller or that with controllable pitch. In the case of driving the propeller with a diesel engine through a reduction gear the application of a controllable pitch propeller makes engine operation with practically constant and optimum rotational speed possible in different navigation conditions, owing to this efficiency of the whole system is the highest. Though it is paid with a much greater complexity of propeller boss mechanism and necessity of application of a separate hydraulic system for driving and controlling the mechanism. This enlarged complexity of the propellers results in dropping their reliability and increasing costs of investment and operation.

An increased reliability and reduced complexity of the system may be reached by using a constant pitch propeller. However for the maintaining of a relatively high efficiency of the propulsion system it is necessary to ensure possibly fluent change, in value and direction, of propeller shaft rotation, that may be as simple as possible executed with the use of a propulsion system fitted with a hydrostatic or electric gear. However it should be stressed that in such gears energy form change occurs two times: first from mechanical energy form on combustion engine shaft to hydraulic or electric one and

then back to mechanical one on propeller shaft. Unfortunately, every change in energy form is associated with a dozen or so percent of energy loss, but there are also reached considerable profits. One of them is, in particular, easiness in transmitting electric energy as well as hydraulic one, that eliminates the necessity of applying long propulsion shafts and provides a large freedom in arranging, in the most favourable way, combustion engines and other heavy power plant equipment. This is a very valuable feature especially for the designed ship intended for navigation in shallow inland waters because it allows to distribute uniformly loads over ship hull and avoid the undesired overloading of ship stern.

Another profits are available by substituting the solid nozzle with rotatable one.

It allows to resign from a traditional rudder and, as a result, to reduce dimensions and weight of steering devices at simultaneous improving ship's manoeuvrability. Application of hydraulic drive and control to nozzle rotation mechanism is most profitable, it means such solution as that commonly used for ship steering devices. It results from the necessity of achieving a precise but relatively slow motion of laying rudder blade or nozzle, maintaining a perfect but simple protection against overloading. The driving of rudder post may be obtained in a simple and cheap way by using hydraulic cylinders and lever systems or complex and more expensive, but compact, mechanisms with hydraulic motors, planetary gear and friction brake. Nevertheless this type of mechanism, but fitted with electric motors, can be found also in diesel–electric propulsion systems.

The next step aimed at possible reduction of the area occupied by power plant devices and their mass is the application of two azimuthal propellers (rotatable thrusters) with round rotation angle ( $360^\circ$ ) of propeller column. Such solution is advantageous because it leads to a higher manoeuvrability of the ship and elimination of relatively long and slender horizontal propulsion shafts which usually require an additional support bearing outside the ship hull.

In view of the low water depth of the discussed navigation route of the designed ship, it was decided to place the propellers in a simple cage structure fixed with the ship hull (Fig. 2) in order to better protect them against damaging in case of hitting the river bed. In the middle of the lower transverse beam of the structure, the body and bushing of the slide bearing of the rotatable propeller column are placed (Fig. 4).

Also, different variants of energy sources were considered. It was concluded that the basic, most profitable, reliable and commonly used source of energy is a light-oil combustion engine. Application of a hybrid propulsion system combined with an additional supply source of energy, e.g. electricity from photovoltaic cell batteries, is not very effective in our climate and it would moreover require to complicate greatly the propulsion system and lead to additional costs and space [5]. Possible application of a compressed gas fuel (methane) was also considered, but one resigned of the alternative in view of necessity of keeping gas in pressure cylinders, which is potentially dangerous.

Based on the above presented factors and conditions it was decided to work out concept designs of two, most technically justified (acc. this author's opinion) solutions of the propulsion systems fitted with two rotatable thrusters, namely:

- diesel-electric system with typical asynchronous squirrel-cage electric motors and frequency converters which make it possible to fluently change rotational speed of a constant pitch screw propeller, and
- diesel-hydraulic system with hydrostatic gear.

The comparative analysis of both the above specified systems for concretely chosen particular units and elements with taking into account their efficiency, mass, dimensions and investment cost was presented in the work [6]. As a result of this analysis it was concluded that a diesel-hydraulic system presented in the further part of this work would be more favourable.

## CONCEPT DESIGN OF DIESEL-HYDRAULIC PROPULSION SYSTEM FOR PUSHER

Below, in Fig. 2 there is presented a schematic diagram of a hydraulic drive and control system with description its units and elements but without giving precise data on each of the selected units.

The system consists of two identical mutually independent systems. Each of them is driven by means of the high-speed piston self ignition engine I, which, through the elastic coupling II, drives the system of the two oil pumps 2 and 3, and also, through the mechanical gear III, the electric generator IV and the oil pump 4.

The pump 3 is a multi-plunger variable-delivery pump, which, together with the constant delivery pump 2 fixed with it, and the control block V associated with it, constitutes the main source of energy oil which supplies the constant absorbing capacity hydraulic motor 11. The motor, through the toothed bevel gear, drives the constant pitch propeller placed in the rotatable nozzle of the column of the azimuthal propeller XIV. In this case the application of the constant pitch propeller was justified due to possible continuous control of rotational speed and direction of the hydraulic motor. This is executed by changing the capacity and oil pressing direction of the pump 3. To this end, there is used the hydraulic servomechanism of the pump, which is consisted of the hydraulic actuator 5 and the electromagnetically controlled proportional distributor 6. The control system of the variable delivery pump 3 is supplied from the constant delivery pump 2. The oil from this pump is delivered through the non-return valve 27 to the filter block behind which it is distributed into four branches:

- to supply the proportional distributor 6 in the block VI,
- to supply the block VII intended for refreshing and ensuring the main system of the pump,
- to limit the lower value of control pressure by connecting with the overflow valve 15,
- to limit the pump capacity to protect the block VIII against overloading.

During regular operation the filtrated oil of an appropriate temperature flows from the control system of the pump through one of the blocks VII and runs into an instantaneously low pressure branch of the main circuit of the variable-capacity pump. Simultaneously, from this branch the same amount of oil, now of a higher temperature, must be removed. The oil flows out through the three-position distributor 10, overflow valve 19 and filter 21 into the oil tank 1. The distributor 10 is controlled by the pressure in the branches of the main circuit of the pump and during its operation always connects the low-pressure branch with the overflow valve 19 whose opening pressure is set up to a value a little lower than that on the overflow valve 15.

The overflow valves 18 located in the block VII serve as emergency valves, preventing both the main branches of the pump against overpressure.

The ship propeller of each of the azimuthal propellers is driven, through the toothed intersecting axis gear of constant reduction ratio, by the hydraulic constant absorbing capacity motor 11 located in the propeller ventral pod. This motor is placed vertically in the ship hull over the propeller and coupled directly with the vertical shaft of the above mentioned gear.

The ship steering functions are executed by rotating the propellers by an arbitrary angle in respect of vertical axis. To this end, there were used two hydraulic constant absorbing capacity motors 12 driving the propeller column through toothed reduction gears. The motors are fed from the constant capacity pump 4 through the non-return valve 27 and the electromagnetically controlled three-position distributor 7 and the block XII with the controlled non-return valves 13. The valves prevent the propeller column against rotation under external loads in case of a pressure drop in the system. If the above mentioned external load appears excessively large, e.g. as a result of hitting the river bed, then one of the two overflow valves 14 located in the block XIII will be opened, that will make the propeller rotation at the rotating moment greater by abt. 20% from the rated one, possible.

The application of two motors and the reduction gear was mainly justified by a desire of reducing dimensions so as to make it possible to place all the three motors in one common plane with maintaining the selected crown bearing of the propeller column. Since in the symmetrical system two smaller motors allow to greatly reduce the loads and, as a result of that, also the dimensions of the toothed gear. The motors are supplied in parallel through the dividers 9 which have two-position and are electromagnetically controlled. They allow to cut out hydraulically a given motor from supply circuit while simultaneously connecting both of its supply pipes together. Owing to this, it is possible to drive the propeller rotation mechanism by only one hydraulic motor while the other one serves as a pump operating for overflow at a slight loss of power. It should be however stressed that the possibly available rotation moment of the propeller will be lower by almost a half from that rated, however it seems to be sufficient for ship course steering during regular long-range navigation.

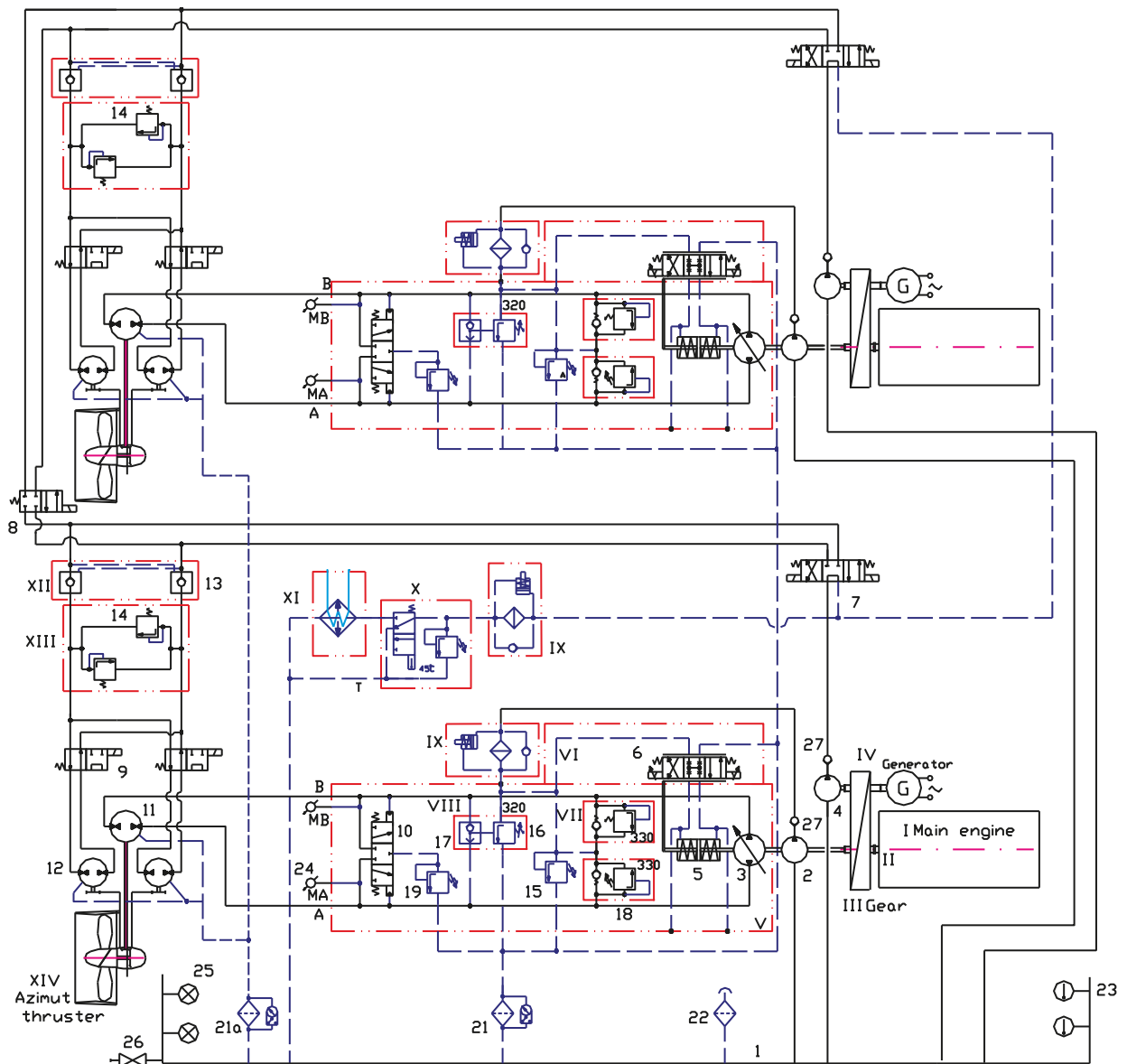


Fig. 2. Schematic diagram of a drive and control system with hydrostatic gear, intended for inland waterway ship

In view of that the duration time of manoeuvres with the use of rotation of the propeller column is only a small part of the whole navigation time, the circuit in question was used also for purifying and cooling the oil in the tank. In the time between manoeuvres the distributor 7 is in the middle position cutting off this way hydraulically the propeller column driving motors from supply and directing all the output of the pump 2 to the block IX – for oil filtering, block X – for temperature control and possibly to the block XI – for oil cooling and further to the tank 1. During execution of manoeuvres the oil reconditioning process is also carried out, but this is the oil coming back from the hydraulic motors 12 which flows into the above mentioned blocks IX, X and XI.

The circuits of the propeller column rotation mechanism of both the propulsion systems can be mutually connected by changing the set position in the two-position electromagnetically controlled distributor 8. This way, it is made possible to control rotation of the both propellers, but

with the speed lower by a half, also during operation of only one propulsion system.

The oil tank 1, common for the both propulsion systems, is equipped with the inlet filter 22, temperature sensors 23, oil level gauges 25 and cut-off valve 26 for oil discharging. Oil leakages from hydraulic motors are led through the outflow filter 21 to the tank 1.

## ARRANGEMENT OF PROPULSION SYSTEM'S CRUCIAL UNITS

The arrangement of particular units of the worked out propulsion system and other crucial power plant elements are schematically shown in Fig. 3.

To simplify the drawing, the oil piping and other minor equipment elements especially those of hydraulic oil tank including various valves, filters, oil cooler and temperature and oil level sensors, were omitted.

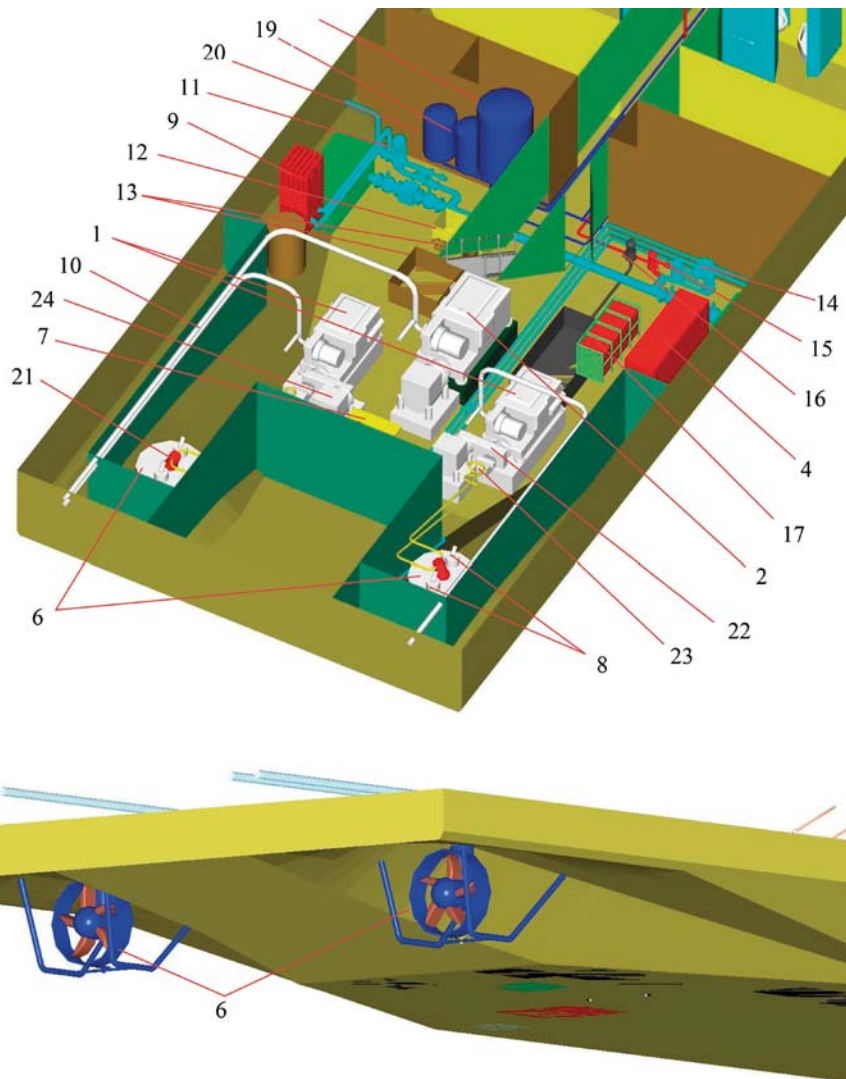


Fig. 3. Simplified arrangement drawing of crucial units of diesel-hydraulic propulsion system as well as other power plant devices of an inland navigation ship.

- Notation: 1 – Combustion engines, 2 – Electric generating set, 4 – Cabinets with electric equipment, 6 – Azimuthal propellers, 7 – Hydraulic oil tank with supply system, 8 – Hydraulic motors with planetary gears for driving rotation mechanism, 9 – Central cooler, 10 – Exhaust gas pipes, 11 – outside water pump, 12 – Lubricating oil tank and transport pump, 13 – Fuel oil tank and transport pump, 14 – Ballast pump, 15 – Fire pump, 16 – Bilge pump, 17 – Electric accumulator batteries, 18 – Hydrophore tank, 19 – Electric water heater, 20 – Water heater, 21 – Hydraulic propeller driving motors, 22 – Mechanical reduction gear, 23 – Hydraulic variable capacity pump, 24 – Electric generating set

## PRELIMINARY DESIGN OF AZIMUTHAL PROPELLER WITH DUCTED SOLID SCREW PROPELLER

The designing of azimuthal propeller was one of the difficult design tasks during execution of this project. Initially it has seemed that an appropriate propeller would be available on the market, but it soon has turned out that the available azimuthal propellers could not fulfil the assumed technical conditions for the ship in question. It was then decided to design a special propeller for that ship with taking into account rules of classification societies, first of all of Polish Register of Shipping. In a short time was prepared a preliminary design of such propeller whose cross-sectional drawing is presented in Fig. 4. Two constructional versions which only slightly differ to each other in form and transverse dimensions of elements for fastening the propeller in the ship's

hull, were prepared. The variant shown in Fig. 4 is adjusted to its assembling from the top. For this reason in the propeller fastening area suitably large openings in the deck and bottom of the ship should be provided in order to make it possible to lower the propeller with the use of a line into its fastening place. After installation of the propeller, a removable cover will be mounted on the opening in the deck. The other variant of the propeller is intended for the installing it upward from an outboard position below the ship bottom. Its merits consist in smaller diameters of assembly plate and opening in the ship bottom as well as a lack of making any opening in the deck. An important drawback is a much more difficult assembling operation for which ship docking is necessary with a properly large distance between dock's deck and ship's bottom, as well as necessity of preparation of a removable transverse beam in the cage protecting the propeller, in which the slide bearing of the propeller column with the nozzle is fastened.

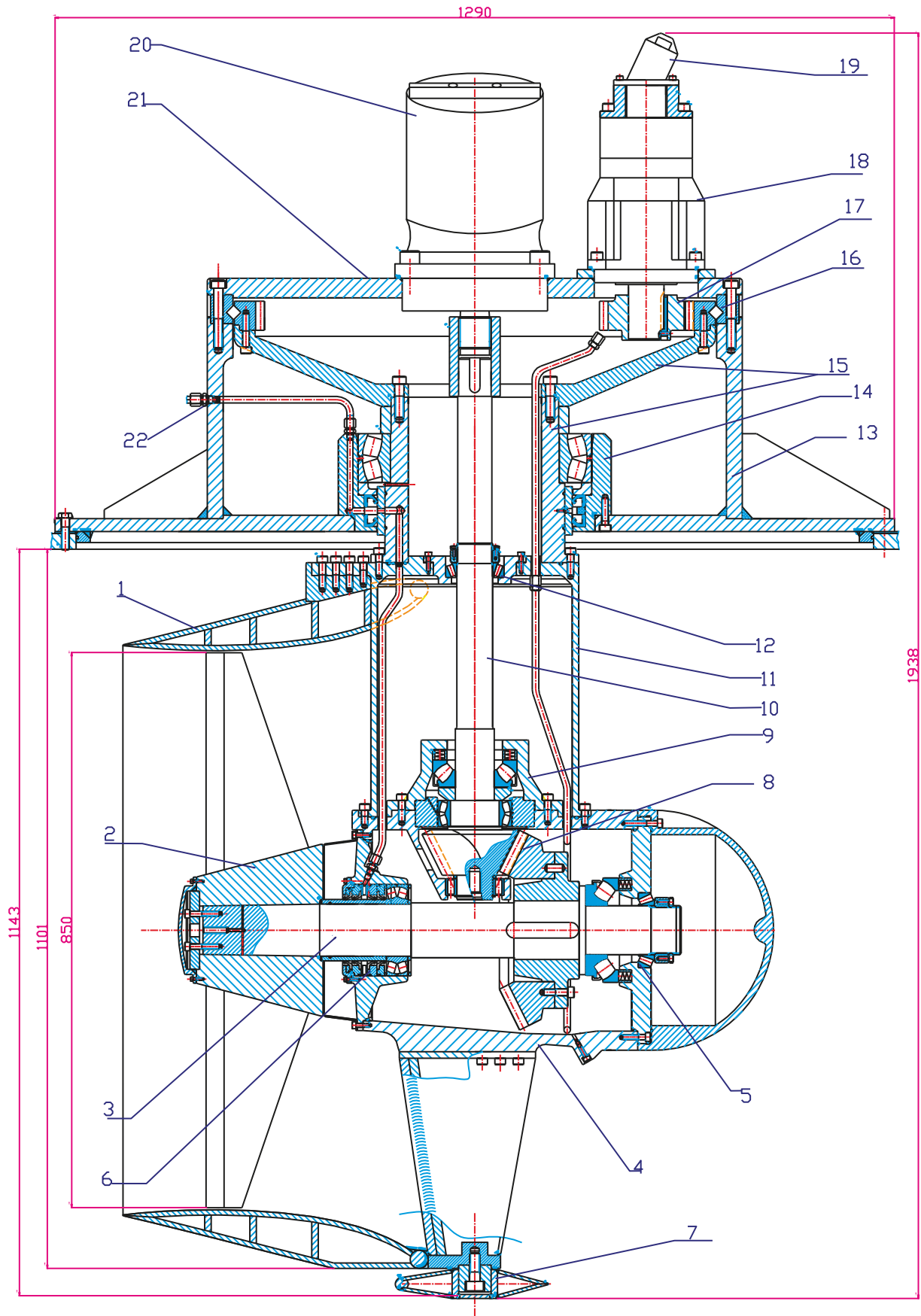


Fig. 4. Assembly drawing of the designed azimuthal propeller with solid screw propeller and hydraulic drive, showing its major units [4].  
 Notation: 1 – nozzle, 2 – screw propeller, 3 – propeller shaft, 4 – pod, 5 – front shaft bearing unit, 6 – rear shaft bearing and sealing unit, 7 – nozzle bearing in protection beam, 8 – angular gear, 9 – lower propulsion shaft bearing unit, 10 – propulsion shaft, 11 – lower part of the column, 12 – upper propulsion shaft bearing unit, 13 – propeller body, 14 – column bearing unit, 15 – upper part of the column, 16 – crown bearing, 17 – column drive bearing, 18 – planetary gear, 19 – column drive hydraulic motor, 20 – propeller drive hydraulic motor, 21 – body cover, 22 – lubrication system piping

## FINAL REMARKS

The concept design, presented in this paper, of the propulsion system for the pusher of two-segment passenger ship intended for Berlin–Kaliningrad waterway route was selected during a final seminar held in 2007 with participation of all consortium members, project reviewers and representatives of Bydgoszcz Shipping Co. However the project was not finally put into execution due to a lack of financial resources. Today, as already mentioned, the dynamic economic development of Poland and resulting fast increase of demand for transport services have caused from the side of the Authority a greater interest in using inland waterways transport.

It should be also stressed that many research centres and technical universities have conducted investigations on developing construction and operation of hydraulic propulsion units and elements with taking into account properties of working medium [7], [8], as well as changeable service conditions, including ambient temperature [9], [10]. There have been also conducted investigations on more and more efficient propulsion systems, including hybrid diesel-electric ones intended for inland navigation ships. Even to mention the design projects and tests of two small ships with electric propulsion systems fed from photovoltaic cells, recently worked out by a team of Ocean Engineering and Ship Technology Faculty, Gdansk University of Technology, [11], [12].

Summing up, this author hopes that the information presented in this paper may be helpful for designers and researchers of novel inland navigation ships in their making important design decisions.

## REFERENCES

1. *Inland waterways transport in Poland* in 2016 ( in Polish). Signalling issue. Polish main statistical authority. Warsaw, 25 August 2017.
2. White Paper 2011. *Roadmap to a Single European Transport Area – Towards a competitive and resource efficient transport system*, European Commission, Brussels, 28 March 2011.
3. W. Hołowko, J. Michalski, K. Rosochowicz: *A design concept of ecological tourist – passenger ship intended for Berlin-Królewiec (Kaliningrad) inland waterway service*. Polish Maritime Research, Special Issue 2006/S2.
4. Dymarski Cz.: *A propulsion system with hydrostatic gear intended for inland navigation ship* (in Polish). In monograph on “Research, construction and production of hydraulic systems”, Cylinder 2006, 26–28 September 2006.
5. Dymarski Cz., Rolbiecki R., Litwin W., Piątek D.: *A concept design of propulsion system and main installations of inland navigation ship*. A chapter of the final report on the project INCOWATRANS – 2006.
6. Dymarski Cz., Rolbiecki R.: *Analysis of two Design Kinds of Propulsion for an Inland Vessel*. Explo-Diesel & Gas Turbine ‘2008’, 5<sup>th</sup> International Scientifically-Technical Conference.
7. Śliwinski P.: *The influence of water and mineral oil on mechanical losses in the displacement pump for offshore and marine applications*. Polish Maritime Research. Vol. 25, S1 (97), 2018.
8. Śliwinski P.: *The influence of water and mineral oil on volumetric losses in a hydraulic motor*. Polish Maritime Research, Vol. 24, SI (93) 2017.
9. Jasinski R.: *Influence of design of hydraulic components on their operation in low ambient temperatures*. Key Engineering Materials, Vol. 490, 2012.
10. Jasinski R.: *Problems of the starting and operating of hydraulic components and systems in low ambient temperature. Part IV. Modelling the heating process and determining the serviceability of hydraulic components during the starting-up in low ambient temperature*. Polish Maritime Research, No. 3, (95) 2017.
11. Litwin W., Leśniewski W., Kowalski J.: *A proposed conversion of propulsion system for inland navigation passenger ship – from conventional to hybrid one* (in Polish). Napędy i sterowanie 5/ 2017.
12. Kowalski J., Leśniewski W., Litwin W.: *Multi-source -supplied parallel hybrid propulsion of the inland passenger ship STA.H. Research work on energy efficiency of a hybrid propulsion system operating in the electric motor drive mode*. Polish Maritime Research No. 3, 2013.

**CONTACT WITH THE AUTHORS**

**Czesław Dymarski**

*e-mail: cpdymars@pg.gda.pl*

Gdańsk University of Technology

Narutowicza 11/12

80-233 Gdansk

**POLAND**

## DIAGNOSTIC MODEL OF CRANKSHAFT SEALS

**Piotr Bzura**

Gdańsk University of Technology, Poland

### ABSTRACT

*The paper presents a research stand being a diagnostic model of radial lip seals used, among others, on crankshafts of piston combustion engines in order to identify the correctness of their operation. The possibility of determining the technical condition of lip seals on the basis of the proposed coefficient of correctness of operation has been described. The basic features of seals influencing their correctness of operation were also described, along with examples of determining the durability limits of lip seals. A modified version of the friction node of the T-02 four-ball apparatus is presented. It allows to check the correctness of sealing lips operation as well as to test the compatibility between the steel shaft, sealing lip and sealed lubricating oil. It was shown that the test results con-firmed the usefulness of the hypothesis that the quality of oil affects the durability of sealing lips and their coefficient of correctness. Additionally, attention was paid to the possibility of analyzing the pumping effect affecting the transition of the seal-shaft system from the state of partial suitability  $S_2$  to the state of full suitability  $S_1$  or to the state of unfitness  $S_3$ , and because the change in the state of such a system is random, it requires a probabilistic analysis.*

**Keywords:** marine gas turbine, inlet air fogging, applicability

### INTRODUCTION

Dynamic crankshaft seals of internal combustion piston engines work properly when there is sufficient lip-to-shaft pressure to ensure permanent compression and maintenance of the thin-layer grease between lip and shaft. In addition, the lip pressure is supported by the oil pumping effect, which is the result of the interaction between the deformed lip and the rotating shaft. Thus, it can be concluded that this tribological system of any internal combustion piston engine consists of its steel crankshaft, its contact sealing lip and the lubricating oil that exists between these elements.

These crankshaft seals have two functions: they maintain the required lubricant layer and prevent contamination from entering from outside (moisture and water and dry particles of various materials, including dust, sand, dirt or other particles such as those produced in manufacturing

processes), which can directly damage the crankshaft bearings of the motor.

In the operating practice of this type of seals it is important to estimate the durability of their operation, which is characterized by the minimal leakage of lubricating oil. Therefore, the durability of any such seal, which is characterized by the correctness of its operation when there is a minimal leakage of oil, can be assessed by means of a post-rightness of operation coefficient. Due to the fact that the preparation of operational tests in this respect requires obtaining preliminary results of laboratory tests, so such tests have been planned and carried out. In these studies, a simplified model of the above mentioned seal was applied, developed on the basis of the friction node of the modified T-02 four-ball apparatus. The results of these tests are presented in the article, the main purpose of which is to present the method of developing the results of tests

carried out at the friction node of the modified T-02 four-ball apparatus using a relational diagnostic model.

The presented relational diagnostic model, whose general graphic form is shown in Fig. 1, fulfils two basic functions:

- theoretical is a special (due to the sealing contact zone adopted as the research objective) reflection of the modeled system,
- practical it is a tool enabling the analysis of discrete stochastic processes in states and continuous in time, the values of which are distinguished such states as:  $S_1$ ,  $S_2$  and  $S_3$  (Fig. 1).

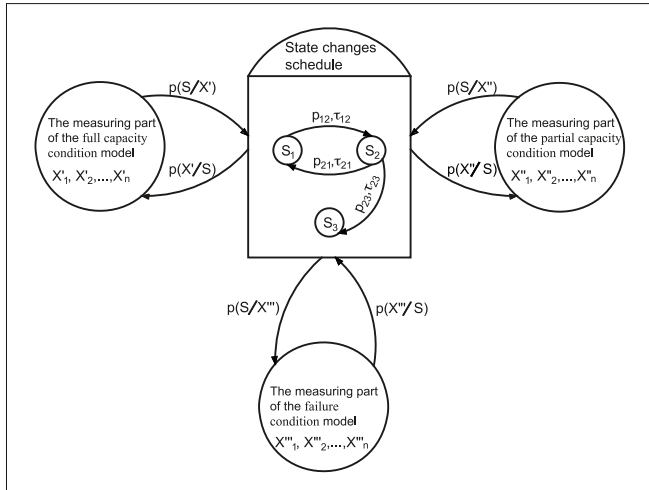


Fig. 1. Rational model of changes in the condition of sealing systems:

$S_1$  – full capacity condition;  $S_2$  – partial capacity condition;  $S_3$  – failure condition;  $p_{ik}$  – probability of process transition from  $S_i$  to  $S_k$  condition;  $\tau_{ik}$  – duration of  $S_i$  condition under condition of transition to  $S_k$  condition;  $i, k = 1, 2, 3$ ;  $X'_1, X'_2, \dots, X'_n$  – observational indicators indicating full capacity status;  $X''_1, X''_2, \dots, X''_n$  – observational indicators indicating incomplete condition status;  $X'''_1, X'''_2, \dots, X'''_n$  – observational indicators indicating zero condition

The conditional probability presented in Fig. 1 can be presented in general terms by means of formulae:

$$P(S/X) = \frac{P(S \cap X)}{P(X)} \quad (1)$$

$$P(X/S) = \frac{P(S \cap X)}{P(S)} \quad (2)$$

Therefore, it should be assumed that the identification of a given technical condition of a lip seal can be determined only taking into account the probability of its occurrence.

The engine crankshaft seal, which will be the subject of research, is a combination of components (sealing lip, crankshaft and sealed substance, i.e. engine lubricating oil), which should ensure maximum reduction of oil leakage.

The above sealing ability is the main characteristic (property) of this type of sealing system and is measured by the mass of the substance escaping through the seal (effluent rate) in relation to the permissible mass of the leaking substance [1, 2, 3].

According to the author, the sealing ability can be assessed by means of the " $W_{PD}$ " coefficient of performance, which can be determined according to the following relation:

$$W_{PD} = 1 - \frac{D_S}{D_{S(dop)}} = 1 - \frac{1}{D_{S(dop)} \Big|_{t_0}^{t_r}} \int_{t_0}^{t_r} D(t) dt \quad (3)$$

At the same time, according to [4, 5, 6, 7]:

$$D_S = L_S \cdot \tau \quad (4)$$

where:

$D_S, D_{S(dop)}$  – actual and permissible ‘harmful’ effects as appropriate;

$\tau$  – duration of one crankshaft revolution;

$L_S$  – “harmful work” during one revolution;

$t_r$  – estimated useful life;

$D(t)$  – a function that describes how the ‘harmful’ effect changes over time;

$t_0$  – is the moment from which the operation of the tested sealing system commenced.

In conditions of full suitability of the sealing system for operation, i.e. when the system is in the state of full suitability  $S_1$ ;  $D_S < D_{S(dop)}$ , the coefficient of correctness of operation  $W_{PD} > 0$ .

In conditions of incomplete usability, i.e. when the system is in the state of partial usability  $S_2$ ;  $D_S = D_{S(dop)}$ , the coefficient of correctness of operation  $W_{PD} = 0$ .

Under fault conditions, i.e. the system is in a state of failure  $S_3$ ;  $D_S > D_{S(dop)}$ , the coefficient of correctness of operation  $W_{PD} < 0$ .

The proposed diagnostic parameter, the  $W_{PD}$  coefficient of correctness of operation enables to check, among other things, the limits of measurement of the strength (durability) of sealing lips, whose basic features will be described in the next chapter.

## DYNAMIC SEALING MECHANISM

The view of the cross-section of the traditionally used lip seal and its scheme with the selection of the main parameters of the construction structure is shown in Fig. 2. The nomenclature used in this figure for its description is the same as that used by Johnston in his work [8].

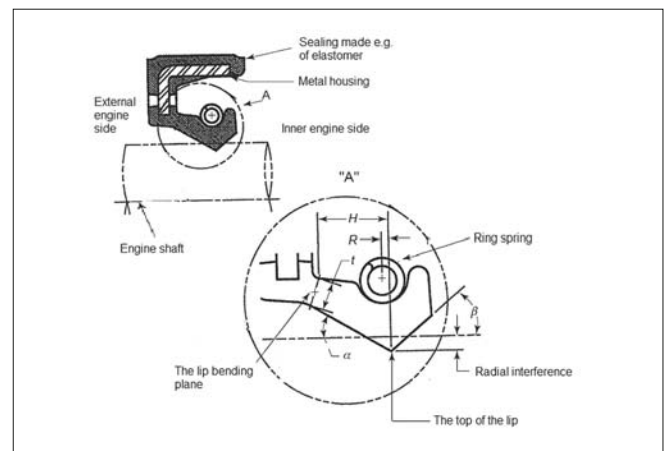


Fig. 2. View of the cross-section and the scheme of the lip seal with an indication of the basic parameters of its construction structure: A – structural detail;

R – distance between spring axis and lip apex; H – lip length;

$\alpha$  – lip external angle;  $\beta$  – lip internal angle; t – thickness of bending plane

The specificity of shaft sealing in the engine hull results from the asymmetry of the seal geometry [8, 9]. The geometry of this seal is characterized by a specific elastomer angle on the oil side of the seal, which is steeper than the angle on the ambient side. Typical design angles, when the seal is in the free state, are in the range of 40–45° for the  $\beta$  attack angle (on the hull-to-body side of the engine) and 25–30° for the  $\alpha$  angle on the envelope side (outside the engine hull). After being installed on the shaft, these angles will change by about 10°, taking the values in the work-state:  $\beta = 50^\circ$  and  $\alpha = 20^\circ$ . A further influence on the asymmetrical distribution of stress is the position of the seal spring. The cross-sectional axis of this spring is moved away from the top of the lip by the size R, usually by 10% of the length of the edge of the length H. This shift is directed towards the inside of the seal. This position of the spring in relation to the seal is important, so that the correct value of the direct edge load can be ensured and the asymmetrical geometry of the seal can be maintained during operation. Moving the axis of the seal by R size ensures the required pressure to the shaft in the external direction without the possibility of excessive lip deformation.

There are two factors that have a significant influence on the sealing performance of lip seals. They provide a permanent pumping of oil that enters the “contact zone” between the lip of the seal and the crankshaft of the engine on the oil side of the seal. This phenomenon is known as inward pumping of oil. The first of these factors is described as a micro-mechanism [8], which provides both load support for oil layer formation and inward pumping (Figure 3), and the second as a macro mechanism which primarily supports the pumping effect.

This micro mechanism has been the subject of many studies and analyses in the last three decades, the most important of which are the results obtained by Salanta [10]. These studies show that the proper effect of oil pumping depends on two important characteristics of the seal:

1. Asymmetrical geometry.
2. The texture of the elastomer surface in the contact zone after the seal has been applied.

The correct functioning of the seal to provide the required shaft sealing in each engine shaft depends significantly on both of these characteristics.

Once the seal is installed, the lip of the seal adheres to the crankshaft, creating a sealing or contact zone with a width of typically 0.2–0.4 mm. When the motor is started, a different texture is visible as a result of lip abrasion in the moulded surface. This is due to the fact that the abrasive material of the lip seal is used to expose the surface with clear thickening or micro-shifting of its layers. Such roughness is deformed by the rotation of the motor shaft so that it is oriented at an angle to the shaft axis, as shown in Fig. 3 [9, 11, 12].

These thickened bumps become micro-elastohydrodynamic wedges that allow both the surface of the elastomer seal to be raised and the oil to be pumped when the engine shaft rotates in both directions. However, as the contact surface on the outside of the engine hull is more extensive than on the inside, the effect of pumping into the inside of the engine hull is stronger than pumping outwards. Therefore, the seal

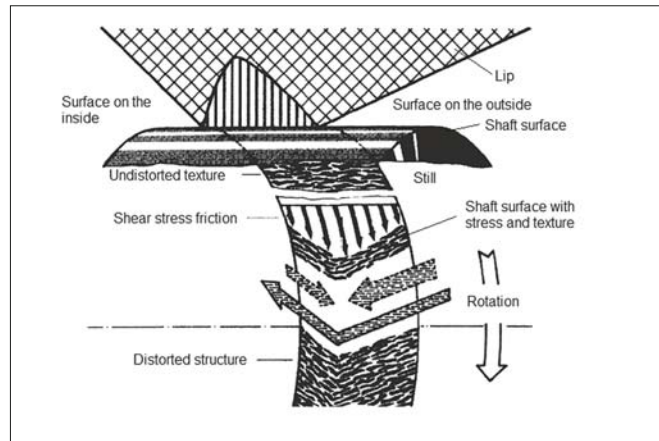


Fig. 3. Diagram of contact lip distortion in the form of irregularities at an angle to the shaft axis

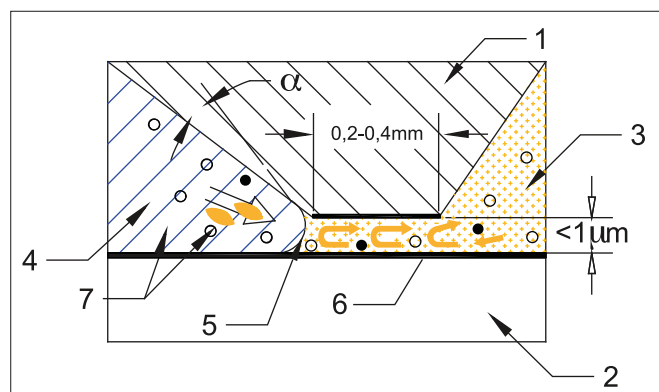


Fig. 4. Flow diagram of the oil film under the sealing lip: 1 – sealing lip, 2 – crankshaft, 3 – inner side (lubricating oil), 4 – outer side (air), 5 – concave meniscus, 6 – flux of recycled oil, 7 – impurities,  $\alpha$  – wetting angle (oil moistens the lip walls of the seal)

has a tendency to return oil and because of that prevents oil leakage outside the engine hull. This action is shown schematically in Fig. 4 [8, 9, 12, 13].

During operation, changes in direction of rotation and loads on the engine crankshaft create new gaps in the structure of the sealing lip. The distribution of the absorption of the seal is then random and ensures proper tightness of the tribological system of the seal as long as the deformation of the structure is reversible. However, after a certain period of operation, the ability of the unevenness of this surface to return to a neutral position when the shaft is held in place will decrease.

As a result, these bumps will have a directional orientation that will always result in a more effective seal in the normal crankshaft rotation than in the reverse direction. This has been demonstrated experimentally [8] by testing the reversal of a new seal and then repeating these tests after several hundred hours of operation.

The correct functioning of lip seals depends not only on the constructional value of the seal, lip edge loading, etc., but also on the sealing material (its elasticity) and other factors, such as micro-inequalities of the engine crankshaft. In further considerations, the main factor influencing the correct functioning of the seal is presented, together with examples of how the performance of the seal is calculated, which determines the performance of the seal.

## THE PARAMETERS OF THE PROPER FUNCTIONING OF THE SEAL

The most important factor negatively influencing the durability of the sealing lip is the heat generation at the point of contact with the shaft. "Harmful" measures to dissipate the heat generated by the friction are one of the key factors in limiting the life of the seal. The harmful effects of friction between the seal and the motor shaft can be demonstrated by considering that a typical 50 or 60 mm diameter shaft seal will consume up to 100 W of power [14].

In addition, the type of lubricating oil that comes into contact with the seal must also be taken into account, as its viscosity will have a direct effect on the dispersed operation ("harmful operation") produced in the friction node, which is formed by the sealing lip, lubricating oil and the engine crankshaft. Most of the generally available empirical data from empirical studies relate to typical lubricants, such as engine oil. This type of lubricant has a dynamic viscosity in the range of 0.005-0.01 [Belt] at the typical working temperature for them  $t = 100^{\circ}\text{C}$ . Lubricants with higher viscosity, such as transmission greases, generate higher shear stresses and thus cause higher friction. Examples supporting these observations are shown in Figure 5, where it can be seen that increasing viscosity in engine oils increases energy consumption by about 30%. Transmission greases, which may have higher viscosities, can further increase energy consumption, because the denser the viscosity of the grease causes a convex-acid increase in lower lip temperature.

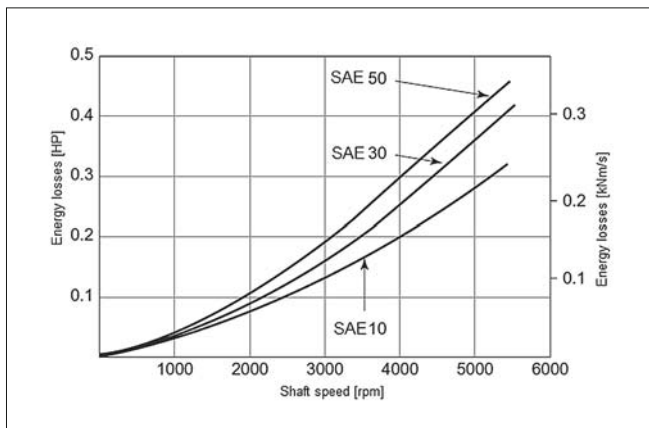


Fig. 5. Effect of viscosity on seal energy consumption. Source: BHR Group

Continuous dissipation of energy in the form of heat has a negative effect on the durability of the seal, which is equal to the value of the correct operation time until the loss of sealing efficiency. However, it is not easy to determine the actual seal life, as it depends on a number of factors, such as the operating temperature, the eccentricity of the spring seat, the speed of rotation, and the type of sealing substance and lubrication.

Figure 6 shows the curves of the estimated seal life, obtained by considering the main factors determining the seal life, such as the rubber material of the seal, lubricant and lip temperature [15].

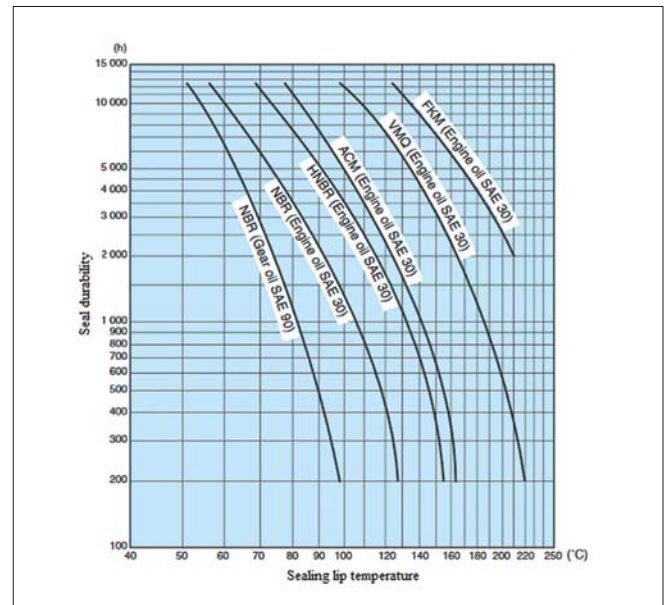


Fig. 6. Lip seal durability estimation curves: FKM - fluorocarbon rubber, VMQ - silicone rubber, ACM - acrylic rubber, HNBR - hydrogenated nitrile rubber, NBR - nitrile rubber. Source: Oil Seals & O-rings. KOYO Sealing Techno CO.,LTD

The results of these studies were taken into account in the author's studies, which were carried out on a laboratory stand enabling, among others, the study of energy losses for various variants of shaft sealings, as tare nodes. This stand and the obtained research results are presented in point 4. of the article (Test stand and results of the seal durability test).

## TEST STAND AND RESULTS OF THE SEAL DURABILITY TEST

The test stand was slightly modified in comparison to the stand described in the paper [7]. A ball of bearing steel with a hardness of 62.7 HRC was placed in the upper grip and treated as a rotating crankshaft. Three rubber balls of hardness in the range 15–80°sh were placed in the lower handle-cartridge in the shape of a bowl and treated as a sealing lip because they are immobilized and pressed against the upper ball with a force of up to 7200 N. This modification made it possible to obtain similar conditions of operation of the stationary friction node (stationary tribological system) to the conditions of operation of the seal, whose elements are the lip seal pressed by a ring spring against the crankshaft of the engine.

In the next part of the article, the values of parameters proving the correctness of the seal and its sealing lip were presented.

## PARAMETERS FOR THE CORRECT FUNCTIONING OF THE SEALING LIP

While testing the correctness of the sealing lip on the modified friction node of the four-ball apparatus T-02, a constant oil temperature of  $20^{\circ}\text{C}$  and a minimum possible constant load of 61.2 N were assumed. As a multitude having

a significant influence on the changes in the value of the correct functioning of the sealing lip, a variable speed of rotation  $n$  of the handle of the upper ball, treated as the crankshaft of the engine, was assumed.

Three model variants of rotary shaft seals were tested:

1. Dry friction node consisting of three rubber balls (seal lip) and one steel ball (crankshaft) without lubricant – symbol A.
2. A friction node consisting of three rubber balls immersed in pure SAE30 lubricating oil and one steel ball – symbol B.
3. A friction node consisting of three rubber balls immersed in SAE30 lubricating oil with additives to improve its quality and one steel ball – symbol C.

For these three variants the following has been determined:  $P_S$  power loss and the coefficient of correctness of operation  $W_{PD}$  of sealing lips on the basis of the algorithm [7], the shortened verse of which is presented in the algorithm in Fig. 7.

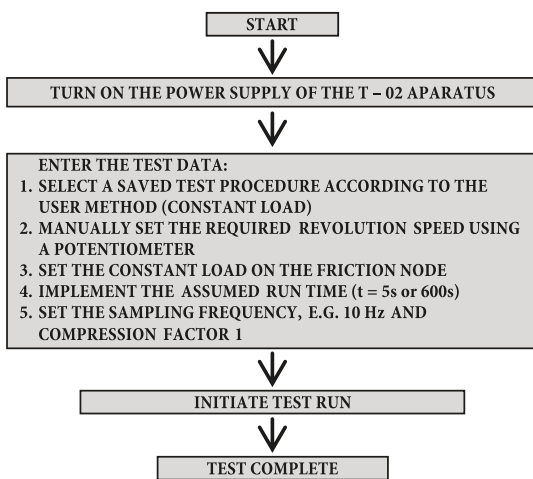


Fig. 7. Algorithm of tests on the measuring stand

The measurements were repeated four times and their mean value was checked on the basis of the t-Student's distribution with a probability of 0.68.

## POWER LOSSES

The test results obtained for speeds  $n = 312, 500$  and  $1450$  rpm are shown in Table 1, which contains the power loss recorded at the start of the applied test. The power loss was determined on the basis of the formula:

$$P_S = \frac{L_S}{\tau} = \frac{2 \cdot \pi \cdot P_r \cdot r \cdot \mu}{\tau} \quad (5)$$

where:

- $L_S = 2 \cdot \pi \cdot P_r \cdot r \cdot \mu$  – “harmful work” during the first rotation of the steel ball fixture;
- $P_r$  – radial load [N];
- $\mu$  – coefficient of friction [-];
- $r$  – shaft radius [m];
- $\tau$  – duration of one rotation of the steel ball fixture.

Tab. 1. Power losses

Rotational speed during test $n$ [rpm]	Power loss [Nm/s]		
	Symbol A	Symbol B	Symbol C
312	1.62	0.84	0.87
500	1.88	1.54	1.40
1450	9.77	5.16	5.02

The presented calculations of power losses show that in a dry friction node the largest dissipation of energy takes place, i.e. for this combination the largest increase of the dissipated “harmful work” takes place. For this reason, in further empirical research, as a measure of the permissible “harmful action” of a seal, the action of a dry friction node is assumed and the coefficient of lawfulness of action of any friction node determines the formula:

$$W_{PD} = 1 - \frac{L_S \cdot \tau}{L_{S(dop)} \cdot \tau} \quad (6)$$

where:

- $L_{S(dop)}$  – “harmful work” of the seal during the first rotation of the steel ball holder at the set speed of the dry friction node;
- $L_S$  – “harmful work” when rotating the steel ball fixture at a set speed of the friction node under test;
- $\tau$  – duration of one rotation of the steel ball fixture.

## COEFFICIENT OF CORRECT OPERATION OF SEALING LIPS

Results of tests lasting 600 seconds, obtained according to the concept presented in the paper [7] and the shortened algorithm Fig. 7 and formulas (5, 6), for rotational speed  $n = 312, 500$  and  $1450$  rpm are shown in Table 2, 3, 4 and Figures 7, 8, 9.

Tab. 2.  $W_{PD}$  seal performance factors for rotational speed 312 rpm

Measurement time [s]	$W_{PD}$ [-]		
	Symbol A	Symbol B	Symbol C
Start	0.00	0.00	0.00
100	failure	0.44	0.41
200		0.43	0.44
300		0.39	0.44
400		0.37	0.44
500		0.37	0.43
600		-0.06	0.46

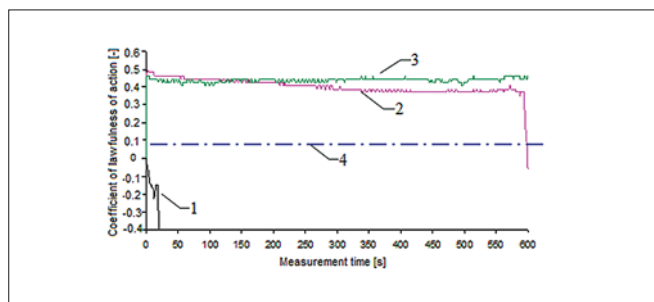
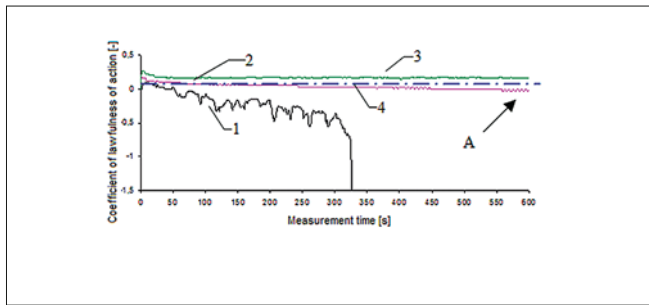


Fig. 8. Comparison of the  $W_{PD}$  seal performance coefficients at rotational speed of 312 rpm: 1 – symbol A; 2 – symbol B; 3 – symbol C; 4 – permissible ‘harmful’ effect

Tab. 3.  $W_{PD}$  seal performance factors for 500 rpm

Measurement time [s]	$W_{PD}$ [-]		
	Symbol A	Symbol B	Symbol C
Start	0.00	0.00	0.00
100	-0.10	0.08	0.15
200	-0.18	0.05	0.18
300	-0.38	0.03	0.18
400	failure	0.03	0.15
500		0.00	0.18
600		0.00	0.15



Detail "A"

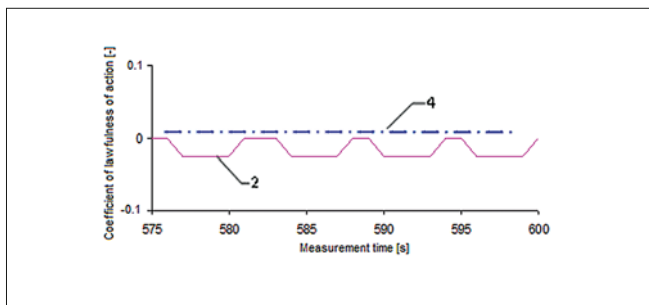


Fig. 9. Comparison of the  $W_{PD}$  seal performance coefficients at rotational speed of 500 rpm: 1 – symbol A; 2 – symbol B; 3 – symbol C; 4 – permissible 'harmful' effect

At a preset load and speed of 312 rpm, for a dry friction node immediately after starting, the coefficient of performance of  $W_{PD} < 0$ , i.e. it is in a state of failure  $S_3$ , which means that the version of the model with symbol A is worthless. On the other hand, the model marked with symbol B lost its full capacity after about 600 seconds and went to the state of incomplete capacity  $S_2$ . The life span of this version of the combination model is approximately 600 seconds. The C-model remains at full capacity throughout the entire test, meaning that the tribological system lasts more than 600 seconds.

In the second series of tests at a given load and speed of 500 rpm on the basis of the obtained test results, it can be stated that:

- in the case of testing a system with symbol A: the system changed from  $S_1$  to  $S_2$  partial capacity after approx. 10 seconds and in the case of partial capacity the seal lasted approx. 250 seconds, after which it went into zero capacity state.
- in the case of testing a system with symbol B: After the system has passed from the full capacity state  $S_1$

Tab. 4.  $W_{PD}$  seal performance factors for 1450 rpm

Measurement time [s]	$W_{PD}$ [-]		
	Symbol A	Symbol B	Symbol C
Start	0.00	0.00	0.00
100	failure	0.03	0.05
200		0.03	0.05
300		-0.03	0.05
400		-0.03	0.05
500		-0.05	0.05
600		-0.05	0.05

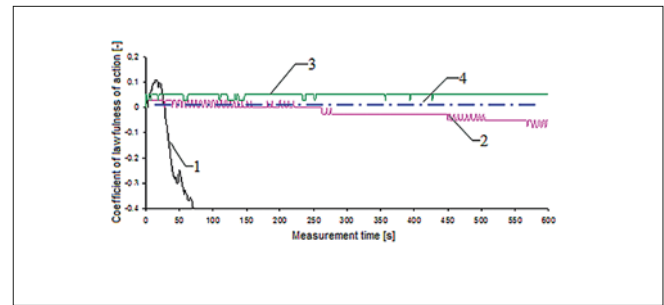


Fig. 10. Comparison of the performance factors at a speed of 1450 rpm: 1 – symbol A; 2 – symbol B; 3 – symbol C; 4 – permissible 'harmful' effect

to the partial capacity state  $S_2$ , an oil pumping effect may be observed, resulting in a specific cooling and reduction of the friction coefficient (detail "A") and a random transition from the full capacity state  $S_1$  to  $S_2$  and vice versa.

- in the case of testing a system with symbol C: as in the previous test, the system remains in full  $S_1$  compliance and has a life expectancy of more than 600 seconds.

In the final series of tests at a given load and speed of 1450 rpm, based on the test results, it can be concluded that:

- for testing a system with symbol A: after approximately 40 seconds, the system has changed from  $S_1$  to  $S_3$  without a regeneration 'test' in the  $S_2$  partial capacity condition,
- in the case of testing a system with symbol B: already after about 80 seconds, the system changed from the  $S_1$  to the  $S_2$  partial capacity status, where, however, due to too high speed, the pumping effect did not prevent the system from going to state of zero capacity after about 400 seconds of durability,
- for testing the C system: as in the previous two tests, the system remains in  $S_1$  full capacity and has a life expectancy of more than 600 seconds.

## FINAL REMARKS AND CONCLUSIONS

The presented diagnostic model enables identification of rotary crankshaft seals of piston combustion engines on the basis of correctness of operation of the friction node of the T-02 four-ball apparatus. The analysis of durability of seals (i.e. friction nodes being tribological systems) was

performed by determining the coefficient of correctness of operation of  $W_{PD}$ , which enabled comparison of three versions of operation. The best  $D_s$  action was found in the case of the tribological system with symbol C, in which the lubricating oil was of the best quality. Therefore, it can be concluded that the hypothesis presented in the paper [7] that the quality of oil affects the correctness of operation of the tested tribological system was finally confirmed, which justifies the need for good research on sealing lips, carried out under the conditions of the actual exploitation of internal combustion engines.

Additionally, the presented research results show that:

1. To interpret the results of the study, a model of the friction phenomenon in the contact area of the sealing lip (rubber balls in the oil sump of the T-02 apparatus friction node) and the crankshaft of the engine (steel ball in the upper grip) were used.
2. After the start-up and first rotation of the friction node, the greatest loss of power per revolution occurred at technically dry friction and then the greatest permissible distortion of the contact lips, i.e. rubber balls, took place.
3. The  $W_{PD}$  sealing lip performance factor entered allows for the separation of capacity and zero capacity states.
4. The observed pumping effect is the result of the tribological system that occurs on both sides of the lip, so that heat exchange takes place.
5. The process, due to the pumping effect, of a system switching from partial  $S_2$  capacity to full  $S_1$  capacity or  $S_3$  zero capacity, is random and therefore requires a probabilistic analysis to determine the probability of  $P(S/X)$  and  $P(X/S)$  as determined by formulae (1) and (2).

The research shows that the diagnostic model proposed by the author to identify the correctness of operation of each tribologic system may be useful for determining the durability of lip seals and for compatibility tests between the sealing lip, crankshaft and sealed lubricating oil.

## REFERENCES

1. Kragelsky V.: *Friction Wear Lubrication*. English translation, Mir Publishers, 1981, Vol. 3, pp. 82–111.
2. Pieter Baart, Bas van der Vorst, Piet M. Lugt & Ron A.J. van Ostayen: *Oil Bleeding Model for Lubricating Grease Based on Viscous Flow Through a Porous Microstructure*, Tribology Transactions, Volume 53, 2010, pp. 340–348.
3. Paszota Z.: *Energy losses in hydrostatic drive*. LABERT Academic Publishing, 2016.
4. Girtler J.: *A method for evaluating theoretical and real operation of diesel engines in energy conversion formulation taking into account their operating indices*. Polish Maritime Research. Vol. 18, No. 3(70), 2011, pp. 31–36.
5. Girtler J.: *The method for determining the theoretical operation of ship diesel engines in terms of energy and assessment of the real operation of such engines, including indicators of their performance*. Journal of Polish Cimac. Vol 6 no. 1, 2011, pp. 79–88.
6. Girtler J.: *Quantitative interpretation of energy-based systems and index of their reliability*. Journal of Polish Cimac. Vol 3 no. 1, 2008, pp. 87–94.
7. Bzura P.: *Influence of lubricating oil improvers on performance of crankshaft seals*, Polish Maritime Research. Special Issue S1 (97) 2018 Vol. 25, pp. 172–177.
8. Johnston D.E.: *Design aspects of modern rotary shaft seals*, Proc. I. Mech. E. 213 (Part J) (1999), pp. 203–214.
9. Flitney R. K.: *Seals and Sealing Handbook (Sixth Edition)*. 2014 Elsevier Ltd., Chapter 3.
10. Salant R.F.: *Soft elastohydrodynamic analysis of rotary lip seals*, Proc. I. Mech. E. Part C J. Mech. Eng. Sci. 224 (12) (2010), pp. 2637–2647.
11. Kammüller M.: *Zur abdichtwirkung von radial wellendichtringen (Dr-Ing thesis)*, Universität Stuttgart, 1986.
12. Baart, P., Lugt, P.M. and Prakash, B.: *Review of the lubrication, sealing and pumping mechanisms in oil and grease lubricated radial lip seals*. Proc. Inst. Mech. Engineers., part J: J. Engineering Tribology, 2009; pp. 347–358.
13. FST Technical Manual 2015. Freudenberg.
14. Jagger E.T. *Rotary shaft seals: the sealing mechanism of synthetic rubber lip seals running at atmospheric pressure*, Proc. I. Mech. E. 171 (1957).
15. Koyo Oil Seals& O-Rings. KOYO Sealing Techno CO., LTD.

**CONTACT WITH THE AUTHORS**

**Piotr Bzura**

*e-mail: pbzura@pg.edu.pl*

Gdańsk University of Technology

Narutowicza 11/12

80-233 Gdansk

**POLAND**

## ENERGY LOSS COEFFICIENTS $k_i$ IN A DISPLACEMENT PUMP AND HYDRAULIC MOTOR USED IN HYDROSTATIC DRIVES

Agnieszka Maczyszyn

Gdańsk University of Technology, Poland

### ABSTRACT

*The article aims at defining and analysing the energy loss coefficients in design solutions of rotating displacement machines, with a piston machine as an example. The energy losses observed in these machines include mechanical loss, volumetric loss, and pressure loss. The scale and relations between these losses in different machines depend on machine design and manufacturing quality, and on operating parameters. The operating parameters, in turn, which affect directly or indirectly the above losses depend on whether the machine works in pump or hydraulic motor regime. The article is also a contribution to the development of a library of  $k_i$  coefficients which define the losses in displacement machines, as the knowledge about these coefficients makes it possible to assess fast and easily the energy efficiency of a machine or drive system at each point of its working area.*

**Keywords:** hydrostatic drive, energy loss rate, pump, hydraulic motor, energy loss coefficients

### INTRODUCTION

The motivation for developing a library of  $k_i$  coefficients defining energy losses in displacement machines was creating the opportunity for fast and easy efficiency assessment of a machine or drive system at each point of its working area (Fig. 1).

In articles [4 ÷ 7], the author has analysed the structure of losses generated in a hydraulic motor as a function of other, loss independent parameters. Fig. 2 presents the loss increase in the direction opposite to that of power flow. It was mentioned in these articles that assessing the energy efficiency of a motor requires prior accurate assessments of mechanical loss, volumetric loss, and pressure loss. In turn, to assess accurately these losses, they should be made depended on relevant parameters which directly determine their scale.

The drive system is not decisive for conditions in which the driven device works. On the contrary, it is the driven device or mechanism which determines the real load or speed of the hydraulic motor used in the hydrostatic drive system. The control structure (of volumetric or throttling type) used for

controlling the hydraulic motor speed should allow the motor to reach the speed required by the driven device.

Working conditions of the device change in time, as a result of loss changes, among other causes [10, 11, 13–15]. Consequently, the working conditions of the hydrostatic system used as the drive also change.

Changes of working parameters of the hydrostatic system are limited by maximal parameter values. In Fig. 1, these maximal values are marked as boundaries of the working area of the system (illustrated by maximal values of motor speed coefficient  $\bar{\omega}_{Mmax}$  and motor load coefficient  $\bar{M}_{Mmax}$ ).

Working conditions of the device can change within the full range of changes of the motor speed coefficient  $\bar{\omega}_M$  and motor load coefficient  $\bar{M}_M$ . The area of changes of these coefficients is limited by the inequalities:  $0 \leq \bar{\omega}_M < \bar{\omega}_{Mmax}$  and  $0 \leq \bar{M}_M < \bar{M}_{Mmax}$ .

The goal of hydrostatic system operation is to meet power requirements of the driven device or machine in the entire range of its working area. It is assumed that the machine can work at each point of the working area, hence the information about its energy efficiency in newly created conditions is

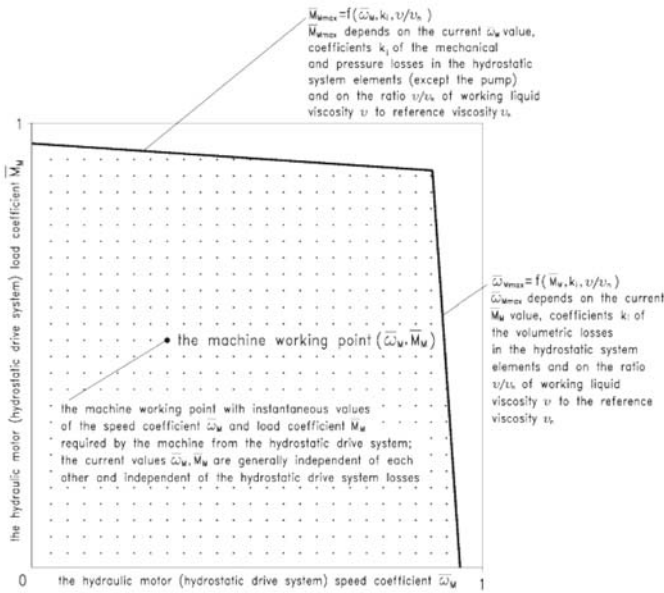


Fig. 1. The range of drive motor speed coefficient  $\bar{\omega}_M$  and motor load coefficient  $\bar{M}_M$  ( $0 \leq \bar{\omega}_M < \bar{\omega}_{Mmax}$ ,  $0 \leq \bar{M}_M < \bar{M}_{Mmax}$ ) in a hydrostatic drive system [9]

important. In practice, however, this information is not available for a machine or system user.

To find the range of the working area of the hydrostatic system driving a machine, we should determine the maximal values of the motor speed coefficient  $\bar{\omega}_{Mmax}$  and motor load coefficient  $\bar{M}_{Mmax}$ . The value of  $\bar{\omega}_{Mmax} = f(\bar{M}_M, k_i, \frac{v}{v_n})$  depends on the current value of the motor load coefficient  $\bar{M}_M$ , the volumetric loss coefficients  $k_i$  in hydrostatic system elements, and the current ratio  $v/v_n$  between the working medium viscosity  $v$  and the reference viscosity  $v_n$ . In turn, the value of  $\bar{M}_{Mmax} = f(\bar{\omega}_M, k_i, \frac{v}{v_n})$  depends on the current value of the motor speed coefficient  $\bar{\omega}_M$ , the mechanical and pressure loss coefficients  $k_i$  in hydrostatic system elements (excluding pump), and the current ratio  $v/v_n$  between the working medium viscosity  $v$  and the reference viscosity  $v_n$ .

To perform the energy balance in the displacement machine (pump or hydraulic motor) used in a hydrostatic drive system, we should add the energy loss rate to the useful (output) power, (see Fig. 2), as it is the output power parameters which are decisive for individual energy loss rates [8].

It is noteworthy that the maximal values of the motor speed coefficient  $\bar{\omega}_{Mmax}$  and the motor load coefficient  $\bar{M}_{Mmax}$ , which define the boundaries of the system's working area, depend on the parameters of the displacement machines used in the system. They also depend on the control structure applied for controlling the hydraulic motor speed, and on losses generated in the remaining elements of the system.

### METHODS TO DETERMINE $k_i$ COEFFICIENTS AND "A" EXPONENTS DESCRIBING THE EFFECT OF INDIVIDUAL PARAMETERS ON ENERGY LOSSES

According to the theory by Z. Paszota [9], the basis for describing losses and energy efficiency of a displacement machine (pump, rotating hydraulic motor) is the diagram of power increase in the drive system in the direction opposite to the power flow direction, (Fig. 2).

The presented formulas make it possible to calculate the value of each individual loss generated in a rotating displacement machine. These formulas contain selected energy loss coefficients  $k_i$ , and "a" exponents that describe the effect of individual parameters on energy losses.

### MODEL OF VOLUMETRIC LOSS IN PUMP AND HYDRAULIC MOTOR

The mathematical model of volumetric loss in pump which takes into account the dependence of the volumetric

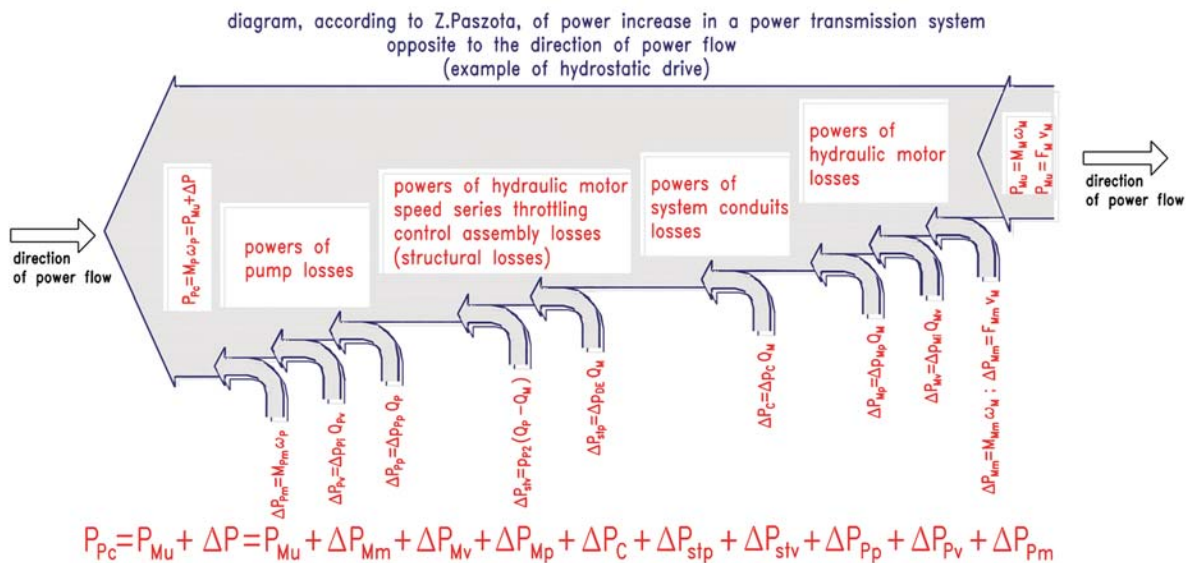


Fig. 2. Diagram of power increase in the hydrostatic drive system, in the direction opposite to that of power flow [9]

loss rate  $Q_{pv}$  in the pump on the induced pressure increase  $\Delta p_{pi}$  in pump's working chambers and on the ratio  $v/v_n$  between oil viscosities has the form [9]:

$$Q_{pv} = k_1 \cdot q_{pt} \cdot n_p \left| \frac{q_{pt}}{v_n} \right|^{\Delta p_{pi} = p_n} \cdot \left( \frac{\Delta p_{pi}}{p_n} \right)^{a_{pv}} \cdot \left( \frac{v}{v_n} \right)^{a_w} \quad (1)$$

where  $k_1$  is the coefficient of the volumetric loss  $Q_{pv}$  generated during one revolution of constant or variable delivery pump shaft for the induced pressure increase  $\Delta p_{pi}$  in the pump equal to the nominal pressure  $p_n$  of the hydraulic system:  $\Delta p_{pi} = p_n$ , and for the reference viscosity  $v_n$  of the working medium. The value of the coefficient  $k_1$  is referenced to the theoretical working volume  $q_{pt}$  of the pump:

$$k_1 = \frac{Q_{pv} \left| \frac{q_{pt}}{v_n} \right|^{\Delta p_{pi} = p_n} \cdot 1}{n_p \left| \frac{q_{pt}}{v_n} \right|^{\Delta p_{pi} = p_n} \cdot q_{pt}} \quad (2)$$

Here,  $q_{pt}$  is the theoretical working volume of the constant delivery pump, and  $n_p$  is the rotational speed of the pump, determined for its theoretical working volume and the temperature corresponding to the reference viscosity  $v_n$ , and for the induced pressure increase  $\Delta p_{pi}$  in pump's working chamber equal to the nominal pressure  $p_n$  of the hydraulic system:  $\Delta p_{pi} = p_n$ .

$(\Delta p_{pi} = p_n)^{a_{pv}}$  represents the effect of the induced pressure increase  $\Delta p_{pi}$  in pump's working chambers on the total amount of losses in the rotating displacement machine. The value of the exponent  $a_{pv}$  varies from  $a_{pv} = 1$  for laminar flow to  $a_{pv} \approx 0,57$  for flow with not fully developed turbulence, and  $a_{pv} = 0,5$  for fully developed turbulent flow. The exact value of the exponent  $a_{pv}$  should be determined experimentally for each pump type.

$v$  is the kinematic viscosity of the working medium (hydraulic oil) for which the volumetric loss rate  $Q_{pv}$  at pump inlet is calculated, and  $v_n$  is the reference kinematic viscosity of the working medium (hydraulic oil), equal to  $v_n = 35 \text{ mm}^2\text{s}^{-1}$ , determined for the atmospheric pressure, i.e. for  $p = 0$ .

$(v/v_n)^{a_{vv}}$  represents the effect of medium viscosity  $v$  on the total amount of volumetric loss in the rotating displacement machine. The value of the exponent  $a_{vv}$  varies from  $a_{vv} = -1$  for laminar leakage flows to  $a_{vv} = -0,14$  for leakage flows with not fully developed turbulence, and  $a_{vv} = 0$  for fully developed turbulent leakage flows. The exact value of the exponent  $a_{vv}$  should be determined experimentally for each displacement pump type.

The volumetric loss rate  $Q_{Mv}$  in working chambers of the hydraulic motor are given by the following mathematical simulation model [9]:

$$Q_{Mv} = k_9 Q_{pt} \left( \frac{\Delta p_{Mi}}{p_n} \right)^{a_{pv}} \left( \frac{n_M}{n_{Mt}} \right)^{a_{nv}} \left( \frac{v}{v_n} \right)^{a_w} \quad (3)$$

where is the coefficient of the volumetric loss  $Q_{Mv}$  determined for: the induced pressure drop  $\Delta p_{Mi}$  equal to the nominal pressure  $p_n$  of the hydraulic system:  $\Delta p_{Mi} = p_n$ , the reference viscosity  $v_n$  of the working medium, and the theoretical

rotational speed  $n_{Mt}$  of motor shaft. The value of the coefficient  $k_9$  is referenced to the theoretical pump delivery  $Q_{pt}$ :

$$k_9 = \frac{Q_{Mv} |q_{pt}; \Delta p_{Mi} = p_n; n_M; v_n}{Q_{pt}} \quad (4)$$

Here,  $(\Delta p_{Mi} = p_n)^{a_{pv}}$  represents the effect of the induced pressure drop  $\Delta p_{Mi}$  in motor's working chambers on the total amount of volumetric loss in the rotating displacement machine. The value of the exponent  $a_{pv}$  varies from  $a_{pv} = 1$  for laminar flow to  $a_{pv} \approx 0,57$  for flow with not fully developed turbulence, and  $a_{pv} = 0,5$  for fully developed turbulent flow. The exact value of the exponent  $a_{pv}$  should be determined experimentally for each motor type.

$(n_M / n_{Mt})^{a_{nv}}$  represents the effect of the rotational speed  $n_M$  of the motor shaft on the volumetric loss rate  $Q_{Mv}$ . The exact value of the exponent  $a_{nv}$  should be determined experimentally for each type of hydraulic motor.

$(v/v_n)^{a_{vv}}$  represents the effect of medium viscosity  $v$  on the total amount of volumetric loss in the rotating displacement machine. The value of the exponent  $a_{vv}$  varies from  $a_{vv} = -1$  for laminar leakage flows to  $a_{vv} \approx -0,14$  for flows with not fully developed turbulence, and  $a_{vv} = 0$  for fully developed turbulent flows. The exact value of the exponent  $a_{vv}$  should be determined experimentally for each motor type.

The models (2.1) and (2.3) of volumetric loss in a displacement machine make it possible to determine very accurately the dependence of the rates  $Q_{pv}$  or  $Q_{Mv}$  in the displacement machine on the induced pressure increase  $\Delta p_{pi}$  or pressure drop  $\Delta p_{Mi}$  in machine's working chambers and on oil viscosity  $v$ , as well as on the rotational speed  $n_M$  of motor shaft in the case of hydraulic motor. The models utilise the coefficients  $k_1$  (in pump) and  $k_9$  (in hydraulic motor) of volumetric loss rates generated at the induced pressure increase  $\Delta p_{pi}$  or pressure drop  $\Delta p_{Mi}$  in chambers equal to the nominal pressure  $p_n$  of the hydrostatic system in which the pump is installed:  $\Delta p_{pi} = p_n$ , or in which the motor is installed:  $\Delta p_{Mi} = p_n$ . The obtained loss values are referenced to the theoretical working volume  $q_{pt}$  of the pump, or, in the case of hydraulic motor, to the theoretical delivery  $Q_{pt}$  of the pump.

## MODEL OF PRESSURE LOSS IN PUMP AND HYDRAULIC MOTOR

The mathematical simulation formula which determines the pressure loss  $\Delta p_{pp}$  in pump channels for varying viscosity  $v$  has the form [9]:

$$\Delta p_{pp} = k_3 p_n \left( \frac{Q_p}{Q_{pt}} \right)^{a_{qp}} \left( \frac{v}{v_n} \right)^{a_{vp}} \quad (5)$$

where  $k_3$  is the coefficient of the pressure loss  $\Delta p_{pp}$  in pump's inner channels and distributor (if exists). This coefficient is determined for the pump delivery  $Q_p$  equal to its theoretical delivery  $Q_{pt}$  and for the reference viscosity  $v_n$  of the working medium. The value of the coefficient  $k_3$  is referenced to the nominal pressure  $p_n$  of the system:

$$k_3 = \frac{\Delta p_{pp}|_{Q_p=Q_{pt}}}{p_n} \quad (6)$$

Here,  $(Q_p / Q_{pt})^{a_{Qp}}$  represents the effect of the flow rate  $Q_p$  of the liquid medium (pump delivery  $Q_p$ ) in the channels on the pressure loss  $\Delta p_{pp}$  in the pump. The value of the exponent  $a_{Qp}$  varies from  $a_{Qp} = 1$  for laminar flow to  $a_{Qp} \approx 1,75$  for flow with not fully developed turbulence, and to  $a_{Qp} = 2$  for fully developed turbulent flow. The exact value of the exponent  $a_{Qp}$  should be determined experimentally for each type of displacement pump.

$(\nu/\nu_n)^{a_{vp}}$  is the effect of medium viscosity  $\nu$  on the total amount of pressure loss in the rotating displacement machine. The value of the exponent  $a_{vp}$  varies from  $a_{vp} = 1$  for laminar flow to  $a_{vp} \approx 0,25$  for flow with not fully developed turbulence, and to  $a_{vp} = 0$  for fully developed turbulent flow. The exact value of the exponent  $a_{vp}$  should be determined experimentally for each type of displacement pump.

The model of pressure loss in hydraulic motor has the form [9]:

$$\Delta p_{Mp} = k_8 p_n \left( \frac{Q_M}{Q_{pt}} \right)^{a_{Qp}} \left( \frac{\nu}{\nu_n} \right)^{a_{vp}} \quad (7)$$

with the coefficient:

$$k_8 = \frac{\Delta p_{Mp}|_{Q_M=Q_{pt}, \nu_n}}{p_n} \quad (8)$$

determining the pressure loss  $\Delta p_{Mp}$  generated in inner channels and distributor of the hydraulic motor at absorbing capacity  $Q_M$  of the motor equal to the theoretical delivery  $Q_{pt}$  of the pump. The value of the coefficient  $k_8$  is referenced to the nominal pressure  $p_n$  of the system in which the hydraulic system is installed.

$(Q_M / Q_{pt})^{a_{Qp}}$  represents the effect of the absorbing capacity  $Q_M$  of the liquid medium in the channels on the pressure loss  $\Delta p_{Mp}$  in the rotating hydraulic motor. The value of the exponent  $a_{Qp}$  varies from  $a_{Qp} = 1$  for laminar flow to  $a_{Qp} \approx 1,75$  for flow with not fully developed turbulence, and to  $a_{Qp} = 2$  for fully developed turbulent flow. The exact value of the exponent  $a_{Qp}$  should be determined experimentally for each motor type.

$(\nu/\nu_n)^{a_{vp}}$  represents the effect of medium viscosity  $\nu$  on the total amount of pressure loss in the rotating displacement machine. The exponent  $a_{vp}$  varies from  $a_{vp} = 1$  for laminar flow to  $a_{vp} \approx 0,25$  for flow with not fully developed turbulence, and to  $a_{vp} = 0$  for fully developed turbulent flow. The exact value of the exponent  $a_{vp}$  should be determined experimentally for each motor type.

The type of the medium flow developed in displacement machine channels is mainly affected by the local flow resistance (flow direction and cross section disturbances) which depends on structural design and dimensions of the machine. The created pressure loss models (2.5) and (2.7) can be applied in analysing an individual machine design to determine experimentally the exact values of the exponent  $a_{vp}$  describing the effect of viscosity, and the exponent  $a_{Qp}$  describing the effect of flow rate on the pressure loss in machine channels. The models utilise the pressure loss coefficients  $k_3$  (in pump) and  $k_8$  (in hydraulic

motor) determined for the flow rate  $Q_p$  or  $Q_M$  in the channel equal to the nominal pump delivery  $Q_{pt}$ , and referenced to the nominal pressure  $p_n$  of the system in which the pump is installed.

## MODEL OF MECHANICAL LOSS IN PUMP AND HYDRAULIC MOTOR

The mathematical model describing the mechanical loss moment  $M_{Pm}$  in the pump with geometric (variable) delivery  $q_{pgv}$  ( $q_{pgv} = b_p q_{pt}$ ) per shaft revolution has the form:

$$\begin{aligned} M_{Pm|\Delta p_{pi}, b_p, \nu} &= (k_{4.1.1} + k_{4.1.2} b_p) M_{Pt} \left( \frac{\nu}{\nu_n} \right)^{a_{vm}} + k_{4.2} M_{Pt} b_p \frac{\Delta p_{pi}}{p_n} = \\ &= \left[ (k_{4.1.1} + k_{4.1.2} b_p) \left( \frac{\nu}{\nu_n} \right)^{a_{vm}} + k_{4.2} b_p \frac{\Delta p_{pi}}{p_n} \right] M_{Pt} = \\ &= \left[ (k_{4.1.1} + k_{4.1.2} b_p) \left( \frac{\nu}{\nu_n} \right)^{a_{vm}} + k_{4.2} b_p \frac{\Delta p_{pi}}{p_n} \right] \frac{q_{pt} p_n}{2\Pi} \quad (9) \end{aligned}$$

Here, the coefficient  $k_{4.1.1}$  expresses the ratio of the mechanical loss moment  $M_{Pm|\Delta p_{pi}=0, b_p=0, \nu_n}$  of the unloaded pump, determined for the delivery  $q_{pgv}$  per pump shaft revolution (pump delivery change coefficient  $b_p$ ) equal to zero:  $q_{pgv} = 0$  ( $b_p = 0$ ) and the working medium reference viscosity  $\nu_n$ , to the theoretical moment  $M_{Pt}$  of the pump:

$$k_{4.1.1} = \frac{M_{Pm|\Delta p_{pi}=0, b_p=0, \nu_n}}{M_{Pt}} = \frac{M_{Pm|\Delta p_{pi}=0, b_p=0, \nu_n}}{\frac{q_{pt} p_n}{2\Pi}} \quad (10)$$

The coefficient  $k_{4.1.2}$  expresses the ratio of the difference between the mechanical loss moment  $M_{Pm|\Delta p_{pi}=0, b_p=1, \nu_n}$  in the unloaded pump, determined for the pump delivery  $q_{pgv}$  per pump shaft revolution (pump delivery change coefficient  $b_p$ ) equal to the theoretical working delivery  $q_{pt}$  of the pump,  $q_{pgv} = q_{pt}$  ( $b_p = 1$ ) and the mechanical loss moment  $M_{Pm|\Delta p_{pi}=0, b_p=0, \nu_n}$  in the unloaded pump, determined for the pump delivery  $q_{pgv}$  per pump shaft revolution equal to zero:  $q_{pgv} = 0$  ( $b_p = 0$ ) and the working medium reference viscosity  $\nu_n$ , to the theoretical moment  $M_{Pt}$  of the pump:

$$\begin{aligned} k_{4.1.2} &= \frac{M_{Pm|\Delta p_{pi}=0, b_p=1, \nu_n} - M_{Pm|\Delta p_{pi}=0, b_p=0, \nu_n}}{M_{Pt}} = \\ &= \frac{M_{Pm|\Delta p_{pi}=0, b_p=1, \nu_n} - M_{Pm|\Delta p_{pi}=0, b_p=0, \nu_n}}{\frac{q_{pt} p_n}{2\Pi}} \quad (11) \end{aligned}$$

The coefficient  $k_{4.2}$  expresses the ratio of the difference between the mechanical loss moment  $M_{Pm|\Delta p_{pi}=p_n, b_p=1, \nu_n}$  in the pump loaded with nominal pressure and the mechanical loss moment  $M_{Pm|\Delta p_{pi}=0, b_p=1, \nu_n}$  in the unloaded pump at the working medium reference viscosity  $\nu_n$ , to the theoretical moment  $M_{Pt}$  of the pump:

$$\begin{aligned}
k_{4.2} &= \frac{\Delta M_{Pm|\Delta p_{pi}, b_p, v_n}}{M_{Pi}} = \frac{\Delta M_{Pm|\Delta p_{pi}, b_p, v_n}}{b_p q_{Pt} \Delta p_{pi}} = \frac{\Delta M_{Pm|\Delta p_{pi}, b_p=1, v_n}}{q_{Pt} \Delta p_{pi}} = \\
&= \frac{M_{Pm|\Delta p_{pi}=p_n, b_p=1, v_n} - M_{Pm|\Delta p_{pi}=0, b_p=1, v_n}}{\frac{q_{Pt} p_n}{2\Pi}} = \\
&= \frac{M_{Pm|\Delta p_{pi}=p_n, b_p=1, v_n} - M_{Pm|\Delta p_{pi}=0, b_p=1, v_n}}{M_{Pt}}, \quad (12)
\end{aligned}$$

Here,  $(v/v_n)^{a_{vm}}$  represents the effect of medium viscosity  $v$  on the mechanical loss moment in the displacement piston machine with medium filling the casing. The value of the exponent  $a_{vm}$  should be determined experimentally for each type of displacement pump.

$\Delta p_{pi}/p_n$  represents the effect of the induced pressure increase  $\Delta p_{pi}$  in pump's working chambers on the total amount of mechanical loss in the rotating displacement machine. According to [9], the assumed value of the exponent  $a_{pm}$  is 1.

The mathematical model of the mechanical loss moment  $M_{Mm}$  in the rotating hydraulic motor with geometrical (variable) absorbing capacity  $q_{Mgv}$  per shaft revolution has the form [9]:

$$\begin{aligned}
M_{Mm|M_M, n_M, b_M, v} &= \left( k_{7.1.1} + k_{7.1.2} \frac{n_M}{n_{Mt}} b_M \right) M_{Mt} \left( \frac{v}{v_n} \right)^{a_{vm}} + k_{7.2} M_M = \\
&\left( k_{7.1.1} + k_{7.1.2} \frac{n_M}{n_{Mt}} b_M \right) \frac{q_{Mt} p_n}{2\pi} \left( \frac{v}{v_n} \right)^{a_{vm}} + k_{7.2} M_M, \quad (13)
\end{aligned}$$

where the coefficient  $k_{7.1.1}$  expresses the ratio of the mechanical loss moment  $M_{Mm}$  in unloaded motor ( $M_M = 0$ ), determined for the motor shaft rotational speed equal to zero:  $n_M = 0$ , theoretical capacity per motor shaft revolution equal to  $q_{Mt}$  (coefficient  $b_M$  of absorbing capacity change per motor revolution:  $b_M = 1$ ), and working medium viscosity equal to  $v_n$ , to the theoretical moment  $M_{Mt}$  of the motor:

$$k_{7.1.1} = \frac{M_{Mm|M_M=0, n_M=0, b_M=1, v_n}}{M_{Mt}}, \quad (14)$$

The coefficient  $k_{7.1.2}$  expresses the ratio of the difference – in unloaded motor:  $M_M = 0$ , at the theoretical capacity  $q_{Mt}$  per motor shaft revolution ( $b_M = 1$ ) and the working medium reference viscosity  $v_n$  – between the mechanical loss moment  $M_{Mm|M_M=0, n_M=n_{Mt}, b_M=1, v_n}$  determined for the theoretical motor shaft rotational speed  $n_{Mt}$  and the mechanical loss moment  $M_{Mm|M_M=0, n_M=0, b_M=1, v_n}$  determined for the motor shaft rotational speed  $n_M$  equal to zero ( $n_M = 0$ ), to the theoretical moment  $M_{Mt}$  of the motor:

$$k_{7.1.2} = \frac{M_{Mm|M_M=0, n_M=n_{Mt}, b_M=1, v_n} - M_{Mm|M_M=0, n_M=0, b_M=1, v_n}}{M_{Mt}}, \quad (15)$$

The coefficient  $k_{7.2}$  expresses the ratio of the difference – at the theoretical capacity  $q_{Mt}$  per motor shaft revolution

( $b_M = 1$ ), the theoretical motor shaft rotational speed  $n_{Mt}$ , and the working medium reference viscosity  $v_n$  – between the mechanical loss moment  $M_{Mm|M_M=M_{Mt}, n_M=n_{Mt}, b_M=1, v_n}$  in the motor loaded with the theoretical moment  $M_{Mt}$  and the mechanical loss moment  $M_{Mm|M_M=0, n_M=n_{Mt}, b_M=1, v_n}$  in the unloaded motor to the theoretical moment  $M_{Mt}$  of the motor:

$$k_{7.2} = \frac{M_{Mm|M_M=M_{Mt}, n_M=n_{Mt}, b_M=1, v_n} - M_{Mm|M_M=0, n_M=n_{Mt}, b_M=1, v_n}}{M_{Mt}}, \quad (16)$$

The ratio  $n_M/n_{Mt}$  represents the effect of the rotational speed on the total amount of mechanical loss in the rotating hydraulic motor. According to [9], the assumed value of the exponent  $a_{nm}$  is 1.

$(v/v_n)^{a_{vm}}$  represents the effect of medium viscosity  $v$  on the mechanical loss moment in the displacement piston motor with medium filling the casing. The exact value of the exponent  $a_{vm}$  should be determined for each type of rotating hydraulic motor.

The mathematical model (2.9) describing the mechanical loss in pump makes it possible to determine precisely the dependence of the mechanical loss moment  $M_{Pm}$  on: the induced pressure increase  $\Delta p_{pi}$  in pump's working chambers, the pump delivery  $q_{Pi}$  per pump shaft revolution, and the oil viscosity  $v$ . The model utilises the mechanical loss coefficients  $k_{4.1}$ ,  $k_{4.1.1}$ ,  $k_{4.1.2}$ , and  $k_{4.2}$ , which provides opportunities for performing simulation tests.

The mathematical model (2.13) describing the mechanical loss moment  $M_{Mm}$  in rotating hydraulic motor makes it possible to determine precisely the dependence of this moment on: the motor shaft rotational speed  $n_M$ , the oil viscosity  $v$ , and the capacity  $q_{Mt}$  per motor shaft revolution. The model utilises the mechanical loss coefficients  $k_{7.1.1}$ ,  $k_{7.1.2}$ , and  $k_{7.2}$ , which provides opportunities for performing simulation tests.

## EXAMINED PUMPS AND MOTORS

The examined pumps and hydraulic motors are shown in Figs. 3 ÷ 7.

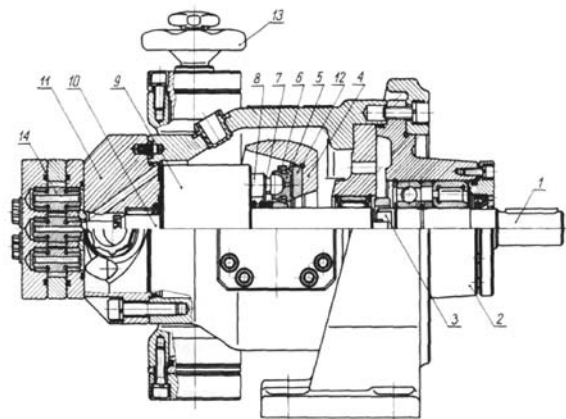


Fig. 3. PTO22-25 variable displacement pump, PZL-HYDRAL [11]; 1 – drive shaft, 2 – attachment drive, 3 – clutch, 4 – swivel disc, 5 – sliding foot, 6 – separator, 7 – spring, 8 – plunger, 9 – cylinder block, 10 – main shaft, 11 – cover, 12 – sliding disc, 13 – control unit

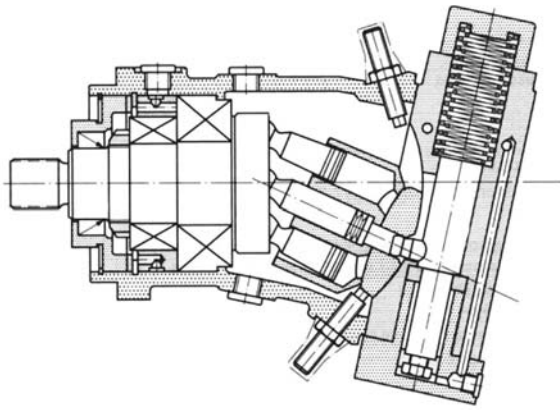


Fig. 4. Variable displacement piston pump (A7V.58R.DR.1.R.P.F.00 by HYDROMATIK) [3]

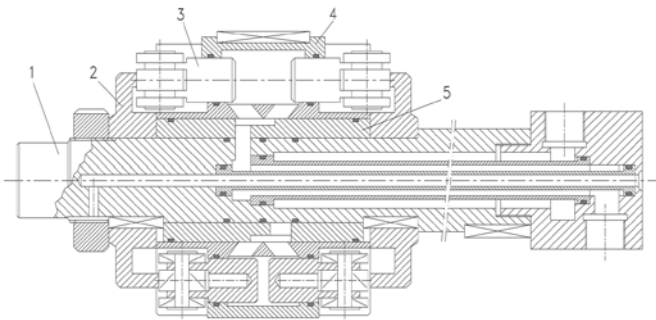


Fig. 5. Structure diagram of a low-speed hydraulic high-torque motor type SWSB with axial arrangement of pistons, HYDROSTER [8]; 1 – drive shaft; 2 – cam equipped with humps; 3 – plunger equipped with bearings; 4 – rotary cylinder block; 5 – distributor bushing

## COMPARING ENERGY LOSS COEFFICIENTS IN PISTON PUMPS

**Table 1** collates the energy loss coefficients  $k_i$  obtained for the examined piston pumps as a result of applying a new perspective to loss and efficiency assessment in rotating displacement machines used in hydrostatic drive and control systems [2, 3, 4, 10]. These coefficients were calculated neglecting the compressibility of the working medium. Constructional solutions of the examined pumps are shown in Figs. 3 and 4.

The coefficient  $k_i$  of the volumetric loss rate  $Q_{pv}$  provides the information about the scale of leakage flows taking place in the displacement machine. The volumetric efficiency  $\eta_{pv}$  can be calculated by subtracting the obtained value of coefficient  $k_i$  from 1. Hence, the volumetric efficiency of the PTOZ2-25 pump was 94,4%. At the same time, the efficiency of the A7V.58R.DR.1.R.P.F.00 pump with  $q_{pt} = 58,227 \text{ cm}^3$  was equal to 93,5%, and increased to 94,3% when its delivery was decreased to  $q_{pt} = 32,20 \text{ cm}^3$ .

The coefficient  $k_3$  of pressure loss  $\Delta p_{pp}$  provides the information about the scale of losses generated in machine's inner channels and distributor. These losses are mainly the effect of local pressure losses resulting from direction and velocity changes of the flowing medium. The pressure efficiency  $\eta_{pp}$  can be calculated by subtracting the obtained value of coefficient  $k_3$  from 1. The pressure efficiency of the examined pumps was relatively high and ranged about  $\sim 99,9\%$ .

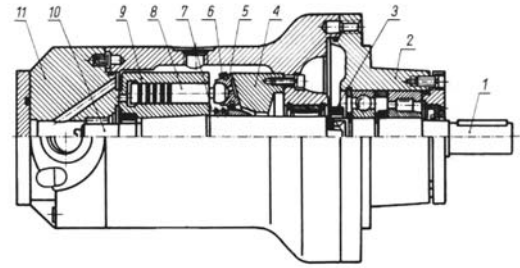


Fig. 6. Hydraulic motor PTO2-16 with constant rotational speed, PZL-HYDRAL [11]: 1 – drive shaft, 2 – drive starter, 3 – clutch, 4 – tread slope, 5 – sliding foot, 6 – separator assembly, 7 – spring, 8 – piston, 9 – rotor, 10 – main shaft, 11 – cover

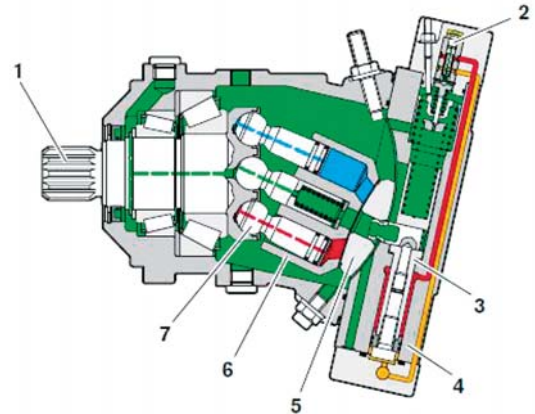


Fig. 7. A6VM variable displacement axial piston hydraulic motor by Bosch Rexroth [12]: 1 – drive shaft, 2 – control piston, 3 – control piston stroke, 4 – body in which the control piston is positioned, 5 – divider, 6 – cylinder block, 7 – piston

The coefficient  $k_{4,1}$  of the mechanical loss moment  $M_{Mm}$  (being the sum of coefficients  $k_{4,1}$  and  $k_{4,2}$ ) provides the information about losses caused by friction between construction elements (bearings, for instance) and between the liquid medium filling the crank chamber and the cylinder block (in piston machines). The largest losses were recorded in the PTOZ2-25 pump.

The coefficient  $k_{4,2}$  of the mechanical loss moment  $M_{Mm}$  provides the information about the scale of the mechanical loss moment increase  $\Delta M_{Pm|\Delta p_{pi}, b, v}$  in the pump, as a result of loading its structural elements with the induced moment  $M_{pi}$  generated by the induced pressure increase  $\Delta p_{Mi}$  in pump's working chambers. The largest losses were recorded in the PTOZ2-25 pump.

The mechanical efficiency  $\eta_{pm}$  of the pump can be calculated by subtracting the obtained sum of coefficients  $k_{4,i}$  from 1. Hence, the mechanical efficiency of the PTOZ2-25 pump was 87,7%, while that of the A7V.58R.DR.1.R.P.F.00 pump with  $q_{pt} = 58,227 \text{ cm}^3$  was 96,4%, and of the same pump with  $q_{pt} = 32,20 \text{ cm}^3$  was 94,6%.

## COMPARING ENERGY LOSS COEFFICIENTS IN PISTON MOTORS

**Table 2** collates the energy loss coefficients  $k_i$  obtained for the examined piston motors as a result of applying a new perspective to loss and efficiency assessment in rotating

Tab. 1. Energy loss coefficients  $k_i$  in displacement piston pumps [2÷4, 10]

		PTOZ2-25	A7V*	A7V**
	$v_n$ [mm <sup>2</sup> s <sup>-1</sup> ]	35	35	35
	$q_{pt}$ [m <sup>3</sup> ]	$16,50 \cdot 10^{-6}$	$32,20 \cdot 10^{-6}$	$58,23 \cdot 10^{-6}$
	$n_{pn}$ [s <sup>-1</sup> ]	16,67	25	25
	$p_n$ [MPa]	16	16	32
	$P_{pc}$ [kW]	4,40	12,88	23,10
$Q_{pv}$	$k_{l=}$	0,056	0,057	0,065
	$a_{pv=}$	-	-	0,97
	$a_{vv=}$	-	-	-0,30
	$k_{3=}$	0,001	0,002	0,001
$\Delta p_{pp}$	$k_{3=}$	0,001	0,002	0,001
	$a_{qp=}$	1,59	-	1,76
	$a_{vp=}$	-	-	0,26
$M_{pm}$	$k_{4,1=}$	0,076	0,039	0,021
	$k_{4,1,1=}$	0,063	-	0,014
	$k_{4,1,2=}$	0,013	-	0,007
	$k_{4,2=}$	0,047	0,015	0,015
	$a_{vm=}$	-	-	0,316

\* – coefficients  $k_i$  and exponents “a” determined for nominal operating parameters of the system in which the A7V.58.DR.1.R.P.F.00 pump was used

\*\* – coefficients  $k_i$  and exponents “a” determined for nominal parameters of the A7V.58.DR.1.R.P.F.00 pump

displacement machines used in hydrostatic drive and control systems [1, 2, 4]. Constructional solutions of the examined motors are shown in Figs. 5 ÷ 7.

The coefficient  $k_{7,1}$  of the mechanical loss moment  $M_{Mm}$  (being the sum of coefficients  $k_{7,1,1}$  and  $k_{7,1,2}$ ) provides the information about losses caused by friction between construction elements (bearings, for instance) and between the liquid medium filling the crank chamber and the cylinder block (in piston machines). The largest losses were recorded in the PTO2-16 motor.

The coefficient  $k_{7,2}$  of the mechanical loss moment  $M_{Mm}$  provides the information about the scale of mechanical loss moment increase  $\Delta M_{Mm}$  in the motor as a result of the increase in motor shaft loading. The largest losses were recorded in the SWSB-63 motor.

The mechanical efficiency  $\eta_{Mm}$  of the hydraulic motor can be calculated by subtracting the obtained sum of coefficients  $k_{7,i}$  from 1. Hence, the mechanical efficiency of the SWSB-63 motor was 96,8%, while that of the PTO2-16 motor was 94,0% and of the A6VM160 motor was 96,2%.

The coefficient  $k_8$  of the pressure loss  $\Delta p_{pp}$  provides the information about the scale of losses generated in machine's inner channels and distributor. These losses are mainly the effect of local pressure losses resulting from direction and velocity changes of the flowing medium. The pressure

Tab. 2. Energy loss coefficients  $k_i$  in displacement piston motors [1, 2, 4]

		SWSB-63	PTO2-16	A6VM
	$v_n$ [mm <sup>2</sup> s <sup>-1</sup> ]	26	35	22
	$q_{Mt}$ [m <sup>3</sup> ]	$639 \cdot 10^{-6}$	$12,74 \cdot 10^{-6}$	$160 \cdot 10^{-6}$
	$n_{Mn}$ [s <sup>-1</sup> ]	2,67	21,54	50
	$p_n$ [MPa]	6,2	16	40
	$P_{Mc}$ [kW]	10,6	4,39	320
$M_{Mm}$	$k_{7,1=}$	0,032	0,060	0,038
	$k_{7,1,1=}$	0,018	0,035	0,002
	$k_{7,1,2=}$	0,014	0,025	0,036
	$a_{vm=}$	0,15	-	-
	$k_{7,2=}$	0,076	0,033	0,036
$\Delta p_{Mp}$	$k_{8=}$	0,039	0,001	0,002
	$a_{qp=}$	1,76	1,87	1,76
	$a_{vp=}$	0,25	-	-
$Q_{Mv}$	$k_{9=}$	0,053	0,047	0,054
	$a_{pv=}$	1,62	0,92	-
	$a_{vv=}$	-0,62	-	-
	$a_{nv=}$	0,12	-	-

efficiency  $\eta_{Mp}$  can be calculated by subtracting the obtained value of coefficient  $k_8$  from 1. The highest pressure efficiency, equal to 99,0%, was recorded for the PTO2-16 motor.

The coefficient  $k_9$  of the volumetric loss rate  $Q_{Mv}$  provides the information about the scale of leakage flows in the displacement machine. The volumetric efficiency  $\eta_{Mv}$  can be calculated by subtracting the obtained value of coefficient  $k_9$  from 1. The lowest volumetric efficiency, approximately equal to 95,5%, was recorded for A6VM and SWSB-63 motors.

## CONCLUSIONS

The presented research is the next step in scientific development of the author involved in creating a library of energy loss coefficients  $k_i$ . This work discusses its practical implementation for assessing the quality of the examined machines.

Each energy loss coefficient  $k_i$  describes a relative value of individual loss in a hydrostatic system element (pump, hydraulic motor, but also in a conduit and the motor speed throttle control unit).

The  $k_i$  coefficients provide the opportunity for assessing proportions and scale of losses, as well as the resulting (volumetric, pressure, and/or mechanical) energy efficiency of an element, being the result of losses generated at the reference viscosity and nominal operating pressure  $p_n$  of the system in which the element is installed.

The information on exact values of the energy loss coefficients  $k_i$  for individual loss types provides opportunities for determining losses and (volumetric, pressure, mechanical, and total) energy efficiency of an element working in the drive system, as well as the total efficiency of the system with a given speed control structure as a function of speed coefficient  $\bar{\omega}_M$  and load coefficient  $\bar{M}_M$  of the hydraulic motor referred to in [9].

Tables 1 and 2 collate the obtained values of  $k_i$  coefficients and such exponents as:  $a_{Qp}$ ,  $a_{vp}$ ,  $a_{pv}$ ,  $a_{vv}$ ,  $a_{vm}$ ,  $a_{nv}$  which describe the effect of such parameters as: flow rate, pressure, rotational speed, and viscosity on individual losses. The values of these coefficients were obtained using the power sum method described in [4, 6], among other tools.

The values of such exponents as:  $a_{Qp}$ ,  $a_{vp}$ ,  $a_{pv}$ ,  $a_{vv}$  provide the information about the type of flow taking place in the examined machine.

The exact value of the exponent  $a_{vm}$  could only be calculated for two machines. It was equal to  $a_{vm} = 0,316$  for the A7V.58.DR.1.R.P.F.00 pump, and to  $a_{vm} = 0,148$  for the SWSB-63 motor.

The article compares the values of energy loss coefficients  $k_i$  for the A7V.58.DR.1.R.P.F.00 pump examined at its nominal parameters [3] and in the conditions of nominal operation of the entire system in which it was installed [10]. The obtained  $k_i$  values are different, as the pump working in conditions which differ from its nominal parameters generates higher energy loss coefficients  $k_i$  and, consequently, has lower efficiency.

## REFERENCES

- Balawender A., Osiecki A., Paszota Z., Klimkiewicz W., Ciepielowski J., *Tests of high-torque medium-pressure hydraulic motor SWSB-63 (in Polish)*. Research work report, Gdansk 1972.
- Czyński M., *Laboratory tests of hydrostatic transmission energy efficiency model (in Polish)*. PhD thesis. Szczecin University of Technology. Faculty of Maritime Technology. Szczecin 2005.
- Koralewski J., *The effect of viscosity on energy losses in variable delivery piston pump (in Polish)*. Factual report of research project No. N N504 4684 33, Agreement No. 4684/TO2/2007/33.
- Maczyszyn A., *Energy analysis of rotating displacement machine structures used in hydrostatic transmissions (in Polish)*. PhD. thesis. Gdansk University of Technology, Faculty of Ocean Engineering and Ship Technology, Gdansk 2014.
- Maczyszyn A., *Evaluation of losses in a hydraulic motor based on the SWSB – 63 motor tests*. Polish Maritime Research. Vol. 17, No 4, 2010, pp. 46–53.
- Maczyszyn A.: *Method of sum of power losses as a way for determining the  $k_i$  coefficients of energy losses in hydraulic motor*. Polish Maritime Research. Vol. 23, No. 2 (90) (2016), pp. 57–63.
- Maczyszyn A.: *Investigation method and mathematical model of pressure losses in hydraulic rotary motor*. Polish Maritime Research. Vol. 25, nr. 1 (97) (2018), pp. 93–98.
- Paszota Z., *Aspects energetiques des transmissions hydrostatiques*. Publications of Gdansk University of Technology, Gdansk 2002.
- Paszota Z., *Energy losses in hydrostatic drive*. Drive investigation method compatible with diagram of power increase opposite to the direction of power flow Lambert Academic Publishing Saarbrücken 2016.
- Skorek G., *Energy characteristics of hydraulic system with proportional control of servomotor fed by constant delivery pump in constant and variable pressure system (in Polish)*. PhD thesis. Gdansk University of Technology, Faculty of Ocean Engineering and Ship Technology, Gdansk 2010.
- Stryczek S.: *Hydrostatic drive (in Polish)*. Volume I Elements. WNT, Warsaw 1997.
- Operating manual for A6VM motor produced by Bosch Rexroth RE 91604-01-B/01.2012 (in Polish).
- Śliwiński P., *The influence of water and mineral oil on mechanical losses in the displacement pump for offshore and marine applications*. Polish Maritime Research. Vol. 25, iss. S1 (97) (2018), pp. 178–188, DOI: 10.2478/pmr-2018-0040;
- Śliwiński P., *The influence of water and mineral oil on volumetric losses in a hydraulic motor*. Polish Maritime Research, Special Issue 2017 S1 (93) 2017 Vol. 24; pp. 213–223 10.1515/pomr-2017-0041.
- Śliwiński P., *Influence of water and mineral oil on the leaks in satellite motor commutation unit clearances*. Polish Maritime Research 3 (95) 2017 Vol. 24; pp. 58–67 10.1515/pomr-2017-0090.

**CONTACT WITH THE AUTHORS**

**Agnieszka Maczyszyn**

*e-mail: [agnieszka.maczyszyn@pg.edu.pl](mailto:agnieszka.maczyszyn@pg.edu.pl)*

Gdańsk University of Technology

Narutowicza 11/12

80-233 Gdansk

**POLAND**

## NUMERICAL INVESTIGATING THE EFFECT OF WATER DEPTH ON SHIP RESISTANCE USING RANS CFD METHOD

Nguyen Thi Ngoc Hoa <sup>a</sup>

Vu Ngoc Bich <sup>a</sup>

Tran Ngoc Tu <sup>b</sup>

Nguyen Manh Chien <sup>b</sup>

Le Tat Hien <sup>c</sup>

<sup>a</sup> Ho Chi Minh City University of Transport, Vietnam

<sup>b</sup> Vietnam Maritime University, Vietnam

<sup>c</sup> Hochiminh City University of Technology, Vietnam National University, Vietnam

### ABSTRACT

*On inland waterways the ship resistance and propulsive characteristics are strictly related to the depth of the waterway, thus it is important to have an understanding of the influence of water depth on ship hydrodynamic characteristics. Therefore, accurate predictions of hydrodynamic forces in restricted waterways are required and important. The aim of this paper is investigating the capability of the commercial unsteady Reynolds–Averaged Navier–Stokes (RANS) solver to predict the influence of water depth on ship resistance. The volume of fluid method (VOF) is applied to simulate the free surface flow around the ship. The hull resistance in shallow and deep water is compared. The obtained numerical results are validated against related experimental studies available in the literature.*

**Keywords:** ship resistance, shallow water, RANS

### INTRODUCTION

In general, for a ship moving in shallow water, the following phenomena may take place due to the interaction between the ship and the seabed [1, 2]:

- water speed around the ship hull increases;
- pressure gradients around the hull increase;
- dynamic trim and sinkage increase;
- ship's wave pattern changes (wave amplitude increases);
- ship resistance increases;
- other ship characteristics (wake field, hull-propeller interaction, maneuverability) change;

The knowledge of ship resistance when navigating through shallow water regions is necessary and important, as correct design of ship propulsion system depends on the accuracy in determining its resistance.

This paper discusses the influence of water depth on ship resistance, with the aim to make inland vessels operate more economically and safely, as well as to reduce their fuel consumption.

There are three types of methods which are used to evaluate ship resistance in shallow water: empirical methods, Computational Fluid Dynamics (CFD) methods, and model towing tank tests.

The model tests give the most reliable results in predicting ship resistance in comparison with the two other methods. But this technique is both expensive and time consuming, so it is usually used after the alternative design stage, when the overall dimensions and the lines plan of the ship have already been optimally chosen.

Some empirical methods, mostly based on towing tank test results, have been proposed by Artjushkov [3], Geerts [4], and Karpov [5], among others, to predict ship resistance in shallow water. These methods are fast and do not require much input data. However, their range of application is often limited, and the lack of accuracy is a problem [6].

Nowadays, fast development of computational resources is making the Computation Fluid Dynamics (CFD) methods become a powerful tool for ship designers in solving problems related to hydrodynamics. Ship resistance calculation is one of

the basic hydrodynamic problems. The benefit of this method is that it allows visualization of several quantities, such as flow streamlines, wave profiles, or pressure distributions, for instance, which are difficult to obtain from experiments. This is a very useful aid for designers to understand the physics of flow phenomena, at least from a qualitative point of view.

Depending on the assumptions made to simplify the fluid equations, a number of CFD approaches can be named that are available to solve hydrodynamics problems. These approaches include: the potential flow theory (panel code), Reynold Averaged Navier-Stokes (RANS) equations, Detached Eddy Simulation (DES), and Large Eddy Simulation (LES). DES and LES approaches require much more computational effort, in terms of meshing and solver time, than the remaining two methods, but they allow to capture small variances of quantities of interest (velocity and pressure). However, in the ship resistance problem we mainly focus on the average values of forces. The RANS method simulates the turbulence using the term called “turbulence model” and gives time averaged mean values for velocity and pressure fields. This way, it consumes less time and requires less computational resources [7].

At the moment, the most popular approach is RANS CFD, as it ensures sufficient accuracy of results for engineering purposes at reasonable computational time. However, the level of accuracy of the numerical simulation significantly depends on practical skills.

There are some authors who performed shallow-water CFD calculations to investigate the influence of shallow water on ship resistance. However, large discrepancies between CFD and experimental data were witnessed for some results obtained by Prakash et al. [8], Pacuraru et al. [9], Patel et al. [10], Tezdogan et al. [11].

This paper presents the theoretical background and application of the RANS method to investigate the effect of water depth on ship resistance, taking into account the detailed setup of simulation to get accurate and meaningful results which agree well with the experiment. The case study is the US Navy Combatant DTMB with the available experimental data making it possible to validate the obtained numerical results on the experiment. The commercial solver Star-CCM+ was used in this study. The main objective of the paper is to assess the accuracy of CFD simulation for ship resistance calculations at different water depths.

The paper is organized as follows: the theoretical background of shallow water effects on ship wave patterns and ship resistance are described in detail in Section 2. The numerical simulation is analyzed and discussed in Section 3. The summary and conclusions are presented in Section 4.

## THEORETICAL BACKGROUND OF RESTRICTED WATER EFFECTS ON WAVE PATTERNS AND SHIP RESISTANCE

When the ship approaches a restricted depth water region, the interaction begins between the ship and the seabed, which leads to the velocity increase and pressure decrease under the

hull, and significant changes in sinkage and trim. All this leads to the increase in potential and skin friction drag, together with the increase in wave resistance. Using the wave theory, the wave velocity  $c$  can be developed in terms of  $h$  and  $\lambda$ , where  $h$  is the water depth from the still water level and  $\lambda$  is the wavelength, crest to crest. Therefore, classifying the water as deep or shallow can be decided based on the ratio of water depth  $h$  to wavelength  $\lambda$ .

For the deep water, the ratio  $h/\lambda$  is approximately assumed as  $h/\lambda \geq 1/2$ .

For the shallow water, the ratio  $h/\lambda$  is  $h/\lambda \leq 1/2$  and  $c = \sqrt{gh}$  is known as the critical speed, where  $c$  is the wave velocity and  $g$  is the acceleration gravity.

Larsson et al. [1] performed shallow water investigations in which they presented wave patterns formed due to a point source in shallow water. Their work led to the introduction of the dimensionless depth Froude number:

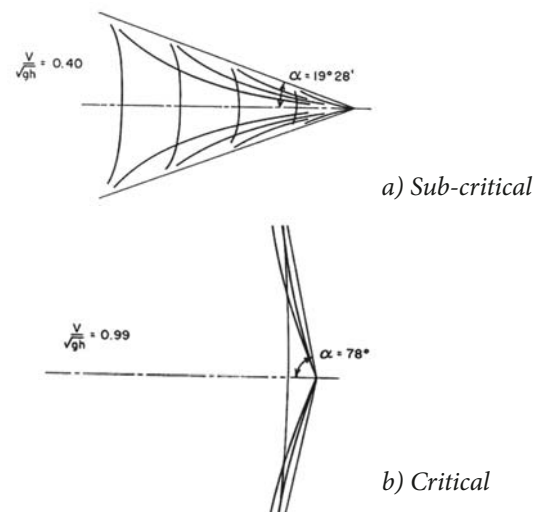
$$Fr_h = \frac{V}{\sqrt{gh}} \quad (1)$$

### SHALLOW WATER EFFECTS ON SHIP WAVE PATTERNS

Obviously, the geometry of the ship’s wave pattern in shallow water is not only dependent on its Froude number but also on its depth Froude number, which modifies the wave length and wave components. Based on the value of  $Fr_h$ , there are three flow regimes:

- Sub-critical  $Fr_h < 1.0$ ;
- Critical  $Fr_h = 1.0$ ;
- Supercritical  $Fr_h > 1.0$ .

The wave system at speeds well below  $Fr_h < 1.0$ , is shown in Figure 1(a). It comprises the transverse wave system and the divergent wave system propagating away from the ship. This wave system might be called the Kelvin wave pattern. When the ship speed nears the critical speed,  $Fr_h = 1.0$  the waves become more perpendicular to the track of the ship, Figure 1(b). At speeds greater than the critical speed, the diverging wave system propagates away from the ship with a certain angle, but in this case the transverse waves are clearly visible [1].



# NUMERICAL SIMULATIONS

## REFERENCE VESSEL

The vessel under study in this paper is the US Navy Combatant DTMB shown in Figure 4. The main reason for selecting this hull is that the hull geometry is published [13] and extensive model test data exists for vessel resistance at different Froude numbers in shallow and deep water. This data comes from tests carried out by the Ship Design and Research Centre CTO S.A. Poland [14, 15]. To provide opportunities for direct comparison, the computations were performed at the model scale with scale factor  $\lambda = 26.69$ , the same as the scale used in model tests.

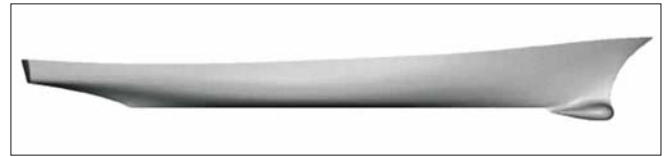


Fig. 4. Geometry of US Navy Combatant DTMB

Tab. 1. Basic parameters of unmanned boats

Description	Ship	Model
Scale factor	$\lambda$	26.69
Length between perpendiculars	$L_{pp}$ (m)	142.0
Length of waterline	$L_{WL}$ (m)	142.18
Breadth	$B$ (m)	19.06
Draft	$T$ (m)	6.15
Volume	$\nabla$ (m <sup>3</sup> )	8425
Wetted surface	$S$ (m <sup>2</sup> )	2972
Longitudinal Center of Buoyancy From AP	LCB/ $L_{pp}$	0.489

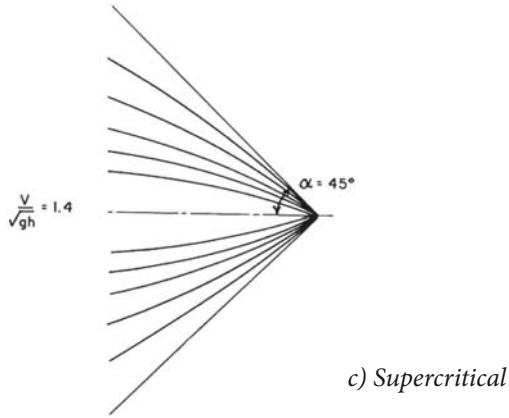


Fig. 1. Pressure patch wave patterns for different  $Fr_h$  [1]

## SHALLOW WATER EFFECTS ON SHIP RESISTANCE

In order to describe fully the effect of shallow water on ship resistance, it is usual to use such parameters as  $T/h$  or  $L/h$ , as well as the depth Froude number  $Fr_h$ . The influence of shallow water on the wave resistance component caused by changes in the wave pattern has already been investigated by Larsson et al. [1]. The results of the Froude number-based resistance experiment regarding to  $L/h$  changes are shown in Figure 2.

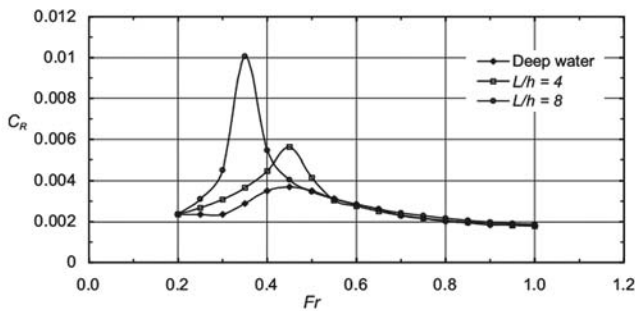


Fig. 2. Influence of water depth on residual resistance coefficient [12]

Figure 3 shows the influence of water depth on the total resistance coefficient as a function of Froude number and depth Froude numbers.

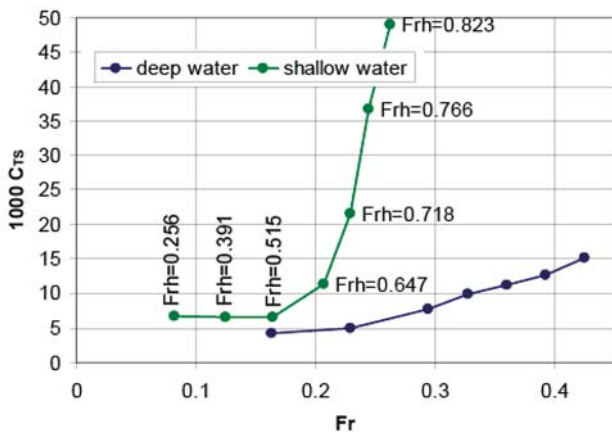


Fig. 3. Influence of water depth on total resistance coefficient

## TEST CASES

The computations were performed on the model scale for the following conditions: design draft  $T_M = 0.23$  m corresponding to the model volume  $\nabla_M = 0.455$  m<sup>3</sup>, and LCB measured from AP equal to 2.602 m in shallow water (water depth  $h_M = 0.46$  m) and in deep water.

The following settings were considered in the simulations:

- Calm water condition;
- Six model scale speeds: 0.597; 0.799; 0.995; 1.199; 1.291; 1.394 m/s for shallow water and deep-water simulations, corresponding to six depth Froude numbers: 0.281, 0.376, 0.469, 0.564, 0.608, 0.656 for shallow water case.
- The vessel is free to trim and sink;
- The hull mass is constant.

The water parameters for all case studies (density, viscosity) corresponded to real values used in the experimental set up (water density  $\rho = 998.7$  kg/m<sup>3</sup>, kinematic viscosity of water  $\nu = 1.079 \times 10^{-6}$  m<sup>2</sup>/s).

## COMPUTATION SETUP

The commercial package Star-CCM+ from Siemens was used for the computation.

### Computational domain and boundary conditions

The size of computational domain and the boundary conditions are important factors that affect the numerical results. For the computational domain, in general, its size should be taken sufficiently large to avoid any wave reflections from the boundary walls that might affect the numerical results. For the ship resistance calculation, the existing flow symmetry makes that only half of the hull (port side) can be simulated, thus reducing the computational time. Based on the recommendations and applications reported in Star-CCM+ [16], the size of the computational domain used in this study was selected as follows: the inlet boundary was located at  $1.5L_{pp}$  from forward perpendicular, while the outlet boundary was located at  $2.5L_{pp}$  from aft perpendicular. The top boundary was located at  $1.5L_{pp}$  from the free surface, and the lateral boundary at  $2.5L_{pp}$  from the center plane. The bottom boundaries for shallow-water and deep-water simulations were located at depth of 0.46 m and  $2.5L_{pp}$  from the free surface, respectively. The free surface was located at  $z = 0$ .

There are several types of boundary conditions offered by the CFD software package. For Star-CCM+, the boundary conditions applied when simulating ship resistance in shallow and deep water are given in Table 2.

Tab. 2. Boundary Conditions

Boundary	Shallow water	Deep water
Inlet	Velocity inlet	Velocity inlet
outlet	Pressure outlet	Pressure outlet
side	Symmetry plane	Symmetry plane
Symmetry	Symmetry plane	Symmetry plane
Top	Velocity inlet	Velocity inlet
Bottom	Moving No-slip wall	Velocity inlet
Ship hull	No-slip wall	No-slip wall

In the case of shallow water simulation, there is an interaction between the ship and the seabed. Therefore, the moving No-slip wall condition was applied on the tank bottom (the bottom moves with the velocity equal to the ship speed), which is similar to the CFD simulation successfully performed by Mark Bettle et. al [17].

### Physics modelling

The computation was carried out using the unsteady Reynold Averaged Navier-Stokes (RANS) equation model. The free surface was modeled with the volume of fluid (VOF) method. Fluid turbulence was simulated employing the Realizable K-epsilon Two-layer model with Two-layer all  $y^+$  wall treatment. To ensure accurate representation of ship motions, Star-CCM+ offers a Dynamic Fluid-Body Interaction

(DFBI) module, which allows the user to select degrees of freedom in which the analyzed structure can move and rotate. For the current study, the ship was free to trim and sink.

Since the ship moves in shallow water, the bottom of the ship is very close to the seabed boundary. To accurately model the movement of the ship above the fixed bottom, the “morphing mesh” was used. When using this mesh, the boundaries of a region can change position and shape over time, due to the motion of the contacting body [16]. Figure 5 shows a simple example of the morphing mesh with the flow through a cylinder with contracting wall.

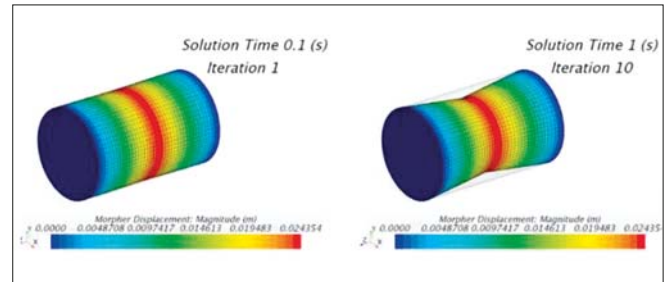


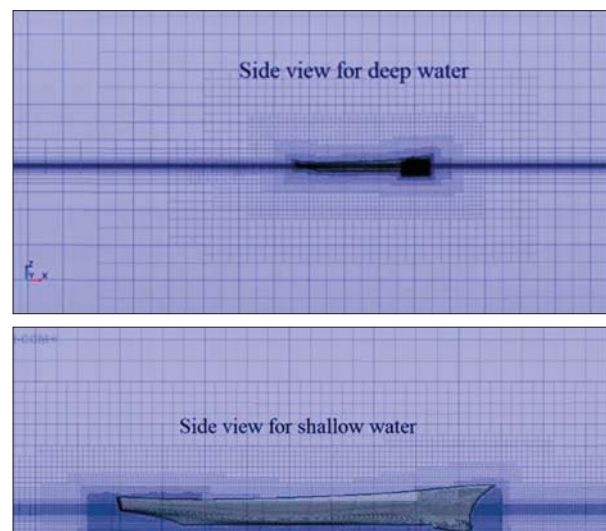
Fig. 5. Example of morphing mesh [16]

### Mesh generation

The mesh used in the calculations was composed of hexahedral cells. The meshing and the flow simulation were conducted by Star-CCM+. The grid generated for DTMB was characterized by concentration of cells around the hull region near the free surface.

To avoid using a fine mesh where unnecessary, a local volume was created for the sonar dome, and particular cell size was assigned. To capture the exact flow behavior near the walls of the wetted surface, prism layers were used to resolve the near-wall flow accurately. The prism layer numbers were selected such as to ensure the average  $y^+$  value of 50 on ship wall boundaries. To capture the flow around the hull near the free surface, a finer mesh was created in the free surface region. The grid at the free surface needed to be small enough to capture the wave elevation.

Figure 6 shows the general view of the coarsest mesh for shallow and deep water.



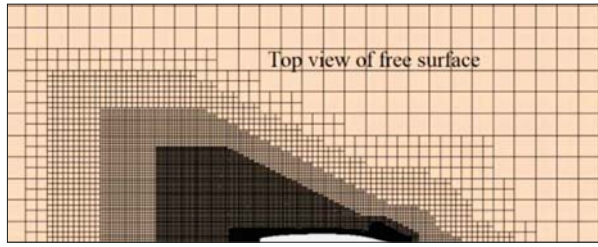


Fig. 6. General view of computational mesh in shallow and deep water

### Selection of time step

One of the key issues determining the numerical accuracy is the time step. For implicit solvers, the time step is decided by flow features. For standard pseudo-transient resistance computations, the recommended time step is related to the  $L/V$  ratio [18]:

$$\Delta t = 0.005 \sim 0.01 L/V, [s] \quad (2)$$

where  $V$  [m/s] is the ship speed and  $L$  [m] is the characteristic length.

## RESULTS AND DISCUSSION

### Mesh independency study

The first step of the research was to carry out the mesh sensitivity study, i.e. to determine the mesh density at which the difference between total resistance values obtained from two subsequent meshes reaches a sufficiently low level. The goal of such a study is to obtain the “grid-independent solution”, i.e. to ensure that further mesh refinement does not improve the quality of the results. In the presented case, the mesh sensitivity was studied for shallow water and deep-water cases at  $V = 1.199$  m/s. The studies were conducted using three grids with the Non-integer grid refinement ratio  $r_G = \sqrt{2}$  (the value recommended by the ITTC-Quality Manual 7.5-03-01-01, 2008 [19]). These grids were referred to as coarse (grid#3), medium (grid#2) and fine grid (grid#1), with the corresponding cell numbers equal to 0.54, 1.23 and 2.85 million, respectively, for shallow water, and 0.65, 1.42 and

2.97 million for deep water. Mesh refinement was done by reducing the cell size in all directions outside the prism layer. The idea here was to keep the same  $y^+$  values, of about 40 to 60, at near-wall cells over the largest part of the wetted hull surface for all six cases.

Table 3 presents the total resistance results obtained for three grids resolutions at  $V = 1.199$  m/s in shallow and deep water. The difference between the EXP data, denoted as  $D$ , and the CFD simulation results, denoted  $S$  in this paper, is defined as:

$$E\%D = \frac{(D - S)}{D} \cdot 100\% \quad (3)$$

The solution changes obtained in simulations performed on two subsequent meshes, such as fine-medium  $\epsilon_{12}$  and medium-coarse  $\epsilon_{23}$ , are defined as follows:

$$\epsilon_{12}\% = (S_1 - S_2) / S_1; \quad \epsilon_{23}\% = (S_2 - S_3) / S_2 \quad (4)$$

The presented cases show that the resistance changes monotonically with mesh density, and the comparison shows quite a good agreement between simulation (CFD) and experimental values (EFD), especially for the fine mesh (the relative error equal to only 3.28% for shallow water simulation and 0.47% for deep water simulation). As a result, the fine mesh was used in further studies.

### Numerical simulation results

Table 4 and Figure 7 compare the predicted and measured total ship resistance values in shallow and deep water for the depth Froude number ranging from 0.281 to 0.656. As can be seen, the difference between the numerically predicted and experimentally recorded ship resistance results varies from 1.45% to 4.47% for the shallow-water simulation and from 0.47% to 3.57% for the deep-water simulation.

Comparing the values of ship resistance components for shallow and deep water is summarized in Table 5 and Figure 8. As can be seen, two of the resistance components increase when the ship moves in shallow water. The change of the friction resistance component can be explained by the

Tab. 3. Total resistance predicted on different grids at  $V = 1.199$  m/s ( $Fr_h = 0.564$ ) in shallow and deep water (Model scale)

Shallow water							
Parameter		EFD(D)	V&V Study			$\epsilon_{32}\%$	$\epsilon_{12}\%$
			Grid#3	Grid#2	Grid#1		
RT[N]	Value	15.291	14.23	14.68	14.79	3.07	0.74
	E%D	/	6.94	4.00	3.28		
Deep water							
Parameter		EFD(D)	V&V Study			$\epsilon_{32}\%$	$\epsilon_{12}\%$
			Grid#3	Grid#2	Grid#1		
RT[N]	Value	12.720	12.98	12.84	12.78	-1.09	-0.47
	E%D	/	-2.04	-0.94	-0.47		

Tab. 4. Comparing predicted ship resistance results with experimental values (model scale)

Parameters	V [m/s]	0.597	0.799	0.995	1.199	1.291	1.393
$R_T$ [N] in shallow water ( $h = 0.46\text{m}$ )	$Fr_h$	0.281	0.376	0.469	0.564	0.608	0.656
	EXP.	4.670	7.282	10.667	15.291	16.695	19.788
	CFD	4.47	7.05	10.28	14.79	16.953	20.08
	Relative error [%]	4.47	3.28	3.77	3.39	-1.52	-1.45
$R_T$ [N] in deep water	EXP.	3.08	5.27	8.25	12.72	14.52	16.98
	CFD	3.19	5.45	8.48	12.78	14.78	17.43
	Relative error [%]	3.57	3.42	2.79	0.47	1.79	2.65

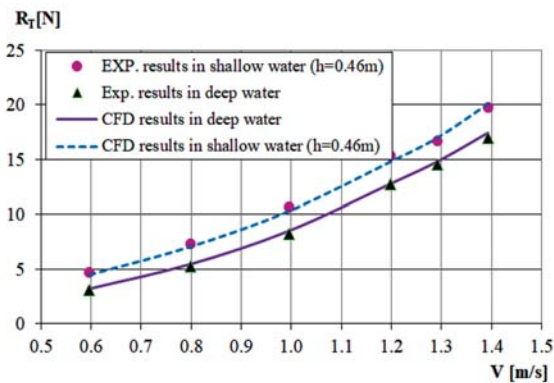


Fig. 7. Comparing predicted ship resistance results in deep and shallow water at different speeds with experimental values

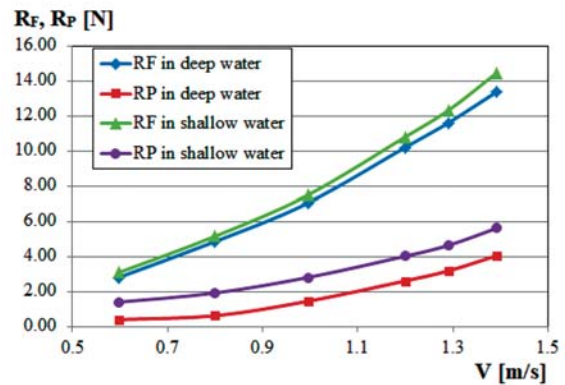


Fig. 8. Changes of ship resistance components in shallow and deep water

Tab. 5. Changes of ship resistance components in shallow and deep water (model scale)

V [m/s]	CFD computation in deep water			CFD computation in shallow water ( $h = 0.46\text{m}$ )			
	$R_T$	$R_F$	$R_P$	$Fr_h$	$R_T$	$R_F$	$R_P$
0.597	3.19	2.80	0.39	0.281	4.47	3.08	1.39
0.799	5.45	4.84	0.61	0.376	7.05	5.14	1.91
0.995	8.48	7.04	1.44	0.469	10.28	7.48	2.80
1.199	12.78	10.18	2.6	0.564	14.79	10.78	4.01
1.291	14.78	11.6	3.18	0.608	16.953	12.316	4.64
1.393	17.43	13.38	4.05	0.656	20.08	14.46	5.62

increasing flow velocity under the keel when the vessel moves from deep to shallow water. This flow velocity change, clearly shown in Figure 9, results from the interaction between the ship and the seabed. The change of the pressure resistance component can be explained by the change of the wave pattern in shallow water, accompanied by significant pressure drop (see Figures 10 and 11).

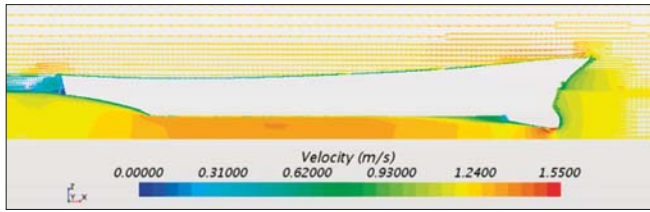
## CONCLUSION

The unsteady RANS calculations were performed to predict the resistance of the DTMB model in shallow

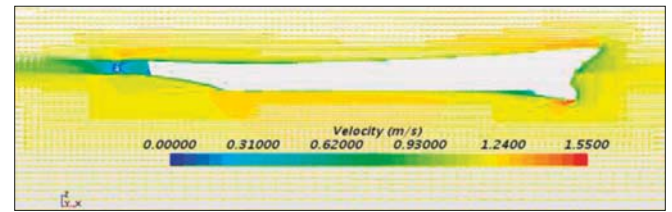
water at different depth Froude numbers. The selected ship speed values were the same as in the towing tank experiments performed in CTO [14, 15]. In all analyses, use was made of the commercial RANS solver Star-CCM+ version 12.02.011.R8.

The predicted ship resistance and model test results were presented for the DTMB model. The CFD results obtained for all simulation cases show quite good agreement with the experiment.

The increase of ship resistance in shallow water, compared to the deep-water case at the same speed, is due flow velocity change under the keel and significant pressure drop along the hull, all this leading to wave pattern change.

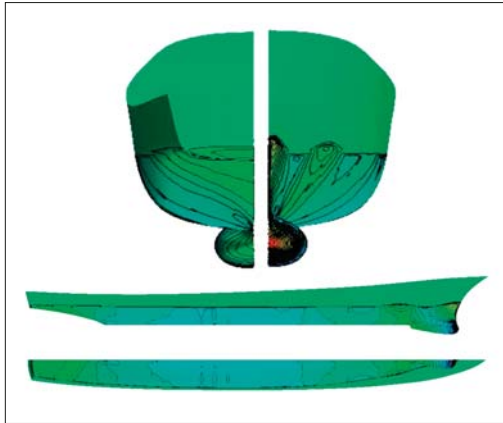


a) Shallow water

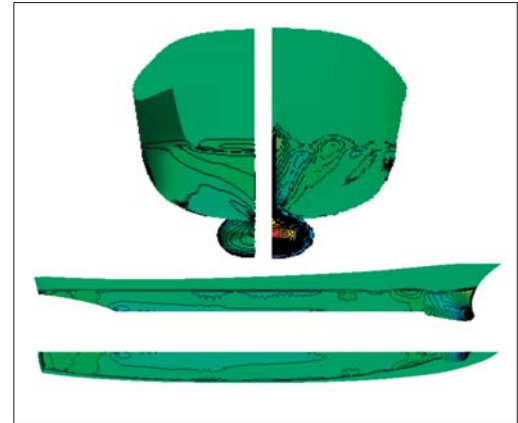


b) Deep water

Fig. 9. Flow velocity distributions under keel in deep and shallow water, at the same speed ( $V=1.199$  m/s)



a) Shallow water



b) Deep water

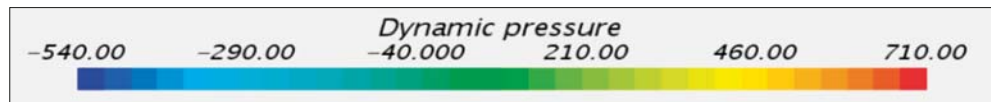
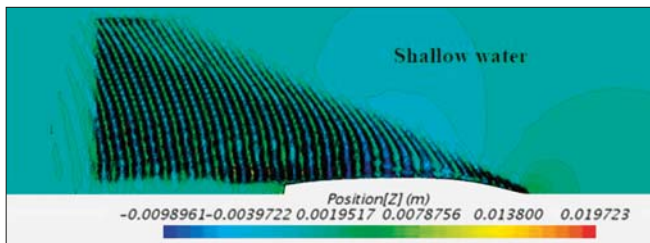
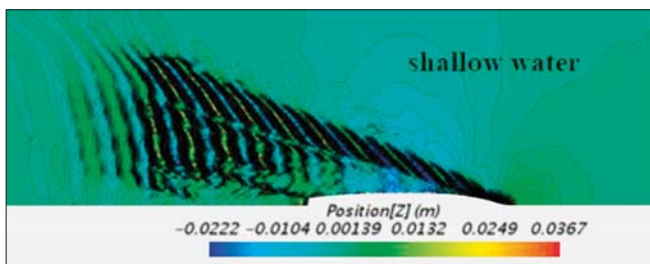
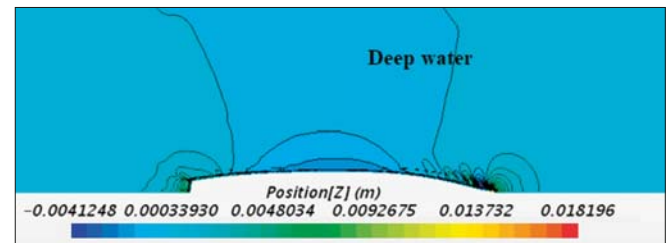


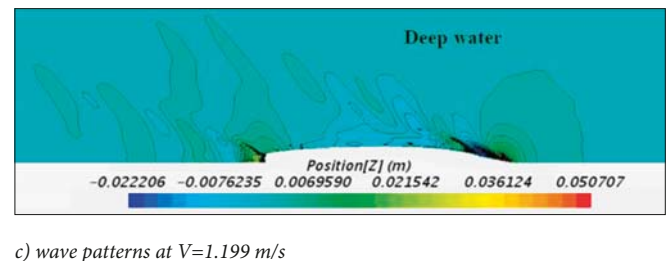
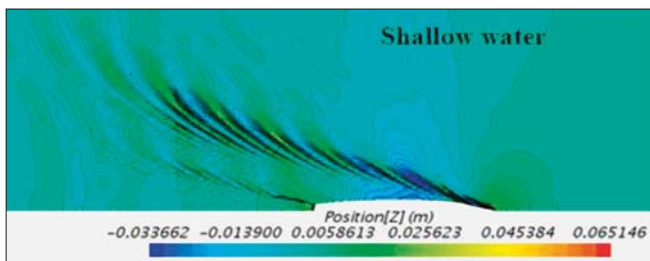
Fig. 10. Dynamic pressure distributions along the hull in deep and shallow water, at the same speed ( $V=1.199$  m/s)



a) wave patterns at  $V=0.799$  m/s



b) wave patterns at  $V=1.199$  m/s



c) wave patterns at  $V=1.199$  m/s

Fig. 11. Wave patterns at different speeds in shallow and deep water

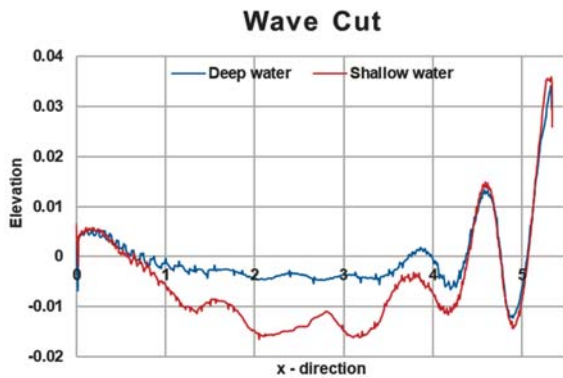


Fig. 12. Wave cut at  $V = 1.199$  m/s in shallow and deep water

The computed values of the resistance components (frictional and pressure) reveal that when the ship moves in shallow water, the pressure resistance component changes more than the friction resistance component, especially at high depth Froude numbers.

Good agreement between CFD computations and model tests illustrates the capability of RANS CFD in solving ship hydrodynamics problems. However, further validation using model tests with final hull form should be carried out to avoid unexpected errors of numerical methods.

## NOMENCLATURE

$B$ [m]	– Ship breadth
$L_{PP}$ [m]	– Length between perpendiculars
$L_{WL}$ [m]	– Length at water level
$\nabla$ [m <sup>3</sup> ]	– Ship volume displacement
$S$ [m <sup>2</sup> ]	– Wetted surface area
$T$ [m]	– Ship draft
$R_T$ [N]	– Total ship resistance
$R_F$ [N]	– Friction resistance component
$R_p$ [N]	– Pressure resistance component
$h$ [m]	– Depth of water
$V$ [m/s]	– Ship speed
$Fr_h$	– Depth Froude number
$\rho$ [kg/m <sup>3</sup> ]	– Water density

## REFERENCES

- Larsson, L. and H. Raven, *Ship resistance and flow*. 2010: Society of Naval Architects and Marine Engineers.
- Bertram, V., *Practical ship hydrodynamics*. 2011: Elsevier.
- Artjushkov, L., *Wall effect correction for shallow water model tests*. NE Coast Institution of Engineers and Shipbuilders., 1968.
- Geerts, S., Verwerft, B., Vantorre, M., and Van Rompuy, F., *Improving the efficiency of small inland vessels*. Proc., 7th European Inland Waterway Navigation Conf., Budapest Univ. of Technology and Economics, Budapest, Hungary, 2010.
- Karpov, A., *Calculation of ship resistance in restricted waters*. TRUDY GII. T. IV, Vol. 2 (in Russian). 1946.
- Linde, F., et al., *Three-Dimensional Numerical Simulation of Ship Resistance in Restricted Waterways: Effect of Ship Sinkage and Channel Restriction*. Journal of Waterway, Port, Coastal, and Ocean Engineering, 2016. 143(1): p. 06016003.
- ITTC 2014 Specialist committee on CFD in marine hydrodynamics—27th ITTC.
- Prakash, S. and B. Chandra, *Numerical estimation of shallow water resistance of a river-sea ship using CFD*. International journal of computer applications, 2013. 71(5).
- Pacuraru, F. and L. Domnisoru. *Numerical investigation of shallow water effect on a barge ship resistance*. in IOP Conference Series: Materials Science and Engineering. 2017. IOP Publishing.
- Patel, P.K. and M. Premchand, *Numerical investigation of the influence of water depth on ship resistance*. International Journal of Computer Applications, 2015. 116(17).
- Tezdogan, T., A. Incecik, and O. Turan, *A numerical investigation of the squat and resistance of ships advancing through a canal using CFD*. Journal of Marine Science and Technology, 2016. 21(1): p. 86–101.
- Molland, A.F., S.R. Turnock, and D.A. Hudson, *Ship resistance and propulsion*. 2017: Cambridge university press.
- <http://www.simman2008.dk/5415/combatant.html>.
- Resistance test report in deep water for DTMB vessel*. CTO, Poland 2017.
- Resistance test report in shallow water for DTMB vessel*. CTO, Poland 2017.
- CD-ADAPCO. *User Guide STAR-CCM+, Version 13.02*. 2018.
- Bettle, M., S.L. Toxopeus, and A. Gerber, *Calculation of bottom clearance effects on Walrus submarine hydrodynamics*. International Shipbuilding Progress, 2010. 57(3-4): p. 101–125.
- ITTC 2011b *Recommended procedures and guidelines 7.5-03-02-03*.
- ITTC-Quality Manual 7.5-03-01-01, 2008.

**CONTACT WITH THE AUTHORS**

**Nguyen Thi Ngoc Hoa**

*e-mail: hoa\_vt@hcmutrans.edu.vn*

**Vu Ngoc Bich**

*e-mail: vubich@hcmutrans.edu.vn*

Ho Chi Minh City University of Transport  
**VIETNAM**

# NUMERICAL AND EXPERIMENTAL STUDY ON SEAKEEPING PERFORMANCE OF A HIGH-SPEED TRIMARAN WITH T-FOIL IN HEAD WAVES

Ang Li <sup>a</sup>

Yunbo Li <sup>b</sup>

<sup>a</sup> Harbin Engineering University, China

<sup>b</sup> Shanghai Maritime University, China

## ABSTRACT

*The longitudinal motion characteristics of a slender trimaran equipped with and without a T-foil near the bow are investigated by experimental and numerical methods. Computational fluid dynamics (CFD) method is used in this study. The seakeeping characteristics such as heave, pitch and vertical acceleration in head regular waves are analyzed in various wave conditions. Numerical simulations have been validated by comparisons with experimental tests. The influence of large wave amplitudes and size of T-foil on the longitudinal motion of trimaran are analyzed. The present systematic study demonstrates that the numerical results are in a reasonable agreement with the experimental data. The research implied that the longitudinal motion response values are greatly reduced with the use of T-foil.*

**Keywords:** trimaran; T-foil; URANS; longitudinal motion; model test

## INTRODUCTION

Improving a ship's seakeeping performance and enhancing its navigational performance under stormy wave conditions has always been crucial research topics in the marine industry. More and more research works on high-performance vehicles and stabilization techniques have been made in recent years. Trimarans are currently of interest for many new high-speed ship projects due to their high level of hydrodynamic efficiency.

Compared with monohull and catamaran, the trimaran has excellent navigation and high-speed performance [1, 2]. Large amount of efforts have been focused on developing experimental and numerical methods to predict the seakeeping performance of trimarans. In the work [3] two different designs for target trimaran were studied. The first one had a round bilge hull and asymmetric side hulls and the other one had a Deep-V hull and symmetric side hulls. Comparison of the resistance and seakeeping qualities of the two different trimaran designs tested in model scale were presented in their paper. In [4] model tests were conducted on multiple trimarans, and the influence of trim, hull form and

outrigger layout on the resistance and seakeeping performance were analyzed. In [5] the effects of the stagger of the side hulls on the motions in heave and pitch of a trimaran hull were investigated. Despite the model experiments were still valuable the use of CFD method was getting in common. CFD approaches widely used by researchers can be classified into two main categories, namely, based on potential theory and RANS method. For the prediction of seakeeping performance some methods could be found in the literature : in [6] the high-speed slender body potential flow theory (also called two and a half dimensional potential flow theory, 2D+t or 2.5D), was first developed. The method effectively solved the shortcomings of the STF method in the prediction of multihull ship seakeeping [7]. In [8] the vertical motions of a trimaran with different Froude numbers were calculated by using 2.5D theory. The authors demonstrated that the results of the 2.5D method for prediction of the trimaran wave-induced motions are in agreement with the experimental results. In [9] a series of model tests in regular head waves were conducted for one trimaran with different outrigger layouts at the Froude numbers of 0.471 and 0.628. The authors pointed out that the numerical model of 2.5D is based on the linear potential flow theory and hence cannot capture the

influence of the violent green water on the heave motions, and that this could cause an error in the numerical results.

In the traditional potential theory viscosity and non-linearity effects are not taken into account, thus it may cause errors. As computational facilities have become more powerful and accessible, CFD tools are now increasingly used to predict ship motions. In [10] a numerical method for the prediction of motion performance of a trimaran with a long bulb and a transom stern was developed and its accuracy was assessed by the comparison with experiments. The unsteady Reynolds-averaged Navier-Stokes equations are solved with the density function technique for the free surface treatment. The research showed that the heave and pitch motions were predicted with reasonable accuracy. In [11] ship motions and added resistance of a high-speed trimaran in regular head waves were predicted by using CFD tools. In [12] CFD tools were used to investigate the optimization of a trimaran yacht equipped with axebow. The study was focused on the analysis of resistance and seakeeping qualities which could provide the best performance to the yacht.

When the trimaran navigates under high speed, the longitudinal motion responses may be large. The vertical acceleration will cause severe seasickness of passengers and crew [13]. In order to reduce longitudinal motion responses of fast ferries, different kinds of motion control devices have been developed to increase comfort of passengers. In recent years, T-foils has been widely installed on fast ferries due to its small size and obvious effects. It is fixed under the bow, providing the restoring force and moment, and it can reduce the pitch and heave motion of the fast ferries [14]. The INCAT corporation engaged in the study of anti-vertical motion appendages, developed fixed and retractable T-foil and cooperated with Maritime Dynamics Inc. (MDI) to design the Ride Control System (RCS) which can adjust the restoring force and moment generated by T-foil when the ship moves in waves [15]. In [14-16] many numerical simulations and model tests of the high speed monohull craft with T-foil and flaps were conducted. The authors pointed out that the vertical acceleration and MSI (Motion Sickness Index) of the fast ferry were reduced by 65 and 35% , respectively , with the actuators moving under control. In [17] an experimental study (model tests) was conducted on a trimaran with controlled T-foil, three different ship models including a bare hull, a hull with non-controlled T-foil and a hull with an active controlled T-foil. In the study, the efficacy of the non-controlled and controlled T-foil were reported and discussed. There are limited studies based on URANS method on the reduction of vertical motion of the trimaran by means of T-foil.

The present study primarily deals with the seakeeping performance of a trimaran with T-foil near the bow in regular head waves, investigated by using experimental and numerical methods.

In the present study, the numerical simulations and experimental tests for the prediction of the ship motions of trimaran with and without T-foil in regular head waves are carried out. The numerical method is based on URANS method. Both free heave and pitch motions in head waves

are simulated. The obtained numerical results are validated with the use of experimental data. During the study, the grid convergence tests are also carried out for the URANS approach. The longitudinal motion of the ship is examined in various wave conditions. Unsteady wave patterns and the time history results of the longitudinal ship motion responses in waves are simulated by using the CFD tool. To investigate the influence of T-foil on hydrodynamic performance of high-speed trimaran in regular head waves, two cases are considered: bare trimaran and trimaran with T-foil. The influence of large wave amplitudes and size of T-foil on the longitudinal motion of trimaran are analyzed.

## DESCRIPTION OF THE TRIMARAN AND T-FOIL

A numerical simulation and small-scale model test of the trimaran were carried out. The body plan of the main hull and outriggers are shown in Fig. 1. The main characteristics of the model are given in Tab. 1.

The dimensions of the T-foil installed on the trimaran model near the bow are indicated in Tab. 2. The T-foil is composed of a vertical foil and an airfoil with the attack angle of  $\pm 5^\circ$ . It is assumed that the counter-clockwise rotation angle of the T-foil is positive. The geometrical image of the trimaran equipped with the T-foil and stern flap is shown in Fig. 2.

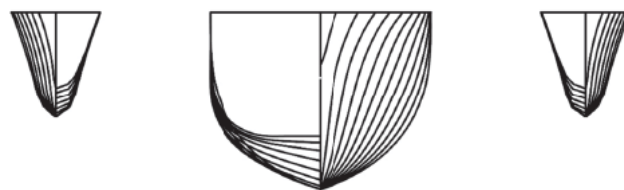


Fig. 1 Lines drawing of the trimaran

Tab. 1 Main characteristics of the trimaran model

Main feature	Value	
	Middle Hull	Side Hull
Length overall (m)	3.343	
Breadth (m)	0.641	
Depth (m)	0.249	
Length at waterline (m)	3.0	1.071
Beam at waterline (m)	0.24	0.051
Draft (m)	0.122	0.043
Displacement (kg)	45.99	
Longitudinal radius of gyration (m)	0.807	
Ratio of main hull displacement and outriggers displacement	14.333	

Tab. 2 Dimensions of the T-foil'

Principal particulars	Value
Airfoil shape	NACA0012
Span (m)	0.144
Chord (m)	0.096
Aspect ratio	1.5
Rotating angle of the flap (°)	
Width of the vertical foil (m)	0.01
Length of the vertical foil (m)	0.060
Height of the vertical foil (m)	0.024
Longitudinal position of installed foil (distance between vertical centre line of foil and 10 <sup>th</sup> theoretical station of the trimaran body) (m)	1.320

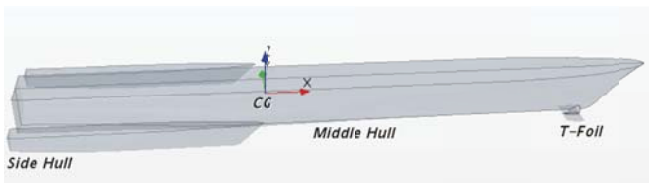


Fig. 2 Geometrical image of the trimaran with T-foil

## EXPERIMENTAL SETUP

Model tests were conducted at the Harbin Engineering University towing tank whose dimensions are: 108 m, 7 m and 3.5 m in length, width and depth, respectively. There is a wave maker at one end of the towing tank, and a wave dissipation bank at the other end of the towing tank. The maximum speed of the towing carriage over the tank is 6.5 m/s. The waves generated by the wave generator are measured with the use of a wave probe. The four - motion measurement device (heave, pitch, roll and surge) is used to measure the ship model motions.

The bare trimaran hull model and the model fitted with a T-foil and stern flap are used for the model tests. The model free to trim and sink was run first in calm water to obtain the basic resistance. The models were then run in a seaway to allow the ship wave-generated motions to be observed. The heave, pitch and vertical acceleration at 19th hull station near the bow in different wave conditions were measured. Fig. 3 shows the experimental setup for the model test.



Fig. 3 Experimental setup for seakeeping tests

The forward speed  $U$  was set at 3.408 m/s, and the corresponding Froude number  $F_n$  was equal to 0.628. For the entire seakeeping tests, the wave amplitude  $\zeta$  changed with wave length. The wavelength  $\lambda$  varied between 1.5 m and 6.75 m, thus the ratio  $\lambda/L$  varied between 0.50 and 2.25. The numerical simulations were conducted in the same test conditions as for the model tests. The CFD simulations and model tests were performed for eleven different conditions listed in Tab. 3, ( identified by their case numbers). The wave encounter frequency  $f_e$  [ Hz] is calculated from the formula  $f_e = \sqrt{g/2\pi\lambda} + U/\lambda$  for head seas (where  $g$  - the gravitational acceleration, and  $U$  - the ship forward speed [ m/s]).

Tab. 3 Simulation and model test conditions

Condition number	Wave length ( $\lambda/L_{pp}$ )	Wave amplitude $\zeta$ (m)	Wave frequency $f$ (Hz)	Encounter frequency $f_e$ (Hz)	$\zeta^*k$
C0 (calm water)	—	—	—	—	—
C1	0.50	0.015	1.020	3.292	0.063
C2	0.75	0.0225	0.833	2.348	0.063
C3	0.88	0.025	0.769	2.060	0.059
C4	1.0	0.03	0.721	1.857	0.063
C5	1.25	0.03	0.645	1.554	0.050
C6	1.38	0.03	0.614	1.437	0.046
C7	1.60	0.04	0.570	1.280	0.052
C8	1.75	0.04	0.545	1.194	0.048
C9	2.0	0.05	0.510	1.078	0.052
C10	2.25	0.05	0.481	0.986	0.047

## NUMERICAL SIMULATION METHOD

This section provides details of the numerical simulation approaches used in this study and discussion of the numerical methods applied to the current CFD model.

## GOVERNING EQUATIONS

An URANS approach was applied to calculate the added resistance and ship motions in regular waves by using the STAR-CCM+ commercial CFD software [18]. The governing equations are the RANS equations and continuity equation for mean velocity of the unsteady, three-dimensional

incompressible flow. The averaged continuity and momentum equations are given by Eq. (1) and Eq. (2) in tensor form in the Cartesian coordinate system.

$$\frac{\partial(\rho\bar{u}_i)}{\partial x_i} = 0 \quad (1)$$

$$\frac{\partial\rho\bar{u}_i}{\partial t} + \frac{\partial}{\partial x_j}(\rho\bar{u}_i\bar{u}_j + \rho\overline{u_i u_j}) = -\frac{\partial\bar{p}}{\partial x_i} + \frac{\partial\bar{\tau}_{ij}}{\partial x_j} \quad (2)$$

where  $\bar{u}$  is the relative averaged velocity vector of flow between the fluid and the control volume,  $\overline{u_i u_j}$  is the Reynolds stresses and  $\bar{p}$  is the mean pressure. For Newtonian fluid under three-dimensional incompressible flow, the mean shear stress tensor  $\bar{\tau}_{ij}$  can be expressed as follows :

$$\bar{\tau}_{ij} = \mu \left( \frac{\partial\bar{u}_i}{\partial x_j} + \frac{\partial\bar{u}_j}{\partial x_i} \right) \quad (3)$$

where  $\mu$  is dynamic viscosity.

The equation for the translation of the centre of mass of the ship body is given as:

$$m \frac{dv}{dt} = f \quad (4)$$

where  $m$  represents the mass of the body,  $f$  is the resultant force acting on the body and  $v$  is the velocity of the centre of mass. An angular momentum equation of the body is formulated in the body local coordinate system with the origin in the centre of the body:

$$M \frac{d\omega}{dt} + \omega \times M \omega = n \quad (5)$$

where  $M$  is the tensor of moments of inertia,  $\omega$  is the angular velocity of rigid body, and  $n$  is the resultant moment acting on the body. The resulting force and moment acting on the ship are obtained from fluid pressure and shear force acting on each boundary face of the body. The translations of the ship are estimated according to the computed velocity and pressure fields in the flow domain.

## PHYSICAL PHENOMENA MODELLING

The “Finite Volume Method” (FVM) was applied to the spatial discretization. The “Volume of Fluid” (VOF) method was used to model the free surface, either with a flat wave in the simulation of calm-water resistance or first-order regular wave in the calculation of ship motion in waves. The VOF model is based on the assumption that the same basic governing equations as those used for a single-phase problem can be solved for all the fluid phases present within the domain, as it is assumed that they will have the same velocity, pressure and temperature. This means that the equations are solved for an equivalent fluid whose properties represent the different phases and their respective volume

fractions. The grid is simply refined to enable the variations in volume fraction to be more accurately captured. In this work, a second-order convection scheme was used throughout all the simulations to accurately capture interface between the phases. The flow equations were solved in a segregated manner by using a predictor-corrector approach. Convection and diffusion terms in the RANS equations were discretized by a second-order upwind scheme and a central difference scheme. The semi-implicit method for pressure-linked equations (SIMPLE) algorithm [19] was used to resolve the pressure-velocity coupling. The turbulent model selected in this study was a SST k- $\omega$  turbulence model which has the ability to simulate the complex flow problems with flow separation and strong adverse pressure gradients. In order to simulate the seakeeping behaviour of the trimaran, the Dynamic Fluid Body Interaction (DFBI) model was used to allow the model to move free in heave and pitch modes. The DFBI model enabled the RANS solver to calculate the exciting force and moments acting on the hull due to wave forces, and to solve the governing equations of rigid body motion to reposition the grid body [20]. The overset mesh allowed all motions to be simulated without the risk of badly deforming cells, thus enabling the simulation of large amplitude motions.

## COMPUTATIONAL DOMAIN, BOUNDARY CONDITIONS AND MESHES

A general view of the computational domain with the trimaran is shown in Fig. 4. The boundary conditions are given in Tab. 4.

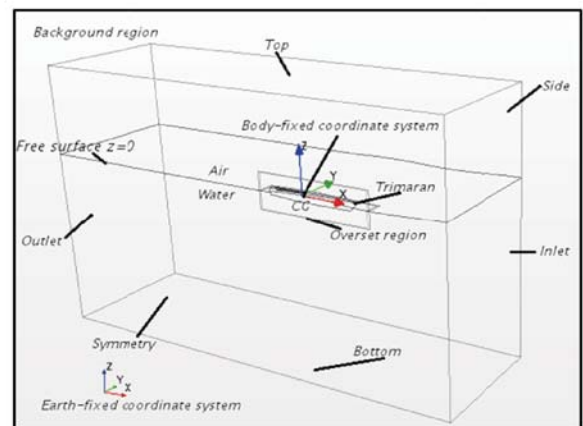


Fig.4 General view of computational domain and boundaries

Tab. 4 Boundary conditions

Boundary	Inlet	Outlet	Side	Bottom	Top	Symmetry	Trimaran
Boundary conditions	Velocity Inlet	Pressure Outlet	Velocity Inlet	Velocity Inlet	Velocity Inlet	Symmetry Plane	No-Slip Wall

Two different coordinate systems were applied to predict ship performance. One is the earth-fixed coordinate system and another one is the moving coordinate system located at the centre of gravity (CG) of the trimaran. The origin of the inertial frames was located on the base line of the ship at its aft perpendicular. The origin of the ship-fixed reference frames was situated at their centre of gravity (CG). First, the flow field was solved, and the exciting force and moments acting on the hull were calculated in the earth-fixed coordinate system. Then, the forces and moments were converted to the moving coordinate system. The motions of the trimaran were described by translations and rotations with respect to the centre of gravity in the earth-fixed coordinate system. The equations of motions were solved to calculate the ship velocities and then they were converted back to the earth-fixed coordinate system. These information sets were then used to find the new location of the ship and grid system. The overset grid system was re-positioned after each time step. The authors of [21] recommend that for simulations in the presence of incident waves, the inlet boundary should be located  $(1\div 2) L_{BP}$  away from the hull, whereas the outlet should be positioned  $(3\div 5) L_{BP}$  downstream to avoid any wave reflection from the boundary walls. The trimaran symmetry about its centre plane of the middle hull allowed to discretize only one-half of the computational domain. Therefore only a half of the trimaran and control volume were considered in all the calculations; thus, the symmetry plane formed the centreline domain face to reduce computational time. The mid-plane of the ship is located at  $y=0$  and ship draught (T) is  $z=0$ . The dimensions of the boundaries are shown in Fig. 5, which gives front and side views of the computation domain.

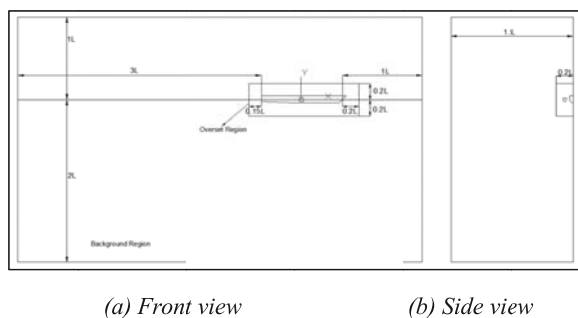


Fig. 5. The dimensions of the computational domain

The inlet boundary was located one model length ahead of the model's forward perpendicular; the outlet boundary - three model lengths behind the model's aft perpendicular; the bottom - two model lengths below the calm water surface; the top - one model length above the calm water surface and one model length between symmetry boundary and side boundary. The velocity-inlet boundary condition was set in the positive  $x$  - direction, where first - order incident regular waves were generated. The velocities of the incident wave were directly set to the inlet boundary to generate the required regular wave. The negative  $x$ - direction was modelled as a pressure-out. The top, bottom and side

boundaries were selected as velocity-inlet. The symmetry plane forms a symmetry condition. The trimaran hull was regarded as a rigid body and set as no-slope wall. In order to prevent the undesirable effect of the reflected waves from the outlet boundary, artificial wave damping capability of the software package [22] was applied to the outlet boundary in background region with a damping length equal to 1.5 ship length.

There are three methods, namely: that of rigid motion, deforming mesh motion and overset mesh, which can be chosen. The rigid motion and deforming mesh motion methods have distinct disadvantages compared to the overset mesh method when simulating bodies with large amplitude motions. The rigid motion approach causes difficulties for free surface refinement, especially in pitch, and deforming meshes may lead to cell quality problems. The authors of [23] showed that the overset grid method was more accurate in the prediction of the motion response of an SSB catamaran under regular wave conditions when heading in the wave. The overset region moves with the hull over a static background region. In fact, using the overset mesh saves computational costs and allows to generate a sufficiently refined mesh configuration around the free surface and the body. Since the overset mesh was used, two different regions, named background region and overset region, were established to simulate ship responses in calm water and waves. An interface was produced between the background region and overset region to transfer fluid information. Mesh generation was performed by using the automatic meshing facility in STAR-CCM+ software. A trimmed cell mesher was employed to produce a high-quality grid for complex mesh generating problems. The ensuing mesh was formed primarily of unstructured hexahedral cells with trimmed cells adjacent to the surface. Prism layers were applied around the trimaran to resolve the turbulent boundary layer at the no-slip surface and mesh control volumes were produced to refine the meshes near the free surface and the hull surface together with the surfaces of anti-pitching appendages. Fig. 6 presents a general view of the computational mesh showing the background and overset domains. As shown in Fig. 6, near the free surface and around the hull, local mesh refinements were applied to resolve the wave pattern and the incident wave field. Fig. 7 provides a closer look at the mesh around the ship hull and anti-pitching appendages.

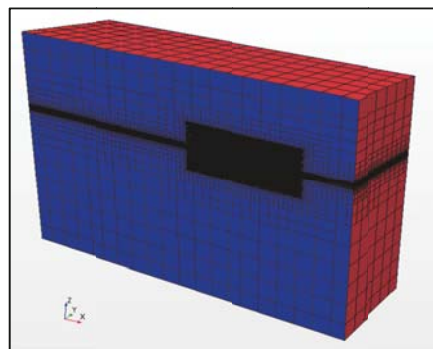


Fig.6 A general view of the meshes for the whole domain

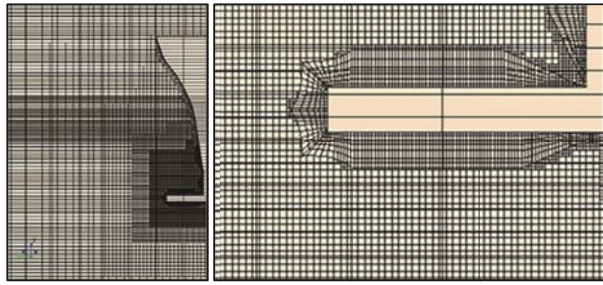


Fig.7 (a) Meshes around the bow (b) Meshes around the T-foil

## VERIFICATION AND VALIDATION FOR CFD SIMULATION

In this section, following the method presented in [24], verification and validation (V&V) was performed to quantify errors and uncertainties in CFD simulations.

It is necessary to mention that the transfer functions of heave, pitch and acceleration motions were calculated as follows:

$$TF_3 = \frac{Z_a}{\zeta_a} \quad (6)$$

$$TF_5 = \frac{\phi}{k\zeta_a} \quad (7)$$

$$A_{19} = \frac{AL_{BP}}{g\zeta_a} \quad (8)$$

Where  $Z_a$ ,  $\Phi$ ,  $A$  and  $\zeta_a$  represent the first Fourier Series (FS) harmonic amplitudes of heave, pitch, acceleration and incident wave amplitude time histories, respectively. Corresponding Fourier transform equations may be referred to [25]. In this paper, the longitudinal motions of heave and pitch were evaluated at the ship's centre of gravity (CG) and the vertical acceleration was evaluated at the 19th hull station near the bow.

## VERTIFICATION

A verification study was carried out to assess the numerical uncertainty  $U_{SN}$ . Grid convergence test was performed at the wave-ship length ratio  $\lambda/L = 1.38$ , which corresponds to the near-resonant physical conditions for heave motion [9], since large motions and accelerations tend to cause the highest numerical errors. The verification parameters included the wave amplitude  $\zeta_a$ , the heave and pitch transfer functions  $TF_3$ ,  $TF_5$  and vertical acceleration at 19th hull station ( $A_{19}$ ) near the bow, respectively.

The convergence studies were performed for three cases by using systematically refined grids and time steps. Often in implicit unsteady simulations, the time step is determined by the flow properties. In [26] there is recommended the use of at least 100 time steps per period for motion responses. In this paper, a small time step (1/256 of the encounter period) was used as a base time step. The coarse and fine mesh systems are derived by reducing and increasing cell numbers per wavelength and cell height on free surface, respectively, by using a factor of  $\sqrt{2}$  [27] as well as cell numbers on and around the ship hull, which is affected by the mesh refinement on free

Tab. 6 Results of grid convergence study.

Parameter	$r_G$	Fine	Base	Coarse	$R_G$	$\delta_G^*(\%S_1)$	$U_G(\%S_1)$	$U_{Gc}(\%S_1)$	$S_c$	EFD (D)
		$S_1$	$S_2$	$S_3$						
$\zeta$	$\sqrt{2}$	28.017	27.831	27.592	0.777	-0.663	5.595	1.644	28.202	28.255
$TF_3$	$\sqrt{2}$	1.490	1.502	1.518	0.774	0.805	6.658	1.951	1.478	1.425
$TF_5$	$\sqrt{2}$	0.982	0.969	0.952	0.747	-1.332	9.108	2.592	0.995	1.039
$A_{19}$	$\sqrt{2}$	87.697	86.917	85.918	0.782	-0.890	7.783	2.297	88.478	88.869

Tab. 7 Results of time step convergence study.

Parameter	$r_T$	Fine	Base	Coarse	$R_T$	$\delta_T^*(\%S_1)$	$U_T(\%S_1)$	$U_{Tc}(\%S_1)$	$S_T$	EFD (D)
		$S_1$	$S_2$	$S_3$						
$\zeta$	$\sqrt{2}$	28.017	27.811	27.545	0.770	-0.732	5.910	1.726	28.222	28.255
$TF_3$	$\sqrt{2}$	1.490	1.505	1.523	0.777	0.968	8.159	2.397	1.476	1.425
$TF_5$	$\sqrt{2}$	0.982	0.968	0.950	0.757	-1.424	10.496	3.024	0.996	1.039
$A_{19}$	$\sqrt{2}$	87.697	86.697	85.408	0.776	-1.140	9.546	2.802	88.697	88.869

surface. The simulation time step is set to be proportional to the grid size [28, 29, 30].

The grid convergence study was carried out with the small time step  $\Delta t = T_e/362$  in three calculations in which the grid size was systematically coarsened by a uniform refinement ratio of  $r_G = \sqrt{2}$  in each direction, while the time step convergence study was carried out with a time step refinement ratio of  $r_T = \sqrt{2}$  on the fine grid. The base and coarse mesh were generated by changing the base size of grid only in the overset region, which means that the background mesh configuration was not altered [20]. This enabled the incident head waves to be modelled efficiently through the computational domain. Otherwise, the incident head waves would not have been captured well with a coarser grid, thus leading to wrong results. Although the mesh changed, the size of prism layers around the hull surface remained the same. The value of yplus on the hull surface were between  $30 \div 100$  as shown in Fig. 8 and Fig. 9. The mesh cell numbers for each mesh configuration are listed in Tab. 5.

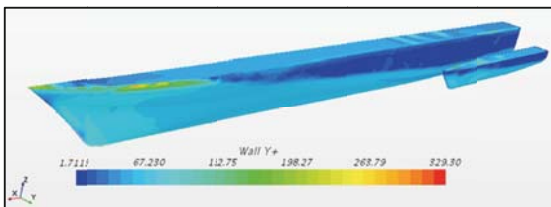


Fig.8 Yplus distribution on the hull surface

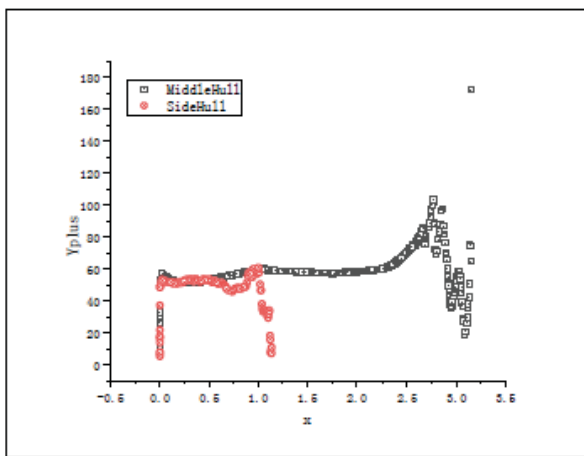


Fig.9 Yplus distribution on the hull surface

Tab. 5 The final cell numbers for each mesh configuration in the grid convergence study.

Grid name	Mesh configuration	Grid number (Million)		
		Background	Overset	Total
$G_1$	Fine	1.092	5.040	6.132
$G_2$	Base	1.092	2.229	3.321
$G_3$	Coarse	1.092	1.055	2.147

The results of grid and time step convergence studies are listed in Tab. 6 and 7. Let's consider the situation of three

solutions corresponding to fine  $S_{k1}$ , base  $S_{k2}$ , and coarse  $S_{k3}$  values for the  $k^{\text{th}}$  input parameter. To assess the convergence condition,  $R_k$  acc. Eq. (9) is used as the convergence ratio:

$$R_k = \frac{\varepsilon_{k21}}{\varepsilon_{k32}} \quad (9)$$

where  $\varepsilon_{k21} = S_{k2} - S_{k1}$  is the difference between the results of base mesh and fine mesh, and  $\varepsilon_{k32} = S_{k3} - S_{k2}$  is the difference between the results of coarse mesh and base mesh. Subscript  $k$  refers to the  $k^{\text{th}}$  input parameter.  $S_c$  is the corrected simulation value calculated as  $S_c = S - \delta^*$  where  $S$  is the simulation results,  $\delta^*$  is the corrected value.  $U_c$  is the corrected uncertainty.

Tab. 8 Results of grid convergence study.

Parameter	(%D)		(%D)	E(%D)
	8.069	2.5	8.447	0.844
	11.014	2.5	11.294	-4.589
	13.137	2.5	13.373	5.463
	12.154	2.5	12.409	1.319

As shown in Tab. 6 and 7, monotonic convergence was achieved for  $\zeta_a$ ,  $TF_3$ ,  $TF_5$ , and  $A_{19}$ . The uncertainty estimated for the wave amplitude, motion transfer functions and vertical acceleration at 19<sup>th</sup> hull station were reasonable small. The grid uncertainty  $U_G$  (9.108%) and the time step uncertainty  $U_T$  (10.496%) are relatively large for the pitch transfer function  $TF_5$  these values are reduced to 2.592% and 3.024% , respectively, when the corrected uncertainties  $U_{Gc}$  and  $U_{Tc}$  are estimated. The time step uncertainties  $U_T$  are generally larger than those of the grid uncertainties  $U_G$ , which indicates that the numerical results are relatively more sensitive to the time step resolution.

## VALIDATION

To determine modelling errors, the numerical results were compared to the experimental data. The experimental data uncertainty was assumed to be of a rather low value  $U_D = 2.5\%$ . The validation uncertainty  $U_v$  and the comparison error  $E$  were calculated and summarized in Tab. 8. As indicated in Tab. 9, the wave amplitude, the heave, pitch transfer function as well as the vertical acceleration can be considered validated since the comparison error  $E$  is smaller than the validation uncertainty  $U_v$ . The uncertainty levels are estimated to be 8.447%, 11.294%, 13.373% and 12.409%, respectively.

## RESULTS AND DISCUSSION

After performing the validation, the main findings of this paper are summarized and discussed as follows.

## WAVE MEASUREMENT

For the purpose of monitoring the waves generated at the inlet, a wave probe located  $0.5 L_{WL}$  [25] in front of the hull was set to record the wave elevation. Fig. 10 shows the recorded time history of the wave elevation at  $\lambda/L = 1.38$ . The mean first-order harmonic wave amplitudes of the last ten encounter periods was  $0.0284$  m. The errors between the simulated wave amplitude and the intended wave amplitude were equal to  $5.33\%$ . The slight difference was considered acceptable for the current cell size and time step. The measured wave amplitudes were used to calculate the motion transfer functions in the CFD simulation.

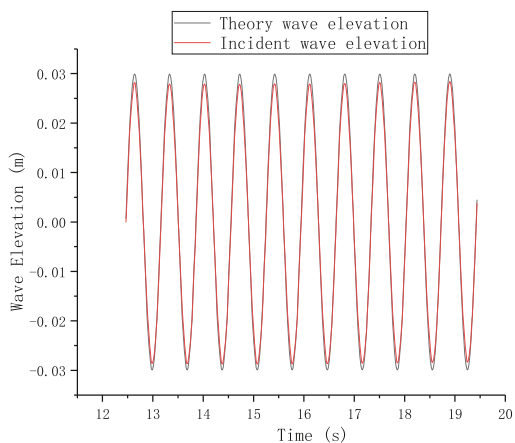


Fig.10 Time history of wave elevation at the wave probe,  $\lambda/L=1.38$

## CALM WATER RESISTANCE OF TRIMARAN WITH AND WITHOUT T-FOIL

To investigate the calm water resistance of the trimaran with and without T-foil, numerical simulations and experimental tests were carried out. Tab. 9 presents the experimental and numerical results of the calm water resistance of the bare trimaran. The total resistance from model tests exceeded the total resistance from numerical simulations by about  $0.92\%$ , which indicates that the numerical method was able to simulate the calm water resistance of the trimaran with a reasonable small error. Tab. 10 shows the experimental and numerical values of the calm water resistance of the trimaran at different values of T-foil attack angle ( $\pm 5^\circ$ ). The total resistance from experimental tests also exceeded the total resistance from numerical simulations. The errors between the experimental (EFD) and CFD results turned out to be  $2.74\%$  for  $-5^\circ$  T-foil attack angle and  $2.62\%$  for  $+5^\circ$  T-foil attack angle, respectively. Compared to the resistance of the bare trimaran in calm water, the resistance of the trimaran with different T-foil attack angles increased by  $8.05\%$  for T-foil ( $-5^\circ$ ): EFD,  $7.17\%$  for T-foil ( $-5^\circ$ ): CFD,  $9.23\%$  for T-foil ( $+5^\circ$ ): EFD,  $6.85\%$  for T-foil ( $+5^\circ$ ): CFD. As a result of the application of the anti-pitching appendage ( i.e.T-foil ) the calm water resistance of the trimaran increased, and for different T-foil attack

angles different resistance characteristics were revealed. Tab. 10 shows that the trimaran with T-foil attack angle of  $-5^\circ$  demonstrates preferable calm water resistance characteristics. Therefore, the T-foil attack angle of  $-5^\circ$  was used as a basic condition in subsequent research on the influence of  $\zeta_a^*k$  and size of T-foil on the trimaran motions.

Tab. 9 Calm water resistance of the trimaran without anti-pitching appendages

	EFD (N)	CFD (N)
Resistance (N)	36.84	36.50
Error $\left  \frac{CFD - EFD}{EFD} \right  (\%)$	---	0.92

Tab. 10 Calm water resistance of the trimaran with different T-foil attack angles

	T-foil (-5): EFD (N)	T-foil (-5): CFD (N)	T-foil (+5): EFD (N)	T-foil (+5): CFD (N)
Resistance (N)	39.804	39.116	40.242	39.186
Error $ CFD - EFD /EFD  (\%)$	---	2.74	---	2.62
$\Delta R \left  \frac{T-Bare}{Bare} \right  (\%)$	8.05	7.17	9.23	6.85

## SHIP MOTION RESPONSE OF BARE TRIMARAN

Following the model tests and numerical simulations of the trimaran with and without anti-pitching appendages in calm water, the motion response of the trimaran was investigated. The Response Amplitude Operators (RAOs) of heave, pitch motions and vertical acceleration at 19<sup>th</sup> hull station were compared with the model test results as shown in Figs. 11-13. In Fig. 11 it can be observed that the CFD method over-estimated the heave response values around the resonant period, while under-estimated the heave response values for short and long wave conditions. Fig. 12 indicated that the CFD method under-estimated the pitch response values around the resonant period. Fig. 13 showed that the CFD method was in a good agreement with the experimental results around the resonant period, while under-estimated the vertical acceleration at 19<sup>th</sup> hull station for short and long wave conditions. In general, the CFD method used in this paper was capable of calculating the longitudinal motions of the bare trimaran with a relative high speed.

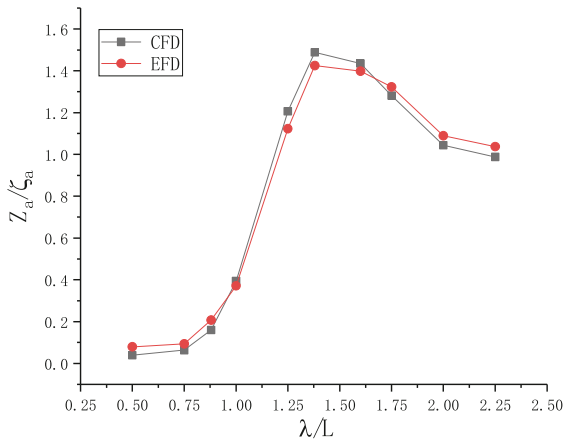


Fig.11 Heave RAO

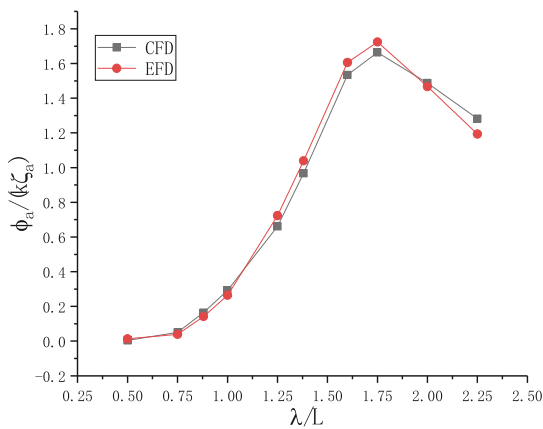


Fig.12 Pitch RAO

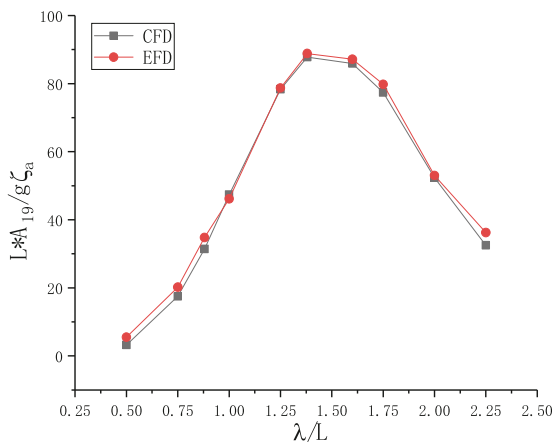


Fig.13 RAO of acceleration at 19<sup>th</sup> hull station ( A19)

## SHIP MOTIONS OF TRIMARAN FITTED WITH T-FOIL

The longitudinal motions of the trimaran at high speed are severe. For the purpose of improving the seakeeping performance of the trimaran, T-foil was used as an anti-pitching appendage to reduce the motion response of the trimaran in waves. The selected wave conditions are

considered identical to those applied to the simulations of the bare trimaran. In considering the calm water resistance characteristics of the trimaran with T-foil, only the T-foil attack angle of  $-5^\circ$  was taken into account in this section.

Response values of heave and pitch motions and vertical acceleration at 19<sup>th</sup> hull station calculated by the CFD method were compared with the results of the experiment as shown in Figs. 14÷16. In Fig. 14 it can be observed that the CFD method under-estimated the heave response values, especially for the short waves ( $\lambda/L < 0.88$ ), which can be explained by that for short waves higher requirements as to grid setting are necessary. The amplitude of the heave response is reduced by 19.6% in case of the CFD method and 13.6% for experimental results. Fig. 15 indicates that the CFD method was in a good accordance with the experimental results. The amplitude of the pitch response is reduced by 39.1% for CFD method and 42.4% for experimental results. Fig. 16 shows that the CFD method a little under-estimated the vertical acceleration at 19<sup>th</sup> hull station. The amplitude of the acceleration is reduced by 41.3% for CFD method and 40.1% for experimental results. Figs. 14÷16 obviously show that the T-foil can significantly reduce the longitudinal motions response values of the trimaran with a high speed.

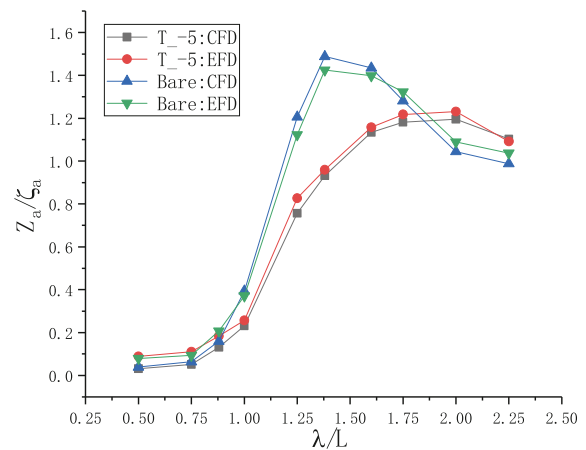


Fig.14 Heave RAO

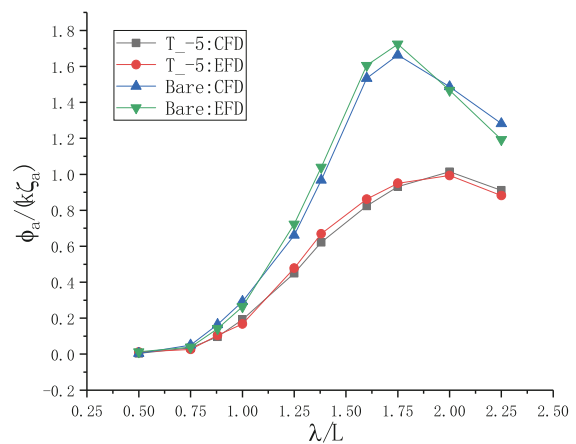


Fig.15 Pitch RAO

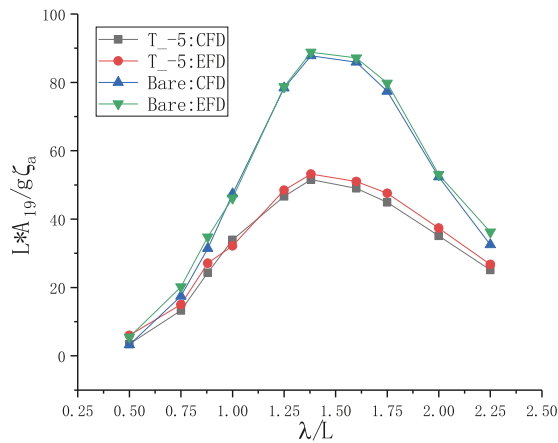


Fig.16 RAO of acceleration at 19<sup>th</sup> hull station (A19)

## SHIP MOTIONS OF TRIMARAN IN THE CONDITION OF $\zeta_a * K = 0.1$

Longitudinal motion characteristics of the trimaran with and without T-foil were investigated in the condition of  $\zeta_a * k$  within the range of 0.046 (longest wave) and 0.063 (shortest wave). In the considered situations, a high amplitude may occur making a different influence on the ship motion in waves. The longitudinal motions of the trimaran with and without T-foil in the condition of  $\zeta_a * k = 0.1$  were investigated. The wave conditions for the CFD calculations are shown in Tab. 11. As can be seen in Tab. 11, the wave amplitude  $\zeta_a$  times wave number is equal to about 0.1.

Tab. 11 Calm water resistance of the trimaran without anti-pitching appendages

Wave length ( $\lambda/L_{pp}$ )	Wave amplitude $\zeta_a$ (m)	$\zeta_a * k$
0.50	0.024	0.101
0.75	0.036	0.101
0.88	0.042	0.100
1.0	0.048	0.101
1.25	0.060	0.101
1.38	0.066	0.100
1.60	0.077	0.101
1.75	0.084	0.101
2.0	0.096	0.101
2.25	0.108	0.101

Response values of heave and pitch motions and vertical acceleration at 19<sup>th</sup> hull station calculated by the CFD method are shown in Figs. 17÷19. In the figures it can be observed that in the wave condition  $\zeta_a * k = 0.1$ , the T-foil played some role in reducing the amplitudes of heave, pitch and acceleration. The

amplitudes of the heave, pitch and acceleration were reduced by 22.72%, 20.93% and 22.16%, respectively. With the wave amplitude increasing, the T-foil had different influence on values of heave and pitch motion and acceleration. The effect of reducing heave motion appeared a little greater, but in contrast, the effect of reducing pitch motion and acceleration became lower, the reduction was from 39.1% to 20.93% for pitch motion and 42.4% to 22.16% for acceleration motion.

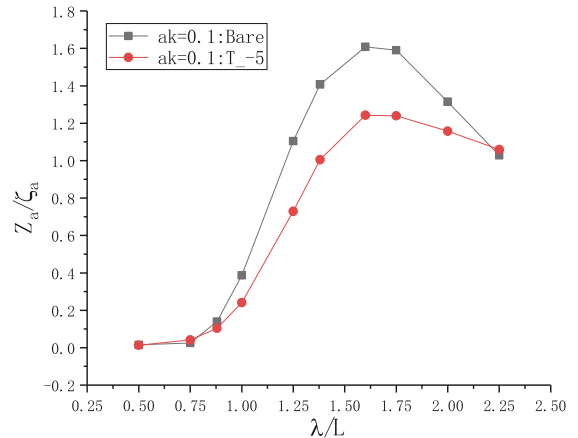


Fig.17 Heave RAO

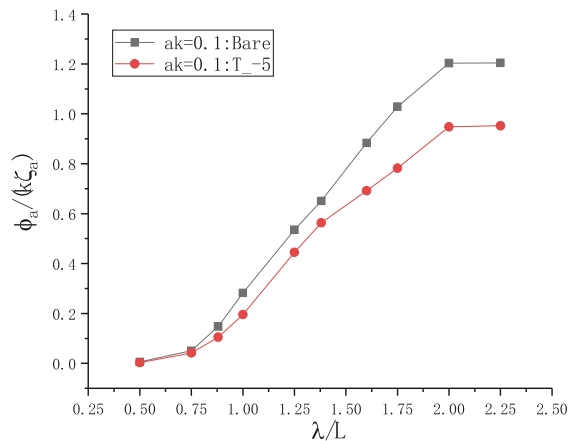


Fig.18 Pitch RAO

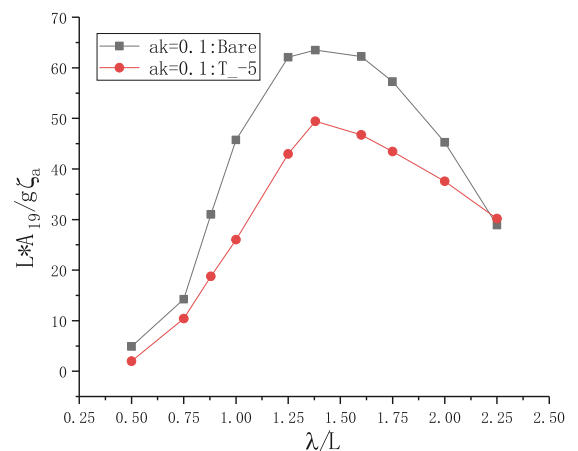


Fig.19 RAO of acceleration at 19<sup>th</sup> hull station (A19)

## INFLUENCE OF T-FOIL SIZE ON TRIMARAN MOTIONS

To investigate the influence of size of T-foil on trimaran motions, three sizes of T-foil were considered. During the CFD simulations, the applied T-foil was of the dimensions decreased and enlarged by 20% in each direction for the horizontal wings, with other parameters unchanged. The dimensions of the so differentiated T-foils are shown in Tab. 12. The T-foil origin size was marked T2.

Tab.12 Dimensions of the different -size T-foils

Principal particulars	T1	T2	T3
Airfoil shape	NACA0012		
Span (m)	0.1152	0.144	0.1728
Chord (m)	0.0768	0.096	0.1152
Aspect ratio	1.5	1.5	1.5
Rotating angle of the flap (°)	-5	-5	-5
Width of the vertical foil (m)	0.01	0.01	0.01
Length of the vertical foil (m)	0.060	0.060	0.060
Height of the vertical foil (m)	0.024	0.024	0.024
Longitudinal position of foil installation place (distance between centre line of vertical foil and 10 <sup>th</sup> hull station of the trimaran) (m)	1.320	1.320	1.320

The response values of heave and pitch motions and vertical acceleration at 19<sup>th</sup> hull station calculated by the CFD method are shown in Figs. 20÷22. In the figures it can be observed that each of the three T-foils of different size produced different effect on the longitudinal motion response values of the trimaran. The trends of the RAOs were the same for the considered different-size T-foils. With the increase of the T-foil dimensions, their effect on pitching stabilization became greater. The amplitudes of the heave, pitch and acceleration were reduced by 17.68%, 15.17% and 13.15% for T1 foil and 29.72%, 25.73% and 31.44% for T3 foil, respectively.

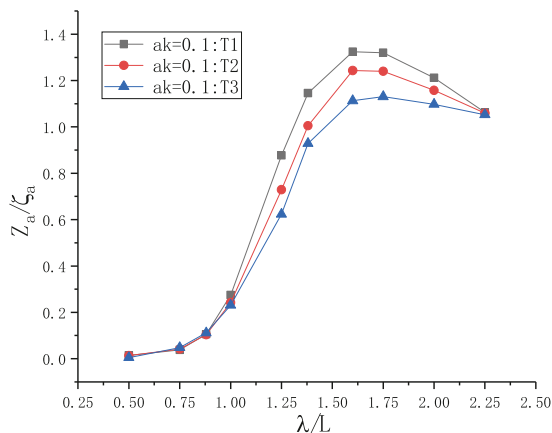


Fig.20 Heave RAO

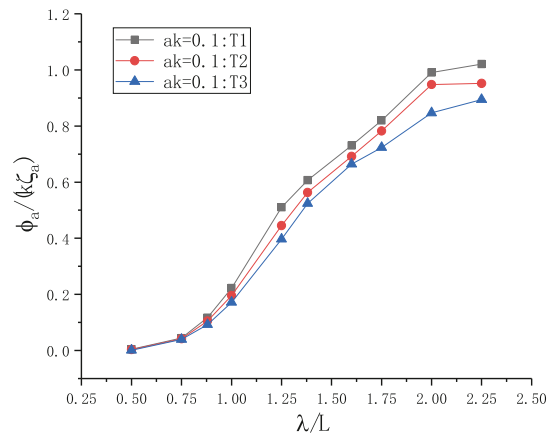


Fig.21 Pitch RAO

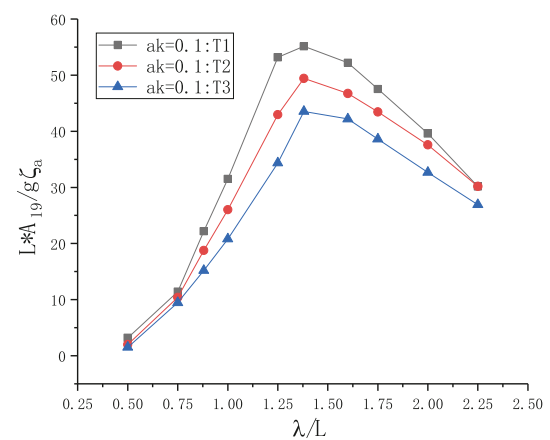


Fig. 22 RAO of acceleration at 19<sup>th</sup> hull station ( A19)

In addition, the influence of the change of T-foil size on the calm water resistance of the trimaran, were studied. Tab. 13 shows the results of the numerical calculations of the calm water resistance of the trimaran with T-foils of different size. Compared to the calm water resistance of the bare trimaran, the resistance of the trimaran with T-foils of different size increased by 5.28% for T1(-5°), 7.17% for T2 (-5°), 11.53% for T3(-5°). With increasing T-foil dimensions, the calm water resistance of the trimaran increases.

Tab.13 Calm water resistance of the trimaran with T-foils of different size

	T1(-5): CFD(N)	T2 (-5): CFD (N)	T3 (-5): CFD (N)
Resistance (N)	38.426	39.116	40.707
$\Delta R (T - Bare)/Bare $ (%)	5.28	7.17	11.53

## CONCLUDING REMARKS AND DISCUSSION

In the present work, to investigate the seakeeping and resistance characteristics of the trimaran at a relative high speed ( $F_n = 0.628$ ), the unsteady RANS method was used

to simulate the calm water resistance of the trimaran, the longitudinal ship motions (heave and pitch) and vertical acceleration at 19<sup>th</sup> hull station for a broad range of wave conditions. The wave conditions covered a series of wavelength  $\lambda$  varying between 1.5 m and 6.75 m, thus the  $\lambda/L$  ratio varied between 0.50 and 2.25.

The longitudinal motion responses of the trimaran at a relative high speed were rather intense. In order to reduce the longitudinal motions of the trimaran a T-foil was used as an anti-pitching appendage which was located at the 19<sup>th</sup> hull station near the bow of the middle hull of the trimaran. The T-foil can significantly reduce the amplitude of the longitudinal motions of the trimaran, but the increase of calm water resistance was a detrimental effect.

All experimental measurements obtained from the model tests were used for comparison with numerical results. Therefore, to avert scaling errors, all numerical investigations were conducted in corresponding model scale.

The STAR-CCM+ unsteady RANS solver was used for the simulation of the trimaran behaviour. The method was extended by an explicit six-degrees-of-freedom solver to compute nonlinear ship motions. CFD simulations have been validated by comparison with results of the experimental tests. The verification study at the resonant frequency demonstrated that the numerical results were more sensitive to the time step than to the mesh size. The validation was positive for all the considered variables.

Comparisons between the experimental results and numerical calculations showed that the unsteady RANS method predicts ship longitudinal motions with a high accuracy.

Compared with the results for the bare trimaran, the use of anti-pitching appendage in the form of T-foil greatly reduced the longitudinal motions. In the wave condition of  $\zeta_a^*k=0.1$ , the amplitudes of the heave, pitch and acceleration were reduced with the help of T-foil by 22.72%, 20.93% and 22.16%, respectively. In the wave condition of  $\zeta_a^*k$  of a value between 0.046 and 0.063, the T-foil produced a little greater effect on heave motion, but its effect on pitch and acceleration was reduced by about 20%. With the increase of T-foil size, the effect of reducing longitudinal motions becomes greater, however, the calm water resistance of the trimaran increases by 5.28% to 11.53% compared with the bare trimaran.

The nonlinear effects on the longitudinal motions of the trimaran in wave of a relatively high amplitude will be further investigated experimentally in the future. The use of T-foil can significantly reduce longitudinal motions but has a negative effect on resistance, therefore the combined use of T-foil and stern flap will be further studied with the aim to realize the comprehensive optimization of resistance and seakeeping performance of the trimaran.

## BIBLIOGRAPHY

1. Davis, M.R., Holloway, D.S.: A comparison of the motions of trimarans, catamarans and monohulls. Australian Journal of Mechanical Engineering, 4(2), (2007). pp. 183-195.
2. Mynard, T. : Numerical and experimental study of wave resistance for trimaran hull forms. Vol.1, (2008), pp.117-132.
3. Brizzolara, S., Capasso, M., Ferrando, M., et al. : Trimaran hull design for fast ferry applications. Int. Conference on Ships Design and Shipping, Nav. 2003.
4. Bertorello, C., Bruzzone, D., Cassella, P., et al. : Trimaran model test results and comparison with different high speed craft. Practical Design of Ships & Other Floating Structures, 1, (2001), pp. 143-149.
5. Hebblewhite, K., Sahoo, P.K. and Doctors, L.J.: A case study: theoretical and experimental analysis of motion characteristics of a trimaran hull form, Ships and Offshore Structures, 2:2, (2007) , pp.149 – 156.
6. Faltinsen, O.M. : Numerical prediction of ship motions at high forward speed. Phil. Trans. R. Soc. , London Ser. A, 334, (1991), pp. 241-252.
7. Salvesen, N., Tuck, E.O., Faltinsen, O.M. : Ship Motion and Sea Loads. SNAME, 1970.
8. Wei, Y.F., Duan, W.Y., Ma, S. : Trimaran motions and hydrodynamic interaction of side hulls, 9th International Conference on Fast Sea Transportation, FAST 2007, pp. 413-421.
9. Wang, S. M., Ma, S., & Duan, W. Y. : Seakeeping optimization of trimaran outrigger layout based on NSGA-II. Applied Ocean Research, 78, (2018), pp. 110-122.
10. Sato, Y., Uzawa, K., Miyata, H. : Validation of motion prediction method for trimaran vessels. International Conference on Numerical Ship Hydrodynamics 2007, (Vol.5).
11. Wu, C.S, Zhou, D.C, Gao, L., et al. :). CFD computation of ship motions and added resistance for a high speed trimaran in regular head waves, International Journal of Naval Architecture and Ocean Engineering, 3(1), (2011), pp. 105-110. doi: <https://doi.org/10.2478/ijnaoe-2013-0051>.
12. Poundra, G.A.P., Utama, I.K.A.P., Hardianto, D., et al. : Optimizing trimaran yacht hull configuration based on resistance and seakeeping criteria. Procedia Engineering, 194, (2017), pp. 112-119.
13. Fang, C.C., Chan, H.S. : An investigation on the vertical motion sickness characteristics of a high-speed catamaran ferry. Ocean Engineering, 34(14), (2007), pp. 1909-1917.
14. Esteban, S., Giron-Sierra, J.M., Andres-Toro, B.D., et al. : Fast ships models for seakeeping improvement studies using

- flaps and t-foil. *Mathematical & Computer Modelling*, 41(1), (2005), pp. 1-24.
15. Haywood A.J., Duncan A.J., Klaka K.P. et al. : The development of a ride control system for fast ferries. *Control Eng. Pract.* 3(5), (1995), pp. 695-702.
  16. Giron-Sierra J.M., Esteban S, Andres D., et al. : Experimental study of controlled flaps and T-foil for comfort improvement of a fast ferry. In: *IFAC Proceedings control applications in marine systems*, vol. 34, (2001), pp. 261-266.
  17. Zong, Z., Sun, Y., Jiang, Y. : Experimental study of controlled T-foil for vertical acceleration reduction of a trimaran. *Journal of Marine Science & Technology*, (2018), pp. 1-12.
  18. CD-Adapco. User guide of STAR-CCM+ , Version 11.0.2, 2016.
  19. Patankar, S.V., Spalding, D.B. : A calculation procedure for heat, mass and momentum transfer in three-dimensional parabolic flows. *Int. J. Heat. Mass Transf.* 15 (2), (2005), pp. 1787-1806.
  20. Tezdogan, T., Demirel, Y.K., Kellett, O., et al. : Full-scale unsteady RANS CFD simulations of ship behavior and performance in head seas due to slow steaming. *Ocean Eng.* 97, (2015), pp. 186-206.
  21. International Towing Tank Conference (ITTC) : Practical guidelines for ship CFD applications. In: *Proceedings of the 26th ITTC*, Rio de Janeiro, Brazil, 2011b.
  22. Choi, J., Yoon, S.B. : Numerical simulations using momentum source wave-maker applied to RANS equation model. *Coast. Eng.* 56 (10), (2009), pp. 1043-1060.
  23. Sun, H.B., Jing, F.M., Jiang, Y., et al. : Motion prediction of catamaran with a semi-submersible bow in wave. *Polish Maritime Research* 1(89) , Vol. 23, 2016 , pp. 37-44.
  24. Stern, F., Wilson, R., Shao, J. : Quantitative V&V of CFD simulations and certification of CFD codes. *International Journal for Numerical Methods in Fluids*, 50(11), (2006), pp. 1335-1355.
  25. Sun, X.S., Yao, C.B., Xiong, Y., et al.: Numerical and experimental study on seakeeping performance of a swath vehicle in head waves. *Applied Ocean Research*, 68, (2017), pp. 262-275.
  26. International Towing Tank Conference (ITTC), Ocean Engineering Committee : Final report and recommendation to the 27th ITTC. In: *Proceedings of the 27th ITTC*, Copenhagen, 2014.
  27. Bøckmann, A., Pakozdi, C., Kristiansen, T., et al. : An Experimental and Computational Development of a Benchmark Solution for the Validation of Numerical Wave Tanks. *ASME 2014, International Conference on Ocean, Offshore and Arctic Engineering* (2014), Vol.2, pp. V002T08A092-V002T08A092.
  28. Kim, M., Hizir, O., Turan, O., et al.: Estimation of added resistance and ship speed loss in a seaway. *Ocean Engineering* 141, (2017), pp. 465-476.
  29. Kim, M., Turan, O., Day, S., et al. : Numerical studies on added resistance and ship motions of KVLCC2 in waves. *Ocean Engineering* 140, (2018), pp. 466-476.
  30. Hizir, O., Kim, M., Turan, O., et al. : Numerical studies on non-linearity of added resistance and ship motions of KVLCC2 in short and long waves. *International Journal of Naval Architecture and Ocean Engineering*, (2018). <https://doi.org/10.1016/j.ijnaoe.2018.02.015>.

#### CONTACT WITH THE AUTHORS

**Ang Li**

*e-mail: liang0301@hrbeu.edu.cn*

College of Shipbuilding Engineering  
Harbin Engineering University  
Harbin  
**CHINA**

**Yunbo Li**

*e-mail: multihull@163.com*

College of Ocean Science and Engineering  
Shanghai Maritime University  
Shanghai  
**CHINA**

# PULSATION SIGNALS ANALYSIS OF TURBOCHARGER TURBINE BLADES BASED ON OPTIMAL EEMD AND TEO

Fengli Wang

College of Marine Engineering, Dalian Maritime University, China

## ABSTRACT

*Turbocharger turbine blades suffer from periodic vibration and flow induced excitation. The blade vibration signal is a typical non-stationary and sometimes nonlinear signal that is often encountered in turbomachinery research and development. An example of such signal is the pulsating pressure and strain signals measured during engine ramp to find the maximum resonance strain or during engine transient mode in applications. As the pulsation signals can come from different disturbance sources, detecting the weak useful signals under a noise background can be difficult. For this type of signals, a novel method based on optimal parameters of Ensemble Empirical Mode Decomposition (EEMD) and Teager Energy Operator (TEO) is proposed. First, an optimization method was designed for adaptive determining appropriate EEMD parameters for the measured vibration signal, so that the significant feature components can be extracted from the pulsating signals. Then Correlation Kurtosis (CK) is employed to select the sensitive Intrinsic Mode Functions (IMFs). In the end, TEO algorithm is applied to the selected sensitive IMF to identify the characteristic frequencies. A case of measured sound signal and strain signal from a turbocharger turbine blade was studied to demonstrate the capabilities of the proposed method.*

**Keywords:** turbocharger turbine blades, pulsation signals analysis, ensemble empirical mode decomposition, Teager energy operator, correlation kurtosis

## INTRODUCTION

As one of the critical systems of marine diesel engine, turbocharger plays an important role in ensuring the power for ship's propulsion provided sustainably and stably by diesel engine, and reducing the impact of exhaust gas emission on the environment. Turbine blades are an important component of the turbocharger, which suffer from periodic vibration and flow induced excitation. Knowing the amplitude of blade vibration is critical to the safe operation of turbochargers, and for this purpose, strain gauge and sound signals may be employed. These signals are often non-stationary and sometimes nonlinear. One such example is the pulsating sound and strain signals measured during engine ramp

mode to find the maximum resonance of turbine blades or during engine transient mode. Because the signal frequency is proportional to engine speed it changes when the speed varies. Traditionally, such signals are analyzed by using Fast Fourier Transformation (FFT) [1]. The Fourier Transformation (FT) is a weighted sum of any signal decomposed into sinusoidal signals each of which corresponds to a fixed frequency. It simply treats the signal as an integral over time. Therefore, it is very effective in analyzing stationary signals which do not change with time. But for non-stationary signals which vary with time, FT is powerless. To overcome this weakness, Yeung used a piecewise FFT to process the compressor pressure pulsation signal. It could accurately detect the precursor signal of compressor instability in the experiment. Although

the piecewise FFT was effective for the instability induced by the slowly developed modal wave, it had a limited effect on the instability caused by the sharp spike pulse [2]. Short Time Fourier Transform (STFT) is a FT with a window that can be varied to improve the treatment to non-stationary signals. However, once the window function is selected the size and shape of the time frequency window are fixed, and the time resolution and frequency resolution of Heisenberg function cannot be optimized at the same time [3]. Wavelets transform (WT) can transform the signal through the scalable and translational wavelets to achieve the localization of time-frequency analysis [4]. However, the WT requires to select an appropriate basis function, and its basis function is fixed and cannot change with the signal. The limited length of the wavelet basis function will also cause the leakage of the signal energy. The WT is essentially a FT with an adjustable window, and the signal in its wavelet window must be stationary, so that it does not get rid of the limitation of Fourier analysis.

Empirical Mode Decomposition (EMD) has been intensively investigated and applied to signal processing. It no longer treats the basis of a signal as sinusoidal, but a function called the intrinsic mode function (IMF) [5]. The amplitude and frequency of IMF can be time-varying, and they are called the instantaneous amplitude and instantaneous frequency, respectively. Unlike the WT which requires to preselect the base function, in the EMD process its base function comes directly from the signal itself, and different signals will produce different basis functions, making EMD potentially superior to the Fourier and wavelet transforms. EMD has been widely applied to nonlinear and non-stationary signal analysis. Its capability to analyze such data has been utilized in various applications. However, the mode mixing is one of the major shortcomings of EMD, and it not only leads to serious abasing in the time-frequency distribution but also makes the physical meaning of individual IMF ambiguous.

To eliminate the defects of EMD, the Ensemble Empirical Mode Decomposition (EEMD) is proposed, which is a noise-assisted data analysis method by adding white noise to the investigated signal [6]. However, in the EEMD process, how to choose suitable amplitude of the added noise and the ensemble number have remained a topic. Wu and Huang described the effect of the added white noise and determined these two parameters by experience [6]. Zhang introduced the principle of adding noise based on the energy ratio of the added white noise and the original signal, but his method considered only the signals composed of two components, and did not study the signal with multiple mode components [7]. Chen proposed an improved method of determining these two parameters in the EEMD process. Due to the influence of noise and modal aliasing, the first IMF cannot represent accurately the high frequency information of the investigated signal [8]. The signal-to-noise ratio (SNR) was introduced by Chang [9]. Yeh presented a novel noise-enhanced data analysis method to determine these two parameters [10]. Wang proposed the criterion of the energy standard difference for adding white noise into the EEMD [11]. However, the premise of proper use of the method is to know beforehand the information

of each component contained in the processed signal. This limits the application of the method to actual signals. Lei uses coloured noise instead of Gauss white noise, which effectively improves the distribution of extreme points, but the research does not establish the criterion of adding noise [12]. Niazy [13] uses the relative root-mean-square error criterion to determine the performance of EEMD, but it does not give a method to select the appropriate noise amplitude. Kong used the distribution of signal extreme points as an evaluation index to determine the optimal amplitude of Gaussian white noise through an ergodic process. However, the noise interval selection in this method still requires to be artificially set, and the pre-treatment time is longer [14]. Therefore, if these two parameters, the amplitude of the added noise and the ensemble number in the EEMD process, can be obtained adaptively according to the actual signals, it will be of a great significance for improving the performance of EEMD.

The pressure pulsations measured on a turbocharger turbine can come from different sources. Detecting the weak useful signal under noise background may become difficult if signal processing error interferes. These authors had encountered such difficulty in their work when processing the strain gauge and sound signals of a turbocharger turbine. This prompted them to search for a possible explanation and a solution to the problem. This paper reports the results of the investigation.

The paper describes a signal processing problem in a small turbocharger turbine and gives an introduction to the theory and algorithms for data processing of pulsation signals from the turbine based on optimal EEMD and TEO. The results of sound and strain signals analysis of the turbine are presented in the following sections of this paper.

## A SIGNAL PROCESSING PROBLEM

The involved turbine is a small turbocharger turbine of Cummins Turbo Technologies for small diesel engine application. In evaluating turbine's high cycle fatigue (HCF) life, some of the turbine blades were strain gauged to measure the blade deformation during turbine operation [15]. Cummins Turbo Technologies has multi-year experience in measuring vibratory blade strain by using strain gauge and has established a good correlation between measured strains and HCF life of their turbine wheels. Fig. 1(a) shows a strain gauged turbine wheel. Due to the small size of the turbine, only one blade was strain gauged. As currently before testing all the blades there is no simple way to determine which blade has the largest vibratory strain due to mistuning effect [16], multiple tests are necessary. But this type of test is time consuming and costly, therefore Cummins Turbo Technologies and Dalian Maritime University are working together to find solutions to reduce experiment time and cost, including a possible use of the sound signature of turbines in operation. For this reason, a microphone was placed a half meter away from turbine exhaust manifold. Fig.1(b) and (c) show such arrangement. The turbocharger was installed

in a gas stand test cell. A burner which can generate inlet gas temperature up to 760°C to drive the turbine wheel, is connected to the turbine housing inlet by using long pipes. A valve controller on the burner is used to control fuel and air flow to achieve the required conditions of steady state turbine inlet pressure and temperature. A blade pass speed sensor is installed into the compressor cover to count impeller blade passing pulses to calculate turbocharger speed during operation.

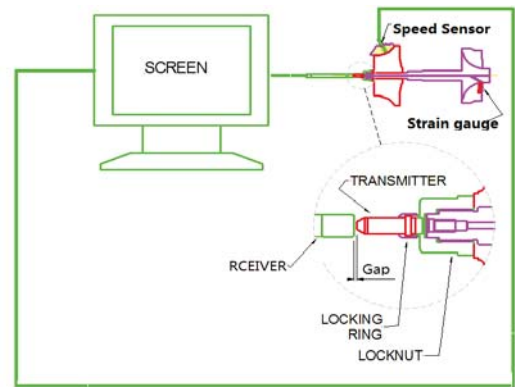
The exducer flap mode of the turbine blades is the concern, and the natural frequency of this mode of the strain gauged blade was measured to be 12,670Hz at stationary and room temperature condition. The turbocharger was run on an engine, and its rotational speed was ramped up and down constantly so that this mode could be excited. Fig. 2(a), (b) and (c) give an example of recorded signals of turbine speed, blade strain and sound, respectively, and signals in Fig. 2(b) and (c) are normalized. These data were taken at a sampling rate of 102.4 KHz. The data in Fig. 2 were analysed, and the results are shown in Fig. 3 and 4 for the measured blade strain and sound, respectively. Fig. 3 gives the power spectrum of the blade strain, based on FFT analysis. The largest peak occurs at the frequency of 13,650Hz.



Turbine blade with strain gauge



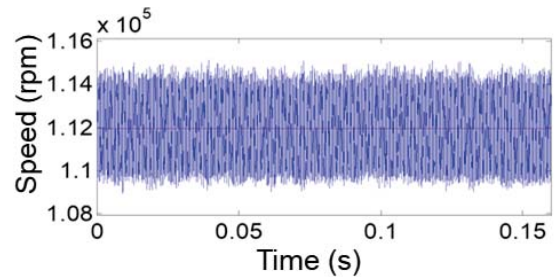
Photo of test rig



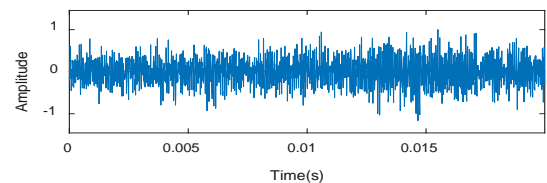
Strain gauge and microphone measuring system

Fig. 1. Strain gauge and microphone for blade strain and turbine sound measurements

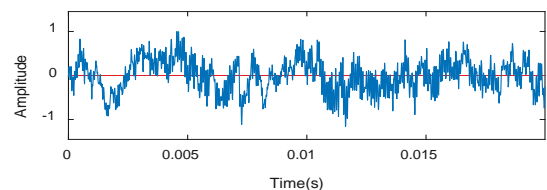
This is an unexpected result: the natural frequency of the first blade mode is 12,670Hz for the blade at room temperature and stationary condition, however one expects that the maximum strain should appear near or at this frequency, due to the combining effects of centrifugal stiffening and Young's modulus reduction of turbine blade material at the hot running condition. The engine frequency order in this case is seven, so the excitation force is relatively small, and small blade strain is expected. But the occurrence of the peak strain at 13,650Hz is puzzling and needs an explanation.



Turbine speed signal



Blade strain signal from the strain gauge



(c) Sound signal from the microphone

Fig. 2. Turbine speed, blade strain and sound signals measured on an engine

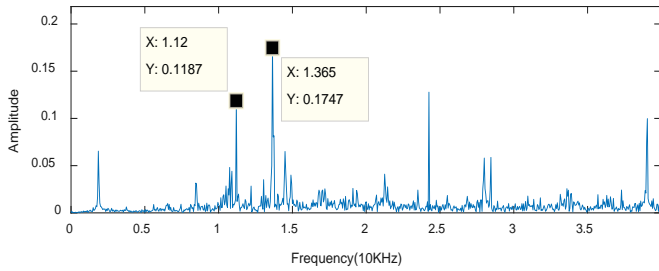


Fig. 3. Power spectrum of the blade strain based on the data in Fig. 2(b) processed by FFT analysis

Fig. 4 shows the power spectrum of the sound signal by using FFT. No frequency near 12,000Hz is found with the FFT results of the sound signal either. At this stage one may not blame the signal analysis for the lack because the blade vibratory signal may be too weak to be picked up by an external microphone. The largest peak of the sound power occurs at 13,050Hz, a frequency very close to compressor blade passing frequency (BPF) which, calculated from the speed signal in Fig. 2(a), is 13067Hz (~112,000rpm/60x7, as the compressor has 7 inducer blades).

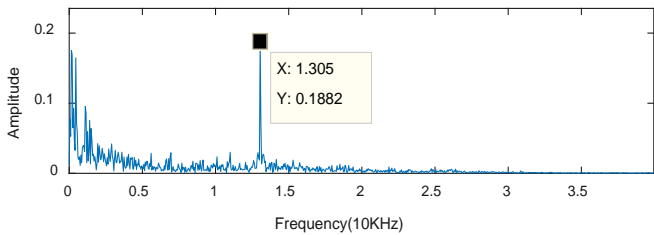


Fig. 4. Power spectrum of the sound signal based on the data in Fig. 2(c) processed by FFT analysis

## NEW THEORY AND METHOD

### OPTIMAL PARAMETERS OF EEMD AND EEMD

EMD is based on the local characteristic time scale of signal and can decompose a complicated signal  $x(t)$  into a number of IMFs,  $c_j(t)$

$$x(t) = \sum_{j=1}^n c_j(t) + r_n(t) \quad (1)$$

The IMFs,  $c_j(t)$ , represent the natural, oscillatory mode embedded in the signal and work as the basis functions which are determined by the signal itself, rather than pre-determined kernels. As a self-adaptive signal processing method, EMD has been widely applied to non-linear and non-stationary signal analysis. However, the decomposition results can suffer from mode mixing which is defined as a single IMF either consisting of signals of widely disparate scales, or a signal

residing in different IMF components. It not only leads to serious abasing in the time-frequency distribution but also makes the physical meaning of individual IMF ambiguous. To overcome the problem of mode mixing, EEMD is developed, which is a noise-assisted data analysis method by adding white noise to the investigated signal [6]. The EEMD algorithm can be given as follows:

- (1) Add a white noise series to the targeted data.

$$X(t) = x(t) + N(t) \quad (2)$$

- (2) Decompose the data with added white noise into IMFs.

$$X(t) = \sum_{j=1}^n c_j(t) + r_n(t) \quad (3)$$

- (3) Repeat step 1 and step 2 again and again, but with different white noise series each time,  $i = 1 \sim m$ ,

$$X_i(t) = x(t) + N_i(t) \quad (4)$$

$$X_i(t) = \sum_{j=1}^n c_j(t) + r_n(t) \quad (5)$$

- (4) Obtain the means of corresponding IMFs as the final result,

$$c_j(t) = \frac{1}{m} \sum_{i=1}^m c_j(t) \quad (6)$$

In the EEMD process, two critical parameters, the amplitude of the added noise and the ensemble number, are to be pre-set. The selection of these two parameters will directly affect the decomposition results of signal.

### OPTIMIZATION OF PARAMETERS FOR EEMD

In the EEMD process of noise aided analysis method, there is no strict theoretical basis for the selection of the amplitude of the added noise and the ensemble number. If the selection of the two parameters is inappropriate, the decomposition error will increase, and the decomposition result may become meaningless. Much investigation carried out for determining these two parameters shows that when the amplitude of the added noise is too small it may not introduce enough changes in the local extremum of the decomposed signal and has little or no effect on the change in the local time span of the original signal; if, however, the amplitude of the added noise is too large, the decomposition error will increase and the original signal characteristics may be destroyed. Once the amplitude of the added noise is determined, a larger value of ensemble number, not considering the computational cost,

will be helpful for reducing the remaining noise in each IMF. However, continuing increasing the ensemble number not only rises the computational effort, but also results in only a minor change in error. Wu and Huang suggested that the amplitude of the white noise  $a_N$  is defined by the amplitude standard deviation  $SD$  of the original signal multiplied by a magnitude factor  $k$ ,  $k$ ,  $a_N = k \times SD$ . The ensemble number  $m$  can be determined by setting the decomposition error. This method is empirical and non-adaptive. Therefore, it would be useful to adaptively determine these two parameters to improve the decomposition capability of EEMD for different signals. In engineering the measured signals are usually composed of background noise, main signal components and some minor signal components. A set of IMFs is obtained by using EEMD for the signal, wherein the main signal component is the IMF with the largest correlation coefficient with the original signal, which is denoted as  $c_{\max}(t)$ . In this way, the EEMD decomposition performance of signals under different amplitudes of white noise can be evaluated by evaluating  $c_{\max}(t)$ . The relative root-mean-square error ( $RRMSE$ ) is introduced to analyze the difference between  $c_{\max}(t)$  and original signal. It is expressed as follows:

$$RRMSE = \sqrt{\frac{\sum_{n=1}^N (x(t) - c_{\max}(t))^2}{\sum_{n=1}^N (x(t) - x_m)^2}} \quad (7)$$

where  $x_m$  is the mean of the original signal,  $N$  is the number of samples in the original signal. If  $RRMSE$  is small or close to zero, it indicates that component  $c_{\max}(t)$  is infinitely close to the original signal, which contains not only the main component of the original signal, but also some noise or some low correlation signal components. This shows that the difference between the component  $c_{\max}(t)$  and the original signal is small, and the decomposition quality of EEMD is not good. In order to get good quality of EEMD,  $RRMSE$  should reach the maximum value, so that the selected IMF,  $c_{\max}(t)$ , contains only the main component of the original signal. This is the desired decomposition result, and the corresponding noise amplitude is the optimal one.

In the proposed adaptive EEMD, the amplitude coefficient of added white noise  $k$  is determined as follows:

(1) First, a small value of ensemble number  $m$  is set, and a small value of  $k$  is chosen as the initial amplitude coefficient for the white noise.

(2) The white noise is added to the original signal for EEMD. The correlation coefficients of each IMF are calculated, and the  $c_{\max}(t)$  which has the largest correlation with the original signal, is selected.

(3) Then  $RRMSE$  between the  $c_{\max}(t)$  and the original signal is calculated.

(4) Gradually increase the amplitude coefficient  $k$  of white noise, keep the ensemble number value  $m$  unchanged, repeat steps (2), (3).

(5) Analyze the trends in  $RRMSE$  with white noise amplitude coefficient  $k$ , when the value of  $RRMSE$  is the maximum, the corresponding white noise is the best one that should be added into EEMD.

Once the amplitude of the added noise is determined, the appropriate value of the ensemble number  $m$  can be determined. In the EEMD process, too large value of  $m$  will lead to a higher computation cost. However, too small value of  $m$  will not be able to cancel out the noise remaining in each IMF. Based on the statistical characteristics of white noise using EMD, Wu found that the product of the energy density of the component IMF and its mean period is a constant [17]. Gao proposed a method to test whether the IMFs of a noisy signal contain useful information [18]. Here, the widely used measure, the signal-to-noise ratio (SNR), is introduced to determine the appropriate value of  $m$ . The procedure is as follows:

(1) Fix the optimal noise level as described earlier, a smaller value of  $m$  is initially chosen as the ensemble number in EEMD.

(2) EEMD is performed and the product of the energy density and the mean period is calculated respectively for the IMFs. The IMFs containing useful information were obtained and the original signal after de-noising is constructed and the SNR value is calculated.

(3) Gradually increase the value of  $m$ , repeat steps (2) until the change in the SNR value is relatively small, and the corresponding value is the reasonable ensemble number for EEMD.

## TEAGER ENERGY OPERATOR (TEO)

The TEO of the time-varying signal is defined as follows, [19-20]:

$$J[x(t)] = [\dot{x}(t)]^2 + x(t) \ddot{x}(t) \quad (8)$$

where  $\dot{x}(t)$  and  $\ddot{x}(t)$  are the first and the second order derivatives of the signal  $x(t)$  relative to time  $t$ , respectively. The output of the TEO tracks the total energy required to produce the signal.

At any given moment, the mechanical energy of the vibration system is the sum of the kinetic energy in the spring and the kinetic energy of the mass block,

$$E = \frac{1}{2} k[x(t)]^2 + \frac{1}{2} m[\dot{x}(t)]^2 = \frac{1}{2} mA^2\omega^2 \quad (9)$$

Applying the TEO defined by Eq. (8) to the harmonic vibration  $x(t)$  described by Eq. (9), one obtains:

$$J[x(t)] = J[A \cos(\omega t + \varphi)] = A^2\omega^2 \quad (10)$$

Comparing Eq. (9) with Eq. (10), one can see that the output of the TEO and the instantaneous total energy of the

harmonic vibration differ only by a constant  $m/2$ , so TEO tracks the total energy required to generate the harmonic vibration.

Traditionally, the signal energy is defined as the square of the amplitude of the signal, representing only kinetic energy or potential energy. Although it may also highlight the transient characteristics of impact type of signals if an impact amplitude is small, the impact component may however be hidden by other components. Because of the high vibration frequency of the transient impact, the TEO method can effectively highlight the transient characteristics of the impact.

The TEO in Eq. (8) is defined for the continuous time signal  $x(t)$ . For the discrete time signal  $x(n)$ , the TEO is transformed into a discrete time signal:

$$J[x(n)] = [x(n)]^2 - x(n-1)x(n+1) \quad (11)$$

For the discrete time signal, TEO requires only three sample data at any time to calculate signal energy. Therefore, it has a good time resolution for the instantaneous changes of signals and can detect transient components in a signal. TEO is only suitable for narrowband signals, and complex multi-component signals, the EEMD of optimal parameters can be employed first to decompose the signals into IMFs. Through screening the sensitive components, the selected component can then be analyzed by using the TEO.

### CORRELATION KURTOSIS

The Correlation Kurtosis (CK) not only retains the characteristics of kurtosis, but also has the characteristics of correlation functions. It is a parameter that reflects the intensity of periodic pulse signals in faulty signals [21]. When applied to the signal of turbine blades, if there is a disturbance in the pressure distributions introduced by the rotating blade, which is similar to an impact signal with a distinct cycle, the kurtosis is large, while the CK of other impact signals will be very small. Moreover, the larger CK the greater the proportion of the blades' disturbance signal in the pressure pulsation signal. Therefore, CK can be used to extract disturbance signals more effectively, and as the screening index of the sensitive components. The first  $m$  IMFs with the maximum correlation kurtosis value are selected as sensitive components. CK is computed as:

$$CK_M(T) = \frac{\sum_{n=1}^N \left( \prod_{m=0}^M X_{n-mT} \right)^2}{\left( \sum_{n=1}^N X_n^2 \right)^{M+1}} \quad (12)$$

where  $X_n$  is the signal sequence,  $N$  is the number of samples in the original signal,  $T$  is the cycle of the pulse signal of interest,  $M$  is the number of cycles of shift.

Based on the above theories and methods, the procedures of the proposed method are as follows:

- (1) The turbine blade signals are decomposed by using EEMD of optimal parameters, the IMFs containing the critical feature information are obtained,
- (2) CK is used to screen the sensitive feature components.
- (3) TEO is applied to the selected sensitive IMFs and the characteristic frequencies of the measured signal are identified.

## APPLICATIONS OF THE PROPOSED METHOD AND RESULTS

### SOUND SIGNAL ANALYSIS

The sound signal in Fig. 2(c) was decomposed by using the EEMD, and the first four IMFs of decomposition results are shown in Fig. 5.

The first IMF,  $c_1(t)$ , contains the impulse characteristic signal, and the marginal spectrum of  $c_1(t)$  is shown in Fig. 6. Both the blade vibration and the blade passing disturbances are captured. Despite this success, the peak of the blade vibration mode in Fig. 6 is not distinct as noise interferes.

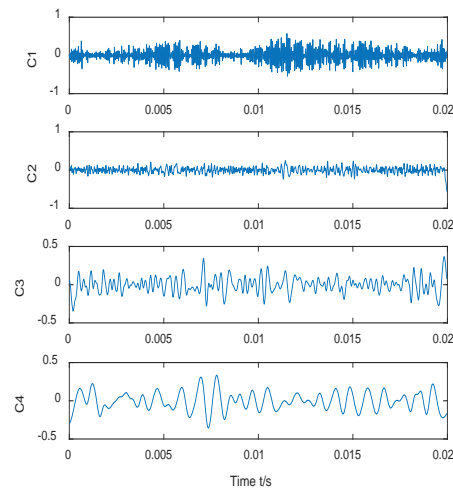


Fig. 5. The first four IMFs of sound signal obtained by using EEMD

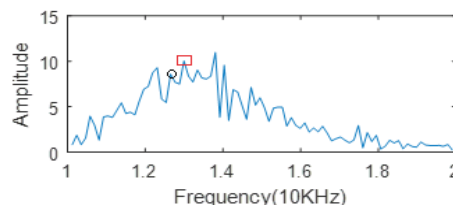


Fig. 6. The marginal spectrum of IMF1 in Fig. 5. The circle mark corresponds to 12,600Hz, and the rectangle mark to 13,000Hz.

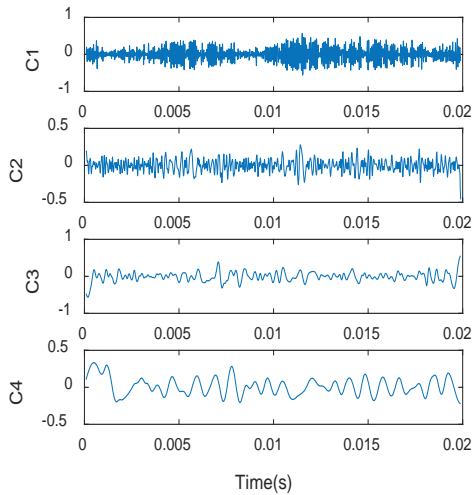


Fig. 7. The first four IMFs of sound signal obtained by using EEMD of optimal parameters

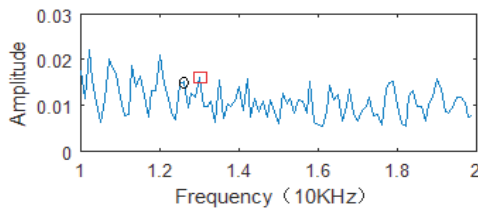


Fig. 8. Teager envelope spectrum of IMF2 in Fig. 7. The circle mark corresponds to 12,600Hz, and the rectangle mark to 13,000Hz.

The same sound signal was again investigated by the proposed new method. Firstly, the EEMD of optimal parameters is applied to the sound signal in Fig. 2(c), and the first four IMFs of the decomposition results are shown in Fig. 7.

As the pressure pulsations can come from different disturbance sources, the disturbance sources information contained in the original signal is decomposed into each component. CK was used as the screening index of the sensitive components to extract the disturbance source feature. The CK values of each IMF component were calculated by using the period of detected components  $T (=1/12670)$ . In accordance with the criterion of maximum CK, the second IMF  $c_2(t)$  was selected as the sensitive component. TEO analysis was then applied to  $c_2(t)$  and the Teager envelope spectrum is shown in Fig. 8. Compared with the results in Fig. 6, the peaks around 12,000Hz ~ 13,000Hz are more distinct and narrower banded. Both the known blade vibration and the compressor blade passing signals are well captured.

## STRAIN SIGNAL ANALYSIS

For the blade strain signal in Fig. 2(b), the strain signal near the natural frequency of the measured turbine blade is very weak form the power spectrum of the blade strain obtained from FFT analysis in Fig.3. The strain signal was next decomposed by using the traditional EEMD, and the first four IMFs of decomposition results are shown in Fig. 9.

The second IMF,  $c_2(t)$ , contains the impulse characteristic signal, and the marginal spectrum of  $c_2(t)$  is shown in Fig. 10. A peak of 12,650Hz is just identifiable. This is likely the pursued vibration mode of the blade. A stronger peak with a higher frequency of 13,070Hz is also present, but the reason of its occurrence is not clear. The FFT result in Fig. 3 has also a large peak at 13,650Hz. So, compared with the FFT, the traditional EEMD was more efficient in identifying the blade mode, but this identification is still weak.

Therefore, the proposed new method was employed for the strain signal. Firstly, the EEMD of optimal parameters was applied to the strain signal in Fig. 2(b), and the first four IMFs of the decomposition results are shown in Fig. 11.

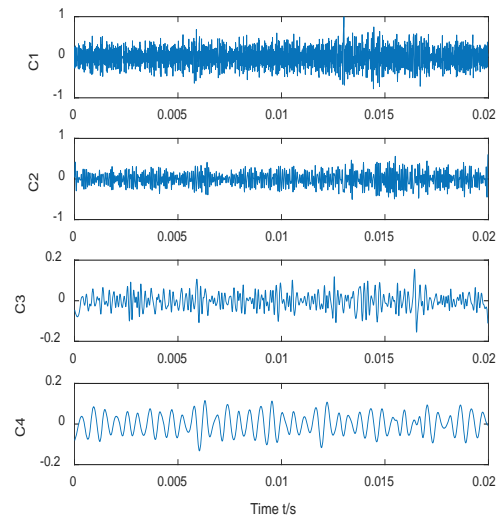


Fig. 9. The first four IMFs of blade strain signal obtained by using traditional EEMD

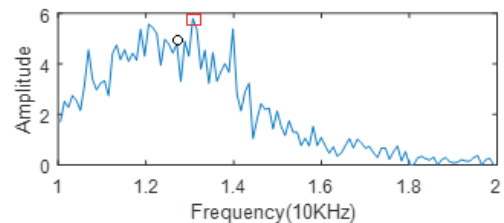


Fig. 10. The marginal spectrum of IMF2 in Fig. 9. The circle mark corresponds to 12,650Hz, and the rectangle mark to 13,070Hz.

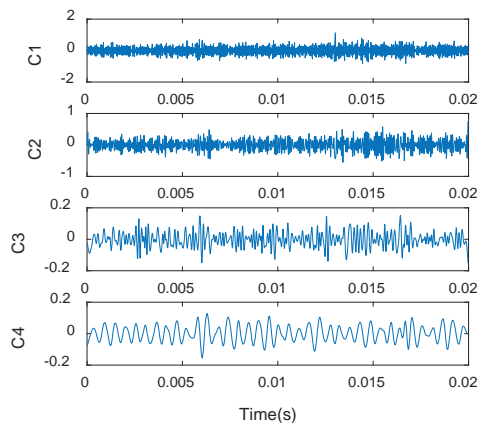


Fig. 11. The first four IMFs of blade strain signal obtained by using EEMD of optimal parameters

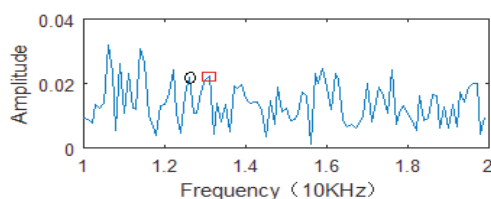


Fig. 12. Teager envelope spectrum of IMF1 in Fig. 11. The circle mark corresponds to 12,650Hz, and the rectangle mark to 13,070Hz

The CK values of each IMF component were calculated by using the period of detected components  $T = 1/12670$ . In accordance with the criterion of maximum CK, the first IMF,  $c_1(t)$ , was selected in this case as the sensitive component. TEO analysis was then applied to  $c_1(t)$  and the Teager envelope spectrum is shown in Fig. 12. In the figure one can clearly observe a distinct peak at 12,650Hz. This result, compared with the result of the traditional EEMD ( Fig. 10) and that of FFT (Fig. 3), again demonstrates the value of the new method.

## CONCLUSIONS

In this research, sound signals and strain gauge signal were used for the identification of the first vibratory mode of turbocharger turbine blades. An optimization method was developed for adaptive determining appropriate EEMD parameters for the measured signals, so that the significant feature components could be extracted from the original vibration signal and separated from background noise and some irrelevant components. By using CK, the sensitive feature component is screened out, which can effectively eliminate interfering components and capture the feature information. TEO enhances the detection of weak impact characteristic frequencies.

Experiments on a turbine wheel were carried out to verify the effectiveness of this method against both FFT and traditional EEMD method. The results show that it can identify the first blade vibratory mode from both the weak sound signal and the strain gauge signal, which was difficult

in this case for conventional FFT technique and to a lesser degree for the traditional EEMD method.

This investigation suggests that it might be possible to identify the characteristics of the first blade vibratory mode of turbocharger turbine rotors by using feature extraction of sound signal. It is of a great importance to determine which blade has the largest vibratory strain due to mistuning effect, and to reduce in this simple way experiment time and cost of strain gauging or tip timing measurement. The current study also shows that there is still some way to go before this aim can be achieved.

## ACKNOWLEDGMENTS

The authors acknowledge the financial support from the Science Research Project of Liaoning Provincial Department of Education(L2015069), the National Science Foundation (11272093) and the Project of the Scientific Research Leaders of Dalian Maritime University (002530).

## BIBLIOGRAPHY

1. H. Hackenberg, A. Hartung: An approach for estimating the effect of transient sweep through a resonance, in: Proceedings of ASME Turbo Expo 2015: Turbomachinery Technical Conference and Exposition, 2015, pp. 1-11.
2. S. Yeung, R. M. Murray: Reduction of bleed valve rate requirements for control of rotating stall using continuous air injection, IEEE International Conference on Control Applications. 1997, pp.683-690.
3. Y. H. Wu, J. Wu, H. Zhang, W. Chu: Experimental and numerical investigation of near-tip flow field in an axial flow compressor rotor-Part II: Flow characteristics at stall inception condition, ASME Turbo Expo 2013: Turbine Technical Conference & Exposition, 2013, pp.67-73.
4. Z. Peng, F. Chu: Application of the wavelet transform in machine condition monitoring and fault diagnostics: a review with bibliography, Mechanical systems and Signal Processing, 18 (2004), pp. 199-221.
5. N. E. Huang, Z. Shen, S.R. Long, M.L. Wu, H.H. Shih, Q. Zheng, N.C. Yen, C.C. Tung, H.H. Liu: The empirical mode decomposition and the Hilbert spectrum for nonlinear and nonstationary time series analysis, Proceedings of the Royal Society of London, Series A, 454(1998) pp. 903-995.
6. Z. H. Wu, N. E. Huang: Ensemble empirical mode decomposition: a noise assisted data analysis method, Advances in Adaptive Data Analysis, 1(2009), pp. 1-41.
7. J. Zhang, R. Q. Yan, R. X. Gao, Z. H. Feng: Performance enhancement of ensemble empirical mode decomposition,

- Mechanical Systems and Signal Processing, 24(2010), pp. 2104-2123.
8. L. Chen, G. Tang, Y. Zi, et al.: Application of adaptive ensemble empirical mode decomposition method to electrocardiogram signal processing, Chinese Journal of Data Acquisition & Processing, 26(2011), pp. 361-366.
  9. Chang K. M., Liu S. H.: Gaussian noise filtering from ECG by Wiener filter and ensemble empirical mode decomposition, Journal of Signal Processing, 64(2011), pp. 249-264.
  10. J. R. Yeh, J. S. Shieh, N. E. Huang: Complementary ensemble empirical mode decomposition: a novel noise enhanced data analysis method, Advances in Adaptive Data Analysis, 2(2010), pp. 135-156.
  11. Y. J. Wang, Y. C. Jiang, S. Q. Kang, G. X. Yang, Y. N. Chen: Diagnosis method of fault location and performance degradation degree of rolling bearing based on optimal ensemble EMD (in Chinese), Chinese Journal of Scientific Instrument, 34(2013), pp. 1834-1840
  12. Y. G. Lei, D. T. Kong, N. P. Li, et al.: Adaptive ensemble empirical mode decomposition and its application to fault detection of planetary gearboxes, Journal of Mechanical Engineering, 50(2014), pp. 64-70.
  13. R. K. Niazy, C. F. Beckmann, J. M. Brady, S. M. Smith: Performance evaluation of ensemble empirical mode decomposition, Advances in Adaptive Data Analysis, 1 (2009), pp. 231-242.
  14. D. T. Kong, Q. C. Liu, Y. G. Lei, W. Fan, X. C. Ding, Z. Wang: The improved EEMD method and its application, The Journal of Vibration Engineering, 28(2015), pp. 1015-1021.
  15. J.A. Kenyon, D.C. Rabe, S. Fleeter: Aerodynamic effects on blade vibratory stress variations, Journal of propulsion and power, 15 (1999), pp. 675-680.
  16. D. Hemberger, D. Filsinger, H J Bauer: Identification of mistuning for casted turbine wheels of small size, in: ASME Turbo Expo2014: Turbine Technical Conference and Exposition, 2014, pp. V01BT24A002.
  17. Z. H. Wu, N. E. Huang: A study of the characteristics of white noise using the empirical mode decomposition method, Proceedings of The Royal Society Series A, 460(2004), pp. 1597-1661.
  18. Y. Gao, E. Sang, B. Liu: Adaptive de-noising algorithm based on EMD (in Chinese), Computer Engineering and Applications, 43(2007), pp. 59-61
  19. A. Potamianos, P. Maragos: A comparison of the energy operator and Hilbert transform approaches for signal and speech demodulation, Signal Processing, 37(1994), pp. 95-120.
  20. J. Kaiser: On a simple algorithm to calculate the 'energy' of a signal, Proceedings of IEEE International Conference on Acoustics, Speech, and Signal Processing, 1(1990), pp. 381-384.
  21. G. McDonald, Q. Zhao, M. Zuo: Maximum correlated kurtosis deconvolution and application on gear tooth chip fault detection, Mechanical Systems and Signal Processing, 33(2012), pp. 237-255.

#### CONTACT WITH THE AUTHOR

**Fengli Wang**

*e-mail: wangfl@dlnu.edu.cn*  
 College of Marine Engineering  
 Dalian Maritime University  
 Linghai Road No.1, Dalian, Liaoning  
 116026 Dalian  
**CHINA**

# DYNAMIC CHARACTERISTIC STUDY OF RISER WITH COMPLEX PRE-STRESS DISTRIBUTION

Luyun Chen

Hong Yi

State Key Laboratory of Ocean Engineering, Collaborative Innovation Center for Advanced Ship and Deep-Sea Exploration, Shanghai Jiao Tong University, Shanghai, China

## ABSTRACT

*In this study, the dynamic characteristic problem of riser structure with complex pre-stress distribution is investigated. At first, the differential equation of the riser structure with complex pre-stress distribution is derived. The analytical expression of the free vibration of a riser structure with complex pre-stress distribution is discussed by using the orthogonal property of the trigonometric series. A top-tensioned riser (TTR) for example, the influences of the amplitude and direction of complex pre-stress on natural frequency and mode shape characteristics are compared. This study provides a new method for addressing the riser structure response problem with complex loading.*

**Keywords:** complex pre-stress, top-tensioned riser (TTR), natural frequency, mode analysis, free vibration

## INTRODUCTION

Owing to the growing demand for crude oil and gas, offshore equipment has been developed for deep-water exploitation. A riser structure, as the key equipment that links the platform and wellhead at the sea base, has become a popular issue in engineering design. In addition to the influence of gravity, riser structures are subjected to wave - and current-induced loading and high-pressure oil and gas. Thus, several dynamic responses, such as parametric and vortex-induced vibrations (VIV), occur in riser structures. The parametric vibration which is caused by the heave of the floating platform might destabilize the straight equilibrium of a riser structure. An accurate prediction of dynamic characteristics is vital to the design, installation and operation of the riser structure. Researchers have conducted numerous studies that involve theoretical analysis, numerical calculation and experimental investigation to investigate the fundamental mechanism of free vibration for the riser structure. The nonlinear resonance that arises from parametric excitation problems has been discussed, and closed-form solutions for the riser have been obtained based on first and second modes through

extensive mathematical manipulations [3,4]. The parametric vibration that is caused by the wave-induced motions of the floating platform is practically important because this vibration can destroy a riser structure [11]. A finite element method has also been used to analyse the influence of water depths, environmental conditions and vessel motions under combined parametric and forcing excitations [10].

Structural natural frequency is an important dynamic property of a riser structure. However, the natural frequencies of a riser structure possess a low modal, and these frequencies are near one another given the structural stiffness problem of risers. A closed-form solution for the natural frequencies and associated mode shapes of axial loading has been deduced by Timoshenko beam theory [6,15]. Based on Spark's theory, the influence on bending stiffness is defined as tension force, and natural frequency and mode are deduced through a segmentation method [12].

Pre-stress (initial stress) often exists in complex structures and may be caused by welding residual stress, structural manufacturing defects, material thermal effects, static external loading, and so on. A riser is a large welded structure, and the welding residual stress in the structure will not be completely

eliminated with the operation of risers. Pre-stress can resist or aid in structural deformation and alter the static and dynamic characteristics of a structure. Pre-stress significantly influences local and global stiffness matrices. The effects of uniform pre-stress distribution on natural frequencies and dynamic responses have been investigated [7,8]. The natural frequencies of a structure may increase or decrease if the pre-stress is considered in terms of uniform Euler-Bernoulli beams under linearly varying fully tensile stress [1,2,11]. The effects of welding residual stress on the added virtual mass and the quality factor of the diaphragm have been presented [14]. In addition, the differential equation of the vibration of a cylindrical shell with welding residual stress has been derived, and a theoretical solution has been presented [9]. The analytic expression of the influence of complex pre-stress force on a riser structure is derived in a previous study, and the VIV response is compared [5]. The influence of complex pre-stress on the mechanical response of risers, especially on their structural dynamic characteristics, requires further study. However, only a few studies have considered the effects of complex pre-stress on the dynamic response of a riser structure.

The main objective of the present study is to investigate the influence of complex pre-stress (welding residual stress) on the natural frequency and modal shape for the dynamic characteristic of a top-tensioned riser (TTR). The developed analytical method to analyze the dynamic behaviour of the riser structures with or without, local area or overall and even non-uniform pre-stress distributions. The outline of the present paper is as follows. A model of complex pre-stress force theory is described in Section 1. The differential equation of the pre-stressed beam is presented in Section 2. A free vibration analytical solution of a riser structure with complex pre-stress is introduced in Section 3. The governing equation of the parametric vibration for the riser structure with complex pre-stress distribution is expressed in Section 4. A numerical analysis is implemented in Section 5. The conclusions are presented in Section 6.

## PRE-STRESS MODEL OF BEAM

Pre-stress (initial stress) typically exists in continuum structures, the influence of complex pre-stress on the static and dynamic characteristics of riser structures, especially on their structural dynamic characteristics, is worthy of study. In the present study, only welding residual stress and axial tension are discussed. These types of pre-stress can be defined as complex pre-stress that is unaffected by external dynamic excitation force. The complex pre-stress that satisfies the linear superposition principle can be expressed as follows:

$$\sigma_r = \sigma_T + \sigma_R \quad (1)$$

where  $\sigma_r$  is the complex pre-stress in the structure,  $\sigma_T$  is the pre-stress caused by axial riser tension force and  $\sigma_R$

is the welding residual stress. In the riser structures, complex pre-stress  $\sigma_r$  is a non-uniform distribution stress and the function of time and space. In the present study, only the axial direction of pre-stress is considered; the complex pre-stress can be written as  $\sigma_r = \sigma_{r,z}$ .

## DIFFERENTIAL EQUATION OF THE PRE-STRESS BEAM

The riser structure can be idealized as a beam structure. The motion equations of beam structure with pre-stress distribution must consider the pre-stress distribution.

### EULER-BERNOULLI BEAM MODEL

In Fig. 1, the length of the beam structure is  $L$ . A rectangular Cartesian coordinate system  $x$ ,  $y$  and  $z$  are used to describe the loading and structure deformations. The original points of the structural member are referred to as a Cartesian coordinate system ( $x$ ,  $y$  and  $z$ ), where the  $z$ -axis is parallel to the longitudinal axis of the beam, whereas  $x$  and  $y$  are the principal axes of the cross-section of the structure. The displacement of the beam satisfies the 'plane cross-sectional assumption'.

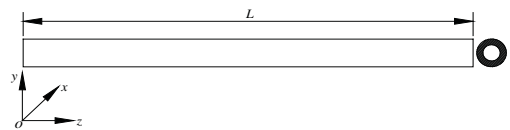


Fig.1. Beam geometry model

A differential element with length  $dz$  is selected, as illustrated in Fig. 2. The internal member forces during the beam structure vibration include two parts. The first part consisted of the moment and axial forces that are caused by dynamic external loading. The second part comprised of the moment and axial forces that are caused by the coupling of complex pre-stress force and dynamic vibration displacement.

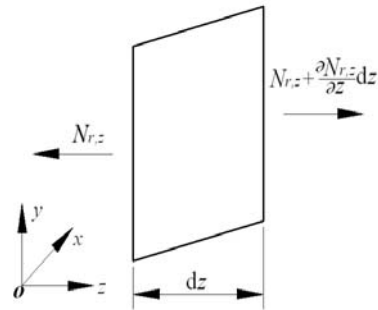


Fig.2. Section force that is caused by complex pre-stress

In the beam structure, the pre-stress  $\sigma_{r,z}$  is distributed along the  $z$ -direction; this pre-stress is a function of variable  $z$ .

The axial internal forces  $\mathbf{N}_{r,z}$  at the end of the differential element can be written as follows:

$$\mathbf{N}_{r,z} = \sigma_{r,z} S \quad (2)$$

where  $S$  is the cross-sectional area of the beam. Based on the beam bending theory, the strain  $\varepsilon_z$  in the differential element can be stated as follows:

$$\varepsilon_z = -y \frac{d^2 w(z,t)}{dz^2} \quad (3)$$

where  $w(z,t)$  is the displacement that is vertical to the symmetry plane. The stress in the beam structure can be expressed as  $\sigma_z = E\varepsilon_z = -Ey \frac{d^2 w}{dz^2}$ . The moment in the differential element can be written as follows:

$$M_z = EI \frac{d^2 w}{dz^2} \quad (4)$$

where  $M_z$  is the moment which is caused by stress  $\sigma_z$ ,  $I$  is the moment of inertia of the beam and  $E$  is Young's modulus of the beam material.

#### COUPLING FUNCTION OF PRE-STRESS FORCE AND VIBRATION DISPLACEMENT

If the beam structure is vibrated by the dynamic external loading, then the coupling function between complex pre-stress and dynamic vibration displacement can be obtained. In addition, the amplitude and distribution of the complex pre-stress are constant during structural vibration. The structural deformation  $l_y$  of the cross-sectional neutral plane with unit length can be expressed as follows:

$$l_y = 1 + \varepsilon_z \quad (5)$$

Based on the 'plane cross-sectional assumption', the volume of the unit length of the beam structure can be stated as follows:

$$V = \int_{-\frac{y}{2}}^{\frac{y}{2}} l_y dy = S \quad (6)$$

In Eq. (6), the volume of the differential element of the beam cross-section is constant. The internal forces  $\mathbf{N}_{r,z}$  will be static while the beam vibrates. Owing to the structural displacement  $w$ , a torsional angle for the  $y$ -axis emerges, and the value of the angle is  $\partial w / \partial z$ .

In the differential element, internal forces  $\mathbf{N}_{r,z}$  are parallel to the  $z$ -direction, the components in the other directions are zero and internal forces  $\mathbf{N}_{r,z}$  includes a component in

the  $y$ -direction. This situation is written as  $\Delta \mathbf{N}_{y,z}$  and can be expressed as follows:

$$\Delta \mathbf{N}_{y,z} = \sigma_{r,z} S \frac{\partial w}{\partial z} \quad (7)$$

In Eq. (7), the component force  $\Delta \mathbf{N}_{y,z}$  depends on the complex pre-stress and dynamic vibration displacement. Then, a new equilibrium equation is obtained for the differential element of the beam structure. This equilibrium equation is defined as a coupling force of complex pre-stress and dynamic vibration displacement, as depicted in Fig. 3.

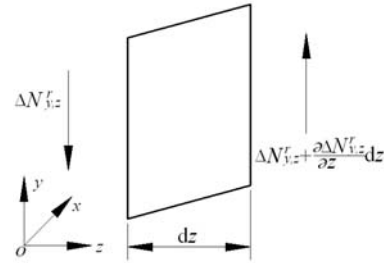


Fig.3. Coupling force of the differential element

#### EQUILIBRIUM EQUATION

The equilibrium equation for internal force and moment are established to address the vibration function of the differential element. Based on the small deformation of beam bending theory, the force in the  $z$ -direction satisfies the equilibrium equation. Then, the equilibrium equation in the  $y$ -direction which combines force  $N_z$  and coupling force  $\Delta \mathbf{N}_{y,z}$  can be stated as follows:

$$\frac{\partial Q_z}{\partial z} dz + \frac{\partial \Delta \mathbf{N}_{y,z}}{\partial z} dz = m \frac{\partial^2 w}{\partial t^2} dz \quad (8)$$

where  $m$  is the mass of the unit length of the beam structure. The moment in the  $y$ -direction satisfies the equilibrium equation because no coupling moment is caused by the complex pre-stress. The moment in the  $z$ -direction can be stated as

$$Q_z dz + \frac{\partial M_z}{\partial z} dz = 0 \quad (9)$$

The differential equation is gained by substituting Eq. (9) into Eq. (8), as follows:

$$\frac{\partial M_z}{\partial z^2} - \frac{\partial \Delta \mathbf{N}_{y,z}}{\partial z} = -\rho S \frac{\partial^2 w}{\partial t^2} \quad (10)$$

where  $\rho$  is the equivalent density of the beam, and  $S$  is the cross-sectional area of the beam.

### MOTION DIFFERENTIAL FORMULATION OF BEAM

The free vibration differential formulation of the beam structure with complex pre-stress can be expressed by substituting Eqs. (4) and (7) into Eq. (10), as follows:

$$EI \frac{\partial^4 w}{\partial z^4} - \frac{\partial}{\partial z} (\sigma_{r,z} S \frac{\partial w}{\partial z}) = -\rho S \frac{\partial^2 w}{\partial t^2} \quad (11)$$

In Eq. (11), the elemental stiffness matrix comprises two parts, that is, the elasticity and geometric stiffness matrices;

the former can be written as  $EI \frac{\partial^4 w}{\partial z^4}$ , while the latter can be defined written as  $C(w, \sigma_{r,z}, t) = -\frac{\partial}{\partial z} (\sigma_{r,z} S \frac{\partial w}{\partial z})$ . This

quasi-linear fourth-order partial differential equation governs

the beam to a general dynamic and distributed external excitation. If the complex pre-stress in the beam structure is zero, then  $C(w, \sigma_{r,z}, t) = 0$ . This scenario represents a free vibration differential formulation of a simple beam structure. The vibration equation will be solved with given boundary conditions.

### FREE VIBRATION OF THE RISER WITH COMPLEX PRE-STRESS DISTRIBUTION

The structural modes and modal problem of the riser with a complex pre-stress distribution are discussed.

#### DEFINITION OF BOUNDARY CONDITIONS

The physical boundary condition at both ends of the riser structure can be modelled as a simple support. The displacement at each end is zero, and the boundary conditions can be written as follows:

$$w(z, t)|_{z=0} = 0, \quad \frac{\partial^2 w(z, t)}{\partial z^2} \Big|_{z=0} = 0, \quad w(z, t)|_{z=L} = 0, \quad \frac{\partial^2 w(z, t)}{\partial z^2} \Big|_{z=L} = 0 \quad (12)$$

Modal decomposition is based on the assumption that the riser mode may be expressed as a sum of eigenmodes or eigenfunctions at any point in time. The solution of Eq. (11) can be obtained with a form of power series expansion. Galerkin's procedure is used to obtain the solution of Eq. (11). The solution of linearized Eq. (11) under the simple support boundary can be expressed as follows:

$$w(z, t) = \phi(z) e^{i\omega t} = \sum_{n=1}^N B_n \sin(n\beta z) e^{i\omega t} \quad (13)$$

where  $z$  is the axial coordinate,  $L$  is the length of the riser,  $t$  is the time parameter,  $w_n(t)$  is the modal weight function and  $\phi_n(z)$  is the mode shape function, where  $n = 1, 2, 3, \dots$ . The mode shapes can be defined as sinusoid functions as follows:  $\phi_n = \sin(n\beta z)$ , where  $\beta = \pi/L$ , and  $\omega$  is the angular frequency.

The free vibration differential formulation of the riser with complex pre-stress can be obtained by introducing orthogonal series  $\sin(\xi\beta z)$  and substituting Eq. (13) into Eq. (11).

$$\int_0^L \sin(m\pi z / L) \cdot \sin(n\pi z / L) dz = 0 \quad \text{exists by using the}$$

orthogonal property of the trigonometric series because  $m \neq n$  integrates the function from  $z = 0$  to  $z = L$ . Then, Eq. (11) can be written as follows:

$$EI(n\beta)^4 B_n - \frac{2}{L} \int_0^L \frac{\partial}{\partial z} (\sigma_{r,z} S \frac{\partial w}{\partial z}) \sin(\xi\beta z) dz = \rho S \omega^2 B \quad (14)$$

$$\text{where } R = -\frac{2}{L} \int_0^L \frac{\partial}{\partial z} (\sigma_{r,z} S \frac{\partial w}{\partial z}) \sin(\xi\beta z) dz \quad \text{which is}$$

defined as the integration item of the complex pre-stress and dynamic vibration displacement.

### SOLUTION OF THE BEAM STRUCTURE

The free vibration of the riser structure with a complex pre-stress distribution is analysed, and the analytical solution for Eq. (14) is discussed as follows:

(1) If the complex pre-stress satisfies the equation  $\sigma_{r,z} = 0$ , then Eq. (14) can be expressed as a vibration function of a simple beam. The solution equation can be written as  $EI(n\beta)^4 = \rho S \omega^2$ .

(2) If the complex pre-stress is in a uniform distribution form, then the pre-stress can be written as  $\sigma_{r,z} S = T_0$ , where  $A$  is the cross-sectional area. The solution equation can be written as  $EI(n\beta)^4 + T_0(n\beta)^2 = \rho S \omega^2$  by substituting the complex pre-stress into Eq. (14). If parameter  $\sigma_{r,z}$  is the tensile stress, then the natural frequency of the beam structure increases. If parameter  $\sigma_{r,z}$  is a compressive stress, then the natural frequency of the beam structure decreases.

(3) If the complex pre-stress is a function of variable  $z$ , then the complex pre-stress is a one-dimensional complex pre-stress distribution problem. The complex pre-stress distribution can be fitted by a trigonometric function and can be expressed as follows:

$$\sigma_{r,z} = \sigma_{r,z0} \cos(g\beta z) \quad (15)$$

where  $\sigma_{r,z0}$  is the amplitude of the complex pre-stress, and  $g$  is an integral number that is not less than 1. Function  $R$  can be obtained by separating the variables and substituting the complex pre-stress function into Eq. (14), as follows:

$$R = -\frac{2\sigma_{r,z0}S}{L} \int_0^L \frac{\partial}{\partial z} [\cos(g\beta z)] \frac{\partial w}{\partial z} \sin(\xi\beta z) dz$$

$$= -\frac{2\sigma_{r,z0}S}{L} \sum_{n=1}^N B_n(n\beta) \int_0^L \frac{\partial [\cos(n\beta z) \cos(g\beta z)]}{\partial z} \sin(\xi\beta z) dz \quad (16)$$

Following the trigonometric function, function  $R$  can be defined as follows:

$$R = -\frac{\sigma_{r,z0}S}{L} \sum_{n=1}^N B_n(n\beta) \int_0^L \frac{\partial \{\cos[(n+g)\beta z] + \cos[(n-g)\beta z]\}}{\partial z} \cdot \sin(\xi\beta z) dz$$

$$= \frac{\sigma_{r,z0}S}{L} \left\{ \sum_{n=1}^N B_n(n\beta^2)(n+g) \int_0^L \sin[(n+g)\beta z] \cdot \sin(\xi\beta z) dz \right.$$

$$\left. + \sum_{n=1}^N B_n(n\beta^2)(n-g) \int_0^L \sin[(n-g)\beta z] \cdot \sin(\xi\beta z) dz \right\} \quad (17)$$

Based on the orthogonal characteristics of the trigonometric function, the solution of Eq. (17) can be written as follows:

$$\int_0^L \sin[(n+g)\beta z] \cdot \sin(\xi\beta z) dz = \begin{cases} L/2 & n+g = \xi \\ 0 & n+g \neq \xi \end{cases} \quad (18.1)$$

$$\int_0^L \sin[(n-g)\beta z] \cdot \sin(\xi\beta z) dz = \begin{cases} L/2 & n-g = \xi \\ -L/2 & n-g = -\xi \\ 0 & |n-g| \neq \xi \end{cases} \quad (18.2)$$

By substituting Eq. (21) into Eq. (17), the function  $R$  can be expressed as follows:

$$R = \begin{cases} \frac{\sigma_{r,z0}S}{2} \sum_{g=1}^N [B_{n-g}(n\beta^2)(n-g) + B_{n+g}(n\beta^2)(n+g)] & n > g \\ \frac{\sigma_{r,z0}S}{2} \sum_{g=1}^N [-B_{n-g}(n\beta^2)(n-g) + B_{n+g}(n\beta^2)(n+g)] & n < g \end{cases} \quad (19)$$

Based on Eq. (19),  $N$  number functions exist and can be written in a matrix form as follows:

$$(\Lambda + R_g)X = 0 \quad (20)$$

where  $X = [w_1(z, t), w_2(z, t), \dots, w_N(z, t)]^T$ , and  $\Lambda = \text{diag}\{EI(n\beta)^4 - \rho S \omega^2\}$  is a diagonal matrix. The element parameter in the diagonal matrix can be written as  $EI(n\beta)^4 - \rho S \omega^2$ .  $R_g$  is a sparse matrix, and the value of function  $R$  is as follows:

If  $p = n$  and  $q = |n - g|$ , then the following equation can be deduced as

$$R_{pq} = \begin{cases} \frac{\sigma_{r,z0}S}{2} (n\beta^2)(n-g), & n > g \\ -\frac{\sigma_{r,z0}S}{2} (n\beta^2)(n-g), & n < g \end{cases} \quad (21.1)$$

If  $p = n$  and  $q = n + g$ , then the following equation can be deduced as

$$R_{pq} = \frac{\sigma_{r,z0}S}{2} (n\beta^2)(n+g) \quad (21.2)$$

(4) If the distribution of the complex pre-stress has high complexity, then the complex pre-stress is a function of variable  $z$  and a one-dimensional complex pre-stress distribution problem. The distribution of the complex pre-stress can be fitted by a trigonometric function and expressed as follows:

$$\sigma_{r,z} = \sum_{g=1}^G \sigma_{r,g} \cos(g\beta z) \quad (22)$$

where  $\sigma_{r,g}$  ( $g = 1, 2, \dots, J-1, J$ ) is the amplitude of the complex pre-stress force.

$N$  number functions exist by substituting the complex pre-stress function into Eq. (6) and can be written in a matrix form as follows:

$$(\Lambda + R)X = 0 \quad (23)$$

where  $\Lambda$  is a diagonal matrix. An increase in the series leads to a change in complex pre-stress influence matrix  $R$  because the complex pre-stress expression is highly complex. Matrix  $R$  is not a sparse matrix. In addition, the series of complex pre-stress follows the linear superposition principle and can be expressed as follows:

$$R = \sum_{g=1}^J R_g \quad (24)$$

## MODAL ANALYSIS

Following the complex pre-stress function, the dynamic response function of the beam structure with complex pre-stress can be obtained because the structural complex pre-stress can be expressed as a trigonometric function. The equations are linear in a beam structure with or without a complex pre-stress distribution, and the determinant factor to the characteristic equation is zero and can be expressed as follows:

$$|\Lambda + R| = 0 \quad (25)$$

In Eq. (25), if no complex pre-stress force distribution ( $R = 0$ ) exists, then this equation can be written as a classical elastic beam free vibration equation. If a complex pre-stress distribution ( $R \neq 0$ ) exists, then the matrix  $\Lambda + R$  is not diagonal. Therefore, the characteristic

equation and structural modes of the free vibration beam with complex pre-stress must be modified.

## FREE VIBRATION OF THE RISER STRUCTURE

### SYSTEM MODELLING

The TTR in a complex ocean environment is discussed to reveal the parametric vibration problem by considering the heaving of the platform and the motion of the tension ring. The riser structure is subjected to a current. The riser structure could be considered a long, continuous, tubular member that is straight and vertical. The boundary conditions at the two ends are known. The heaving of a floating platform which induces axial tension fluctuation in the riser structure is considered. The top of the riser is connected to the main body of the platform through a compensator. The heave compensator can be simplified as an equivalent spring with stiffness  $K$ .

Several hypotheses for the riser structure are defined as follows. (1) The material and mechanical properties are uniform along the overall of the riser structure. (2) The tension variation along the riser length varies linearly with depth. (3) Only the cross-flow vibration is considered, whereas the in-line vibration was excluded. (4) The effect of the shear strain is minimal and can be neglected. In addition, the pipe wall behaves elastically; that is, no internal damping was considered.

In this study, a rectangular Cartesian coordinate system is defined to establish the deformation of the riser structure, as demonstrated in Fig. 4.

In Fig.4, the sea surface is set as the origin of the coordinate system, the  $x$ -axis is parallel to the flow velocity and the  $z$ -axis is measured from the top of the riser.

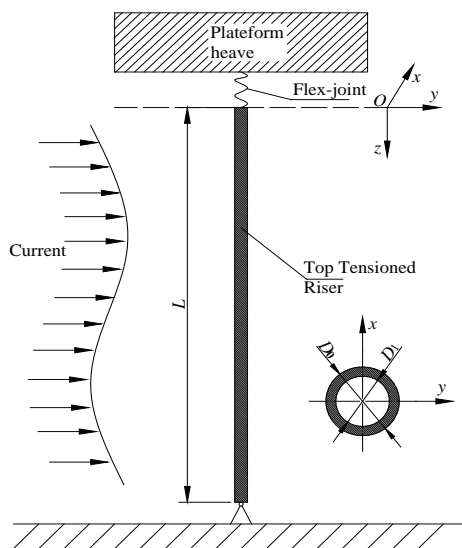


Fig. 4. Mechanical model and reference frame of the riser

Owing to the neglected effects of rotational inertia, the motion equations in the two principal vertical planes are identical and can be derived independently for each plane because of the symmetry of the riser cross-section. The riser structure can move only in the plane of the figure (i.e., in the  $z$ -direction). The lateral deflection ( $w(z, t)$ ) is considered minimal in which every cross-section remains plane perpendicular to the axis, and the riser structure can be modelled as a beam structure.

### FREE VIBRATION EQUATION OF THE RISER

Owing to the assumption of the riser structure, the governing equation of the lateral deflection  $w(z, t)$  of the riser structure by vibration can be written in the form of the following partial differential equation:

$$EI \frac{\partial^4 w(z, t)}{\partial z^4} - \frac{\partial}{\partial z} [T(z, t) \frac{\partial w(z, t)}{\partial z}] + (m_r + m_f + m_a) \frac{\partial^2 w(z, t)}{\partial t^2} + c_s \frac{\partial w(z, t)}{\partial t} = f(z, t) \quad (26)$$

where the first term is the bending stiffness of the riser structure; the second term is the axial riser tensioning force; the third term is the inertia of the riser structure and includes the riser structure, internal fluid and fluid addition masses.  $EI$  is the bending stiffness of the riser structure,  $T(z, t)$  is the effective axial tension of the riser,  $w(z, t)$  is the displacement that is vertical to the riser structure axis,  $z$  is the axial position and  $t$  is the time parameter.

In the partial differential equation,  $m_r = \frac{1}{4} \rho_s \pi (D_0^2 - D_1^2)$  is the mass per unit length of the riser,  $m_f = \frac{1}{4} \rho_f \pi D_1^2$  is the mass per unit length of the internal fluid and  $m_a = \frac{1}{4} C_a \rho_w \pi D_0^2$  is the mass per unit length of the added

mass; in addition, the influence of the motion of internal fluid in the riser structure is omitted.  $D_0$  is the outer diameter of the riser,  $D_1$  is the inner diameter of the riser,  $\rho_s$  is the riser structural density,  $\rho_f$  is the water density,  $\rho_w$  is the internal fluid density and  $C_a$  is the added mass coefficient.  $c_s$  is the damping parameter of the riser structure and is defined as 0 in the present study.

### PARAMETRIC FORCE

The effect of tension in the riser includes static and dynamic components. The static component of the tension results from the pretension imposed by the heave compensator and submerged weight. The dynamic component is caused by the heaving of the platform. This tension component depends only on time given the assumption of inextensibility. If the

platform vibrates harmonically, the effective tension can be expressed as follows:

$$T(z,t) = T_0 - W_a z + K a \sin(\pi) \quad (27)$$

where  $T_0 = Sg(\rho_s - \rho_w)f_{top}L$  is the static tension on the top of the riser, and  $f_{top}$  is the top tension coefficient.  $W_a$  is the submerged weight of the riser per unit length which is equal to  $m_r + m_f + m_a$ .  $K$  is the stiffness of the heave compensator. Parameters  $\tau$  and  $a$  are the amplitude and frequency of the heave of the platform, respectively. In the structural vibration analysis, if the effective axial tension is defined, then the structural modes and structural modal of the riser can be obtained, and the analytical solution of the dynamic response can be obtained.

Based on Eq. (1), the complex pre-stress force in the riser structure is  $\sigma_{r,z} = \frac{[T_0 - W_a z + K a \sin(\pi)]}{S}$ , where  $T_0$  is the static axial tension force,  $U_m z$  is the influence of gravity,  $K\mu$  is the amplitude of dynamic axial tension force and  $\tau$  is the frequency of platform heaving. The partial differential equation of a deepwater riser structure can be obtained by substituting Eq. (27) into Eq. (14) and can be written as follows:

$$EI \frac{\partial^4 w(z,t)}{\partial z^4} - \frac{\partial}{\partial z} [\sigma_{r,z} S \frac{\partial w(z,t)}{\partial z}] + (m_r + m_f + m_a) \frac{\partial^2 w(z,t)}{\partial t^2} + c_s \frac{\partial w(z,t)}{\partial t} = f(z,t) \quad (28)$$

Eq. (28) is a modified function of the riser structure that considers the complex pre-stress force distribution. The traditional differential equation of the deepwater riser structure is compared, and the parameter of pre-stress  $\frac{\partial}{\partial z} [\sigma_{r,z} S \frac{\partial w(z,t)}{\partial z}]$  is obtained. The description of the stress conditions of the riser structure is comprehensive. If the axial tension and welding residual stress are defined, then the structural modes and structural modal of the riser and the solution of the dynamic response can be determined.

## NUMERICAL RESULT AND DISCUSSION

### MODEL DESCRIPTION

The design parameters of the riser structure for the numerical analysis of the parametric vibration problem are listed in Table 1. The effects of complex pre-stress on the natural frequency and mode shape of the riser are compared. The design parameter is similar to that in Reference [13].

Tab. 1. Design parameters of the model system

Parameter	Symbol	Values	Unit
Length	$L$	1000	m
Outer Diameter	$D_0$	0.30	m
Thickness	$t$	0.025	m
Young's Modulus	$E$	2.1E11	Pa
Material Density	$\rho_s$	7850	kg/m <sup>3</sup>
Density of Water	$\rho_w$	1025	kg/m <sup>3</sup>
Density of Oil	$\rho_f$	800	kg/m <sup>3</sup>
Equivalent Coefficient	$\lambda$	10	m
Top Tension Coefficient	$f_{top}$	1.3	-
Addition Mass Coefficient	$C_a$	1.0	-
Stiffness of Compensator	$K$	320000	N/m
Heave Amplitude	$\mu$	5	m
Heave Frequency	$\tau$		s

### MODELLING OF WELDING RESIDUAL STRESS

Two types of welding residual stress distribution are compared to analyse the influence of welding residual stress on the dynamic characteristics of the riser. The two types of stress are mixed tensile and compressive residual stresses.

The three types of welding residual stress distribution are as follows. Distribution model I is a tensile stress. Distribution model II is a tensile stress with a maximum amplitude that is smaller than that of Distribution model I. Distribution model III is defined as mixed tensile and compressive residual stresses.

The welding residual stress in the riser follows for a non-uniform distribution. Based on the common welding technology for risers, the peak value of stress is distributed periodically by a certain distance. In the present study, every 2 m is defined as peak stress, and the welding residual stress is zero at the end of the riser structure. The welding residual stress in the riser can be fitted by a trigonometric series. Five peaks with the characteristics of the periodic distribution of welding residual stress are illustrated in Fig. 5 to describe the welding residual stress distribution.

Fig. 5(a) depicts Distribution model I of the welding residual stress; a positive value denotes the tensile stress.

Fig. 5(b) exhibits Distribution model II of the welding residual stress, and a positive value denotes the tensile stress. The peak value of the welding residual stress in Fig. 5(b) is less than that in Fig. 5(a).

Fig. 5(c) presents Distribution model III of the welding residual stress. A negative value denotes the compressive stress, and a positive value denotes the tensile stress. The absolute value is similar to that in the Distribution model I compared with the values displayed in Figs. 5(a) and 5(b).

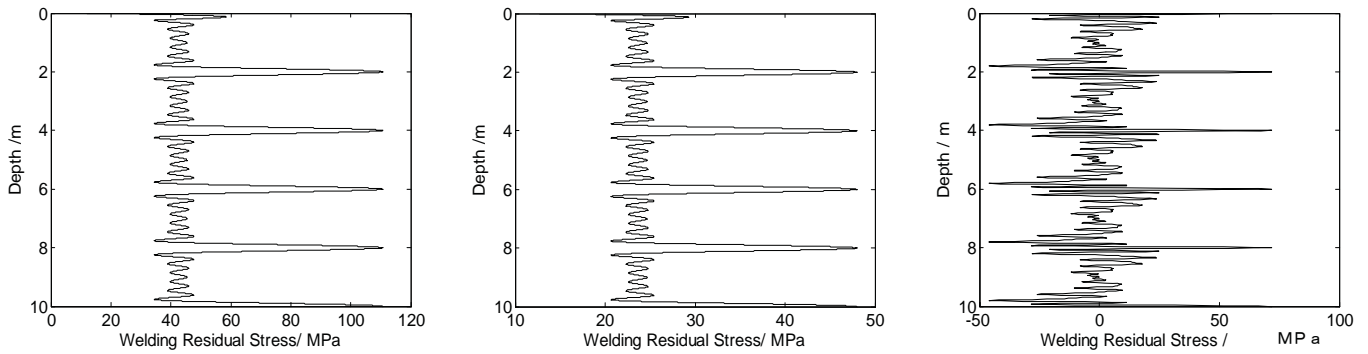


Fig. 5. Distribution model of the welding residual stress

### EFFECT OF WELDING RESIDUAL STRESS ON NATURAL VIBRATION FREQUENCY

Based on the function of the welding residual stress, the complex pre-stress in the riser can be written as  $\sigma_{r,z} = \frac{[T_0 - U_m z + K\mu \sin(\alpha)]}{A} + \sigma_R$ . The vibration characteristics of the riser can then be obtained.

#### (1) Constant axial loads

Constant axial loading is also considered, in which the sole weight is neglected. The complex pre-stress in the riser structure can be written as  $\sigma_{r,z} = T_0 / A$ . The mode shapes of the riser structure can be written as  $EI \frac{d\phi^4(z)}{dz^4} - T_0 \frac{d\phi^2(z)}{dz^2} - (m_r + m_f + m_a)\omega^2 \phi(z) = 0$ .

The mode function of the vertical tube under fixed axial force can be calculated by using the method of separation of variables.

#### (2) Varying axial loads

Vertical pipe weight and internal tension are considered. The complex pre-stress in the riser structure can be written as  $\sigma_{r,z} = (T_0 - W_a z) / A$ . The mode function of the vertical tube under fixed axial force can be calculated by using the method of the separation of variables, and the modes are not standard sine functions.

#### (3) Varying axial loading and welding residual stress

In this case, the welding residual stress, vertical pipe weight and internal tension are considered. The values of the welding residual stress are obtained from the measurement data of the riser structure or through a numerical simulation analysis. The cosine function is used to fit the welding residual stress parameter. The welding residual stress in the riser can be written as  $\sigma_{r,z} = \sum_{g=1}^{18} \sigma_{r,zg} \cos(g\beta z)$ , and the distribution

of welding residual stress is exhibited in Figs. 5(a), 5(b) and 5(c). The complex pre-stress in the riser can be written as

$$\sigma_{r,z} = \frac{T_0 - U_m z}{A} + \sum_{g=1}^{18} \sigma_{r,zg} \cos(g\beta z)$$

By substituting the complex pre-stress into Eq. (3), the differential formulation can be written as follows:

$$EI \frac{d\phi^4(z)}{dz^4} - [T_0 - U_m z + A \sum_{g=1}^{18} \sigma_{r,zg} \cos(g\beta z)] \frac{d\phi^2(z)}{dz^2} + W_a \frac{d\phi(z)}{dz} - (m_r + m_f + m_a)\omega^2 \phi(z) = 0$$

Table 2 summarizes the natural frequencies of the riser structure with variation from the first to the tenth order. Table 2 indicates that the complex pre-stress exerts a significant effect on the natural frequency of the riser. If the welding residual stress is positive, then the natural frequency of the riser will increase. If the welding residual stress is negative, the natural frequency of the riser will decrease. In addition, the influence of complex pre-stress on natural frequency becomes increasingly significant with the increase in order. These results show that the peak value of the welding residual stress distribution is in evident in natural frequency because the range of the riser in the peak area is relatively narrow. Table 2 indicates that analysing the influence of the welding residual stress is necessary for the riser design.

Tab.2. Comparison of the natural frequencies of the riser

Order	Constant axial force	Axial force and sole weight	Welding residual stress mode I	Welding residual stress mode II	Welding residual stress mode III
1	0.257	0.190	0.273	0.240	0.176
2	0.514	0.381	0.545	0.478	0.360
3	0.771	0.572	0.818	0.718	0.546
4	1.029	0.764	1.092	0.959	0.733
5	1.287	0.957	1.367	1.200	0.923
6	1.547	1.153	1.642	1.442	1.115
7	1.807	1.350	1.918	1.686	1.309
8	2.069	1.550	2.196	1.931	1.507
9	2.332	1.752	2.476	2.178	1.707
10	2.596	1.956	2.757	2.427	1.910

## MODES OF THE RISER STRUCTURE

The first-order to sixth-order modes of the riser structure are illustrated in Fig. 6. The modes are not standard sine functions.

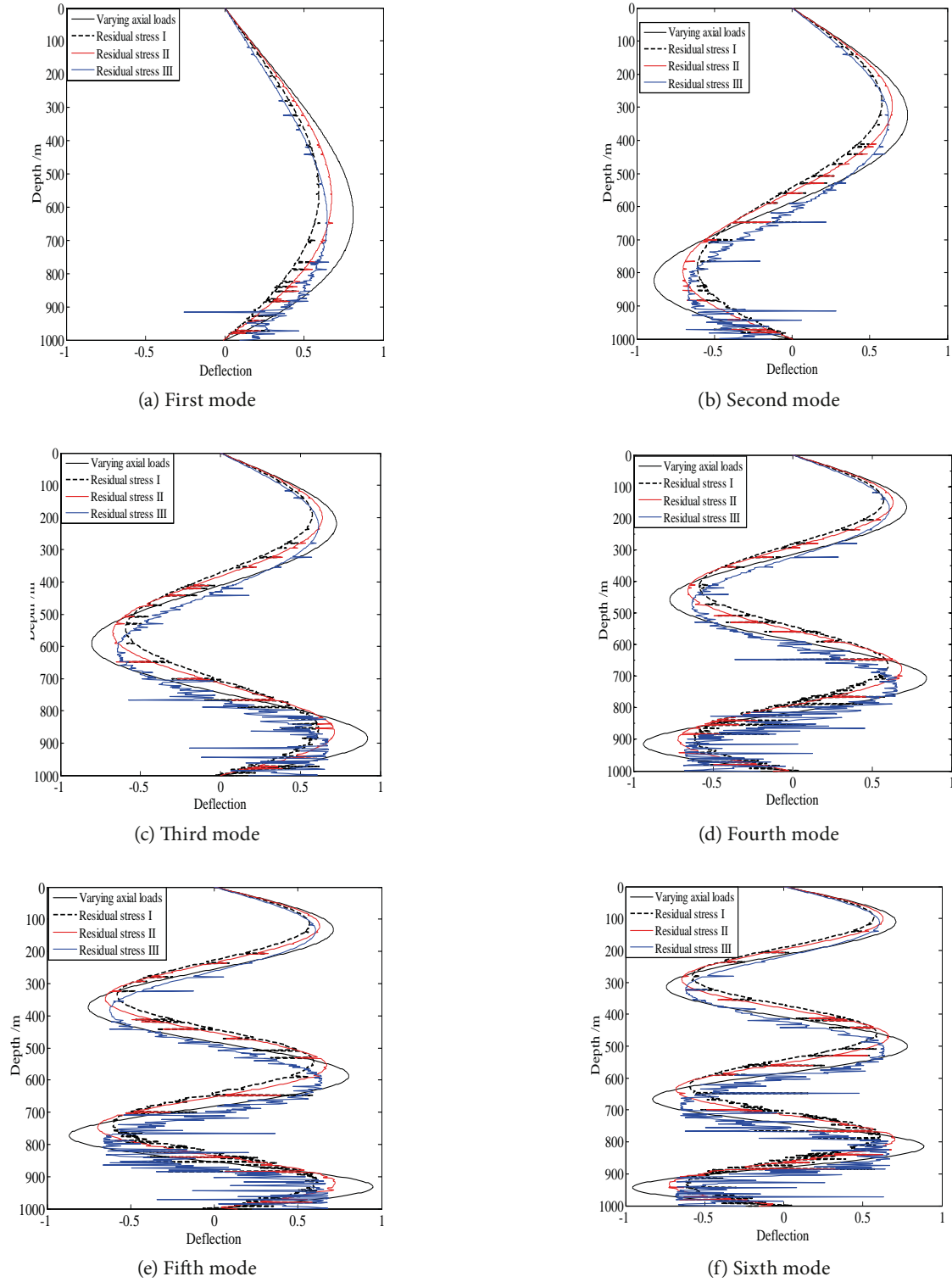


Fig.6 First six mode shapes in different loading cases

In Fig. 6, the maximum amplitude of the mode is moved to the bottom when the sole weight is considered. Welding residual stress significantly affects the mode shapes of the riser structure. The mode shapes become increasingly complex when the welding residual stress is considered. The influence of the welding residual stress on the riser structure vibration mode is evident. The mode shape of the riser becomes a rough curve with mutation when the welding residual stress exists. The mutation direction depends on the direction of the welding residual stress because the welding residual stress had changed the local stiffness of the riser.

## CONCLUSIONS

In this study, a new approach to analysing the dynamic characteristics of the riser structure is proposed to investigate the influence of the welding residual stress on the natural frequency and modal shape. A corresponding differential equation is established. The numerical results show that complex pre-stress force significantly influences parametric vibration. The distribution of complex pre-stress causes the resonance point of the riser to migrate, and the migration direction corresponds to the complex pre-stress direction. The mode shape is not a smooth curve, and the distortion direction depends on the amplitude of complex pre-stress. The approach that is proposed in this study can be applied to address the uniform or non-uniform distribution stress force problem, thereby extending the research area of the application for pre-stress problems.

## ACKNOWLEDGES

This work was partially supported by the Fund of State Key Laboratory of Ocean Engineering (Grant No: 1507). This support is gratefully acknowledged by the authors.

## REFERENCES

1. Ashwear, N., A. Eriksson: Natural frequencies describe the pre-stress in tensegrity structures, *Computers and Structures*. 138(2014):162-171.
2. Bigoni, D., Gei, M., Movchan, A.B: Dynamics of a prestressed stiff layer on an elastic half space: filtering and band gap characteristics of periodic structural models derived from long-wave asymptotics, *Journal of the Mechanics and Physics of Solids*. 56(2008):2494-2520.
3. Chatjigeorgiou, I.K., Mavrakos, S.A: Nonlinear resonances of parametrically excited risers-numerical and analytic investigation for  $\Omega=2\omega_1$ , *Computers and Structures*. 83(2005): 560-573.
4. Chatjigeorgiou, I.K: On the Parametric excitation of vertical elastic slender structures and the effect of damping in marine applications, *Applied Ocean Research*. 26(2004): 23-33.
5. Chen, L.Y., Li, L.X., Yang, N: Analysis of vortex-induced vibration of marine riser under the consideration of pre-stress force distribution, *Journal of Shanghai Jiaotong University*. 51(2017):476-484. (In Chinese)
6. Chen, Y.F., Chai, Y.H., Li, X., et al: An extraction of the natural frequencies and mode shapes of marine risers by the method of differential transformation, *Computers and Structures*. 87(2009):1384-1393.
7. Hamed, E., Frostig, Y: Natural frequencies of bonded and unbonded prestressed beams-prestress force effects, *Journal of Sound and Vibration*. 295(2006):28-39.
8. Li, J., Li, W., Shen, R., et al: Coupled bending and torsional vibration of nonsymmetrical axially loaded thin-walled Bernoulli-Euler beams, *Mechanics Research Communications*. 31(2004): 697-711.
9. Liu, Y., Chen, L.Y: The effect of weld residual stress on the free vibrational characteristics of cylindrical shell through the analytical method, *Journal of Vibroengineering*. 18(2016):334-348.
10. Park, H., Jung, D.H. A finite element method for dynamic analysis of long slender marine structures under combined parametric and forcing excitations, *Ocean Engineering*. 29(2002):1313-1325.
11. Patel, M.H., Park, H.I: Combined axial and lateral responses of tensioned buoyant platform tethers, *Engineering Structures*.17(1995):687-695.
12. Senjanovic, I., Ljustina, A.M., Parunov, J: Natural vibration analysis of tensioned risers by segmentation method, *Oil & Gas Science and Technology*. 61(2006):647-659.
13. Tang, Y.G., Shao, W.D., Zhang, J., et al: Dynamic Response Analysis for Coupled Parametric Vibration and Vortex-induced Vibration of Top-tensioned Riser in Deep-sea, *Engineering Mechanics*. 30(2014):282-286. (In Chinese).
14. Wu, H.Y., Zhou, S.J: Dynamic response of sensor diaphragm with residual stress in contact with liquids, *Journal of Sound and Vibration*. 333(2014):3702-3708.
15. Wu, J.S., Chen, C.T: Wave-Induced Vibrations of an Axial-Loaded Immersed Timoshenko beam carrying an Eccentric Tip Mass with Rotary Inertia, *Journal of Ship Research*. 54(2010):15-33.
16. Zhang, L.M., Chen, W.J., Dong, S.L: Natural vibration and wind-induced response analysis of the non-fully symmetric Geiger cable dome, *Journal of Vibroengineering*, 16(2014): 31-41.

## CONTACT WITH THE AUTHORS

**Chen Luyun**

*e-mail: [cluyun@sjtu.edu.cn](mailto:cluyun@sjtu.edu.cn)*  
State Key Laboratory of Ocean Engineering  
Shanghai Jiaotong University  
800 Dongchuan road  
200240 Shanghai  
**CHINA**

**Yi Hong**

*e-mail: [1841666106@qq.com](mailto:1841666106@qq.com)*  
State Key Laboratory of Ocean Engineering  
Shanghai Jiaotong University  
800 Dongchuan road  
200240 Shanghai  
**CHINA**

# THE ENERGY EFFICIENCY GAP IN TURKISH MARITIME TRANSPORTATION

Olgun Konur

Murat Bayraktar

Murat Pamik

Barış Kuleyin

Mustafa Nuran

Dokuz Eylul University, Izmir, TURKEY

## ABSTRACT

*The Turkish Merchant Shipping Industry has recently witnessed an increasing awareness of the importance to minimize environmental pollution and fuel oil consumption. Together with certain non-governmental organizations and media concerns about environmental protection, the International Maritime Organization (IMO) has been strict on controlling undesirable effects on the environment and, consequently, forcing shipping companies to minimize their emissions. Besides, today's highly advanced technology companies over the world have developed various innovative systems that can be utilized to minimize carbon emission, thus giving assurance to relevant investors that their investments are most likely to turn out well with a considerable financial gain in the short or long term. Despite all such favorable developments, in a general look, shipping companies seem reluctant in making use of technologies providing efficiency in energy consumption. This reluctance has eventually brought about the term "Energy Efficiency Gap". This research conducts a questionnaire, created by Acciaro et al. [1], among the shipping companies in Turkey. 20 respondent companies, who represent 26 percent of the Turkish owned merchant marine fleet of over 1000 gross tonnage in terms of deadweight cargo capacity, participated in the research. The Pearson correlation analysis was used, and interpretations were made according to the obtained statistical values. The aim of the research was to identify reasons and points restraining the use of new technologies regarding energy efficiency, as well as to develop proposals for the innovators in this field about how to overcome this handicap concerning technical and managerial aspects of gaining energy efficiency.*

**Keywords:** Energy efficiency gap; Maritime transportation; Energy efficiency technologies; Carbon emission

## INTRODUCTION

The onset of environmental problems in the world has prompted authorities to take preventive actions to reduce ship-borne exhaust emissions. As a result of both these actions, and growing economic concerns of the maritime industry, the energy efficiency improving applications have become of great importance in ships in recent years.

IMO has made a quick response to the environmental protection calls. They conducted various studies to reduce the ship-based emissions and started to regulate the ship transportation industry by implementing new rules. The Regulations for the Prevention of Air Pollution from Ships

were added to the Annex VI Convention with the 1997 protocol by amending the MARPOL 73/78 Convention. These regulations entered into force on May 19, 2005. The MARPOL Annex VI regulates the arrangements made to limit the ozone layer by depleting ship emissions of nitrogen oxides (NO<sub>x</sub>) and sulphur oxides (SO<sub>x</sub>) in exhaust gases [33]. In 2009, IMO published the Second IMO Greenhouse Gas Study which revealed that the ship-based CO<sub>2</sub> emissions were projected to increase significantly in the coming decades. Depending on future economic and energy developments, the analyzed scenarios projected an emission increase by 50% to 250% in the period to 2050 [6]. Further actions with additional regulations on efficiency and emissions could

mitigate the emissions growth. Therefore, applications of the Energy Efficiency Design Index (EEDI) and the Ship Energy Efficiency Management Plan (SEEMP) were accepted in July 2011. EEDI was made mandatory by the Marine Environment Protection Committee (MEPC) for new ships and SEEMP for all ships [19, 30].

There has to be a SEEMP plan specifically prepared for vessels [18]. In spite of these preventive actions, new projections still show an increase in some greenhouse gas emissions, considering the increasing demand for fossil fuels. As a result of Tier III and Tier IV engines entering the world fleet, the emissions of nitrogen oxides increase at a lower rate than CO<sub>2</sub> emissions. The emissions of particulate matters show an absolute decrease until 2020, and sulphurous oxides continue to decline through to 2050, mainly because of MARPOL Annex VI requirements imposed on the sulphur content of fuels [17].

The policymakers' initiation to reduce the global warming potential from ship-based emissions has become an inevitable cause of innovation acceleration in this field [32]. The international regulations in force give limited time to the maritime transportation industry to adopt the requirements [40]. Both the engine suppliers, and other parties related to the emission reduction technologies are still studying hard to innovate products satisfying the goals of the above-mentioned Annex VI amendments. All in all, the emergence of new and modified emission reduction technologies in recent few years, and also energy efficiency improving technologies, has been a great challenge for the maritime transport industry.

Reducing fuel costs via using eco-friendly applications is another point of view for the sustainability of these innovations. As the cost-effectiveness potential of the emission reduction technologies grows with time [11], the feasibility of the products affects the willingness of more shipping companies to use them in their fleet. However, in practice, the implementation of economically viable technologies to marine vessels is going slower than expected in the worldwide market because of some "barriers to energy efficiency", as defined in the literature [1]. The energy efficiency gap [23] is another term which defines barriers to energy efficiency. According to Klemick and Wolverton [26], the energy efficiency gap is defined as the difference between the amount of energy that is currently consumed and the amount that should be consumed, relative to some notion of the optimal level. In the shipping industry, innovative products that provide energy efficiency with cost efficiency are developing very fast in recent years. This situation creates an expanding energy efficiency gap on marine vessels because of some barriers to the implementation of energy efficient end-products [41].

## LITERATURE REVIEW

Considering the current and oncoming IMO legislations, the technologies reducing emission and improving energy efficiency in the field of marine transportation systems have been enhanced significantly. Bedford et al. [3] described

a direct water injection system that is operated by injecting water into the combustion chamber via a separate nozzle from the fuel to reduce NO<sub>x</sub> emissions by 50-60% under high loads and eliminate harmful effects of bad combustion [8, 45]. As explained in the study by Kristensen [26], the operating principle of the exhaust gas recirculation system (EGR) is to recirculate some of the engine exhaust gas back to the engine. The mixing of the exhaust gas with the intake air increases the specific heat of the intake mixture, which leads to a reduction in the ignition temperature and reduces the oxygen concentration in the combustion chamber. A significant reduction is observed in the number of nitrogen oxides produced due to the combustion temperature decrease. The EGR system allows approximately 20% reduction of NO<sub>x</sub> emissions. The Selective Catalytic Reduction (SCR) process chemically transforms the NO<sub>x</sub> molecule into molecular nitrogen and water vapor. A nitrogen-based reagent, such as ammonia or urea, is injected into the exhaust gas in the exhaust line. The hot flue gas and the reagent are passed through a catalyst. The reactant emitted by the catalyst selectively reacts with NO<sub>x</sub> at a certain temperature range and in the presence of the catalyst and oxygen.

The global fuel fleet consumes approximately 330 million tons of fuel annually. Approximately, 80-85% of these consumed fuels contain sulphur. At present, liquefied natural gas (LNG), liquid petroleum gas (LPG), electric energy, solar power, biodiesel, and methanol are at the top of alternative fuels used in the maritime industry [7]. In terms of environmental emissions, the use of LNG as fuel plays an important role as an emission reducer, with the ratios of CO<sub>2</sub> emissions up to 20%, sulphur oxides (SO<sub>x</sub>) up to 100%, Nitrogen oxides (NO<sub>x</sub>) up to 90%, and particulate matter (PM) up to 99% [20]. LNG will be an alternative fuel that meets stringent ECA requirements because it emits small quantities of NO<sub>x</sub> [47]. Considering the environment-friendly feature of LNG, propulsion of LNG fueled ships comes to an important point [5]. Also, the cost of liquefying natural gas is almost the same compared to IFO 380, according to the data taken at February 2019 [10, 46].

The solar energy technology transforms solar energy into electricity and thermal energy. Every square meter of the earth's surface draws about 1000 Watts of energy from the sun [13]. Solar energy provides a clean, environment-friendly, and non-consumable source of energy for humanity. The cost of energy acquired from the sun is also falling steadily due to the competition in this market [16]. Although there are significant advantages offered by solar energy, it is necessary to keep in mind some defects while utilizing this energy source [14]. Wind energy technologies convert the mechanical energy into electrical energy by taking advantage of the kinetic energy of the wind. The kinetic energy of the airflow drives the wind turbine blades and the drive shaft, thus providing mechanical energy to the wind turbine generator [21]. Furthermore, there are some other technologies that utilize wind forces to assist the propulsion of ships. One of them is wind kites that use kite power for ship propulsion. Another option is the wing sails that consist of different types of sails or wings. The Flettner

rotor technology, which uses the Magnus effect to provide the ship with harnessing wind energy, has been started to develop in recent years [29].

Hull cleaning is a method that leads to a significant reduction in daily fuel consumption, as well as to increasing the energy efficiency of vessels in a very cost-effective way [2].

Waste heat recovery systems have gained great significance for ship owners in the last decade, following their many land-based applications [28]. Thermoelectric generators seem suitable for small scale commercial applications. On the other hand, large-scale applications, such as ships, require Rankine-based systems which can potentially offer greater environmental gains and better energy efficiency than thermoelectric generators [25].

Most of the literature studies refer to the energy efficiency gap in the industrial sectors such as textile [44], household [38], paper [42], ceramics [31], and construction [15] industries. Financial matters related with investing into energy efficiency are also discussed in several studies [4, 9, 34, 36, 43].

There are limited studies in the literature which concern the energy efficiency gap issue for marine transportation systems. SEEMP and EEDI regulations seem to have an inspiring role for both academic and institutional studies. Jafarzadeh and Utne [22] propose a framework for overcoming barriers to the energy efficiency in the shipping industry. The framework is designed in 5 steps, and starts with identifying the barriers and categorizing them. The categorized barriers are analyzed and ranked by any suitable multi-criteria decision making (MCDM) methods in step 2. Possible measures for overcoming the identified barriers are assigned. Then, interactions between the barriers are identified in step 3 and 4. Step 5 is about documentation of the results, with a feedback loop due to possible reductions in the previous barriers.

Poulsen and Sornn-Friese [37] have studied the influence of the third-party ship management to energy efficiency. Lack of information on energy efficiency, lack of energy training, and lack of time to produce and provide reliable energy efficiency information are highlighted as barriers to ship operations with third-party ship management.

Barriers to improving the energy efficiency in short sea shipping are discussed by Johnson et al. [24] in their action research designed case study. The collaboration of two shipping companies for implementing an energy management system to their fleet is examined with active participation of researchers to the implementation process. Discussions and results are mainly focused on what best practices could be in an energy management plan when considering the SEEMP requirements. Another outcome derived from that case study was the understanding of barriers which may hinder the companies in achieving energy efficient operations.

Fridell et al. [12] describe several parameters to improve the energy efficiency in shipping by exemplifying the Latin American and Caribbean regions. Barriers to energy efficiency between different modes of transport in these regions are well defined. Uncertainties about the future fuel cost, high rate of technological risks, stakeholder influences, ship owner-charterer agreements, low second-hand values, and the lack

of capital stock within shipping companies have been seen as the major factors affecting the implementation of energy-efficient technologies. Also, the shore-side electricity (cold ironing) method has been seen as a good option to reduce the emissions in populated coastal areas.

Rehmatullaa et al. [39] conducted a survey with the participation of 200 shipping companies, mostly from Europe. The implementation of over 30 energy efficiency and CO<sub>2</sub> emission reduction technologies were surveyed. The study shows that the companies tend to implement technologies which offer energy efficiency gains. This tendency indicates an equal distribution among the design, hydrodynamic, and machinery measures by selecting only a number of different measures in each category. Small energy efficiency gains at the ship level, when accompanied with low initial costs and high payback rate, are the motivations for most of the implementation choices.

The study of Acciaro et al. [1] provides a good understanding of relevant barriers to the implementation of energy efficiency improving technologies among the Norwegian Ship-owners' Association members. A newly developed questionnaire, which was verified by DNV GL experts and the representatives of the Norwegian Shipowners' Association, was utilized to gain a better understanding of barriers to the implementation of new technologies among Norwegian shipping companies. 12 CO<sub>2</sub> abatement technologies were taken into account in the study. A set of barriers to the shipping industry related energy efficiency were defined as a result of interviews with DNV experts and shipping companies, and an intensive literature review. These barriers are categorized as: safety and reliability, technical uncertainty, behavioural barriers, market constraints, financial and economic constraints, and complexity. As a result of the study, operational measures appear to have lower barriers than hardware measures. Immature technologies also show higher barrier levels. An active role of the policy maker through financial incentives and revision of existing regulation is suggested to be effective in overcoming these barriers.

## METHODOLOGY

This study aims to assess the energy efficiency gap in Turkish maritime transportation by conducting the questionnaire created by Acciaro et al. [1] among 20 different shipping companies representing 26 percent of the Turkish merchant marine fleet of over 1000 gross tonnage in terms of deadweight cargo capacity. The responses have been received from the employees carrying on the duties of ship owner, general manager, technical manager, inspector, designated person ashore (DPA), human resources manager, master, and engineer in pioneer companies of the Turkish merchant marine fleet, as can be seen from the demographic structure of participants in Fig. 1.

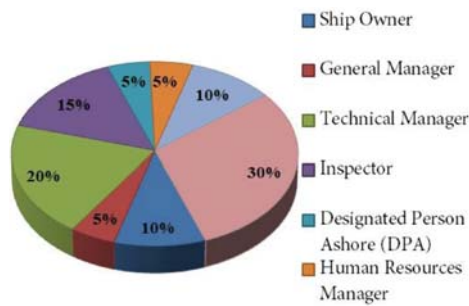


Fig. 1. Hierarchical distribution of survey participants

Among the most effective and widely used techniques, the Pearson's correlation analysis was applied to establish the framework for barriers to emission reducing and energy efficiency improving technologies. The correlation analysis is a statistical method used to test the relationship between two variables or the relationship of one variable with two or more variables. The purpose of the correlation analysis is to see how the dependent variable (y) changes when the independent variable (x) changes. In order to perform the analysis, both variables must be continuous and have normal distribution. The result of the correlation analysis shows whether there is a linear relationship between the variables or not (See Tab. 1). In the former case, the correlation coefficient is calculated from this relation [35].

Tab. 1. Intervals of correlation coefficient R [35]

R Values	Comments
0,00 - 0,25	Very Poor
0,26 - 0,49	Poor
0,50 - 0,69	Medium
0,70 - 0,89	High
0,90 - 1,00	Too High

The emission reducing and energy efficiency improving technologies are described in Tab. 2, together with their abbreviations used when discussing the results in Section 4.

Tab. 2. Emission reducing and energy efficiency improving technologies

Technology Description	Description	Abbreviation
Speed reduction	More efficient speed for operation	SR
Voyage performance	Route determination based on weather conditions and trim, draft control etc. systems to improve operation performance	VP
Friction reducing technologies	Ship resistance reduction	FRT
Propeller enhancing devices	Increasing efficiency by taking advantage of propeller characteristics	PE
Electrical connection from the shore	Connecting shore electricity to the ship in ports	EC
Reducing the need for auxiliary power	Reduction of needed power such as light, heat and electric motor	RN

Technology Description	Description	Abbreviation
Waste heat recovery	Systems that can recover part of exhaust gas heat energy	WH
Development of the main engine	Main engine control and efficiency improvement	DME
Solar energy	Utilizing solar energy for electricity generation	SE
LNG (Liquefied natural gas)	Using gas fuels instead of diesel-based fuels	LNG
Wind energy	Using wind power for electricity generation on the vessel	WP
Fuel cell	Energy production from natural gas or other hydrogen-containing gases	FC

Barriers to the implementation of new technologies for exhaust emissions have been addressed to the participants to determine the level of these barriers (see Tab. 3).

Tab. 3. Barriers to the implementation of new technologies

Level of knowledge	Safety issue for the crew and ship
Purchase and installation costs	Reliability issue for the crew and ship
Effectiveness in reducing exhaust emissions	Degree of compliance with current regulations
Ease of initial installation	Ease of implementation to ship considering the charter agreement
Ease of use	Suitability to the company
Level of their technical maturity	

The conditions affecting these issues have been expressed in eleven headings. The statements related to the implementation of new technologies aiming at reducing exhaust emissions are shown in Tab. 4. The barriers to the implementation of new technologies shown in Tab. 5 have been surveyed according to their significance levels to get the effective results about the research question.

Tab. 4. Statements related to the implementation of new technologies aiming at reducing exhaust emissions in the participant's shipping company

Installation costs are very expensive	IC
Operating costs are too high	OC
There are a lot of uncertainties with respect to their costs	UC
The initial installation is very difficult	IID
It is very difficult to use	DU
There are a lot of uncertainties with respect to their effectiveness	UE
Safety risk of the ship increases with their utilization	SR
The know-how about the new technologies is not reliable	TR
The company has not reached the capacity to afford new technologies	CC
Charter agreements restrain the use of these technologies	CH

Tab. 5. Barriers to new technologies that indicate significance levels

Complexity of operation	CO
Operating costs	OC
Technical maturity	TM
Current regulations	CR
Complexity of initial installation	CII

Integration difficulties in the system	IDS
Technical data	TD
Lack of information	LOI
Charter agreements	CA
Organizational maturity	OM
Safety	S
Lack of awareness	LOA
Installation cost	IC
Access to capital	AC
Lack of incentives	LI
Reliability	R

## RESULTS AND DISCUSSION

According to the data obtained from the questionnaires, the importance levels of barriers to the implementation of new technologies are illustrated in Fig. 2.

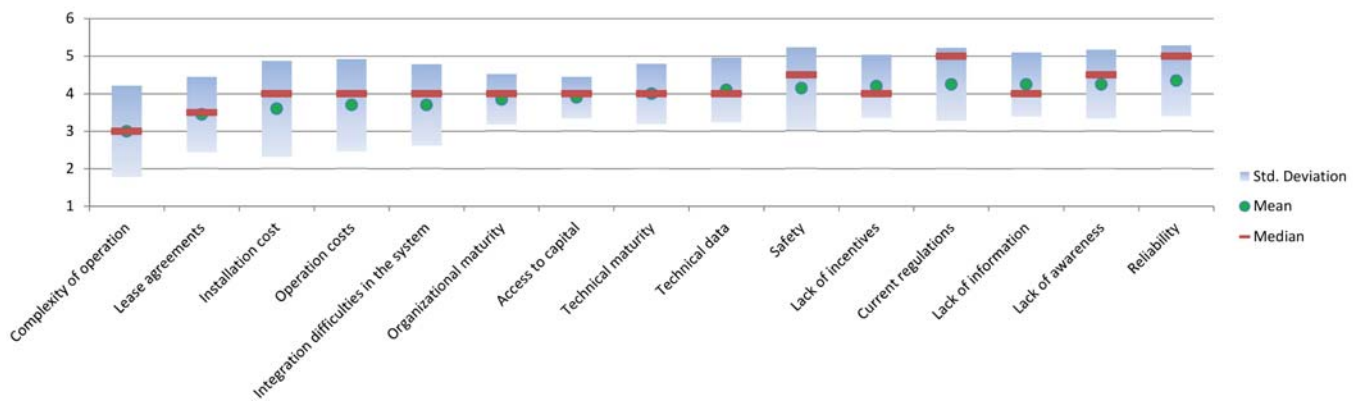


Fig. 2. Importance levels of emission reducing and energy efficiency improving technology barriers

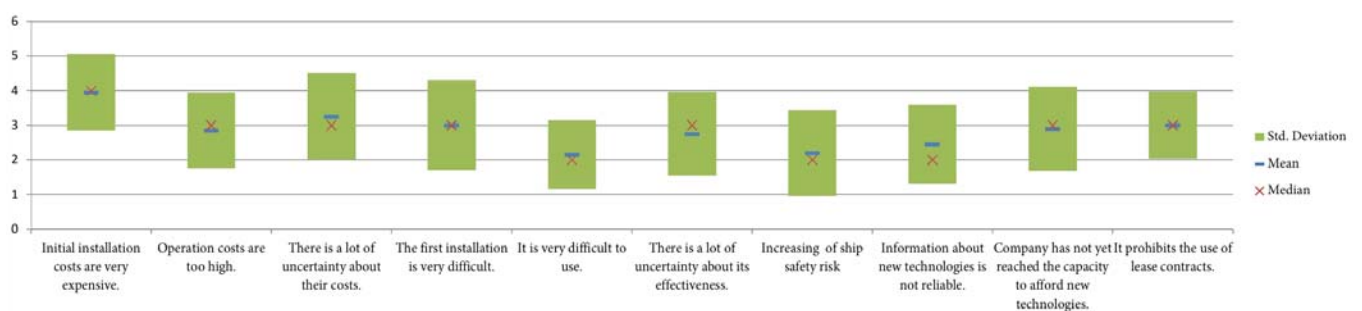


Fig. 3. Agreement levels to the statements related to new technologies aiming at reducing the exhaust emissions

Reliability, lack of awareness, lack of information, and current regulations are observed as the most critical points considering the willingness of the companies to implement these technologies. The remaining measures also show a close importance level. Only the complexity of operation and the initial installation stage have a lower significance level compared to other barriers. This situation can be interpreted

that the shipping companies are confident with their crew to operate these technologies with proper familiarization. The companies that provide the emission reducing devices also appear to be trusted by the shipping companies in the context of the ability to install the products with professional workmanship and in a time-effective manner.

The participants mostly agree on high cost of initial installation (See Fig. 3). The uncertainties with respect to the cost of new technologies are another strong factor to be considered seriously. On the other hand, these technologies are assessed to be easily operated systems according to multiple point of views.

The correlation analysis presents the strongest relationship between the operating cost (OC) and the installation cost (IC), as expressed in Table 6. Besides, the operating cost (OC) has significant relation with the complexity of operation (CO). No connection has been established between these and other barriers. These relations state that the shipping companies agree on that the technologies are both costly and complex systems to implement and operate.

Tab. 6. Pearson correlation coefficients of selected barriers to the implementation of new technologies

	OC	CO	IC
OC		0,68**	0,94**
CO	0,68**		0,75**
IC	0,94**	0,75**	

\*\* Correlation is significant at the 0.01 level (2-tailed).

The results shown in Tab. 7 illustrate that the technological advancement in the field of emission reduction and energy efficiency improvement has failed to provide a reliable source of know-how according to the shipping companies' point of view. The correlation factor of 0.822 between SR and TR in the same table shows that the safety and reliability issues are highly related with each other, and that the insufficient know-how has raised concern about the increased risk to ship's safety.

Tab. 7. Pearson correlation coefficients of agreement levels to the statements related to new technologies aiming at reducing exhaust emissions

	SR	TR	UC	DU
SR		0,822**	-	0,533*
TR	0,822**		-	-
UC	-	-		0,564**
DU	0,533*	-	0,564**	

\*\* Correlation is significant at the 0.01 level (2-tailed)  
 \* Correlation is significant at the 0.05 level (2-tailed)

Figure 4 compares the average barrier levels of the technologies to their suitability to the company and the familiarity of the companies to the technologies. Fuel cell (FC), wind power (WP), LNG, and solar power (SP) technologies possess the highest barrier levels, respectively.

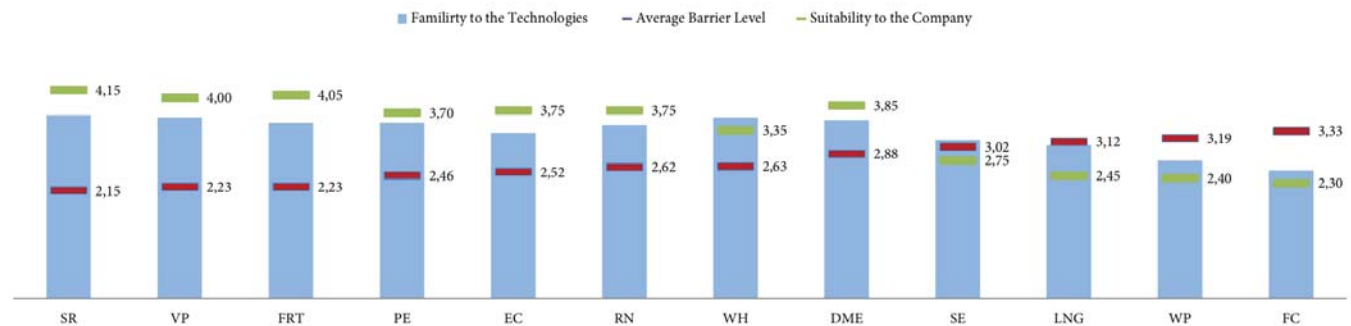


Fig. 4. Comparing average barrier levels of technologies to the suitability to the company and familiarity to the technologies

These technologies are also indicated as unsuitable to be applied. Speed reduction (SR), friction reducing technologies (FRT), and voyage performance (VP) have been found most appropriate applications for the companies due to the requirements of considerably lower cost and complexity than other innovations. In this context, the companies look reluctant to utilize costly and complex applications related to emission reduction and energy efficiency improvement, as well. The participating companies generally score just above the average in terms of technology familiarity, which reveals that more cooperation needs to be developed between the academicians, policy makers, technology developers, and end-users.

## CONCLUSION

The paper evaluates barriers to the implementation of new technologies which aim at reducing exhaust emissions and improving energy efficiency in the Turkish maritime transportation industry. This evaluation bases on the questionnaire created by Acciaro et al. [1], and its results are discussed.

Reliability is deduced as the most important barrier against the implementation of the emission reducing and energy efficiency improving technologies to the Turkish merchant marine fleet. The most significant relationship among the barriers is found between the operating cost and the installation cost, with the R value of 0.937.

As expected, the costs are generally the main topic, but also the uncertainties about operational measures and payback periods make it difficult to convince the shipping companies to utilize innovative products of the emission reduction technology. The shipping companies regard the operational measures as more suitable to the company, as these measures require lower initial and operational costs. The know-hows about these technologies are considered as insufficient and unreliable, which raises concern about the increased risk to ship's safety. Therefore, reliable information must be provided, and the risk status concerning the safety of operations must be eliminated to increase the application density of the technologies by the shipping companies.

The study of Acciaro et al. [1] aimed to find the barriers in the Norwegian shipping industry. As a result of the study, operational measures appeared to have lower barriers than hardware measures. The same pattern is observed among the Turkish shipping companies. Renewable energy and LNG technologies have the highest barrier scores for both countries. Maturity levels of the technologies and cost considerations have possessed a high barrier level. An active role of Norwegian policymakers through financial incentives has also been suggested. In comparison, the Turkish maritime transportation is basically in the need to revise the existing regulations to be effective, along with incentives, in overcoming these barriers. The reliability and safety issues are among the most important issues for both countries.

In this respect, it is suggested that the university-industry cooperation should be well-established in the emission reduction and energy efficiency improvement technology fields to accelerate the innovative products with reliable source

of information. In that way, the payback periods and the initial costs may be decreased as a solution to the main concern of end-users, and the energy efficiency gap would be narrowed in the Turkish maritime transportation industry.

## ACKNOWLEDGEMENTS

We want to express our sincere thanks to Acciaro, Hoffmann, and Eide for their support in providing us with the questionnaire they have developed. We also acknowledge the shipping companies who have participated in the survey and considered this research as an enlightening guide to the energy efficiency gap problem of Turkish maritime transportation.

## REFERENCES

1. Acciaro, M., Hoffmann, P.N., Eide, M.S., 2013. The energy efficiency gap in maritime transport. *Journal of Shipping and Ocean Engineering*. 3(2013), 1-10.
2. Adland, R., Cariou, P., Jia, H., Wolff, F.C., 2018. The energy efficiency effects of periodic ship hull cleaning. *J. Clean. Prod.* 178, 1–13. <https://doi.org/10.1016/j.jclepro.2017.12.247>.
3. Bedford, F., Rutland, C., Dittrich, P., Raab, A., Wirbeleit, F., 2000. Effects of direct water injection on DI diesel engine combustion. No. 2000-01-2938. SAE Technical Paper.
4. Bergmann, A., Rotzek, J.N., Wetzel, M., Guenther, E., 2017. Hang the low-hanging fruit even lower - evidence that energy efficiency matters for corporate financial performance. *Journal of Cleaner Production* 147(2017), 66-74. <http://dx.doi.org/10.1016/j.jclepro.2017.01.074>.
5. Boylston, J.W., 2011. LNG as a fuel for vessels some design notes. [http://leg.wa.gov/JTC/Documents/Studies/LNG/LNGFuelDesignNotes\\_060911.pdf](http://leg.wa.gov/JTC/Documents/Studies/LNG/LNGFuelDesignNotes_060911.pdf). (Accessed 20 October 2017)
6. Buhaug, O., Corbett, J.J., Eyring, V., Endresen, O., Faber, J., Hanayama, S., Lee, D.S., Lee, D., Lindstad, H., Markowska, A.Z., Mjelde, A., Nelissen, D., Nilsen, J., Palsson, C., Wanquing, W., Winebrake, J.J., Yoshida, K., 2009. Prevention of air pollution from ships - Second IMO GHG Study. MEPC 59/INF.10. International Maritime Organization, London, UK.
7. Chryssakis, C., Balland, O., Tvete, H.A., Brandsæter, A., 2014. Alternative fuels for shipping chain. Position paper: 17-2014. <https://transportemaritimoglobal.files.wordpress.com/2014/01/dnv-gl-alternative-fuel-2014-positionpaper.pdf>. (Accessed 09 November 2017)
8. Deal, A.L., 2013. Liquefied natural gas as a marine fuel. NEPI Working Paper. <http://www.glmri.org/downloads/LngMisc/NEPI%20LNG%20as%20a%20Marine%20Fuel%205-7-13.pdf>. (Accessed 18 October 2017)
9. DeCanio, S.J., Watkins, W.E., 1998. Investment in energy efficiency: do the characteristics of firms matter? *The review of economics and statistics*. 80(1), 95-107. <http://dx.doi.org/10.1162/003465398557366>.
10. DNV GL, 2019. Current price development oil and gas. <https://www.dnvgl.com/maritime/lng/current-price-development-oil-and-gas.html>. (Accessed 12 March 2019)
11. Eide, M.S., Longva, T., Hoffmann, P., Endresen Ø., Dalsøren, S.B., 2011. Future cost scenarios for reduction of ship CO2 emissions. *Maritime Policy & Management*, 38(1), 11-37. <https://doi.org/10.1080/03088839.2010.533711>.
12. Fridell, E., Winnes, H., Styhre, L., 2013. Measures to improve energy efficiency in shipping. *FAL Bulletin*, 324(8). <http://www.transportportal.se/energieffektivitet/measures%20to%20improve%20energy%20efficiency%20in%20shipping.pdf>. (Accessed 09 May 2017)
13. Genesis Energy, 2010. Solar energy. <http://www.electrocity.co.nz/images/factsheets/solar%20energy.pdf>. (Accessed 12 November 2017)
14. Gromicko, N., 2012. Disadvantages of Solar Energy. <https://www.nachi.org/disadvantages-solar-energy.htm>. (Accessed 12 November 2017)
15. Gupta, P., Anand, S., Gupta, H., 2017. Developing a roadmap to overcome barriers to energy efficiency in buildings using best worst method. *Sustainable Cities and Society*, 31(2017), 244–259. <http://dx.doi.org/10.1016/j.scs.2017.02.005>.
16. Hoeven, V.D.M., 2011. Solar energy perspectives. [https://www.iea.org/publications/freepublications/publication/solar\\_energy\\_perspectives2011.pdf](https://www.iea.org/publications/freepublications/publication/solar_energy_perspectives2011.pdf). (Accessed 12 November 2017)
17. IMO, 2014. Third IMO GHG study 2014: executive summary and final report. <http://www.imo.org/en/OurWork/Environment/PollutionPrevention/AirPollution/Documents/Third%20Greenhouse%20Gas%20Study/GHG3%20Executive%20Summary%20and%20Report.pdf>. (Accessed 15 October 2017)
18. IMO, 2017. MARPOL73-78: brief history - list of amendments to date and where to find them. <http://www.imo.org/en/KnowledgeCentre/ReferencesAndArchives/HistoryofMARPOL/Documents/MARPOL%2073-78%20Brief%20History%20-%20List%20of%20amendments%20and%20how%20to%20find%20them.htm>. (Accessed 04 January 2018)

19. IMO, 2019. Energy efficiency measures. <http://www.imo.org/en/OurWork/Environment/PollutionPrevention/AirPollution/Pages/Technical-and-Operational-Measures.aspx>. (Accessed 13 March 2019)
20. International Gas Union, 2015. World LNG report-2015 edition. [http://www.igu.org/sites/default/files/node-page-field\\_file/IGUWorld%20LNG%20Report-2015%20Edition.pdf](http://www.igu.org/sites/default/files/node-page-field_file/IGUWorld%20LNG%20Report-2015%20Edition.pdf). (Accessed 14 November 2017)
21. International Renewable Energy Agency, 2012. Wind power. [https://www.irena.org/DocumentDownloads/Publications/RE\\_Technologies\\_Cost\\_Analysis-WIND\\_POWER.pdf](https://www.irena.org/DocumentDownloads/Publications/RE_Technologies_Cost_Analysis-WIND_POWER.pdf). (Accessed 11 November 2017)
22. Jafarzadeh, S., Utne, I.B., 2014. A framework to bridge the energy efficiency gap in shipping. *Energy* 69(2014), 603-612. <https://doi.org/10.1016/j.energy.2014.03.056>.
23. Johnson, H., Andersson, K., 2011. The energy efficiency gap in shipping: barriers to improvement. Paper presented at International Association of Maritime Economists (IAME) 2011 Annual Conference, Santiago de Chile.
24. Johnson, H., Johansson, M., Andersson, K., 2014. Barriers to improving energy efficiency in short sea shipping: an action research case study. *Journal of Cleaner Production* 66(2014), 317-327. <https://doi.org/10.1016/j.jclepro.2013.10.046>.
25. Karvonen, M., Kapoor, R., Uusitalo, A., Ojanen, V., 2016. Technology competition in the internal combustion engine waste heat recovery: A patent landscape analysis. *J. Clean. Prod.* 112, 3735-3743. <https://doi.org/10.1016/j.jclepro.2015.06.031>.
26. Klemick, H., Wolverton, A., 2013. Energy-efficiency gap. In *Encyclopedia of Energy, Natural Resource, and Environmental Economics*, ed. Jason Shogren, 74-81.
27. Kristensen, H.O., 2012. Energy demand and exhaust gas emissions of marine engines. *Clean Shipping Currents*, 1(6), 18-26.
28. Larsen, U., Pierobon, L., Haglind, F., Gabriellii, C., 2013. Design and optimisation of organic Rankine cycles for waste heat recovery in marine applications using the principles of natural selection. *Energy* 55, 803-812. <https://doi.org/10.1016/j.energy.2013.03.021>.
29. Lele, A., Rao, K.V.S. 2016. Ship propulsion strategies by using wind energy. In 2016 International Conference on Emerging Technological Trends (ICETT) (pp. 1-6). IEEE. <https://doi.org/10.1109/ICETT.2016.7873693>
30. Marine Pollution Annex VI 2018 EEDI and SEEMP <https://www.marpol-annex-vi.com/eedi-seemp/>(Accessed 19 February 2019)
31. Manrique, R., Vásquez, D., Vallejo, G., Chejne F., Amell, A.A., Herrera, B., 2018. Analysis of barriers to the implementation of energy efficiency actions in the production of ceramics in Colombia. *Energy* 143(2018), 575-584. <https://doi.org/10.1016/j.energy.2017.11.023>.
32. Mickwitz, P., Hyvättinen, H., Kivimaa, P., 2008. The role of policy instruments in the innovation and diffusion of environmentally friendlier technologies: popular claims versus case study experiences. *Journal of Cleaner Production* 16S1 (2008), 162-170. <https://doi.org/10.1016/j.jclepro.2007.10.012>.
33. Ministry of Transport, Maritime Affairs and Communications (Ulaştırma, Denizcilik ve Haberleşme Bakanlığı), 2017. 1978 Protokolü ile Değişik, 1973 Tarihli Denizlerin Gemiler Tarafından Kirletilmesinin Önlenmesine Ait Uluslararası Sözleşme (MARPOL 73/78). <http://imo.udhb.gov.tr/TR/19Marpol.aspx>. (Accessed 05 November 2017).
34. Nehler, T., Rasmussen, J., 2016. How do firms consider non-energy benefits? empirical findings on energy-efficiency investments in Swedish industry. *Journal of Cleaner Production* 113(2016), 472-482. <https://doi.org/10.1016/j.jclepro.2015.11.070>.
35. Pearson, K., 1895. Notes on regression and inheritance in the case of two parents. *Proceedings of the Royal Society of London*. 58, 240-242.
36. Polzin, F., 2017. Mobilizing private finance for low-carbon innovation – a systematic review of barriers and solutions. *Renewable and Sustainable Energy Reviews* 77(2017), 525-535. <http://dx.doi.org/10.1016/j.rser.2017.04.007>
37. Poulsen, R.T., Sornn-Friese, H., 2015. Achieving energy efficient ship operations under third party management: How do ship management models influence energy efficiency? *Research in Transportation Business & Management* 17(2015), 41-52. <https://doi.org/10.1016/j.rtbm.2015.10.001>
38. Reddy, B.S., 2003. Overcoming the energy efficiency gap in India's household sector. *Energy Policy* 31(2003), 1117-1127. [https://doi.org/10.1016/S0301-4215\(02\)00220-3](https://doi.org/10.1016/S0301-4215(02)00220-3).
39. Rehmatullaa, N., Calleyab, J., Smith, T., 2017. The implementation of technical energy efficiency and CO2 emission reduction measures in shipping. *Ocean Engineering* 139(2017) 184-197. <http://dx.doi.org/10.1016/j.oceaneng.2017.04.029>.

40. Ruan, Y., Hang, C.C., Wang, Y.M., 2014. Government's role in disruptive innovation and industry emergence: the case of the electric bike in China. *Technovation* 34(2014), 785–796. <https://doi.org/10.1016/j.technovation.2014.09.003>.
41. Styhre, L., Winnes, H., 2013. Energy efficient shipping – between research and implementation. Paper presented at IAME2013 Conference, Marseille, France.
42. Thollander, P., Ottosson, M., 2008. An energy efficient Swedish pulp and paper industry- exploring barriers to and driving forces for cost-effective energy efficiency investments. *Energy Efficiency* 1(1), 21-34. <https://doi.org/10.1007/s12053-007-9001-7>.
43. Thomson, P.B., 1997. Evaluating energy efficiency investments: accounting for risk in the discounting process. *Energy Policy*, 25(12), 989-996. [https://doi.org/10.1016/S0301-4215\(97\)00125-0](https://doi.org/10.1016/S0301-4215(97)00125-0).
44. Trianni, A., Cagno, E., 2012. Dealing with barriers to energy efficiency and SMEs: Some empirical evidences. *Energy* 37(2012), 494-504. <http://dx.doi.org/10.1016/j.energy.2011.11.005>.
45. Wärtsilä Encyclopedia of Marine Technology, 2017. Direct Water Injection (DWI). [https://www.wartsila.com/encyclopedia/term/direct-water-injection-\(dwi\)](https://www.wartsila.com/encyclopedia/term/direct-water-injection-(dwi)). (Accessed 19 December 2017)
46. Ycharts, 2019. Henry hub natural gas spot price chart. [https://ycharts.com/indicators/natural\\_gas\\_spot\\_price](https://ycharts.com/indicators/natural_gas_spot_price). (Accessed 12 March 2019)
47. Yoon, B., Shin, J., Lee, S., 2018. Technology assessment model for sustainable development of LNG terminals. *J. Clean. Prod.* 172, 927–937. <https://doi.org/10.1016/j.jclepro.2017.10.187>.

## CONTACT WITH THE AUTHORS

**Olgun Konur**

*e-mail: olgun.konur@deu.edu.tr*

**Murat Bayraktar**

*e-mail: murat.bayraktar@deu.edu.tr*

**Murat Pamik**

*e-mail: murat.pamik@deu.edu.tr*

**Barış Kuleyin**

*e-mail: baris.kuleyin@deu.edu.tr*

**Mustafa Nuran**

*e-mail: mustafa.nuran@deu.edu.tr*

Dokuz Eylül University  
Dokuz Eylül Üniversitesi Denizcilik Fakültesi Tınaztepe  
Yerleşkesi 35160 Buca İZMİR  
35160 İzmir  
**TURKEY**

# POWER PERFORMANCE OF THE COMBINED MONOPILE WIND TURBINE AND FLOATING BUOY WITH HEAVE-TYPE WAVE ENERGY CONVERTER

Esmail Homayoun

Hassan Ghassemi

Hamidreza Ghafari

Amirkabir University of Technology, Tehran, Iran

## ABSTRACT

*This study deals with a new concept of near-shore combined renewable energy system which integrates a monopile wind turbine and a floating buoy with heave-type wave energy converter (WEC). Wave energy is absorbed by power-take-off (PTO) systems. Four different shapes of buoy model are selected for this study. Power performance in regular waves is calculated by using boundary element method in ANSYS-AQWA software in both time and frequency domains. This software is based on three-dimensional radiation/diffraction theory and Morison's equation using mixture of panels and Morison elements for determining hydrodynamic loads. For validation of the approach the numerical results of the main dynamic responses of WEC in regular wave are compared with the available experimental data. The effects of the heaving buoy geometry on the main dynamic responses such as added mass, damping coefficient, heave motion, PTO damping force and mean power of various model shapes of WEC in regular waves with different periods, are compared and discussed. Comparison of the results showed that using WECs with a curvature inward in the bottom would absorb more energy from sea waves.*

**Keywords:** combined renewable energy, monopile wind turbine, heaving buoy, power take off

## INTRODUCTION

Ocean energy resources have a great potential of providing renewable energy in the form of wind, waves and tidal currents. Over the last decade, among ocean renewable energy resources, offshore wind energy utilisation has been rapidly developed mainly in the form of the monopile fixed-bottom platform wind turbines (WT) in near shore wind farms. Other fixed-bottom platforms used in near shore wind farms are tripod and jacket ones[1].

Compared to wind, wave energy represents an energy resource with a higher power density. The wave renewable energy can be absorbed by using various wave energy converters (WEC) such as oscillating water column,

oscillating body and overtopping [2]. Although various types of WEC systems have been proposed, this technology is actively developing and it is not mature enough for large-scale commercial application.

In a site where wind and waves coexist, it might be beneficial to combine a WT and a WEC system by sharing support structure and power substations. It would be beneficial for utilizing the ocean space more efficiently and reducing the cost of manufacturing, installation and maintenance.

So far, many studies on the combined concept of WT and WECs have been conducted and reported by several researchers. Most of the studies on such combined systems have been done for different floating support platforms and type of WECs.

Based on the semi-submersible floating platform, three combined WT and WEC systems have been proposed. Alves [3] studied the combined concept of WT and an oscillating water column WEC with a V-shape semi-submersible floating support structure. They showed that the economic cost could be reduced by sharing the mooring and power infrastructure. Other combined concepts were proposed based on the semi-submersible floating support structure of WT, which consists of three rotating-flap types WECs [4, 5], and a point-absorber WEC [6].

Bachynski and Moan [7] introduced a combined concept of WT and three point absorber WECs based on tension-leg-platform (TLP) floating support structure. In their work, the effects of point absorber WEC on TLP were studied in operational conditions.

Most of the studies on the combined concept based on floating support platform have been done for the spar-type platform. The spar - torus combination (STC) is consisted of the 5 MW WT of National Renewable Energy Laboratory (NREL) and a torus- point-absorber WEC, introduced and developed by Muliawan et al. [8, 9, 10]. Further numerical and experimental studies of the STC system in survival mode were conducted by Wan et al. [11, 12, 13, 14]. In their model tests they examined several phenomena such as Mathieu instability, wave slamming and vortex- induced motions.

There is limited number of research works about the conceptual design of the combined systems based on the fixed-bottom platforms in the shallow water zones. For the first time, a new concept of a combined fixed-bottom monopile WT and a heave WEC was proposed by Ren et al. [15]. This system is named 'MWWC' (Monopile-WT-WEC-Combination). Ren and Ma [16] compared numerical and experimental results of the MWWC system in both regular and irregular waves. In MWWC concept, the floating buoy can move along the monopile tower to absorb wave energy through a power take-off (PTO) system. A schematic picture of the MWWC system is shown in Fig. 1.



Fig. 1. A schematic picture of the MWWC system

In this paper, four different model shapes of WEC heaving buoys of the MWWC system are selected. At first, the function of the MWWC concept system is described and various

model shapes of WEC are discussed. Then, the numerical results for one model of the WEC system are validated by the experimental data. Finally, the results of the main dynamic responses such as added mass, damping coefficient, heave motion, PTO damping force and mean power for various model shapes of WEC in regular wave with different periods are compared and discussed by using the ANSYS-AQWA software.

## GEOMETRIC AND FUNCTIONAL DESCRIPTION OF THE MWWC SYSTEM

The MWWC concept considered in this study is inspired by the STC system developed by the Norwegian University of Science and Technology (Norges Teknisk Naturvitenskapelige Universitet = NTNU) [8, 9]. The monopile is a type of platform which is used for most of the offshore wind turbines in the shallow water zones [1]. Hence the spar floating platform in the STC system is replaced with the bottom- fixed monopile platform.

In this concept, the wind turbine is a 5 MW NREL reference turbine [17] (Notice that in the present study, the 5 MW NREL wind turbine is parked ) and the WEC system is inspired by the 'Wavebob' solution developed in Ireland [18]. The Float which is the main component of the Wavebob is replaced by the monopile platform. Therefore, the floating buoy of the Wavebob is connected directly to the platform and it can be moved along the monopile tower.

The water depth for the operation of MWWC system is 15 m. The overall view of this system and the sketch of WEC are shown in Fig. 2, and the main characteristics of the system are listed in Tab. 1.

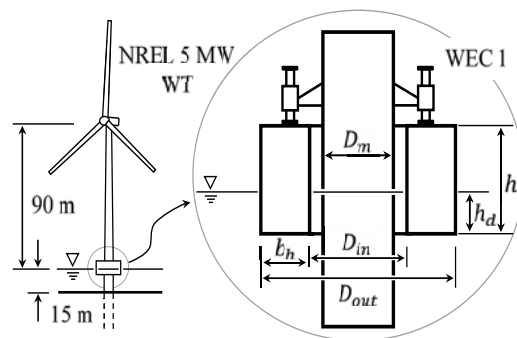


Fig. 2. The overall view of the MWWC system and the sketch of WEC system

Tab. 1. The main characteristics of the MWWC system

Parameters	Symbol	WEC1	Unit
Monopile diameter	$D_m$	6.0	m
Inner diameter	$D_{in}$	8.0	m
Outer diameter	$D_{out}$	16.0	m
Height	$h$	8.0	m
Draft	$h_d$	3.0	m
Bottom breadth	$b_h$	4.0	m

Parameters	Symbol	WEC1	Unit
PTO damping coefficient	$B_{pto}$	2.0e6	Ns/m
Centre of mass	C.G	(0,0,-1)	m

The wave energy is absorbed by the heave motions through a PTO system. In the STC system, the PTO system has been simplified by the linear PTO stiffness ( $K_{pto}$ ) and linear PTO damper ( $B_{pto}$ ) [10]. In MWWC system, just two linear PTO dampers ( $B_{pto} = 2e6 \text{ Ns/m}$ ) are used. A sketch of the PTO system is shown in Fig. 3.

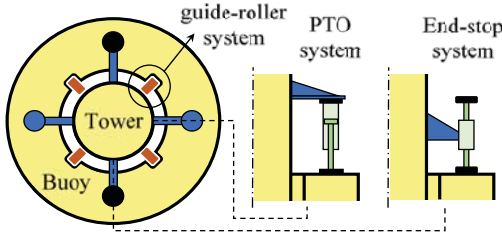


Fig. 3. A sketch of the linear guide-roller system and the end-stop system

Four linear guide-roller systems have been incorporated between the heave WEC system and the monopile. Therefore, the WEC system can move vertically along the monopile tower and its horizontal motions are limited. In addition, two end-stop systems have been used to limit the excessive heave motion in harsh environmental conditions. A sketch of the linear guide-roller system and end-stop system is shown in Fig. 3.

Three other shapes of WEC system, WEC2, WEC3 and WEC4, have been selected to be compared with the WEC as WEC1, which were studied by Ren et al. [15] at first. The sketch of the three WEC systems is shown in Fig. 4. The similarities between all the models of WECs and the model of WEC1 consist in the same displacement, inner diameter, height, draft and location of centre of mass. On the other hand, the main differences are in their outer diameter and shape of their bottoms; values of the parameters are listed in Tab. 2.

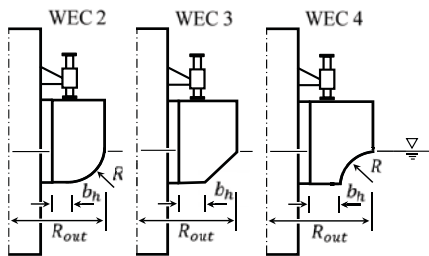


Fig. 4. The sketch of three different types of the WEC system

Tab. 2. The main characteristics of other types of WEC system (unit: meter)

Parameters	Symbol	WEC2	WEC3	WEC4
Outer radius	$R_{out}$	9.908	9.453	9.009
Curvature radius	$R$	5.0	-	5.0
Bottom breadth	$b_h$	2.908	2.453	2.009

## NUMERICAL MODELLING

Dynamic responses and power performance of the MWWC system have been investigated in both time and frequency domains based on the boundary element method in ANSYS-AQWA software in which the hydrodynamic loads acted on the structures are calculated by means of the three-dimensional radiation/diffraction theory and Morison's equation.

In this simulation, two rigid bodies have been modelled as a fixed monopile platform wind turbine and a heaving buoy. The bodies are connected together by the guide-roller system at their interfaces, therefore the WEC system can be moved vertically by waves along the monopile tower.

The wave elevation in a regular linear Airy wave is expressed as follows:

$$\zeta(x, t) = \frac{H}{2} \cos(kx + \omega t) \quad (1)$$

where  $H$  is the wave height;  $k$  is the wave number;  $\omega$  is the wave frequency;  $t$  is the time. The wave number and wave frequency are expressed by wave length ( $\lambda$ ) and wave period ( $T$ ):

$$k = 2\pi/\lambda, \quad \omega = 2\pi/T \quad (2)$$

The motion in heave direction of the WEC system is described by the equation (3):

$$\begin{aligned} [M + A_z] \ddot{z}(t) + [B_z + B_{PTO}] \dot{z}(t) \\ + [C_z + K_{PTO}] z(t) = F_0 \cos(\omega t) \end{aligned} \quad (3)$$

in which  $M$  and  $A_z$  are the buoy mass and the added mass in heave direction;  $\ddot{z}(t)$ ,  $\dot{z}(t)$  and  $z(t)$  are the acceleration, velocity and displacement;  $B_z$  and  $C_z$  represent the hydrodynamic damping coefficient and the restoring stiffness of the buoy;  $B_{PTO}$  and  $K_{PTO}$  are the linear PTO damping and stiffness coefficients, respectively;  $F_0$  is the amplitude of external excitation force in heave direction. The solution of the equation(3) for the steady condition is:

$$z(t) = z_a \cos(\omega t - \varepsilon) \quad (4)$$

where  $z_a$  is the amplitude of the WEC heaving motion, and  $\varepsilon$  is the phase angle of the WEC motion in relation to the exciting force. The amplitude of the WEC motion is given by:

$$z_a = \frac{F_0 / (C_z + K_{PTO})}{\sqrt{(1 - \Lambda^2)^2 + (2\xi\Lambda)^2}} \quad (5)$$

in which  $\Lambda$  is the tuning factor, and  $\xi$  is the non-dimensional damping factor. They can be expressed as follows:

$$\Lambda = \omega / \omega_z \quad (6)$$

$$\xi = \frac{B_z + B_{PTO}}{2\sqrt{(M + A_z) \times (C_z + K_{PTO})}} \quad (7)$$

where  $\omega_z$  is the natural frequency of heave motion and it can be calculated as follows:

$$\omega_z = \sqrt{(C_z + K_{PTO}) / (M + A_z)} \quad (8)$$

The damping force of the PTO system can be expressed as follows:

$$F_{PTO} = B_{PTO} \dot{z} \quad (9)$$

and the WEC instantaneous power can be calculated by using the PTO damping force in the equation (9) as follows:

$$P_{WEC} = F_{PTO} \dot{z} = B_{PTO} \dot{z}^2 \quad (10)$$

## MESH STUDY

The ANSYS-AQWA software employs Hess-Smith constant panel method, hence the structure wetted surface is divided into triangular or quadrilateral panels. Hydrodynamic panel models which include WEC and a part of the substructure are shown in Fig. 5.

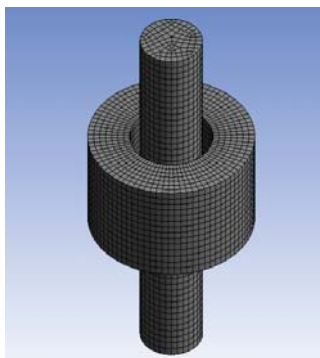


Fig. 5. MWWC panel models in ANSYS-AQWA software

In order to obtain the appropriate size of the elements to get accurate results from numerical simulation, the number of elements changed several times for both the WEC heave motion and the mean WEC power in typical regular wave case. The examined number of WEC elements in this study is illustrated in Figs. 6 and 7.

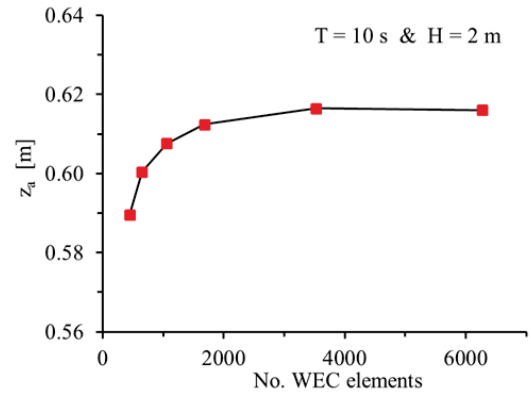


Fig. 6. Mesh study for heave motion of WEC in typical regular wave case

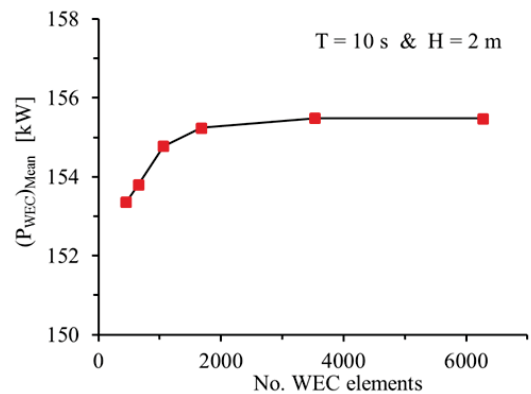


Fig. 7. Mesh study for mean WEC power in typical regular wave case

In Fig. 6 and Fig. 7 it can be seen that initially, with increasing the number of elements, changes in WEC heave motion and mean WEC power are significant. It is also clear that after applying more than 3528 elements for WEC, the changes in the parameters in question are reaching smaller and smaller values. Hence, numerical simulation of this model in ANSYS-AQWA software with using this number of elements will be of good accuracy.

## VALIDATION

In order to verify the simulation results from ANSYS-AQWA software, the numerical results of the main dynamic responses of WEC1 have been compared with the experimental results obtained from the model test in State Key Laboratory of Coastal and Offshore Engineering. The amplitude of WEC heave motion, the PTO damping force and the Mean power obtained from the comparisons for different regular wave periods and wave height, are shown in Figs. 8, 9 and 10.

## RESULTS AND DISCUSSIONS

To get the general performance of the different model shapes of WEC system, numerical results for regular wave conditions are compared and discussed. The simulations have been done for different wave periods and 2 m wave height. Added mass and damping coefficient of different shapes of WEC system are shown in Fig. 11 and Fig. 12.

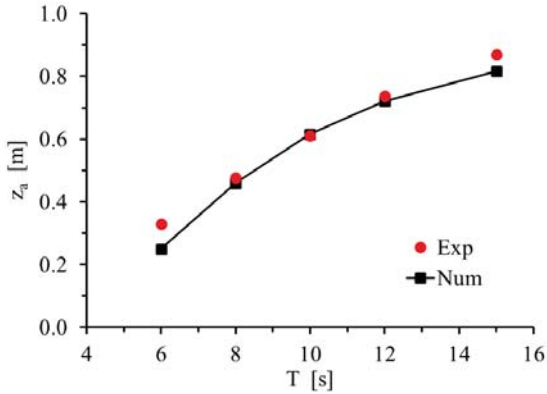


Fig. 8. Comparison of the WEC heave motion between experimental data and numerical results for typical regular waves ( $H = 2m$ )

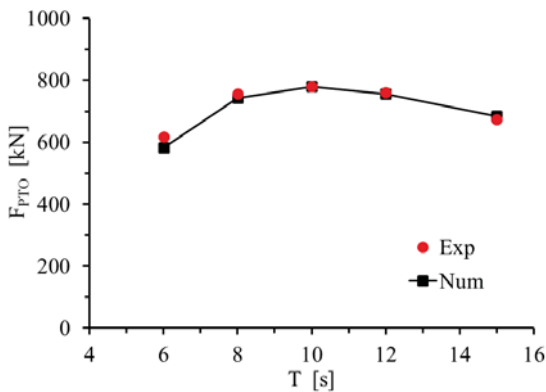


Fig. 9. Comparison of the PTO damping force between experimental data and numerical results for typical regular waves ( $H = 2m$ )

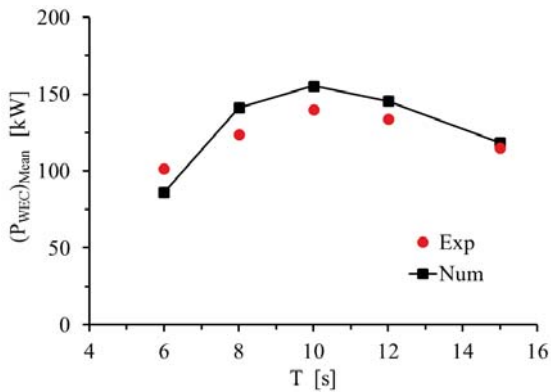


Fig. 10. Comparison of the mean WEC power between experimental data and numerical results for typical regular waves ( $H = 2m$ )

It is observable that the numerical result of WEC1 for the regular wave and the test data reported by Ren et al. [16] are in a good agreement. The main reason for the difference between numerical and experimental results is the viscous effect in the scale test model.

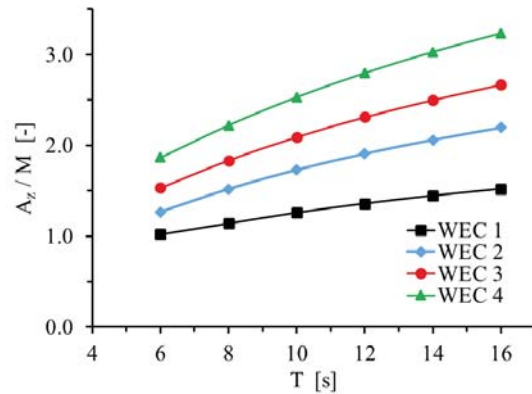


Fig. 11. Comparison of the buoy added mass for different shapes of WEC ( $H = 2m$ )

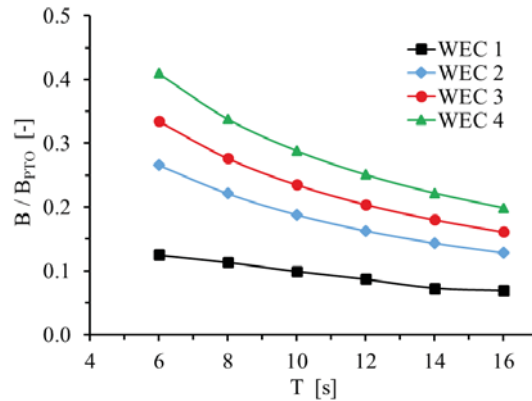


Fig. 12. Comparison of the buoy damping coefficient for different shapes of WEC ( $H = 2m$ )

In Fig. 11 it can be seen that the added mass of WECs gradually increases as wave period increases, while in Fig. 12 the damping coefficient gradually decreases for all the different shapes of WEC system. Also, it is clear that the model WEC4 has greater added mass and damping coefficient in comparison with the other model shapes of WEC system in the same conditions. In addition, the amplitude of WEC heave motion for its various shapes is illustrated in Fig. 13.

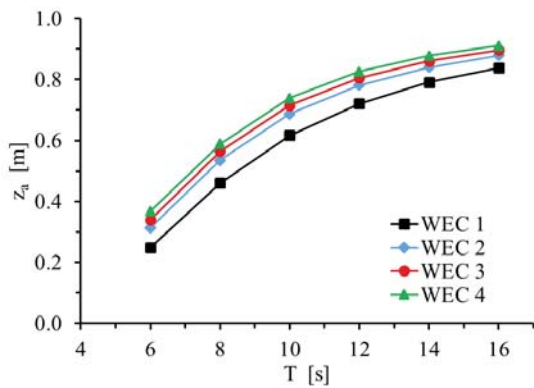


Fig. 13. Comparison of the heave motion for different shapes of WEC ( $H = 2m$ )

As shown in Fig. 13, the amplitude of WEC heave motion increases as wave period increases. In case of the larger wave periods, the amplitude of WEC heave motion gets closer to the amplitude of the regular wave. Also, it is clear that the model WEC4 has greater heave motion amplitude in comparison with the other model shapes of WEC system in the same conditions.

By using the equations (9) and (10), the PTO damping force and the mean power for various shapes of WEC system are calculated ; their amplitudes based on wave period are illustrated in Fig. 14 and Fig. 15.

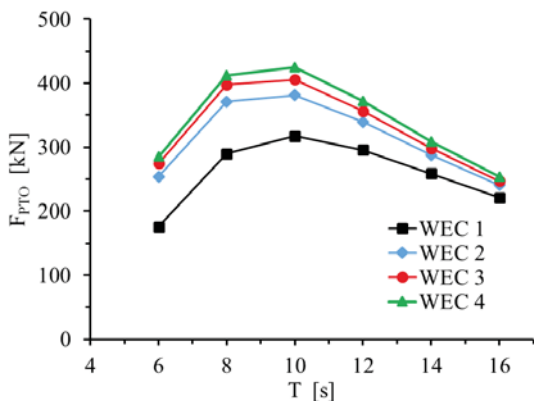


Fig. 14. Comparison of the PTO damping force for different shapes of WEC ( $H = 2m$ )

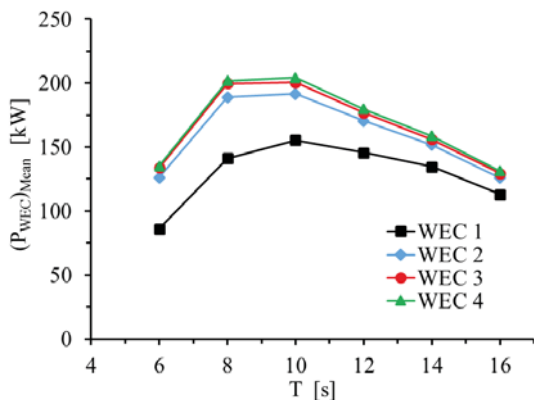


Fig. 15. Comparison of the mean WEC power for different shapes of WEC ( $H = 2m$ )

It can be seen that ,when the wave period increases, the PTO damping force and the mean WEC power first increase to the maximum value and then gradually decrease. This trend is similar in almost all model shapes of WEC. It is estimated that the maximum power generated by the WEC system is at about  $T = 10 s$  for all model shapes of WEC. Also, the model WEC4 has the best power performance in comparison with the other model shapes of WEC system in the same conditions.

The time history results obtained from ANSYS-AQWA for the typical regular wave case ( $T = 10 s$  and  $H = 2 m$ ) are presented in Figs. 16, 17 and 18. In the figures, the heave motion, damping PTO force and mean WEC power have been compared for different models of the WEC, whose amplitude have previously been displayed for different wave periods ( $T = 6 - 16 s$ ). It is obvious that the model WEC4 has a better performance than other model shapes of WEC system in the same conditions.

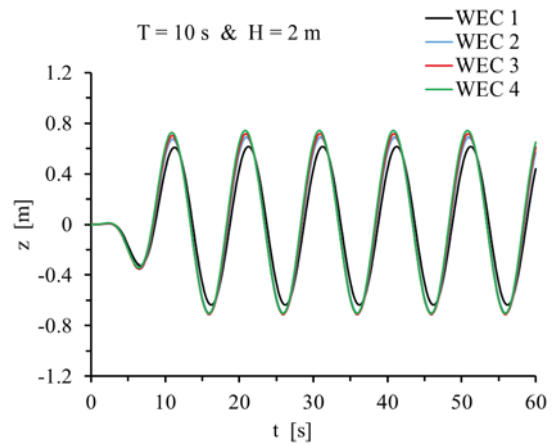


Fig. 16. Comparison of time histories of the WEC heave motion

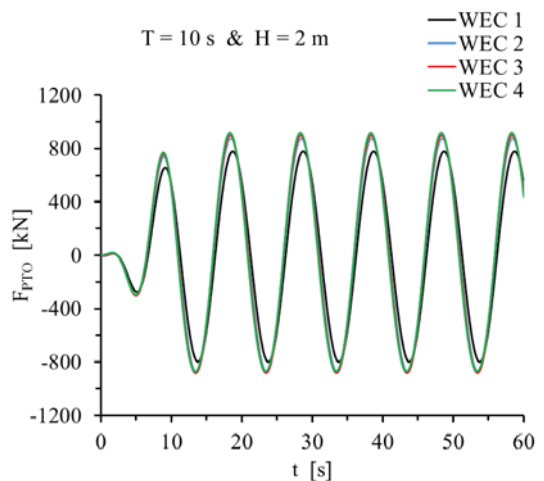


Fig. 17. Comparison of time histories of the PTO damping force

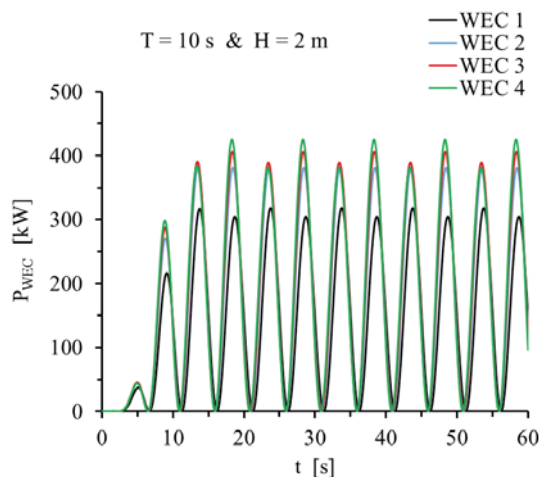


Fig. 18. Comparison of time histories of the WEC power

## CONCLUSIONS

In order to observe the dynamic responses of the different shapes of WEC heaving buoy in regular wave conditions, numerical simulations have been performed by using ANSYS-AQWA software. The following conclusions can be derived from the study of numerical simulation results:

- The added mass of WECs and the amplitude of WECs heave motion increase as the wave period increases.
- The damping coefficient of WECs decreases as the wave period increases.
- The PTO damping force and the mean WEC power first increase to the maximum value and then gradually decrease as the wave period increases.
- The model shape of WEC4 has the best power performance in comparison with the other model shapes of WEC in the same conditions.

The comparison of the results of the numerical simulation showed that using WECs with a curvature inward in the bottom would absorb more energy from sea waves for the MWEC system.

## BIBLIOGRAPHY

1. Pérez-Collazo, C., D. Greaves, and G. Iglesias, *A review of combined wave and offshore wind energy*. *Renewable and Sustainable Energy Reviews*, 2015. **42**: pp. 141-153.
2. Antonio, F.d.O., *Wave energy utilization: A review of the technologies*. *Renewable and sustainable energy reviews*, 2010. **14**(3): pp. 899-918.
3. Aubault, A., et al. *Modeling of an oscillating water column on the floating foundation WindFloat*. in : ASME 2011 30<sup>th</sup> International Conference on Ocean, Offshore and Arctic Engineering. 2011. American Society of Mechanical Engineers.
4. Luan, C., et al. *Modeling and analysis of a 5 MW semi-submersible wind turbine combined with three flap-type Wave Energy Converters*. in : ASME 2014 33rd International Conference on Ocean, Offshore and Arctic Engineering. 2014. American Society of Mechanical Engineers.
5. Michailides, C., et al. *Effect of flap type wave energy converters on the response of a semi-submersible wind turbine in operational conditions*. in : ASME 2014 33rd International Conference on Ocean, Offshore and Arctic Engineering. 2014. American Society of Mechanical Engineers.
6. Peiffer, A., D. Roddier, and A. Aubault. *Design of a point absorber inside the WindFloat structure*. in : ASME 2011 30th International Conference on Ocean, Offshore and Arctic Engineering. 2011. American Society of Mechanical Engineers.
7. Bachynski, E.E. and T. Moan. *Point absorber design for a combined wind and wave energy converter on a tension-leg support structure*. in : ASME 2013 32nd International Conference on Ocean, Offshore and Arctic Engineering. 2013. American Society of Mechanical Engineers.
8. Muliawan, M.J., et al., *Extreme responses of a combined spar-type floating wind turbine and floating wave energy converter (STC) system with survival modes*. *Ocean Engineering*, 2013. **65**: pp. 71-82.
9. Muliawan, M.J., M. Karimirad, and T. Moan, *Dynamic response and power performance of a combined spar-type floating wind turbine and coaxial floating wave energy converter*. *Renewable Energy*, 2013. **50**: pp. 47-57.
10. Muliawan, M.J., et al. *STC (Spar-Torus Combination): a combined spar-type floating wind turbine and large point absorber floating wave energy converter—promising and challenging*. in : ASME 2012 31st International Conference on Ocean, Offshore and Arctic Engineering. 2012. American Society of Mechanical Engineers.
11. Wan, L., Z. Gao, and T. Moan, *Experimental and numerical study of hydrodynamic responses of a combined wind and wave energy converter concept in survival modes*. *Coastal Engineering*, 2015. **104**: pp. 151-169.
12. Wan, L., Z. Gao, and T. Moan. *Model test of the STC concept in survival modes*. in : ASME 2014 33rd International Conference on Ocean, Offshore and Arctic Engineering. 2014. American Society of Mechanical Engineers.
13. Wan, L., et al., *Experimental and numerical comparisons of hydrodynamic responses for a combined wind and wave energy converter concept under operational conditions*. *Renewable Energy*, 2016. **93**: pp. 87-100.

14. Wan, L., et al., *Comparative experimental study of the survivability of a combined wind and wave energy converter in two testing facilities*. Ocean Engineering, 2016. **111**: pp. 82-94.
15. Ren, N., et al. *Dynamic Response of a Combined Mono-Pile Wind Turbine and Heave-Type Wave Energy Converter System*. In : ASME 2017 36th International Conference on Ocean, Offshore and Arctic Engineering. 2017. American Society of Mechanical Engineers.
16. Ren, N., et al., *Experimental and numerical study of hydrodynamic responses of a new combined monopile wind turbine and a heave-type wave energy converter under typical operational conditions*. Ocean Engineering, 2018. **159**: pp. 1-8.
17. Jonkman, J.M., *Definition of the Floating System for Phase IV of OC3*. 2010: Citeseer.
18. Rourke, F.O., F. Boyle, and A. Reynolds, *Renewable energy resources and technologies applicable to Ireland*. Renewable and Sustainable Energy Reviews, 2009. **13**(8): pp. 1975-1984.

## CONTACT WITH THE AUTHORS

### Hassan Ghassemi

*e-mail: gasemi@aut.ac.ir*

Department of Maritime Engineering  
AmirKabir University of Technology  
Hafez Ave., Tehran  
**IRAN**

### Esmail Homayoun

*e-mail: homayoun73223@gmail.com*

Department of Maritime Engineering  
AmirKabir University of Technology  
Hafez Ave., Tehran  
**IRAN**

### Hamidreza Ghafari

*e-mail: hamidghafari230@yahoo.com*

Department of Maritime Engineering  
AmirKabir University of Technology  
Hafez Ave., Tehran  
**IRAN**

# SHIP MANEUVERING PREDICTION USING GREY BOX FRAMEWORK VIA ADAPTIVE RM-SVM WITH MINOR RUDDER

Bin Mei <sup>a</sup>  
Licheng Sun <sup>a</sup>  
Guoyou Shi <sup>a</sup>  
Xiaodong Liu <sup>b</sup>

<sup>a</sup> Dalian Maritime University, The People's Republic of China

<sup>b</sup> Dalian University of Technology, The People's Republic of China

## ABSTRACT

*A grey box framework is applied to model ship maneuvering by using a reference model (RM) and a support vector machine (SVM) (RM-SVM). First, the nonlinear characteristics of the target ship are determined using the RM and the similarity rule. Then, the linear SVM adaptively fits the errors between acceleration variables of RM and target ship. Finally, the accelerations of the target ship are predicted using RM and linear SVM. The parameters of the RM are known and conveniently acquired, thus avoiding the modeling process. The SVM has the advantages of fast training, quick simulation, and no overfitting. Testing and validation are conducted using the ship model test data. The test case reveals the practicability of the RF-SVM based modeling method, while the validation cases confirm the generalization ability of the grey box framework.*

**Keywords:** ship maneuvering; reference model; linear support vector machine; grey box framework; similarity rule

## INTRODUCTION

A report by the International Maritime Organization (IMO) pertaining to the global use of autonomous systems indicated that autonomous ships may be launched soon [1]. Ship maneuvering modeling is the key element of ship motion prediction (kinematics and kinetics), simulation and control of autonomous ship navigation, and collision avoidance [2]. Ship maneuverability has received increasing attention from the shipping industry.

Generally, there are several primary methods based on captive model test, free model test, full-scale trials, and computational fluid dynamics (CFD) [2-4] which are used for maneuvering simulations. The reports of the International

Towing Tank Conference (ITTC) offer a broad overview of many available ship modeling methods [4]. To obtain the ship hydrodynamic force and ascertain the hydrodynamic coefficients, captive model tests, such as planar motion mechanism (PMM) and circular motion test (CRM), and other complicated and expensive tests, must be used repeatedly [5]. CFD is a crucial method for theoretical calculations and has a long history. As the performance of computers has been improving with time, CFD can be utilized much more effectively. However, CFD analyses need human experience to build a suitable grid, and remain excessively time-consuming for online ship motion prediction [3]. The overview of methods to develop a ship maneuvering model reveals that system identification has a significantly lower

cost and requires considerably lower effort. However, this method is not as precise as the free running model test, the captive model test, or CFD [4]. This implies that, despite their drawbacks, the captive model tests and CFD realize a more accurate model. Therefore, to increase its accuracy, the system identification method should be improved on the basis of free model tests and full-scale sea trials.

The system identification method fits the test data and conducts generalization ability simultaneously. When a ship is sailing on the sea, its sailing conditions change constantly due to the action of environmental disturbances and changing load conditions. For ship motion control and prediction, the system identification method can simulate the future trajectory and velocity by using sensors. Researchers of ship motion identification modeling have made many attempts to deal with this problem [6-13], and their results are classified as white box, black box, and grey box identification.

For white box system identification, Abkowitz introduced an EKF to identify model parameters during ship sea trials [6]. Other researchers used partial least squares regression, multi-innovation least squares (MILS), and linear support vector machine (LS-SVM) approaches to verify the parameters [7-9]. However, the parameters could not be identified using partial least squares regression for a ship in motion under wind or wave disturbances, and MILS and LSVM did not yield accurate simulations. Kallstrom used the pseudo random binary sequence (PRBS) as the maneuver signal [10]. Yoon applied ridge regression to figure out the parameters, and improved the PRBS and D-optimal maneuver scheme [11]. Sutulo and Soares presented an offline system modeling method using five different learning metrics and genetic algorithm (GA) based parameter optimization [12]. However, the GA only obtains the learning parameters with a fixed interval on the basis of theoretical or database methods.

Many studies have been conducted on black box system identification. Haddara obtained an optimal effect by estimating derivatives with neural networks, but the network training was time consuming [13]. Wang (2015) proposed a fuzzy neural network for system identification modeling [14]. Faller presented a maneuvering motion model by using a recursive neural network (RNN), for which a number of numerous turning circle and zigzag maneuvers were utilized as training tests [15]. Moreira proposed an RNN maneuvering simulation model for turning circle and zigzag maneuvers, but this method also required a lot of training tests [16]. Oskin presented an RNN to identify a ship motion response model that neglects ship speed prediction [17]. On the basis of multiple tests, Bai used the locally weighted learning to predict maneuvering motion by using the black box structure. However, the maneuver scheme for identification was not suitable as good seamanship handling required [18]. Zhu used a least squared SVM and optimized it with the artificial bee colony method, but the surge velocity was not verified for a zigzag test [19]. Luo proposed a method in which the reconstruction of sample data was identified using an SVM, and no verification was conducted for the turning test [20]. Thus, system identification methods require considerable ship

motion test data and have poor generalization ability. For the grey box identification, Wang used SVM to get the ship maneuvering model without ship's principal particulars [26].

Motivated by these observations, we aim to address the problems in ship motion identification. Despite improvements in the precision of system identification for ship motion since the ITTC 2005, some difficulties have not been overcome yet.

Firstly, it is not very feasible to use simulation data for system identification. When the simulation test data is without noise, it has higher quality and can be easily used for identification. However, in practical scenarios, the test data contains measurement errors and disturbances from the sea environment. Secondly, the period, frequency and other characteristics of the input signals in the simulation test, such as the sinusoidal rudder angle and pulse signals [14], and the PRBS and D-optimal signals [10,11], are relatively broad. However, a sinusoidal rudder angle cannot be easily obtained for the steering control system. Moreover, for sea trials, the IMO proposed a maximum allowable rudder angle ( $+20^{\circ}/-20^{\circ}$ ) as a test scheme standard for ship maneuverability. Therefore, although the identification of simulation data is better than trial data, it is difficult to obtain training data in full-scale trials.

The sea trials are only conducted in light ballast or heavy ballast conditions. Therefore, for using the data of the ship trial test as the identification data, the ship maneuvering ability should be converted from the ballast condition to the full load condition [21]. Thus, the sea trial test is not convenient for identification modeling. This implies that the test data under the full load condition are more suitable for ship operation with inadequate excitation. The aim of this study is to improve the precision of identification modeling and to reduce the data set for identification, thus reducing the effort, time, and cost required for modeling. These problems are addressed using the features of the reference model (RM).

## PROBLEMS AND PRELIMINARIES

The aim of the grey box approach is to model ship maneuvering and describe the trajectory and velocity of the ship during navigation on the sea. In this section, the problems of ship maneuvering are presented and simplified. Then, the grey box structure is correlated with ship velocities and accelerations, and utilized to address the aforementioned problems.

### PROBLEMS

During sea navigation, the ship motion is typically described in three degrees of freedom (3 DOF). A 3-DOF model is equivalent to a horizontal plane model with surge, sway, and yaw motion. There are two assumptions for this model. Assumption A: On the basis of the rigid-wall boundary condition, the free surface is regarded as a fixed horizontal plane [22]. Assumption B: The 3-DOF model is a specific horizontal plane model. The motions can be decoupled into

longitudinal and lateral motions. Moreover, sway and yaw are coupled. On the basis of these assumptions, the model can be described as Equation (1) [23]:

$$\begin{cases} m - X_{\dot{u}} \dot{u} = f_1(u, v, r, \delta) \\ (m - Y_{\dot{v}}) \dot{v} + (mx_G - Y_{\dot{r}}) \dot{r} = f_2(u, v, r, \delta) \\ (mx_G - N_{\dot{v}}) \dot{v} + (I_z - N_{\dot{r}}) \dot{r} = f_3(u, v, r, \delta) \end{cases} \quad (1)$$

where  $m$  represents the mass of the ship;  $x_G$  represents the gravity center of ship's mass;  $(x, y)$  is the trajectory of the ship's gravity center;  $\psi$  is the ship course;  $u, v, r$  are the velocities of surge, sway, and yaw motion, respectively;  $I_z$  is the moment of inertia; and  $X_{\dot{u}}, Y_{\dot{v}}, Y_{\dot{r}}, N_{\dot{v}}$  and  $N_{\dot{r}}$  are constants. Equation (1) can be rewritten as Equation (2):

$$\begin{cases} \dot{u} = f_1 / (m - X_{\dot{u}}) \\ = G_1(u, v, r, \delta) \\ \dot{v} = \frac{(I_z - N_{\dot{r}}) \cdot f_2 - (mx_G - N_{\dot{v}}) \cdot f_3}{(m - Y_{\dot{v}})(I_z - N_{\dot{r}}) - (mx_G - N_{\dot{v}})(mx_G - Y_{\dot{r}})} \\ = G_2(u, v, r, \delta) \\ \dot{r} = \frac{(m - Y_{\dot{v}}) \cdot f_3 - (mx_G - N_{\dot{v}}) \cdot f_2}{(m - Y_{\dot{v}})(I_z - N_{\dot{r}}) - (mx_G - N_{\dot{v}})(mx_G - Y_{\dot{r}})} \\ = G_3(u, v, r, \delta) \end{cases} \quad (2)$$

The ship hydrodynamics functions  $G_1, G_2$ , and  $G_3$  on the right-hand side of Equation (2) are purely related to the ship maneuver state  $(u, v, r, \delta)$ , which determines ship accelerations.

## PRELIMINARIES OF THE GREY BOX FRAMEWORK

To resolve the ship maneuvering problem, system identification modeling is used to quantify the relationship between ship motion velocities and accelerations. RM-SVM is a grey box framework used for system identification. In this section, the concepts of general grey box and RM-SVM are introduced. Then, the framework and flowchart of RM-SVM are presented.

Based on Ljung's description [24], combining the identification model with a nonlinear static model and a linear dynamic model gives a slate grey model. The RM, being a concept from adaptive control [25], is an approximate model of the controlled object. For ship maneuvering, an existing mathematical model can be used as RM, which is a nonlinear static model. Hence, as presented in Figure 2, the nonlinear static model, the RM, and the nonlinear ship motion model are identical and belong to the same category. Then, a linear SVM is used as the learning algorithm, which is equivalent to a linear dynamic model. The dynamic model approximates the error between the target ship and the RM. The conceptual evolution path of the slate grey model, RM,

and ship motion grey box identification model is presented in Figure 1.

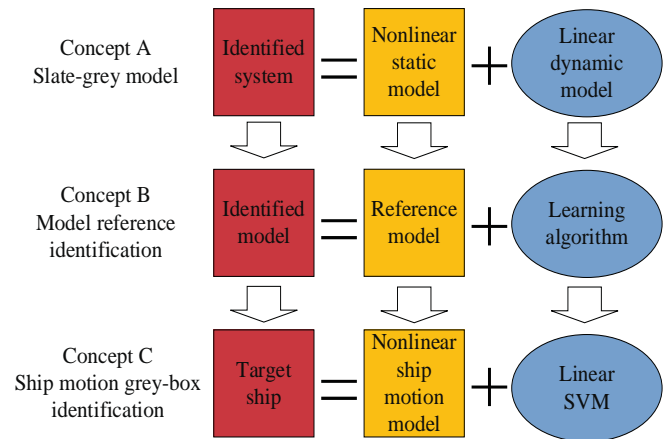


Fig. 1. Conceptual evolution path of the slate grey box, reference model, and ship motion grey box identification frameworks

It is noteworthy that the SVM has been used as grey box [26]. There are three differences between SVM and RM-SVM, although SVM is used in RM-SVM. As shown in Figure 2, firstly, the outputs of SVM and RM-SVM are different. Secondly, the accelerations consist of RM and errors between RM and target ship. Thirdly, the system in SVM is a discrete-time system, while in RM-SVM it is a continuous-time system. Therefore, RM-SVM is different from SVM. Furthermore, SVM is an artificial intelligent (AI) algorithm in RM-SVM, and can be replaced by any other regression algorithm, e.g. neural network, decision trees, and logistic regression. Since the RM can be verified and advanced, RM modeling provides robust estimation of ship velocities when SVM fails.

As presented in Figure 2.b, ship maneuvering is a time-consuming task, and accelerations are selected as inputs and output of the grey box system. The steps of grey box modeling are as follows:

- a: Select an existing nonlinear ship maneuvering motion model as the RM.
- b: Convert the target ship velocities  $u_T, v_T$ , and  $r_T$  to the RM velocities  $u_R, v_R$ , and  $r_R$ , respectively.
- c: Calculate the RM accelerations  $\dot{u}_R, \dot{v}_R$ , and  $\dot{r}_R$ , and the RM velocities  $u_R, v_R$ , and  $r_R$ ; the rudder angle is  $\delta_R$ .
- d: SVM compensates the acceleration errors of the target ship and the RM.
- e: Adaptively tune the SVM parameter.

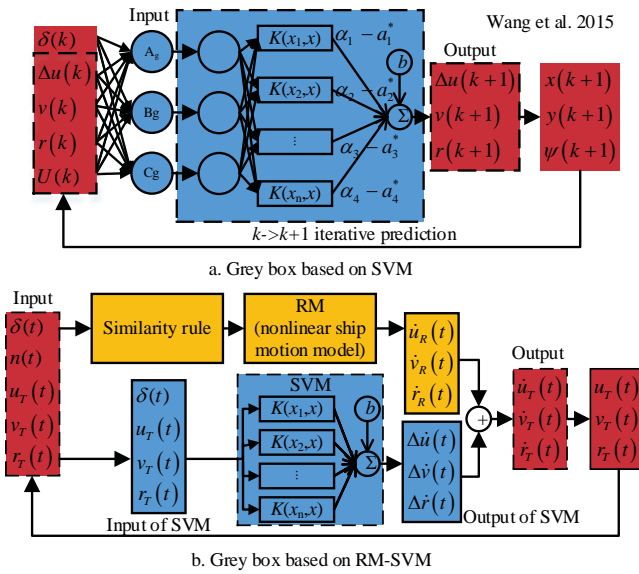


Fig. 2. Comparison of grey box framework based on SVM [26] and RM-SVM for ship motion identification modeling

## GREY BOX MODELING

In this section, the details and content of the application of the RM-SVM are presented. Firstly, the RM is selected, and then the target ship velocities are converted to the RM. As the third step, the SVM is obtained for use in the RM-SVM. Finally, adaptive tuning of the SVM parameter is done.

### SELECTION OF RM

Several models used for ship maneuvering were mentioned in [19]. Nonlinear static models, such as the response model of sway motion, the Mathematical Maneuvering Group (MMG) response model, and the Abkowitz model, can be employed as the RM. It is crucial to select a suitable RM from the existing models. The selected RM should be most suitable for the target ship.

On the basis of [27], we consider the particular vector  $\mathbf{p}$  as the feature of the ship. Moreover,  $Cb$ , is the ship block coefficient,  $Lpp$  is the length between perpendiculars,  $B$  is the ship beam,  $T$  is the ship draught,  $V_0$  is the speed of the designed ship, and  $Ar$  is the rudder area. Thus, we obtain Equation (3):

$$\mathbf{p} = (Cb, Lpp / B, B / T, Lpp / V_0, Ar / (Lpp \cdot T)) \quad (3)$$

The matrices  $\mathbf{P}$  comprise  $\mathbf{p}$ , which can be expressed as Equation (4):

$$\mathbf{P} = (\mathbf{p}_1, \dots, \mathbf{p}_i, \dots, \mathbf{p}_m)^T = \begin{pmatrix} Cb_1 & Cb_2 & \dots & Cb_n \\ Lpp_1 & Lpp_2 & \dots & Lpp_n \\ B_1 & B_2 & \dots & B_n \\ T_1 & T_2 & \dots & T_n \\ Lpp_1 & Lpp_2 & \dots & Lpp_n \\ V_{01} & V_{02} & \dots & V_{0n} \\ Ar_1 & Ar_2 & \dots & Ar_n \\ Lpp_1 T_1 & Lpp_2 T_2 & \dots & Lpp_n T_n \end{pmatrix} \quad (4)$$

Let  $\boldsymbol{\eta}_i = (\mathbf{p}_{i1}, \dots, \mathbf{p}_{ij}, \dots, \mathbf{p}_{in})^T$ ;  $m = 5$ ;  $i = 1, 2, \dots, m$ ; and  $j = 1, 2, \dots, n$ . Then, the normalization of the particular matrix  $\mathbf{P}$  can be given as Equation (5):

$$\zeta_i = \frac{\boldsymbol{\eta}_i}{\|\boldsymbol{\eta}_i\|_2} = \frac{\boldsymbol{\eta}_i}{(\mathbf{p}_{i1}^2 + \dots + \mathbf{p}_{ij}^2 + \dots + \mathbf{p}_{in}^2)^{\frac{1}{2}}} \quad (5)$$

Let  $\mathbf{Q} = (\zeta_1, \zeta_2, \dots, \zeta_n)^T$  and  $(\mathbf{q}_1, \mathbf{q}_1, \dots, \mathbf{q}_n) = \mathbf{Q}^T$ . The normalization particular vector is  $\mathbf{q}_i$ . Then, the coefficient  $\gamma_i$  of the relationship between  $\mathbf{q}_1$  and can be written as Equation (6):

$$\begin{aligned} \gamma_i &= \frac{COV(\mathbf{q}_1, \mathbf{q}_i)}{\sigma(\mathbf{q}_1)\sigma(\mathbf{q}_i)} \\ &= \frac{E(\mathbf{q}_1 \mathbf{q}_i) - E(\mathbf{q}_1)E(\mathbf{q}_i)}{\{E(\mathbf{q}_1^2) - E^2(\mathbf{q}_1)\}^{\frac{1}{2}} \{E(\mathbf{q}_i^2) - E^2(\mathbf{q}_i)\}^{\frac{1}{2}}} \\ &= \frac{\sum \mathbf{q}_1 \mathbf{q}_i - \frac{\sum \mathbf{q}_1 \sum \mathbf{q}_i}{n}}{\{(\sum \mathbf{q}_1^2 - \frac{(\sum \mathbf{q}_1)^2}{n})(\sum \mathbf{q}_i^2 - \frac{(\sum \mathbf{q}_i)^2}{n})\}^{\frac{1}{2}}} \end{aligned} \quad (6)$$

The ship corresponding to the maximum  $\gamma$  is most similar to the target ship and is selected as the RM. In other words, the order and structure of the selected RM are approximately equal to those of the target ship.

### CONVERSION OF VELOCITIES

The target ship and the RM have differently designed standard states, therefore the velocities of the target ship should be converted to the RM. Two conversion methods have been proposed by SNAME [28] and Norrbin [29]. In this study, the normalization forms from the study by SNAME [28] were introduced, including ship surge, sway and yaw motion, and rudder angle. These states are expressed as Equation (7):

$$\begin{cases} u_R = u_T (V_{0R} / V_{0T}) \\ v_R = v_T (V_{0R} / V_{0T}) \\ r_R = r_T (V_{0R} / Lpp_R) / (V_{0T} / Lpp_T) \\ \delta_R = \delta_T \end{cases} \quad (7)$$

where  $(\cdot)_T$  represents the target ship and  $(\cdot)_R$  represents the RM. Here,  $v$  is the service speed and  $L_{pp}$  is the length between perpendiculars.

According to Equation (2), the accelerations of the RM are expressed as Equation (8):

$$\begin{cases} \dot{u}_R = G_{1R}(u_R, v_R, r_R, \delta_R) \\ = G_{1R}(u_T \frac{V_{0R}}{V_{0T}}, v_T \frac{V_{0R}}{V_{0T}}, r_T \frac{V_{0R}}{L_{ppR}} \frac{L_{ppT}}{V_{0T}}, \delta_T) \\ \dot{v}_R = G_{2R}(u_R, v_R, r_R, \delta_R) \\ = G_{2R}(u_T \frac{V_{0R}}{V_{0T}}, v_T \frac{V_{0R}}{V_{0T}}, r_T \frac{V_{0R}}{L_{ppR}} \frac{L_{ppT}}{V_{0T}}, \delta_T) \\ \dot{r}_R = G_{3R}(u_R, v_R, r_R, \delta_R) \\ = G_{3R}(u_T \frac{V_{0R}}{V_{0T}}, v_T \frac{V_{0R}}{V_{0T}}, r_T \frac{V_{0R}}{L_{ppR}} \frac{L_{ppT}}{V_{0T}}, \delta_T) \end{cases} \quad (8)$$

## SVM

On the basis of the flowchart of ship motion grey box modeling, the function relating the RM and the target ship is modeled through regression learning algorithms, such as SVMs, neural networks, Gauss regression models, and decision trees. In this study, the SVM was utilized [30].

The RM velocities,  $\mathbf{x} = (u_T, v_T, r_T, \delta_T)$ , are defined as the state variables. Then, the acceleration error between the target ship and RM is  $\mathbf{y} = (G_{1T} - G_{1R}, G_{2T} - G_{2R}, G_{3T} - G_{3R})$ . Consider surge acceleration as an example. The Lagrangian function of the linear SVM for the surge acceleration error is defined as Equation (9):

$$\begin{aligned} L(w_1, b_1, e_1, a_1) &= \frac{1}{2} w_1^T w_1 + \frac{1}{2} C_1 \sum_{i=1}^n e_{1i}^2 \\ &- \sum_{i=1}^n a_{1i} \{ w_1^T \varphi(\mathbf{x}_i) + b_1 + e_{1i} - y_{1i} \} \end{aligned} \quad (9)$$

By using sequential minimal optimization (SMO) to solve the Lagrangian function, the regression function  $\mathbf{y}_{1i}$  is obtained as Equation (10):

$$\mathbf{y}_{1i} = \sum_{i=1}^n a_{1i} K(\mathbf{x}, \mathbf{x}') + b_1 \quad (10)$$

where  $C_1$  is the regularization factor,  $e_1$  is the regression error,  $w_1$  is the weighted function,  $b_1$  is the bias, and  $K(\mathbf{x}, \mathbf{x}')$  is the linear kernel function written as  $\mathbf{x} \cdot \mathbf{x}'^T$ .

Thus, the surge acceleration of the target ship is  $\mathbf{y}_{1i} + G_{1R}$ . Similarly, the acceleration of the target ship can be expressed by Equation (11):

$$\begin{cases} \dot{u}_T = \mathbf{y}_{1i} + G_{1R} = \\ \sum_{i=1}^n a_{1i}(u_T, v_T, r_T, \delta_T) \cdot (u_T, v_T, r_T, \delta_T)^T + b_1 \\ + G_{1R}(u_T \frac{V_{0R}}{V_{0T}}, v_T \frac{V_{0R}}{V_{0T}}, r_T \frac{V_{0R}}{L_{ppR}} \frac{L_{ppT}}{V_{0T}}, \delta_T) \\ \dot{v}_T = \mathbf{y}_{2i} + G_{2R} = \\ \sum_{i=1}^n a_{2i}(u_T, v_T, r_T, \delta_T) \cdot (u_T, v_T, r_T, \delta_T)^T + b_2 \\ + G_{2R}(u_T \frac{V_{0R}}{V_{0T}}, v_T \frac{V_{0R}}{V_{0T}}, r_T \frac{V_{0R}}{L_{ppR}} \frac{L_{ppT}}{V_{0T}}, \delta_T) \\ \dot{r}_T = \mathbf{y}_{3i} + G_{3R} = \\ \sum_{i=1}^n a_{3i}(u_T, v_T, r_T, \delta_T) \cdot (u_T, v_T, r_T, \delta_T)^T + b_3 \\ + G_{3R}(u_T \frac{V_{0R}}{V_{0T}}, v_T \frac{V_{0R}}{V_{0T}}, r_T \frac{V_{0R}}{L_{ppR}} \frac{L_{ppT}}{V_{0T}}, \delta_T) \end{cases} \quad (11)$$

## ADAPTIVE TUNING OF SVM

The insensitive band  $\varepsilon$  is the SVM parameter that should be tuned. This parameter determines the incorrect sample data to be ignored in the SMO solver. In this study, adaptive tuning based on the pattern search algorithm has been introduced. The search range of  $\varepsilon$  is  $[0, 1]$ . The parameters  $\varepsilon_1$ ,  $\varepsilon_2$ , and  $\varepsilon_3$  are insensitive bands for surge, sway, and yaw accelerations in Equation (11), respectively. As presented in Figure 3, the following search steps are performed:

- Step 1: Prepare the training data for the RM-SVM;
- Step 2: Initialize  $\varepsilon_1, \varepsilon_2$ , and  $\varepsilon_3$  in the SVM.
- Step 3: Conduct the pattern search.
  - Step 3.1: Generate the mesh grid of  $\varepsilon_1, \varepsilon_2$ , and  $\varepsilon_3$  ranges
  - Step 3.2: Conduct SMO on the SVM.
  - Step 3.3: Simulate the training test.
  - Step 3.4: Calculate the Pearson correlation coefficient  $\lambda$  between the heading angles obtained from the training test and simulation.
  - Step 3.5: If the coefficient  $\lambda$  is less than the threshold, then repeat Steps 3.1 to 3.5. Otherwise, go to Step 4.
- Step 4: Record the optimal values of  $\varepsilon_1, \varepsilon_2$ , and  $\varepsilon_3$ .

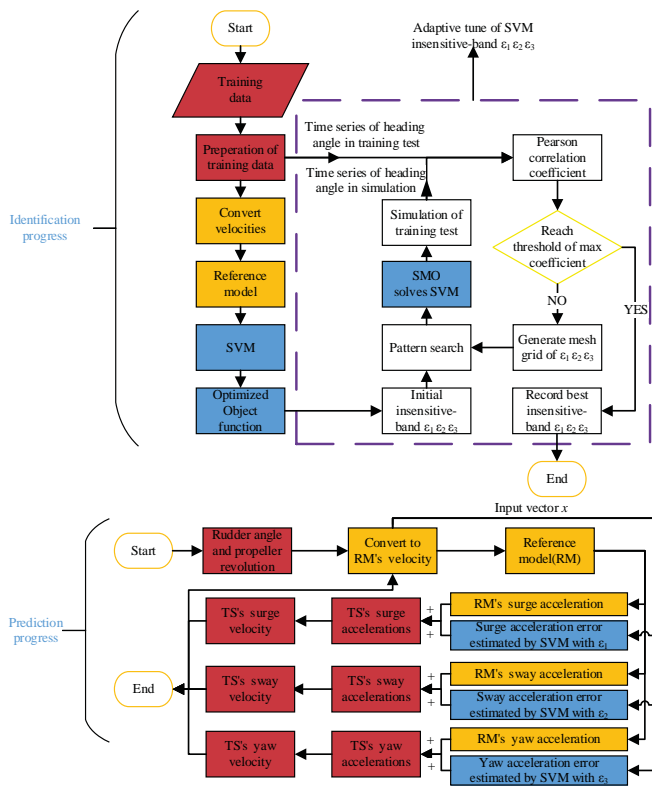


Fig. 3. Adaptive tuning of insensitive bands in SVM and RM-SVM based prediction

## PREPARATION

To verify the effectiveness of grey box modeling for ship maneuvering, a free running model test was used and the training test was simulated. Then, the free running model test was validated for estimating the generalization ability.

## TEST DATA

KVLCC2 is a benchmark ship used for validation of ship maneuvering models, performed using the system based maneuvering simulation method, CFD-based maneuvering simulation method, and other no simulation methods. Its particulars are presented in Table 1. The data from these two faculties were converted using the prime system [22].

Tab. 1. Particulars of target ship KVLCC2

Particulars	model	Full scale
Scale	45.7	1
Length (m)	7.0	320.0
Maximum breadth (m)	1.17	58.0
Draught (m)	0.46	20.8
Block coefficient	0.81	0.81
Maximum rate of rudder (°)	15.8	2.34
Service speed (knots)	1.18	7.9

The free running model test in basin generates sample points with sampling frequency of 1 Hz. The test type, the rudder angle, and other maneuver scheme information of the test data for study cases are given in Table 2. The tests were performed in the basin, in which the max test rudder of the zigzag maneuver is less than or equal to 20°. Therefore, the test data with minor rudder angle was used to identify the RM-SVM. As presented in Table 3, a relatively small amount of training data was used compared to other studies [15][18][31], and the validation data was different from the training data.

Tab. 2. Training and validation data

Training cases			
Test type	Rudder and heading angle	Sample points	Port/starboard
Zigzag test	10°/10°	520	starboard
Zigzag test	10°/10°	565	port
Zigzag test	20°/20°	606	starboard
Zigzag test	20°/20°	684	port
Validation cases			
Test type	Rudder angle	Sample points	Port/starboard
Turning circle	35°	1610	starboard
Turning circle	-35°	1151	port

Tab. 3. Comparing test data in the current study and related studies

Training data		Current study	Bai [18]	Wang [31]	Hess [15]
Zigzag	Contained	Yes	Yes	Yes	Yes
	NO. of Case	4	4	2	2
	Max rudder	20	30	20	20
Turning circle	Contained	No	Yes *	Yes	Yes
	NO. of Case	No	4*	2	4
	Max rudder	No	30	15	35
Validation test different from training		Yes	No	No	No

The 20°/20° zigzag test is presented as an example in Figure 4. Spline filters were used to indicate sway velocity and sway acceleration.

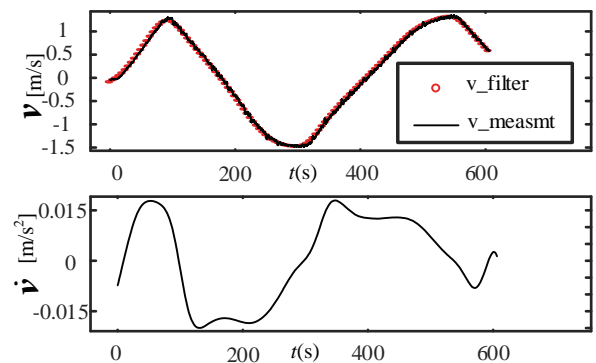


Fig. 4 Sway velocity and acceleration obtained from the filter

## RM FOR KVLCC2

Four RMs were used for selecting a proper RM for KVLCC2 [21][23]. The particulars are presented in Table 4. On the basis of the selection conducted to obtain suitable progress in grey box modeling, the correlation coefficients  $\gamma$  between the RMs and KVLCC2 were estimated (-0.5758, 0.8510, -0.8873, and -0.7228). The maximum  $\gamma$  was 0.8510. Therefore, the “Tanker” was selected as the RM.

Tab. 4. Particulars of the Tanker RM

Name	KVLCC2	Mariner [23]	Tanker [23]	SR108 [21]	PCC [21]
Structure	***	Abkowitz	Abkowitz	MMG	MMG
$C_b$	0.90	0.60	0.83	0.56	0.55
$L_{pp}/B$	5.52	6.95	6.39	6.89	5.60
$B/T$	2.79	3.10	2.58	2.99	3.93
$L_{pp}/V_0$	40.1	20.9	37.0	14.1	$\approx 18.0$
$Ar/(L_{pp}T)$	1/48.7	1/83.1	$\approx 1/61.0$	1/45.8	1/39.8

## ERRORS BETWEEN RM AND KVLCC2

Following Equation (7), the velocities of KVLCC2 were converted to those of the RM Tanker. Moreover,  $u_R$ ,  $v_R$ ,  $r_R$ , and  $\delta_R$  were selected as the inputs for Tanker, and the outputs were  $\dot{u}_R$ ,  $\dot{v}_R$ , and  $\dot{r}_R$ . Figure 5 compares the accelerations  $\dot{u}_R$ ,  $\dot{v}_R$ , and  $\dot{r}_R$  with  $\dot{u}_T$ ,  $\dot{v}_T$ , and  $\dot{r}_T$ . The result of the comparison is approximated by a line. The relationship coefficients are 0.99, 0.94, and 0.87, which implies that the nonlinear dynamics of KVLCC2 is very well replicated by the Tanker.

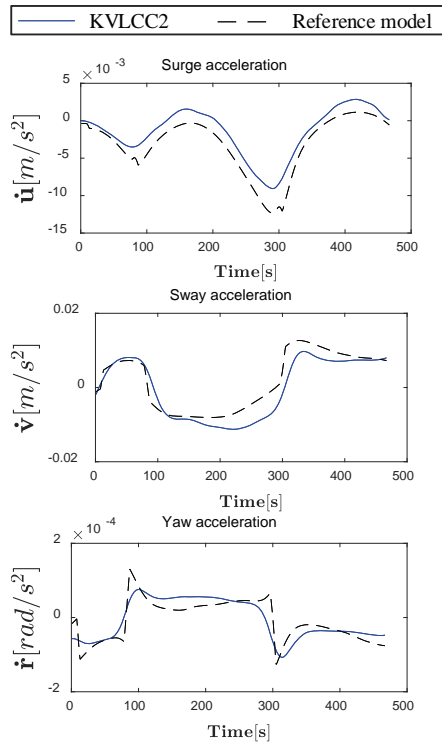


Fig. 5. Comparing accelerations of KVLCC2 and RM

## CASE STUDIES

In order to illustrate the prediction performance of the presented grey box model based on RF-SVM, four zigzag tests:  $10^\circ/10^\circ$ ,  $-10^\circ/-10^\circ$ ,  $20^\circ/20^\circ$ , and  $-20^\circ/-20^\circ$  were used for training. After that, two validation cases of  $35^\circ$  and  $-35^\circ$  turning circle were tested.

## ADAPTIVE TUNING OF INSENSITIVE BAND

The parameters  $\varepsilon_1$ ,  $\varepsilon_2$ , and  $\varepsilon_3$  are the insensitive bands for surge, sway, and yaw accelerations. On the basis of adaptive tuning steps, a  $20^\circ/20^\circ$  zigzag test was chosen as the simulation test. The Pearson correlation coefficient  $\lambda$  of the heading angle in the  $20^\circ/20^\circ$  zigzag test was calculated. The optimal insensitive bands obtained from the pattern search correspond to the maximum value of coefficient  $\lambda_{\max}$ . As presented in Figure 6,  $\varepsilon_1$ ,  $\varepsilon_2$ ,  $\varepsilon_3$ , and  $\lambda$  change with the iteration of the pattern search and converge to 0.005, 1, 1, and 0.993, respectively.

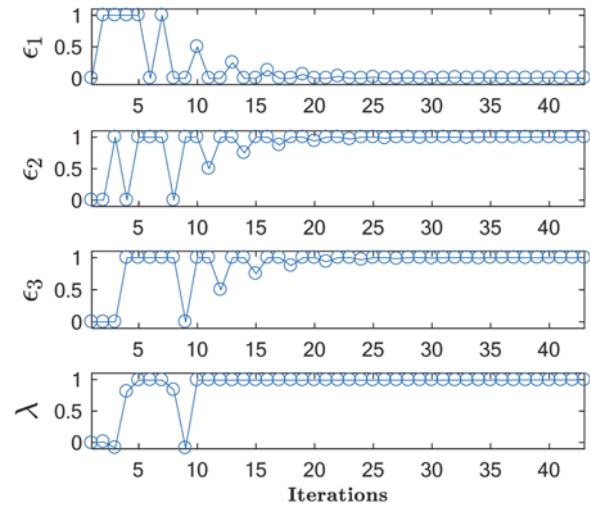


Fig. 6 Iterations of  $\varepsilon_1$ ,  $\varepsilon_2$ ,  $\varepsilon_3$ , and  $\lambda$

## TRAINING CASE FOR $20^\circ/20^\circ$ ZIGZAG MANEUVER

To assess the effectiveness of the RM-SVM approach, a training case was simulated. By using Equation (10), the  $20^\circ/20^\circ$  zigzag maneuver was predicted and the heading, velocities, and trajectory were acquired. Then, the results were compared with those of the CFD method from Hyundai Maritime Research Institute (HMRI) presented by Sung [32] and model experiments from NMRI presented by Yasukawa [33]. The results of the above three methods were further compared with those from the free running model test called EXP-MARIN and performed at the Maritime Research Institute Netherlands (MARIN). However, the studies [32] and [33] have included headings rather than velocities. The variables presented in Figure 7 were made dimensionless using the method proposed by Norrbin [29].

Figure 7 shows that RM modeling has the advantages of robust prediction and base estimation. Especially, the base estimation of ship velocities by RM is labeled, and more accurate estimation of RM-SVM is shown.

The first and second overshoot angles (OSA) are presented in Table 5. Their comparison reveals that the RM-SVM has optimal performance and prediction accuracy for the training data. The prediction of the training test is not very accurate. When the overfitting occurs, the training data fits effectively, but lower accuracy is attained for the validation data. The accuracy of the prediction for the training test of the 20°/20° zigzag maneuver is acceptable, which implies that the validation test has an optimal generalization ability.

Tab. 5. OSA predictions of 20°/20° zigzag maneuver obtained from various methods

Methods	EXP-MARIN	EFD-NMRI	RM-SVM	CFD-HMRI
1st OSA	13.8	10.9	11.8	11.7
2nd OSA	14.9	17.0	14.3	16.5

the presented method using the RM-SVM. On the basis of Equation (11), the 35° turning circle case was used for RM-SVM performance validation. After that, the results of the CFD-PMM simulation from the Shanghai Jiao tong University (CFD-SJT) [34], the experimental fluid dynamics (EFD) method from NMRI (proposed by Hironori Yasukawa) [33], and the CFD of HMRI developed by Sung and Park [32] were collected. The results of these methods and the proposed method were compared with the EXP-MARIN free running model test, which is considered most accurate. The surge, sway, and yaw speeds are included in CFD-SJT merely. Thus, the velocities obtained using the proposed method were compared with those obtained using CFD-SJT. Moreover, the trajectory obtained using the proposed method was compared with those from EFD-NMRI, CFD-HMRI, and CFD-SJT.

The time-histories of variables predicted by the aforementioned methods for 35° turning circle test are given in Figure 8.

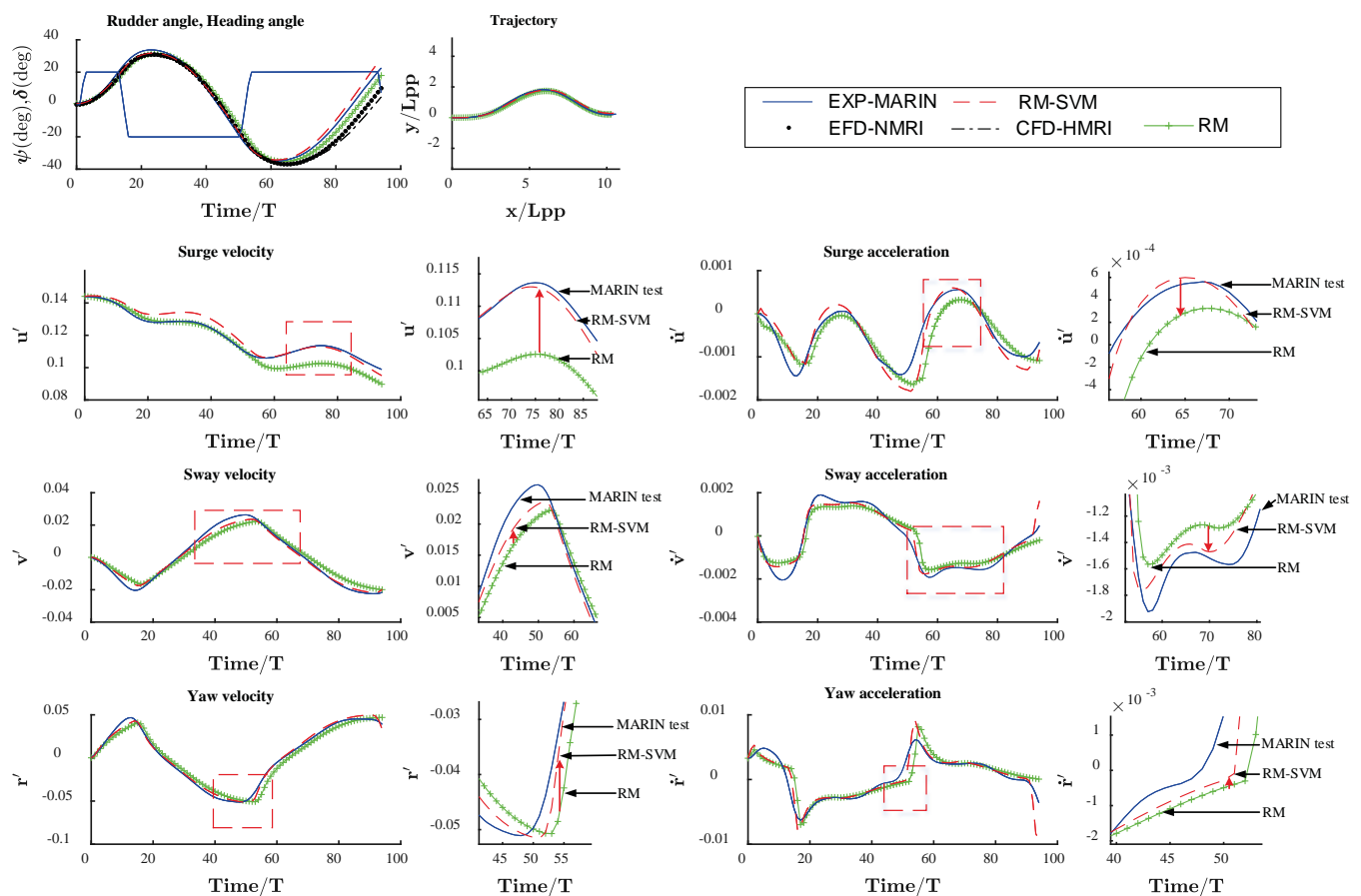


Fig. 7. Prediction variables of 20°/20° zigzag test

## VALIDATION CASE FOR GENERALIZATION ABILITY OF 35° TURNING CIRCLE

Being an AI algorithm, SVM should be verified. The same refers to the RM-SVM grey box. Therefore, a validation case was simulated to show the generalization ability of

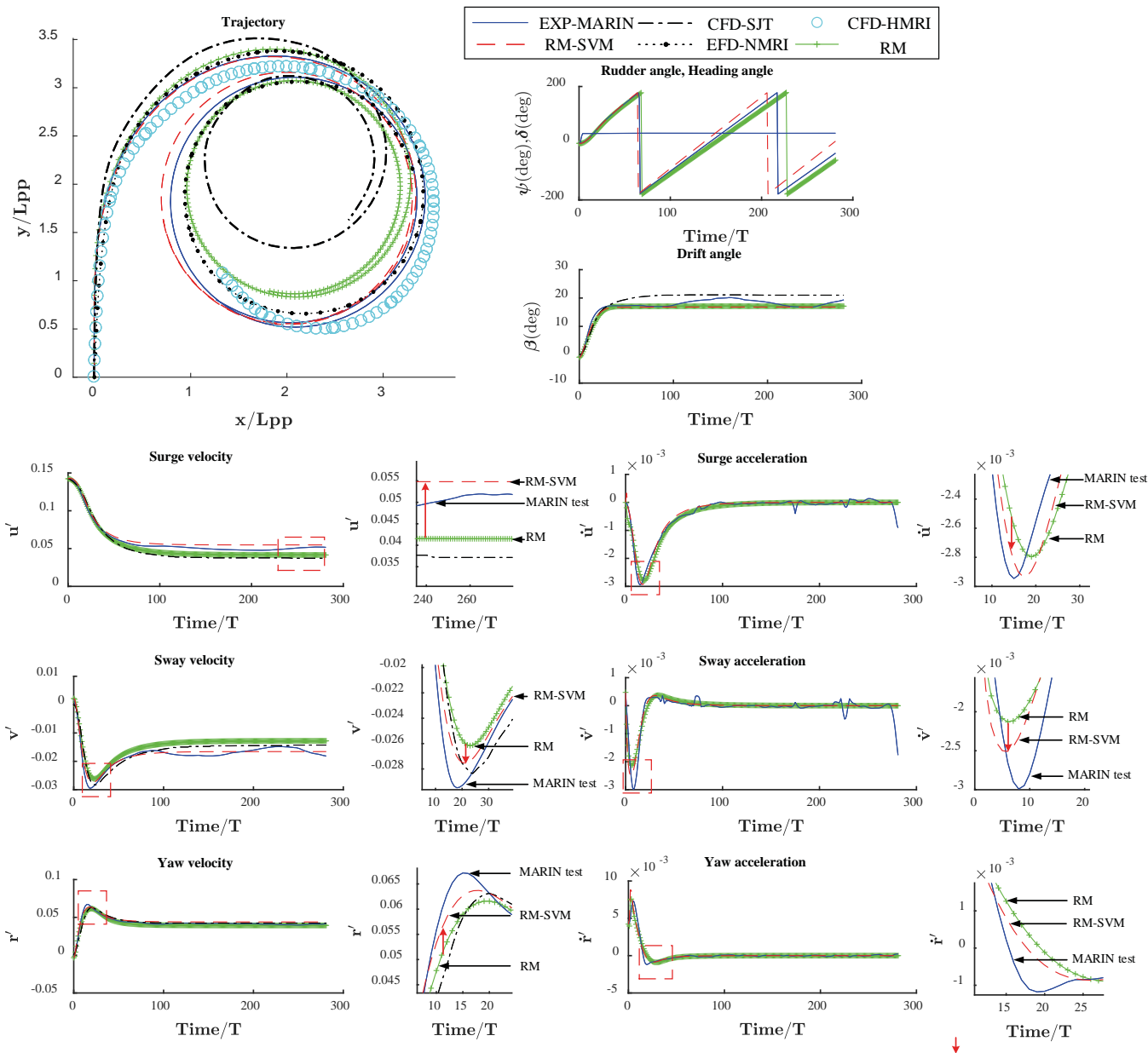


Fig. 8. Prediction variables of 35° turning circle for generalization ability validation

### VALIDATION CASE FOR GENERALIZATION ABILITY OF -35° TURNING CIRCLE

The geometries of the turning circles obtained using different methods are compared in Table 6. The precision of the advance predicted by RM-SVM is outstanding, while the predicted tactical diameter obtained from RM-SVM is average.

Tab. 6. Advances and tactical diameters predicted by different methods for the 35° turning circle case

Methods	EXP-MARIN	EFD-NMRI	RM-SVM	CFD-HMRI	CFD-SJT
$A_D$	3.25	3.31	3.22	3.12	3.63
$D_T$	3.34	3.36	3.20	3.4	2.87

The -35° turning circle is another validation case for verifying generalization ability of the proposed method. As presented in Figure 9 and Table 7, the variables in the method proposed by Norrbin are dimensionless. The advance predicted by the RM-SVM is similar to the best of those predicted by other methods, while the tactical diameter is average. The approximation ability of RM is shown in Figure 9.

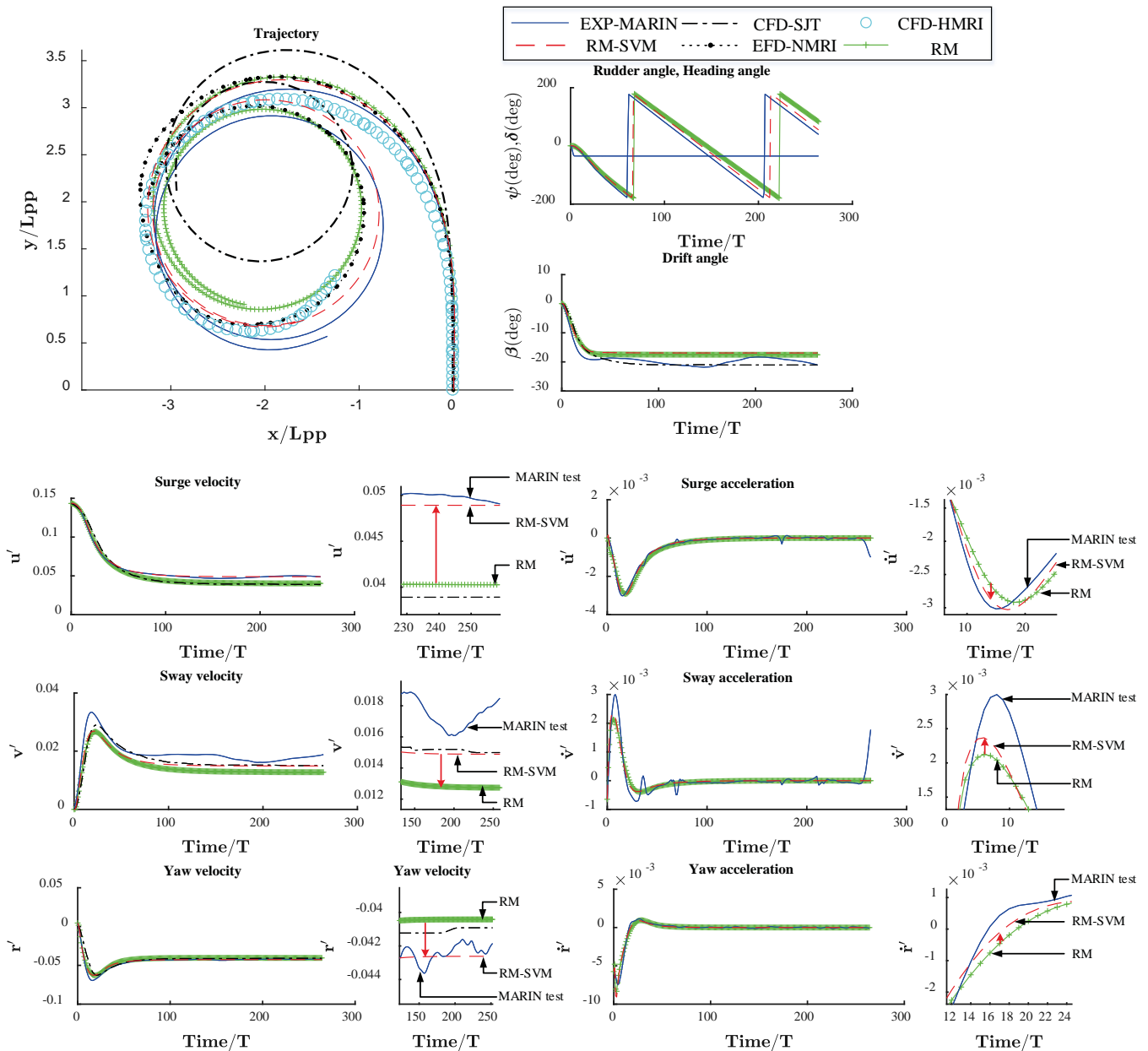


Fig. 9. Prediction variables of  $-35^\circ$  turning circle for generalization ability validation

Tab. 7. Advances and tactical diameters predicted by different methods for the  $-35^\circ$  turning circle case

Methods	EXP-MARIN	EFD-NMRI	RM-SVM	CFD-HMRI	CFD-SJT
$A_D$	3.25	3.26	3.26	3.00	3.75
$D_T$	3.34	3.26	3.24	3.14	2.88

## ANALYSIS

The kinetic variables obtained from the simulations of the zigzag maneuver and turning circles indicate that the ship motion identification matches the target ship

KVLCC2. The RM-SVM predicts the ship trajectory with high accuracy. Thus, the prediction of the  $20^\circ/20^\circ$  zigzag maneuver performed as the training test proves the effectiveness, and the predictions of the  $35^\circ$  and  $-35^\circ$  turning circle tests present the generalization ability of the RM-SVM approach. What is noteworthy, the simulations of the  $35^\circ$  and  $-35^\circ$  turning circle tests require only several seconds, whereas the full-scale test requires 25 min. Hence, the simulations can present the real-time performance of the RM-SVM, which is crucial for a ship handling simulator. What is more, the accelerations predicted by RM-SVM are highly accurate and can be utilized when taking decisions in ship course and track control.

However, there are some issues which have not been considered in the proposed method. The first is the effect of ship rolls on the ship maneuvering motion, due to the fact that the 3-DOF model was used in this study. The second

issue refers to the fact that the 35° or –35° turning circle tests had just one free running model test result. This implies that the uncertainty analysis of captive and free running model test could not be performed; thus, there is a certain error. The third issue is related with the fact that the scale of ship model used in this paper is 45.7. The scale effects of CFD-SJT and EXP-NMRI were not analyzed in detail, and they can be a source of differences in comparison.

## CONCLUSIONS

The RM-SVM based grey box model structure and adaptive tuning for ship motion identification modeling is presented. The key technologies and skills applied are: RM selection, velocity conversion using the similarity rule, and adaptive SVM tuning. The RM-SVM has a simple structure and requires shorter training and simulation times compared with other models. By analyzing earlier studies, we can find that ship modeling based on AI system identification is a time-consuming work, while the RM-SVM simulation requires less time. Illustrative examples presented in the paper demonstrate the generalization ability and feasibility of the RM-SVM approach. Furthermore, this RM-SVM scheme of adaptive tuning used for insensitive band in SVM has been proved to be effective.

In this study, three crucial results were obtained. Firstly, compared with the CFD and other related methods, the prediction accuracy of the proposed RM-SVM method is high. As an identification method for ship maneuvering, the prediction of the RM-SVM makes some progress since the ITTC 2008. Secondly, RM-SVM uses less data and a minor rudder as the identification data than other system identification methods, which yields greater generalization ability. Thirdly, RM shows the approximation ability and provides the base estimation for ship maneuvering.

However, RM-SVM has some inherent drawbacks. It neglects ship hydrodynamic coefficients, such as those in Abkowitz, ship module, or MMG model, and no information about ship flow field is provided, unlike the CFD method. Furthermore, the input variables for SVM are not optimal and need some further theory in the aspect of mechanism principle. For instance, the turbulence of rudder and propeller position cannot be precisely estimated. In this context, future studies should focus on ship maneuvering modeling which will take into consideration sea disturbances, uncertainty analysis, and ship roll.

## ACKNOWLEDGMENTS

This study was partially supported by the National Natural Science Foundation of China under Grant no. 51579025. We also thank MARIN for sharing the model test data.

## BIBLIOGRAPHY

1. IMO (International Maritime Organization). Regulatory scoping exercise for the use of maritime autonomous surface ships (MASS), MSC 99-WP.9 Report of the working group, London: IMO, (2018).
2. Knud Benedict, Caspar Krueger, Gerd Milbradt, Michèle Schaub, simulation -augmented maneuvering system to support autonomous ships from the shore in different loading conditions, Autonomous Ship Technology Symposium 2016, Amsterdam, (2016).
3. Guo C. Y., Li X. Y., Wang S., Zhao D. G. A numerical simulation method for resistance prediction of ship in pack ice. *Journal of Harbin Engineering University*, (2016), 37(2):145-150.
4. ITTC (International Towing Tank Conference). The maneuvering committee, final report and recommendations to the 25th ITTC. Kgs. Lyngby, Denmark: ITTC, (2008).
5. Jia X, Yang Y. Ship motion mathematical model. Dalian, China: Dalian Maritime University Press, (1999).
6. Abkowitz M A. Measurement of hydrodynamic characteristics from ship maneuvering trials by system identification. *Transactions of Society of Naval Architects and Marine Engineers*, (1980), (88): 283-318.
7. Luo W L, Zou Z J. Identification of response models of ship maneuvering motion using support vector machines. *Journal of Ship Mechanics*, (2007), 11(6): 832-838.
8. Yin J C, Zou Z J, Xu F. Parametric Identification of Abkowitz Model for Ship Maneuvering Motion by Using Partial Least Squares Regression. *Journal of Offshore Mechanics & Arctic Engineering*, (2015), 137(3):031301- 031308.
9. Zhang G. Q, Zhang, Zhang X K, Pang H S. Multi-innovation auto-constructed least squares identification for 4 DOF ship maneuvering modelling with full-scale trial data. *ISA Transactions*, (2015), 58:186.
10. C Källström, Åström, Karl Johan, Identification and Modelling of Ship Dynamics, volume 7015: Lund (Sweden): Identification and Modelling of Ship Dynamics, (1972)
11. Yoon H K, Rhee K P. Identification of hydrodynamic coefficients in ship maneuvering equations of motion by Estimation-Before-Modeling technique. *Ocean Engineering*, (2003), 30(18):2379-2404.
12. Sutulo S, Soares C. G. Offline system identification of ship maneuvering mathematical models with a global optimization algorithm. *Marsim 2015: International Conference on Ship Maneuverability and Maritime*

- Simulation. Tyne and Wear, United Kingdom: Newcastle University, (2015).
13. Haddara M R, Wang Y. Parametric identification of maneuvering models for ships. *International Shipbuilding Progress*, (1999), 46(445):5-27.
  14. Wang N, Er M J, Han M. Large Tanker Motion Model Identification Using Generalized Ellipsoidal Basis Function-Based Fuzzy Neural Networks Design Automation Conference. *Proceedings. ACM/IEEE. IEEE*, (1988):205-210.
  15. Faller H. D., W. Simulation of Ship Maneuvers Using Recursive Neural Networks [C]. *Twenty-Third Symposium on Naval Hydrodynamics*, National Academies Press, 2000.
  16. Moreira L., Soares C G., Dynamic model of maneuverability using recursive neural networks. *Ocean Engineering*, (2003), 30(13):1669-1697.
  17. Oskin D. D. Neural Network Identification of Marine Ship Dynamics Control Applications in Marine Systems. (2013):191-196.
  18. Bai W. W., Ren J. S., Li T. S. Multi-Innovation Gradient Iterative Locally Weighted Learning Identification for A Nonlinear Ship Maneuvering System. *China Ocean Engineering*, (2018), 32(3):288-300.
  19. Zhu M, Hahn A, Wen Y, et al. Identification-based Simplified Model of Large Container Ships Using Support Vector Machines and Artificial Bee Colony Algorithm. *Applied Ocean Research*, (2017), 68:249-261.
  20. Luo W, Li X. Measures to diminish the parameter drift in the modeling of ship maneuvering using system identification. *Applied Ocean Research*, (2017), 67:9-20.
  21. Kijima K, Toshiyuki K, Yasuaki N, et al. On the maneuvering performance of ship with the parameter of loading condition. *Jour of The Soc of Naval Architects of Japan*, (1990), 168(3): 141-148.
  22. Newman J. *Marine Hydrodynamics*. MIT, 1977.
  23. Fossen T I. *Handbook of Marine Craft Hydrodynamics and Motion Control*. (2011).
  24. Ljung L. Perspectives on system identification. *Annual Reviews in Control*, (2008), 34(1):1-12.
  25. Ioannou P A, Sun J. *Robust Adaptive Control*. Springer London, (2015).
  26. Wang X G, Zou Z J, Hou X R, et al. System identification modelling of ship maneuvering motion based on support vector regression. *Journal of Hydrodynamics*, 2015, 27(4):502-512.
  27. IMO, Revision of the interim standards for ship maneuverability ship maneuvering data submitted by the Republic of Korea, (2000), sub-committee on ship design and equipment, 44th session, Agenda item 4.
  28. SNAME. *Nomenclature for treating the motion of a submerged body through a fluid*. Technical and Research Bulletin. New York: The Society of Naval Architects and Marine Engineers, (1950).
  29. Norrbin Nils H., *Theory and Observations on the Use of a Mathematical Model for Ship Maneuvering in Deep and Confined Waters*, Publication No.68 of SSPA. Sweden, (1970)
  30. Ho C H, Lin C J. Large-scale linear support vector regression. *Journal of Machine Learning Research*, (2012), 13(1):3323-3348.
  31. Wang X, Zou Z, Ren R, et al. Black-box modeling of ship maneuvering motion in 4degrees of freedom based on support vector machines. *Shipbuilding of China*, (2014), 55(3):147-155.
  32. Sung Y J, Park S H. Prediction of Ship Maneuvering Performance Based on Virtual Captive Model Tests. *Journal of the Society of Naval Architects of Korea*, (2015), 52(5):407-417.
  33. Yasukawa H, Yoshimura Y. Introduction of MMG standard method for ship maneuvering predictions. *Journal of Marine Science & Technology*, (2015), 20(1):37-52.
  34. Liu H, Ma N, Gu X. Maneuvering Prediction of a VLCC Model Based on CFD Simulation for PMM Tests by Using a Circulating Water Channel ASME 2015, *International Conference on Ocean, Offshore and Arctic Engineering*. (2015):41548-41545.

## CONTACT WITH THE AUTHORS

**Bin Mei**

*e-mail: meibindmu@163.com*

**Licheng Sun**

*e-mail: 13910219827@163.com*

**Guoyou Shi**

*e-mail: allenimitsg@163.com*

Dalian Maritime University

NO. 1 Linghai Road

116026 Dalian

**CHINA**

**Xiaodong Liu**

*e-mail: xdliuros@hotmail.com*

Dalian University of Technology

No.2 Lingong Road, Ganjingzi District

Dalian City

Liaoning Province

116024 Dalian

**CHINA**

## CFGFRPT PILES WITH A CIRCULAR CROSS-SECTION AND THEIR APPLICATION IN OFFSHORE STRUCTURES

Eligiusz Mieloszyk

Marcin Abramski

Anita Milewska

Gdańsk University of Technology, Poland

### ABSTRACT

*The possibilities of using concrete piles in a polymer composite reinforced with glass fibres in offshore facilities were shown. Laboratory tests of CFGFRPT type piles compressed axially and in eccentric compression for the analysis of CFGFRPT piles were used. Methods of analysis of dynamic systems for mathematical modelling of the displacement of the hammer in the pile driving process were applied. The possibilities of combining CFGFRPT piles, including the creation of hybrid piles were also presented. For example, concrete piles can be combined with concrete piles in a polymer composite reinforced with glass fibres with different fibre beam angles. The possibilities of using such hybrid piles in offshore facilities were indicated.*

**Keywords:** concrete-composite piles, composite reinforcement, beam angle, hybrid piles

### INTRODUCTION

Using concrete and composite, it is possible to construct piles with a circular cross-section of different lengths and diameters. These are, for example, CFGFRPT piles (Concrete Filled Glass Fibre – Reinforced Polymer Tubes), i.e. piles in the form of a concrete-filled tube made of glass fibre reinforced polymer composite. A pipe made of composite, used to constrain concrete (called “concrete confinement”), shall be called a pile coating.

It is obvious that a pile structure constructed in this way has mechanical and durability features of concrete as well as of the composite and its reinforcements – in this case, of glass fibres. This combination of materials creates new construction and operation possibilities also for piles used in offshore facilities.

The matrix material is one of the basic factors affecting the process of production and exploitation of the composite material. For the production of composite materials, virtually all groups of manufactured polymeric materials are used, as the polymers themselves generally meet the conditions set for

the components of composite materials. They are corrosion-resistant and lightweight. Their presence greatly minimizes the disadvantages of high-strength fibres, including glass fibres. This is especially true for the brittleness of these fibres [7].

As stated in [7], [23], the first synthetic resins were polyester resins. They are the most frequently used polymer matrices in composites, mainly in glass fibre reinforced composites [7]. Epoxide resins with great possibilities of modifying their properties are also frequently used [7]. They are resistant to the direct influence of water, including seawater. The material of the matrix is also thermosetting epoxy resins mainly due to high mechanical strength, significant chemical resistance and good electrical insulation properties. Contact with water does not adversely affect the properties of this material. So it is advisable to use piles in a composite or fibre-reinforced composite coating in the design and construction of offshore facilities.

As we shall see further, composite materials produced on the basis of resins with reinforcement in the form of glass fibres (Glass Fibre Reinforced Polymer, GFRP – [1]) are exposed to various damage occurring during their operation. Typical



Fig. 1. Stereoscopic view of the fracture of a pipe sample made of glass fibre reinforced composite



Fig. 2. Destruction (debonding) of a pipe made of glass fibre reinforced composite

types of damage that composite materials undergo include: fatigue cracks in the matrix or in the reinforcing fibres, fibre and matrix debonding, and in the case of multilayer materials the damage also include delamination. The crack propagation in the reinforced composite causes the warp crack approaching the fibre and then it develops on the other side of the fibre. At the same time, propagation of the crack occurs along the fibre-warp interface, with the fibre remaining intact. It is only later that the fibre ruptures and is pulled out of the matrix, it disperses the energy of the crack propagation (Fig. 1).

In the case where the composite consists of several fibre layers forming the laminate, the crack propagation process in the material, selecting the path requiring the smallest energy, leads to stratification of the laminate [9], [17], [21]. This is clearly seen in Fig. 2.

If the composite material cracks, its development is important. The correct hypothesis of the development of the crack provides for the determination of the time interval when the crack is subcritical, i.e. the fracture does not develop rapidly, leading to the ultimate fatigue scrap. The methods of fracture mechanics allow estimation of the time of safe work of the structure in conditions where the crack has already occurred. Fatigue hypotheses of linear fracture mechanics can, therefore, be useful in systems monitoring the technical condition of composite structures, where apart from the detection and location of damage it is important to determine the level of risk associated with this fracture. Crack development hypotheses are usually described using ordinary differential equations [13].

As has been mentioned, concrete is introduced into the cylindrical shell (coating) of a reinforced composite. In longitudinally compressed concrete elements with an external coating, the transverse deformation of the concrete due to restraint is limited. As a result, the core concrete of such a construction element operates in a three-axial compression state.

Depending on the type of pile-soil interaction and the manner of transferring loads by the pile to the soil, for the testing of piles, it is possible to use laboratory tests of columns with the same structure as the aforementioned

pile. It can be assumed that in such a case there is a certain mathematical isomorphism between the column and the pile. This relationship will be used in this work. The paper does not deal with pile-soil interaction problems.

## PILES AND CFGFRPT PILES

The preparation of the foundation of the naval structure includes, among others, strengthening the soil foundation. One method of reinforcing the ground is piling. Prior to the piling process, subsoil recognition must be carried out which can be layered [20]. This can be done with the use of static penetration. In the test, a static push probe uses two

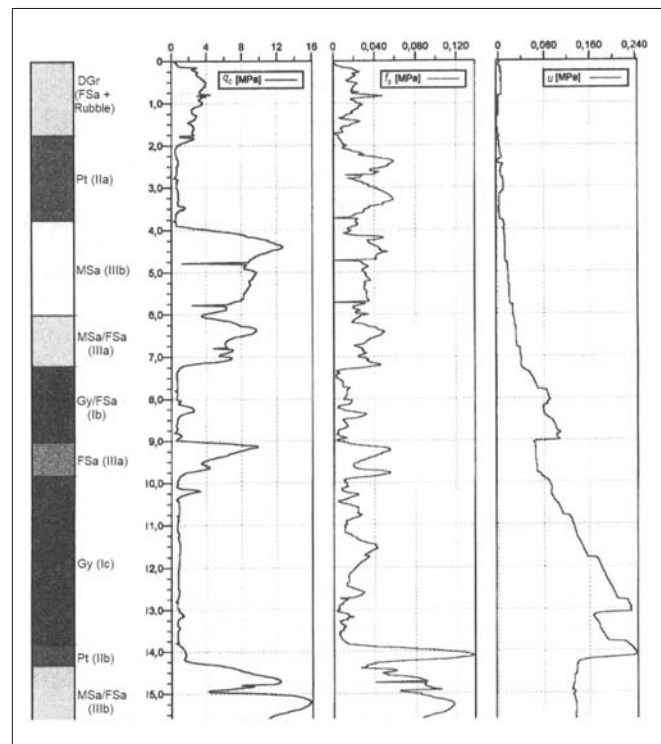


Fig. 3. An example of the CPTU test result at the selected probing point (node) [19]

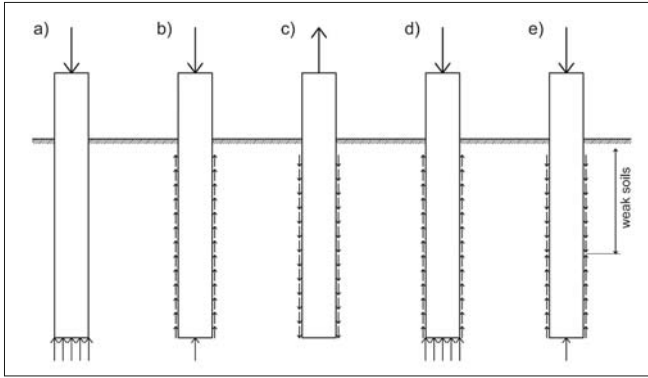


Fig. 4. Scheme of transferring loads through a vertical pile to the soil

methods of penetration. One of them is the CPT method without measurement of water pressure in soil pores and the other – CPTU method with measurement of water pressure in soil pores. The results of such recognition can be presented by means of appropriate graphs (Fig. 3). The diagrams show resistance on the probe cone  $q_c$ , friction on the friction sleeve  $f_s$ , pressure of water in the pores of the soil  $u$ .

The basic task of the pile, as well as the foundation [11], is to transfer loads to the deeper soil layers. That is to more durable layers than the layers through which it passes, e.g. through seabed sediments [8]. Passing loads through a vertical pile to the ground can be done in many ways (Fig. 4): through the base (Fig. 4a), through the pile side, as: push-in (Fig. 4b) or anchor – pulled out (Fig. 4c), through the base and pile side (Fig. 4d) and taking into account negative friction (Fig. 4e), which may occur when the pile is driven through low-bearing soils, non-consolidated e.g. silt, peat, sediments [5].

The pile can be made in the ground or embedded in the ground vertically or diagonally, individually, in groups [4] or rows.



Fig. 6. Sea corrosion of piles [10]

Steel, concrete, reinforced concrete piles (pre-compressed) can be driven into the soil by hammering or pressing. They can be formed with or without a cast pipe (drilled piles). Pallets or impact and vibrating hammers are used to drive in a pile. In the case of offshore works, work is performed using floating floats, special pontoons, work platforms or special vessels. Drilled piles are made using drills. An example of using piles is shown in Fig. 5.

The piles used in offshore facilities are exposed to sea corrosion of concrete and steel (Fig. 6).

Sea corrosion of concrete piles is the destruction of the concrete in seawater. This may be chemical or biological corrosion. The first one includes: corrosion caused by water of low transient hardness (concrete leaching of binder components easily soluble in soft water – leaching corrosion), corrosion resulting from reaction between cement components and aggressive compounds dissolved in seawater (magnesium corrosion), corrosion consisting of on the formation and settling of water-insoluble salt crystals in concrete pores causing concrete disintegration (sulphate corrosion).



Fig. 5. Offshore platforms with connecting bridges [10]

Biological corrosion is caused by the activity of marine pests (pholas dactylus, molluscs, crustaceans). There is also chloride corrosion of reinforced concrete piles, leading to mechanical damage of concrete, occurring when chlorides get to the reinforcement and cause corrosion.

Sea corrosion of steel piles is the destruction of steel piles and steel reinforcement inserts in reinforced concrete piles as a result of seawater.

The piles in the composite or reinforced composite coating, i.e. CFGFRPT piles, are more resistant to the negative impact of seawater on concrete or steel. The mechanical properties of the reinforced coating also cause that such piles are more resistant to lateral forces caused by sea waves. The applied cover limits carbonization of concrete and its cyclical freezing and thawing with penetrating water, thus increasing the lifespan of piles exposed to seawater.

In the case of engineering applications, it is worth bearing in mind that composite-concrete piles, in addition to the features described above, are also characterized by high aesthetic values. For example, directing the laser beam to the GFRP (Glass Fibre Reinforced Polymer) composite gives an interesting effect – Fig. 7.



Fig. 7. The effect of directing a laser light beam on the GFRP composite

As stated in [25] piles for offshore structures have been implemented in the USA in CFGFRPT technology for many years. The use of these piles in the US is regulated by the standard [3], published in 2014 by the world-recognized standardization organization ASTM International. For example, in [24], the use of 28.3 m long piles and of 42 cm outside diameter for the construction of a wharf cover is described. The quays of the port are located in the moderate cold climatic zone with cold winters. The coating walls were 7 mm thick and were made of polymer material reinforced with continuous glass fibre (i.e. roving) type E (fibre made of boron-aluminum-silicon glass). The piles were made outside the construction site.

## LABORATORY TESTS

Cylindrical tubes with a length of 2 m, outer diameter of 0.2 m and medium wall thickness from 5.8 to 7.1 mm were prepared for the tests. The pipes were made of a composite (polyester resin) reinforced with glass fibres E in the form of roving with different beam angles: 20°, 55°, 85°. The beam angle is the angle between the tangent to the winding curve (roving curve) and the generating line of the cylinder. In the laboratory of the Faculty of Civil and Environmental Engineering of the Gdańsk University of Technology, the composite piles (coating) and piles filled with C30/37 concrete according to the Eurocode



Fig. 8. A sample in a hydraulic press



Fig. 9. Destroyed composite coating

were tested. Composite piles and composite piles filled with concrete will also be called samples.

Samples of coating and concrete-filled composite pipes of different beam angles of glass fibres were compressed in a strength hydraulic press manufactured by the Swiss company Walter + Bai AG, model 102/5000-HK4, with a capacity of 5000 kN and with a press piston extension from 0 to 100 mm (Fig. 8). Loading was controlled by a fixed extension of the press piston, or displacement. Due to the assumption (Figure 4a), the samples worked like squeezed poles. A single experiment lasted several dozen minutes until the sample was destroyed – Fig. 9. (See also Fig. 1 and Fig. 2.). Examples of registered test results for compressed samples are shown in Figure 10.

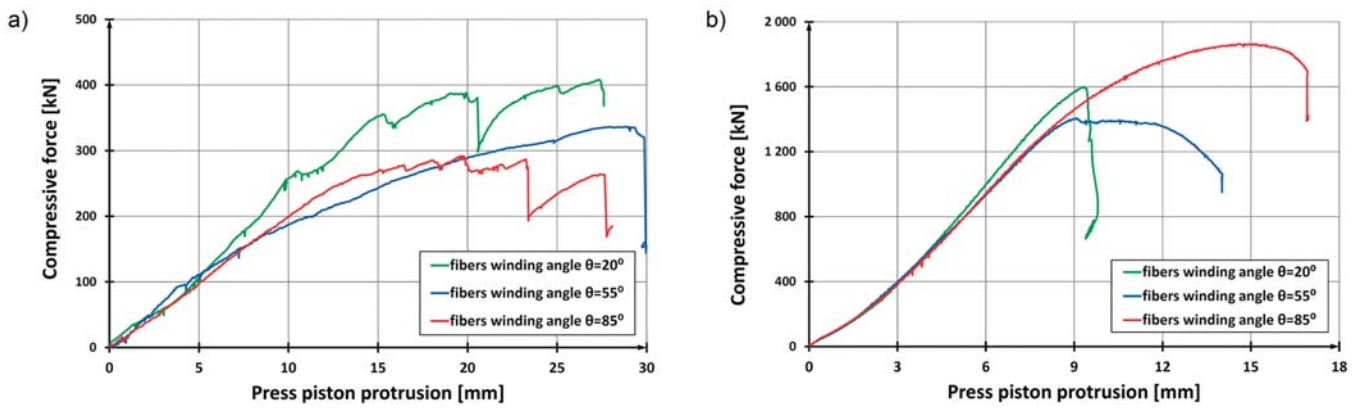


Fig. 10. Relation between force and displacement for: a) coating, b) composite pipe filled with concrete

The experiments carried out show that the load capacity and post-critical behaviour of the samples tested experimentally are determined by the angle of the beam of the glass fibres in the applied coating. Differences in the load capacity of the samples resulting from the different direction of the fibre winding in the coating are up to approximately 30%.

The research shows that the brittle way of destruction (Fig. 1 and Fig. 2) and the low post-load bearing capacity eliminate the piles in the coating with an angle of the beam of fibres close to 20° for offshore applications. This is particularly important where the bearing capacity of offshore structure is important.

Coats with a fibre beam angle close to 20° are characterized by increased longitudinal compression strength (in the described studies by as much as 100%) and a larger modulus of longitudinal elasticity. These advantages, however, are of little relevance to the shortcomings of these composite tubes described earlier.

More details on experiments and laboratory tests can be found in [1], [2].

In offshore structures, piles are exposed to horizontal forces due to the waves of seawater and work simultaneously on compression and bending. This fact was taken into account in the laboratory studies by introducing the replacement piling concept. It is a pile, whose behaviour under the influence of horizontal forces is modelled as the behaviour of an eccentrically compressed pillar supported articulated at both ends.

The columns subjected simultaneously to axial compression and bending are generally designed as eccentrically compressed. The magnitude of the eccentrically compressive axial force  $e$ , compressive  $N$  is the quotient of the bending moment  $M$  and that force  $N$ , acting in the considered cross-section of the pile. A commonly used practical method of calculating the load-bearing capacity of eccentrically compressed concrete columns is the use of nomograms representing the so-called curves of interaction of normal force  $N$  and bending moment  $M$ , simultaneously affecting the cross-section of the column. Such curves can also be made for steel or composite steel-concrete poles, corresponding to the respective piles. Fig. 11 shows an illustrative interaction curve for a CFST (Concrete-Filled Steel Tube) composite column.

The area inside the curve is safe for the load capacity of the column section, and outside – it is dangerous. Similarly, for the pile being modelled here.

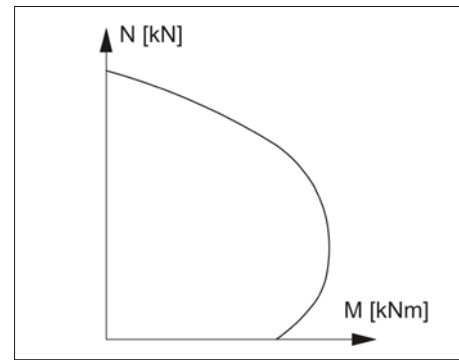


Fig. 11. An interaction curve for a cross-section of an exemplary steel-concrete composite column of the CFST type

Analyzing the impact of horizontal loads on the pile's load capacity, experimental studies of nine eccentrically compressed CFGFRPT columns [1] were used. The samples were made in the same way as the axially compressed samples described earlier. The test conditions of all samples were virtually identical (temperature, humidity, sample preparation, etc. [1], [2]). Among the eccentrically compressed samples, six were compressed on the eccentricity  $e = 26$  mm, and the remaining three – eccentricity  $e = 52$  mm. The first of these values  $e$  corresponds to the boundary of the cross-sectional core. This means that the six described samples experienced the kind of eccentric compression that on one of the edges of the cross-section normal stresses were equal to zero (without taking into account the effects of the second-order). The group of the six examined elements was divided into two subgroups: three were tested as standard, and the remaining three were loaded before the actual test with ten load cycles in the force range from 105 kN to 750 kN. This accounted for a maximum of 88% load capacity of previously tested eccentrically compressed  $e = 26$  mm, not loaded cyclically.

As it turned out, the impact of bending on the load capacity was significant (Fig. 12). As expected, the load capacity of the columns decreased with the increase of eccentricity.

The visible effect of the deadweight capacity of the CFGFRPT samples tested were coating cracks along the fibres

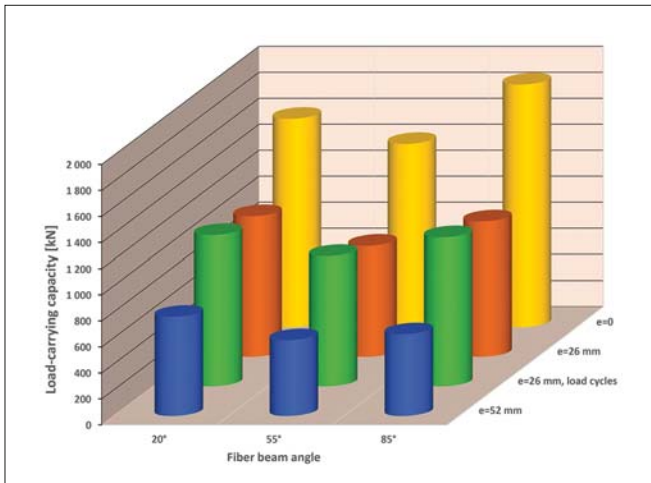


Fig. 12. Load capacity results obtained in experimental studies of CFGFRPT samples

(coat with 20° fibre bundle) or global buckling (coatings with beam angles of 55° and 85°). In the case of the latter, the composite of the coat showed after the test in the central zone (in the zone with the greatest curvature during buckling and at the post-coating step) cracking of the resin matrix, both on the tension side and on the compression side. No damage was observed in the pressure zone of the samples.

CFGFRPT samples with 20° beam were characterized by the most brittle way of destruction. However, they were not the least bearing ones. Certainly, this was due to the high load-bearing capacity of the coating itself, which (without the core) turned out to be twice as large after the test than for the other two types of fibreglass beam.

Attention should also be paid to the fact that in each of the four test series the lowest load capacities were recorded for CFGFRPT samples with a fibre beam angle of 55°. The probable reason for this was the fact that on the one hand they were characterized by low longitudinal strength of the coating, and on the other – the medium ability to excite the triaxial state of compression in the core concrete. However, to confirm this conclusion, a larger number of samples should be tested.

When discussing the results obtained for compressed samples on the eccentricity of  $e = 26$  mm, one should notice a clearly beneficial effect on their bearing capacity of a series of ten cyclic loads carried out prior to the fundamental destructive load. All samples subjected to cyclic loads proved to be more efficient than their counterparts not subjected to these loads. The average percentage difference for the three pairs of samples was 11.4% of the lower load-bearing capacity.

## MATHEMATICAL DESCRIPTION OF THE SELECTED PROBLEM

The driving of piles in the composite coating into the ground is also performed by the hammering method [5], i.e. using impact hammers. This method meets the requirement of the American standard [3]. According to it only the tip of the pile

with a length of 61 cm can suffer damage when driving a pile. In this process, there is also the propagation of vibrations in the pile and in the ground. The process of propagation of vibrations in the ground can be members/elements using analogue models [14]. The impact of the hammer on the pile head can be treated as collisions of the respective masses and analyzed using methods from [16]. The masses  $m_1$ ,  $m_2$  can correspond respectively to the pile weight and hammer mass.

In modelling, all these situations are specific cases of generalized dynamical systems [13] and lead to continuous or discrete dynamic systems [12], [13]. In the first case, the description uses differential equations, and in the second one – difference equations. The results are recorded in the form of continuous  $u$  or discrete  $u_k$  signals. Due to their large diversity in the analysis of the obtained results and further applications, the signal parameters are used along with probabilistic methods [18]. For example, the average of signals is used to average the signal. This parameter for the continuous signal  $u$  in interval  $\langle t_1, t_2 \rangle$  is given by the formula

$$\bar{u} = \frac{1}{t_2 - t_1} \int_{t_1}^{t_2} u(t) dt \quad (1)$$

This parameter is also used in the analysis of signals registered in the CPTU probing process (Fig. 3).

In pile-soil interaction models, rheological elements of the type springs, slide and piston responsible for the inner stickiness can be used [15].

Pile driving is accompanied by various processes. Among them is the displacement  $u_m$  of the hammer.

Taking the designations as in [12] we get a continuous dynamic system described in [12] by the differential equation

$$S^3 u_m + 2nS^2 u_m + p^2 S u_m = 0, \quad (2)$$

where

$$2n = \frac{\beta + \gamma \lambda m_m + \frac{\gamma c_p m_m}{E_p A_p}}{m_m + \lambda \beta m_m + \beta \frac{c_p m_m}{E_p A_p}} \quad (3)$$

$$p^2 = \frac{\gamma}{m_m + \lambda \beta m_m + \beta \frac{c_p m_m}{E_p A_p}}, \quad (4)$$

while

$$S = \frac{d}{dt}$$

In the expressions (3) and (4), the following designations were adopted:

- $E_p$  – substitute modulus of elasticity depending on the modulus of elasticity of concrete and steel or composite,
- $A_p$  – the cross-sectional area of the pile,
- $m_m$  – hammer mass,
- $c_p$  – the velocity of stress waves propagation in the pile,
- $\gamma$  – constant defining the increase in the permanent settlement of pile head,
- $\lambda$  – constant defining the permanent deformation of the pile head,
- $\beta$  – constant taking into account the frictional pressure in the pile head.

Dynamic system (2) is a chain connection of an oscillating element and an integrating element – Fig. 13.

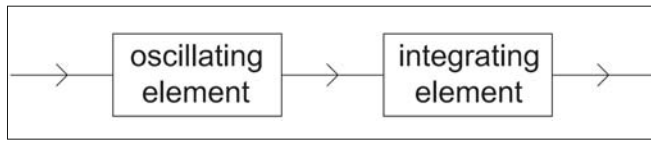


Fig. 13. Chain connection of the oscillating and integrating elements

If so, then the properties of the dynamic system (2) are derived from the connected chains of the oscillating and the integrating elements. The response of the system (2) can be determined using the methods of determining the response of complex dynamic systems [13]. These methods allow formulating patterns for the response of complex dynamic systems. These formulas use formulas for the response of individual members/elements of the system [13]. Directly from these formulas, it follows that the response of the dynamic system (2) with conditions

$$\begin{aligned}
 u_m(0) &= 0 \\
 \dot{u}_m(0) &= \sqrt{2gh} = v_m \\
 \ddot{u}_m(0) &= -\frac{\beta v_m}{\gamma} p^2
 \end{aligned}$$

( $g$  – standard acceleration due to gravity,  $h$  – hammer release height) is given by the formula

$$\begin{aligned}
 u_m &= \frac{v_m}{\sqrt{p^2 - n^2}} [(p^2 - 2n^2) \exp(-nt) \sin \sqrt{p^2 - n^2} t + \\
 &+ 2\sqrt{p^2 - n^2} n (1 - \exp(-nt) \cos \sqrt{p^2 - n^2} t) - \\
 &- \frac{\beta v_m}{\lambda \sqrt{p^2 - n^2}} [\sqrt{p^2 - n^2} (1 - \exp(-nt) \cos \sqrt{p^2 - n^2} t) - \\
 &- n \exp(-nt) \sin \sqrt{p^2 - n^2} t] \quad (5)
 \end{aligned}$$

when

$$p^2 > n^2.$$

Based on the properties of the components of the system, one can infer the properties of a complex system. The properties of generalized dynamic systems [13] show that the spectral transmittance of the system (2) is the product of the transmittance of the oscillating element and the integrating element, and this facilitates the analysis of such systems in the frequency domain.

In complex systems, for example in the case of work of the piles in groups, as is the case in offshore facilities, the work of piles can be analyzed using numerical methods [4].

## COMBINING PILES AND CREATING HYBRID PILES

There are known methods of joining prefabricated concrete piles with a square cross-section. These methods allow for the efficient joining of piles at the construction site using steel joints (Fig. 14).

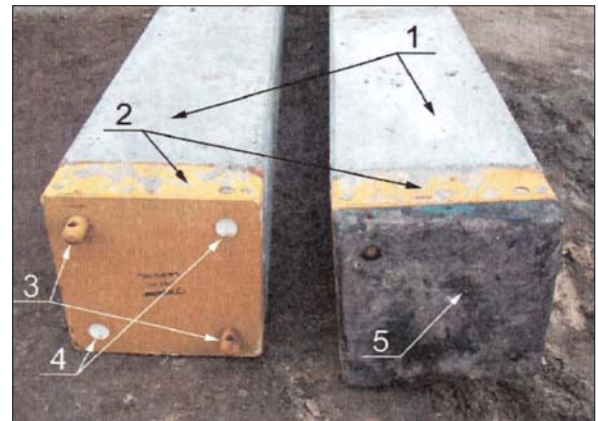


Fig. 14. Prefabricated piles with steel joints [6]: 1 – reinforced concrete piles, 2 – steel joints, 3 – steel bolts with holes for connecting bolts, 4 – steel sleeves for pins with safety plugs, 5 – Teflon washer protecting bolts during pile driving

Using the method of joining piles with 0.4 x 0.4 m cross-section shown in [6], one can propose a method of joining circular piles in a composite coating. On the lower end of the upper pile an “empty roller” without one base (pile shoe) is placed on the pile coating – Fig. 15. The upper end of the lower pile is finished with a full steel cylinder (Fig. 15). The pile shoe and the steel roller together with the pins and sleeves constitute the so-called steel CFGFRPT pile connector.

The steel joint should be anchored in the concrete pile core to a depth of about 1.10 m [6], in the form of spindle extensions with steel bars  $\varnothing 20$  mm. Similarly, as in [6] for piles 0.4 x 0.4 m, it is proposed to use connectors with two pins and two sleeves or with four bolts and four sleeves. The connectors are integrated respectively with four or eight pins  $\varphi 18.8$  mm, made of stainless steel with a design strength of 400 MPa. In the case of the first, these bolts will carry 515 kN, and in the case of the second 1030 kN [6]. In any case, it is the maximum pulling force acting on the pile, which will be transferred by the connecting pins working as double-sided pins.

Between the steel elements of the pile connector, a Teflon washer or a polyurethane spacer (Fig. 15) should be introduced, modelled on polyurethane pads, for example type PWE6094. Due to its properties, it will ensure good cooperation between the contacting surfaces of the steel joint.

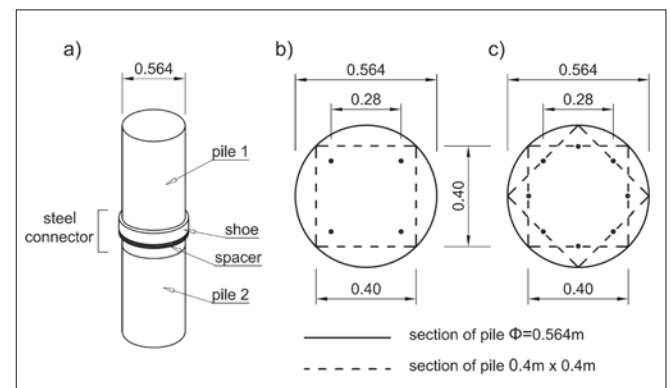


Fig. 15. Steel joint for circular piles in a composite coating: a) diagram for joining piles, arrangement of bolts and sleeves: b) two bolts and two sleeves, c) four bolts and four sleeves (Dimensions in Fig. 15b and 15c are based on a pile with a 0.4 x 0.4 m cross-section)

Additionally, the spacers are resistant to cyclic loads ( $3 \times 10^6$  cycles) or temperature changes. They have insulating properties (including electrical). They have a long service life – even after 10 years of use, the physical and strength tests of the spacers give good results. The applied spacer in the steel joint will fulfil a similar beneficial role in the steel connection of the piles, as the spacers in rail connections.

When more than two piles are connected to each other, the initial and final piles have one element of the steel joint (respectively the shoe and the other element of the joint). The remaining piles have complete joints, as in Fig. 15.

As has already been mentioned, piles of offshore facilities are exposed to corrosion of concrete and steel under the influence of the seawater environment. Marine corrosion is primarily limited to zones of varying levels of the seawater surface, especially to splash zones. There its intensity is the greatest. In principle, offshore steel structures are corrosion resistant only when they are permanently submerged in seawater. Mainly at greater depths, where oxygen access is limited. The average increase in corrosion of steel offshore facilities is about 0.10 mm per year. However, the strongest corrosion occurs at a depth of about 0.5 m below the average level of the water surface, because at this level seawater has a higher content of oxygen and salt than on the surface.

From these facts, it appears that at least in the zone directly above and below the surface of the seawater surface, it is worth using CFGFRPT piles that are resistant to seawater. It is enough, therefore, to use hybrid piles. A hybrid pile is a combination of a pile without a coating with a pile in a composite coating (Fig. 16).

In the subsurface zone, it may be a part with a composite coating of a hybrid pile, and below this zone, it may be a part without a composite coating. Both parts of the hybrid pile are connected with each other by a steel joint (Fig. 15).

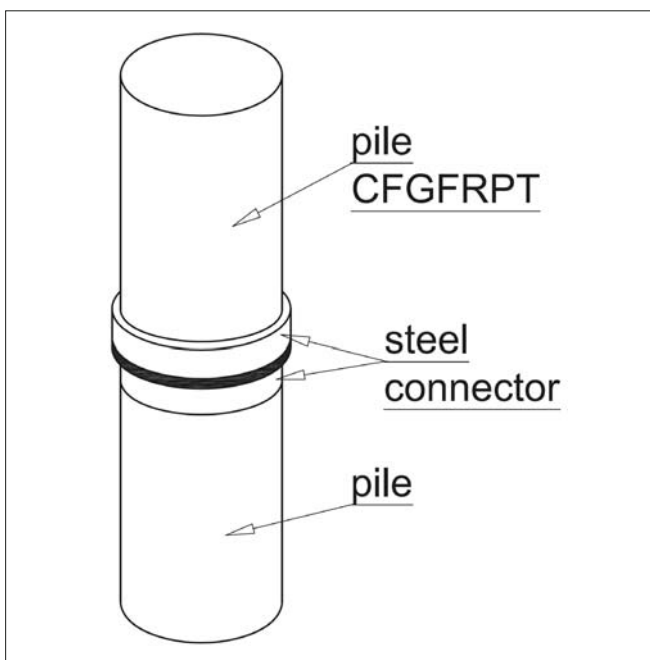


Fig. 16. Hybrid pile scheme (a combination of pile with no coating with pile in composite coating)

## CONCLUSION

The use of a composite concrete pile coating prevents physical, chemical and biological degradation of concrete and steel. It limits the carbonization of concrete and its cyclical freezing and thawing with penetrating water, thus increasing the lifetime of piles exposed to seawater in offshore facilities.

CFGFRPT piles are characterized by the simplicity of their technology (i.e. concreting and the possibility of driving them in the ground by classical methods) and high aesthetics.

The introduction of the concept of isomorphism between the pile and the column allowed the use of laboratory tests of piles in the reinforced composite coating to determine the behaviour of a certain type of piles.

Eccentric compression of the samples allowed to assess the impact of simultaneous axial compression and bending of the pile on its life.

The mechanical properties of the glass fibre reinforced coatings also cause that these types of piles are more resistant to lateral forces caused by sea waves.

A significant influence of the beam angle of the glass fibres on the work of piles has been demonstrated.

It is advisable to use combined piles (hybrid piles) in surface water zones.

The use of hybrid piles is an important form of corrosion protection for piles of offshore facilities.

Serial connection of basic elements of dynamic systems is beneficial from the point of view of mathematical modelling of problems related to the functioning of piles.

To increase the load-bearing capacity of the soil substrate other methods can be used to improve its quality [22].

Coatings made of glass fibre reinforced composites are easy to be recycled, for example, using the energy method.

The use of CFGFRPT piles and hybrid piles in offshore infrastructure facilities is fully justified.

## REFERENCES

1. Abramski, M. *Short-time load-carrying capacity of columns with a circular cross-section made of FRP tubes filled with concrete. Experiments, theory, design.* Gdansk University of Technology, Gdansk, 2019.
2. Abramski, M., Mieloszyk, E., and Milewska, A. Determination of the shape of the CFGFT cylindrical column based on laboratory tests (in preparation).
3. ASTM. D7258-14: Standard Specification for Polymeric Piles. 2014.
4. Van Eekelen, S.J.M. The 2016-update of the Dutch Design Guideline for Basalt Reinforced Piled Embankments. In *Advances in Transportation Geotechnics 3. The 3rd International Conference on Transportation Geotechnics (ICTG 2016)*. Procedia Engineering, 2016, pp. 582–589.

5. Gwizdała, K. *Pile foundation. Technologies and calculations (in Polish)*. Wydawnictwo Naukowe PWN, Warsaw, 2019.
6. Gwizdała, K. and Kowalski, J. *Prefabricated driven piles (in Polish)*. Gdansk, 2005.
7. Leda, H. *Polymer composites with continuous filaments (in Polish)*. Wydawnictwo Politechniki Poznańskiej, Poznań, 2000.
8. Magda, W. Comparison of soil models in the thermodynamic analysis of a submarine pipeline buried in seabed sediments. *Polish Maritime Research*, 24, 4 (2017), 124–130.
9. Mazumdar, S.K. *Composites Manufacturing: Materials, Product, and Process Engineering*. CRC Press, 2002.
10. Mazurkiewicz, B. *Encyclopedia of marine engineering (in Polish)*. Fundacja Promocji Przemysłu Okrętowego i Gospodarki Morskiej. Oficyna Morska., Gdansk, 2009.
11. Meyer, Z. *Engineering calculations of settlement on foundations (in Polish)*. ZAPOL Publishing, Szczecin, 2012.
12. Mieloszyk, E. *Operational calculus and the dynamics of mechanics in the civil and hydro – engineering (in Polish)*. Gdansk University of Technology, Gdansk, 1998.
13. Mieloszyk, E. *Non-classical operational calculus in application to generalized dynamical systems (in Polish)*. Polish Academy of Sciences Scientific Publishers, Gdansk, 2008.
14. Mieloszyk, E. and Grulkowski, S. Analog modeling in qualitative analysis of vibration propagation. *Transportation Overview*, 9 (2017), 18–21.
15. Mieloszyk, E. and Milewska, A. Modeling of soil interaction using generalized dynamical systems. In *11th Baltic Sea Geotechnical Conference. Geotechnics in Maritime Engineering*. Gdansk, 2008, pp. 735–742.
16. Mieloszyk, E., Milewska, A., and Grulkowski, S. Effect of vehicle motion stability after impact / crash on traffic safety. *MATEC Web of Conferences*, (2018), 1–9.
17. Ochelski, S. *Experimental methods in mechanics of fibre composites (in Polish)*. Wydawnictwa Naukowo-Techniczne, Warsaw, 2004.
18. Puła, W. and Zaskórski, Ł. Estimation of the probability distribution of the random bearing capacity of cohesionless soil using the random finite element method. *Structure and Infrastructure Engineering*, 11, 5 (2015), 707–720.
19. Sikora, Z. *Static probing. Methods and application in geoen지니어ing (in Polish)*. Wydawnictwa Naukowo-Techniczne, Warsaw, 2006.
20. Szypcio, Z. and Dołżyk, K. The bearing capacity of layered subsoil. *Studia Geotechnica et Mechanica*, 28, 1 (2006), 45–60.
21. Vasiliev, V. and Morozov, E. *Mechanics and Analysis of Composite Materials*. Elsevier, 2001.
22. Wyroślak, M. Dynamic soil improvement by hybrid technologies. In *Geotechnical Engineering for Infrastructure and Development*. ICE Publishing, 2015, pp. 1469–1474.
23. *Plastics – Guide*. Wydawnictwa Naukowo-Techniczne, Warsaw, Poland, 2000.
24. Information and promotion materials of the Lancaster Composite. Select Installations – Port Hadlock, Washington State. 2013. <http://www.lancastercomposite.com/installation08.html>.
25. Information and promotion materials of the Lancaster Composite. Lancaster CP40 Pile. Design Guide. Fibreglass/concrete composite marine piling. 2014.

## CONTACT WITH THE AUTHORS

**Eligiusz Mieloszyk**

*e-mail: eligiusz.mieloszyk@pg.edu.pl*

**Marcin Abramski**

*e-mail: marcin.abramski@pg.edu.pl*

**Anita Milewska**

*e-mail: animilew@pg.edu.pl*

Gdańsk University of Technology

Narutowicza 11/12

80-233 Gdansk

**POLAND**

# OPTIMIZING THE SHAPE OF A COMPRESSION-IGNITION ENGINE COMBUSTION CHAMBER BY USING SIMULATION TESTS

Ireneusz Pielecha

Jerzy Merkisz

Poznan University of Technology, Poland

## ABSTRACT

*Modern solutions used in compression-ignition internal combustion engines are quite similar to each other. The use of high-pressure, direct fuel injection results in high combustion rates with controlled exhaust emissions. One of the combustion system quality criteria is to obtain adequately high thermodynamic indicators of the combustion process, which are obtained through, among others, the right combustion chamber geometry. Its shape influences the fuel atomization process, turbulence of fuel dose, evaporation and the combustion process. Optimizing the combustion chamber shape is one of the decisive factors proving the correct execution of the combustion process. This article presents the methodology of choosing the combustion chamber shape (changes of three selected combustion chamber dimensions) by using the optimization methods. Generating multidimensional data while maintaining the correlation structure was performed by using the Latin hypercube method. Chamber optimization was carried out by using the Nelder-Mead method. The combustion chamber shape was optimized for three engine load values (determined by the average indicated pressure) at selected engine operating conditions. The presented method of engine combustion chamber optimization can be used in low and high speed diesel propulsion engines (especially in maritime transport applications).*

**Keywords:** CI engine combustion system, combustion process thermodynamic analysis, combustion chamber optimization

## INTRODUCTION

The internal combustion engine design quality is defined by its operational indicators. Currently the engine capability of meeting the emission limits can be considered an additional indicator of structure quality. These two indicators mean that internal combustion engines must meet various, often widely different requirements.

The operating indicators for four-cycle low-speed internal combustion engines are currently rather large. The average indicated pressure of two-stroke engines is about 2.1 MPa with a specific fuel consumption value (dual fuel mode – methane injection) of 129 g/kWh (i.e. MAN B&W G35ME-C10.5-GI). The brake mean effective pressure (BMEP) of four-stroke engines ranges from 2.25 MPa with a specific fuel consumption (SFC) of 186 g/kWh (gas mode) (i.e. MAN

L51/60DF) up to 2.83 MPa at SFC reaching 175.5 g/kWh ( $n = 720$  rpm) (i.e. MAN L32/44CR) [7].

Compression-ignition engines also gain slightly higher values. The Wartsila 31 engine has a BMEP of 3.1 MPa (at  $n = 750$  rpm) and a power of 610 kW/cyl. [15].

One of the main systems responsible for the internal combustion engine design quality is the combustion system along with the fuel supply system. The main problem in that case is the shape of the combustion chamber. Its shape and dimensions depend on the method of fuel injection and atomization, the fuel dose turbulence size, and the combustion process. The formation of exhaust components, with particular focus on the nitrogen oxides and solid particles emission, is an important aspect of the combustion chamber shape. The use of dual-fuel (liquid and gas fuels) combustion systems [11] does not allow to fully optimize this structure, as it would

necessitate meeting requirements related to different fuel properties that are at times in opposition to each other. The use of fuel additives [10] also allows to control the combustion process, but to a lesser extent than the optimal shape of the combustion chamber.

## IMPACT OF THE COMBUSTION CHAMBER SHAPE ON ENGINE OPERATING INDICATORS

Experimental research on combustion chamber optimization in stationary CI engines was carried out by Vedharaj et al. [14]. The impact of the trapezoidal and toroidal chamber (one cylinder, four stroke engine (S x D – 87.5 x 110 mm) using the Kapok methyl ester and diesel blend (KME – diesel blends) was tested. As a result, it was found that exhaust emission can be reduced by using the TCC (toroidal combustion chamber) and an increase of the BTE (brake thermal efficiency) can be reached.

Similar studies with using the chambers: Hemispherical, Straight Sided, Toroidal and Re-entrant Toroidal were conducted by Channappagoudra et al. [2] powering the CI engine with the B20 fuel. The best parameters of engine operation and exhaust emission indicators were obtained by using the Re-entrant Toroidal chamber.

Experimental studies along with model ones were conducted by Khan et al [5]. He analyzed the experimental Hemispherical chamber and development of the fuel stream and compared the tests with theoretical models containing the Toroidal Re-entrant (TR) and standard toroidal chamber. Simulation results show that spray angle significantly affects the mixing and combustion process for all three bowl geometries and that the engine having TR combustion chamber gives better performance (generate a strong squish and turbulence).

Simulations of the combustion chamber shape were carried out by Gaffor and Gupta [3]. Using the rectangular shape of the combustion chamber, they showed that a low d/D ratio (bowl diameter to cylinder diameter) increases NO emission and decreases soot emission due to the high combustion rate within TDC.

Similar simulation research on combustion chamber optimization was conducted by Navid et al. [9] and Taghavifar [13]. The results of the works relate to high compression ratios (19.5:1). The exhaust emission values were not analyzed in these works. In [9] several optimization methods were compared and a high similarity of the obtained results was noted.

## AIM AND SCOPE OF RESEARCH WORK

The aim of the simulation research is to find the combustion chamber shape which exhibits the maximum indicator values of thermodynamic process in the form of the brake mean effective pressure. It is possible to choose a different indicator, however, in traction applications of low-speed internal combustion engines, the requirements concerning exhaust emissions are not the ones which play the most important role.

For this reason, an indicator has been chosen which allows to make significant changes in the shape of the combustion chamber (by changing selected quantities of its shape).

The scope of the work related to optimization concerns: 1) pressure analysis in the combustion chamber, 2) heat dissipation rate, 3) total heat released, 4) change of excess air coefficient, 5) indicated engine efficiency, 6) mechanical efficiency and 7) exhaust emission analysis of the combustion process (NO and soot emission).

## RESEARCH METHODOLOGY

### COMBUSTION CHAMBER GEOMETRY

For simulation analysis an example (typical) combustion chamber of a CI engine was chosen. The scope of the simulation work concerned the change of the following design variables (Fig. 1):

- Combustion chamber radius – R3,
- Distance between the piston and the engine head – TDC,
- The depth of the combustion chamber at its centre – Tm

in order to obtain the maximum indicated mean effective pressure – IMEP.

As a result of changing the listed values, the combustion process itself changes due to the fuel dose preparation process being altered (change of compression ratio due to the change in the combustion chamber size, resulting in different compression pressure values during ignition, with consequences in the form of thermodynamic and emission impact of the process).

### THE BOUNDARY AND INITIAL CONDITIONS OF THE SIMULATIONS

The simulation tests were carried out in typical operating conditions of a medium-speed engine (such as a marine engine) by using the AVL FIRE software [1]. The characteristics of engine geometry are presented in Tab. 1. The initial and boundary conditions of the simulation tests are listed in Tab. 2. The thermodynamic gas characteristics during compression were provided and the used calculation models described. Important data regarding fuel injection are presented in Tab. 3.

Tab. 1. Characteristics and parameters of the engine used in simulations

No.	Parameter	Unit	Value
1.	Number of cylinders	-	1
2.	S x D	mm x mm	85 x 90
3.	Connecting rod length	mm	94
4.	$\epsilon$ (initial)	-	16

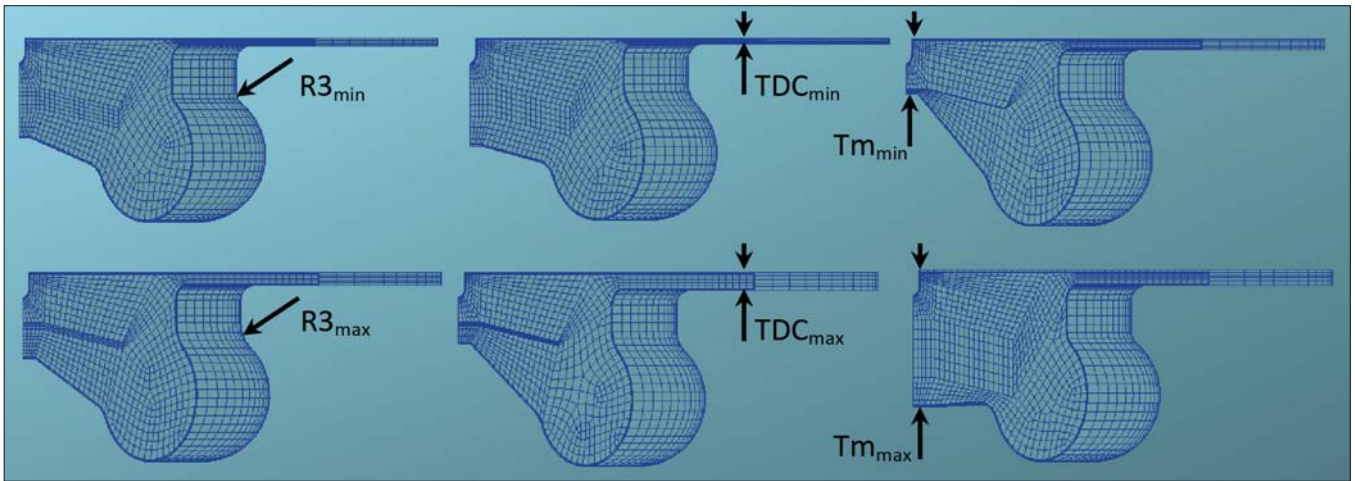


Fig. 1. Combustion chamber shape with changing design variables

Tab. 2. Simulation parameters

No.	Description	Unit	Value
1.	Engine speed	rpm	1000
2.	Start of simulation	deg	540
3.	End of simulation	deg	800
4.	Initial cylinder pressure	MPa	0.15
5.	Initial fuel dose temperature in the cylinder	K	380
6.	Initial wall temperature: piston liner	K	575
	head	K	475
		K	550
7.	Initial turbulent kinetic energy (TKE)	m <sup>2</sup> /s <sup>2</sup>	10
8.	Initial turbulent length scale	m	0.003
10.	Breakup model	Wave	
10.	Evaporating model	Dukowicz	
9.	Wall model	Walljet1 (Naber&Reitz)	
10.	Combustion model	Coherent Flame Model: ECFM-3Z Autoignition: Two-stage	
10.	Model NO	Extended Zeldovich	
11.	Soot model	Kinetic Model	

Tab. 3. Fuel injection conditions

No.	Parameter	Unit	Value
1.	Start of injection (SOI)	deg	719
2.	Injection time	ms	1
3.	Fuel mass	mg	12; 20; 40
	Fuel temperature	K	330.15

In the wave disintegration model of the droplet the initial increase in turbulence on the fluid surface is used along with the increase in the wavelength and other physical and dynamic parameters of the injected fuel. Two disintegration systems can be distinguished: for small and high speeds. The Dukowicz model was used to simulate evaporation of fuel droplets [1]. It is based on typical coefficients of heat and mass exchange, with the assumptions that 1) the spheres are symmetrical, 2) the film on the surface of fuel drops is quasi-permanent, 3) the temperature of the droplets is uniform along its diameter, and 4) the drop surface is in a thermal liquid-gas balance. Walljet model (wall model) is based in principle on the spray/wall impingement model of Naber and Reitz [8]. The concept is that in the working engine conditions a vapor cushion is formed under the droplets and that they rebound or slide along the walls. The ECFM combustion model (Extended Coherent Flame Model) applies to a turbulent premixed combustion regime, using a chemical time scale, integral length scale and turbulence intensity. The extended Zeldowicz model concerns the formation of nitrogen oxides through three reactions:  $N_2 + O$ ;  $N + O_2$  and  $N + OH$  [1, 4]. The basis of the kinetic model (soot model) is a detailed chemical reaction scheme for the calculation of soot formation and oxidation (the complete model contains over 100 reactions; 7 oxidation reactions of various hydrocarbons have been implemented in AVL Fire software) [1].

#### METHOD OF GENERATING MULTIDIMENSIONAL DATA

By using the DVI (Design Variation Interface) module of the AVL Fire software, the design variables of the following basic values have been assigned:

$R3 - 0.00242857$  m (variation  $\pm 50\%$ ),

$Tm - 0.00121429$  m (variation  $\pm 50\%$ ),

$TDC - 0.00886429$  m (variation  $\pm 50\%$ ).

To generate multidimensional data while maintaining the correlation structure, the Latin-Hypercube method was used [12]. This method divides the design space of every

factor  $n$  (each variable) evenly into 10 levels. There is only one point on each project ? level. In the columns of the designed matrix there are  $n_k$  combinations with the same probability of occurring. Because the matrix is randomly generated, there may be a correlation between the columns. The structure associated with 10 research samples was used for the analysis (Fig. 2).

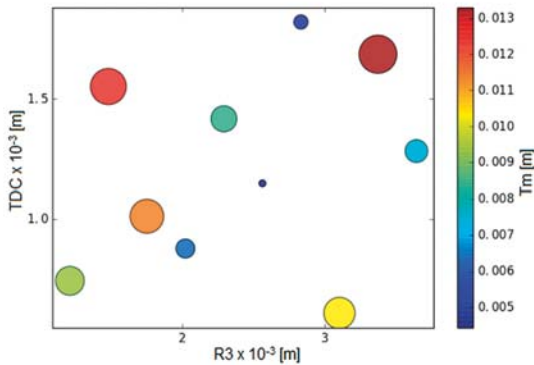


Fig. 2. The method of selecting initial data for optimization of three variables – 2D view

The initial data generated this way was subject to further optimization.

### OPTIMIZATION PROCEDURE

The optimization task was based on the Nelder-Mead method (*downhill simplex method*) [6]. To simplify: it consists of a gradual transformation of the simplex (in the three-dimensional space it is a tetrahedron) in such a way that in each next iteration the worst point can be replaced with a specially created new one.

In the optimization task, the target function (maximization of average indicated pressure) takes the form:

$$f(R3, Tm, TDC) = \max \quad (1)$$

where the starting values of design variables and their variability ranges (restrictions) are as given previously.

The generated starting data (10 solutions) and optimization conditions created more than 20 configurations of combustion systems, whose target function was maximized (max IMEP).

The research was carried out by using the ESE Diesel software from the AVL Fire package [1]. For each case, a new mesh was generated and calculations were made for modification of design variables (R3, Tm, TDC) in the range of 540 to 800 deg on the crankshaft. Changes in the shape of the combustion chamber resulted in thermodynamic changes (with special regard to IMEP as a target function) and emission changes for these combustion processes.

### OPTIMIZATION OF THE COMBUSTION CHAMBER IN THE ASPECT OF ENGINE LOAD

The analysis of optimal solutions was carried out individually for each engine load value. The assessment of optimal design variables indicates that the variation of the variables depends on the engine load (Fig. 3). The largest differences were obtained for changes in the value of the variable R3, where, with increasing engine load, the optimal value of this variable is not predictable.

A complete analysis of changes in the design variable values is presented in Fig. 4. It shows that increased load requires:

- reducing the size of radius R3,
- reducing the TDC value

and an undefined change in the size of Tm (average engine load causes a drop of this value – Fig. 4b, while other loads increase it). Analysis of changes in the search for individual variables (Fig. 4) indicates the same directions of changes of these values regardless of the load. However, the obtained results of the target function are not similar. The first 10 attempts created on the basis of the Latin hypercube are the same (same values of design variables), which does not result in identical changes of the target function. For this reason, point 11 (Fig. 4) is similar to the values of design variables leading to the maximization of the target function in the first ten attempts.

The combustion chamber optimization should result in different values of compression and combustion pressure. Such conditions should also cause differential thermodynamic properties of the combustion process and exhaust emissions. Their analysis was carried out in the next part of the article.

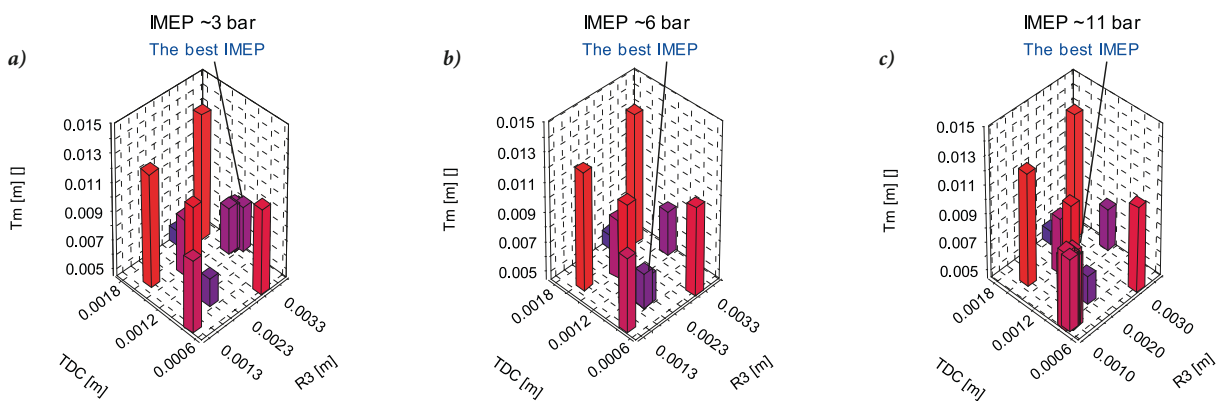


Fig. 3. Three-dimensional layout of operational indicators within the combustion chamber optimization with three IMEP load values: a) 3 bar, b) 6 bar, c) 11 bar

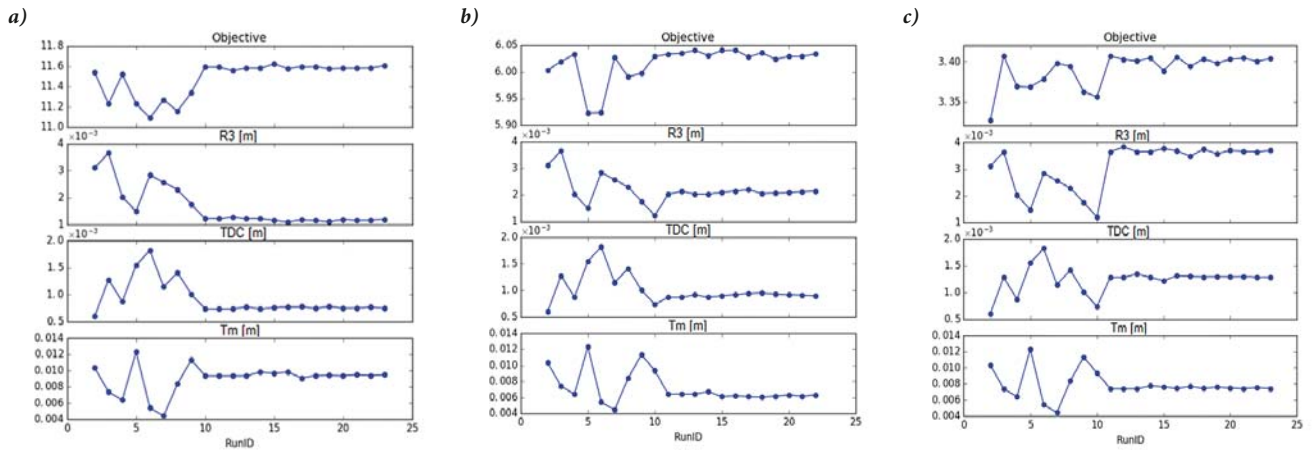


Fig. 4. One-dimensional change of three operating indicators as a part of the combustion chamber optimization with three values of the initial IMEP load: a) 3 bar, b) 6 bar, c) 11 bar

## THERMODYNAMIC ANALYSIS RESULTS

$$\text{CoV}(X) = Y_{\text{av}}/\sigma \quad (2)$$

Comparison of the final compression pressure values indicates significant changes in this variable when the shape (and volume) of the combustion chamber changes. The maximum and minimum values of compression pressure are the same as they result from the first 10 settings of the combustion chamber (Latin hypercube – Fig. 4 – vertical red line). These values are as follows:  $P_{\text{comp}} = 5.68$  and  $7.07$  MPa, respectively. However, the research values are already different and result from searching for the optimal solution.

For each load, the coefficient of variation of the X value is determined as:

where:  $Y_{\text{av}}$  is the mean measured value of Y,  $\sigma$  – standard deviation.

At low load (IMEP = 3 bar) the coefficient of variation  $\text{CoV}(P_{\text{comp}})$  is 3.3%, with load increase of 4.4% and 4.8%, respectively. This means increasing the final compression pressure ( $P_{\text{comp}}$ ) together with the search for the optimum value of the indicated mean effective pressure (Fig. 5a). The change in the final compression pressure resulted in much larger changes in the maximum combustion pressure. The coefficients of variation  $\text{CoV}(P_{\text{max}})$  corresponding to the increased load are respectively: 2.78%; 3.64% and 4.33%. Similarly to  $\text{CoV}(P_{\text{comp}})$  also  $\text{CoV}(P_{\text{max}})$  attains higher values when increasing the load.

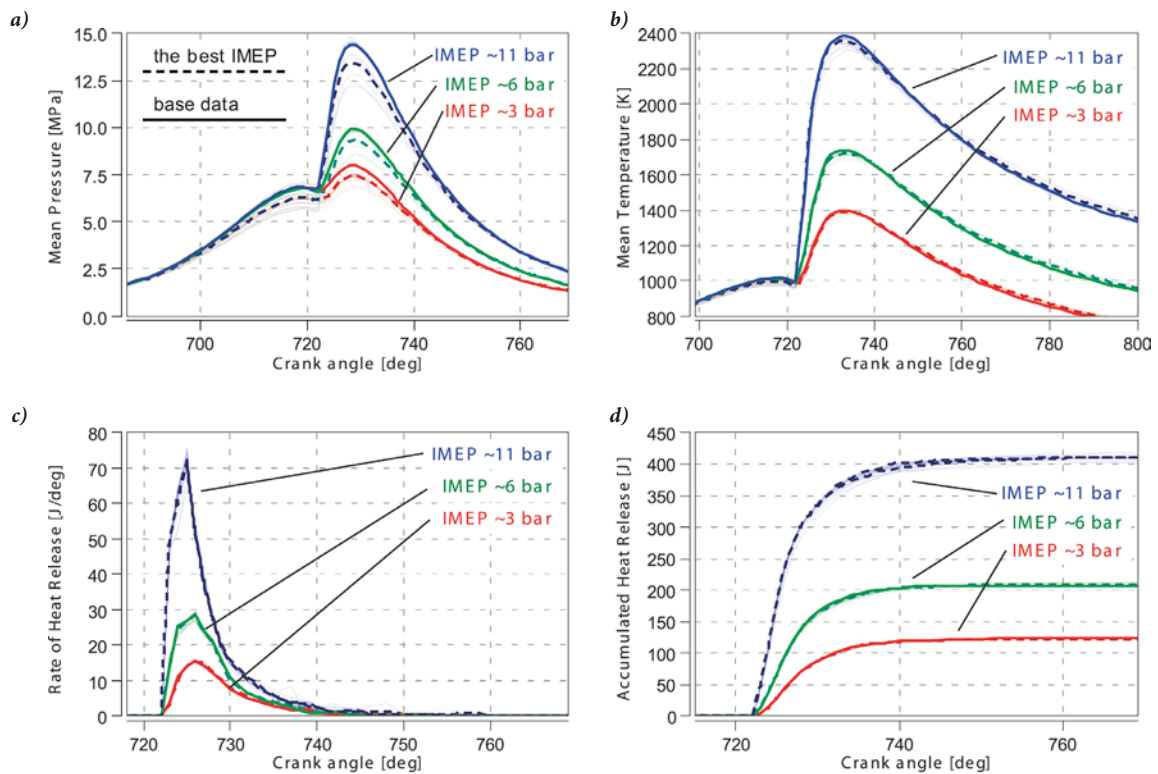


Fig. 5. Thermodynamic indicator changes of the combustion process for combustion chamber optimization with three IMEP load values: 3 bar, 6 bar, 11 bar: a) combustion pressure, b) average process temperature, c) heat recovery rate, d) heat value

## EXHAUST EMISSION ANALYSIS

Such results indicate that it is more difficult to obtain an optimal solution at a higher load value (this is not caused by the irregularity of engine operation). Larger  $CoV(P_{max})$  values when increasing the load also indicate that the initial conditions for the search of the maximum of the target function (max IMEP) adopted on the basis of the Latin hypercube are quite different.

The special feature of such procedure is also the situation that – despite different values of pressure changes in the cylinder ( $P_{comp}$  and  $P_{max}$ ) – other thermodynamic process indicators (temperature, heat recovery rate and heat delivered) have similar characteristics. This means that it is possible to shape the target function by using the variability of design values in a fairly wide range. The optimal values of thermodynamic indicators, marked with a dashed line, can easily be distinguished from the pressure characteristic in the cylinder, but the deviations of the remaining values from the optimal value are small (Fig. 5b–d).

Initial values of the combustion chamber design variable settings (R3,  $T_m$ , TDC) result in small changes in the internal combustion engine operating indicators. The IMEP variability coefficient at different settings takes values below 1.3% (at the maximum load) – Fig. 6a. Indicated engine efficiency is maintained at 33 to 37% (assuming maximum values at partial load) – Fig. 6b. The lowest specific fuel consumption value was obtained at the average engine load and reached 233 g/kWh. The engine mechanical efficiency increases with the load and reaches a maximum of 80% (Fig. 6c). The maximum dispersion of the excess air coefficient is  $CoV(\lambda) = 0.27\%$ , which is the smallest value analyzed.

The analysis of nitrogen oxide share was based on the Extended Zeldovich model [4]. The local temperature value in the combustion chamber plays a significant role in this model. Analysis of the process mean temperature value (Figure 5b) indicates that the value of nitric oxide concentration will also be subject to high variability. The results of the NO concentration simulation are shown in Fig. 7. The values for the optimal combustion chamber fulfilling the target function indicates the NO concentration greater than the base values but still below the maximum values. It follows that it is possible to design a combustion chamber to maximize IMEP while maintaining average nitric oxide concentration values. Determining the NO emission (expressed in g/kWh) should result in values below the maximum as a result of the presented characteristics changes (Fig. 7a). Similar concentration levels were obtained for greater engine loads. In both subsequent cases, the optimal chamber geometry allows obtaining NO concentration values below the maximum values (Fig. 7b and 7c).

The soot concentration was determined based on the kinetic model. The basis of this model is a detailed chart of chemical reactions to calculate the formation and oxidation of soot [1]. The differences in the quantities are small (Fig. 8) due to the high soot concentration in the flame in the initial combustion phase. The formation of soot in the cylinder increases with the increase in engine load. The maximum values are proportional to the engine load. Optimal dimensions of the combustion chamber (to reach the maximum value of the target function)

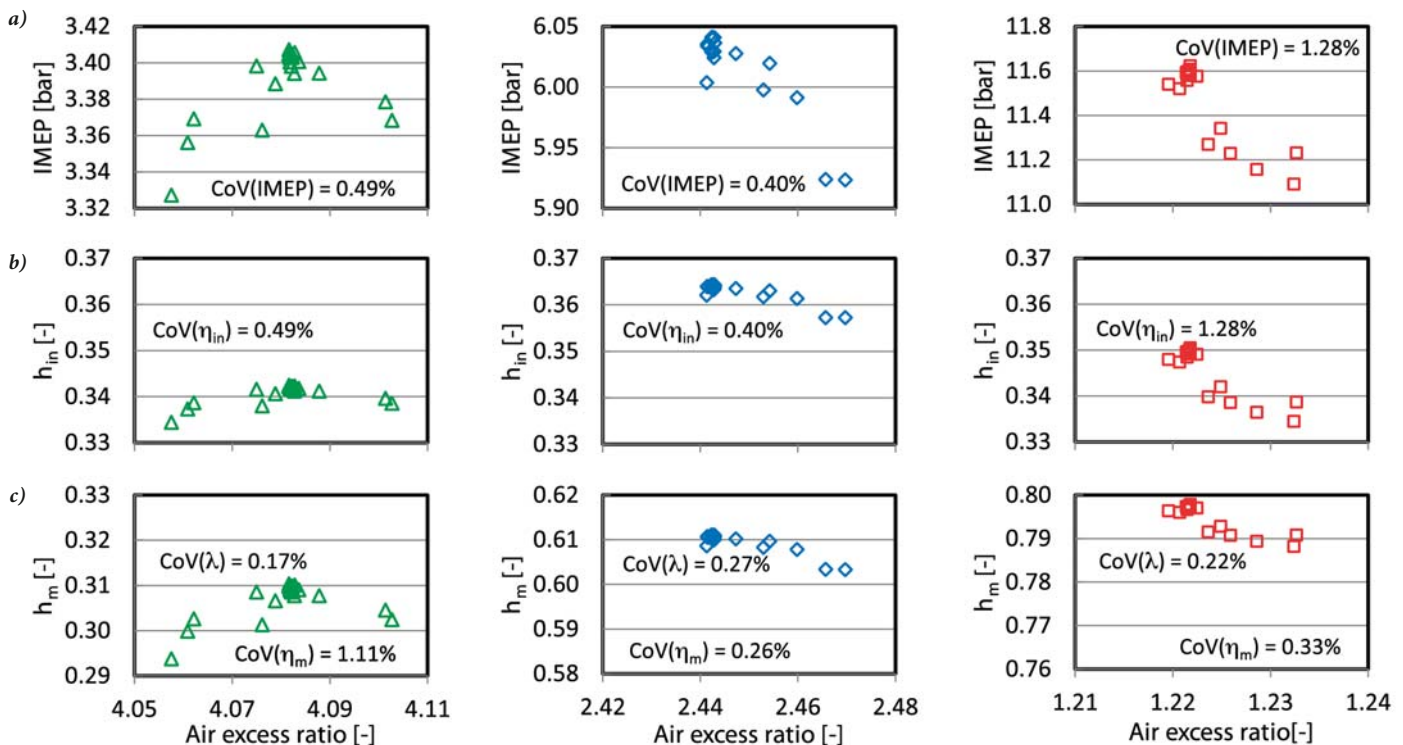


Fig. 6. Analysis of engine operating indicator changes: a) indicated mean effective pressure IMEP, b) indicated efficiency  $\eta_{in}$ , c) mechanical efficiency  $\eta_m$  in function of the excess air coefficient resulting from changes in the shape of the combustion chamber

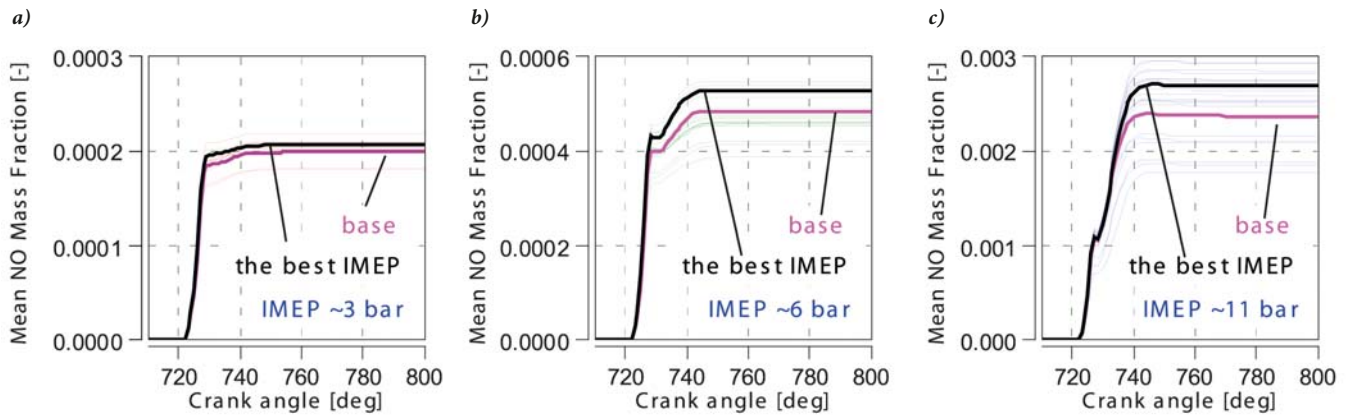


Fig. 7. Mass proportions of nitrogen oxide for various engine loads along with the initial values and corresponding to the optimal dimensions of the combustion chamber to maximize the target function: a) IMEP = 3 bar, b) IMEP = 6 bar, c) IMEP = 10 bar

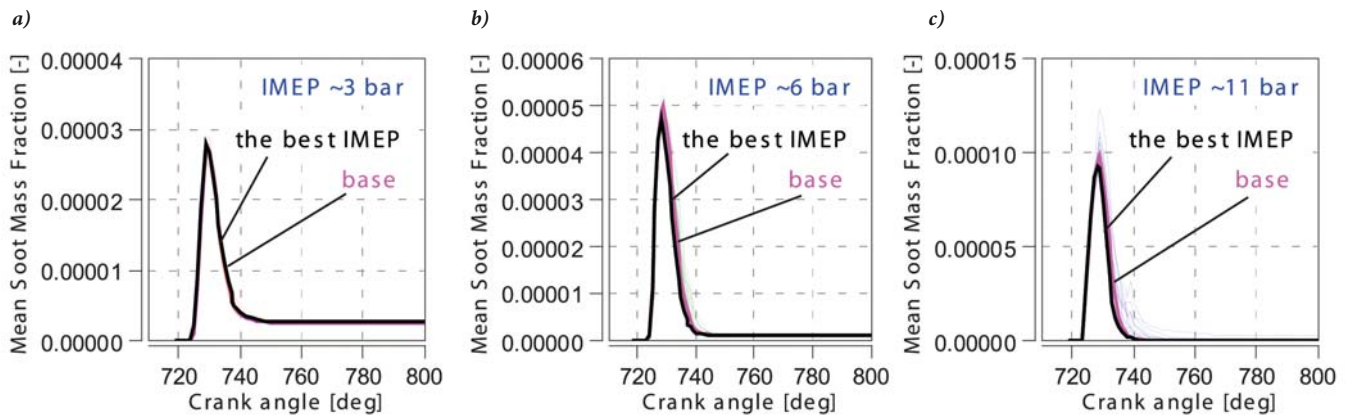


Fig. 8. Mass proportions of soot for various engine loads along with marked initial values and corresponding to optimal dimensions of the combustion chamber to maximize the target function

indicate very similar soot formation processes in the engine cylinder. There are no significant differences between the soot concentration values for the default and optimal chamber. The maximum values for the optimal chamber were found at medium and high load values, equal to 6.1% and 5.6%, respectively. At the lowest load value, the concentration value increased slightly (by 3.7%).

## CONCLUSIONS

Simulation tests allow to optimize the combustion system based on accepted criteria; one of them may be the maximization of the indicated mean effective pressure (liberality of regulations concerning the exhaust emission levels related to internal combustion engines in marine applications allows to maximize operational indicators rather than emission ones).

A summary of the combustion chamber shape tests is presented in Fig. 9. The optimal variable sizes (R3, Tm and TDC) for different engine load values with the maximization of the target function (max IMEP) have been indicated.

Optimal combustion chamber designs (depending on the engine load) indicate a limitation of the so-called harmful area (TDC size) created by the compression stroke of the piston. This limits the formation of soot and hydrocarbons.

Decreasing the Tm value leads to a charge turbulence increase in the combustion chamber, increasing the intensity of the pre-flame processes resulting in an IMEP value increase. At high fuel doses, the value of R3 is limited, which allows to increase the decomposition intensity of the injected fuel droplets when interacting with the combustion chamber walls. This is confirmed by the data from Fig. 4, indicating the limitation of the radius when increasing the engine load.

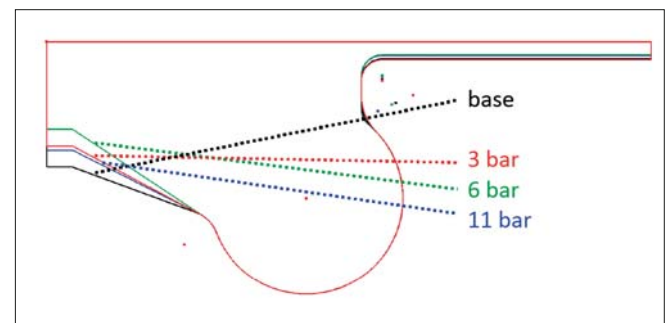


Fig. 9. Optimal combustion chamber shapes at different engine loads

This article presents an analysis of changes in selected design values in order to obtain the criterion set for which the highest values of IMEP was reached.

The results of the performed simulation tests led to the following conclusions:

1. Optimization of combustion chamber of a internal-combustion low-speed engine in the aspect of increasing its operating indicators is a complex issue and does not lead to obtaining unambiguous variables. In the analyzed variants, the change in the engine load resulted in different optimal values of design variables.
2. The choice of the parameters R3, Tm and TDC is not unambiguous. Increasing the load causes:
  - a) Decreasing the value of the radius R3,
  - b) Reducing the TDC value,
  - c) An ambiguous change in the value of Tm (medium load causes a decrease of this value, but other loads increase it).
3. The analysis of optimal combustion chambers indicates that it is possible to achieve large changes in the values of compression pressure and combustion pressure; the changes do not cause large fluctuations of thermodynamic indicators in the form of: process temperature, heat release rate and heat output.
4. The sensitivity of the method was also evaluated during the analysis of nitric oxide and soot. It was found that the changes in nitric oxides are significant. In this case the differences in the extreme values reached 17% (for IMEP = 3 bar), 29% (for IMEP = 6 bar) and 37% (for IMEP = 11 bar). Differences from the soot concentration analysis were found not similar to the above mentioned (the change in their values were 12%, 14% and 29% respectively as the load increased).
6. Maehara N., Shimoda Y.: *Application of the genetic algorithm and downhill simplex methods (Nelder–Mead methods) in the search for the optimum chiller configuration*. Applied Thermal Engineering, 61(2), 2013, pp. 433–442.
7. Marine engine programme. MAN energy solution. 2nd edition 2018. www.marine.man-es.com
8. Naber J.D., Reitz R.D. *Modeling engine spray/wall impingement*. SAE Technical Paper 880107.
9. Navid A., Khalilarya S., Abbasi M.: *Diesel engine optimization with multi-objective performance characteristics by non-evolutionary Nelder-Mead algorithm: Sobol sequence and Latin hypercube sampling methods comparison in DoE process*. Fuel, 228, 2018, pp. 349–367.
10. Pielecha I., Pielecha J., Skowron M. et al.: *The influence of diesel oil improvers on indices of atomisation and combustion in high-efficiency engines*. Polish Maritime Research, 3(95), vol. 24, 2017, pp. 99–105.
11. Pielecha I., Wislocki K., Cieřlik W. et al.: *Application of IMEP and MBF50 indexes for controlling combustion in dual-fuel reciprocating engine*. Applied Thermal Engineering, 132, 2018, pp. 188–195.
12. Shields M.D., Zhang J.: *The generalization of Latin hypercube sampling*, Reliability Engineering & System Safety, 148, 2016, pp. 96–108.
13. Taghavifar H.: *Towards multiobjective Nelder-Mead optimization of a HSDI diesel engine: Application of Latin hypercube design-explorer with SVM modeling approach*. Energy Conversion and Management, 143, 2017, pp. 150–161.
14. Vedharaj S., Vallinayagam R., Yang W.M. et al.: *Optimization of combustion bowl geometry for the operation of kapok biodiesel – Diesel blends in a stationary diesel engine*. Fuel, 139, 2015, 561–567.
15. Wartsila Solutions for Marine and Oil & Gas Markets. Wartsila 2018, wartsila.com.

## ACKNOWLEDGEMENTS

This work has been done under AVL University Partnership Program.

## REFERENCES

1. AVL FIRE, ESE Diesel, Emission Module, Version 2017.
2. Channappagoudra M., Ramesh K., Manavendra G.: *Comparative study of standard engine and modified engine with different piston bowl geometries operated with B20 fuel blend*. Renewable Energy, 133, 2019, pp. 216–232.
3. Gafoor A.C.P., Gupta R.: *Numerical investigation of piston bowl geometry and swirl ratio on emission from diesel engines*. Energy Conversion and Management, 101, 2015, pp. 541–551.
4. Heywood J.: *Internal Combustion Engine Fundamentals*. McGraw-Hill Book Company, New York 1988.
5. Khan S., Panua R., Bose P.K.: *Combined effects of piston bowl geometry and spray pattern on mixing, combustion and emissions of a diesel engine: A numerical approach*. Fuel, 225, 2018, pp. 203–217.
6. Maehara N., Shimoda Y.: *Application of the genetic algorithm and downhill simplex methods (Nelder–Mead methods) in the search for the optimum chiller configuration*. Applied Thermal Engineering, 61(2), 2013, pp. 433–442.
7. Marine engine programme. MAN energy solution. 2nd edition 2018. www.marine.man-es.com
8. Naber J.D., Reitz R.D. *Modeling engine spray/wall impingement*. SAE Technical Paper 880107.
9. Navid A., Khalilarya S., Abbasi M.: *Diesel engine optimization with multi-objective performance characteristics by non-evolutionary Nelder-Mead algorithm: Sobol sequence and Latin hypercube sampling methods comparison in DoE process*. Fuel, 228, 2018, pp. 349–367.
10. Pielecha I., Pielecha J., Skowron M. et al.: *The influence of diesel oil improvers on indices of atomisation and combustion in high-efficiency engines*. Polish Maritime Research, 3(95), vol. 24, 2017, pp. 99–105.
11. Pielecha I., Wislocki K., Cieřlik W. et al.: *Application of IMEP and MBF50 indexes for controlling combustion in dual-fuel reciprocating engine*. Applied Thermal Engineering, 132, 2018, pp. 188–195.
12. Shields M.D., Zhang J.: *The generalization of Latin hypercube sampling*, Reliability Engineering & System Safety, 148, 2016, pp. 96–108.
13. Taghavifar H.: *Towards multiobjective Nelder-Mead optimization of a HSDI diesel engine: Application of Latin hypercube design-explorer with SVM modeling approach*. Energy Conversion and Management, 143, 2017, pp. 150–161.
14. Vedharaj S., Vallinayagam R., Yang W.M. et al.: *Optimization of combustion bowl geometry for the operation of kapok biodiesel – Diesel blends in a stationary diesel engine*. Fuel, 139, 2015, 561–567.
15. Wartsila Solutions for Marine and Oil & Gas Markets. Wartsila 2018, wartsila.com.

## CONTACT WITH THE AUTHORS

**Ireneusz Pielecha**

*e-mail: ireneusz.pielecha@put.poznan.pl*

**Jerzy Merkisz**

*e-mail: jerzy.merkisz@put.poznan.pl*

Poznan University of Technology

Piotrowo 3

60-965 Poznan

**POLAND**

# PARAMETRIC METHOD APPLICABLE IN CALCULATING BREAKOUT FORCE AND TIME FOR LIFTING AXISYMMETRIC OBJECTS FROM SEABED

Jan P. Michalski

Gdańsk University of Technology, Poland

## ABSTRACT

*The issue of calculating parameters for lifting objects of axisymmetric shapes from the seabed is studied. The article presents the results of numerical simulation examination of the equation formulated by Foda for the force needed to extricate the object from the seabed depending on soil and water parameters, extrication speed, and object diameter. The simulations were performed within the range of parameters characteristic for real applications, and their results were used for deriving approximate algebraic formulas applicable in engineering practice of lifting objects resting on seabed.*

**Keywords:** extricating objects from seabed; designing subsea recovery activities; predicting the breakout force

## INTRODUCTION

The engineering practice in lifting objects from the seabed, such as a sunken shipwreck, a submarine, of a ballast anchor, for instance, reveals that the force needed to extricate the object from the seabed can be a multiple of its weight in water. The knowledge of this phenomenon and physical relations which describe it, along with the ability to predict the force, speed, and time needed for extricating the object from the seabed, can be a useful tool in both preparing the recovery procedure and selecting necessary instrumentation.

Empirical observations, quoted in [7] and [13] for instance, and experimental tests, such as those described in [2] and [3], give the evidence that the phenomenon of object sucking to the seabed results from local pressure differences generated in water and in the porous seabed soil when the object is extricated from the seabed. The global effect of this phenomenon is the increasing sucking force when the object is moved away from the seabed, along with the resulting increase of the force needed to extricate it,

above its static weight in water. Correct force assessment is essential when lifting such objects as ballasts, dead anchors, tanks resting on the seabed, construction plates, underwater pipelines, or shipwrecks. A wide spectrum of the quoted examples testifies that the issue of object extrication from seabed is of high importance in widely understood ocean engineering activities.

The literature review on the subject reveals that the value of the extrication resistance force is related in a complicated way with the time and speed of object extrication, and with hydraulic and mechanical properties of the seabed soil and water in it. One of main difficulties when conducting experimental investigations of the above phenomenon is that its real physical and geometric conditions cannot be precisely modelled in the laboratory scale. As a consequence, the results of laboratory experiments cannot be easily extrapolated to real conditions, the more so that the laws of similitude for this phenomenon have not been well-defined [12] and there is a need to refer to the theoretical knowledge and analytical methods. A conceptual sketch of the studied issue is given in Fig. 1.

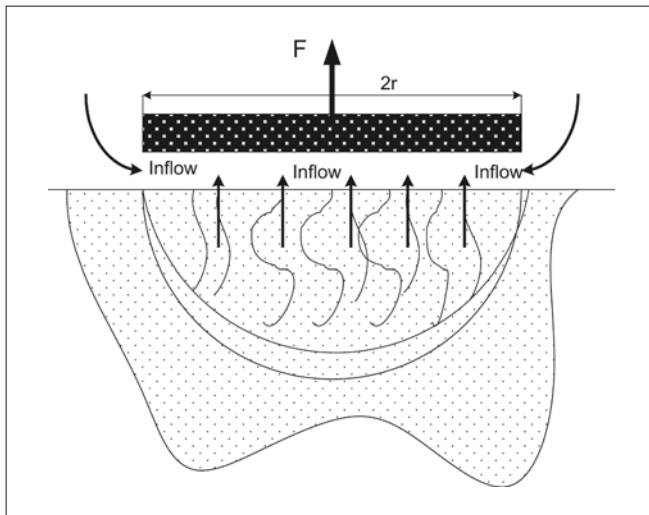


Fig. 1. Conceptual sketch of the phenomenon of object extrication from porous seabed

## PURPOSE AND SCOPE

The well-known methods to determine forces needed to lift an object resting on the seabed are either simple, with low assessment accuracy resulting from neglecting a number of important parameters of the phenomenon (for instance, the formula given by Poinc [10]), or take into account many essentials at the expense of high complication of mathematical description and difficulties in calculating parameters important for engineering practice.

The purpose of the study reported in this article was developing a method to determine essential parameters for the technology of object lifting from seabed, which would have simple mathematical structure and the accuracy comparable with that of advanced theoretical methods, thus being applicable in engineering practice.

However, the applicability of the developed method has some limitations, as its range comprises only basic extrication parameters, such as the shape and dimensions of the lifted object, the extrication force, speed, and time, the total time of the breakout phenomenon, and the time after which the sucking action of the seabed on the object disappears. The motivation and inspiration for undertaking this task was the research done within the framework of the previous project [9]. An attempt to use the Foda model for practical calculations was presented in [12], while more systematic studies were conducted by Liu [6]. However, the results of these studies were only described in an internal report and are not widely available.

## LITERATURE REVIEW ON THE SUBJECT

The force needed for extricating a body from the seabed can be roughly assessed using non-structural approximate empirical relations, such as the formula proposed by Poinc [10], which says how much the force needed to extricate the object from the seabed is larger than the weight of the

object in water. This force/weight ratio is calculated taking into account the type of seabed, starting from stony and ending with clay type. In the Poinc formula, the suction force only depends on the type of base soil, which is a major simplification, as both practical experience and performed experiments show that the extrication force, speed, and time are mutually dependent.

It results from the laboratory tests performed by Basinski [2], [3] that the extrication resistance force, also referred to as the suction force, can reach a large value, which is also confirmed by reports from excavation works cited both by the author and in [14]. Basinski's motivations for undertaking labour-intensive experimental investigations was that the available literature contains insufficient amounts of model test data for reliable generalisation concerning their scaling to real objects.

In the tests performed by Basinski, the dimensions of the extricated object are large (up to 30 cm), compared to the dimensions of soil particles. In the light of his research, the course of object extrication from granular soil during the phase of suction force action is as follows. The applied external lifting force reduces the pressure under the rigid body base with respect to the surrounding hydrostatic pressure. The reduced pressure distribution under the object base changes when the object rests freely on the soil surface, and is uniform when the object is embedded into the soil. The pressure reduction generated by the object motion propagates into the soil, and the appearing pressure gradient initiates the flow of the water filling the soil structure (pores).

At object edges, the pressure difference makes that the water flows faster under the object base, as a result of which the soil becomes more liquefied and is washed out. The water flow generates relatively large forces of inertia of water masses and friction forces between water particles moving up and soil particles, all this leading to the reduction of soil cohesion and lifting up of part of soil particles. With the increasing gap between the rigid body base and the soil, the motion resistance in the gap decreases and the amount of water flowing through it increases.

Theoretical analyses of the above issue are based on the concept of boundary layer in porous medium. It is assumed that in direct vicinity of the seabed surface, the dynamics of motion of the water filling the soil pores differs from that inside the soil medium. This assumption is justified by the fact that the value of the suction force depends on the speed of extricating the object from the seabed, as well as on the type and cohesion of the soil, the air content in the water, the geometry and dimensions of the object, and on how deep the object is embedded into the soil.

Based on the varying pressure distribution generated by the force used to extricate the object from the seabed, three phases of the phenomenon can be named. In the first phase, which lasts until the stability of the soil structure skeleton is lost, the breakout force is mainly composed of adhesive and cohesive forces acting on the contact surface between the extricated body and the soil. In the second phase, starting after the soil stability is lost, the dominating force is the resistance of the water flowing through the soil, while in the

third phase – the resistance of the water flowing through the gap between the object and the seabed. This scheme provides an opportunity for extracting the static breakout resistance, acting until the time of clear beginning of motion, and the kinetic extrication resistance, acting in the phase of object motion.

Sawicki [13] considers the issue in which the lifted object moves uniformly and rectilinearly in the direction of action of gravity forces. The structure of the water reservoir bottom is modelled as the porous body filled with two-phase compressible liquid. The compressibility of the liquid is described by the parameter  $\beta$ , the value of which depends on water aeration in pores. The elasticity of the porous medium structure is assumed and defined by the parameter  $G$ . This medium property plays a vital role in modelling flows in pores during rapid appearance of negative pressure (suction). The third important parameter is the seabed porosity coefficient  $n$ , the values of which do not differ much in the examples analysed in the literature.

An interesting mathematical model of axisymmetric object extrication from the seabed is proposed by Foda [4], who makes a series of simplifying assumptions to derive a formula describing the pressure decrease between the seabed structure and the adhering object at the time of object motion initiation. Making use of Biot's theory about properties of flows in porous-elastic bodies and assuming that the flow in pores obeys Darcy's law, the author derives formulas describing the dynamic pressure distribution and the resulting force of object suction to the bottom of water reservoir.

For the adopted assumptions, Foda obtained formulas being the solutions for axisymmetric objects (with respect to vertical axis) and slender objects. The advantage of the Foda method in the aspect of practical applications is its prognostic value – the delivered solutions include the phenomenon referred to as “breakout”, well-known from practice, which consists in the appearance of maximal breaking force after some time from the beginning of object extrication from the seabed, followed by fast decrease of the sucking force. A detailed analysis of assumptions made and results obtained by Foda [4] was done by Mei et al. [7] who stressed the importance of the use of different models of soil structure depending on its type.

## CONCEPT AND RESULTS OF THE STUDY

The prognostic quality of the Foda method [4] justifies its use for systematic simulation studies covering a wide range of practically used parameter values and expected to provide data applicable for deriving simple and useful approximation formulas, without need to solve complicated equations such as Eq. (1) or Eq. (1).

According to Foda [4], for the motion with nonuniform extrication speed, the force  $F$  with which the axisymmetric object is sucked to the seabed is given by Abel's differential-integral equation:

$$F(t) = \pi \cdot r^2 \cdot \alpha \cdot \int_0^t \left[ 1 - \frac{2 \cdot I_1(f_o \cdot r)}{f_o \cdot r \cdot I_0(f_o \cdot r)} \right] \cdot \left( \frac{d\Delta}{d\tau} \right) \frac{d\tau}{(t-\tau)^{1/2}} \quad (1)$$

When the extrication speed  $w$  is uniform, the extrication force is given by the integral equation:

$$F(t) = \pi \cdot r^2 \cdot \alpha \cdot w \cdot \int_0^t \left[ 1 - \frac{2 \cdot I_1(f_o \cdot r)}{f_o \cdot r \cdot I_0(f_o \cdot r)} \right] \cdot \frac{d\tau}{(t-\tau)^{1/2}} \quad (2)$$

The symbols in the above equations have the following meaning:

$$\alpha = \frac{1+m}{m} \cdot \left[ \frac{\frac{G}{k}}{\pi \cdot m \cdot (1-2 \cdot \nu) + \frac{\pi(1-2 \cdot \nu)}{2 \cdot (1-\nu)}} \right]^{\frac{1}{2}} \quad (3)$$

$$f_o = \left( \frac{6 \cdot \mu}{\alpha \cdot w^3} \right)^{\frac{1}{2}} \cdot t^{-\frac{7}{4}} \quad m = \frac{n \cdot G}{(1-2 \cdot \nu) \cdot \beta} \quad k = \frac{\beta}{\gamma} \quad (4)$$

Names and values of parameters used in the simulation studies are as follows:

$t$	– extrication time;
$w$	– extrication speed;
$r$	– radius of the object;
$I_0(\cdot)$	– zero-order modified Bessel function of first kind;
$I_1(\cdot)$	– first-order modified Bessel function of first kind;
$\Delta$	– object displacement distance;
$G = 10^7 \text{ N/m}^2$	– shear modulus of seabed solid;
$\beta = 10^7 \text{ N/m}^2$	– bulk modulus of porous fluid (partial saturation);
$k = 10^{-10} \text{ m}^3 \text{ s/kg}$	– soil permeability coefficient;
$n = 0.3$	– seabed porosity coefficient;
$\mu = 1.325t / (\text{m} \cdot \text{s})$	– water viscosity coefficient;
$\gamma = 10^4 \text{ N/m}^3$	– specific weight of water;
$m = 0.9$	– ratio of solid skeleton elasticity to fluid elasticity;
$\nu = 0.333$	– Poisson's ratio of solid-fluid system;

The following ranges of parameters were considered interesting from the point of view of engineering practice and used in the performed simulations:

– set of object radii:

$$r \in \{1.00 \text{ m}, 5.00 \text{ m}, 10.00 \text{ m}\};$$

– set of uniform extrication speeds:

$$w \in \{10^{-3} \text{ m/s}, 10^{-4} \text{ m/s}, 10^{-5} \text{ m/s}, 10^{-6} \text{ m/s}, 10^{-7} \text{ m/s}\};$$

– limiting value of extrication force decay  $F_{decay} = 10 \text{ N}$ .

At low extrication speeds, solving numerically Eq. (2) becomes difficult, as in this case the argument  $f_o$  in Eq. (4) takes high values, which exceed the applicability range of

classical formulas for calculating Bessel functions. In this case, use was made of asymptotic formulas given in [1], [5], [8], [11]. After some preliminary tests, the following approximation was selected for simulation calculations:

$$\frac{I_1(x)}{I_0(x)} \cong \exp\left(\frac{-1}{2 \cdot x}\right) \text{ for } x > 800 \text{ with } : O\left(\frac{-1}{x^2}\right) \quad (5)$$

The extrication forces and gap dimensions calculated from Eq. (2) are shown in Fig. 2, Fig. 3 and Fig. 4, for different object dimensions. In these figures, the logarithmic scale was used, as the values of the presented parameters differ by several orders of magnitude. Continuous lines are graphical representations of solutions of Eq. (2) with respect to the extrication force, while broken lines illustrate the size of the gap between the seabed and the object, depending on the extrication speed and time.

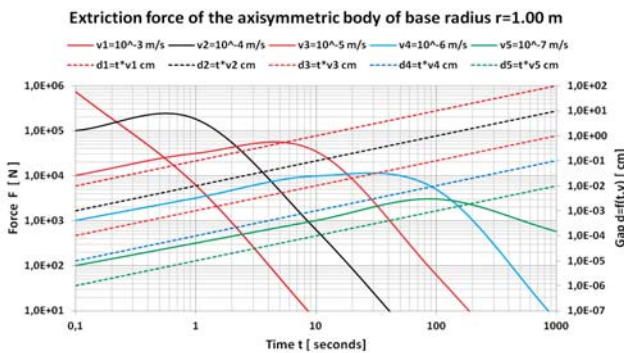


Fig. 2. Time-histories of extrication force and gap size at different extrication speeds;  $r = 1 \text{ m}$

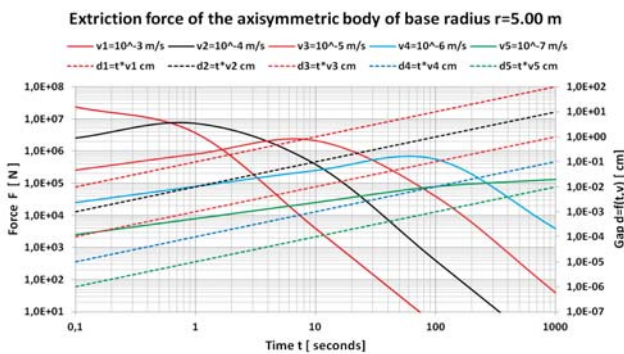


Fig. 3. Time-histories of extrication force and gap size at different extrication speeds;  $r = 5 \text{ m}$

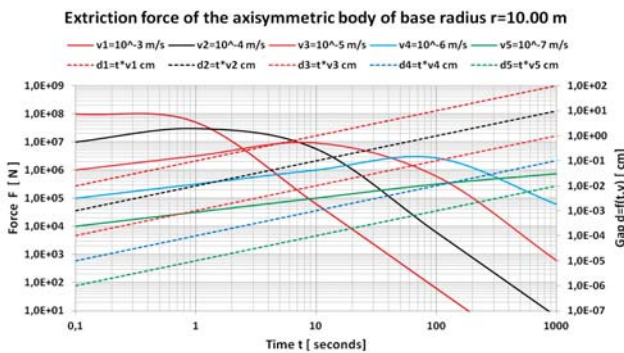


Fig. 4. Time-histories of extrication force and gap size at different extrication speeds;  $r = 10 \text{ m}$

The maximal extrication force  $F_{max}$ , often referred to as the “breakout force”, and the time  $T_{max}$  after which this force appears were calculated, for different object sizes and extraction speeds, from the precondition for the existence of extremum of suction force characteristic:

$$\frac{dF(t)}{dt} = \pi \cdot r^2 \cdot \alpha \cdot w \cdot \frac{d}{dt} \int_0^t \left[ 1 - \frac{2 \cdot I_1(f_o \cdot r)}{f_o \cdot r \cdot I_0(f_o \cdot r)} \right] \cdot \frac{d\tau}{(t-\tau)^{1/2}} = 0 \quad (6)$$

The maximum forces  $F_{max}$  calculated from Eq. (6) are shown in Fig. 5 as continuous lines.

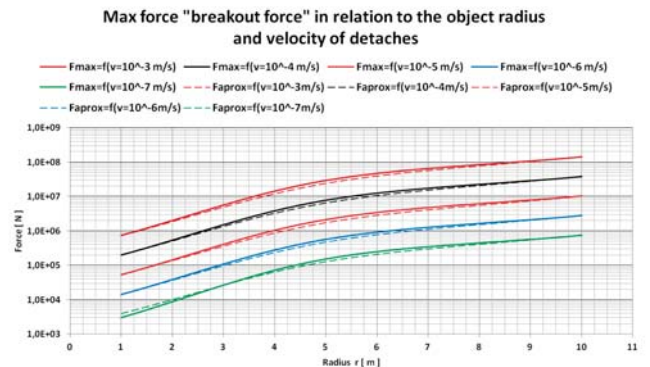


Fig. 5. Maximal extrication forces (breakout forces) as functions of object size and extraction speed

An interesting parameter of the study is the time  $T_{decay}$ , after which the sucking action of the seabed on the extricated object decays. It was assumed that the decrease of the sucking force below  $F_{decay} = 10 \text{ N}$  means the decay of the suction effect of seabed, after which the further process of object lifting becomes a classic task of object moving in water, where the resistance force depends on the shape and weight of the object and the speed of its lifting.

The time  $T_{decay}$  was determined by solving the following equation for time  $t$ :

$$F_{decay} - \pi \cdot r^2 \cdot \alpha \cdot w \cdot \int_0^t \left[ 1 - \frac{2 \cdot I_1(f_o \cdot r)}{f_o \cdot r \cdot I_0(f_o \cdot r)} \right] \cdot \frac{d\tau}{(t-\tau)^{1/2}} = 0 \quad (7)$$

The calculated values of  $T_{max}$  after which the maximum forces occur are shown in Fig. 6 as continuous lines, while the time  $T_{decay}$  after which the sucking effect of seabed decays are represented by broken lines.

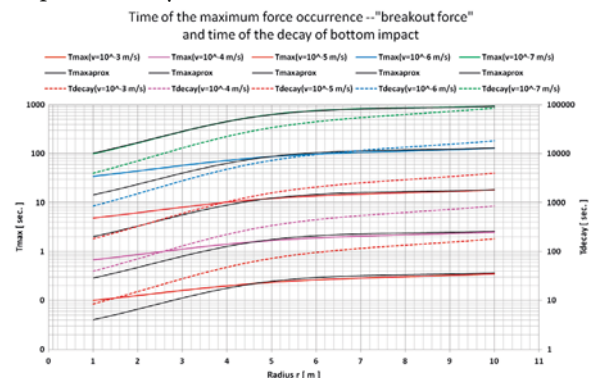


Fig. 6. Time  $T_{max}$  of the occurrence of breakout force  $F_{max}$  and time  $T_{decay}$  of suction force decay

The results of simulation calculations comprise discrete characteristics which represent relevant relations for fixed values of parameters  $r_i$  and  $w_i$ :

$$- F_{max i} = f(r_i, w_i);$$

$$- T_{max i} = f(r_i, w_i);$$

$$- T_{decay i} = f(r_i, w_i).$$

The sets of discrete values of these characteristics were used for deriving simple and continuous algebraic formulas which relatively precisely approximate the original discrete characteristics. The adopted measure of accuracy of the obtained approximations was the square of the relative mean error. From among the tested hypothetical formulas approximating the maximum force characteristics, the best approximation was given by the formula:

$$approx F_{max} = 94.85 \cdot w^{0.569} \cdot (r^{0.7364} + 0.663)^{4.048} \quad (8)$$

In Eqs. (8), (9) and (10), the extrication speed  $w$  is expressed in [mm/s], the object radius  $r$  in [m], and time in [s].  $approx F_{max}$  is the maximum force value expressed in [kN].

The values of the force  $approx F_{max}$  are shown in Fig. 5 as broken lines, which provides opportunities for comparing them with original values (continuous lines) for different extrication speeds and different object sizes. The force  $approx F_{max}$  only represents the suction force, which means that it should be enlarged by the weight of the object in water when calculating parameters for the lifting device.

A similar approach was used when deriving the approximating formulas  $approx T_{max}$  for the time after which the maximum force occurs, and  $approx T_{decay}$  for the time after which the sucking effect of seabed decays. For the former case, the best approximation had the form:

$$approx T_{max} = 0.101 \cdot w^{-0.852} \cdot (r^{1.96} - 0.96)^{0.286} \quad (9)$$

In Fig. 6, coloured continuous lines represent the original solutions, while thin black lines present the relations given by Eq. (9).

For the time  $approx T_{decay}$  after which the action of the sucking force decays, the best approximation was:

$$approx T_{decay} = 8.55 \cdot w^{-2/3} \cdot (r^{0.973} - 0.00028)^{1.37} \quad (10)$$

In Fig. 6, coloured broken lines represent the relations given by Eq.(10). In Eq. (9) and Eq. (10) the speed  $w$  is expressed in [mm/s], the object radius in [m], and time in [s].

## SAMPLE METHOD APPLICATION

The extrication speed and time are to be assessed for a circular object of  $r = 2.40$  m, assuming that the available lifting force is 350 kN.

Placing the force and object radius values into Eq. (8) and performing some algebraic operations leads to the relation:  $0.08104 = w^{0.569}$ . Raising both sides of the equation to a power of  $\frac{1}{0.569} \cong 1.757$  gives the speed  $w = 0.08104^{1.757} \cong 0.012$  mm/s. After placing the speed and object radius values into Eq. (9) we get the time after which the maximum force occurs,  $T_{max} \cong 6.7$  s, and the gap size at this time,  $d_{max} \cong 0.08$  mm. Finally, placing the same values into Eq. (10) gives us the time after which the suction force decays,  $T_{decay} \cong 521$  s, and the corresponding gap size,  $d_{decay} \cong 6.2$  mm.

The presented results of the study can make a basis for developing a programme of laboratory experiments, while practical applicability of the proposed method consists in fact that the above calculations can be performed using a simple calculator.

## REFERENCES

1. Amos D. E.: *Computation of Modified Bessel Functions and Their Ratios*. Mathematics of Computation Vol. 28, No. 125 (Jan., 1974).
2. Basiński T.: *Resistance force during extricating a rigid body from sandy bottom of water reservoir (in Polish)*. Archiwum Hydrotechniki. Vol. XVI, No. 4, 1969.
3. Basiński T.: *Laboratory tests of resistance force during extricating a large rigid body from the bottom of natural water reservoir (in Polish)*. Rozprawy Hydrotechniczne. No. 23, Instytut Budownictwa Wodnego PAN, 1969.
4. Foda M.A.: *On the extrication of large objects from the ocean bottom (the breakout phenomenon)*. Journal of Fluid Mechanics. Vol 117, 1982.
5. Gautschi W., Slavik J.: *On the Computation of Modified Bessel Function Ratios*. Mathematics of Computation. Vol. 32, No. 143 (Jul., 1978), pp. 865-875.
6. Liu C.L.: *Ocean sediment holding strength against breakout of imbedded objects*. Tech. Rep. US Naval Civil Engineering Laboratory, Port Hueneme, California, 1969.
7. Mei C.C., Yeung R.W., Liu K.F.: *Lifting of a large object from a porous seabed*. Journal of Fluid Mechanics. Vol 152, 1985.
8. Mathematics.: <https://math.stackexchange.com>.
9. Michalski J.P.: *Design method and study of autonomous hydro-location module for measuring and examining physical phenomena in marine environment (in Polish)*. Prace Naukowo-Badawcze WOiO, No. 01/PR/2010, Gdansk University of Technology.
10. Poinc W.: *Maritime Rescue (in Polish)*. Wydawnictwo Morskie. Gdynia 1966.

11. Ramy S., Ehab S., Ali H., Tasneem A.: *A Simple and Efficient Approximation to the Modified Bessel Functions and Its Applications to Rician Fading*. IEEE GCC Conference and exhibition, Doha, Qatar 2013.
12. Robakiewicz M.: *Breakout force needed to extricate a rigid body from the bottom of a natural water reservoir (in Polish)*. Inżynieria Morska. No. 4/1985.
13. Sawicki A.: *Soil suction forces and the breakout phenomenon*. Studia Geotechnica et Mechanica. Vol. XVII, No. 1–2, 1995.
14. Sawicki A., et al.: *New Type of Bottom Protection in Harbors – Design Metod*. Journal of Waterway, Port, Coastal, and Ocean Engineering. July/August, 1998.

## CONTACT WITH THE AUTHORS

**Jan P. Michalski**

*e-mail: janmi@pg.edu.pl*

Gdańsk University of Technology  
Narutowicza 11/12  
80-233 Gdansk  
**POLAND**

# INTRODUCTION TO COASTAL HF MARITIME SURVEILLANCE RADARS

**Prof. Dimov Stojce Ilcev**

Durban University of Technology (DUT), South Africa

## ABSTRACT

*This paper presents the main technical characteristics and working performances of coastal maritime surveillance radars, such as low-power High-Frequency Surface Wave Radars (HFSWR) and Over the Horizon Radars (OTHR). These radars have demonstrated to be a cost-effective long-range early-warning sensor for ship detection and tracking in coastal waters, sea channels and passages. In this work, multi-target tracking and data fusion techniques are applied to live-recorded data from a network of oceanographic HFSWR stations installed in Jindalee Operational Radar Network (JORN), Wellen Radar (WERA) in Ligurian Sea (Mediterranean Sea), CODAR Ocean Sebsorsin and in the German Bight (North Sea). The coastal Imaging Sciences Research (ISR) HFSWR system, Multi-static ISR HF Radar, Ship Classification using Multi-Frequency HF Radar, Coastal HF radar surveillance of pirate boats and Different projects of coastal HF radars for vessels detecting are described.*

*Ship reports from the Automatic Identification System (AIS), recorded from both coastal and satellite Land Earth Stations (LES) are exploited as ground truth information and a methodology is applied to classify the fused tracks and to estimate system performances. Experimental results for all above solutions are presented and discussed, together with an outline for future integration and infrastructures.*

**Keywords:** HFSWR, OTHR, JORN, WERA, ISR, AIS, LES, LPA, LRA, DOA, DDC, PCI, RCS

## INTRODUCTION

Over the years there have been many systems developed to serve coastal HF maritime surveillance radars, but more known are HFSWR and OTHR. They use the frequency band of 3-30 MHz to provide a large coverage that could extend up to 200 NM in range. Thus, the primary benefits of the HF-band for coastal radars are over the horizon capability, sky-wave and groundwave propagation modes, which simplified signal generation and processing requirements. Traditional system design for coastal surveillance radars includes large bistatic HF transmit and receive arrays with a substantial geographic footprint since a wide aperture array is used to provide the

needed resolution for detecting surface targets while reducing clutter. Although proven to be effective, the infrastructure requirements of these systems generally render them large, quite costly and not environmentally friendly and immobile, creating major limitations for wide deployment. However, the increased emphasis on homeland security applications such as maritime surveillance for enhanced safety at sea, national security and enforcement continues to drive the need for efficient mobile and low-cost HFSWR and OTHR systems. In order to meet the demands of homeland security applications while keeping the costs, environmental impact and infrastructure requirements at a minimum, novel integrated HF radar system designs are required.

## COASTAL ISR HFSWR SYSTEM

The coastal HFSWR and OTHR radars are a highly cost-effective remote sensing technology for measuring waves, swell direction and for monitoring the movements and detecting of ships and aircraft at over the horizon ranges including pirate boats. The US Imaging Sciences Research (ISR) company is currently developing a low cost, compact HF Phase Array Radar to measure directional wave spectra along a single radial line offshore, without requiring beam steering. The project of ISR is being funded for this work as a Bureau of Ocean Energy Management by NOAA National Oceanographic Partnership Program (NOPP) participant.

However, a bistatic HF radar has been developed for application to ocean current mapping and especially for ship vector tracking. The radar can operate in a multi-frequency mode, so that it can map ocean current vertical shear and can provide more robust ship tracks than single frequency HF radars. This tracking robustness is achieved by avoiding target fading due to echo nulls from frequency and azimuth variations in ship radar cross-section that occur using a single radar frequency. The radar is fully digital in frequency generation and reception and has no RF receiver components because the received antenna signals are digitized at the HF frequency directly. The system uses Analogue-to-Digital (A/D) conversion rates sufficiently high to maintain the 2 to 1 frequency ratio required for the highest radar frequency of interest to avoid frequency aliasing.

The newly developed radar acquisition code provides real-time range compression so that data files that are stored in the processor are In-phase and Quadrature (I/Q) samples, at a much less dense rate than the original digitized signal time series. Thus, the bistatic capability is based on accurate system timing and radar frequency. These are provided at each of two or more radar sites by rubidium clocks and GPS timing, accurate for the first pulse to 50-ns to initiate data acquisition in the bistatic mode. Once acquisition is initiated, the rubidium clocks at each site maintain much more accurate frequency and time stability to allow Doppler velocity measurements accurate to 2  $\mu$ Hz at 25 MHz operating frequency.

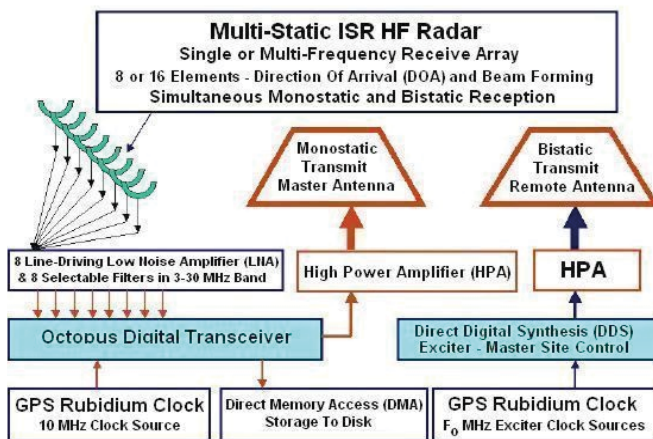


Fig. 1. System Layout of Typical Bistatic Two-site HF Radar – Courtesy of Manual: by ISR [1]

The primary site requires an 8 or 16-element receive array, and both primary and satellite bistatic-illuminator sites have a modest 2 or 4-element monopole transmit antenna pair. This bistatic approach reduces the coastal space requirements because of the need for just one receive-antenna array per radar system.

These systems can be operated with a pair of bistatic transmitters, either side of the receive site, to expand the spatial coverage. Using such an approach, these units could be staggered to create a system of few radars, providing continuous coverage along a coastline, alternating transmit and receive sites. This type of arrangement could be used to provide robust ship tracking along a country's coastline, and a modest estimate of type and tonnage of all vessel traffic based on target echo strength. Due to its digital approach, the cost of these radars is substantially lower than that of existing single coastal HF radars, none of which have multi-frequency capability [1, 2, 3, 4].

## MULTI-STATIC ISR HF RADAR

The ISR Company has developed a bistatic HF radar for robust ship tracking in coastal seas and ocean current mapping based on purely digital receiver and transmission technology. The bistatic capability represents an upgrade from the previous system, requires use of accurate system clocks and absolute time referencing in order to operate in a bistatic mode. These are provided by GPS timing and rubidium clocks. Initially, the system was comprehensively tested in the VHF-band and some of those results are presented here. The VHF-band allows for shorter range and wider bandwidth usage than can be achieved at HF frequency. The technology transfers directly to HF frequencies, with slower A/D conversion rates required due to lower radar frequencies and corresponding lower Nyquist frequencies, named after engineer Harry Nyquist, as  $\frac{1}{2}$  of the sampling rate of a discrete signal processing system.

A layout of the bistatic radar is shown in **Figure 1** for a 2-site system, with the master site on the left and a bistatic transmitter shown on the right. The heart of the radar is the Octopus transceiver card, which has both a programmable pulsing capability and 8-receive channels per card. For a 16-element array, a second Octopus Receiver card provides eight additional channels of receives capability. At the bistatic transmit-only site, an Exciter card is used to generate the pulsed waveforms.

Typically, the radar is operated with up to a 20% duty cycle pulse compressed waveform, fully programmable by the operator. For long-range operation, for example, a 100  $\mu$ s pulse is transmitted (forcing a 15 Km blind area around the area), which is compressed to 10  $\mu$ s, achieving a 20 dB pulse compression gain. Thus, this allows a 250 W peak power pulse to be compressed to the equivalent of a 5 KW pulse using frequency-modulated pulse waveforms.

The receive array at the master site receives both monostatic echoes from pulses transmitted at the master site, as well

as bistatic echoes from pulses transmitted at the slave site. The pulses can either be interleaved on ping-pong like time sequence or can be transmitted simultaneously at two different radar frequencies with non-overlapping frequency content.



Fig. 2. Multi-Frequency Radar Transmit LPA and Receive LRA –  
Courtesy of Paper: by Trizna [5]

Additionally, one array could use orthogonal phase modulated waveforms simultaneously for optimal use of frequency-time bandwidth. In the case of multi-frequency operation, more complicated antennas at both, transmit and receive end, which must be used to accommodate the desired bandwidth. It is developing a low-cost single-frequency system that will use off the shelf antenna components to minimize cost and space requirements. A multi-frequency system covering the full 3-30 MHz HF band requires wideband antennas and switchable narrowband filters to assure good signal to noise ratios for reliable ship tracking. The long-periodic array is most suitable for such a wide operating bandwidth. Operation over a smaller fraction of the HF band, as might be required for long-range application in order to minimize radar propagation losses in the surface wave mode, might, for example, require only a 3-10 MHz bandwidth. One can achieve this by using transmit antennas in a short two or four element transmit array, with trap antennas or multi-mode elements with several resonances that have low reflection and good standing wave ratios at several frequencies in the desired band. For receiving antennas for multi-frequency radar, loop antennas provide good bandwidth and some directivity to minimize reception of the transmitted pulse.

A new transmit radar antenna was designed for broadband operation over the entire 3-30 MHz band, a modified Log Periodic Antenna (LPA), many of which are shown in **Figure 2**. However, more compact designs are feasible for operation at pre-specified selected frequencies of four or eight in number, e.g. for operational current shear maps. The LPA antenna provides full tunability to any frequency in the HF band and is suggested for target classification applications, such as small and large ships or current shear experiments.

The receive Loop Receive Array (LRA) antenna is based on a loop design, three of which are shown in **Figure 2**. The ISR internal broad preamplifiers provide impedance matching to the loop over the 3-30 MHz filtered output. These elements can be arranged for Direction-of-Arrival (DOA) processing. A small 4-element loop array requires less space than long linear arrays, and is useful for current mapping and ship classification, but could not be used for measurement of

directional wave spectra. For this latter application, long arrays of between 8 and 32 elements, in groups of 8, can be built using an Octopus transceiver, supported by up to three OctRec cards, all of which are time-locked to the master clock on the Octopus card.

## COMPONENTS OF HF RADAR

The DOA processing is a monostatic model, which typically has 4-elements designed for space-limited applications where large receive arrays could not be deployed. This system contains transmit antenna 4-element monopole array with sidelobe control and landward null, receive antenna beamforming array of 4-elements, receive element single-frequency system (resonant monopole), radar receiver Quadrapus, radar Pre-Amplifier Filter (PAF) box with 4-channel pre-amplifier (configurable with up to 8 narrowband or broadband filters for each channel if multi-frequency option is desired), multi-frequency option wideband transmit antenna and loop receive antennas for 3-30 MHz range.

The Phased Array of Multi-static HF Radar contains transmit antenna 2-element monopole array, receive antenna beam formed by 8-elements array of, receive element with single frequency system (reduced-size loop), radar receiver Octopus and 8-channel radar PAF box.

Bistatic DOA model is a 2 or 3 site bistatic radar where all signal reception and processing is done at the master site, with remote sites used for transmission only. Unambiguous target tracks and vector velocities are determined at the master site, using echoes received, master monostatic transmission and one or two bistatic signal echoes from the radar remote sites. Control of the remote sites is achieved by radio networking protocol and remote PC control. It contains transmit antenna 4-element monopole array with sidelobe control and landward null, receive antenna beamforming array of 4 elements, receive element single-frequency system (resonant monopole), radar receiver ISR Quadrapus, 4-channel PAF box with configurable up to 8 narrow bands or broadband filters for each channel of multi-frequency option wideband transmit antenna (loop receive antennas for 3-30 MHz range) [2, 3, 4, 5].

## NETWORKS OF HF RADAR

Each of the above models can be configured to operate as part of a multi-static network of radars, as each card has access to Universal Time (UT) on board using a GPS receiver as part of the basic system. Both Differential GPS and RSAS capabilities are available as added options, primarily for other mobile radar applications. Under this networked approach, each radar operates within its own time slot. Thus, a two-sited phased array radar would operate using alternate pulse time slots, so as to allow interleaved operation using the

same radar frequency. Planned options include using such a pair to receive each other bistatic signal echoes as well, thus mixing monostatic and bistatic operations at both sites. This is useful for target classification and current shear measure, as is described elsewhere on these web sites:

<https://tel.archives-ouvertes.fr/tel-01312183/document>;  
<http://cdn.intechweb.org/pdfs/6891.pdf>; <http://www.imd.gov.in/section/dwr/dynamic/radarfaq.pdf>, etc.

Each model also can be configured with a multi-frequency option, requiring loop receive and multi-frequency transmit antenna or also as desired to be configured as a system to additional requirements. The system also offers a Rubidium clock option, which provides extremely low phase noise, important for high dynamic range applications, such as sea state monitoring using 2nd-order Doppler echoes or for target (ship) detecting, classification and tracking.

### TYPES OF HF RADAR TRANSCEIVERS

The Octopus transceiver card family presents a state of the art digital radar capability that forms the basis of the system. It utilizes the miniaturization of RF components in the design of new radar capabilities and provides transmit and receive capability on one PCI card. It offers programmable pulse generation capability with 1 to 100 MHz bandwidth programmability, and eight digital receiver channels using 8-bit A/D converters for the receiver section for the first step of acquisition, followed by additional onboard processing that increases the dynamic range of the recorded signal.

The single Octopus transceiver supports an 8-element receive array and can be used with up to three additional OctalRec receiver cards to increase the receive aperture to as many as 32 elements. Receiver output data are two-byte words, achieved by either repetitive pulse averaging or digital down-conversion I/Q data generation. In the case of averaging, up to 256 consecutive echoes can be averaged, providing 2-byte output real data. For Digital Down Converter (DDC) processing, the gain is the ratio of 95 MHz divided by the desired output rate (~ pulse bandwidth). For an 8-ms pulse, 125 KHz bandwidth, a gain of  $95/125=760$  is achieved, with I/Q pairs generated and stored at 4-bytes output format. On-board averaging is also available to more fully utilize the 4-byte output word size.

The waveform generation capability ranges from a few KHz to 100 MHz, with user-defined programmable pulse envelope control, in addition to ISR provided cosine-squared, square wave, and triangle envelopes. The signals are generated using Direct Digital Synthesizer chips with a square waveform, fed to a mixer with a user-defined pulse envelope, resulting in a pulse waveform with RF spectrum characteristics that will satisfy HF-band requirements. Software graphical-user-interface is provided that allows the user to program the transceiver according to the desired specifications for the application at hand, stores the parameter file for future use, and then executes the acquisition.

The program can be run on a periodic basis using a task scheduler for continuous data collection. The Octopus card

currently operates under Microsoft Windows and Linux platforms and the Octopus transceiver fits in standard full-sized Peripheral Component Interconnect (PCI) slot (full height and length card) utilizing components of PLX Technology with a PCI9054 chip to communicate with the PCI bus. The Quadrapus transceiver is 4-channel version of the Octopus, designed for use with DOA Radar or four (fewer) receive antennas with other identical characteristics to the Octopus.

The OctRec receiver card is basically the same design as the Octopus transmitter, but without the transmitter capability. It is designed for use in larger phased array radars with 16 to 32 elements. One or more OctRec receiver cards are then used in tandem with an Octopus transceiver, which generates master A/D timing for the OctalRec cards. In the future, it will offer other passive sensing systems based on the OctalRec digital receiver. In such a way, the QuadRec receiver card is basically a Quadrapus card without the transmitter capabilities [2, 3, 4, 6].

### SHIP CLASSIFICATION USING MULTI-FREQUENCY HF RADAR

The ability to operate multi-frequency HF radar allows one to classify ships and small boats. One makes use of the radar frequency dependence of the echo strength or Radar Cross Section (RCS) of individual ships. This occurs because for vertical polarization at HF frequencies, the echo strength is typically dominated by vertical structures of the order of a quarter radar wavelength, such as masts, antennas and stowed fishing lines, so in the case of large ships, the bow and stern vertical rise from the water. Use of the 3-30 MHz range encompasses quarter wavelength ranges between 2.5 to 25 meters in height.

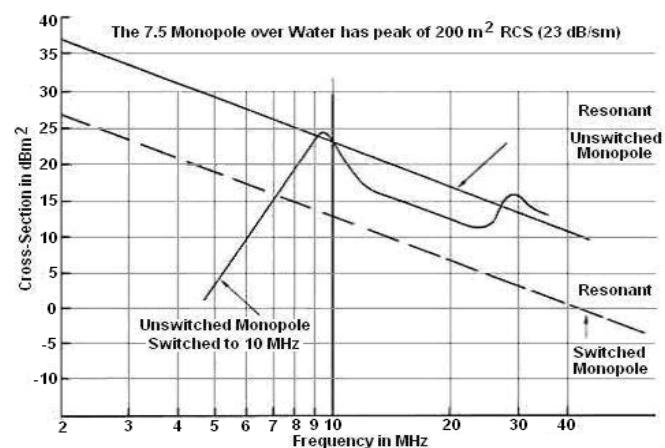


Fig. 3. Radar Measurements of Small Boats – Courtesy of Paper: by Trizna [7]

The additional use of bistatic illumination, where a second (or more) transmitter is placed a few tens of miles from the receiver site, either on land or on an offshore platform and ship at sea, adds an additional dimension to the RCS dependence. When two or more vertical structures are illuminated using a bistatic geometry, they can produce RCS maxima and

minima that vary with bistatic aspect angle, as well as ship aspect or heading, relative to the receive site. The first figure below shows the radar cross-section frequency dependence of an ungrounded vertical mast 7.5 meters high. The shape of the region around the maximum is based on a mast width of about 10-cm and will narrow/broaden with smaller/larger diameter masts. The solid line intersecting the Y-axis at  $\sim 37$  dBm<sup>2</sup> represents the locus along which this curve is slid for taller or shorter masts of the one-quarter length of the radar wavelength. More than one mast, or a tall radio antenna and a mast, can be considered as a pair of monopoles of corresponding lengths, and the RCS of the combination is a function of their spacing and aspect relative to the radar transmitter and receiver. Radar Measurements are done using the radar cross-section for a small boat, illustrated in **Figure 3** and is seen to be well represented by a monopole resonant at 16.6 meters length, plus some additional monopole elements that are responsible for the other peaks.

Radar Modeling is a design in which two masts resonant at 8 and 12 MHz, separated by 7.5 meters were used to calculate the RCS as a function of bistatic angle for a second transmitter. The ships heading is toward the receive antenna. The effects of the changing illumination angle for coherent addition of the scatter from the two monopoles is rather complex, but can be used to classify targets using such models [2, 3, 4, 7].

## COASTAL HF RADAR SURVEILLANCE OF PIRATE BOATS

The deployment of a network of HFSWR systems is a complex task with many factors to be considered, particularly when the radars are expected to perform multiple roles. Failure to treat the sitting problem with appropriate care could seriously degrade performance in one or more radar missions. Here is described a practical technique for HFSWR network design, based to the multi-objective optimization, which has to demonstrate its efficacy in the context of a hypothetical two-radar system deployed in the Strait of Malacca and off Somalia Coast, a major waterway along which many critical surveillance requirements for tracking of pirate boats have been identified. The results confirm that quite disparate criteria can be taken into account with this research approach and that this methodology can be extended to higher and successful dimensions.

### SYSTEM ARCHITECTURE FOR ANTI PIRACY MISSION IN STRAIT OF MALACCA

The HFSWR surveillance network is a highly cost-effective remote sensing technology for measuring waves and currents including monitoring the movements of ships and aircraft, at over-the-horizon ranges. To place this in a specific context, the nominal performance of two representative HFSWR systems, such as the Low-Cost Civilian Radar and a more sophisticated Military Radar are summarized in **Table 1**.

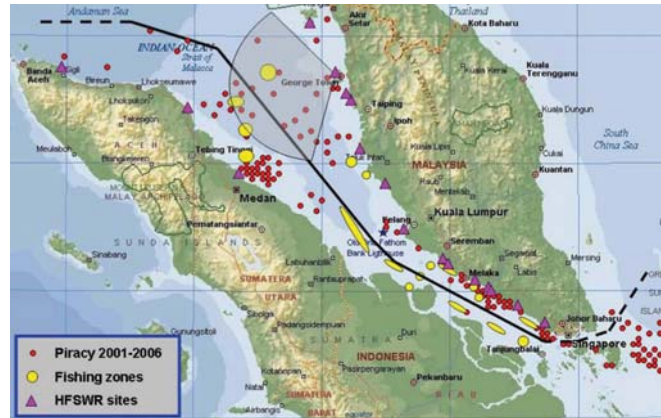


Fig. 4. Radar HF Surveillance and Remote Sensing of Pirate Ships – Courtesy of Paper: by Anderson [8]

Tab. 1. Performances of Civilian and Military Systems

Observable	Typical Performance			
	Low-cost Civilian Radar		Military Radar	
	Max, Range (Km)	± Accuracy	Max, Range (Km)	± Accuracy
Surface Current	60 - 200	0.02 - 0.20 m/s	350 - 450	0.02 - 0.10 m/s
Wave Height	30 - 100	10 - 25%	150 - 259	10 - 20%
Wind Direction	50 - 150	30 <sup>0</sup> - 60 <sup>0</sup>	320 - 400	20 <sup>0</sup> - 60 <sup>0</sup>
Wind Speed	30 - 100	20%	200 - 250	20%
Large Ships	50 - 180	0.5 - 3 Km	300 - 450	0.5 - 3 Km
Fishing Boats	20 - 65	0.5 - 2 Km	120 - 280	0.5 - 2 Km
Small Ships	10 - 25	0.5 - 1 Km	70 - 150	0.5 - 1 Km

In the above table, normal performance of representative HFSWR systems against generic mission is presented. It is noted that coverage and accuracy are dependent on sea conditions, target behaviour and other factors, consideration that is indicated here by citing the range within, in which each parameter usually lays. **Figure 4** is shown the primary shipping channel in the Strait of Malacca covered by the HFSWR system, along with the locations of the main fishing zones and the areas with the highest incidence of piracy. To provide prospective coverage, the HFSWR system is deployed at a coastal radar located in George Town on Pulau Pinang Island in the Strait of Malacca. No other sensor possesses the same combination of over-the-horizon radar coverage, day-night operation with ability to detect non-cooperating targets, remote sensing of sea conditions, ships and low cost per unit area under surveillance. While some HFSWR systems have been deployed with a single mission in mind, it is increasingly recognized that the versatility of this technology supports a variety of applications.

For instance, one might wish to detect and track shipping and pirate boats in the Strait of Malacca but also to measure surface currents so that risks of collision or grounding can be minimized and any transport of pollution predicted. The most important task of anti-piracy mission in the future will be to prevent the piracy activities by deploying additional HFSWR systems in Strait of Malacca and insure more security and safety of ships and crews onboard. Accordingly, one must resort to numerical optimization techniques in a multidimensional parameter space if one is to deploy a radar to best advantage. Moreover, a single surveillance radar can

measure only one component of the instantaneous velocity vector of a moving target. At this point, for detecting and tracking of ships and aircraft, observing target motion over time removes this limitation and the full velocity vector can be estimated

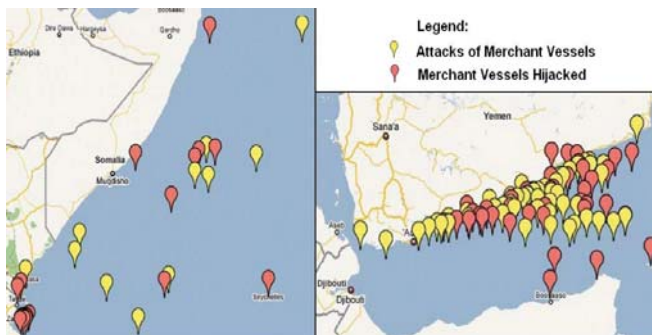


Fig. 5. Reported Piracy Incidents at Somalia Coast and the Gulf of Aden – Courtesy of Booklet: by OCIMF [9]

### DEPLOYMENT OF HFSWR FOR ANTI PIRACY MISSION OF THE SOMALI AND ADEN COASTS

The navigational dangers of collision and grounding of ships in the area of Somalia and the Gulf of Aden are serious problems for a long time. Armed attacks on merchant vessels transiting this area have increased in frequency over the past years. In fact, there were 140 approaches and at least 39 vessels actually detained by pirates in 2008 by source of The UK Maritime Trade Operations (UKMTO). Such acts have usually been conducted with the use or threat of violence, which can be particularly traumatic for those directly involved, as well as their families.

The Oil Companies International Marine Forum (OCIMF) is a voluntary association of oil companies having an interest in the shipment and terminalling of crude oil and oil products, which mission is to organize with its membership on matters relating to the safe shipment of crude oil and oil products, including marine pollution and safety. The Terminal Operators (SIGTTO) have an initiative with the aim of providing practical information to assist seafarers faced with potential or actual acts of piracy operating in the waters of Somalia and Aden.

**Figure 5 (Left)** shows a diagram of area to the South of the Horn of Africa, which is associated with Somali piracy in 2008 with events of 9 attacks on merchant's vessels, of which 8 were fired at and 10 merchant vessels hijacked.

**Figure 5 (Right)** shows a diagram in the area Gulf of Aden with the total number of reported 92 incidents by pirate boats. During 2008 in this area pirates organized 60 attacks on merchant's vessels, 31 vessels were fired at and 32 merchant vessels hijacked.

This High-Risk Area covers the ocean waters where attacks were frequent during past years, so to prevent actions of pirates in this area a minimum of two HFSWR installations have to be deployed, one at Somalian coast and another in the Gulf of Aden [2, 3, 4, 8].

### COASTAL HF JINDALEE OPERATIONAL RADAR NETWORK (JORN)

Jindalee was the first such project taken up in the 1960s as a bistatic OTHR system controlled from the Jindalee Facility at Alice Spring (JFAS) in central Australia, where two separate transmitter and receiver sites were deployed. The main OTHR transmitter was located at Harts Range and the receiver was located at Mount Everard. However, the other radar system is an ionospheric sounder known as the Frequency Management System (FMS).

The JORN HF Radar is the OTHR network that can monitor mobile movements at sea and in the air across 37,000 Km<sup>2</sup> and it has an official range of 3,000 Km. It is used in the defence of Australia and can also monitor maritime operations, wave heights and wind directions. On 2 April 2003, Jindalee was joined with two other OTHR systems and formed what is today known as JORN system. These three radars are dispersed across Australia, at Longreach in Queensland, Laverton in Western Australia and Alice Springs in the Northern Territory, to provide surveillance coverage of Australia's Northern approaches, as shown in **Figure 6 (A)**. This figure depicts the locations of the three OTHR systems and the JCC, and highlights the coverage of all three surveillance radars. The Alice Springs and Longreach radars cover an arc of 90° each, whereas the Laverton OTHR coverage area extends through 180°.

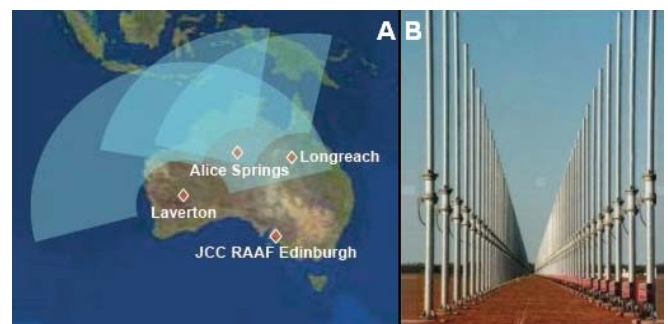


Fig. 6. Coverage Areas and Receiving Antenna of JORN – Courtesy of Paper: by Air Force/Saun [10/11]

Radar data from these three sensors is conveyed to the JORN Coordination Centre (JCC) within the Air Force's No 1 Radar Surveillance Unit (IRSU) at Royal Australian Air Force's (RAAF) Base Edinburgh in South Australia. The IRSU site is tasked by higher headquarters to operate the JORN capability on a daily basis.

The OTHR systems operate on the Doppler principle, where an object can be detected if its motion toward or away from the radar is different from the movement of its surroundings. They are typically made up of a very large fixed transmitter and receiver antennas called arrays, which receiving antenna is illustrated in **Figure 6 (B)**. The location and orientation of these arrays determine the lateral limits or arc of radar's coverage. The extent of OTHR coverage in range within this arc is variable and principally dependent on the state of the ionosphere. The OTHR systems do not

continually “sweep” an area like conventional radars but rather “dwell” by focusing the radar’s energy on a particular area, referred to as a “tile” within the total area of coverage. The transmitted HF energy can be electronically steered to illuminate other “tiles” within the OTHR networks coverage as required to satisfy operational tasking or in response to intelligence inquire. A disadvantage of this system is that it can detect metal vessels, while it is improbable that an OTHR will detect wooden boats. In such a way, the JORN system cannot be used for tracking small wooden boats of pirates [3, 10, 11].

The combination of these three systems, JORN, can detect all sea and air Doppler moving targets in the area between 1,000 and 3,000 Km North of the radar sites. It is also the key component of the sea-air gap surveillance system in Australia by ensuring a surveillance area with an arc of almost 180° wide and out to 2,000 Km from the Australian coastline. The detailed characteristics of JORN transmit antenna can be found in **Figures 7 (A)**, which shows the transmission antenna array of JORN near Longreach, in Queensland. **Figure 7 (B)** demonstrates an interior view of the JORN Co-ordination centre at RAAF Edinburgh, South Australia.

All radar surveillance systems normally have a problem with the bend of the Earth surface. The maximum range of the detecting radars is limited by the radio horizon, which is slightly far away than the optical horizon. The early HF communication systems have made use of ionospheric refraction to obtain spectacularly long ranges for most of the twentieth century.

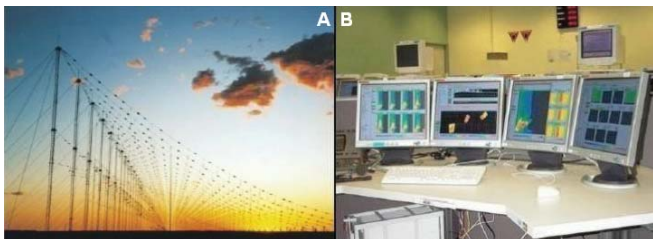


Fig. 7. JORN Transmit Antenna and Coordination Centre – Courtesy of Thesis: by Liu [12]

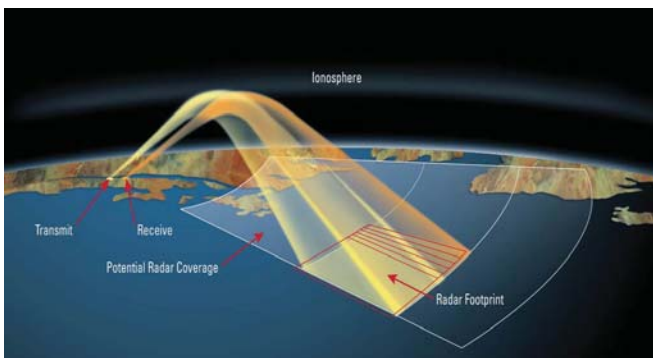


Fig. 8. Key JORN Operating Principles – Courtesy of Paper: by JORN [10]

The idea of actually radiating via the ionosphere and detecting the backscatter returning by the same path did not seem credible until coherent processing became practical

in the early 1960s. **Figure 8** presents the key JORN operating principles to transmit signals on HF frequency via ionosphere towards radar coverage and to receive reflected signals. The ionosphere is the upper part of the atmosphere extending from 75 to 450 Km above the Earth’s surface that consists of particles that have been ionized by solar radiation emitted by the Sun. Thus, the state of the ionosphere depends on the level of solar activity. Other more localized phenomena also affect the stability and/or structure of the ionosphere, which are a combination of these phenomena and solar events, which determines the quality of ionosphere support for HF/SWR or OTHR operations [3, 10, 12].

Therefore, the ability of JORN remote sensing HF radar is to see beyond the horizon with a range that dwarfed conventional radar made it an invaluable tool for detecting seagoing ships. The HF Radar is able to send signals via ionosphere towards its radar footprint or to potential radar coverage and receive reflected signals from targets at footprint and from ionosphere.

**Figure 9** illustrates a diagram of the International Amateur Radio Union (IARU) that Transmit Site sends the HF signal to the ionosphere and after reflected signal from ionosphere goes to the targets, such as ships and aircraft. In the opposite direction, HF radar detects signals in Receive Site reflected from both targets via ionosphere, which finally have to be processed in Control Site [13].

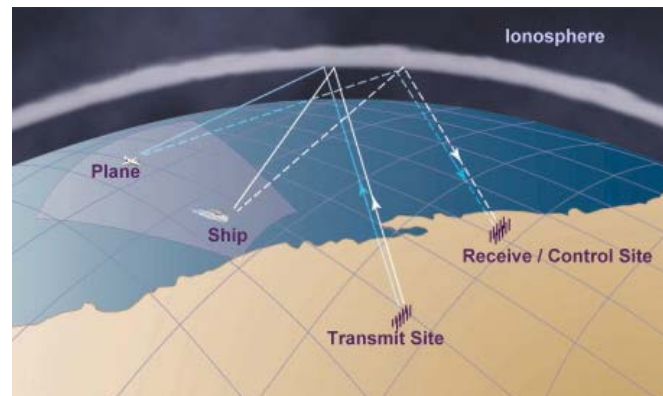


Fig. 9. Transceiver/Control Sites of HF Radar – Courtesy of Paper: by Hadel [13]



Fig. 10. Wellen Radar in Ligurian Sea – Courtesy of Paper: by Schlick [14]

## DIFFERENT PROJECTS OF COASTAL HF RADARS FOR VESSELS DETECTING

The HF surface wave radars have been identified to be a gap-filling technology for maritime domain awareness as a key factor in coastal activities for detecting and tracking of vessels in deep-sea and coastal navigation, for enhanced safety and security, improved national security (terrorism, drug smuggling, etc.) and environmental sea protection (marine protected areas, fishery monitoring and regulation, oil spills, etc.). Therefore, the HF surveillance radar is a strong candidate to become a component of any large sea area for vessel-monitoring network. This research realized several design options for an HF radar and ship monitoring system, such as multiple or single frequency, multiple or single sites or method of target bearing determination, such as Multiple Signal Classification (MUSIC) or real aperture antenna. It also presents a model of the SNR for ship detecting by HF radar and as well as observational examples of ship detecting with single and multifrequency HF radars. Finally, it suggests future experiments about tracking of pirate ships and draws conclusions. The further discussion has to estimate the primary metrics for assessing performance for ship tracking radars with Probabilities of detecting ( $P_d$ ) and false alarm ( $P_{fa}$ ) including their variation with parameters such as range, azimuth and frequency, and number of observing modes.

There are many different projects of Coastal HF Radars for detecting and tracking seagoing ships, but here will be introduced the network coverages of the German Wellen Radar (WERA) and the US SeaSonde.

**1. WERA HF Radar** – This type of HF coastal surveillance radar was employed in May 2009 in an international project known as “NURC BP09 Experiment” by the NATO Research Centre (NURC) of La Spezia, Italy, Department of Information Engineering, University of Pisa, Italy and Institute of Oceanography, University of Hamburg, Germany. The NURC effective maritime situational awareness project deployed a Maritime Surveillance System (MSS) that includes vessel ground truth and contact simulation, sensor processing, data fusion, anomaly detecting, sensor management and performance evaluation. Two WERA systems operating at 12.5 MHz have been installed at the Italian coast for experimental and evaluation purpose.

**Figure 10** illustrates a map depicting the HF setup in the Ligurian Sea near La Spezia town in Italy. The red dot shows the location of a Meteo and a wave rider buoy, which were deployed for validation purposes. The Ligurian Sea setup is depicted showing the overlap area in which the current and wave retrieval is performed as well as the range.

The WERA HF radar system transmits an average power of 30 W but it achieves detecting ranges up to 200 Km, which are far beyond the conventional microwave radar coverage. Due to external noise, radio frequency interference and different kinds of clutter, special techniques of target detecting such as ships using the WERA system have to be applied. For a 12-hour period, HF radar data have been recorded and processed. The target locations detected by the HF radar using

the proposed adaptive technique are passed to a tracking filter to track the ship position. In order to estimate the performance of the radar detecting and tracking techniques, these ship locations are compared with the ship positions recorded by the VHF AIS.

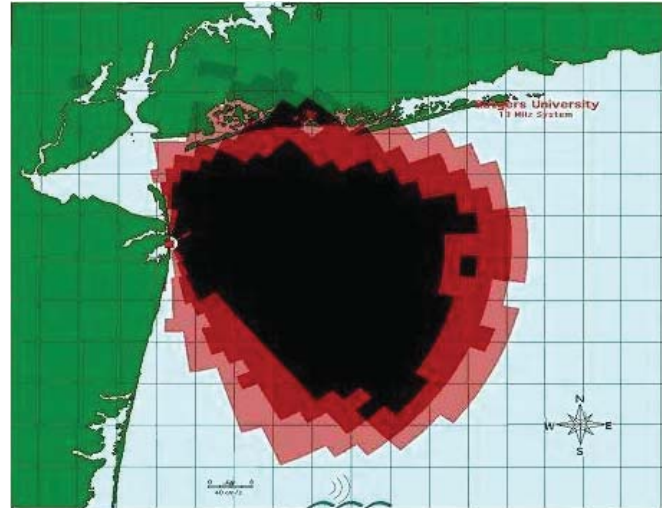


Fig. 11. SeaSonde Radial Coverage Map – Courtesy of Paper: by Glen [15]

The WERA surveillance network was developed at the German University of Hamburg in 1996 to allow a wide range of working frequencies, spatial resolution and antenna configurations in order to operate as low power oceanographic radar providing simultaneous wide-area measurements of surface currents, ocean waves, wind parameters and detecting of ships. This HF Radar system is based on a modular design that can be easily adapted to the requirements of an actual application.

**2. SeaSonde HF Radar** – Present SeaSonde HF radars have been designed to map surface currents, but are able to track surface vessels in a dual-use mode. The US Rutgers University in New Jersey and CODAR Ocean Sensors from Mountain in California, have collaborated on the development of vessel detecting and tracking capabilities from the compact HF radars, demonstrating that ships can be detected and tracked by multistatic HF radar in a multiship environment while simultaneously mapping ocean currents.

Furthermore, the same vessel is seen simultaneously by the radar-based on different processing parameters, mitigating the need to preselect a fixed set and thereby improving detecting performance. The radar was deployed in Sea Bright, New Jersey, 40 Km south of the Battery in New York City. It was direction-finding type radar, SeaSonde Remote Unit code SSRS-100, manufactured by CODAR Ocean Sensors and was installed in October 2008. The radar's primary function was the measurement of surface currents, which are provided in real-time to the NOAA National HF Radar Network. The radar also has the dual-use capability to detect the location of ships at sea.

**Figure 11** illustrates the spatial and temporal radial vector coverage for ocean currents of the radar over a 1-week period,

which coincided with the ship detecting exercise. The radial coverage map is presented in the area of the SeaSonde at Sea Bright, New Jersey, over a 1-week period. The color map illustrates the temporal coverage along the radial grid (black = 75%, red = 50% and pink = 25%). The radar collected range data, which are a time series of the complex echo signal voltages before Doppler processing. These range files are the result of the first Fast Fourier Transform (FFT) of the frequency-modulated continuous-wave received signal.

The range data were collected using an FFT length of 512 points. With a 2-Hz sweep of the radar, each range file encompasses 256 sec of coherent integration time. There were a total of 15 range files over the hour-long period. However, the time on the computer and all the subsequent files it generates are synchronized to atomic time via GPS by the Macintosh operating system. The SeaSonde HF radar consists of a compact receive antenna with three elements, such as two-directional crossed loops and an omnidirectional monopole, a monopole transmit antenna and hardware housed within a climate-controlled enclosure. The radar transmits a radio wave with a centre frequency of 13.46 MHz and a bandwidth of 50 kHz. The bandwidth of the radar sets the spatial range resolution of the system, which was about 3 Km for this particular bandwidth. Separate transmit and receive radar antennas were used for this study spaced at least one a wavelength apart, which is approximately 23 m at the 13 MHz radio band. A ship with a vertical structure of a quarter wavelength (6 m) is the minimum-sized optimal reflector [3, 4, 14, 15].

NATO Science and Technology Organization (STO) Centre for Maritime Research and Experimentation (CMRE) during the Battlespace Preparation 2009 (BP09) campaign. In such a way, ship reports from the AIS data, recorded from both coastal and satellite-based stations are exploited as ground truth information and a methodology is applied to classify the fused tracks and to estimate system performances. **Figure 12 (Right)** illustrates the AIS contacts recorded at Busum and Wangerooge stations on 4th August 2013. A total of 620 different AIS-carrying ships (grey) were recorded that day, with 299 only in the fusion region (blue line perimeter). In fact, this number is far greater than previous conducted, and the performance assessment procedure requires that the AIS reports are interpolated (black) on the radar timestamps [2, 3, 16].

## CONCLUSION

Modern radar systems design offers advanced features such as automatic tracking of vessels in coastal waters and geographical mapping. Geographical masks or areas can be introduced to define forbidden zones, speed limit zones, traffic separation zones etc. However, in order to detect and track ocean-going ships and especially small vessels trying to evade authorities, sophisticated methods of detection and tracking are required. At this point, specialized software algorithms are developed, which ensure successful tracking even in extremely difficult weather and sea conditions have to fulfil the following requirements:

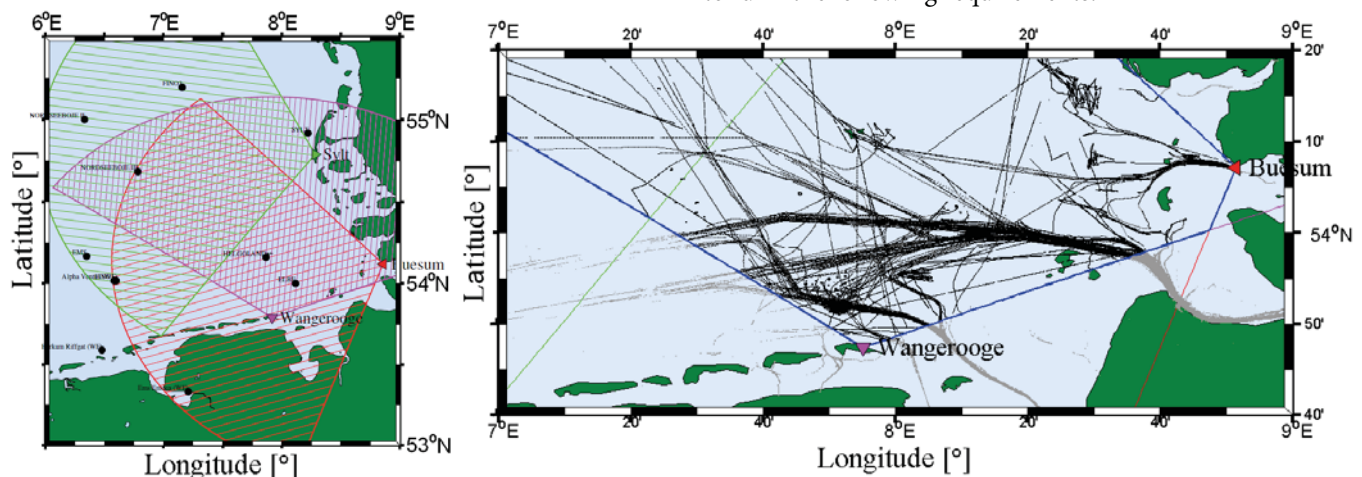


Figure 12. Setup of the HFSW radars in the German Bight and AIS Ship Routes – Courtesy of Paper: by Grasso [16]

**3. German Bight HF Radar** – In the context of ships surveillance, a cost-effective long-range early-warning sensor for ship detection and tracking, which provide data fusion techniques to live-recorded data from a network of oceanographic HFSW radars installed in the German Bight (North Sea), shown in **Figure 12 (Left)**, where Sylt is green, Busum (red) and Wangerooge (magenta) are demonstrated. This experimentation closely follows the one conducted in the Ligurian Sea (Mediterranean Sea) by

- High probability of detection and low false alarm rate;
- Ability to discriminate between close targets;
- Noise and clutter suppression processing techniques;
- Stable tracking and rapid manoeuvre detection;
- Analysis of target movements to identify suspicious behaviour patterns; and
- The application of predefined alarms that respond to entry into zones or in close proximity to other targets.

The coverage area of fixed coastal radar stations can be quickly recognized and the illegal traffic can be directed outside of the existing coverage areas. The radar coverage

areas can be extended and continuously changed by use of transportable radar stations. In this way, the detection zones can be made unpredictable and hence their employment increases the probability of preventing illegal activities. The portable radar stations can be housed inside equipment containers, which can be moved around by helicopter or a lorry. If a more rapid deployment of radar stations is required, the radar sensor can be housed inside a van. Thus, in both cases the radar sensors are self-contained, having power generators, air-conditioning and radio communications.

The International Ship and Port Facility Security (ISPS) Code has been adopted and approved by the International Maritime Organization (IMO) to address the threat to the maritime industry posed by terrorism and other illegal activities. The Code was approved in December 2002 and became a law on 1st July 2004. The implementation of ISPS code calls for improved detection of small craft in littoral waters. The use of radar sensors is a primary tool in the detection of small unfriendly vessels. In most cases the high quality radar data may be the only source of information indicating the position and movements of vessels posing security threats. Therefore, a careful choice of radar parameters is very important for the detection and discrimination of small targets.

## REFERENCES

1. Isik C. & Others, "Principles of Integrated Maritime Surveillance Systems", Kluwer, Norwell, MA, 2000.
2. Ilcev D.S., "Global Mobile Communication, Navigation and Surveillance (CNS)", DUT, Durban 2012.
3. ISR, "HF Surface Wave Radars", Imaging Science Research (ISR), Burke, VA, 2015.
4. Fabrizio G., "High Frequency over the Horizon Radar", McGraw-Hill, New York, 2013.
5. Trizna D.B., "A Bistatic HF Radar for Current Mapping and Robust Ship Tracking", Paper, Burke, VA, 2010.
6. Ilcev D.S., "Maritime Communication, Navigation and Surveillance (CNS)", Presentation, DUT, Durban 2014.
7. Trizna D.B. & Xu L., "Microwave and HF Multi-Frequency Radars for Dual-Use Coastal Remote Sensing Applications", Paper, Paper, Burke, VA, 2005.
8. Anderson S.J., "Optimizing HF Radar Siting for Surveillance and Remote Sensing in the Strait of Malacca", IEEE Transactions on Geoscience and Remote Sensing, Vol. 51, No 3, Piscataway, NJ, 2013.
9. OCIMF, "Piracy - The East Africa/Somalia Situation", Oil Companies International Marine Forum, London, 2008.
10. Air Force, "Jindalee Operational Radar Network", Fact Sheet, Canberra, Australia, 2015.
11. Saun G., "Jindalee Operational Radar Network", Department of Defense, Edinburgh, Australia, 2015.
12. Liu B.Y., "HF Over-the-Horizon Radar System Performance Analyzes", Thesis, Naval Postgraduate School, Monterey, CA, 2007.
13. Hadel W., "Radar Systems on Shortwave", International Amateur Radio Union (IARA), Newington, CT, 2015.
14. Schlick T. & Others, "Evolution of a HF-Radar Ship Detection Algorithm by Comparison to AIS and SAR Data", NATO Undersea Research Center/University of Hamburg, La Spezia, Italy/Hamburg, Germany, 2011.
15. Glen S.M. & Others, "Performance Evaluation of SeaSonde High-Frequency Radar for Vessel Detection", CODAR Ocean Sensors, Mountain View, CA, 2010.
16. Grasso R. & Others, "A Network of HF Surface Wave Radars for Maritime Surveillance Preliminary Results in the German Bight", NATO STO CMRE, La Spezia, Italy, 2014.

## CONTACT WITH THE AUTHOR

**Prof. D.S. Ilcev, BSc, MSc, PhD**

*e-mail: ilcev@dut.ac.za, tel.: +27827650817*  
 Master Mariner  
 Chairman of Spice Science Centre (SSC)  
 and Postgraduate Studies at:  
 Durban University of Technology (DUT)  
 45 Bencorrum, 183 Prince Street,  
 Durban 4001  
**SOUTH AFRICA**

# MODEL PREDICTIVE SUPER-TWISTING SLIDING MODE CONTROL FOR AN AUTONOMOUS SURFACE VEHICLE

Hossein Nejatbakhsh Esfahani  
Rafal Szlapczynski  
Gdańsk University of Technology, Poland

## ABSTRACT

*This paper presents a new robust Model Predictive Control (MPC) algorithm for trajectory tracking of an Autonomous Surface Vehicle (ASV) in presence of the time-varying external disturbances including winds, waves and ocean currents as well as dynamical uncertainties. For fulfilling the robustness property, a sliding mode control-based procedure for designing of MPC and a super-twisting term are adopted. The MPC algorithm has been known as an effective approach for the implementation simplicity and its fast dynamic response. The proposed hybrid controller has been implemented in MATLAB / Simulink environment. The results for the combined Model Predictive Super-Twisting Sliding Mode Control (MP-STSMC) algorithm have shown that it significantly outperforms conventional MPC algorithm in terms of the transient response, robustness and steady state response and presents an effective chattering attenuation in comparison with the Super-Twisting Sliding Mode Control (STSMC) algorithm.*

**Keywords:** autonomous Surface Vehicle, Model Predictive Control, Sliding Mode Control, Super-Twisting Algorithm, Chattering Attenuation

## INTRODUCTION

Marine robots have been drastically improved during the last decade until today. Their applications are very extensive, ranging from inspection tasks to accomplishing complex underwater explorations. Based on this, the maritime robotic platforms can be grouped into underwater and surface robots. As for the first group, we can refer to the underwater manipulators, autonomous underwater vehicles and autonomous underwater vehicle-manipulator systems. For the second group, there are unmanned surface vehicles and autonomous surface ships. Designing a high performance control system for the robotic platforms is a paramount challenge, particularly in case of Autonomous Surface Vehicle

(ASV). However, due to the high nonlinearity terms in ASV dynamics and uncertainties resulting from inertia parameter variation, a robust control algorithm should be adopted for taking these uncertainties and external disturbances into account. As to the literature about the marine robotic control and navigation systems, some research works upon the navigation area have been accomplished in [20-22]. Regarding marine robotics control area, an optimal SMC was adopted in which the adjustable parameters of the sliding mode controller were estimated by using wavelet mutation [1]. In [2] a robust strategy based on Time Delay Control (TDC) algorithm and Terminal Sliding Mode (TSM) was designed to control an Underwater Vehicle-Manipulator System (UVMS). In this work TDC was regarded to enhance robustness feature and

tracking accuracy. Also, the gains of SMC were adaptively tuned by the fuzzy inference system. Concerning chattering reduction of SMC algorithm, the authors of [3] presented a new reaching mode including exponential function to illuminate chattering frequencies. The robustness issue of MPC has always been a challenge in designing robust nonlinear model predictive controllers (NMPC). An NMPC was used for an Unmanned Surface Vehicle (USV) in [4]. In this research a conventional MPC was used in which the robustness however might be not guaranteed. Also, the sea environmental disturbances have not been considered there. In [5], a back-stepping control approach combined with sliding mode control algorithm was designed to cover the trajectory tracking problem of an under-actuated USV. An autonomous robotic boat was presented in [6] and a nonlinear model predictive control (NMPC) was adopted for its controller. However, the uncertain nonlinearities, resulting from the changes in inertia and drag matrices of the robotic boat, were not taken into account there. Another weakness of the work in question was neglecting the influences due to winds, waves and ocean current disturbances. Two kinds of MPC controllers, including NMPC, were proposed in [7], which solved a constrained multi-variable nonlinear programming problem and Linearized MPC (LMPC), designed to solve a constrained quadratic programming problem by means of on-line iterative optimization. However, again the environmental disturbances (winds, waves and currents) were not taken into account. In [8], a nonlinear disturbance observer was designed to estimate unknown parameters and external disturbances. However, this observer was able to estimate only constant disturbances. A control law for path tracking of marine vessel was adopted in [9], where a singular perturbation method was used to decompose the system into two Lyapunov theory based control subsystems. Some research projects concerning adopting the higher order sliding mode algorithms such as super-twisting for control of the maritime autonomous robots, were carried out in [10,11]. In [12] there were presented two control algorithms for the trajectory tracking of an autonomous marine platform, in which the input constraints and disturbances induced by constant ocean currents were regarded. In this research the first approach was based on a Lyapunov design strategy, while the second was developed by adopting a MPC algorithm. For tuning of gains in a PID controller, in [13] a self-regulator PID was designed in which coefficients have been regulated by the fuzzy rules. A robust multi-loop control scheme including Integral Sliding Mode (ISM) loop and MPC loop has been presented in [16] where the ISM role is to reject uncertain terms due to unknown dynamics. In [17], a novel perturbation compensating algorithm was proposed to reach the more accurate path tracking in the presence of environmental disturbances, which finally led to a robust MPC. As to other kinds of nonlinear control of marine vehicles, some approaches based on back-stepping algorithm have been implemented in [18,19].

In this research, the proposed control law is designed based on the sliding mode function, model predictive control and

super-twisting concepts. The motivation is to reach the ability to explicitly deal with state and input constraints as well as fast dynamic response from MPC and the good robustness attributes from SMC and super-twisting, particularly in presence of severe external disturbance. However, we have to face two challenges with adopting the MPC for trajectory tracking goals. The first one is obtaining an acceptable robustness of MPC and the second – avoiding large overshoot caused by fast settling time. Hence, we design an improved MPC based on the sliding function and add a super-twisting part to the control law in order to manage the aforementioned problems.

The rest of this paper is organized as follows. In the next section an ASV dynamical model associated with all of the time-varying external disturbances and uncertainties is described. The third section is dedicated to explain the proposed approach of model predictive super-twisting sliding mode control. In the fourth section the computer simulation results and their mutual comparison are shown to confirm a high performance of the proposed control. Discussion of the simulation results is provided in the fifth section and the conclusion is finally given in the sixth section.

## AUTONOMOUS SURFACE VEHICLE

The nonlinear dynamics of ASV can be described in the form of 3- DOF motion as follows

$$\begin{cases} M\dot{v} + C(v)v + D(v)v = \tau_c + MR^T(\psi)\Gamma \\ \dot{\eta} = R(\psi)v \end{cases} \quad (1)$$

where velocity and position vectors are defined as  $v = [u, v, r]^T$  and  $\eta = [x, y, \psi]^T$ , respectively. The coordinate frames regarding surge, sway and yaw motions are shown in Fig. 1. In the aforementioned equation, the rotation

matrix  $R(\psi) = \begin{bmatrix} \cos(\psi) & -\sin(\psi) & 0 \\ \sin(\psi) & \cos(\psi) & 0 \\ 0 & 0 & 1 \end{bmatrix}$  is used to transfer coordinates from the Body-Fixed Frame (BFF) to the Earth-Fixed Frame (EFF).

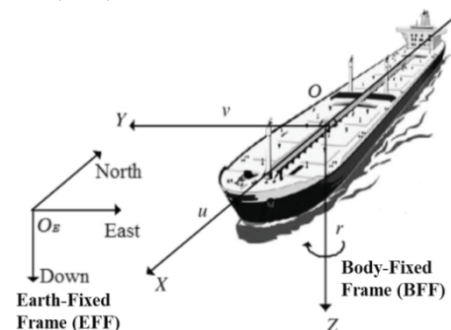


Fig. 1. The earth-fixed frame and body-fixed frame [14]

For presenting the Eq. (1) in a standard form based on position vector, we can rewrite it using the property of the rotation matrix  $\dot{\eta} = R(\psi)v$  as follows :

$$M(\eta)\ddot{\eta} + C(\eta, \dot{\eta})\dot{\eta} + D(\eta, \dot{\eta})\dot{\eta} = \tau_c + \tau_d \quad (2)$$

where, all the related components of each matrix in the equation (2) were presented by analogy with the dynamics of robotic manipulators [23].  $\tau_c = [\tau_x, \tau_y, \tau_N]^T$  and  $\tau_d = MR^T(\psi)\Gamma$  and are control inputs and external disturbances, respectively. These time-varying external disturbances are induced by the winds, waves and ocean currents, which are expressed by the vector of  $\Gamma = [\Gamma_u, \Gamma_v, \Gamma_r]^T$ . The disturbances are considered for applying to the ASV with 3 DOFs, in which their respective vectors can be modeled as follows [15]

$$\begin{cases} \Gamma_u = 0.1v^3 + 0.06u + 0.01\sin(t) \\ \Gamma_v = ur + 0.1u + 0.01\sin(t) \\ \Gamma_r = 0.4ur + v^2 + 0.01\sin(t) \end{cases} \quad (3)$$

$$M = \begin{bmatrix} m_{11} & m_{12} & m_{13} \\ m_{21} & m_{22} & m_{23} \\ m_{31} & m_{32} & m_{33} \end{bmatrix} \in \mathbb{R}^3, M(\eta) \in \mathbb{R}^3, C(\eta, \dot{\eta}) \in \mathbb{R}^3, D(\eta, \dot{\eta}) \in \mathbb{R}^3$$

are constant inertia matrix, time-varying inertia matrix, time-varying Coriolis matrix and time-varying hydrodynamic damping matrix including both linear and nonlinear parts, respectively [23]. Indeed, with taking into account the nonlinear damping parts, the matrix  $D(\eta)$  is changed to the form  $D(\eta, \dot{\eta})$  and nonlinear coefficients ( $d_{ij}$ ) are dependent on velocity vector  $\dot{\eta} = R(\psi)v$ .

## MODEL PREDICTIVE SUPER-TWISTING SMC

### SLIDING MODE-BASED MPC

In the proposed sliding mode model predictive control approach, a control input  $u(t)$  is designed for the tracking of a desired trajectory at the next time  $(t + t_h)$  by minimization of the following cost function.

$$J = f(\sigma(t + t_h), \eta(t + t_h), \tau_c(t)) \quad (4)$$

where  $\sigma(t + t_h)$  is a predicted sliding surface,  $\eta(t + t_h)$  is a  $t_h$ -step ahead prediction of the output state and  $t_h > 0$  is a prediction horizon. The tracking error, sliding surface and its first derivative are defined as:

$$e(t) = \eta - \eta_d \quad (5)$$

$$\sigma(t) = \dot{e} + \lambda e \quad (6)$$

$$\dot{\sigma}(t) = \ddot{e} + \lambda \dot{e} \quad (7)$$

where  $\eta$  and  $\eta_d$  and are actual and desired output states. Let us consider the predicted sliding surface approximately as follows

$$\sigma(t + t_h) = \sigma(t) + t_h \dot{\sigma}(t) \quad (8)$$

We can adopt a state vector of sliding surface as  $Q(t) = \begin{bmatrix} \sigma \\ \dot{\sigma} \end{bmatrix}$  and express the prediction model of sliding surface as follows:

$$\sigma(t + t_h) = T(t_h)Q(t) \quad (9)$$

where,  $T(t_h) = [I_{nn} \quad t_h * I_{nm}]$  and  $I_{nn}$  is an identity matrix.

The cost function based on the predicted sliding surface is presented upon the future horizon as

$$J = \frac{1}{2} \int_0^{t_d} (\sigma(t + t_h))^T (\sigma(t + t_h)) dt_h \quad (10)$$

An acceptable accuracy for the MPC algorithm can be achieved by tuning  $t_d$ . By the prediction model of sliding surface (9), the  $J$  can be rewritten as follows :

$$\begin{aligned} J &= \frac{1}{2} \int_0^{t_d} (\sigma(t + t_h))^T \sigma(t + t_h) dt_h \\ &= \frac{1}{2} \int_0^{t_d} (T(t_h)Q(t))^T (T(t_h)Q(t)) dt_h \\ &= \frac{1}{2} (Q(t))^T R(Q(t)) \end{aligned} \quad (11)$$

where:  $R = \int_0^{t_d} T(t_h)^T T(t_h) dt_h$

$$= \begin{bmatrix} t_d * I_{nn} & \left(\frac{t_d^2}{2}\right) * I_{nn} \\ \left(\frac{t_d^2}{2}\right) * I_{nn} & \left(\frac{t_d^3}{3}\right) * I_{nn} \end{bmatrix} \quad (12)$$

Substituting the equation (12) in (11), the cost function can be expressed based on sliding function and its first derivative as follows:

$$J(\sigma, \dot{\sigma}) = \frac{1}{2} t_d \sigma^2 + \frac{1}{2} t_d^2 \sigma \dot{\sigma} + \frac{1}{2} t_d^3 \dot{\sigma}^2 \quad (13)$$

We can rewrite the dynamic equation of ASV as follows:

$$\ddot{\eta}(t) = -M(\eta)^{-1}(C(\eta, \dot{\eta})\dot{\eta} + D(\eta, \dot{\eta})\dot{\eta}) \dots \dots + M(\eta)^{-1}\tau_c(t) \quad (14)$$

Also, in accordance to combination of the equations (5), (6) and (7), the first derivative of sliding surface can be obtained as

$$\dot{\sigma} = \ddot{\eta} + \lambda\dot{e} - \ddot{\eta}_d \quad (15)$$

Let us present the cost function as follows:

$$\dot{\sigma} = \ddot{\eta} + \lambda\dot{e} - \ddot{\eta}_d \quad (16)$$

where:  $J_1(\sigma) = \frac{1}{2}t_d\sigma^2$  and  $J_2(\sigma, \dot{\sigma}) = \frac{1}{2}t_d^2\sigma\dot{\sigma} + \frac{1}{2}t_d^3\dot{\sigma}^2$ .

The condition for to minimizing  $J$  is

$$\frac{\partial (J)}{\partial \tau_c} = 0 \quad (17)$$

Based on the equations of (14) and (15), we can see  $\tau_c(t)$  in the second part of cost function  $J_2(\sigma, \dot{\sigma})$ . Therefore, we can regard the minimization of the  $J$  subject to the  $\tau_c(t)$  as follows:

$$\frac{\partial (J)}{\partial \tau_c} = \frac{\partial (J_2)}{\partial \tau_c} = 0 \quad (18)$$

Hence, the optimal control law is:

$$\tau_{mp-smc}(t) = \hat{M}(\eta) \left( \ddot{\eta}_d - \lambda\dot{e} - \frac{3}{2t_d}\sigma \right) \dots \dots + \hat{C}(\eta, \dot{\eta})\dot{\eta} + \hat{D}(\eta, \dot{\eta})\dot{\eta} + p(\eta, \dot{\eta}, \ddot{\eta}) \quad (19)$$

where,  $p(\eta, \dot{\eta}, \ddot{\eta}) = [\hat{M}(\eta) - \tilde{M}]\ddot{\eta} + \hat{C}(\eta, \dot{\eta})\dot{\eta} + \dots + \hat{D}(\eta, \dot{\eta})\dot{\eta} - \tau_d$  is a perturbation part including inherent uncertainties ( $\tilde{M}, \tilde{C}, \tilde{D}$ ) and time-varying disturbances ( $\tau_d$ ).

$\hat{M}, \hat{C}$  and  $\hat{D}$  are regarded as nominal and known parts of the dynamical model. In the next section we adopt a super-twisting term for adding to the equation (19) in order to compensate the perturbation part ( $p$ ) and improve robustness property in the proposed hybrid control algorithm.

### SUPER TWISTING CONTROL LAW

The derivation of sliding surface can be performed as follows:

$$\begin{aligned} \dot{s} &= \ddot{e} + \lambda\dot{e} = \ddot{\eta} - \ddot{\eta}_d + \lambda\dot{e} = \\ &\hat{M}^{-1}[\tau_c - \hat{C} - \hat{D}] - \ddot{\eta}_d + \lambda\dot{e} \end{aligned} \quad (20)$$

The standard form for a super-twisting algorithm can be expressed as:

$$\begin{cases} \dot{s} = -k_1\xi(s)\text{sign}(s) + z \\ \dot{z} = -k_2\text{sign}(s) \end{cases} \quad (21)$$

where  $\xi(s) = \text{diag}(|s_1|^{\frac{1}{2}}, |s_2|^{\frac{1}{2}}, |s_3|^{\frac{1}{2}})$  and  $k_1, k_2$  are diagonal positive matrices.

$$\text{sign}(s) = \begin{cases} 1 & , & s > 0 \\ 0 & , & s = 0 \\ -1 & , & s < 0 \end{cases} \quad (22)$$

By using Eq. (20) and Eq. (21), the super-twisting control law is expressed as follows:

$$\tau_c = \hat{M} \left\{ \begin{aligned} &\ddot{\eta}_d - \lambda\dot{e} - k_1\xi(s)\text{sign}(s) \\ &-k_2 \int_0^t \text{sign}(s)dt \end{aligned} \right\} + \dots \dots \dots \hat{C} + \hat{D} \quad (23)$$

### PROPOSED HYBRID CONTROL LAW

In the proposed approach, to assure robustness of the hybrid control law against external disturbances and uncertainties, the following super-twisting term ( $\tau_{st}$ ) must be added to the optimal control law (19).

$$\begin{cases} \tau_{st}(t) = -k_1\xi(\sigma)\text{sign}(\sigma) + z \\ \dot{z} = -k_2\text{sign}(\sigma) \end{cases} \quad (24)$$

Finally, with taking into account the sliding mode MPC part (19) and the super-twisting term (24), the proposed control law is expressed as follows :

$$\tau_{mp-stsmc}(t) = \tau_{mp-smc}(t) + \tau_{st}(t) \quad (25)$$

The proposed control system of ASV is shown in Fig. 2.

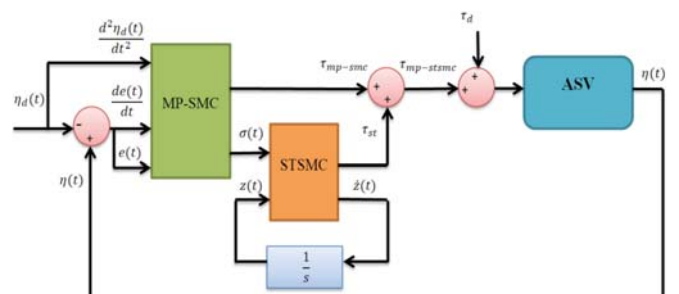


Fig. 2. Schematic diagram of the proposed Model Predictive Super-Twisting Sliding Mode Controller (MP-STSMC)

## COMPUTER SIMULATION RESULTS

In this section, the results of three simulated controllers including Super-Twisting Sliding Mode Controller (STSMC), Model Predictive Controller (MPC) and proposed Model Predictive Super-Twisting Sliding Mode Controller (MP-STSMC) are presented. The comparative outputs are shown in Fig. 3, Fig. 4 and Fig. 5 for the path following, tracking errors and control inputs, respectively.

In the mathematical modeling of ASV, the nonlinear parts of the damping coefficients are also significant elements taken into account in these simulations. They are described as follows [15]:

$$\begin{aligned}
 d_{11} &= 0.72 + 1.33|u| + 5.87u^2 \\
 d_{22} &= 0.8896 + 36.5|v| + 0.805|r| \\
 d_{23} &= 7.25 + 0.8451|v| + 3.45|r| \quad (26) \\
 d_{32} &= 0.0313 + 3.96|v| + 0.13|r| \\
 d_{33} &= 1.9 - 0.08|v| + 0.75|r|
 \end{aligned}$$

Other damping coefficients  $3 \times 3$  in the damping matrix are assigned to zero. And, the constants in inertia matrix are assigned as follows [15]:

$$M = \begin{bmatrix} m_{11} & m_{12} & m_{13} \\ m_{21} & m_{22} & m_{23} \\ m_{31} & m_{32} & m_{33} \end{bmatrix} = \begin{bmatrix} 25.8 & 0 & 0 \\ 0 & 33.8 & 1.0115 \\ 0 & 1.0115 & 2.76 \end{bmatrix}$$

The equations of desired paths with the initial conditions  $[0 \ 0 \ 0]^T$  and simulation time  $t = 40$  sec. are as follows:

$$\eta_d(t) = \begin{cases} x_d = 0.5 \text{ m} \\ y_d = 0.1 \cos\left(\frac{\pi}{20}t\right) \text{ m} \\ \psi_d = \pi \cos\left(\frac{\pi}{20}t\right) \text{ rad} \end{cases} \quad (27)$$

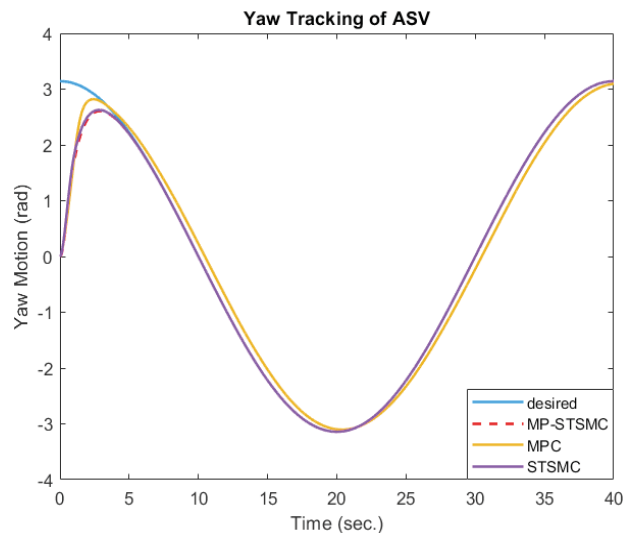
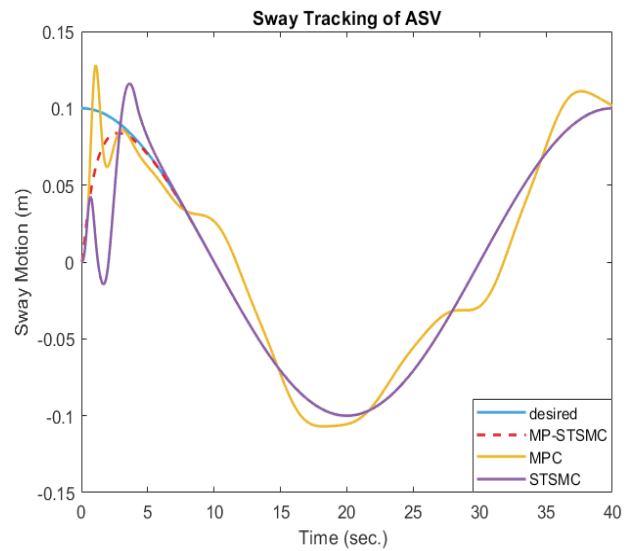
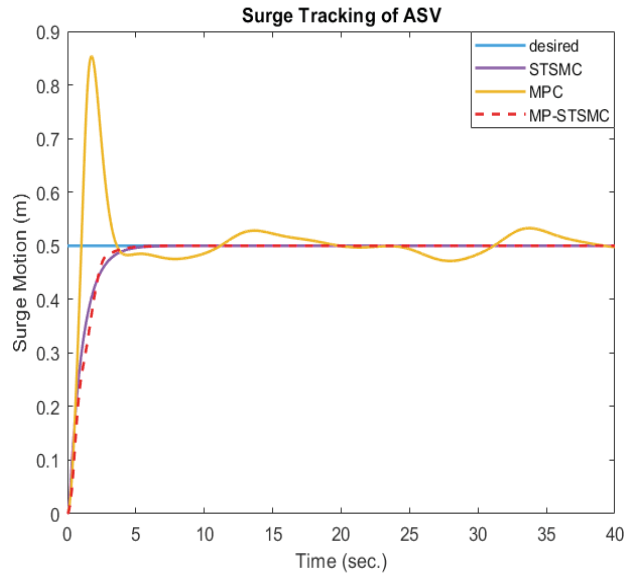


Fig. 3. Path Following

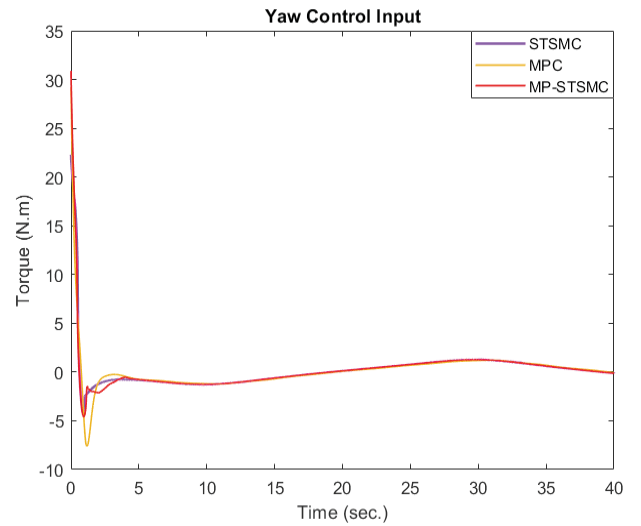
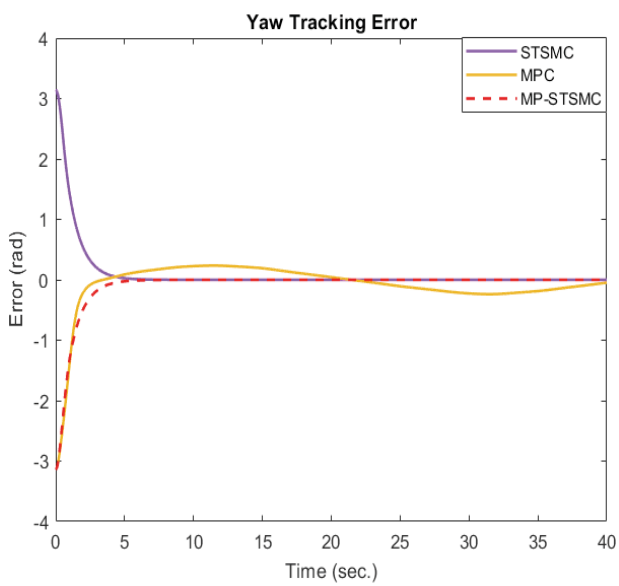
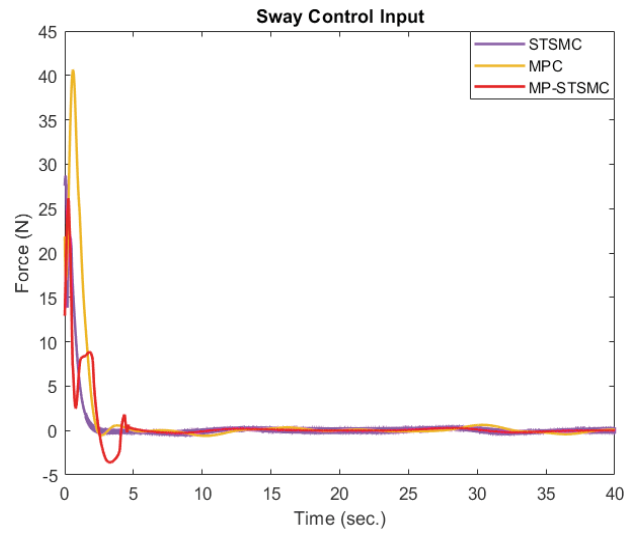
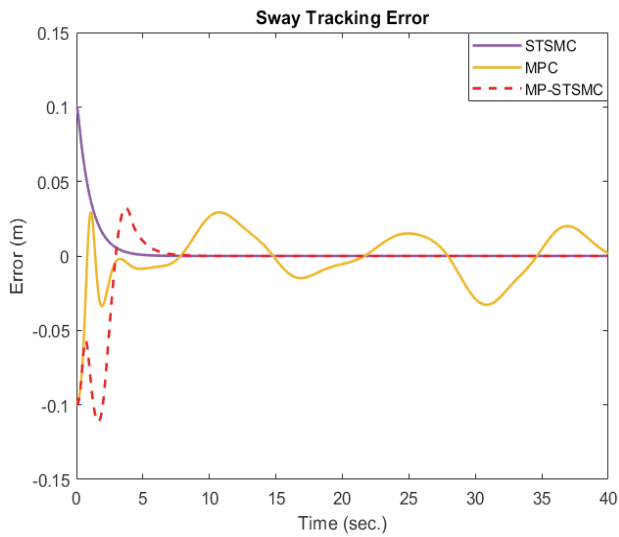
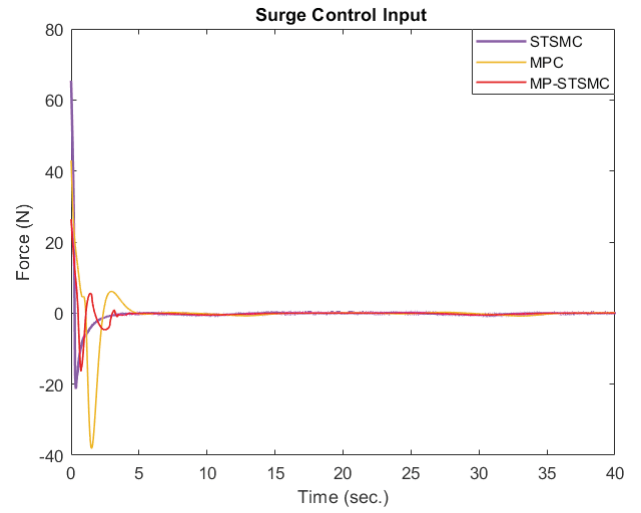
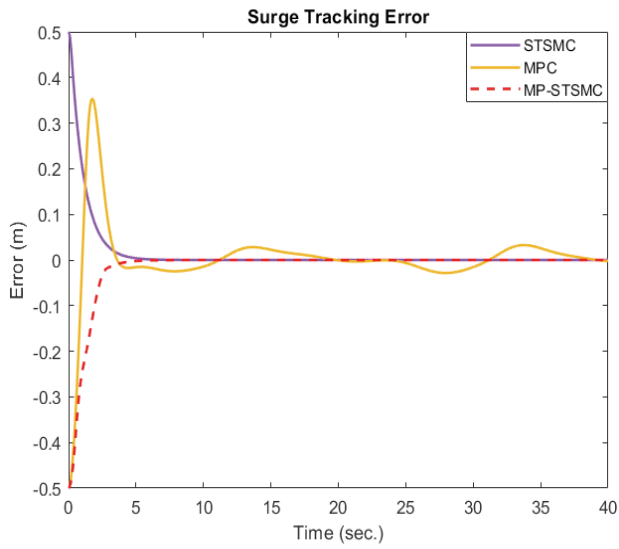


Fig. 4. Tracking Errors

Fig. 5. Control Inputs

As to chattering attenuation in the proposed algorithm in comparison with the super-twisting method, we have

provided Fig. 6 containing zoomed control inputs to compare the signals in terms of chattering effect.

The chattering is due to the assuming of the function in the switching term in a discontinuity in a super-twisting control law. The chattering phenomenon can be also induced by perturbations which compel ASV to leave the sliding mode in dynamic motion. For suppressing this phenomenon one solution is the using of a continuous term  $s$  with a boundary layer instead of discontinuous part  $\text{sign}(s)$  and, as another effective way, we can use the higher-order sliding mode controllers such as super-twisting algorithm. However, the chattering, particularly in steady-state response, is still present on control input as shown in Fig. 6, which let the tracking error to oscillate around the origin. In the proposed MP-STSMC, we can achieve the high robustness attribute of STSMC as well as drastically reduce steady-state chattering in finite time of tracking (see a chattering suppression scheme). Nevertheless, the chattering phenomenon, even with a very low amplitude in super-twisting SMC leads to the dissipation of a large quantity of fuel or energy in manoeuvring thrusters and propeller system, as well as to a rapid wear of mechanical actuators. Also, these high frequencies may excite unmodeled dynamics.

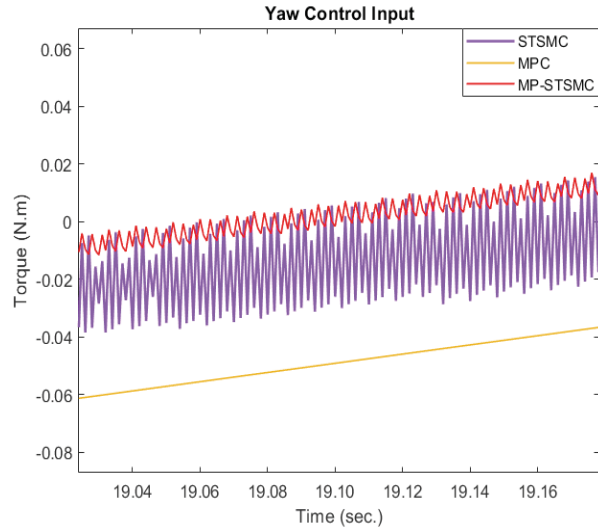


Fig. 6. Zoom in View of Control Inputs

## ANALYSIS AND DISCUSSION OF RESULTS

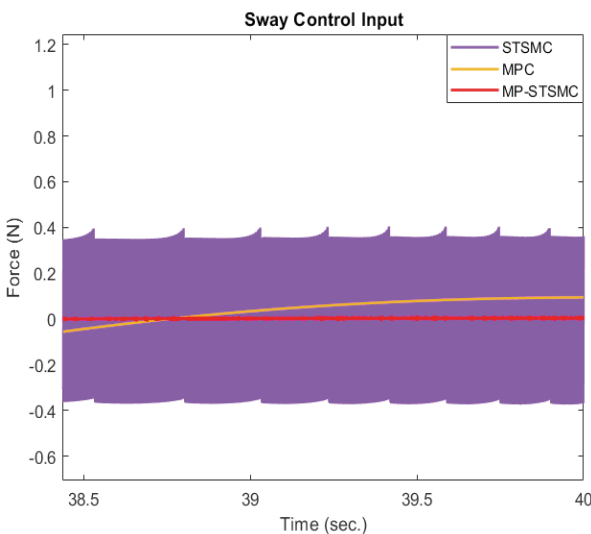
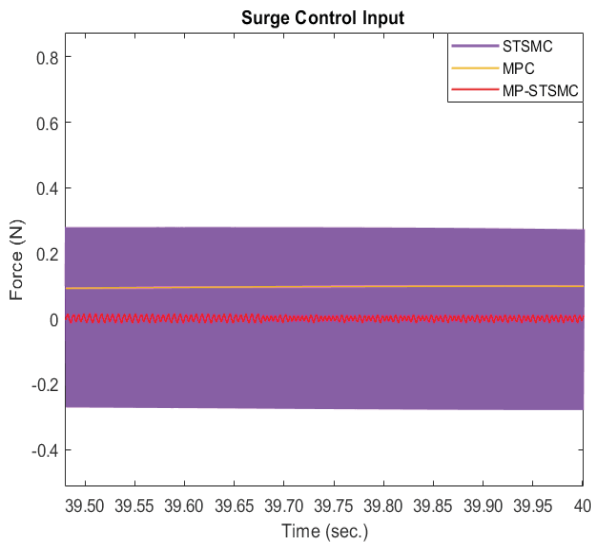
The analyzing of outputs resulting from the three controllers can be done in most nonlinear control theories in terms of four common properties:

- *Transient response*
- *Steady-State response*
- *Robustness*
- *Chattering phenomenon*

Based on the tracking errors depicted in Fig. 4, an undesired overshoot is obviously observed in MPC algorithm during surge trajectory tracking. Indeed, this severe overshoot has been stemmed from the fast dynamic property of MPC approach. However, we can see a smooth transient response for the STSMC and proposed MP-STSMC. Also, due to a lack of robustness of a conventional MPC, an inaccurate trajectory tracking and an undesired steady state response are observed in Fig. 3 and Fig. 4, respectively. Concerning STSMC and MP-STSMC, an acceptable accuracy as well as high robustness has been observed in presence of time-varying external disturbances. As it is illustrated in Fig. 5, we have a reduction in control efforts of MP-STSMC in comparison with STSMC because of optimization feature present in MPC. Finally, it is easily to argue that both proposed and STSMC algorithms bring about an accurate trajectory tracking, however there are two additional advantages of the proposed MP-STSMC in contrast to STSMC. The extra advantages include optimal control efforts and chattering attenuation, shown in Fig. 6.

## CONCLUSION AND FUTURE OUTLOOK

Regarding suitable control system in terms of real-time implementation for marine robotics platforms, particularly autonomous surface vehicles and unmanned ships, MPC



algorithm can be an interesting choice. To model predictive controllers fast dynamic response and simplicity in their implementation into autonomous systems can be attributed. However, a paramount challenge for applying the MPC is its robustness against external disturbances and model uncertainties. In this research, the authors considered the weaknesses of MPC and developed an improved robust MPC to remove the lack of robustness in conventional MPC.

The new hybrid strategy consists of two main parts. The first part is a sliding mode-based MPC law, in which a Proportional Derivative (PD) sliding surface is considered a function which to be optimized by MPC. The second part is the super-twisting term which has been regarded to deal with the robustness of MPC. In the meanwhile, by using this robust strategy, the transient and steady-state responses of conventional MPC have been also enhanced. Super-twisting sliding mode control algorithm is an effective control method in the robust control category. However, due to switching structure of sliding mode algorithms, including first-order and higher-order sliding mode controllers, they have been associated with generating of chattering in their control inputs. In general, super-twisting method can be considered a chattering attenuation strategy among sliding mode controllers. However, for some applications with high external disturbances and complex cases such as control of autonomous surface vehicles in disturbed environment, the super-twisting algorithm might not be able to attenuate the chattering effectively. Therefore, the proposed algorithm MP-STSMC has drastically eliminated the chattering from STSMC algorithm.

Briefly, the presented robust MPC strategy offers a trade-off between a fast real-time controller and a robust controller. In the proposed approach, a high performance controller was developed in terms of transient response, robustness, optimal control efforts and steady-state response. As to future work, these authors intend to find a perfect mathematical proof procedure for stability analysis of the proposed control algorithm by using an approach based on Lyapunov theory.

## BIBLIOGRAPHY

1. Esfahani, H. N., Azimirad, V., Eslami, A., Asadi, S.): *An optimal sliding mode control based on immune-wavelet algorithm for underwater robotic manipulator*. Proceedings of the 21st Iranian Conference on Electrical Engineering (ICEE), Mashhad, Iran, 2013.
2. Esfahani, H. N., Azimirad, V., Danesh, M.: *A time delay controller included terminal sliding mode and fuzzy gain tuning for underwater vehicle-manipulator systems*. Ocean Engineering, Vol. 107, (2015) pp. 97-107.
3. Esfahani, H. N., Azimirad, V., Zakeri, M.: *Sliding Mode-PID Fuzzy controller with a new reaching mode for underwater robotic manipulators*. Latin American Applied Research, vol. 44(3), (2014), pp. 253–258.
4. Liu C., Zheng H., Negenborn R.R., Chu X., Wang L.: *Trajectory tracking control for underactuated surface vessels based on nonlinear Model Predictive Control*. In: Corman F., Voß S., Negenborn R. (eds) Computational Logistics. ICCL 2015. Lecture Notes in Computer Science, vol 9335, (2015), pp. 166-180. Springer, Cham. (Proceedings of the 6th International Conference, ICCL 2015, Delft, The Netherlands).
5. Liu, J., Luo, J., Cui, J., Peng, Y.: *Trajectory Tracking Control of Underactuated USV with Model Perturbation and External Interference*. Proceedings of the 3rd International Conference on Mechanics and Mechatronics Research (ICMMR 2016). Chongqing, China, 2016. DOI: 10.1051/mateconf/20167709009.
6. Wang, W., Mateos, L.A., Park, S., Leoni, P., Gheneti, B., Duarte, F., Ratti, C., Rus, D.: *Design, Modeling, and Nonlinear Model Predictive Tracking Control of a Novel Autonomous Surface Vehicle*. Proceedings of the IEEE International Conference on Robotics and Automation (ICRA), pp. 6189–6196. Brisbane, Australia, 2018. DOI: 10.1109/ICRA.2018.8460632.
7. Zheng, H., Negenborn, R.R., Lodewijks, G.: *Trajectory tracking of autonomous vessels using model predictive control*. IFAC Proceedings Volumes. vol. 19, (2014) no. 3, pp. 8812–8818. (Proceedings of the 19th IFAC World Congress, Cape Town, South Africa, August 24-29). DOI: 10.3182/20140824-6-ZA-1003.00767.
8. Abdelaal, M., Fr, M., Hahn, A.: *Nonlinear Model Predictive Control for trajectory tracking and collision avoidance of underactuated vessels with disturbances*. Ocean Eng., Vol. 160, (2018), pp. 168–180.
9. Yi, B., Qiao, L., Zhang, W.: *Two-time scale path following of underactuated marine surface vessels: Design and stability analysis using singular perturbation methods*. Ocean Eng., Vol. 124, (2016), pp. 287–297.
10. Valenciaga, F.: *A second order sliding mode path following control for autonomous surface vessels*. Asian Journal Control, vol. 16(5), (2014), pp. 1515–1521.
11. Tanakitkorn, K., Phillips, A.B., Wilson, P.A., Turnock, S.R.: *Sliding mode heading control of an overactuated hover-capable autonomous underwater vehicle with experimental verification*. Journal of Field Robotics, vol. 35(3), (2017), pp. 396–415.
12. Hung, N.T., Rego, F., Crasta, N., Pascoal, A.M.: *Input-Constrained Path Following for Autonomous Marine Vehicles with a Global Region of Attraction*. IFAC-PapersOnLine, vol. 51(29), pp. 348–353. (Proceedings of the 11th IFAC Conference on Control Applications in Marine Systems, Robotics, and Vehicles, CAMS-2018. Opatija, Croatia, 2018.

13. Jamalzade, M.S., Koofgar, H.R., Ataei, M.: *Adaptive fuzzy control for a class of constrained nonlinear systems with application to a surface vessel*. Journal of Theoretical and Applied Mechanics, vol. 54(3), (2016), pp. 987-1000.
14. Fossen, T.I.: *Handbook of Marine Craft Hydrodynamics and Motion Control*, John Wiley & Sons, Ltd., 2011.
15. Fu, M., Yu, L.: *Finite-time extended state observer-based distributed formation control for marine surface vehicles with input saturation and disturbances*. Ocean Eng., Vol. 159, (2018) , pp. 219–227.
16. Incremona, G. P., Ferrara, A., Magni, L.: *Hierarchical Model Predictive/Sliding Mode Control of Nonlinear Constrained Uncertain Systems*. IFAC-PapersOnLine, vol. 48(23), (2015) , pp. 102-109. (Proceedings of the 5th IFAC Conference on Nonlinear Model Predictive Control, NMPC-15. Seville, Spain).
17. Esfahani, H. N: *Robust Model Predictive Control for Autonomous Underwater Vehicle–Manipulator System with Fuzzy Compensator*. Polish Maritime Research (forthcoming), 2019. 10.2478/pomr-2019-00139.
18. Witkowska, A, Smierzchalski, R.: *Adaptive dynamic control allocation for dynamic positioning of marine vessel based on backstepping method and sequential quadratic programming*. Ocean Engineering, Vol. 163, (2018) , pp. 570-582.
19. Witkowska, A, Smierzchalski, R.: *Adaptive Backstepping Tracking Control for an over-Actuated DP Marine Vessel with Inertia Uncertainties*. International Journal of Applied Mathematics and Computer Science , Vol. 28(4), (2018), pp. 679-693.
20. Lisowski, J.: *Analysis of Methods of Determining the Safe Ship Trajectory*. TRANSSNAV-International Journal On Marine Navigation And Safety Of Sea Transportation, Vol. 10(2), (2016) , pp. 223-228.
21. Lisowski, J.: *Optimization-supported decision-making in the marine mechatronics systems*. Solid State Phenomena, vol. 210, (2014), pp. 215-222.
22. Tomera, M.: *Ant colony optimization algorithm applied to ship steering control*. Procedia Computer Science, vol. 35, (2014) , pp. 83-92. (Proceedings of the Knowledge-Based and Intelligent Information & Engineering Systems, 18th Annual Conference, KES-2014. Gdynia, Poland).
23. Fang, Y.: *Global output feedback control of dynamically positioned surface vessels : an adaptive control approach*. Mechatronics, Vol. 14, (2004) , pp. 341–356. DOI: 10.1016/S0957-4158(03)00064-3.

## CONTACT WITH THE AUTHORS

**Hossein Nejatbakhsh Esfahani**  
*e-mail: hossein.esfahani@pg.edu.pl*

**Rafal Szlapczynski**  
*e-mail: rafal.szlapczynski@pg.edu.pl*

Gdansk University of Technology  
 Faculty of Ocean Engineering and Ship Technology,  
 Department of Marine Mechatronics  
 G. Narutowicza 11/12  
 80-233 Gdansk  
**POLAND**

# APPLICATION OF THE OPTIMIZATION METHODS TO THE SEARCH OF MARINE PROPULSION SHAFTING GLOBAL EQUILIBRIUM IN RUNNING CONDITION

**Aleksandr Ursolov**

Admiral Makarov National University of Shipbuilding, Ukraine

**Yuriy Batrak**

Intellectual Maritime Technologies, Ukraine

**Wiesław Tarelko**

Gdansk University of Technology, Poland

## ABSTRACT

*Full-film hydrodynamic lubrication of marine propulsion shafting journal bearings in running condition is discussed. Considerable computational difficulties in non-linear determining the quasi-static equilibrium of the shafting are highlighted. To overcome this problem the approach using two optimization methods (the particle swarm method and the interior point method) in combination with the specially developed relaxation technique is proposed. The developed algorithm allows to calculate marine propulsion shafting bending with taking into account lubrication in all journal bearings and exact form of journal inside bearings, compared to results of most of the publications which consider lubrication only in the aft most stern tube bearing and assume rest of bearings to be represented by points. The calculation results of typical shafting design with four bearings are provided. The significance of taking into account lubrication in all bearings is shown, specifically more exact values of bearings' reactions, shafting deflections, minimum film thickness and maximum hydrodynamic pressure in the stern tube bearing in case of considering lubrication in all bearings.*

**Keywords:** marine propulsion shafting, bearing lubrication, fluid-structure interaction, finite-element method, optimization

## FORMULATION OF THE PROBLEM

Bearings are one of the most important parts of a ship's propulsion system. Therefore, at the design stage, it is crucial to ensure whether bearings and especially an aft stern tube bearing operate properly under the specified operational conditions (propeller loads, ship motions at the rough sea, hull deflections etc.). For this, it is necessary to have reliable information about the interaction between the shafting and bearings which are spatially positioned in a certain way. The spatial location of the bearings is achieved through the shaft alignment procedure, which is vital for the shaft line safe operation. Improper shafting alignment could lead to the lack of hydrodynamic lubrication and cause the rapid temperature

rise, whipping, melting or burning of non-metallic bearing bushes during manoeuvring or even normal operation. To determine the optimal bearing positions, it is necessary to be able to reliably and effectively calculate the static equilibrium of the shaft line with regard to lubrication. More precisely, it is a quasi-static equilibrium because it comes about the running shafting. The external loads applied to the operating shafting are averaged and considered constant, shafting vibration being neglected.

The determination of the interaction between the shafting and bearings in operation belongs to the class of problems of non-linear fluid-structure interactions (FSI). To solve it, a number of solutions are to be found: shafting elastic bending, lubrication for each of the shafting's bearings and

elastic deflections of bearing bushes, which is essential for water lubricated bearings with non-metallic bushes [10, 11] (the latter is beyond the scope of the present paper).

The complexity of the listed tasks solutions is caused by the fact that in properly lubricated bearings, the shaft is lifted by the developed hydrodynamic pressure which depends on the lubrication film thickness. In turn, the lubrication film thickness is determined by the journal position and curvature (the aft stern tube bearing has a high  $L/D$  ratio, therefore, the journal curvature should not be ignored since it affects hydrodynamic pressure considerably). Furthermore, the position of the journal as well as hydrodynamic pressure distribution is unknown before calculation. Therefore, shafting deflections and hydrodynamic pressure depend on each other and iterative techniques should be applied to this FSI problem to find the static equilibrium position of the system.

## LITERATURE REVIEW

The paper subject is not new and has been presented by the other authors in similar formulations. However, some of them consider lubrication of the aft stern tube bearing only, some of them use simplified lubrication models and some do not clarify the method of the global equilibrium search.

Mourelatos and Parsons [12] presented the method for determining equilibrium position of the shafting with the water lubricated stern tube bearing but the rest of the bearings are considered non-lubricated point supports. The divergence nature of the shafting-bearings system which fails successive numerical simulation is illustrated and the optimization based approach for the equilibrium search is introduced. The deformation of bearings' bushes is taken into account.

Vulic [20] highlighted the importance of considering lubrication fluid film in shaft alignment design in contrast to the commonly used approach to neglect it. He presented the method to find equilibrium position of shafting with taking lubrication into account, however bearing model is represented by approximation of Reynolds equation solution for bearing with relative length of  $0 < L/D \leq 2$  so any modifications of bearing surface (wear, double sloping etc.), elastic deflection of polymer or rubber bush and journal bending inside bearing cannot be taken into account. The difficulties in the convergence of successive iteration approach are also mentioned.

Xing and et al. [25] consider the behaviour of the marine propulsion shafting using Multi-Body Dynamics approach implemented in ANSYS software. Lubrication of the bearings and bearing bush elastic deflections have been considered and it has been shown that investigation of the marine stern tube bearings lubrication should be performed with taking journal curvature into account. Unfortunately, no method's details or its convergence has been presented in the paper.

Similarly, Andreau et al. [1] stated that they solved the global equilibrium problem taking bush elastic deflections into account by means of the iterative procedure, but no

clarification of an equilibrium search method and its convergence have not been done.

Gurr and Ruifs [6] consider lubrication based on the Reynolds equation solving only for the stern tube bearing, the other bearings were represented by the simplified lubrication model neglecting misalignment. The used iterative scheme also is not discussed.

There are also papers, e.g. [7, 5, 24, 25] which consider only isolated perfectly aligned isolated bearings and provide calculation methods for journal eccentricity and attitude angle without global shafting equilibrium.

Hirani et al. [7] provide a rapid method for determining design parameters of the bearing by taking into account oil flow and temperature effects. The heuristic closed form solution of the Reynolds equation is used for determining pressure distribution.

Kraker et al. [5] presented the computational method of solving the mixed elastic-hydrodynamic problem. The iterative secant method is used to find the eccentricity of the journal and the pseudo-dynamic stepping is used to prevent numerical instability of the staggered scheme between Reynolds equation and bearing bush deformation by introducing artificial damping in the structure.

Xie et al. [24, 25] provide a Stribeck curve calculation method and investigate the influence of the main bearing design parameters on it. Three models of bearing performance for boundary lubrication, mixed lubrication and hydrodynamic lubrication regimes are considered.

From the above, it follows that, despite the fact that many researchers dealt with the described problem, there are no generally accepted reliable methods which fully would meet the authors' requirements.

## METHOD

In the proposed method, the local deflections of journals and bushes under the hydrodynamic pressure are not considered. While ignoring the journal local deflection is a commonly used hypothesis, ignoring bush deflections is valid only for metal bearings bushes. The algorithms for elastic-hydrodynamic modeling of polymer and rubber bearings, which take local elastic bush deflections into account, are under development now.

The method is limited only to pure hydrodynamic lubrication and does not consider any solid contact between the journal and bearing bush.

## SHAFT BENDING

The shafting elastic deflections are determined by solving the system of linear algebraic equations of the finite element method (FEM) for the beam theory:

$$[K]\{u\} = \{q_w\} + \{q_p\} + \{q_l\} \quad (1)$$

where  $[K]$  is a stiffness matrix of the shafting;  $\{u\}$  is a nodal displacement vector;  $\{q_w\}$  is a vector of the weight loads;  $\{q_p\}$  vector of the propeller hydrodynamic loads;  $\{q_j\}$  is a vector of loads from the hydrodynamic pressure which is initially unknown and to be found iteratively. The coordinate system accepted in the present paper is the following: the initial point is at the aft end of a shafting;  $x$ -axis is directed forward along shafting;  $y$ -axis is directed to the port side;  $z$ -axis is directed upward.

The Timoshenko beam element stiffness matrix [14] is used. It was reduced so as to take into account only lateral linear and angular displacements in the vertical and horizontal planes. Shear area coefficient for the beam element with the circular cross-section is calculated according to the recommendations [8].

## LUBRICATION

The Reynolds equation [19] for lubrication under full hydrodynamic regime is solved numerically:

$$\frac{d}{dx} \left( h(x, y)^3 \cdot \frac{d}{dx} p(x, y) \right) + \frac{d}{dy} \left( h(x, y)^3 \cdot \frac{d}{dy} p(x, y) \right) = 6\mu U \frac{d}{dy} h(x, y), \quad (2)$$

where  $h(x, y)$  is lubrication film thickness, m;  $p(x, y)$  is hydrodynamic pressure, Pa;  $U = 0.5d\omega$  is linear velocity of the journal surface, m/s;  $d$  is journal diameter, m;  $\omega$  is journal spin speed, rad/s. In Eq. (2), the  $x$ -axis is directed along bearing and the  $y$ -axis is directed around the bearing bush circumference. The procedure presented in [15] was applied to Eq. (2) in order to derive the stiffness matrix of the lubrication film finite element. The temperature and viscosity of the lubricant are supposed to be defined and constant throughout the lubrication film. Despite the fact that viscosity and temperature variations of the lubricant are important for journal bearing load carrying capacity, they are assumed defined and constant throughout the lubrication film for simplicity. The viscosity variation effect will be considered in further research.

Although FEM allows setting arbitrary bush shape, for simplicity, the grooveless cylindrical bush surface was only considered. Lubrication film thickness is defined as follows:

$$h(x, y) = \frac{\Delta}{2} - e(x) \cdot \cos \left( \frac{y}{d + \Delta} - \varphi_e(x) \right), \quad (3)$$

where  $\Delta$  is bearing diameter clearance, m;  $e(x)$  and  $\varphi_e(x)$  eccentricity and attitude angle of journal, respectively. Position of the journal depends on the spatial position of the shafting and bearing:

$$e(x) = \sqrt{y_j^2(x) + z_j^2(x)}; \quad (4)$$

$$\varphi_e(x) = -\text{atan2}(y_j(x), z_j(x)); \quad (5)$$

$$y_j(x) = W_y(x) - w_y - \alpha_z(x - x_c); \quad (6)$$

$$z_j(x) = W_z(x) - w_z + \alpha_y(x - x_c); \quad (7)$$

where  $W_y(x)$  and  $W_z(x)$  are shafting deflections,  $w_y$  and  $w_z$  are lateral bearing axis offsets,  $\alpha_z$  and  $\alpha_y$  are angular bearing axis slope,  $x_c$  is the longitudinal position of the bearing length middle.

After solving Eq. (2), the pressure is integrated at the circular direction and then transformed to nodal loads  $\{q_j\}$  in the vertical and horizontal planes to be applied to the journal.

## OPTIMIZATION

The static equilibrium of the shafting is reached when sums of all forces and moments acting on the shafting are equal to zero:

$$\sum P_z = \sum P_y = 0; \quad (8)$$

$$\sum M_z = \sum M_y = 0. \quad (9)$$

The possible way to fulfill these conditions is described below. Following the method [12], the auxiliary point support is introduced in the middle of each bearing that allows solving the shafting bending equations. The support position in the transverse section can be specified by non-dimensional cylindrical coordinates

$$\bar{e} = \frac{e}{0.5\Delta}, \quad \bar{\varphi}_e = \frac{\varphi_e}{\pi}, \quad (10)$$

where  $\bar{e}$  is non-dimensional eccentricity,  $\bar{\varphi}_e$  is non-dimensional attitude angle. When the pressure distribution in the bearings corresponds to the shafting equilibrium position, reactions of all auxiliary supports in the vertical and horizontal planes are to be equal to zero as if the auxiliary supports have disappeared. Therefore, fulfillment of the first condition of equilibrium Eq. (2) could be represented as the following optimization problem:

$$\text{Minimize } F(X) = \sum_{j=1}^m \bar{R}_i^2 = \sum_{j=1}^m (\bar{R}_{z_j}^2 + \bar{R}_{y_j}^2); \quad (11)$$

$$X = \{\bar{e}_1, \bar{\varphi}_{e1}, \dots, \bar{e}_j, \bar{\varphi}_{ej}, \dots, \bar{e}_m, \bar{\varphi}_{em}\}; \quad (12)$$

$$\text{over } 0 \leq \bar{e}_j < 1; \quad (13)$$

subject to:

$$-1 \leq \bar{\varphi}_{ej} \leq 1, \quad (14)$$

where  $\bar{R}_j$  is the reaction of the  $j$ -th auxiliary support,  $\bar{R}_{z_j}$  and  $\bar{R}_{y_j}$  are its vertical and horizontal projections, respectively,  $m$  is the number of lubricated bearings in the system. The general number of variables  $X$  is twice a number of lubricated bearings in the scheme.

It should be mentioned that in [12], the objective function is based on the minimizing difference between journal deflections in two positions: when it is fixed by the auxiliary support and when it is supported only by hydrodynamic pressure. However, this approach is unacceptable in the case of several lubricated bearings, because at least two bearings have to be considered as fixed point supports without lubrication in order to provide constraints for the shafting finite element model. Moreover, the deflections, in contrast to bearing reactions, are not integral values so this approach cannot provide stable convergence of the iterative procedures when lubrication of several bearings is considered.

It is well known that there is no universal best optimization method but there are methods that are most applicable to the certain problem. To find an appropriate method to solve this problem, a number of optimization methods (such as interior point method, trust region method, sequential quadratic programming, active set method, Nelder-Mead simplex algorithm, Hooke-Jeeves or pattern search, genetic algorithm, simulated annealing, particle swarm method) were tested. It was found that the interior point method and the particle swarm method are the most appropriate for this problem. The particle swarm method [9, 13, 18] is effective for searching approximate global minimum, but it is too slow for searching the final result. In contrast, the interior point method [4, 21, 22] searches the minimum of the function successfully and fast, but only if the initial point of optimization is close to the solution point. Therefore, the sequential application of these two methods proved to be the most effective in this case. It is significant that an advantage of the particle swarm method use at the first stage is growing with the growth of a lubricated bearings number in the calculation and there is no need to use it in the case of one lubricated bearing in the scheme, e. g. only a aft stern tube bearing. When a number of similar calculations should be done (e. g. different rotation speeds) then the auxiliary supports' position from the previous solution could be used as an initial point for the new one without preliminary using the particle swarm method, which significantly speeds up the calculation.

The solution of the optimization problem is satisfactory if the objective function  $F(X) < 0.01$  N. Otherwise, bearing auxiliary supports remain loaded and equilibrium purely due to hydrodynamic pressure is not reached. It was found during testing different cases that it is enough to use 20 particles and 20 iterations of the particle swarm method in order to localize the objective function minimum.

## RELAXATION TECHNIQUE

In the applied approach, auxiliary support fixes the position of journal centre point in space but the journal can freely rotate relative to this point so optimization can meet only the first condition of equilibrium Eq. (8). Applying the optimization methods to fulfil conditions Eq. (8) and Eq. (9) simultaneously leads to a significant increase in the number of variables which makes such approach not effective for practical use. The fact is that moments generated by the hydrodynamic pressure relative to auxiliary support point are very sensitive to a journal angular position and this relation is highly nonlinear, especially for bearings with high  $L/D$  ratio.

Therefore, the special relaxation approach was developed to reach convergence in the searching shafting equilibrium including the condition of Eq. (9). The proposed relaxation is somewhat similar to the pseudo-dynamic approach in [5]. However, the present method simulates not only damping but also inertia in order to avoid looping. The procedure uses two previous pressure distributions to correct the pressure in the current iteration, which is to be applied to the journal:

$$p_i^* = C_1 p_i + C_2 p_{i-1}^* + C_3 p_{i-2}^*, \quad (15)$$

where  $p_i$  is pressure calculated at present iteration;  $p_{i-1}^*$  and  $p_{i-2}^*$  are two previously used corrected pressures.

The weight coefficients  $C_1$ ,  $C_2$  and  $C_3$  are derived from the following conditions:

- Coefficient  $C_1$  is the main and determines the part of the directly calculated pressure at the present iteration. For stabilization, at the initial critical  $n$  steps it increases linearly up to set  $C_1(n)$  value and after that it remains constant.
- Coefficients  $C_2$  and  $C_3$  which correspond to the parts of the pressure at two previous iterations, have a constant relative proportion.
- Coefficients  $C_1$ ,  $C_2$  and  $C_3$  are so set that the sum of them are to be equal to one:  $C_1 + C_2 + C_3 = 1$ .

The coefficients derived from the mentioned conditions are the following:

$$C_1(i) = \min(C_1(n), (C_1(n) - C_1(2)) \frac{i-2}{n-2} + C_1(2)); \quad (16)$$

$$C_2(i) = \frac{1 - C_1(i)}{1 + C_2/C_3}; \quad (17)$$

$$C_3(i) = 1 - C_1(i) - C_2(i). \quad (18)$$

The dependences of Eq. (16)-(18) can be fully defined by the parameters  $C_1(2)$ ,  $C_1(n)$ ,  $n$  and  $C_2/C_3$ , that are constant for the algorithm and were found from the systematic calculations of different shafting models.

The cycle of equilibrium search is ended if one of the conditions is fulfilled:

- moments of corrected pressure  $p_i^*$  for each bearing relative to the corresponding auxiliary support points in the vertical  $M_y$  and horizontal  $M_z$  planes differ from the values at the previous iteration and from non-corrected moments of the pressure calculated at the present iteration by the value lesser than acceptable error  $\Delta M$ ;
- an iteration number  $i$  is greater than set maximum  $i_{max}$ .

The latest condition provides end of the cycle to stop the current optimization step and start a new one.

These conditions could be written as follows:

$$\left( \left| \frac{M_y(p_i^*) - M_y(p_{i-1}^*)}{M_y(p_i^*)} \right| \leq \Delta M \wedge \left| \frac{M_z(p_i^*) - M_z(p_{i-1}^*)}{M_z(p_i^*)} \right| \leq \Delta M \wedge \left( \left| \frac{M_y(p_i^*) - M_y(p_i)}{M_y(p_i^*)} \right| \leq \Delta M \wedge \left| \frac{M_z(p_i^*) - M_z(p_i)}{M_z(p_i^*)} \right| \leq \Delta M \right) \vee i \geq i_{max}, \quad (19)$$

where  $\wedge$  and  $\vee$  are AND and OR logical operators,  $M_y$  and  $M_z$  are determined as follows:

$$M_y(p) = \int_{-0.5L}^{0.5L} \int_{-\pi}^{\pi} x \cos \varphi p(x, \varphi) d\varphi dx; \quad (20)$$

Unlike the other papers, at each step of the cycle, the calculation is performed for every lubricated bearing so that equilibrium is found iteratively by taking interaction between bearings into account. This interaction impacts the exact journal positions and pressure and ignoring it could lead to incorrect results.

## APPLICATION OF THE METHOD

The presented method is illustrated by the calculation of a somewhat simplified typical shafting design with four lubricated bearings. The shafting scheme and dimensions are illustrated in Fig. 1, shaft diameter  $d = 0.5$  m is constant along the shafting, i.e. and the four-blade propeller with diameter  $D = 5.6$  m is located at  $x = 0.7$  m. Shafts are made of steel with following properties: elastic modulus  $E = 2 \cdot 10^4$  MPa, Poisson ratio  $\nu = 0.3$ , density  $\rho = 7850$  kg/m<sup>3</sup>. General parameters and mesh discretization of the bearings are listed in Tab. 1.

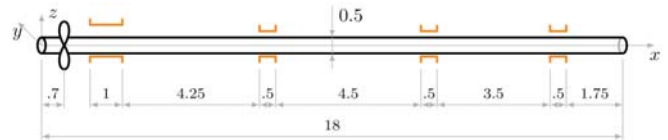


Fig. 1. Dimensions of the shafting model (in meters)

Tab. 1. General characteristics of the bearings

Bearing number	Length $\Delta$ , m	Clearance $\Delta$ , mm	Viscosity $\mu$ , Pa s	Long. grid step $dx$ , m	Circ. grid step $d\varphi$ , deg.
1	1	0.8	0.02	0.025	2
2, 3, 4	0.5	0.4	0.02	0.05	4

Hydrodynamic propeller loads significantly impact the shafting bending and, therefore, the bearing pressure. The propeller loads highly depend on the rpm so the developed method should be able to find the solution (if it exists) for different rpm values. According to [3], mean values of the propeller loads can be defined as:

$$P_y(\omega) = 0.050P_x(\omega); \quad P_z(\omega) = 0.048P_x(\omega); \quad (22)$$

$$M_y(\omega) = 0.350M_x(\omega); \quad M_z(\omega) = 0.284M_x(\omega); \quad (23)$$

where  $P_x$  and  $M_x$  are thrust and torque, respectively, (N and Nm), their values being depended on rotational speed. Calculations have been performed for rotational speed range from 60 to 120 rpm with the step of 20 rpm.

In order to assess the effect of bearings lubrication on the stern tube bearing performance, two types of calculation were provided:

- all bearings are considered lubricated;
- only the stern tube bearing is considered lubricated.

The shafting is loaded by:

1. the distributed shaft weight  $q = 0.25d^2\pi\rho g = -15.1$  kN/m, where  $g = 9.81$  m/s<sup>2</sup> is the acceleration of gravity;
2. concentrated propeller weight with taking buoyancy into account  $P_w = -127.5$  kN;
3. hydrodynamic propeller loads, listed in Tab. 2.

Tab. 2. Hydrodynamic propeller loads

rpm	$P_x$ , kN	$P_y$ , kN	$P_z$ , kN	$M_x$ , kNm	$M_y$ , kNm	$M_z$ , kNm
60	210.8	10.5	10.1	198.9	69.6	56.5
80	374.7	18.7	18.0	353.7	123.8	100.4
100	585.5	29.3	28.1	552.6	193.4	156.9
120	843.1	42.2	40.5	795.8	278.5	226.0

## RESULTS AND DISCUSSION

The calculation has been performed at each rotation speed by using both optimization methods when lubrication of all bearings is considered, and only the interior point method when only the stern tube bearing is considered lubricated. The number of iterations for each of the method and total objective function calls are listed in Tab. 3. As expected, in the case of considering all bearings lubricated, the iteration number is greater than in the case when only the aft stern tube bearing is considered lubricated due to the growth of number of variables in optimization. It should be mentioned that when only the interior point method was applied to the case considering lubrication in all bearings, no solution has been found. This highlights the importance of using both optimization methods when several bearings are considered lubricated.

Tab. 3. Computational effort

	All bearings	Only aft stern tube bearing
Particle swam, number of iterations	20	0
Interior point, number of iterations	56...70	24...30
Number of objective function calls	1147...1430	109...130

The hydrodynamic pressure moment convergence in case of the use of the simple successive iterations and proposed relaxation method, is shown in Fig. 2. It can be clearly seen that the simple successive approximations (see Fig. 2a) have not converged whereas pressure relaxation Eq. (15) accurately determines journal angular position (see Fig. 2b). It shows the effectiveness of the relaxation method.

Fig. 3 shows hydrodynamic pressure in the stern tube bearing at the different speeds in the case of all lubricated bearings. There are significant pressure peaks at 60 and 120 rpm (Fig. 3d and 3a) caused by edge loading. It indicates that the method can be used for any possible hydrodynamic pressure distribution. The dependencies of maximum pressure  $p_{max}$  and minimum lubrication film thickness  $h_{min}$  in the stern tube bearing on rpm are illustrated in Fig. 4. As can be expected, with the decreasing of minimum film thickness, the maximum pressure in the bearing becomes greater. It should be noted that the ignoring of lubrication in the intermediate bearings has led to the error in maximum pressure in stern tube bearing, equal to 30% in case of the aft edge loading (60 rpm) and 22% in case of the forward edge loading (120 rpm). It illustrates the importance of considering lubrication of all bearings.

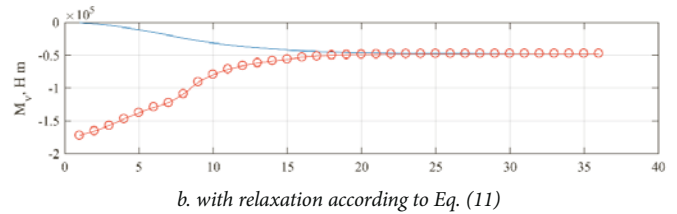
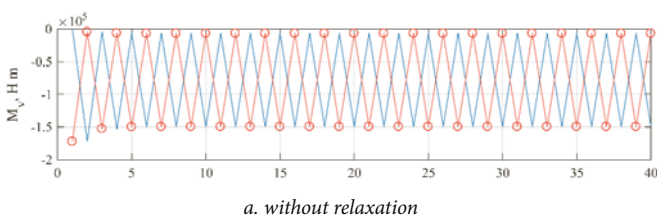


Fig. 2. Plot of stern tube vertical moment convergence: (—o—) – moment of the directly calculated pressure  $p$ , (—) – moment of the corrected pressure  $p^*$

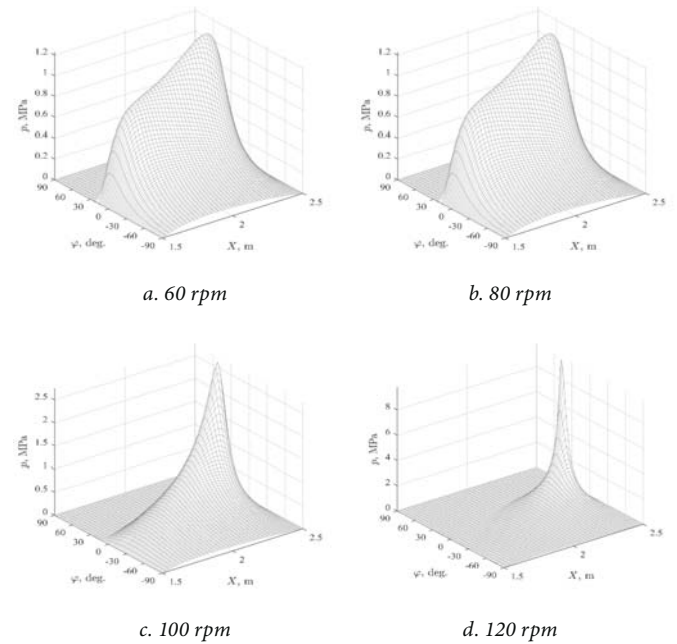


Fig. 3. Hydrodynamic pressure in the aft stern tube bearing

The eccentricity distributions of the bearing journals at the different speeds are illustrated in Fig. 5. The propeller loads cause a significant misalignment in the stern tube bearing, a small journal slope in the second bearing and almost no slope in other bearings. It should be noted that slope sign is changed with the growth of rpm.

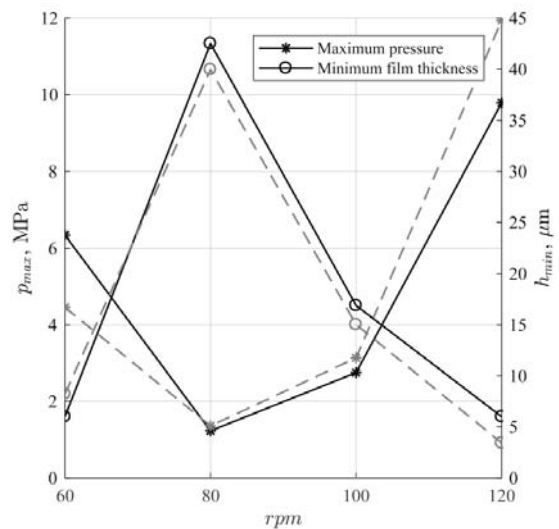


Fig. 4. Characteristics of the aft stern tube bearing: (—) – for all lubricated bearings, (---) – for the aft stern tube lubricated bearings only

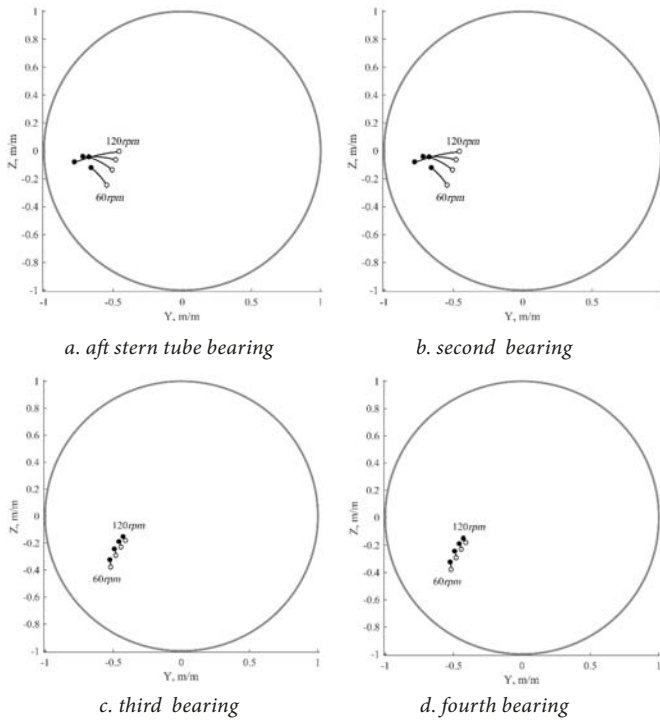


Fig. 5. Journal position inside clearance circle of bearings:  $\circ$  – at the fore bearing edge,  $\bullet$  – at the aft bearing edge

The deflections of the shafting at 60 and 120 rpm in the vertical and horizontal plane are shown in Fig. 6 and Fig. 7, respectively. The solid lines correspond to the shaft deflections in the case of all lubricated bearings and dashed lines in the case when only stern tube bearing lubrication is considered. The shaft deflection magnitudes rise in the horizontal plane and journal slope sign changes in the vertical plane because of the propeller loads increase with the rotational speed increase. It should be noted that ignoring lubrication in the intermediate bearings leads to changes in the shafting deflections and the corresponding position of the aft stern tube bearing journal up to 4% of its diameter clearance therefore the estimation of shafting operation could be incorrect.

The bearings reactions  $R$  are depicted in Fig. 8 and one can see that with the rise of rpm, load redistribution occurs between 1<sup>st</sup> and 2<sup>nd</sup> bearings so that reaction on the 2<sup>nd</sup> one increased two times from 60 to 120 rpm. However, reactions of the third and fourth bearings changed a little.

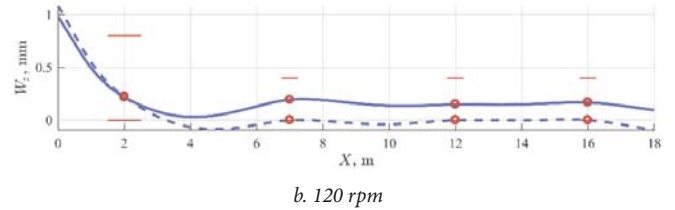
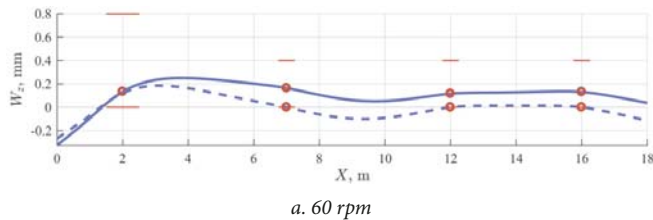


Fig. 6. The vertical projection of the shaft deflections: (—) – for all lubricated bearings, (- -) – for aft stern tube lubricated bearing only

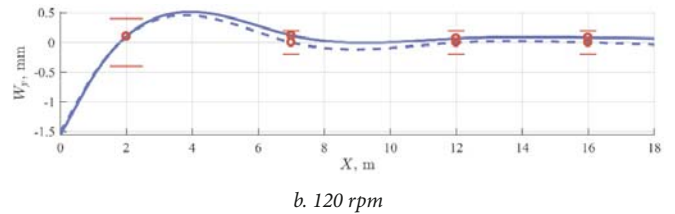
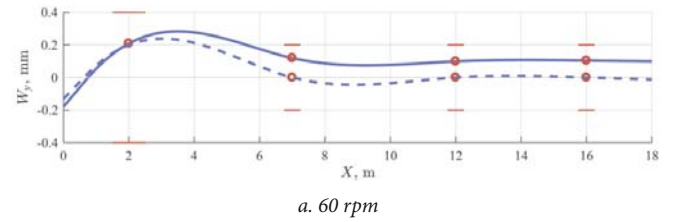
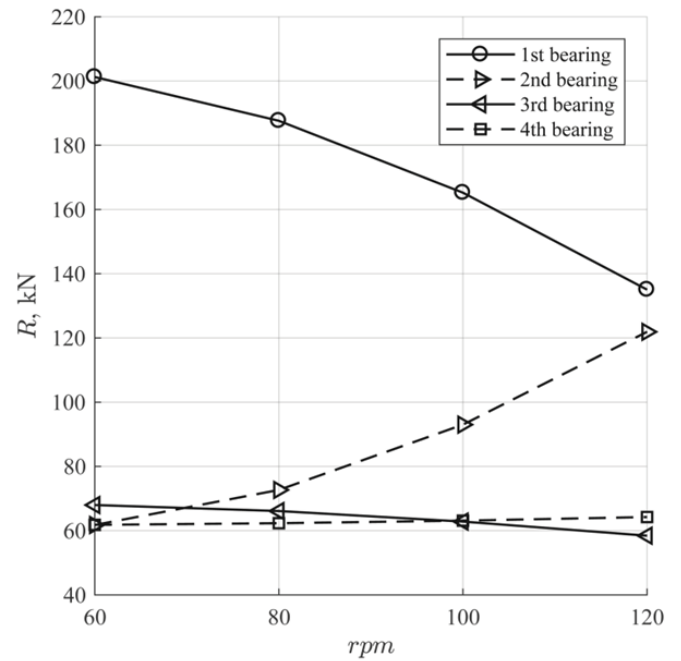


Fig. 7. The horizontal projection of the shaft deflections: (—) – for all lubricated bearings, (- -) – for aft stern tube lubricated bearing only



## CONCLUSIONS

The proposed method allows to perform propulsion shafting static calculation with taking into account a number of lubricated bearing in the model affecting each other even if significant journal slope and bearing edge loading occurs. The method is free of assumptions such as the constant slope of the journal, point representation of the intermediate bearings, restrictions for value of L/D ratio and bearing surface cylindricity. Thereby, it allows a designer to perform the deep precise analysis of the system and more qualitative offset optimization at the design stage. It should be mentioned that reliable determination of the aft stern tube bearing lubrication is essential for providing its reliability and performance prediction.

In such FSI calculation, the convergence is the most challenging issue. The method is based on the optimization approach and thus provides the stable loopless convergence of the journal linear position. However, due to the adopted approach with auxiliary artificial support, the additional cycle is required to find the angular position of the bearing journals. The developed relaxation technique provides stable convergence between angular journal positions and hydrodynamic pressure so that not only the force equilibrium condition but also the moment equilibrium condition is fulfilled.

Results show that lubrication of all bearings has a significant impact on the shafting deflection in the vertical and horizontal plane, the maximum pressure of the stern tube bearing and bearings' reactions and should not be ignored in the alignment design under operational conditions. It should be especially emphasized that bearing lubrication analysis in shaft alignment design should take the global shafting quasi-static equilibrium into account because bearings can affect each other. Neglecting lubrication of some bearings could lead to incorrect aft stern tube lubrication modelling.

The further research in this field is of interest, specifically bearing bush elastic deflections are also to be included in the algorithm, which is essential for rubber and polymer bushes so that the general algorithm will be the same, but the pressure will be found iteratively with the bush deflection. In addition, lubrication under boundary and mixed regimes are also to be included in the algorithm in the future, that is important for heavy loaded bearings and startup-shutdown conditions. The developed method is to be included into the ShaftDesigner software [2, 16, 17].

## BIBLIOGRAPHY

1. Andreau C., Ferdi F., Ville R. et al.: *A method for determination of elastohydrodynamic behavior of line shafting bearings in their environment*. In Proceedings of ASME/STLE International Joint Tribology Conference, San Diego, 2007. DOI:10.1115/IJTC2007-44056.
2. Batrak Y.: *New CAE package for propulsion train calculations*. International conference on computer applications in shipbuilding, 3, Vol. 2., (2009). pp. 187–192.
3. Batrak Y. A., Shestopal V. P., Batrak R. Y.: *Propeller hydrodynamic loads in relation to propulsion shaft alignment and vibration calculations*. Proceedings of the Propellers/Shafting Symposium., 2012.
4. Byrd R. H., Hribar M.E., Nocedal J.: *An interior point algorithm for large-scale nonlinear programming*. SIAM J Optimization, 9(4) , (1999), pp. 877–900. DOI:10.1137/S1052623497325107.
5. de Kraker A., Ostayena R. A. J. and Rixen D. J.: *Calculation of Stribeck curves for (water) lubricated journal bearings*. Tribology International, 40, (2007), pp. 459–469. DOI:10.1016/j.triboint.2006.04.012.
6. Gurr C., Rulfs H.: *Influence of transient operating conditions on propeller shaft bearings*. Journal of Marine Engineering and Technology, 7(2) (2008), pp. 3–11. DOI:10.1080/20464177.2008.11020209.
7. Hirani H., Rao T. V., Athre, K. et al.: *Rapid performance evaluation of journal bearings*. Tribology International, 30 (11) (1997), pp. 825–834. DOI:10.1016/S0301-679X(97)00066-2
8. Hutchinson J. R.: *Shear coefficients for Timoshenko beam theory*. Journal of Applied Mechanics, 68(1), (2001), pp. 87-92. coefficientsfortimoshenkobeamtheory.
9. Kennedy J., Eberhart R.: *Particle swarm optimization*. Proceedings of ICNN'95 - International Conference on Neural Networks, Vol 4, (1995), pp. 1942–1948. DOI:10.1109/ICNN.1995.488968.
10. Litwin W.: *Water-lubricated bearings of ship propeller shafts - Problems, experimental tests and theoretical investigations*. Polish Maritime Research, 4(62), Vol 16, (2009) , pp. 42–50.
11. Litwin W.: *Influence of main design parameters of ship propeller shaft water-lubricated bearings on their properties*. Polish Maritime Research, 4(67), Vol 17, (2010), pp. 39–45.
12. Mourelatos Z.P., Parsons M. G.: *Finite-element analysis of elastohydrodynamic stern bearings*. SNAME Transactions, 93(11), (1985), pp. 225–259.
13. Poli R.: *Analysis of the publications on the applications of particle swarm optimisation*. Journal of Artificial Evolution and Applications, 2008. DOI:10.1155/2008/685175.
14. Przemieniecki J. S.: *Theory of matrix structural analysis*, Dover Publications Inc., New York, 1968.

15. Segerlind L. J. (1976). *Applied Finite Element Analysis*, 1 ed., John Wiley and Sons Inc., New York/London/Sydney/Toronto.
16. ShaftDesigner – the shaft calculation software (2018). Retrieved from <http://www.shaftdesigner.com/>.
17. ShaftDesigner – the shaft calculation software by IMT (2018). Retrieved from <http://shaftsoftware.com/>.
18. Shi Y., Eberhart R. A.: *Modified particle swarm optimizer*. 1998 IEEE International Conference on Evolutionary Computation Proceedings. IEEE World Congress on Computational Intelligence (Cat. No.98TH8360), 1998, pp. 69–73. DOI:10.1109/ICEC.1998.699146.
19. Stachowiak G. W., Batchelor A. W.: *Engineering tribology*, Butterworth Heinemann. 2001.
20. Vulic N.: *Advanced shafting alignment: Behaviour of shafting in operation*. Brodogradnja, 52, (2004), pp. 203–212.
21. Waltz R., Morales J., Nocedal J. et al.: *An interior algorithm for nonlinear optimization that combines line search and trust region steps*. Mathematical Programming, 107(3), (2006) , pp. 391–408. DOI:10.1007/s10107-004-0560-5.
22. Wright M. H.: *The interior-point revolution in optimization: history, recent developments, and lasting consequences*. Bulletin of the American Mathematical Society, 42, (2005), pp. 39–56.
23. Xie Z., Rao Z., Ta N. et al.: *Investigations on transitions of lubrication states for water lubricated bearing. Part I: determination of friction coefficients and film thickness ratios*. 68(3), (2016) , pp. 404–415. DOI: 10.1108/ILT-10-2015-0146
24. Xie Z., Rao Z., Ta N. et al.: *Investigations on transitions of lubrication states for water lubricated bearing. Part II: further insight into the film thickness ratio lambda*. Industrial Lubrication and Tribology, 68(3), (2016), pp. 416–429. DOI: 10.1108/ILT-10-2015-0147
25. Xing H., Wu Q., Wu Z. et al.: *Elastohydrodynamic lubrication analysis of marine sterntube bearing based on multi-body dynamics*. In 2012 International Conference on Future Energy, Environment, and Materials, 2012, pp. 1046–1051. DOI:10.1016/j.egypro.2012.01.167.

## CONTACT WITH THE AUTHORS

**Aleksandr Ursolov**

*e-mail: [aleksandr.ursolov@nuos.edu.ua](mailto:aleksandr.ursolov@nuos.edu.ua)*

Admiral Makarov National University of Shipbuilding  
Ukraine Heroes av. 9  
45000 Mykolaiv  
**UKRAINE**

**Yuriy Batrak**

*e-mail: [yuriy.batrak@marine-software.com](mailto:yuriy.batrak@marine-software.com)*

Intellectual Maritime Technologies  
Buznika str. 5  
45000 Mykolaiv  
**UKRAINE**

**Wieslaw Tarelko**

*e-mail: [wieslaw.tarelko@pg.edu.pl](mailto:wieslaw.tarelko@pg.edu.pl)*

Gdansk University of Technology  
Gabriela Narutowicza Street 11/12  
80-233 Gdansk  
**POLAND**

# APPLICATION OF THERMO-CHEMICAL TECHNOLOGIES FOR CONVERSION OF ASSOCIATED GAS IN DIESEL-GAS TURBINE INSTALLATIONS FOR OIL AND GAS FLOATING UNITS

Oleksandr Cherednichenko

Serhiy Serbin

Admiral Makarov National University of Shipbuilding, Ukraine

Marek Dzida

Gdańsk University of Technology, Poland

## ABSTRACT

*The paper considers the issue of thermo-chemical recovery of engine's waste heat and its further use for steam conversion of the associated gas for oil and gas floating units. The characteristics of the associated gas are presented, and problems of its application in dual-fuel medium-speed internal combustion engines are discussed. Various variants of combined diesel-gas turbine power plant with thermo-chemical heat recovery are analyzed. The heat of the gas turbine engine exhaust gas is utilized in a thermo-chemical reactor and a steam generator. The engines operate on synthesis gas, which is obtained as a result of steam conversion of the associated gas. Criteria for evaluating the effectiveness of the developed schemes are proposed. The results of mathematical modeling of processes in a 14.1 MW diesel-gas turbine power plant with waste heat recovery are presented. The effect of the steam/associated gas ratio on the efficiency criteria is analyzed. The obtained results indicate relatively high effectiveness of the scheme with separate high and low pressure thermo-chemical reactors for producing fuel gas for both gas turbine and internal combustion engines. The calculated efficiency of such a power plant for considered input parameters is 45.6%.*

**Keywords:** thermo-chemical heat recovery, gas turbine engine, diesel engine, associated gas, steam reforming, efficiency, methane number

## INTRODUCTION

The development of the global economy generates growing demand for oil and gas. At the same time, there is a decrease in the number of promising mainland deposits. The vector of fossil hydrocarbon extraction is steadily shifting to the area of the continental shelf. Over 37% of the world oil production and 28% of gas production come from fields located on the shelf [1]. Essentially, these deposits are located in the Middle East, Brazil, the Gulf of Mexico, the North and Caspian seas, and on the Arctic shelf. The recently discovered offshore oil and gas deposits are about 10 times larger than newly discovered land deposits. The development of the continental shelf deposits creates the basis for providing the

world economy with hydrocarbon raw materials for the long perspective.

Oil and gas floating units are located at significant distances from the coast. At the same time, various technologies and technical means are successfully applied and developed for various climatic conditions. An increasing number of oil and gas production facilities are related to deep water (0.4...1.5 km) and ultra deep water (over 1.5 km). The process of oil and gas extraction from the sea shelf is energy intensive, and with the increase of extraction depth the energy costs also grow higher. At the same time, the emissions of greenhouse gases produced by power plants increase as well.

The need to solve the problems of improving fuel efficiency and reducing harmful emissions during power equipment

operation is a paradigm for designing power plants for marine vessels and ocean engineering objects. All this requires defining new promising ways to improve the efficiency of oil and gas production power plants.

## IDENTIFICATION OF THE INVESTIGATION OBJECT

Low-speed two-stroke diesel engines (2SDE) are most widespread in the ship power industry. 2SDE have high efficiency and can work on cheap heavy grades of fuel oil. The efficiency of such power plants can be improved due to the recovery of energy resources [2]. Large weight and size indicators of such engines do not allow their use in power plants of oil and gas floating units.

The main thermal engines used in power installations of oil and gas floating units are gas turbine engine (GTE) and medium speed four-stroke diesel engine (4SDE). Despite the fact that the efficiency of internal combustion engines is higher, the advantage is given to GTEs, as they better satisfy the requirements of ensuring high power with small weight and size parameters.

A large number of publications are devoted to solving the problem of increasing the efficiency of gas-turbine engines for oil and gas production facilities. One of the ways to increase this efficiency can be humidification of the air entering the GTE compressor [3]. The most widespread way to increase gas turbine unit efficiency is to use the heat of the waste gas in the combined gas-steam turbine cycle. Combined-cycle power plants of this type have been installed on three Norwegian gas fields [4]. It was revealed that large mass and dimensions of the steam-turbine circuit equipment [5] restrain the use of such technologies at oil and gas production facilities.

Fuel characteristics largely determine the performance indicators of thermal engines, including GTE [6]. 4SDE and GTE are dual-fuel engines, adapted to operate on gaseous and liquid fuels. The associated gas, separated from crude oil, can also be used as a fuel. The composition of the associated gas varies and it can contain a lot of heavier hydrocarbons [7-11].

The use of such a fuel in an internal combustion engine can cause problems associated with significant influence of fuel composition on the engine's working process. The methane number is the measure of resistance of the gas fuel to knock. Leading manufacturers of marine internal combustion engines restrict the lower limit of the fuel methane number (MN). For example, for Wartsila dual-fuel engines, fuels with methane number WMN <46.8 are not recommended for use. Moreover, the molar methane content should not be less than 70%, and H<sub>2</sub> should not be more than 30% [12].

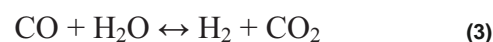
The authors have carried out calculations of the methane number for associated gases with different compositions [7-11]. The calculations were carried out using the Wartsila Methane number calculator, as well as the method of the Gas Research Institute [13]. The results of the MN and Low Calorific Value (LCV) calculations are presented in Table 1.

Tab. 1. Parameters of associated gas

Parameters	Value				
	A1	A2	A3	A4	A5
Designation of associated gas					
Chemical compound (% mol)					
Reference source	[7]	[8]	[9]	[10]	[11]
Methane (CH <sub>4</sub> )	68.00	62.77	73.7	64.48	67.32
Ethane (C <sub>2</sub> H <sub>6</sub> )	15.00	15.07	6.70	11.98	17.66
Propane (C <sub>3</sub> H <sub>8</sub> )	9.00	6.64	6.10	8.75	8.95
Butane (C <sub>4</sub> H <sub>10</sub> )	5.00	2.40	3.89	3.84	4.20
Pentane and Heaver (C <sub>5</sub> +) )	1.00	1.12	3.70	2.02	1.87
Hydrogen Sulfide (H <sub>2</sub> S)	-	2.80	0.20	0.57	-
Carbon Dioxide (CO <sub>2</sub> )	1.00	9.20	1.34	0.63	-
Nitrogen (N <sub>2</sub> )	1.00	-	4.37	3.73	-
Water vapor (H <sub>2</sub> O)	-	-	-	4.00	-
Methane Number Calculation					
Wärtsilä Methane Number (WMN)	<46.8	<46.8	<46.8	<46.8	<46.8
GRI methods:					
Linear coefficient relation (GRI LCR MN)	27.5	47.3	42.6	21.5	26.1
Hydrogen/carbon ratio relation (GRI H/C MN)	64.4	53.4	61.2	53.3	67.9
Low Calorific Value Calculation					
LCV, MJ/kg	46.3	38.6	44.0	42.9	47.9

To prepare the associated gas for use as fuel in an internal combustion engine, Wartsila developed the steam reforming based GasReformer Technology. According to this technology, the methane number of the fuel gas is improved by converting heavier hydrocarbons into synthesis gas and methane [14]. The patented Wärtsilä GasReformer executes the conversion of the associated gas with steam reforming on nickel catalysts (Ni/MgAl<sub>2</sub>O<sub>4</sub>). Since nickel catalysts are very sensitive to sulfur compounds, frequent desulfurization is envisaged. In addition, during the gas reformer operation, intense deactivation of the nickel catalyst takes place due to carbon deposition on the catalyst surface. The installation is designed to work with 4...12 MW 4SDE Wärtsilä engines. The claimed efficiency is 44.5%.

Steam reforming of hydrocarbon fuels is accompanied by endothermic reactions of steam reforming (1) and decomposition (2) requiring external heat supply (+ΔH), as well as exothermic reaction (-ΔH) of water-gas shift (3):



The main components of the synthesis gas that can be obtained as a result of steam reforming are H<sub>2</sub>, CO, CO<sub>2</sub>,

CH<sub>4</sub> and H<sub>2</sub>O. During steam reforming of hydrocarbon fuels, an increase of the process pressure results in the shift of the conversion efficiency region to a high temperature zone. At the same time, the pressure of the gaseous fuel supplied to the gas turbine engine is 1.5...3 MPa, while to the 4SDE, the gaseous fuel is fed at a pressure of 0.5...0.6 MPa. The conversion executed at pressures close to atmospheric can be effective at lower process temperatures, but it requires considerable power inputs to compress the obtained synthesis gas before it enters the engine.

Thermo-chemical conversion of heavy hydrocarbons into synthesis gas can be carried out using plasma-chemical methods [15, 16, 17]. The plasma-chemical technologies are used to intensify the process of burning the synthesis gas of various composition, including low LCV [18, 19, 20].

One of the promising ways to improve the power plant efficiency is the use of engine's exhaust energy to support endothermic reactions of steam reforming of hydrocarbon fuels with different compositions.

The previously conducted researches have shown that the thermal potential of the secondary energy resources in the internal combustion engine does not provide opportunities for efficient conversion of associated gas components. On the other hand, the temperature range of the exhaust gases in modern commercial GTEs enables efficient conversion of heavy hydrocarbons being part of the associated gas.

The diagram of the combined diesel-gas turbine power plant with thermo-chemical heat recovery (COGED+TCR) is considered in [21]. This diagram presents steam reforming of natural gas or cargo vapor products on LNG gas carriers. The heat source for conversion is the heat of GTE off-gases.

The COGED+TCR installation can be applied on oil and gas floating units which utilize the associated gas with different composition as a fuel.

## CHARACTERISTICS OF POWER PLANTS WITH CONVERSION OF ASSOCIATED GAS FOR OIL AND GAS FLOATING UNITS

Figure 1 shows two variants of the combined COGED+TCR installation. The plant consists of a gas turbine unit based on a simple cycle gas turbine engine and two dual-fuel 4SDEs. All engines run on products of associated gas reforming. The heat of the GTE exhaust gas is utilized in a thermo-chemical reactor and a steam generator.

In the diagram with single reactor (Fig. 1A), the conversion of the associated gas is carried out at the pressure corresponding to the feed pressure in the internal combustion engine (0.6 MPa). This moderate process pressure implies a shift in the effective conversion range to a region of relatively low temperatures corresponding to the GTE exhaust gas temperature. The synthesis gas obtained in the reactor is passed to the dehydrator. The drained synthesis gas has a significantly lower content of non-combustible components, which significantly simplifies the processes of mixture formation and combustion. The disadvantage with respect

to gas turbine engines is that dehydration of the synthesis gas results in the loss of thermal potential of the steam-and-gas mixture. Further, the dried synthesis gas is divided into two streams. The first stream is passed to the internal combustion engine, while the second stream is compressed in the compressor to the feed pressure in the GTE (1.5 MPa). The water obtained in the dehydration process returns to the cycle.

In the second case (Fig. 1B), two reactors are provided – with high pressure of 1.5 MPa and low pressure of 0.6 MPa. From the high-pressure reactor, which has a sufficiently high temperature, the steam-and-gas mixture flows into the combustion chamber, like in the STIG cycle. After leaving the low-pressure reactor, the synthesis gas undergoes the dehydration process and is further fed to the internal combustion engine.

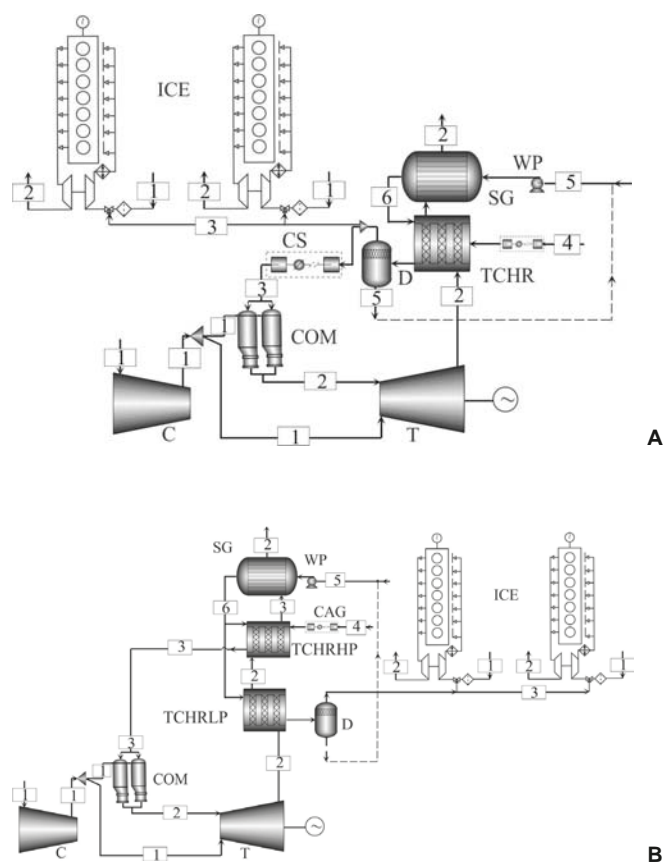


Fig. 1. Simplified calculation schemes of a COGED+TCR plant. A – scheme with single unit reactor, B – scheme with double unit reactor. Designations: 1 – air, 2 – gas, 3 – syngas, 4 – associated gas, 5 – water (steam), C – compressor; CAG – associated gas compressor; COM – combustor; CS – syngas compressor; D – degasifier; SG – steam generator; T – gas turbine; TCHR, TCHRHP, TCHRHP – thermo-chemical reactor; WP – water pump

The applicability range of the developed COGED+TCR diagrams was evaluated using mathematical modelling of processes. In this modeling, the power plant was structurally considered as a system of three functionally interconnected subsystems:

- energy subsystem, in which the chemical energy of the fuel is converted into mechanical and thermal energy;

- recovery subsystem, designed to convert the waste heat of the energy subsystem into mechanical and thermal forms of energy;
- associated gas conversion subsystem.

The range of applicability of the proposed diagrams can be comprehensively evaluated based on the efficiency of use of the chemical energy of the associated gas and the efficiency of the thermo-chemical conversion of heavy hydrocarbons being part of the associated gas.

As the criterion of the fuel energy efficiency, the efficiency of the installation was provided:

$$\eta = \frac{N_{combi}}{m_{\Sigma f} \cdot LCV} \quad (4)$$

where  $N_{combi}$  is the power output of the combined plant, and  $m_{\Sigma f}$  is the fuel mass flux.

$$N_{combi} = i \cdot N_{GTE} + j \cdot N_{4SDE} \quad (5)$$

$$m_{\Sigma f} = m_{\Sigma GTE} + m_{\Sigma 4SDE} \quad (6)$$

In Eqs. 5 and 6,  $i$  and  $j$  are the numbers of gas turbine and diesel engines,  $N_{GTE}$ ,  $N_{4SDE}$  are the power outputs of the gas turbine and diesel engines, and  $m_{\Sigma GTE}$ ,  $m_{\Sigma 4SDE}$  are the fuel mass fluxes of the gas turbine and diesel engines, respectively.

The plant power and the associated gas LCV are considered as constants. In this case, the efficiency criterion is the function of change of fuel consumption rate

$$\eta = f(\Delta m_{\Sigma f}) \quad (7)$$

where  $\Delta m_{\Sigma f}$  is the change of consumption rate of the associated gas fed to the gas turbine engine, or to the internal combustion engine.

As criteria of the efficiency of thermo-chemical conversion of heavy hydrocarbons contained in the associated gas, two parameters were taken:

- the rate of conversion of the corresponding hydrocarbon (ethane, propane, butane, pentane);
- the methane number, defined as WMN and GRI Linear Coefficient Relation MN.

The conversion rate is defined as

$$\xi = \frac{(q_{in}^m - q_{out}^m)}{q_{in}^m} \quad (8)$$

where  $q_{in}^m$  is the mole fraction of the corresponding hydrocarbon in the associated gas, and  $q_{out}^m$  is the mole fraction of the corresponding hydrocarbon in the fuel gas fed to the internal combustion engine.

The methane number defined as WMN and GRI LCR MN was used as the criterion of energy efficiency of the

thermo-chemical conversion of heavy hydrocarbons contained in the fuel gas fed to the internal combustion engine.

The WMN was determined using the on-line Wäertsilä Methane number calculator program. To calculate the GRI LCR MN, the following dependency was considered [13]:

$$\begin{aligned} \text{GRI LCR MN} = \\ = 1.445 \cdot (137.78 \cdot x_1 + 29.948 \cdot x_2 - 18.193 \cdot x_3 - \\ - 167.062 \cdot x_4 + 181.233 \cdot x_5 + 26.994 \cdot x_6) - 103.42 \end{aligned} \quad (9)$$

In Eq. 9,  $x$  represents the mole fraction of an individual component:  $\text{CH}_4 = x_1$ ;  $\text{C}_2\text{H}_4 = x_2$ ;  $\text{C}_3\text{H}_8 = x_3$ ;  $\text{C}_4\text{H}_{10} = x_4$ ;  $\text{CO}_2 = x_5$ ;  $\text{N}_2 = x_6$ .

The basis for the mathematical model of the gas turbine block is the extended GTE calculation which takes into consideration total pressure losses. The combustion chamber model is based on combined chemical and phase equilibrium, while to determine the composition of the components, the Gibbs free energy for reaction products is minimized. Note that the obtained synthesis gas has a low calorific value and high content of non-combustible impurities, therefore it is advisable to use a plasma-chemical intensification system to initiate the burning process in the gas turbine combustion chamber [22, 23].

The rate of the waste gas heat required for fuel conversion was determined from the thermo-chemical reactor heat balance.

The modeling of the power plants was based on the gas turbine engine UGT 2500 and two medium-speed 4SDE engines Wäertsilä 6L50DF. The total plant power was 14.1 MW.

The simulation of the GTE processes was carried out for the parameters of the basic turbo-compressor unit, with the following restrictions:

- fixed GTE power (2.7 MW);
- fixed gas turbine inlet temperature ( $T_3 = 1223$  K);
- environmental parameters according to ISO 3046-1:2002.

With regard to the 4SDE engine Wäertsilä 6L50DF with fixed power (5.7 MW) and total energy consumption at 100% load (7.41 MJ/kWh), the change in fuel consumption in terms of LCV associated gas supplied to the power plant was determined.

Mathematical modelling of the processes in the plant has revealed that the diagram shown in Fig. 1A has low fuel energy efficiency. The energy consumed for compressing the dried synthesis gas to the GTE feed pressure is larger than the increase in energy efficiency due to steam reforming of the associated gas. As a result, the efficiency of the installation shown in the diagram in Fig. 1A is comparable to or lower than the baseline plant efficiency without TCR. The efficiency calculation of thermo-chemical conversion parameters showed complete conversion of heavy hydrocarbons (Fig. 2).

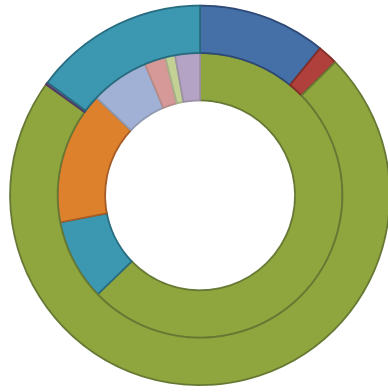


Fig. 2. Comparing chemical compounds (% mol) of the associated gas (inner ring) with the resulting synthesis gas conversion products (outer ring)

The results of modelling of the processes in the power plant shown in Fig. 1B have demonstrated good effectiveness of this scheme. Due to the steam reforming of the associated gas and the use of the potential of the steam-gas mixture, the mass flow rate of the associated gas used as GTE fuel decreased by 19...20% (Fig. 3), which resulted in the increase of the gas turbine unit efficiency by 6.8%.

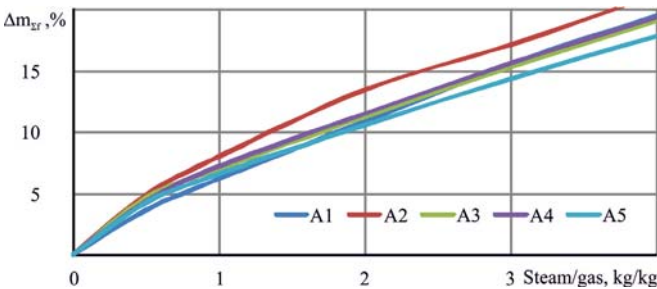


Fig. 3. Decrease in mass flow rates of associated gases with different compositions depending on the water/gas ratio (mass)

As a result of the use of thermo-chemical heat recovery of the waste gas, the calculated efficiency of the COGED+TCR unit (45.6%) increased by 3% compared with the basic COGED power plant. This result is comparable to the declared Wärtsilä GasReformer data.

The performed simulation made it possible to determine the composition of the synthesis gas obtained as a result of conversion of associated gases with different compositions (Table 2).

Tab. 2. Parameters of fuel gases fed to internal combustion engines

Parameter	Value				
Designation of base associated gas (Tab. 1)	A1	A2	A3	A4	A5
Chemical compound of fuel gas fed to internal combustion engine, (% mol)					
Hydrogen (H <sub>2</sub> )	12.7	10.7	11.7	11.4	12.9
Water vapor (H <sub>2</sub> O)	1.7	1.7	1.7	1.7	1.7
Methane (CH <sub>4</sub> )	74.0	71.3	73.4	73.7	74.6

Parameter	Value				
	Carbon Oxide (CO)	0.2	0.2	0.1	0.2
Carbon Dioxide (CO <sub>2</sub> )	10.6	14.6	10.3	10.4	10.7
Nitrogen (N <sub>2</sub> )	0.8	1.5	2.8	2.6	
Calculated Wärtsilä methane number	78	82	77	78	87
Calculated GRI LCR methane number, Eq. (6)	78	84	76.7	77.6	79.3
LCV, MJ/kg	35.7	28.1	30.5	34.7	36.2

The efficiency calculations of the thermo-chemical conversion of heavy hydrocarbons in associated gases with different compositions have shown that the obtained values correspond to the Wärtsilä requirements for the methane number and chemical composition of the fuel gas.

The main characteristics of the COGED+TCR unit with separate high and low pressure thermo-chemical reactors are given in Table 3.

Tab. 3. Design product specification of COGED+TCR unit with separate high and low pressure thermo-chemical reactors (total power 14.1 MW)

Parameter	Unit	Value
Pressure:		
high pressure reactor	MPa	1,4
low pressure reactor		0,6
Temperature of synthesis gas:		
high pressure reactor – in/out	K	714/680
low pressure reactor – in/out		675-660
Specific mass flow rate per 1 MW shaft power:		
feed gas mass flow rate		165-170
total steam demand:	kg/(MW·h)	300-350
of which recycled boiler water		120-140
of which fresh water		180-210
Energy consumption for compressors and pumps	kW	25-30

## FINAL CONCLUSIONS

The use of thermo-chemical conversion to recover the heat from the engine's exhaust gas and further utilization of this heat for steam reforming of heavy hydrocarbons expand the possibilities of using the associated gas as fuel in power plants for oil and gas floating units.

It is rational to carry out thermo-chemical conversion of the associated gas in a COGED+TCR unit with separate high and low pressure thermo-chemical reactors to produce fuel gas for both gas turbine engines and internal combustion engines.

COGED+TCR power plants make it possible to combine attractive advantages of low weight and size of a marine gas turbine engine without reducing the energy efficiency.

In this work, only the thermodynamic analysis of the COGED+TCR power plant is presented. An additional feasibility study is needed to fully assess the application range of such an installation for oil and gas floating units.

## BIBLIOGRAPHY

1. WOR 3 (2014): *Marine Resources – Opportunities and Risks*. Retrieved from <https://worldoceanreview.com/en/wor-3/>
2. Olszewski W., Dzida M. (2018): *Selected Combined Power Systems Consisted of Self-Ignition Engine and Steam Turbine*. Polish Maritime Research, No.1, Vol. 25, 198–203.
3. Domachowski Z., Dzida M. (2019): *Applicability of Inlet Air Fogging to Marine Gas Turbine*. Polish Maritime Research, No.1, Vol. 26, 15–19.
4. Mazzetti M. J., Nekså P., Walnum H. T., Hemmingsen A. T. (2014): *Energy-Efficient Technologies for Reduction of Offshore CO<sub>2</sub> Emissions*. Oil and Gas Facilities, February 2014, 8996.
5. Szymaniak M. (2018): *Steam Turbine Stage Modernisation in Front of the Extraction Point*. Polish Maritime Research, No.2, Vol. 25, 116–122.
6. Sarnecki J., Bialecki T., Gawron B., Głab J., Kamiński J., Kulczycki A., Romanyk K. (2019) *Thermal Degradation Process of Semi-Synthetic Fuels for Gas Turbine Engines in Non-Aeronautical Applications*. Polish Maritime Research, No.1, Vol. 26, 65–71.
7. Michael Farry (1998) *Ethane from associated gas still the most economical*. Retrieved from <https://www.ogj.com/articles/print/volume-96/issue-23/in-this-issue/gas-processing/ethane-from-associated-gas-still-the-most-economical.html> , Accessed 20 May 2019.
8. Al-Saleh M.A., Duffuaa S.O., Al-Marhoun M.A, Al-Zayer J.A. (1991): *Impact of crude oil production on the petrochemical industry in Saudi Arabia*. Retrieved from [https://www.researchgate.net/publication/256569784\\_Impact\\_of\\_crude\\_oil\\_production\\_on\\_the\\_petrochemical\\_industry\\_in\\_Saudi\\_Arabia/figures](https://www.researchgate.net/publication/256569784_Impact_of_crude_oil_production_on_the_petrochemical_industry_in_Saudi_Arabia/figures).
9. Nguyen T., Elmegaard B., Pierobon L., Haglind F., Breuhaus P. (2012): *Modelling and analysis of offshore energy systems on North Sea oil and gas platforms*. 53-rd International Conference of Scandinavian Simulation Society, SIMS 2012. Retrieved from [https://www.researchgate.net/publication/263973093\\_Modelling\\_and\\_analysis\\_of\\_offshore\\_energy\\_systems\\_on\\_North\\_Sea\\_oil\\_and\\_gas\\_platforms/figures?lo=1](https://www.researchgate.net/publication/263973093_Modelling_and_analysis_of_offshore_energy_systems_on_North_Sea_oil_and_gas_platforms/figures?lo=1).
10. Foss M. M. (2004): *Interstate natural gas quality specifications & interchangeability*. Center for Energy Economics. Retrieved from [http://www.beg.utexas.edu/files/energyecon/global-gas-and-lng/CEE\\_Interstate\\_Natural\\_Gas\\_Quality\\_Specifications\\_and\\_Interchangeability.pdf](http://www.beg.utexas.edu/files/energyecon/global-gas-and-lng/CEE_Interstate_Natural_Gas_Quality_Specifications_and_Interchangeability.pdf).
11. Oil & Gas Industry Overview (2019): *Crude Oil and Natural Gas: From Source to Final Products*. Retrieved from [https://www.ihrdc.com/els/po-demo/module01/mod\\_001\\_02.htm](https://www.ihrdc.com/els/po-demo/module01/mod_001_02.htm).
12. WÄRTSILÄ (2019): *Wärtsilä Methane number calculator*. Retrieved from <https://www.wartsila.com/products/marine-oil-gas/gas-solutions/methane-number-calculator>.
13. ISO/TR 22302:2014 (2014): *Natural gas. Calculation of methane number*.
14. WÄRTSILÄ (2015): *Wärtsilä GasReformer*. Retrieved from [https://www.offshore-europe.co.uk/\\_\\_novadocuments/31687?v=635089663131000000](https://www.offshore-europe.co.uk/__novadocuments/31687?v=635089663131000000).
15. Gatsenko NA., Serbin SI. (1995). *Arc plasmatrons for burning fuel in industrial installations*, Glass and Ceramics, vol. 51 (11-12), 383–386
16. Matveev I. B., Tropina A. A., Serbin S. I., Kostyuk V. Y. (2008): *Arc modeling in a plasmatron channel*. IEEE Trans. Plasma Sci., No.1, Vol. 36, part 2, 293–298.
17. Serbin SI, Matveev IB, Goncharova MA (2014). *Plasma Assisted Reforming of Natural Gas for GTL. Part I*, IEEE Trans. Plasma Sci., vol. 42, no. 12, pp. 3896-3900
18. Matveev I., Matveeva S., Serbin S. (2007): *Design and Preliminary Result of the Plasma Assisted Tornado Combustor*. Collection of Technical Papers - 43rd AIAA/ASME/SAE/ASEE Joint Propulsion Conference, Cincinnati, OH, AIAA 2007-5628, Vol. 6, 6091-6098.
19. Matveev I., Serbin S. (2012): *Investigation of a reverse-vortex plasma assisted combustion system*. Proc. of the ASME 2012 Heat Transfer Summer Conf., Puerto Rico, USA, HT2012-58037, 133-140.
20. Matveev I., Serbin S., (2006): *Experimental and Numerical Definition of the Reverse Vortex Combustor Parameters*. 44th AIAA Aerospace Sciences Meeting and Exhibit, Reno, Nevada, AIAA-2006-0551, 6662-6673.
21. Cherednichenko O., Serbin S. (2018): *Analysis of Efficiency of the Ship Propulsion System with Thermochemical Recuperation of Waste Heat*. J. Marine. Sci. Appl. No.1, Vol. 17, 122-130.
22. Serbin S.I. (2006): *Features of liquid-fuel plasma-chemical gasification for diesel engines*. IEEE Trans. Plasma Sci., 6, No.vol. 34, 2488-2496.
23. Serbin S.I. (1998): *Modeling and Experimental Study of Operation Process in a Gas Turbine Combustor with a Plasma-Chemical Element*. Combustion Science and Technology, Vol. 139, 137-158.

## CONTACT WITH THE AUTHORS

**Oleksandr Cherednichenko**

*e-mail: cherednichenko.aleksandr65@gmail.com*

**Serhiy Serbin**

*e-mail: serbin1958@gmail.com*

Admiral Makarov National University of Shipbuilding

Heroyiv Ukraine av. 9

54025 Mykolaiv

**UKRAINE**

**Marek Dzida**

*e-mail: dzida@pg.edu.pl*

Gdańsk University of Technology

11/12 Gabriela Narutowicza Street

80-233 Gdańsk

**POLAND**

## THE PROBLEM OF BALLAST WATER IN MONTENEGRO PORTS AND POSSIBILITY OF ITS TREATMENT

Ivana Ćipranić

Marija Jevric

Goran Sekulic

Sreten Tomovic

University of Montenegro, Montenegro

### ABSTRACT

*The problem of ballast water has been present in the world for the last hundred years, but it has grown and become more complex with the increasing intensity of overseas traffic. Introduction of various species from different parts of the world threatens flora and fauna, especially regarding small and closed seas, such as the Adriatic Sea. New species cause an interruption of the existing food chain which keeps the natural balance and purity of the sea. Many domicile organisms in the sea have been disappearing due to changes in environmental conditions, which significantly impairs the sea-water quality. This paper deals with different possible ways of sea and port protection from ballast water, starting with administrative measures, up to proposals of technologies by which those waters could be treated. The problem of ballast water is of particular concern in the Montenegrin part of the Adriatic Sea, and the protection proposal is given.*

**Keywords:** Adriatic Sea, ballast water, marine protection, water treatment

### INTRODUCTION

Various human activities, whether on land or on the seashore, consequently lead to a violation of the natural balance of the sea bottom and the shore itself. There are a wide spectrum of activities which negatively affect natural conditions of the sea. Those are: sailing, oil platform placement, uncontrolled discharge of used and industrial waste waters, illegal construction, etc. These activities can contribute to the appearance of various pollutions, both on land and in the sea. As a result, the input of nutrients increases, along with the amount of sediments, pathogens, non-biodegradable toxic substances, radio-active substances, oil, and different kinds of waste. A special problem in the majority of seas is the emergence of new species in them, both plants and animals. With their appearance, the violation of the previously established natural balance occurs, wherein new species are usually those that push away or completely destroy original ones, usually spreading new diseases in the sea [3]. It is necessary to emphasize that these new species

are most commonly related to the presence of the so-called “red tide” and other algal bloom, especially in big sea ports. The origin, i.e. the source of new species, is most frequently ballast water from ships (this work pays special attention to it) but it could also be the production of new channels as the sea confluence, or, for example, some projects related to the improvement of fostering of new fish species.

### BALLAST WATERS

Ballast water, as its name suggests, is meant to increase ship stability, and by that, to increase the safety of the sail.

Ballast water was introduced into the practice of sailing about 160 years ago, when the first ship with a double bottom was built. Before that, some firm elements, made of cement or lead for instance, were used as an extra load for supporting balance or stability (in fact, this method is still used on smaller watercrafts). Nowadays, large ships use ballast water because without it, it would be impossible to sail safely. The ballast water is pumped out in the starting port, where the load is

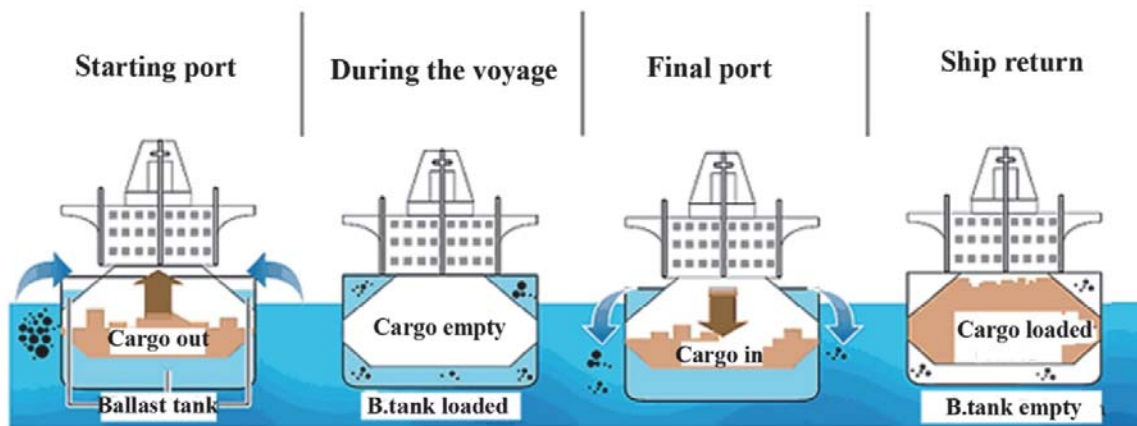


Fig. 1. Loading and discharge of ballast water [15]

being embarked and the waters' role is shifted to the load transported by the ship (Fig.1) There are various ways of ballast water distribution on boats, depending, above all, on the purpose of the ship. Usually, the water is placed in special reservoirs located on the sides of the ship. New-generation tankers, with double hull, also have these reservoirs situated under the transported cargo. They need to have sufficient volume to enable safe sailing of the ship.

### THE INFLUENCE OF BALLAST WATER ON THE ECOLOGICAL BALANCE IN THE ADRIATIC

In 1903, when Asian phytoplankton alga *Caulerpa* appeared in the North Sea, it was noticed that the ballast water transported between various seas and its pumping out may result in migration of different forms of organisms. This also indicated that the natural balance in the water can be disturbed by ballast water discharge [4]. When gathering sea water as ballast, local organisms are also taken, and many of them survive on the ship until they are pumped out into the water. In the past, this problem was not paid much attention until it was noticed that the effects of this migration can be negative. Strong development of maritime transport brought enormous amounts of transported ballast water, and thus, a much greater possibility of species migration. Today, it is estimated that annually, 3-7 billion tons of ballast water is transported in the world, and with it, more than 7,000 various species of animals and plants are migrated [21].

As it can be seen in Figures 2, 3 and 4, the amount of ballast water discharged by the Montenegrin shore, i.e. near its ports, in 4 years' time is within the range of some 3-10 billion tons. While it is still less than in most of the endangered zones of the Mediterranean Sea, it is enough to call for paying more serious attention to this matter, considering the position of the Montenegrin coast and possible effects.

Data about the import of foreign life forms in ballast water into the Adriatic Sea are not reliable, as the Adriatic is one of the richest seas in number of fish species. But at the same time, only a small species population is represented. Besides that, the Adriatic is a warm, shallow and closed sea

with slow sea current changes. One of the visible and known consequences of ballast water discharge is the so-called "sea blooming", or the reproduction of *Caulerpa taxifolia*, a plant which has been transported from tropical seas into the Adriatic, where it is able to survive thanks to mutation and fast expansion, creating a grass carpet on sand, silt, or stone, the kinds of bottoms the Adriatic is made of. This plant causes an interruption of the existing food chain that has sustained the natural balance and purity of the Adriatic, because many maritime organisms disappear as a result of the environment change and the violation of sea water quality.

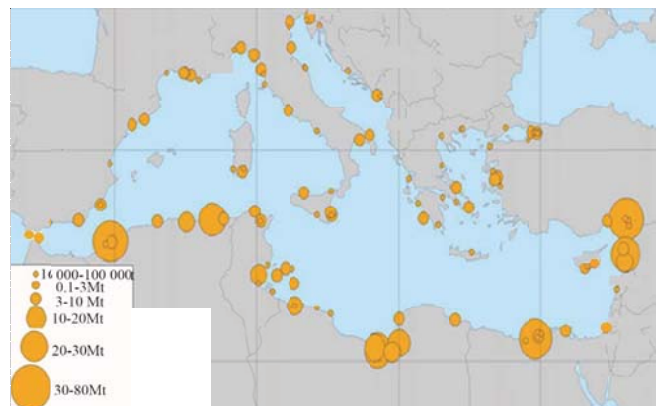


Fig. 2. Ballast water discharge at Mediterranean Sea in years 1999 – 2005 [19]



Fig. 3. Adriatic Sea, main ports [10]

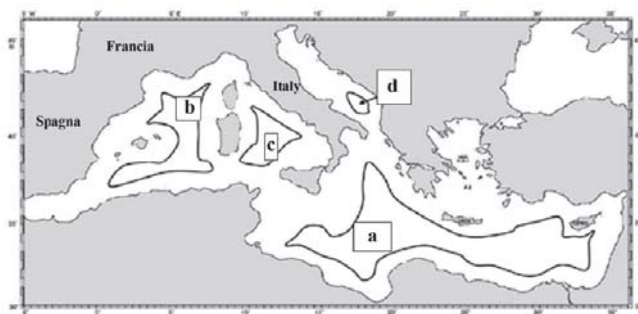


Fig. 4. Areas in Mediterranean Sea for Ballast Water Exchange [11]

The International Maritime Organization (IMO, specialized UN organization) has adopted the Convention on the Prevention of Marine Pollution by Dumping of Wastes and Other Matter (13. 02. 2004.), according to which all ships are supposed to execute the exchange of ballast water at a distance of 200 nautical miles from land, and at a depth higher than 200m, so they can sail into the port with clear ballast. This Convention entered into force on 8th September 2017 [7].

Montenegro didn't have a legal solution to the ballast water issue, even though this problem was discussed and concern was expressed. A series of international contracts, such as: London Convention on the Prevention of Marine Pollution; OPRC convention (on oil pollution preparedness, response and cooperation) and its following Protocol to hazardous and noxious substances; International Convention for the prevention of pollution from Ships (MARPOL convention); Protocol of Barcelona Convention for the protection of the Mediterranean have been ratified and their implementation is being supervised by IMO. Also, Montenegro is a participant in two sub-regional projects concerning the protection of the Adriatic Sea. The first project relates to the announcement of the Adriatic as a particularly sensitive maritime area in accordance to resolutions and decisions of IMO. It predicts introducing measures for the protection of the maritime ecosystem of the Adriatic, which, besides other things, will specifically regulate the exchange of ballast water. The project is in the final adjustment phase on the regional level, after which its consideration will be followed by the governments of the countries in the Adriatic region. The second project refers to the measures associated and regulated by the exchange of ballast water according to the previous project. This is a perennial project helped by the reference organizations (IMO, UNEP, Regional Marine Pollution Emergency Response Center for the Mediterranean Sea/REMPEC) [8], and its goal is to create a Mediterranean strategy which addresses the transfer of hazardous aquatic microorganisms and pathogens through the exchange of ballast ship water and sediments. [17] Being conscious of the importance of this issue, the Adriatic countries approached the common EU project named BALMAS (Ballast water management for Adriatic Sea protection), which lasted from November 2013 to March 2016 and resulted in adopting the strategy and management plans in all the countries participating in the project (Italy, Slovenia, Croatia, Bosnia and Herzegovina, Albania, and

Montenegro). This project assumes ballast water control in 12 Adriatic ports (in Montenegro, the ballast water is controlled in the Port of Bar) [6].

Being conscious of the fact that the Adriatic Sea is being sailed on more and more, no matter whether by cargo or cruise ships, yachts, or domicile inhabitants' watercrafts, the countries surrounding the Adriatic have advised this manner of ballast water discharge into their parts of Adriatic and have marked the sea itself a particularly protected marine area. It must also be noted that Croatia forbids the exchange of ballast water in their part of Adriatic. After adopting the Guidance on Ballast Waters Management, unauthorized ballast water exchange in their part of Adriatic is controlled by monitoring the entrance, speed, course, and port of anchoring of some tankers. However, this also poses the question as to where the ballast water of ships sailing into the Croatian part of the sea can be discharged, once it is prohibited in there. The Montenegrin part of Adriatic is the first stop where it could be done. It should be emphasized that the Montenegrin government has adopted a law on marine protection from pollution from watercraft objects. A significant part of this law is devoted precisely to ballast water, and the solutions proposed are in accordance with positive European experience concerning that issue.

The Bay of Kotor, which represents a unique natural entity and tourist attraction in the last few years, has become a regular destination for anchoring of big ships – cruise ships in particular. Keeping in mind that the average ballast capacity of these ships is 3,000 cubic meters, it cannot be denied that this can pose a substantial threat to the already sensitive bay of Kotor. There is no control system of ballast water upon cruise ship arrival, nor is it mandatory to give any report on possessing systems for its treatment. The expected changes of the Adriatic Sea sailing directions and the growing volume of so-called yachting tourism increase the risk of the entrance of hazardous foreign species.

In order to protect the Montenegrin part of the Adriatic Sea, the first step should certainly be determining the zero state in ports where cargo and cruise ships are anchoring, and based on that, adopting the required measures of protection.

## POSSIBLE TECHNIQUES FOR BALLAST WATER TREATMENT

There are numerous techniques that can be used to minimize and prevent the entrance of various aquatic organisms with ballast water [1], [9], [14], [16]. The most efficient way is ballast water processing, which can be performed when filling ballast tanks, during voyage, during ballast discharge, or after shifting into the system for ballast storage on land. The criteria required for each ballast treatment are: it has to be safe (for both the ship and crew), it has to be acceptable for the environment (i.e. it should not cause more environmental damage than benefits); it has to be applicable (on ship design and on the procedure); it has to be economically justified and biologically efficient (in the sense of removing, destroying or,

by some other influence, decreasing marine organisms and pathogens in ballast water) [9].

The most basic and, at the same time, the most efficient way which would prevent the expansion of undesirable organisms transported in ballast water would be prohibition of ballast water discharge into ports. In that case, ballast water would be pumped out into special ballast tanks situated in ports or beside them. That option includes further mechanical, thermal, chemical, and radiation treatment of ballast water (if necessary) intended to destroy any organisms in it (Fig. 5). However, this solution is, primarily, quite expensive and requires large space in ports. There should be reservoirs built in ports for collecting ballast water, and this water should be treated through mentioned phases. One of the options is that the purifying plants could also be installed on the ships, but that is an even more expensive solution [9]. In an attempt to solve this problem, some suggestions have appeared to exchange ballast water on the open sea, where there are less endangered maritime life forms and where the foreign coastal organisms would hardly survive [2],[16]. It is well-known that organisms from the open ocean cannot survive in coastal waters and their specific conditions. However, this suggestion has a basic disadvantage; it can be efficient only in ocean sailing, while for the conditions of sailing in smaller and closed seas, such as the Adriatic, where routes are close to the shore, it is not a viable solution [9]. This method is prescribed and used in America and Australia, where all the ships need to exchange ballast water in the ocean, and then a check is performed in the ports to verify that the exchange has been carried out, which is easy to identify because there is a huge difference in species from the open ocean and those from coastal areas [16].

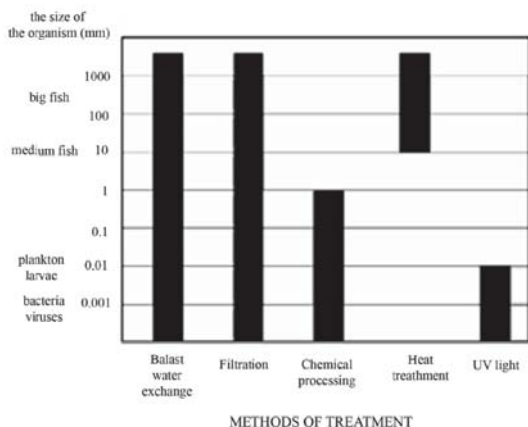


Fig. 5. Possible methods of ballast water treatment and possibility of changes depending on the size of organisms in the ballast water [1]

The thermal method seems very acceptable [12], as it makes it possible to use the waste energy from cooling ship's diesel engines. Two systems are possible for thermal treatment of ballast water. They are based on water circulation in open or closed circle. Thermal treatment of ballast water by circulation in the open circle is based on rinsing of ballast water supported by heating. Processing of ballast water by UV radiation, ozone, hydrogen peroxide, biocides, and

filtration [13] are rather theoretical solutions, as the data on the optimal ratio of the most efficient method, the factory size and energy spending, the starting price of building it, as well as the expenses of the operation and maintenance is still missing. The circulation circle means no ballast discharge, i.e. complete processing of the ballast water taken from the starting port is performed inside it. The processing in closed circulation can be performed according to biological criteria of short and medium exposure of organisms to heating [16].

A brief evaluation of ballast water treatment methods is shown in Table 1, where N means unknown, 1 – unacceptable, 2 – bad, 3 – partly acceptable, and 4 – acceptable method.

Tab. 1. Evaluation of ballast water treatment methods [9]

Treatment method	Safety	Biological efficacy	Environmental friendliness
Filtration	4	1	4
Hydrocyclone separation	4	1	4
Centrifugal separation	4	1	4
UV radiation	4	2	3
Ultrasound	3	2	3
Thermal treatment	3	2 - 3	4
Biocides	2	3	1
Ozonation	2	1	3
Pulsed plasma	3	N	N
Deoxidation	N	2	3
Coating tanks	3	1	2
Combined methods: hydrocyclone separation/UV radiation	4	3	3

The practice has shown that none of the ballast water treatment methods alone is efficient enough to remove all unwanted species of organisms out of ballast reservoirs. That is why the combination of different methods has been suggested as the most effective solution (Fig.6). Generally, the proposed treatment procedure has two levels: primary processing, during which larger organisms and particles are removed, and secondary processing, which aims at removing smaller organisms [9], [16].

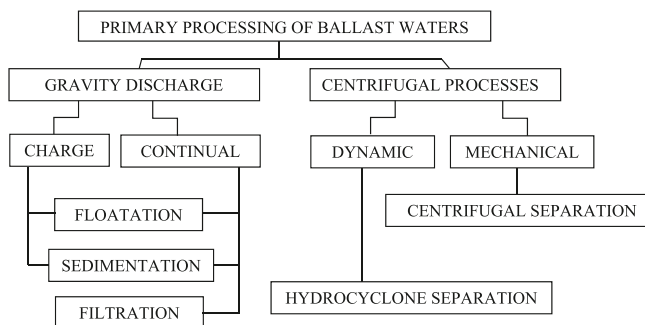


Fig. 6. Overview of possible processes of primary ballast water processing [2]



Fig. 7. Scheme and pictures of filter for ballast water treatment [16]

The primary methods remove larger organisms and sediments, thus preparing the ballast for further processing using other methods. With centrifugal processes, the effect of separation of harder particles is even 10,000 times greater when compared to the gravitational process (Fig.7). Of all the possible methods of primary processing, the greatest effect is achieved using automatic auto-purifying filters and hydrocyclone separators, due to their appropriate dimensions, direct attachment to ballast water systems, automatic work, and simple maintenance in practice. The process of filtration continually implemented through permeable grids for liquid and solid phases (of the diameter of particles smaller than the diameter of grids) is particularly simple and effective [1], [12].

This process can be performed even during the discharge of ballast reservoirs. The advantage of water filtration during their charge is that the filtered organisms remain in their natural environment. If the ballast water is filtered during reservoir discharge, it is essential to properly put off the filtered dead organisms.

The filtration equipment is still quite expensive, both to purchase and for ship assembly. What is more, its price is growing due to the reduced size of microorganisms that should be filtered. That is the basic disadvantage of this method which prevents its unconditional recommendation. But the new legal regulations about marine protection will force many ship owners to apply this treatment, in spite of its high price.

## CONCLUSIONS

Distribution of hazardous organisms with ballast water from the far seas increases threats to the ecological system of the Adriatic Sea, especially in the Montenegrin part. This endangers the survival of various ecosystems, as well as of many different branches of industry in coastal areas, especially tourism as the major resource. Keeping in mind that ballast water is a necessary element of ship's safety, and that without maritime transport, world goods exchange is impossible - the solution to this problem must be achieved in a techno-economic way. A long-term solution for this problem specific to the Adriatic Sea and part of the Montenegrin coast

is possible, and it requires developing the technology of processing ballast water on ships. Until then, the problem can be eased by the measures of national legislation and regional cooperation among all the countries in the Adriatic region.

## REFERENCES

1. Albert R., Everett R., Lishman J. and Smith D. (2010): *Availability and efficacy of ballast water treatment technology: background and issue paper*. Information report to Scientific Advisory Board, EPA.
2. Balaji R., Yaakob O. (2011): *Emerging ballast water treatment technologies: a review*. Journal of Sustainability Science and Management 11(1): 126-138.
3. Drake J M., Lodge D. M. and Lewis M. (2005): *Theory and Preliminary Analysis of Species Invasions from Ballast Water: Controlling Discharge Volume and Location*. The University of Notre Dame.
4. Fileman T., Vance T. (2010): *Ballast water: a question of balance*. Marine Scientist 33: p. 22-25.
5. [http://globallast.imo.org/poster4\\_english.pdf](http://globallast.imo.org/poster4_english.pdf)
6. <http://www.balmas.eu>
7. International Maritime Organization (2005): *Ballast Water Management Ballast Convention International Convention for the Control and Management of Ships' Water and Sediments*. London, p.138.
8. IMO/UNEP (2004): Regional Information System. Part C: Databanks and Information Services. Section 2: *List of Alerts and Accidents in the Mediterranean*. Retrieved from: <http://www.rempec.org>
9. Kurtela Ž., Komadina P. (2010): *Application of Hydrocyclone and UV Radiation as a Ballast Water Treatment Method*. Traffic and Environment (Ecology), Dubrovnik, Croatia.
10. Lušić Z., Kos S. (2006): *The Main Sailing Routes in the Adriatic*. Naše more: Journal of marine sciences, pp. 198-205, ISSN 0469-6255
11. Markovina R., Blagojević B., Ban D. (2007): *"Družba adria" project – managing ballast water problems*. Naše more: Journal of marine sciences, vol.54, No.5-6.

12. Mountfort D, Dodgshun T, Taylor M (2001): *Ballast water treatment by Heat—New Zealand Laboratory & Shipboard trials*. First International ballast water treatment R&D symposium. Proceedings, pp 45–50. Retrieved from <http://globallast.imo.org/wp-content/uploads/2014/11/Mono5.pdf>
13. *Review of treatment options available*. (2003) General background on management and treatment options, Report No. 13, Department of Agriculture, Fisheries & Forestry – Australia, [www.affa.gov.au](http://www.affa.gov.au), Commonwealth of Australia.
14. Rigby G. (2004): *Ballast water treatment technology; choosing the best options*. Proceedings of Conference on the Control and management of ship's ballast water and sediments.
15. Singh B. (2017): *Everything You Wanted to Know About Ballast Water Exchange and Management Plan*. Retrieved from: <https://www.marineinsight.com/maritime-law/everything-you-wanted-to-know-about-ballast-water-exchange-and-management-plan/>
16. Tsolaki E., Diamadopoulos E. (2010): *Technologies for ballast water treatment: a review*. Journal of Chemical Technology & Biotechnology, Vol. 85, No. 1: 19-32.
17. UNEP (2005): *Mediterranean strategy on ships' ballast water management*.
18. Voigt M., Gollasch S. (2000): *Ballast Water: The Latest Research and Methods of Treatment*. 3rd Annual conference "Managing Environmental Risk in the Maritime Industry", London, UK.
19. [www.pfst.unist.hr](http://www.pfst.unist.hr)
20. [www.lr.org/en/ballast-water-management/](http://www.lr.org/en/ballast-water-management/)
21. [www.researchgate.net/publication/301821711\\_Effect\\_of\\_Ballast\\_Water\\_on\\_Marine\\_and\\_Coastal\\_Ecology](http://www.researchgate.net/publication/301821711_Effect_of_Ballast_Water_on_Marine_and_Coastal_Ecology)

## CONTACT WITH THE AUTHORS

**Ivana Ćipranić**

*e-mail: ivanacipranic@yahoo.com*

University of Montenegro  
 Faculty of civil engineering  
 Cetinjski put. b.b. Podgorica  
 382 Podgorica  
**MONTENEGRO**